Structural Dynamics and Control Interaction of Flexible Structures

NASA

Structural Dynamics and Control Interaction of Flexible Structures

Edited by
Robert S. Ryan and Harold N. Scofield
George C. Marshall Space Flight Center
Huntsville, Alabama

TABLE OF CONTENTS

Part 1

iii

TABLE OF CONTENTS (Continued)

*Pages 693 to 1430 are published under separate cover.

TABLE OF CONTENTS (Continued)

Page

TABLE OF CONTENTS (Concluded)

WORKSHOP ON STRUCTURAL DYNAMICS AND CONTROL
INTERACTION OF FLEXIBLE STRUCTURES

MSFC, Morris Auditorium

April 22, 23, 24, 1986

A Workshop on Structural Dynamics and Control Interaction of
Flexible Structures was held at the Marshall Space Flight
Center to promote technical exchange between the structural
dynamics and control disciplines, foster joint technology,
and provide a forum for discussing and focusing critical
issues in the separate and combined areas. This workshop
was attended by approximately 150 people from Government,
industry, and universities. This document contains all the
papers presented. The workshop was closed by a panel
meeting. Panel members' viewpoints and their responses to
questions are included.

Robert S. Ryan
Workshop Co-Host

Harold N. Scofield
Workshop Co-Host

WORKSHOP ON STRUCTURAL DYNAMICS AND CONTROL INTERACTION OF FLEXIBLE STRUCTURES

Jointly Sponsored by OAST and MSFC, NASA

Marshall Space Flight Center, Alabama 35812

April 22-24, 1986

Tuesday, April 22, 1986

8:00   Registration - Lobby, Building 4200

SESSION 1

8:30   Morris Auditorium, Building 4200

Welcome	J. E. Kingsbury, MSFC
Workshop Overview	Dr. J. Blair, MSFC
Future Direction of NASA on Control/ Structures Research	L. Pinson, LaRC (for S. Venneri, Hdq.)
Overview of OAST's Large Space Systems · Controls Research and Technology Program	J. DiBattista, Hdq.
Status of the Mast Experiment	B. R. Hanks, J. L. Allen, Jr., A. Fontana, LaRC
Large Space Structures Ground Experiment Checkout	H. B. Waites, MSFC
Identification of Large Space Structures A State-of-the-Practice Report	T. K. Hasselman ASCE, AS Task Commit. on Ident. of LSS

12:30   Lunch

Tuesday, April 22, 1986

SESSION 2

(Concurrent Sessions on Structures and Control)

1:00   Structures Session 2A - Tulon Bullock, Chairman
        Morris Auditorium, Building 4200

Active Damping Experiments   G. C. Horner, LaRC

A General Method for Dynamic Analysis   R. C. Engels, UTSI
of Structures

Dynamic Behavior of a Large Flexible   N. G. Fitz-Coy and
Space Station During Space Shuttle   J. E. Cochran, Jr.,
Orbiter Docking   Auburn Univ.

Transient Response for Interaction   A. Prabhakar and
of Two Dynamic Bodies   L. G. Palermo, MMC

3:00   Structures Session 2B - Ronald E. Jewell, Chairman
        Morris Auditorium, Building 4200

Mover II - A Computer Program for Model   J. D. Chrostowski,
Verification of Dynamic Systems   T. K. Hasselman,
                                                    Eng. Mech. Assoc.

Considerations in the Design and   P. E. McGowan, LaRC
Development of a Space Station
Scale Model

Verification of Large Beam-Type   C. G. Shih, J. C. Chen,
Space Structures   J. A. Garba, JPL

Verification of Flexible Structures   B. K. Wada and
by Ground Test   C. P. Kuo, JPL

4

April 22, 1986 (Concurrent Sessions on Structures and Control)

1:00   Control Session 2A - Leonard Meirovitch, Chairman
            P106, Building 4200

Optimum Mix of Passive and Active   L. Rogers, W-P AFB
Control for Space Structures

1-CAT: A MIMO Design Methodology   J. R. Mitchell,
                                               J. C. Lucas,
                                               Control Dynamics

Inter-Stable Control Systems   G. von Pragenau, MSFC

Status Report and Preliminary Results of   J. P. Williams, LaRC
the Spacecraft Control Laboratory

3:00   Control Session 2B - J. L. Junkins, Chairman
            P106, Building 4200

Flexible Spacecraft Control Simulation   J. Bossi, Boeing

Improving Stability Margins in   B. T. Oranc and
Discrete-Time LQG Controllers   C. L. Phillips, Auburn

An Overview of Research Conducted by   R. C. Montgomery,
the Spacecraft Control Branch on the   LaRC
NASA LaRC Grid

Space Station Structural/Control   C. R. Larson
Interaction (Payload Pointing and Micro-G)   Rockwell/SD

Wednesday, April 23, 1986

SESSION 3

(Concurrent Sessions on Structures and Control)

8:00   Structures Session 3A - T. K. Hasselman, Chairman
          Morris Auditorium, Building 4200

SAFE Dynamic Flight Experiment   R. W. Schock, MSFC

Application of Robust Projection   M. H. Bantell, Jr.
Operators to the Control of Flexible   Boeing
Structures with Uncertain Parameters

Dynamics of Trusses Having   J. M. Chapman
Nonlinear Joints   Boeing

Equivalent Beam Modeling Using   J. M. Chapman
Numerical Reduction Techniques   Boeing

10:30   Structures Session 3B - Wayne B. Holland, Chairman
          Morris Auditorium, Building 4200

Dynamic Characterization of a Vibrating   J. S. Townsend,
Beam with Periodic Variation in Bending   MSFC
Stiffness

Structural Dynamic System Model   J. C. Chen,
Reduction   T. L. Rose,
                                               B. K. Wada, JPL

Space Telescope Reaction Wheel Assembly   R. E. Jewell, MSFC,
Vibration Damping System   P. Davis and
                                               J. Wilson, Sperry

12:30   Lunch

April 23, 1986   (Concurrent Sessions on Structures and Control)

8:00   Control Session 3A - George B. Doane, III, Chairman
            P106, Building 4200

Stiffness Control for Active Damping   J. L. Fanson and
                                              J. C. Chen, Jr.

A Quasi-Analytical Method for Non-   J. L. Junkins and
Iterative Computation of Nonlinear   R. C. Thompson, Texas A&M;
Controls   J. D. Turner, Cambridge
                                             Research

Decentralized Control of Large Space   D. K. Lindner, VPI
Structures via the GHR

Control of Flexible Structures and   J. S. Pyle and
the Research Community   C. R. Keckler, LaRC

10:30   Control Session 3B - Robert Skelton, Chairman
            P106, Building 4200

Impact of Space Station Appendage Vibrations R. Hughes, GE
on the Pointing Performance of Gimballed
Payloads

Maneuvering and Vibration Control of   L. Meirovitch and
Flexible Spacecraft   R. D. Quinn, VPI

Hubble Space Telescope Disturbances   J. P. Sharkey, MSFC
Caused by High Gain Antenna Motions

Preliminary Evaluation of a Reaction   H. H. Woo and
Control System for the Space Station   J. Finley, RI/SD

12:30   Lunch

April 23, 1986

SESSION 4

1:00   Integrated Session 4A - Don Skoumal, Chairman
        Morris Auditorium, Building 4200

Dual Keel Space Station Control/   J. W. Young,
Structures Interaction Study   F. J. Lallman,
                                          P. A. Cooper, LaRC

High Speed Simulation of Flexible   A. D. Jacot,
Multibody Dynamics   R. E. Jones,
                                          C. Juengst, Boeing

On the Application of Lanczos Modes   R. R. Craig, Jr.
to the Control of Flexible Structures   U. of Texas

Modal Testing and Slewing Control   J. N. Juang, LaRC
Experiment for Flexible Structures

MEOP Control Design Synthesis: Optimal   David C. Hyland and
Qualification of the Big Four Tradeoffs   Dennis Bernstein,
                                          Harris Corp.

3:00   Integrated Session 4B - Harry J. Buchanan, Chairman
        Morris Auditorium, Building 4200

Vibration Isolation for Line of Sight   J. J. Rodden,
Performance Improvement   H. Dougherty,
                                          W. Haile, LMSC

A New Semi-Passive Approach for Vibration K. Kumar and
Control in Large Space Structures   J. E. Cochran, Jr.
                                          Auburn Univ.

Crew Motion Forcing Functions from   B. Rochon, JSC
Skylab Flight Experiment and
Applicable to Space Station

Modeling of Controlled Structures   M. Zak, JPL
with Impulsive Loads

5:00   Tour

6:30   Social Hour, Redstone Officer's Club

7:30   Dinner

8

Thursday, April 24, 1986

SESSION 5

8:00   Critical Issues Forum

Control	Structures	Integrated
Morris Aud./4200	P106/4200	P110/4200
S. Seltzer	B. Wada	L. Pinson

(Concurrent Sessions on Integrated and Structures/Integrated)

10:30   Structures Integrated Session 5 - Carleton Moore, Chairman
         Morris Auditorium, Building 4200

Notes on Implementation of Coulomb   R. J. VanderVoort,
Friction in Coupled Dynamical Simulations   R. P. Singh, DYNACS

On the Control of Structures by   D. R. Edberg and
Applied Thermal Gradients   J. C. Chen, JPL

Finite Element Models of Wire Rope for   J. E. Cochran, Jr.
Vibration Analysis   N. G. Fitz-Coy,
                                                Auburn Univ.

Experimental Characterization of   R. Ikegami and
Deployable Trusses and Joints   S. Church, Boeing
                                                D. Kienholz and
                                                B. Fowler, CSA Eng.

10:30   Integrated Session 5 - Don McCutcheon, Chairman
         P106, Building 4200

System Identification for Large Space   J. C. Chen and
Structure Damage Assessment   J. A. Garba, JPL

Space Station Structures and Dynamics   E. W. Ivey,
Test Program (Proposed)   C. J. Moore,
                                                J. S. Townsend, MSFC

Analytical Determination of Space   F. C. Liu, UAH
Station Response to Crew Motion and
Design of Suspension System for
Microgravity Experiments

Space Station Structural Dynamics/   M. Pinnamaneni, MMC
Reaction Control System Interaction Study

12:30   Lunch

9

SESSION 6

1:00   Panel
            Morris Auditorium

            Dr. G. F. McDonough, MSFC, Chairman
            Dr. John L. Junkins, Texas A&M
            Dr. Roy R. Craig, Jr., U. of Texas
            Dr. Robert Skelton, Purdue University
            Dr. Sherman Seltzer, Control Dynamics
            Dr. Larry Pinson, LaRC
            Dr. Ken Richards, MMC

3:00   Adjourn

WORKSHOP ON STRUCTURAL DYNAMICS AND CONTROL
INTERACTION OF FLEXIBLE STRUCTURES

Tuesday, April 22, 1986

SESSION 1

Welcome	J. E. Kingsbury, MSFC
Workshop Overview	Dr. J. Blair, MSFC
Future Direction of NASA on Control/ Structures Research	L. Pinson, LaRC (for S. Venneri, Hdq.)
Overview of OAST's Large Space Systems Controls Research and Technology Program	J. DiBattista, Hdq.
Status of the Mast Experiment	B. R. Hanks, J. L. Allen, Jr., A. Fontana, LaRC
Large Space Structures Ground Experiment Checkout	H. B. Waites, MSFC
Identification of Large Space Structures A State-of-the-Practice Report	T. K. Hasselman ASCE; AS Task Commit. on Ident. of LSS

WORKSHOP ON STRUCTURAL DYNAMICS
AND
CONTROL INTERACTION OF FLEXIBLE STRUCTURES
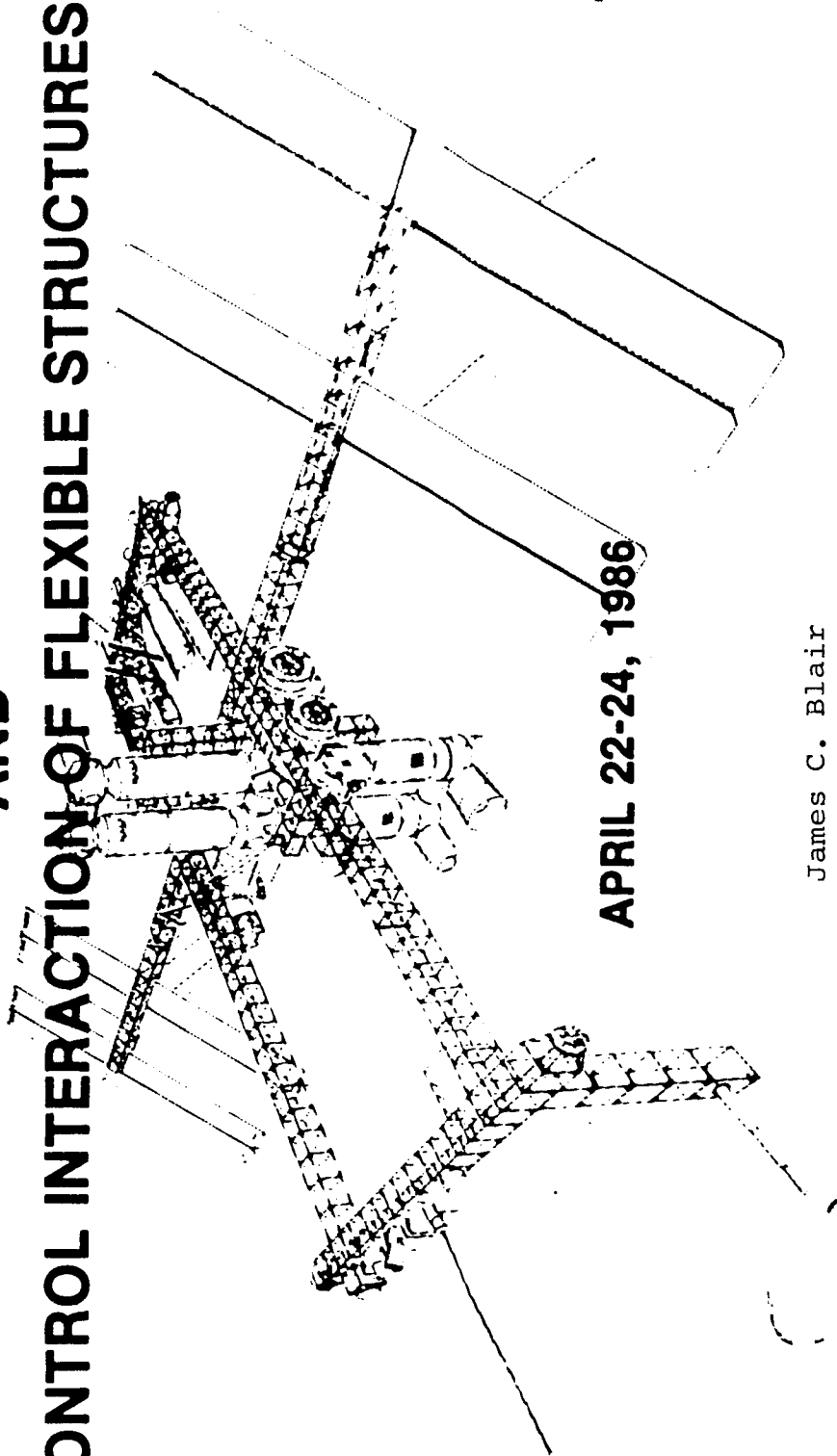
APRIL 22-24, 1986

James C. Blair

NATIONAL AERONAUTICS AND SPACE ADMINISTRATION

MSFC
MARSHALL SPACE FLIGHT CENTER

OAST
OFFICE OF AERONAUTICS &
SPACE TECHNOLOGY

WORKSHOP ON STRUCTURAL DYNAMICS

AND

CONTROL INTERACTION OF FLEXIBLE STRUCTURES

THEME: INTERACTION

PURPOSE: PROVIDE A FORUM FOR ENCOURAGING INTERACTION BETWEEN STRUCTURAL
          DYNAMICS AND CONTROL DISCIPLINES

          IDENTIFY ISSUES AND AREAS OF EMPHASIS IN STRUCTURE-CONTROL
          INTERACTION FOR THE NEXT GENERATION OF FLEXIBLE SYSTEMS.

WORKSHOP ON STRUCTURAL DYNAMICS AND CONTROL
INTERACTION OF FLEXIBLE STRUCTURES
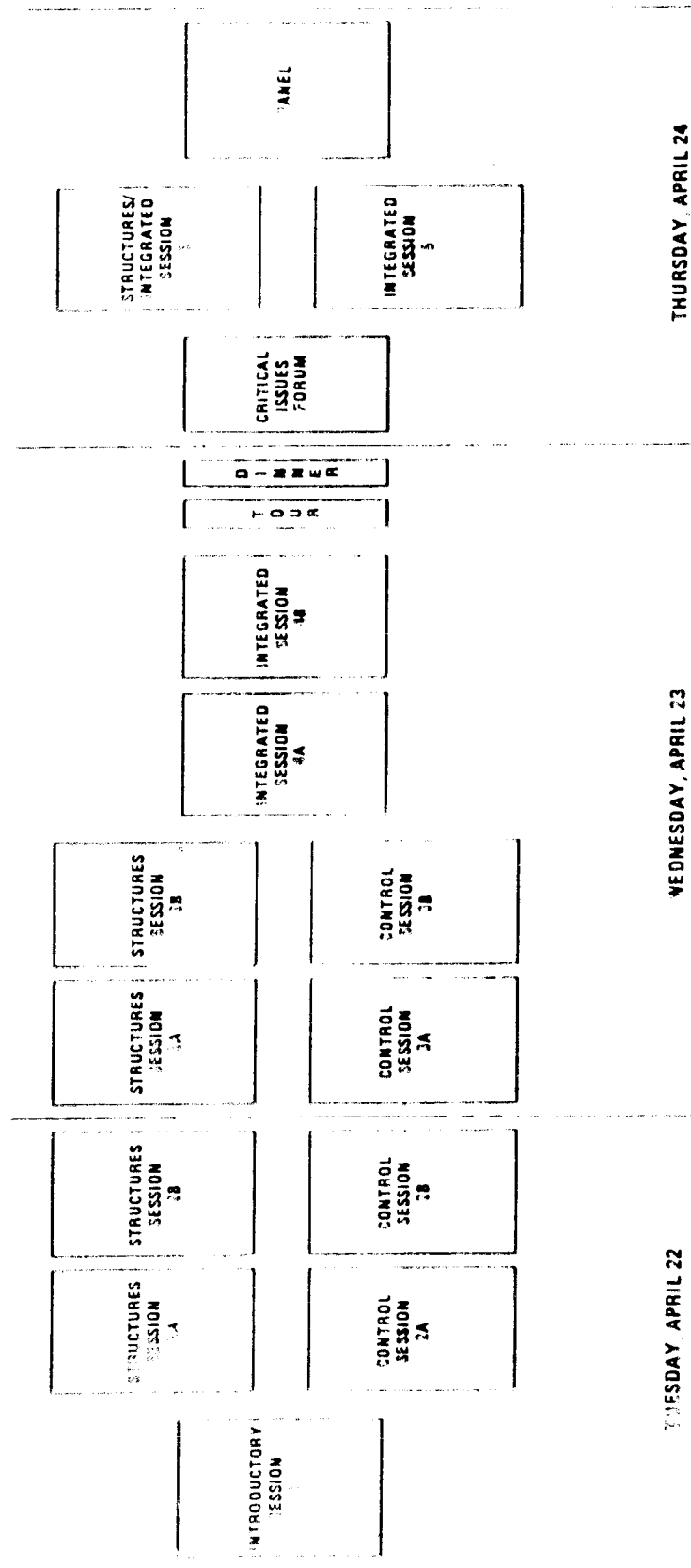
WORKSHOP ON STRUCTURAL DYNAMICS AND CONTROL
INTERACTION OF FLEXIBLE STRUCTURES

INTRODUCTORY SESSION 1

STRUCTURES SESSION 2A — CONTROL SESSION 2A

STRUCTURES SESSION 2B — CONTROL SESSION 2B

STRUCTURES SESSION 3A — CONTROL SESSION 3A

STRUCTURES SESSION 3B — CONTROL SESSION 3B

INTEGRATED SESSION 4A

INTEGRATED SESSION 4B

DINNER

TOUR

CRITICAL ISSUES FORUM

STRUCTURES/INTEGRATED SESSION 5 — INTEGRATED SESSION 5

PANEL

TUESDAY, APRIL 22 **WEDNESDAY, APRIL 23** **THURSDAY, APRIL 24**
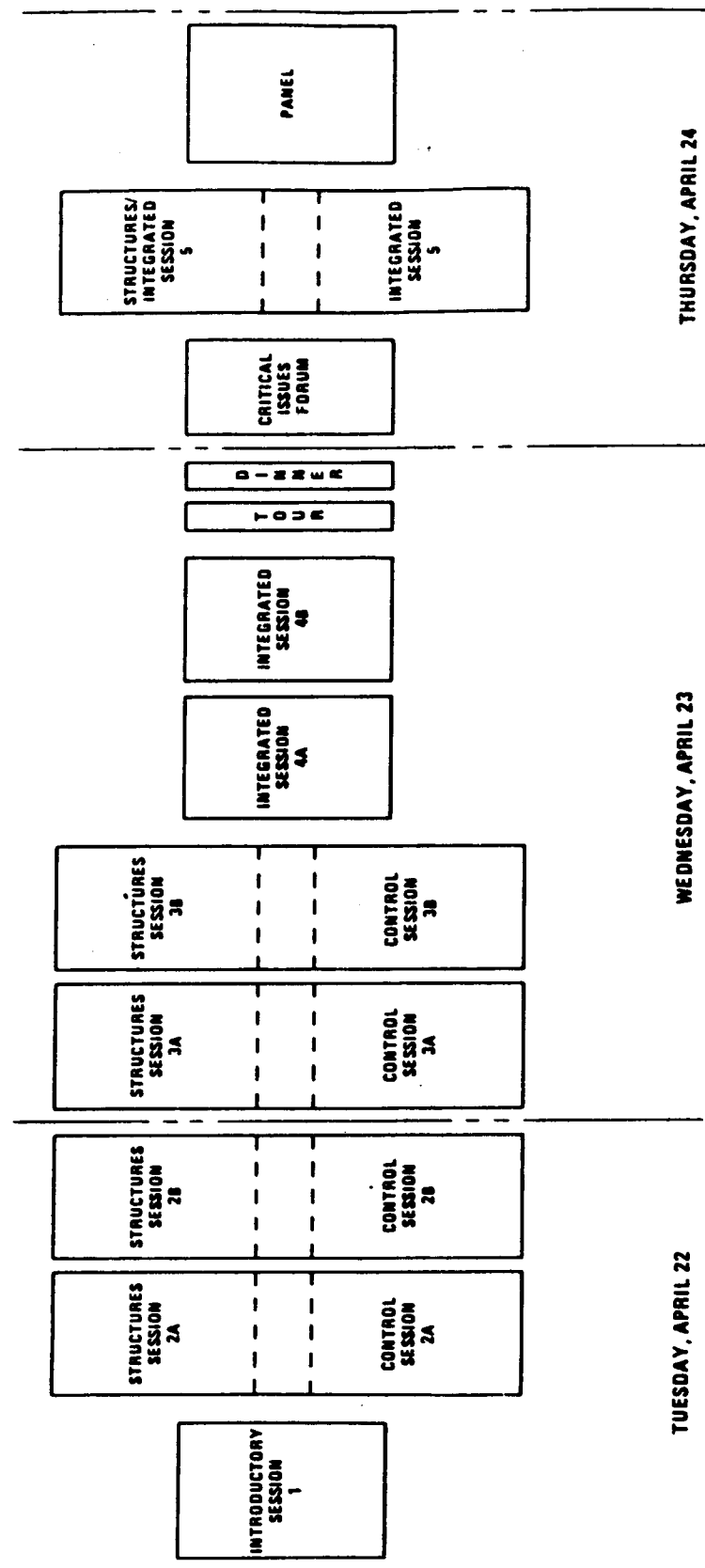
QUESTIONS

PROCESS

o   HOW CAN WE BEST ENHANCE INTERACTION BETWEEN STRUCTURES
    AND CONTROL DISCIPLINES?

o   WHAT ARE CONSIDERATIONS FOR INTERACTION WITH OTHER DISCIPLINES
    - OPTICS, THERMAL, MATERIALS, OTHERS?

o   WHAT ORGANIZATIONAL APPROACHES IMPROVE WORKABLE COMMUNICATION
    PATHS AMONG DISCIPLINES?

QUESTIONS

STRUCTURES INTERACTION

o   WHAT EFFECT DOES AN INTERACTIVE PERSPECTIVE HAVE ON
    THE STRUCTURES DISCIPLINE?

o   WHAT IS A SUITABLE APPROACH FOR TREATING NONLINEARITIES
    OF MULTI-JOINTED SYSTEMS?

o   WHAT IS TRADEOFF BETWEEN MODEL SIZE/COMPLEXITY AND
    NECESSARY PARAMETER VARIATIONS?

QUESTIONS

CONTROL INTERACTION

o   WHAT EFFECT DOES AN INTERACTIVE PERSPECTIVE HAVE ON THE
    CONTROL DISCIPLINE?

o   WHAT IS THE REQUIREMENT/OUTLOOK FOR DEVELOPING "NON-INTRUSIVE"
    CONTROL SENSORS AND EFFECTORS?
    -- OR DELIBERATELY-INTRUSIVE EFFECTORS?

o   WHAT ARE PRACTICAL APPROACHES FOR BRINGING SOPHISTICATED
    CONTROL SCHEMES TO APPLICATION ON REAL SYSTEMS?

QUESTIONS

VERIFICATION

o HOW DO WE VERIFY "UNTESTABLE" STRUCTURAL CONFIGURATIONS?

o WHAT IS BEST APPROACH TO TECHNICALLY-ADEQUATE, AFFORDABLE VERIFICATION OF ADVANCED CONTROL CONCEPTS?

o HOW DO WE INSURE SUFFICIENT LOCAL-EFFECT MODELING FOR STRUCTURES WHICH WILL BE TESTED ON-ORBIT?

20

OVERVIEW OF OAST'S LARGE SPACE SYSTEMS CONTROLS
RESEARCH AND TECHNOLOGY PROGRAM

John DiBattista, NASA Headquarters

It's a pleasure to be here in Huntsville to talk about the subject that's of quite a bit of interest to a few people in the audience and to myself. As Bob said, I've been concerned with this technology since about 1978 when we had the large space systems technology program introduced into OAST and into the agency. I think back then the biggest driver we had for a system that would utilize this technology or a system that really showed the need for such a technology was the old solar powered satellite. Those days, we thought in 1986, oil would be a $100 a barrel and we would have a need for it, but its $10 a barrel.

At that time when we started with LSST, we had largely a structures, materials, and assembly kind of technology program with very little really in controls, and it was through the solar powered satellite program and through our work in LSST that we really developed a case for the controls portion of the control of flexible structures. That was not an easy thing to do as many of you remember in the period of time when we were working the problem. We set up in those days a team that still functions at four centers. Marshall has been a member since the start, Langley has contributed a lot in theoretical areas, with Johnson and, of course, JPL. That team is still in place, and I've always thought that when we combined the research center and the flight center, we had the best mix of people and we would make the fastest progress in the program. I'll probably talk a little more about this later.

I thought bringing on the controls portion with the structures portion would enhance the ability of both programs. I think that's been borne out to garner more funds for the disciplines. As I said, Marshall has been a major contributor as have all of our centers. I'll probably talk more about Marshall as I'm here in Huntsville than I will the other cetners.

First chart please. This to my mind is the first large space modern structure that we put in space. As Larry said it is an OAST technology experiment program, or was. It features a large solar array on the longeron mast. It was 100 feet long, about 8 feet wide, and had a very low natural frequency of 0.03 Hz. It had very high damping. I can remember back in like 1980 when Paul Holloway, who was the Deputy Director of Langley, said, you know, we ought to get a measurement system

Advanced Solar Observatory On The Space Station
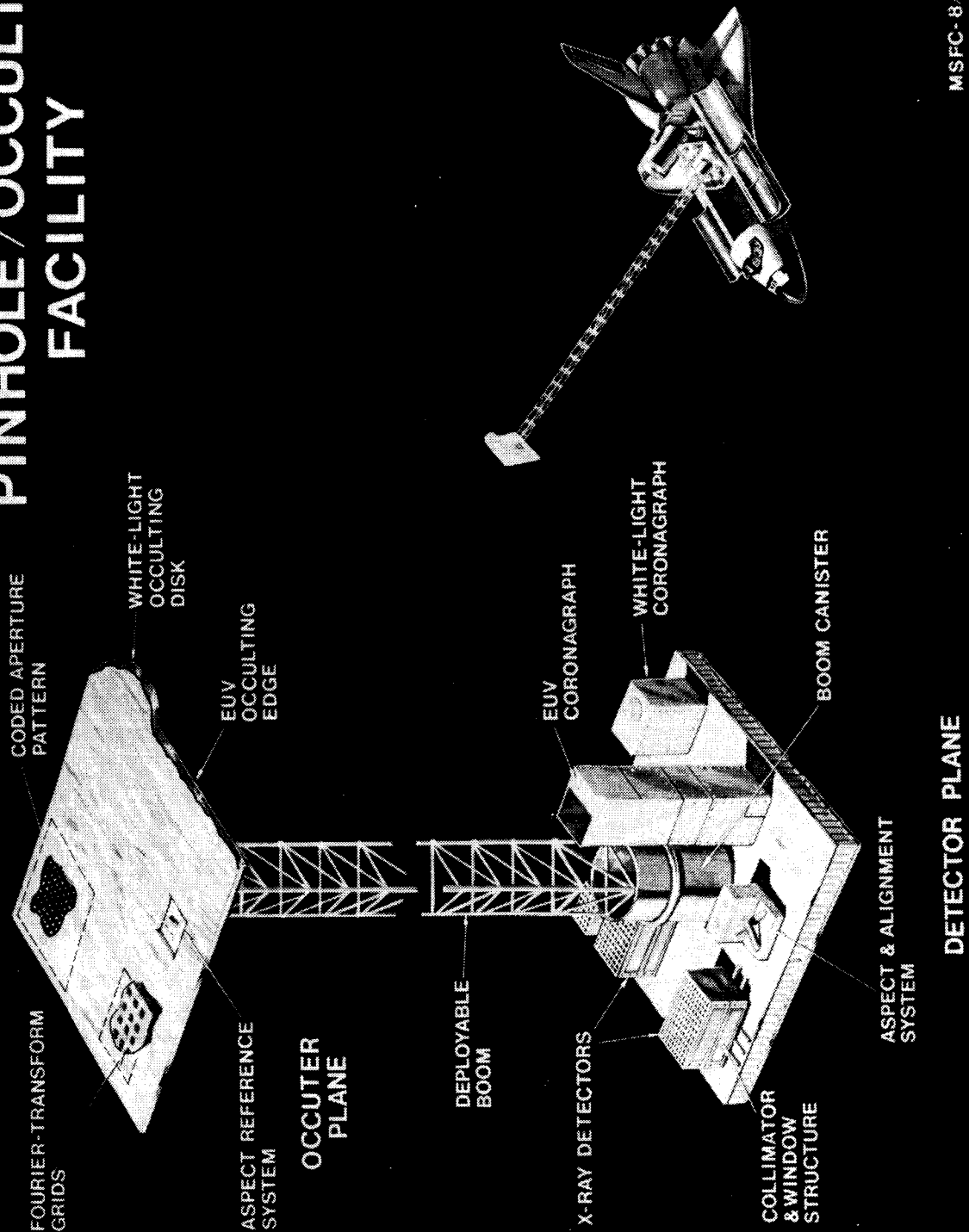
MSFC 9/84-PM 1652
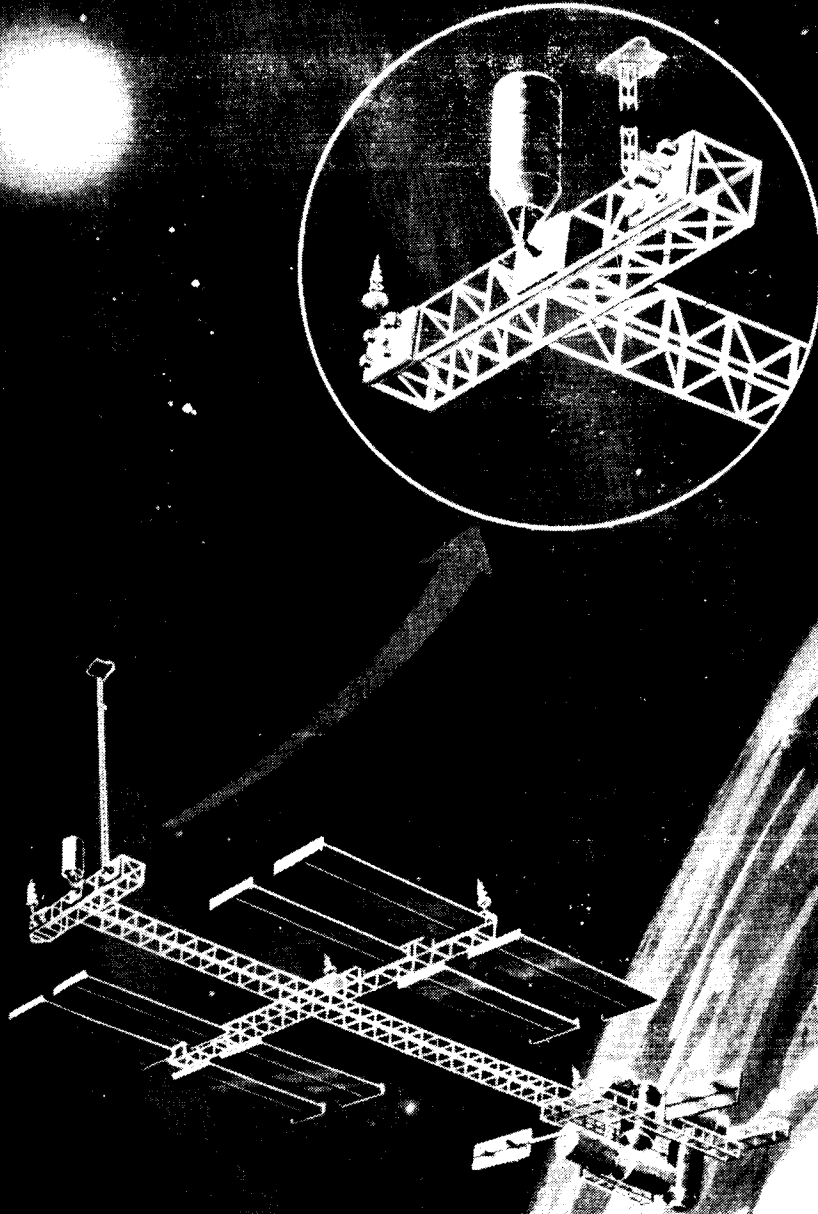
on that. We found some bucks in Headquarters to fund Langley
to do basically the photogrammetry experiment, as Larry
pointed out to you that's what the dots are for. A little
later, Congress gave us another million or million and half
dollars specifically for research in large space structures,
and we funded Ball Brothers, or we funded Marshall who then
selected Ball Brothers to come up with another way, a CCD
array way, of monitoring behavior of that array. I thought
those measurements systems were a major contributor to the
success of the SAFE experiment and utilizing the data. Right
now, the centerpiece of our program is COFS. I think Larry
showed it to you. Contrary to what he said; COFS is a major
controls experiment, and we will destructure the structural
dynamics work on it. We're still getting together. But, in
terms of a multi-center approach to this problem, I think and
I know, we are going to use and you're going to see it a
little later here at Marshall. We are going to be using the
vertical test facility which we built up down here and have
supported over a number of years to test out algorithms that
people propose for COFS I or COFS II. We'd use that along
with other ground facilities in the selection of the controls
algorithms that would be tested in space on the COFS I. I
think that's a very fine statement to say that the Centers can
come together, can cooperate in structures and controls as a
unit to formulate and advance this basic technology.

Next chart please. You hear about many systems that will be
the first users of control of flexible structures technology.
For me, I think this is one of the leading candidates. I
think it may be the pin hole occulter facility. In here, we
have to point this at the sun very stably, and we have to hold
or maintain this mass which has many holes in it to a very sub
arc second angle of relationship to the phase where we
basically have a focal plane. I think you can see where the
data that we generate from the COFS then can come back to
Marshall and can help them in doing a brand new, undoable
program with the current state of technology, a program that's
important to a lot of X-ray scientists in the world today.

Next chart please. You see the reason I've got this chart is
basically it gets me from this flight device on the Shuttle,
shows it on the Space Station, but it really gets me to this
particular device which I really think is going to require in
the end the control of flexible structure technology base that
we are developing and that the people in this room are
advancing. Maybe not for IOC but I still don't believe this
is the case. I think IOC may use some elements of our
technology because we will have flight data when IOC occurs.

PINHOLE / OCCULTER FACILITY

CODED APERTURE PATTERN

WHITE-LIGHT OCCULTING DISK

EUV OCCULTING EDGE

FOURIER-TRANSFORM GRIDS

ASPECT REFERENCE SYSTEM

OCCULTER PLANE

DEPLOYABLE BOOM

X-RAY DETECTORS

EUV CORONAGRAPH

WHITE-LIGHT CORONAGRAPH

BOOM CANISTER

COLLIMATOR & WINDOW STRUCTURE

ASPECT & ALIGNMENT SYSTEM

DETECTOR PLANE

MSFC- 8/82-ST 2849 A
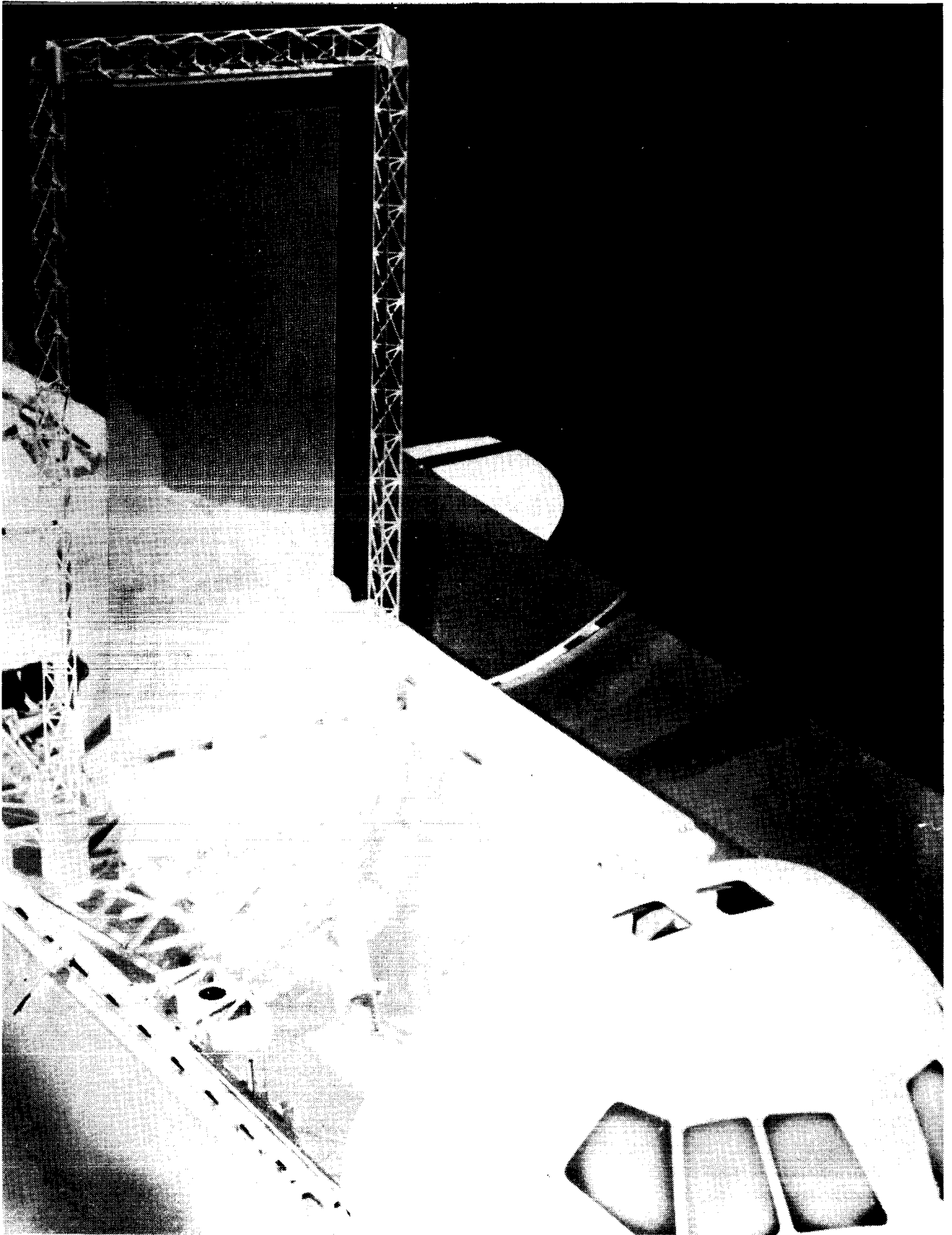
Certainly, the growth of Space Station will simply require this technology. In looking at the current state of affairs, if you look at SDIO, Air Force, look at NASA systems that we are talking about, and even looking at potential commercial systems, like the large mobile communications satellite, I think the field is burgeoning. It's kind of like, and I ran into this with RF engineers in communications, they think RF engineers drive the system concepts for large antennas, not structures guys, and not controls guys. The offset configuration you see for large antennas came from the RF world, not from the controls or structures world. If those guys think they can solve the RF problem, then why can't the controls and structures guys support them using very few resources so that they can optimize the payload portion of the spacecraft in doing the job. So, we are going to be very fortunate, because not only the RF guys but laser guys, everybody is going to be designing systems where we have to supply the know-how and really enable the systems.

That kind of leads me into the last two or three points. I want everybody here to understand that the control of flexible structures is not just an evolutionary technology. What we are talking about here is a revolutionary technology. We need breakthroughs in this technology if we are going to enable some of the large space systems that are handily bandily shown on the charts up here and not this one in particular but when you look at that large, deployable reflector which is, I guess, visible UV submillimeter system, 10 to 20 meters, but when you look at the current concepts and configurations people are showing, you recognize that what we are doing is dragging technology from the '60's and the '70's out into the '90's and the year 2000. When you really look at that technology and you compare it to our Space Telescope background and costing, where Space Telescope probably cost us a billion and half dollars, you really like that LDR that is shown in those configurations and those systems studies are five billion dollars plus, plus machines. We're not going to have those machines until we understand or we can figure out how to do the controls problem and the structures problem where we can implement those systems in a much cheaper version. I think that's absolutely true.

Let me say a few words on dollars in the area. As I said, I think it has been absolutely beneficial that the controls and the structures people got together, or get together so that we can get more funding in the area. I sometimes think that they see each other as competitors for the dollars, and in reality,

you are allies for the dollars against many other disciplines like propulsion or like power in other places. I don't know if I said it in my talk, but in 1978, NASA had, I believe, all of $200,000 in controls and today we have $6 million. DARPA had a much larger program at that time, but now SDIO has an even larger program. So in 1978 to today, I would say the program has grown probably three orders of magnitude at the least. We are at least $20 million if you look at the controls technology, the structures technology, flight experiments technology, if you look at NASA, SDIO, and IRD in industry. It's probably more than that. So, it's been a very substantial growth.

The last thing I would like to do is give a perspective on how I've seen this field develop. I think we spent the last 10 years, and I really mark it I think from the time I really became familiar with it or associated with it, but I'll use the word modern. When you're really addressing control of flexible structures, I think the last 10 years have been 10 years of trying to define the problem, understand the problem, bring the structures and controls people together, to solve the problem. The next 10 years I see as one where we are going to carry out many, by the way, and in those 10 years, we will still be working to bring the structures and controls people together. Okay, the next 10 years, I see, as centered on flight experiments in space, ground experiments supporting those flight experiments, getting an empirical base to support the analytical methods we are developing, and in turn, enriching our analytical methods. I think COFS I, II, and III are clearly going to be pathfinders to do that. I think that even the other agencies, SDIO, the Air Force, other people have got to come forth and get on that program because NASA has to take rather clear direction, and I think they will follow and support us.

We will still, by the way, in the next 10 years, be bringing structures and controls people together. And in the third 10 years, say 1996-2006, I see as the time of implementation of that technology in a limited form, because I don't believe we are going to come to the end of the road in the technology of control of flexible structures in 30 years. I think it's going to be as viable technology for people to study and work in as aeroelasticity has been for the last 40 years and continues to be. So, I guess I would like to leave you with the idea that you are working in a field that is clearly a long term field that will take a lot of work, there are breakthroughs in the field to be made. Let me say one last

point (should have said this earlier). In the COFS program,
we found a very interesting thing. We found that in looking
at the algorithms, many of them that we were looking at exceed
the available capacity for the machines to do the computation.
I guess that's not unusual. If people are now coming up with
new algorithms that were never needed on the old spacecraft
because they were rigid body, then nobody ever flight
qualified the machine to those specs.   So, I guess what I'm
saying is over the next 10 years, 20 years, we have a rich
field, there will be a lot of advancement made in computation
capability, a lot of advancement in getting the current
computation capability into space, and that might be an issue
you might talk about in your critical issues. How do you
formulate a program where we can advance the state of flight
qualified computers for controls systems, because I do believe
controls systems and control of flexible structures will be
the driver for a lot of different disciplines and hardware
that will go into space.   Thanks.

STATUS OF THE MAST EXPERIMENT

BRANTLEY R. HANKS

ANTHONY FONTANA

JOHN L. ALLEN

NASA LANGLEY RESEARCH CENTER

INTRODUCTION

The control of flexible structures is a research topic of high interest and importance in developing future spacecraft, particularly very large or very rapidly maneuvered craft. It is an interdisciplinary problem that involves combining advanced structural dynamics analysis and identification techniques with advanced control methods. Many sophisticated mathematical control techniques for flexible structures have been devised. The basic problem is that most of them require a relatively accurate mathematical model of the system under control including the dynamics of both the structure and the control system components. Obtaining such a model for either subsystem traditionally has required great effort including a significant validation step based on test data. This is complicated further in the interdisciplinary case by the fact that the control system is using the mathematical model to decide where, when and how hard to apply forces, in a fraction of a vibratory oscillation. Requirements on the accuracy and the computational speed of the mathematical calculations in the control computer are far greater than, say, a dynamic loads analysis or a rigid-body control maneuver. Iteration and updating based on measured responses becomes an on-line part of the control process. Instability is a constant threat, especially for higher frequency modes or poorly measured/modelled responses.

Because of the quantum increase in complexity over proven methods, promising techniques for the control of flexible structures must be validated in actual hardware experiments before committing to their use in actual spacecraft missions. The Mast experiment system serves as a focus for such validation. It is the first in a series of experiments under the Control of Flexible Structures (COFS) Program at the NASA Langley Research Center.

THE CONTROL OF FLEXIBLE STRUCTURES (COFS) PROGRAM

The Mast hardware is being developed for the COFS-I Project under the COFS Program. The figure shows the currently envisioned hardware foci for the first three projects under this program. Beginning with a 60m shuttle-orbiter-attached, deployable beam for COFS I, the complexity of structures advances with each level. COFS II adds a three-dimensional motion aspect with rigid-body slewing of a flexible body attached to the Mast structure. Both COFS I and COFS II are planned for both ground and in-orbit tests to calibrate the usefulness of ground tests in the validation process. The planned COFS III hardware is a ground test article which is a scale model of Space Station. Refined calibration of the ground experiments is expected to be made using orbital data obtained as a natural part of Space Station development rather than by special flight experiments.

CONTROL OF FLEXIBLE STRUCTURES PROGRAM

COFS I
Beam Dynamics & Control
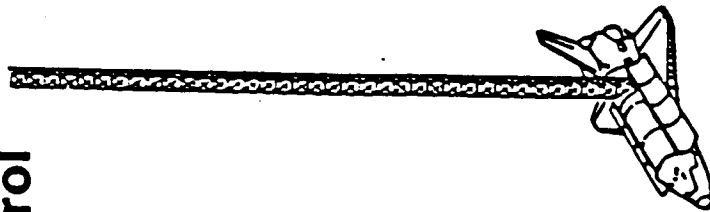
COFS II
Three-Dimensional Dynamics & Control
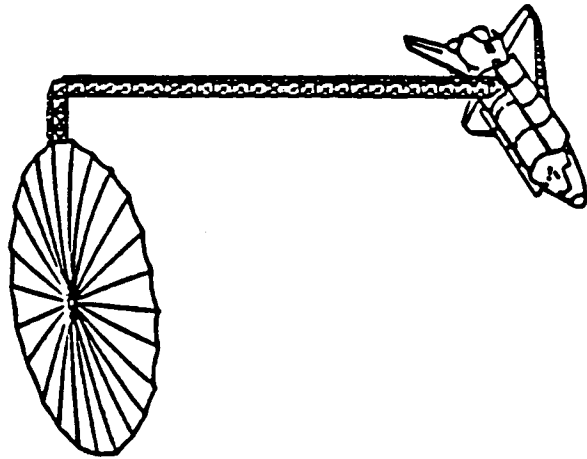
COFS III
Multi-Body Dynamics & Control
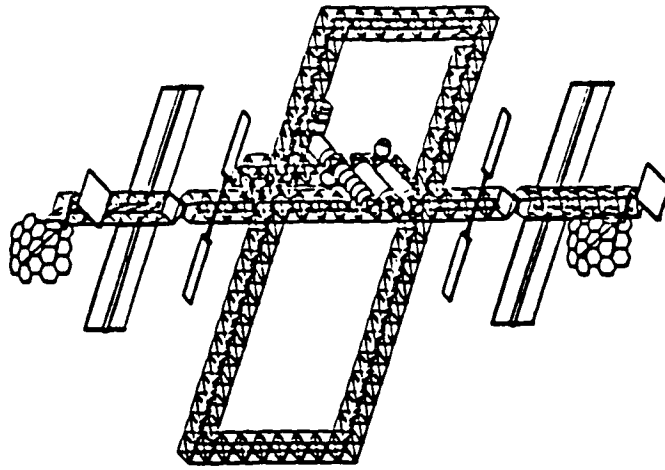
CONTROL OF FLEXIBLE STRUCTURES - COFS I TECHNOLOGY GOALS

The COFS I hardware is intended to provide hardware for general experimentation by the Control Structures Interaction (CSI) research community, including government, academia and industry. As such, it is designed to accommodate a variety of potential research objectives and technology goals. The figure overviews the primary goals.

Several facets of hardware testing and analysis are planned in order to achieve the desired research results. The 60m beam shown on the previous figure is to be tested dynamically on the ground and in orbit. Both excitation/identification and controls tests are planned using proof-mass actuators located at the tip of the beam and at three locations along its length. A capability for exciting/measuring/controlling 10 flexible modes is baselined. Tests on substructures, joints and control components are planned to assist in the development of refined analyses. In addition, scale models will be tested (in ground tests only) to ascertain the validity of using such models to reduce gravity effects in ground tests of proposed flight systems.

33

CONTROL OF FLEXIBLE STRUCTURES

COFS I TECHNOLOGY GOALS

- VALIDATE GROUND TEST METHODS

- DEVELOP & VALIDATE IN-SPACE TEST METHODS

- VERIFY CSI ANALYTICAL TOOLS

- ASSESS SCALING EFFECTS

- EVALUATE DISTRIBUTED CONTROLS METHODS

34

COFS I (MAST) FLIGHT SYSTEM

The Mast flight hardware is currently being designed under contract with Harris Corporation, overviewed in the accompanying figure. The beam, being developed under a subcontract to Astro Aerospace Corporation, is a foldable-longeron graphite epoxy structure with titanium joints. It is of statically determinate design and is intended to be unaffected structurally by temperature changes. A control system consisting of distributed sensors, actuators, control computer and associated data handling equipment is being designed to allow experiments in structural dynamics and a wide variety of vibration control methods. Detailed design has been under way for about six months with a final design completion expected in 1987.

COFS I (MAST) FLIGHT SYSTEM

CONTRACT – AWARDED NOVEMBER 25, 1985

PRIME CONTRACTOR – HARRIS CORP., MELBOURNE, FL

SUB CONTRACTORS

- ASTRO AEROSPACE – BEAM/DEPLOYER
- DELCO – EXCITATION/CONTROL COMPUTER
- SCI SYSTEMS INC. – GROUND SUPPORT EQUIPMENT
  – HOUSEKEEPING COMPUTER

DURATION* – 36 MONTHS + 12 MONTHS POST–DELIVERY SUPPORT

PRODUCTS – FLIGHT SYSTEM INCLUDING BEAM, SENSORS, ACTUATORS AND ELECTRONICS; MATHEMATI–CAL MODELS AND SIMULATOR; GROUND SUPPORT EQUIPMENT

*MAY BE AFFECTED BY RECENT 10–MONTH SLIP OF LAUNCH DATE TO OCTOBER 1990.

MAST FLIGHT SYSTEM SIMULATOR (MFSS)

In order to develop algorithms for excitation and control of the COFS I system, a dedicated ground simulator is being developed. Real time simulation of all significant dynamic effects including actuators, structure and computer delays is to be included. This simulator will serve for determining the best candidate algorithms as well as for validating software during development.

MAST FLIGHT SYSTEM SIMULATOR (MFSS)

OBJECTIVE:

PROVIDE A DEDICATED COMPUTER WHICH PERMITS REAL-TIME SIMULATION OF STRUCTURAL DYNAMIC RESPONSE TO ACTIVE CONTROLS

PURPOSE:

- VALIDATE CONTROLS ALGORITHM SOFTWARE
- SUPPORT FLIGHT ALGORITHM SELECTIVE PROCESS

MAST GROUND TEST CHALLENGES STATE OF THE ART

Validation of mathematical models and control designs by ground tests has been a traditional standard. However, as lightweight space structures become large in dimension, gravity effects combined with low-frequency/high-amplitude response combine to significantly degrade the quality of the test. Traditional soft suspensions used to support the structure for test must have combined properties of low mass, low stiffness and large displacement excursions which are well beyond the state of the art. The alternative is to conduct tests to validate mathematical models which include suspension system dynamics and to analytically remove the suspension system effects to predict on-orbit performance. This too is not a well-developed technology. The Mast systems will be dynamically ground tested as shown in the figure using a relatively interactive suspension which requires careful modeling to extract its effects. Thus ground testing technology development is an integral part of the program.

MAST GROUND TEST CHALLENGES STATE OF ART

LaRC HANGAR ANNEX

LOWEST NATURAL FREQUENCY ≈ .15 Hz

60 M

15 M

CABLES

MAST FLIGHT HARDWARE

40
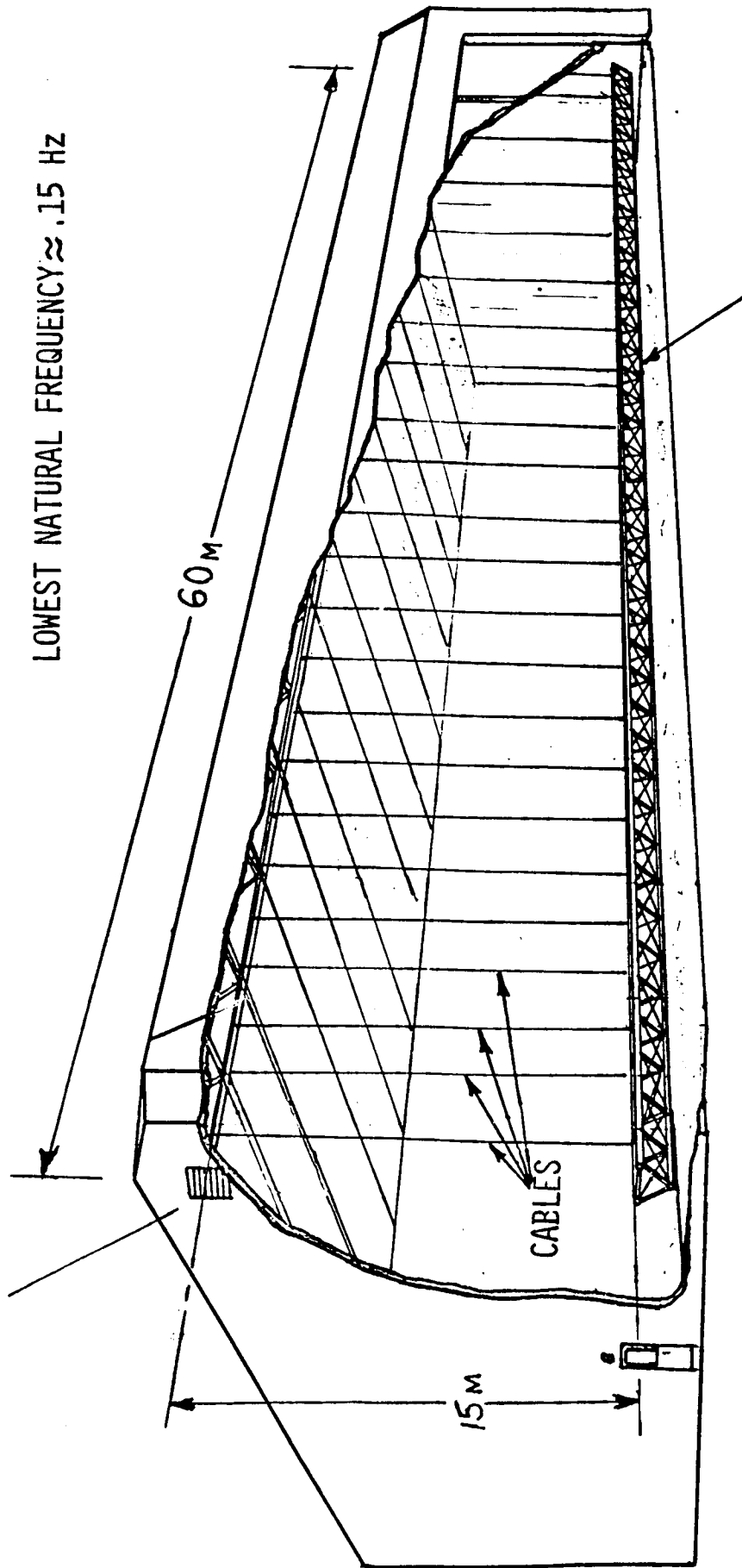
20M LABORATORY BEAM (MINI MAST)

In order to develop mathematical modeling and test techniques for the Mast hardware in advance of flight hardware delivery, a 20m laboratory beam called the Mini Mast is being built. It is based on an early design and is similar to the flight Mast in geometry but has somewhat different joint kinematics. Early static, dynamic and controls tests using this beam in various test configurations will be conducted. Also tests of joints and suspension techniques will be conducted to better understand the importance of these factors in mathematical modeling.

20M LABORATORY BEAM (MINI-MAST)

- DEPLOYABLE; GRAPHITE & TITANIUM; SIMILAR TO FLIGHT BEAM

- BEING BUILT BY ASTRO AEROSPACE.

- TO BE USED FOR PRELIMINARY DEVELOPMENT OF ANALYSIS, CONTROL & TEST METHODS

42

COFS I – BEAM DYNAMICS & CONTROLS TECHNOLOGY SCHEDULE

The attached figure shows the preliminary schedule for the COFS I Program as of May 1986. This schedule is likely to be modified as further information on the space shuttle flight schedule becomes available. As currently planned, the Mast hardware would be delivered to NASA, where the ground model tests will be conducted, in mid-1989. The first flight would occur in late 1990 with a second to follow one year later. The first flight would emphasize structural dynamics and system identification with relatively simple controls experiments. The second flight would permit more advanced control algorithms to be tested on the same hardware, taking advantage of the improved knowledge of the system dynamics obtained from the first flight.

CONTROL OF FLEXIBLE STRUCTURES

COFS I – BEAM DYNAMICS & CONTROLS TECHNOLOGY

MAJOR TASKS	FY	85	86	87	88	89	90	91	92
● MINI-MAST 20M BEAM DESIGN, FABRICATION & TEST			DELIVERY						
● SCALED MODEL DESIGN, FABRICATION & TEST					AWD	DEL. 1/2 SCALE	DEL. 1/4 SCALE	TEST COMPL.	
● EXPERIMENT MODELING, SIMULATION & SOFTWARE DEVELOPMENT									
● MAST FLIGHT SYSTEM DESIGN & FABRICATION				CDR		DELIVERY			
● MAST FLIGHT SYSTEM GROUND TEST									
● GUEST INVESTIGATORS PROGRAM		DEAR COLLEAGUE LETTER		AWD.					
● MAST FLIGHT TESTS									
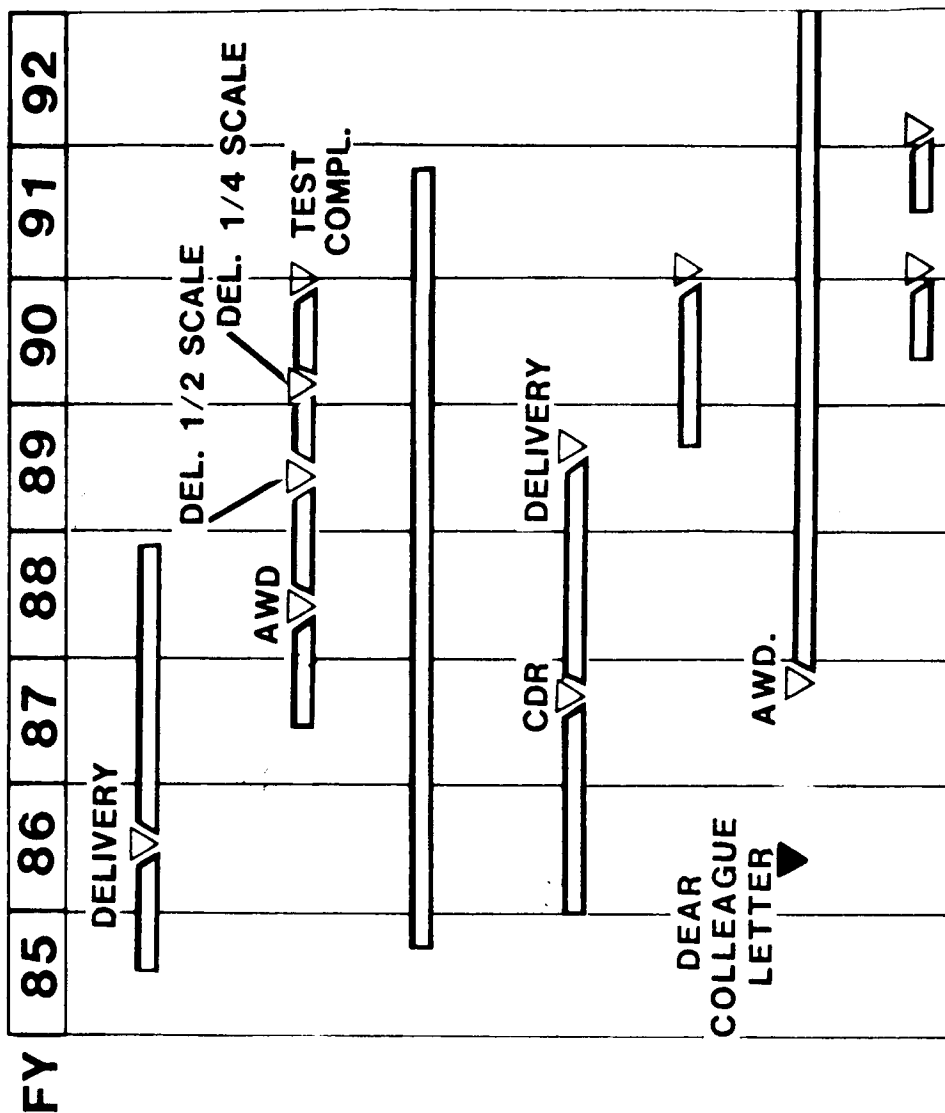
PRELIMINARY

GUEST INVESTIGATOR PROGRAM

Because the Mast is an experimental apparatus for testing/validating analytically developed tools, the opportunity for participation by the research community is being made available. This program is overviewed in the figure. Participation is possible in a variety of roles ranging from receiving and analyzing data to development of control algorithms for on-orbit experiments.

GUEST INVESTIGATOR PROGRAM

OBJECTIVE:

TO PROVIDE OPPORTUNITIES FOR AND PROMOTION OF GENERIC RESEARCH BOTH GROUND AND IN-SPACE AMONG INDUSTRY/ UNIVERSITY AND GOVERNMENT FOR THE DEVELOPMENT OF CONTROLS/STRUCTURES INTERACTION TECHNOLOGY

APPROACH:

ESTABLISH GROUND AND IN-SPACE FACILITIES WHICH PROVIDE FOR INDIVIDUAL AND/OR COMPANY EXPERIMENTS AT MINIMUM COST

PAYOFF:

- BROAD BASE FOR ADVANCED CSI METHODOLOGIES
- DISSEMINATION OF PROGRAM DATA & FINDINGS WITHIN CSI COMMUNITY
- IN-SPACE RESEARCH AWARENESS

GUEST INVESTIGATOR OPPORTUNITIES

Some examples of typical guest investigator studies as listed in the figure. Potential studies are not limited to these activities. Studies which do not require hardware changes are most likely to be acceptable because of the cost and schedule impact involved in changing space qualified hardware. A Call for Proposals has been issued with final proposals due on August 29, 1986. These proposals are technically "unsolicited" and hence discussion of their nature and objectives, as well as possible implementation problems, with NASA investigators is allowed on an individual basis.

GUEST INVESTIGATOR OPPORTUNITIES

(TYPICAL)

- STRUCTURAL DYNAMICS
- FLEX-BODY CONTROL ALGORITHMS
- SYSTEM IDENTIFICATION ALGORITHMS
- FLIGHT & GROUND TEST METHODS
- MATH MODELLING
- VIBRATION SUPPRESSION
- ANALYSIS OF GROUND & IN-SPACE TEST DATA
- FLIGHT TESTING OF UNIQUE HARDWARE

48

COFS I GUEST INVESTIGATOR (GI) PROGRAM
PROPOSAL EVALUATION CRITERIA

The primary factor in selection of proposals for the GI program is technical merit. The figure shows, however, that other factors are important in order to keep the activity manageable and to maximize benefit to the technical community.

COFS I GUEST INVESTIGATOR PROGRAM

PROPOSAL EVALUATION CRITERIA

1. TECHNICAL MERIT

2. RELEVANCE TO COFS GOALS

3. PROGRAMMATIC ISSUES

   – COST

   – ACCOMMODATIONS

   – MIX OF EXPERIMENTS

   – TECHNOLOGY NEEDS

4. INVESTIGATOR/ORGANIZATION EXPERIENCE

GUEST INVESTIGATOR SELECTION PROCESS
COMMITTEE STRUCTURE

The selection of participants in the GI program will be made by four committees as shown in the figure. Initial ratings of all proposals and suggested selections will be made by a Technical Evaluation Committee comprised of nine members from four NASA Centers and the Jet Propulsion Laboratory. No more than two voting members from any one Center will be involved. After the initial technical selection, the proposals will be reviewed for cost and management factors by a Business Evaluation Committee. Also, an Accommodations Committee will screen the selected proposals for possible adverse safety, hardware integration and schedule incompatibility factors which may require changes or rejection of the proposal. Finally, an Experiments Evaluation Committee will review findings and recommendations of the other committees and make a final prioritized recommendation to the NASA Headquarters Control Structures Interaction Steering Committee, which makes final selections. This selection process is due to be completed in the first quarter of 1987 with final contract/grant awards made approximately four months later.

GUEST INVESTIGATOR SELECTION PROCESS

COMMITTEE STRUCTURE

COMMITTEE	MEMBERS	RESPONSIBILITIES
●TECHNICAL EVALUATION	CHAIRMAN: COFS PI JSC JPL MSFC LaRC GSFC	●TECHNICAL ASSESSMENT ●CATEGORIZE ●PRIORITIZE
●BUSINESS EVALUATION	CHAIRMAN: COFS BUSINESS MANAGER LANGLEY STAFF PRICING COST ANALYSIS CONTRACTS	●EXPERIMENT COST ●PRICING CONTROL ●MANAGEMENT STRUCTURE
●ACCOMMODATIONS EVALUATION	CHAIRMAN: COFS PROJECT MANAGER MSFC JSC	●ACCOMMODATIONS ●INTEGRATION ●SAFETY
●EXPERIMENTS EVALUATION	CHAIRMAN: LaRC DIRECTOR FOR SPACE MSFC LaRC JSC JPL GSFC	●FINDINGS TO CSI STEERING COMMITTEE

52

COFS GI PROGRAM-FUNDING PLAN

The funding plan for the COFS I GI program, as of May 1986, is shown in the accompanying chart. This plan is based on the original expected flight date in late 1989. However, some spreading out of the funding to cover the expected October 1990 flight date is likely to occur. In any case, the total funds available is about $4M. This will be distributed among investigators and will undoubtedly control the total number of investigators supported. Opportunities for cost-sharing through memorandums of understanding will be explored where mutual benefit warrants.

53

COFS GUEST INVESTIGATOR PROGRAM

FUNDING PLAN*

INVESTIGATOR FUNDS, $,K

	FY87	88	89	90	BTC	TOTAL
COFS I	400	850	1250	1300	200	4000

FLIGHT SOFTWARE DEVELOPMENT FUNDS, $,K

	FY87	88	89	90	BTC	TOTAL
COFS I	–	1400	2400	200	–	4000

*MAY BE AFFECTED BY RECENT 10–MONTH SLIP OF LAUNCH
DATE TO OCTOBER 1990.

SUMMARY

A flight experiment apparatus for the in-orbit study of structural dynamics and control issues is being built under contract. This apparatus, a 60M-long deployable truss-beam with distributed proof-mass actuators, is planned for flight on board the space shuttle in the early 1990's. It is being designed to accommodate structural dynamics, system identification and active vibration suppression experiments and is backed by a comprehensive ground test program. Participation as experiments by members of the research community is being made available in a Guest Investigator program. Opportunities exist in a variety of specific technical areas including structural modeling, test techniques, control algorithm design and parameter estimation as well as many others. The ultimate goal is the validation and/or verification of critical analytical developments to the point that they may be considered flight ready.

55

SUMMARY

- MAST EXPERIMENT IS COMBINED GROUND TEST, ORBITAL FLIGHT TEST AND ANALYSIS OF A DEPLOYABLE BEAM UNDER THE COFS PROGRAM

- PROVIDES VEHICLE FOR RESEARCH IN STRUCTURES STRUCTURAL DYNAMICS, AND CONTROL ISSUES

- CONTRACT FOR FLIGHT SYSTEM IS UNDER WAY

- GUEST INVESTIGATOR PROPOSALS BEING ACCEPTED FROM UNIVERSITIES, INDUSTRY, AND GOVERNMENT

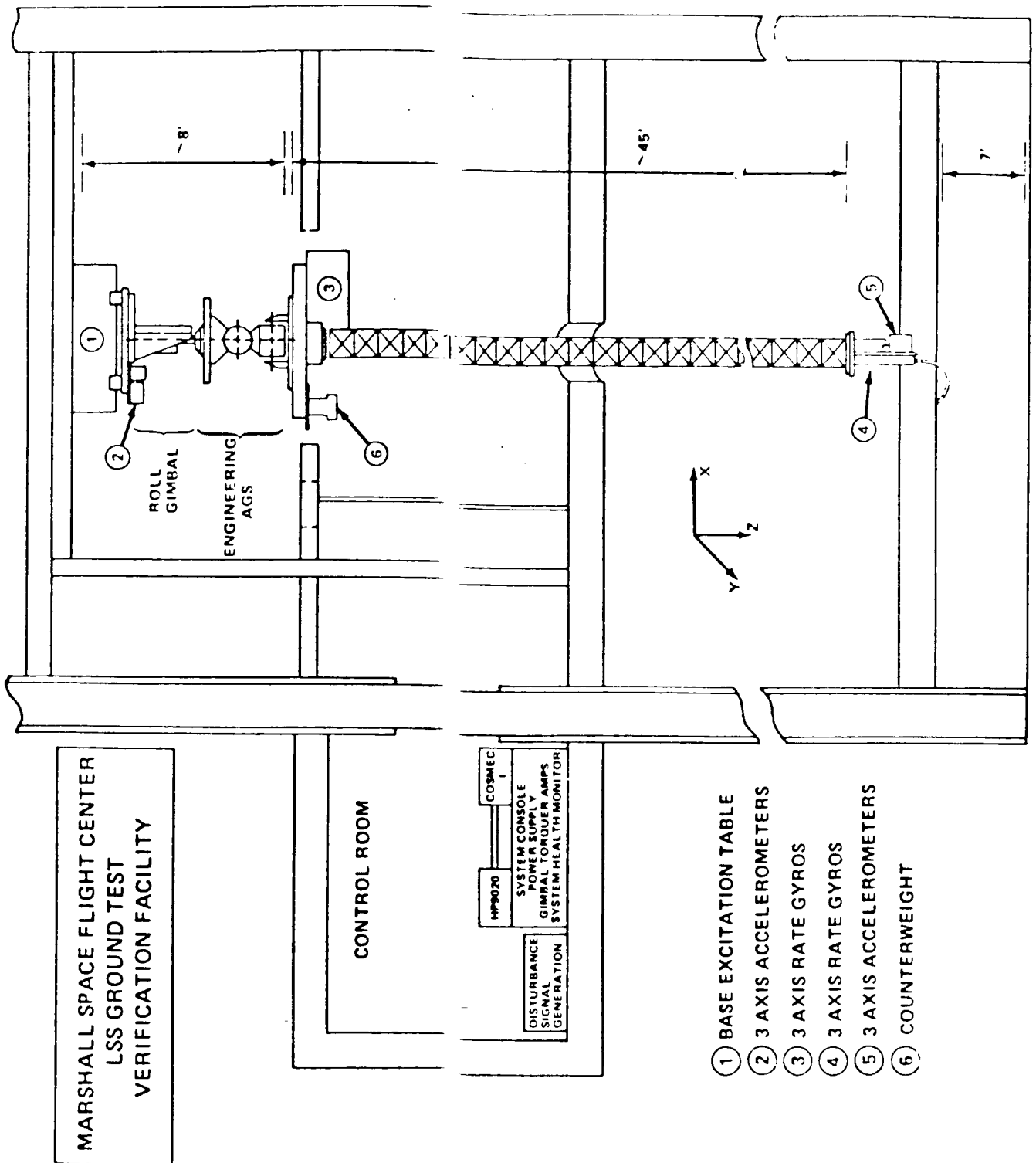LARGE SPACE STRUCTURES
GROUND EXPERIMENT CHECKOUT

HENRY B. WAITES
NASA/MARSHALL SPACE FLIGHT CENTER
HUNTSVILLE, AL

WORKSHOP ON STRUCTURAL
DYNAMICS AND CONTROL INTERACTION
OF FLEXIBLE STRUCTURES

APRIL 22-24, 1986
MSFC, AL

NASA Marshall Space Flight Center has developed a facility in which closed loop control of Large Space Structures (LSS) can be demonstrated and verified. The main objective of the facility is to verify LSS control system techniques so that on-orbit performance can be ensured. The facility consists of an LSS test article or payload which is connected to a 3-axis angular pointing mount assembly that provides control torque commands. The angular pointing mount assembly is attached to a base excitation system which will simulate disturbances most likely to occur for Orbiter and DOD payloads. The control computer contains the calibration software, the reference systems, the alignment procedures, the telemetry software, and the control algorithms. The total system is suspended in such a fashion that the LSS test article has the characteristics common to all LSS.

The first version of the LSS/GTV facility is shown schematically on the facing page. It consisted of an ASTROMAST beam mounted to the faceplate of the Angular Pointing System (APS). The APS, in turn, is mounted to the Base Excitation Table (BET). Six separately packaged inertial measurement assemblies comprise the control system sensors. The signals from these sensors are received and processed in the COSMEC-I data gathering system. The COSMEC-I interfaces with a Hewlett Packard HP9020 desktop computer which processes the control algorithms, transmits control actuator commands to the COSMEC-I system, and stores data as they are collected during test runs; it then provides post-experiment data reduction and off-line displays. The COSMEC-I processes the control command from the HP9020 to the associated effector(s) to complete the closed loop system.

MARSHALL SPACE FLIGHT CENTER
LSS GROUND TEST
VERIFICATION FACILITY

CONTROL ROOM

MP9020

COSMEC

SYSTEM CONSOLE
POWER SUPPLY
GIMBAL TORQUER AMPS
SYSTEM HEALTH MONITOR

DISTURBANCE
SIGNAL
GENERATION

ROLL GIMBAL

ENGINEERING AGS

① BASE EXCITATION TABLE
② 3 AXIS ACCELEROMETERS
③ 3 AXIS RATE GYROS
④ 3 AXIS RATE GYROS
⑤ 3 AXIS ACCELEROMETERS
⑥ COUNTERWEIGHT

59

Six separately packaged inertial measurement assemblies comprise the control system sensors. Two of the packages, containing 3-axis translational accelerometers, are identical. One is mounted on the mast tip and the other on the lower surface of the BET. Three other packages contain Skylab ATM (Apollo Telescope Mount) rate gyroscopes and are mounted on the APS faceplate (see top of facing page). The sixth package, the Kearfott Attitude Reference System (KARS), is located on the mast tip along with the remaining accelerometer package.

The Kearfott Attitude Reference System (KARS) includes three rate gyros and three accelerometers. The KARS unit is mounted to the test article tip as shown on the bottom of facing page, so that the sensors provide information about the tip motion. The rate gyros have a resolution of approximately 50 arc-sec/sec about two axes and 90 arc-sec/sec about the third axis. The KARS rate gyro bandwidth is about 70 Hz.

The ATM rate gyros are mounted to the APS payload mounting plate. The minimum resolution for the ATM gyros is approximately two arc-sec/sec. The gyros operate in a fine mode, which has a bandwidth of 12 Hz, and a coarse mode which has a bandwidth of 40 Hz.

The two 3-axis accelerometer packages incorporate six Kearfott 2401 accelerometers. The minimum resolution for each of these units is 11 microg's, and their bandwidth is 25 Hz.

The signals from these instruments are read by the COSMEC-I data gathering system and are processed by the HP9020 according to the particular control strategy under scrutiny. The control actuator signals are then transmitted to the APS as inputs to the dynamical system.

ORIGINAL PAGE IS
OF POOR QUALITY
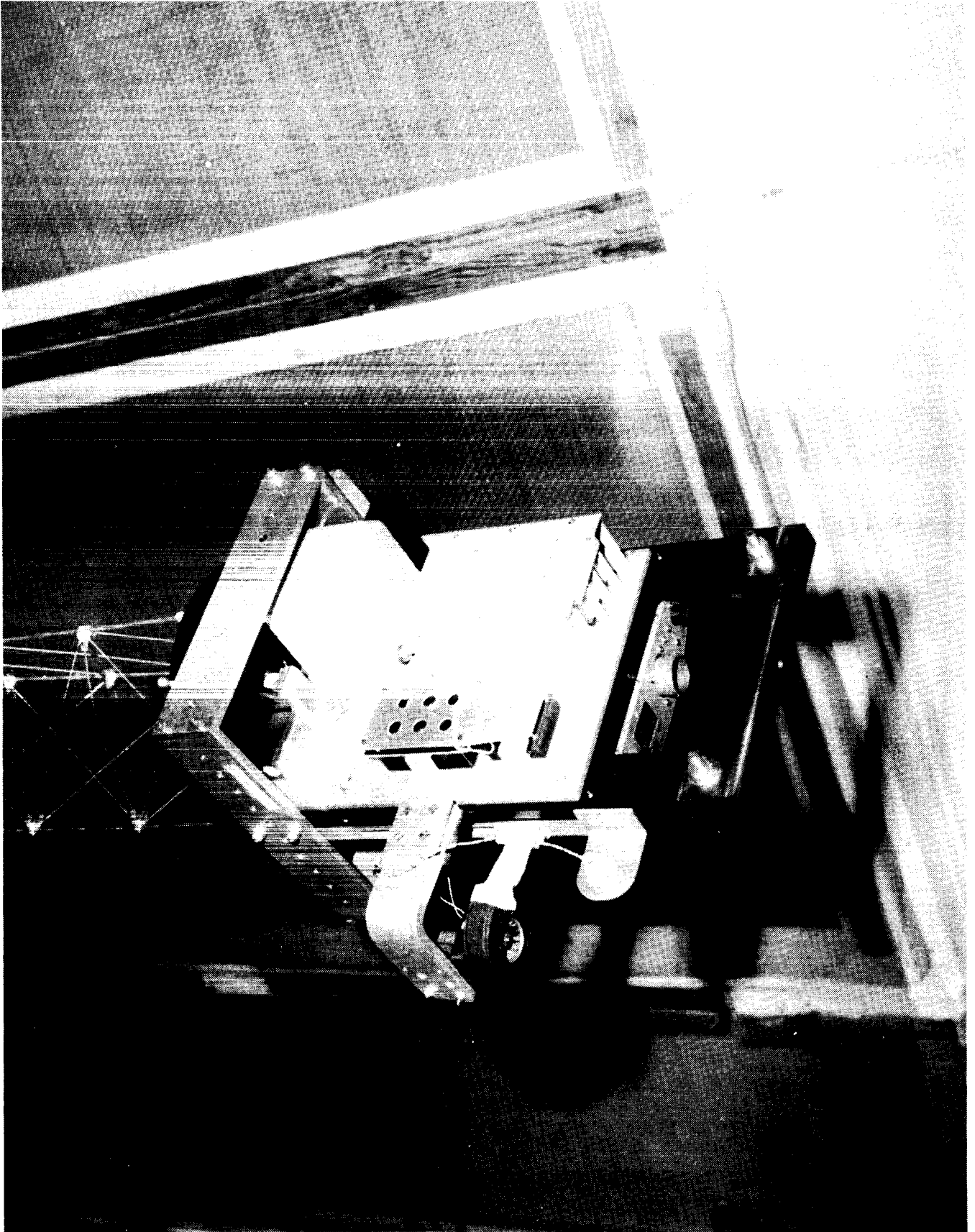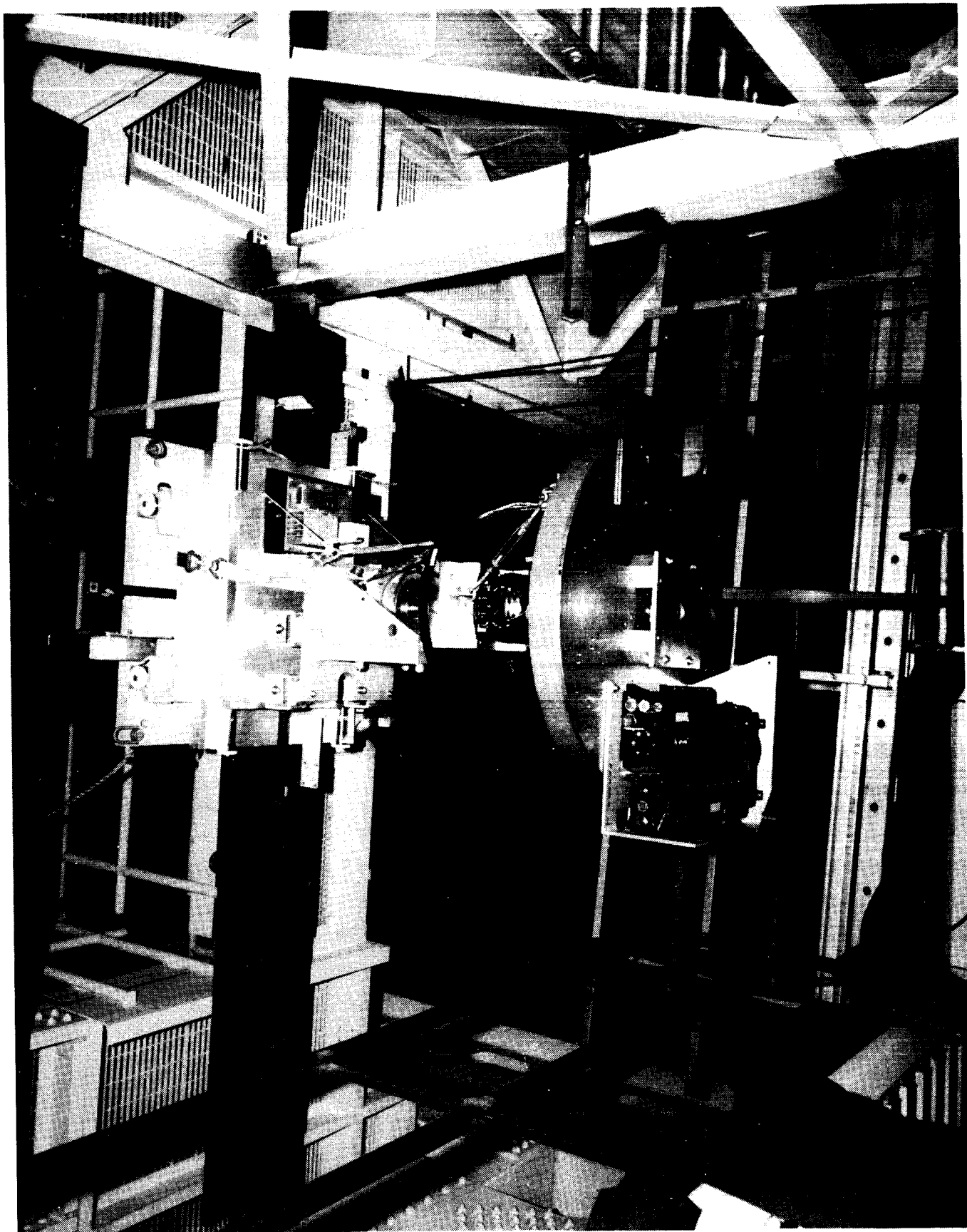
The signals from the sensors are utilized by the control computer and processed according to the control law under consideration. The COSMEC-I is the I/O computer which is used for data acquisition for the sensors and command output processing for the effectors. The COSMEC-I is a highly modified AIM-65 microcomputer system. It was developed originally by MSFC for the solar heating and cooling program. As a result, the development cost was not underwritten by the LSS/GTV facility.

The main purposes of the HP9020 control computer are to acquire the sensor inputs from the COSMEC-I, keep up with the laboratory coordinate system, process the control algorithm commands for the APS, and store control and sensor data for post-processing. The COSMEC-I and the HP9020 performs these tasks with twelve sensor inputs and three torque outputs, while maintaining a 50 Hz sampling rate. With the addition of the ANALOGIC array processor for the HP9020, the computational efficiency will increase by twenty-fold.
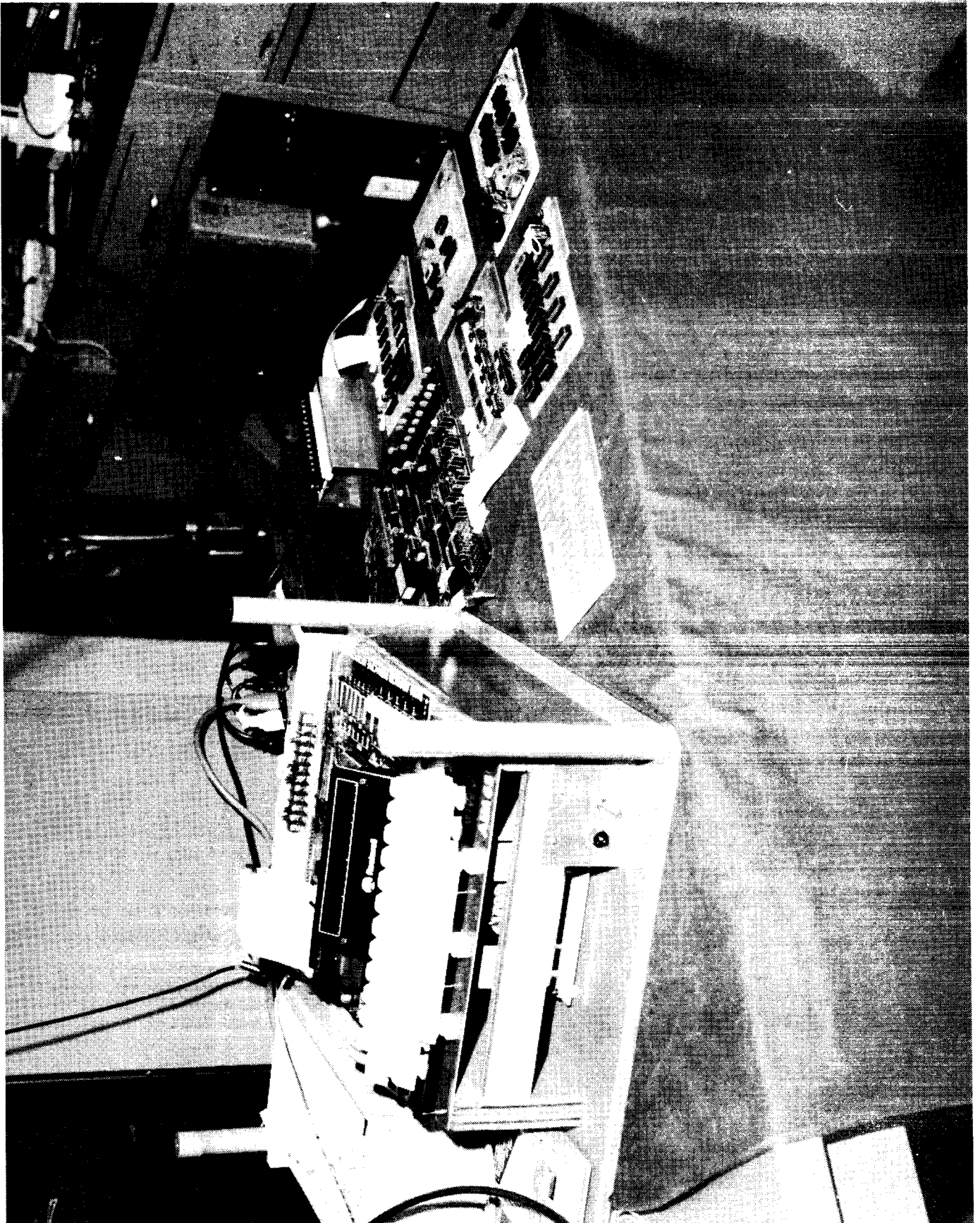
The test structure is mounted to the payload mounting plate of an Angular Pointing System (APS). The APS provides the control inputs for the initial configuration system and the cruciform-modified system. The APS actuators are the Advanced Gimbal System engineering model, produced by Sperry for the Spacelab program, and a third (roll) gimbal designed and built inhouse (as were the amplifiers used to drive the gimbal torquers). The roll gimbal, serving the vertical axis, is suspended by an air bearing which requires approximately 85 psi to operate. The roll gimbal provides a means of rotating the entire system to produce different test scenarios. The air bearing is connected to a Base Excitation Table (BET) which is free to translate in two directions. This actuator assembly setup, with its low friction torques, permits control in three angular directions. With the added roll gimbal, the test article can be rotated about its center line so that different test setups can be achieved.

In the initial research and technology task, the effectors for the LSS/GTV control system are three torque motors which are capable of providing control torques about three axes. The bottom two gimbals can generate up to 51 N-M of torque, and the roll or azimuth gimbal can generate up to 10 N-M of torque. The bandwidth limitation for all three gimbals is 100 Hz. The APS amplifiers receive torque commands from the COSMEC-1 digital processor in the form of analog inputs over the range of -10 to +10 volts. This saturation represents the current limit of 27 amps which is built into the APS servo amplifiers. Because the APS servo amplifier outputs a current which is proportional to torque, the control law algorithm was designed to produce torque command signals. The gimbal torquers are shown on the facing page.
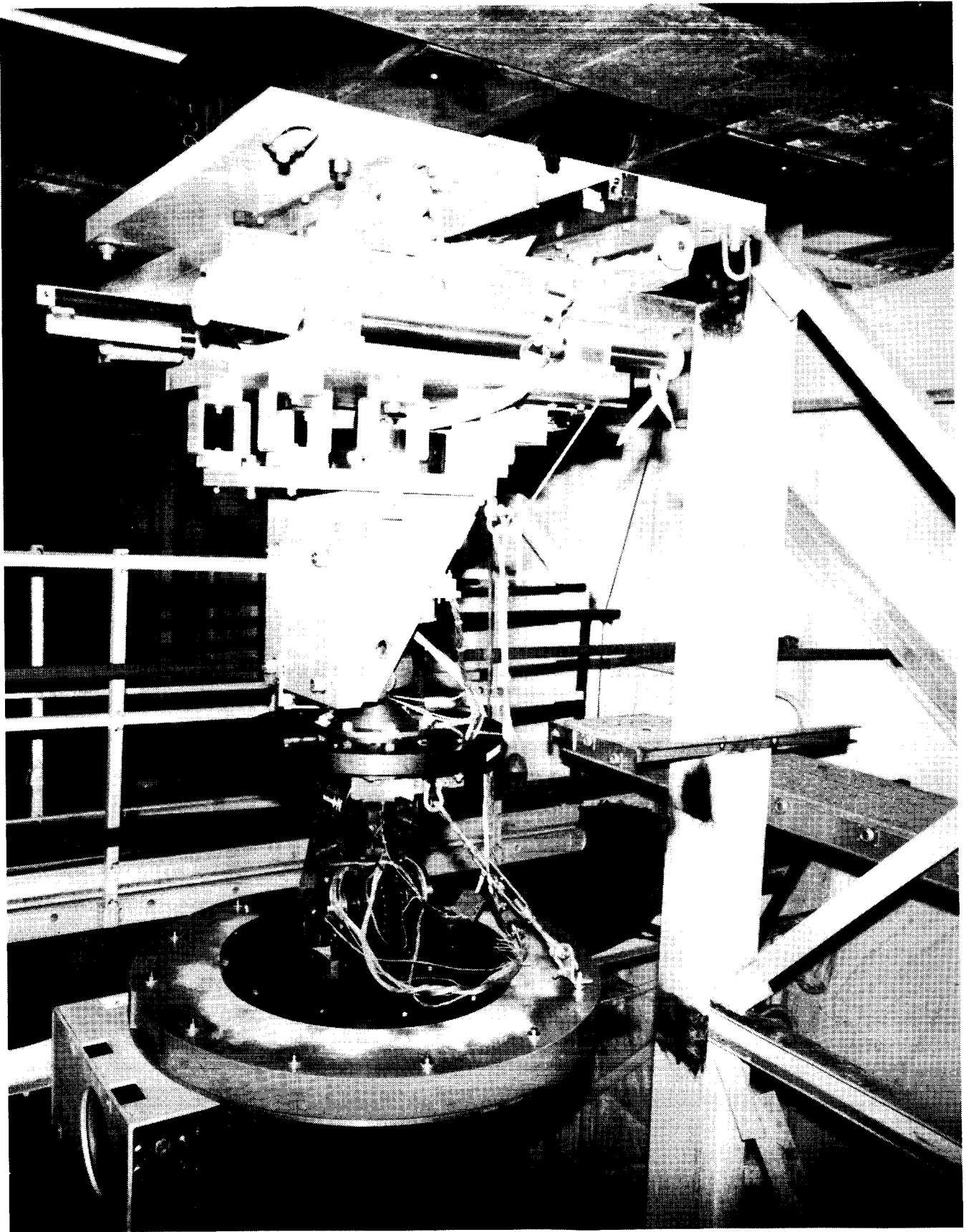
All of the GTV configurations need a device to excite the system in a consistent manner so that the effectiveness of the different control methodologies can be determined. Initially, these disturbances will represent either an astronaut pushoff, or a Reaction Control System thruster firing, or a free flyer disturbance. The Base Excitation Table (BET) which is attached to the building support structure, is shown on the facing page. It provides a means of producing such disturbance inputs. The BET is comprised of signal generators (deterministic or random noise), DC conditioning amplifiers, hydraulic servo controllers, and an oscillograph. The DC conditioning amplifiers are used to scale the signal generator while the signal conditioners are used to condition the electronic deflection indicator motion monitors for display. The oscillograph is used for recording the actual motion of the BET.

The precise motion of the BET is obtained by supplying a commanded voltage input to the BET servo control system. The BET movements are monitored by the directional feedback electronic deflection indicators which are fed back to the servo controllers. The servo controllers compare the commanded input voltage to the electronic deflection indicators and automatically adjust the position of the BET. The closed loop controller allows any type of BET movement within the frequency limitations of the hydraulic system.
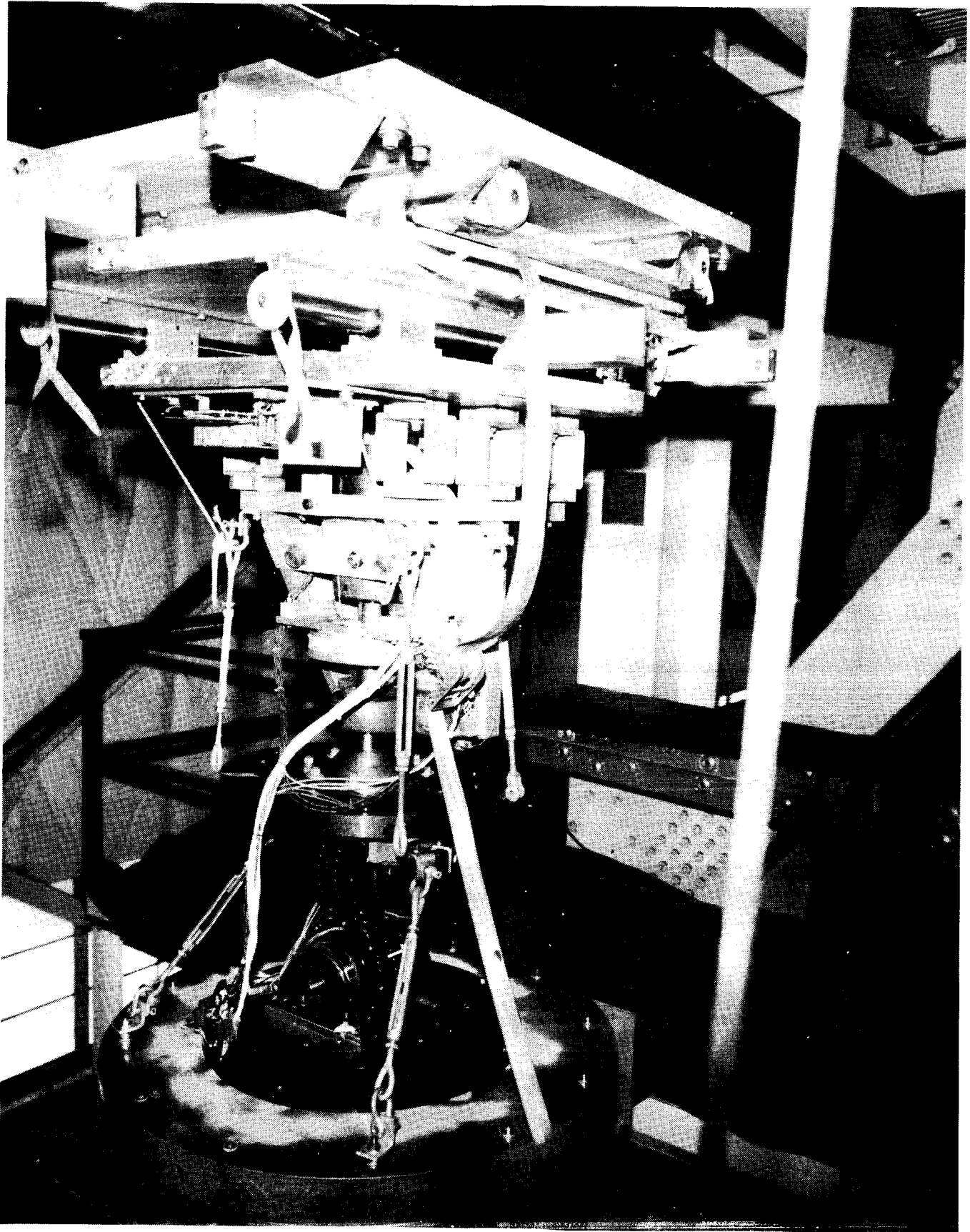
One of the important aspects of the LSS/GTV is to verify the analytical model of the test article. The procedure is to describe the structure mathematically as well as possible, then perform structural tests on the test article, and finally to factor these results into the mathematical model.

One of several modeling efforts included the APS, BET, and instrument packages. This model was used as an aid in conducting the modal test on the structure in this configuration. Again, the test data were used to refine the corresponding structural model. The table, in the upper facing page, provides the corresponding synopsis of the modal frequencies as predicted pre-test, measured, and "tuned." Turning was accomplished by varying the inertial properties which were poorly known and the bending and torsional stiffness which change with the different gravity loading in this configuration. Examination of the percentage errors in table previously mentioned shows the refinement of the model.

The modeling was then expanded to include the cruciform structure at the ASTROMAST tip which was added to obtain more LSS-like pathologies, i.e., closely spaced modal frequencies. The "model-test-tune" procedure described in the previous paragraph was carried out for this configuration in order to produce a high fidelity model of the LSS/GTV experiment structure. The modal frequencies and damping for the two previous measured models are shown in bottom facing page table. The results described as "local modes," in this table primarily involve deformation of the cruciform arms.

The last modal test that was performed was to determine the effects of connecting cables to the various components on the test structure. All the cabling was stripped off the stiff external wrapping and sufficient length and coiling was provided to reduce any cabling effect on the structural dynamics. The acquired test data conclusion is that no significant modal shifts occurred when the cables were connected.

69

TABLE 1. Structural Natural Frequencies Without Cruciform

MODE #	DESCRIPTION	ORIGINAL ANALYTICAL	MEASURED	Δ(%)	TUNED ANALYTICAL	Δ(%)
1	RB (xy-plane)	0.00				
2	RB (yz-plane)	0.00				
3	RB (torsion)	0.00				
4	1st Bend (yz-plane)	0.14	0.14	0.0	0.14	0
5	1st Bend (xz-plane)	0.15	0.15	0.0	0.15	0
6	1st Torsion	1.18	0.99	19.0	1.02	3
7	2d Bend (xz-plane)	1.27	1.33	4.5	1.29	3
8	2d Bend (yz-plane)	1.40	1.80	22.0	1.64	9
9	3d Bend (xz-plane)	3.02	3.30	8.5	3.34	1
10	3d Bend (yz-plane)	3.91	3.94	0.0	4.31	11
11	4th Bend (xz-plane)	6.69	8.06	17.0	8.10	0
12	4th Bend (yz-plane)	7.03	8.13	14.0	8.21	1
13	2d Torsion	8.42	9.60	12.0	9.61	0

TABLE 2. Summary of LSS/GTV Modal Test Results

Description	W/o Cruciform			W/Cruciform		
System Mode	Freq Hz	% Damp	TSS	Freq Hz	% Damp	TSS
1st Bndg (x)	0.144	0.35	002	No Data	No Data	N/A
" (y)	No Data	No Data	N/A	No Data	No Data	N/A
2nd Bndg (x)	1.33	1.33	002B	1.36	1.9	005
" (y)	1.83	1.88	002A	1.83	1.9	004
3rd Bndg (x)	3.38	1.76	002B	3.24	1.7	005
" (y)	3.9	2.2	002A	3.74	2.0	004
4th Bndg (x)	8.06	2.9	003	6.36	1.1	005
" (y)	8.13	4.5	003	6.67	1.85	004
1st Torsion	0.991	0.44	001	0.377	0.56	006
2nd Torsion	9.6	1.1	001	3.02	0.34	007
Local Modes						
Y Bndg	N/A	N/A	N/A	0.38	0.53	008
"	"	"	"	1.149	0.53	008
"	"	"	"	6.418	0.70	008
"	"	"	"	6.876	0.44	008
"	"	"	"	7.326	0.415	008
"	"	"	"	7.706	0.156	008
Z Bndg	N/A	N/A	N/A	1.143	0.79	008
"	"	"	"	6.756	1.09	008
"	"	"	"	7.062	1.23	008

The original test configuration had all the desired LSS characteristics except the densely-packed vibrational modes. Several design configuration changes were considered so that this important missing structural constraint could be implemented. The configuration change which could effect the densely-packed modes was the addition of a cruciform structure at the tip of the ASTROMAST. To a degree, the new configuration approximates an antenna or a radar system.
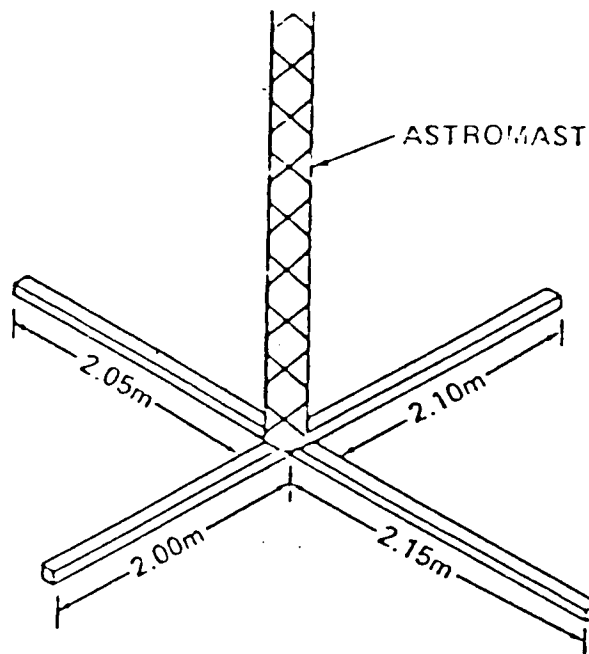
THE CRUCIFORM STRUCTURE

FOR SIMULATION PURPOSES, THE 4 ALUMINUM BARS WERE PLACED AT THE TIP OF THE BEAM, IN ACTUALITY, THEY ARE TO BE LOCATED AT THE END OF THE TIP BRACKET. THE RODS VARY IN LENGTH FROM 2.00m TO 2.15m. THEY ALL HAVE A CONSTANT CROSS-SECTION OF 1/4" x 1/4".

| MODE #	FREQ. (Hz)
1–5	0.0 (RIGID BODY)
6	.382
7	1.052
8	1.149
9	1.154
10	1.157
11	1.219
12	1.254
13	1.266
14	1.287
15	1.409
16	2.973
17	3.520
18	3.870

MODES, MODAL, FREQUENCIES FOR COMBINED STRUCTURE

The first test article is a spare Voyager ASTROMAST built by ASTRO Research, Inc. It was supplied to MSFC by the Jet Propulsion Laboratory (JPL). The ASTROMAST is extremely lighweight (about five pounds) and approximately 45 feet in length. It is constructed almost entirely of S-GLASS. It is of the type flown on the Solar Array Flight Experiment-I (SAFE-I).

When fully developed, the ASTROMAST exhibits a longitudinal twist of about 280°. This twist contributes to the coupling between the torsional and bending modes.

As previously stated, the second test article consists of the ASTROMAST with a cruciform attached to the tip. The cruciform structure, which is made of aluminum, weighs eight pounds and is shown on the facing page. The cruciform rods vary in length from 2.00m to 2.15m. They all have constant cross-section of 1/4" X 1/4".
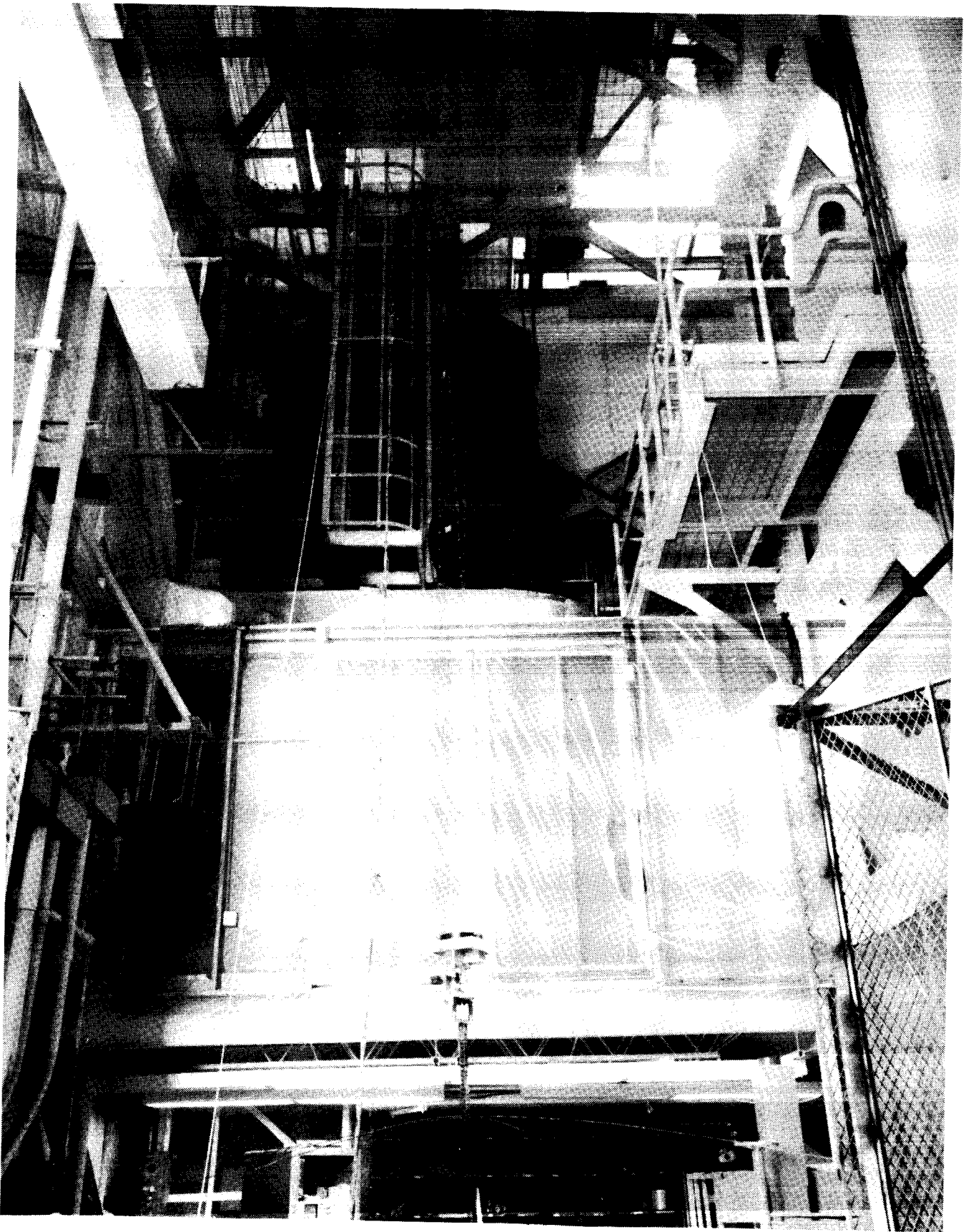
The initial control design for the Ground Facility for Large Space Structures Control Verification (GF/LSSCV) was a centralized control system. The initial centralized control system uses a triad of ATM rate gyros as sensors and the APS as the effectors. The closed loop block diagram is shown in the facing page viewgraph. The quaternions are input to filters which are used to "smooth" the position coordinates and derive a "smooth" rate. The position and rate are multiplied by constant gains to form the effector commands. The effector commands torque the APS gimbals so as to reduce the ATM rate gyro signals in an asymptotic manner. The generic control equations are also shown on the same facing page viewgraph.
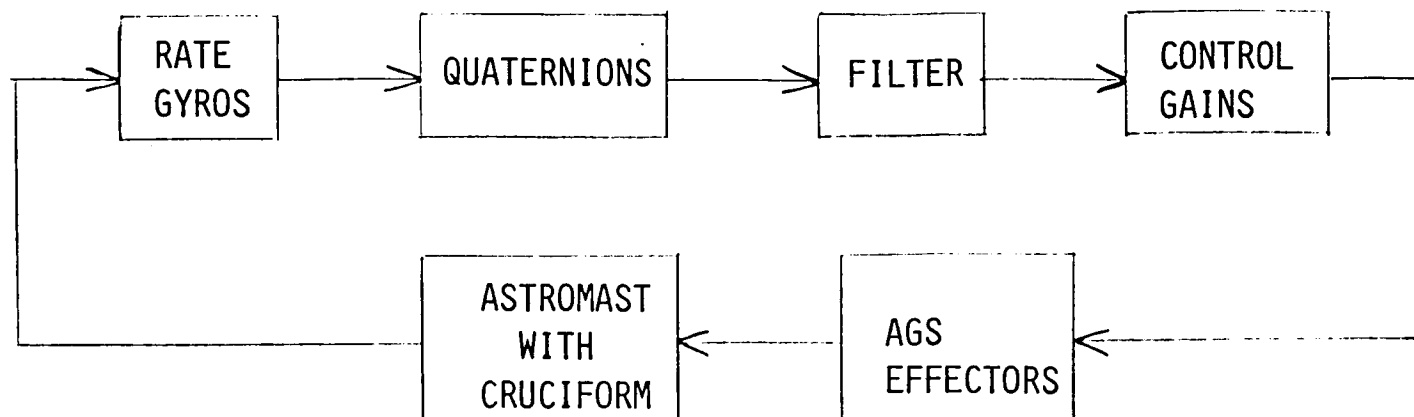
$$Z(I+1) = DZ(I) + EQ(I)$$

$$W(I) = GZ(I)$$

$$U(I) = K\ W(I)$$

WHERE $Q(I)$: 3X1   QUATERNION VECTOR AT THE I^{TH} CYCLE

                $Z(I)$: 6X1   FILTER STATE AT THE I^{TH} CYCLE

                $W(I)$: 6X1   FILTER OUTPUTS

                $U(I)$: 3X1   EFFECTOR COMMANDS

The modal control verification is tabularized on the facing page viewgraph. The table consists of the following: (1) axis (X,Y) see viewgraph 1 for axis identification, (2) open loop test giving modal frequency and damping, (3) analytic closed loop in terms of modal frequency and damping, and (4) closed loop tests which comprise modal frequency and damping.

The open loop test can be compared with the previous modal verification viewgraph. The open loop test was included with the modal control verification to show the amount of damping increase in both the analytical predictions and the actual test results. As can be seen from the table, the control system increases the damping in all of the modes that were tested. These results should not be too surprising. The pleasant results of the table are in the agreements in the analytically closed loop model and the test article. The worst error in frequency is 6.25% at 4.01 Hz and the worst error in damping is 60% at 0.139 Hz. Although the damping error is large, it is in the right direction i.e., more damping than predicted. Typical open and closed loop test plots are shown after the modal control verification table.

MODAL CONTROL VERIFICATION

AXIS X,Y	OPEN LOOP (T)		CLOSED LOOP (A)		. CLOSED LOOP (T)	
	Hz	ζ	Hz	ζ	Hz	ζ
X	0.138	0.0187	0.135	0.023	0.138	0.0567
Y	0.138	0.0187	0.135	0.023	0.138	0.029
X	0.1515	0.041	0.139	0.028	0.1515	0.064
Y	0.1515	0.0167	0.139	0.028	0.1515	0.0567
X	1.33	0.0233	1.38	0.0933	1.6	0.085
Y	1.33	0.0233	1.38	0.0933	1.33	0.11
X	1.66	0.0355	1.85	0.051	1.83	0.085
Y	1.66	0.0258	1.85	0.051	1.739	0.11
Y	3	0.01	3.04	0.096	3	0.045
X	3.75	0.032	4.01	0.066	4.25	0.065

T   IMPLIES TEST

A   IMPLIES ANALYTIC

Y BASE RATE GYRO
Y TORQUER

X BASE RATE GYRO
X TORQUER

79
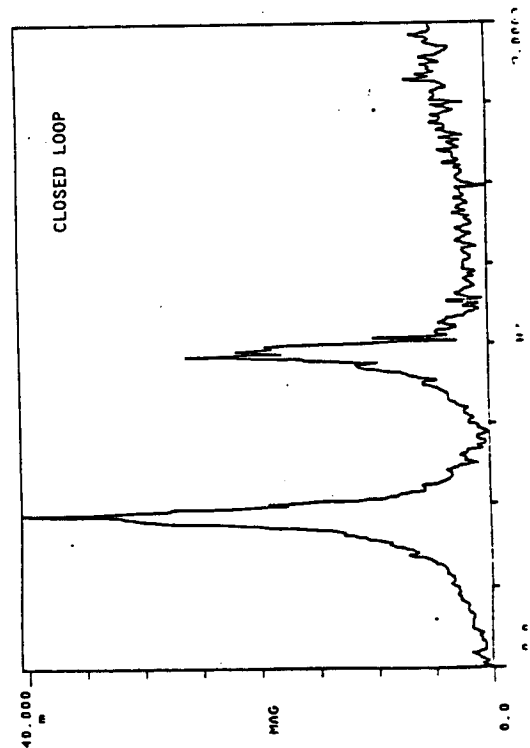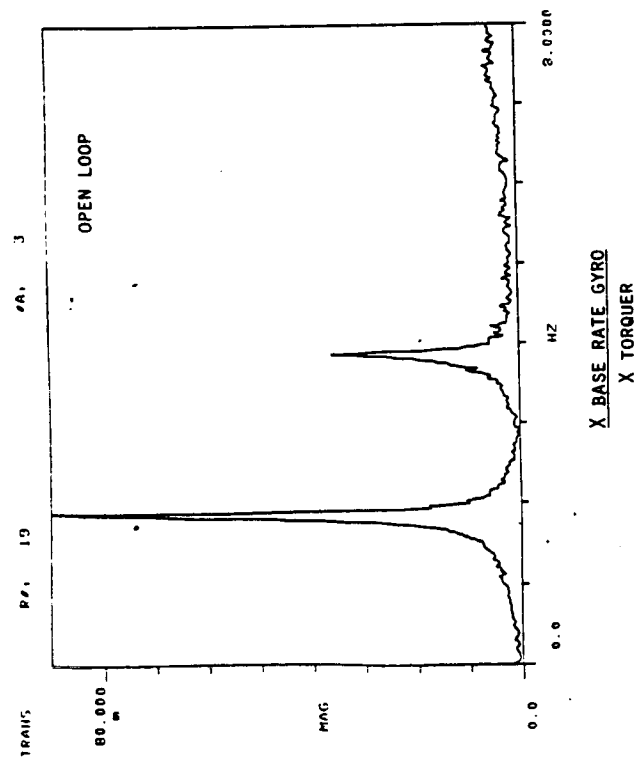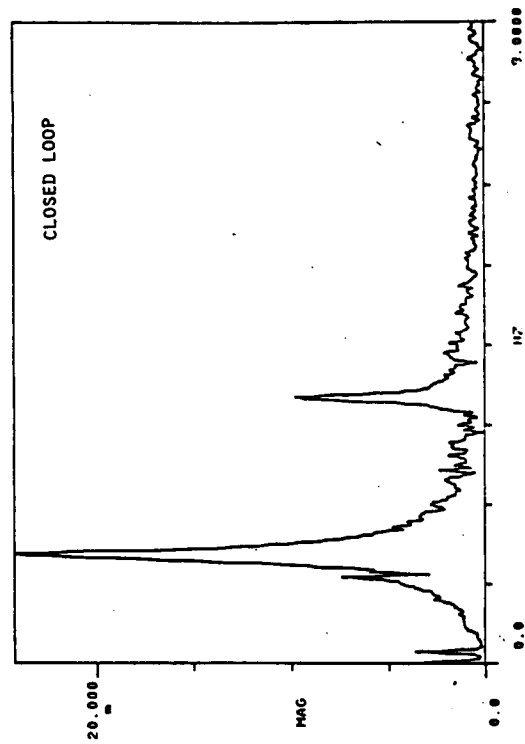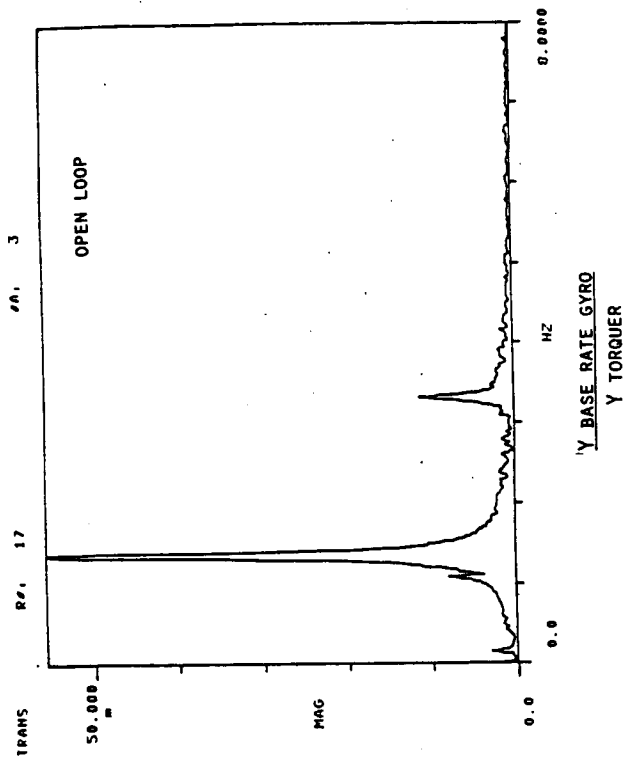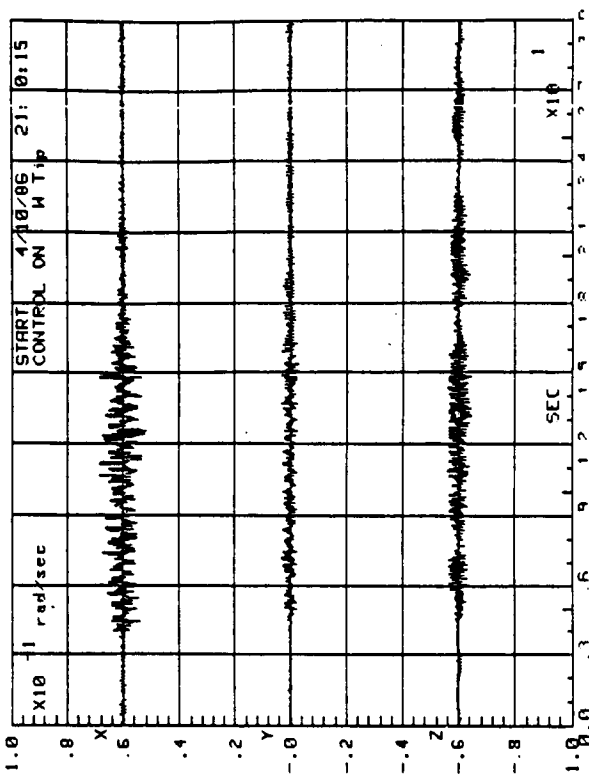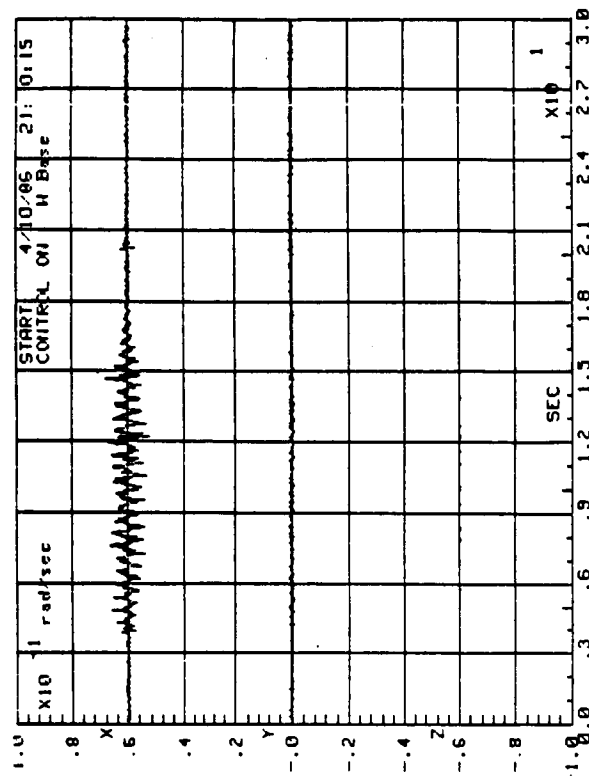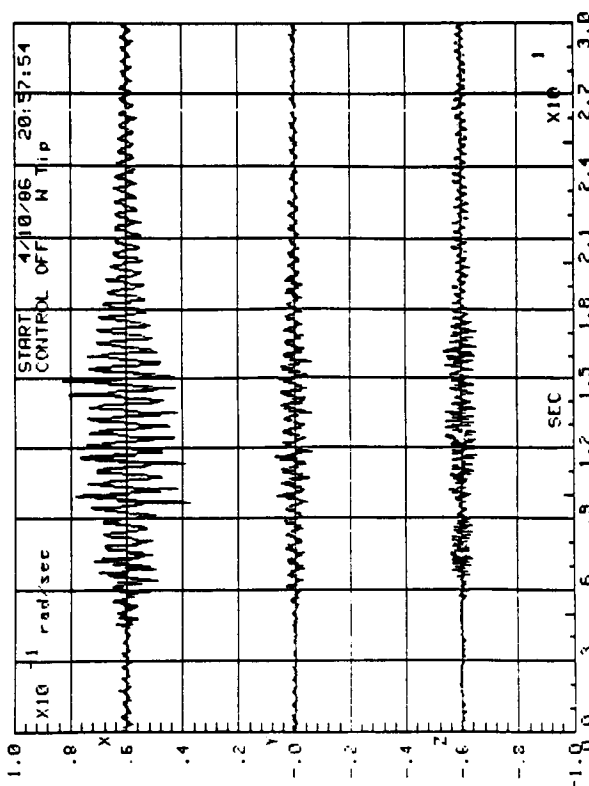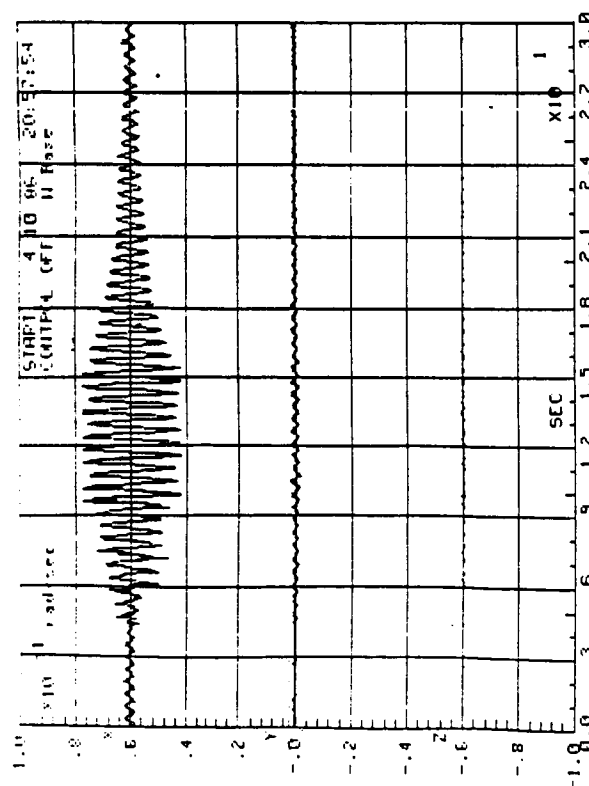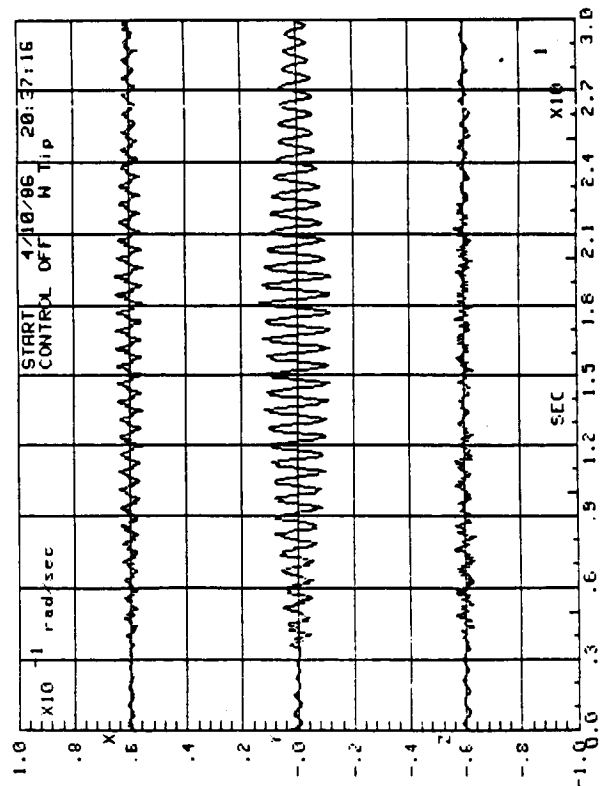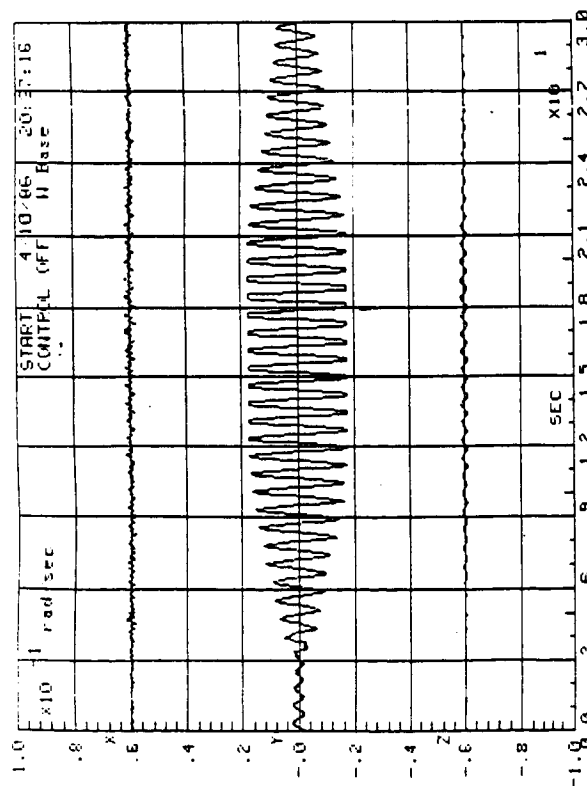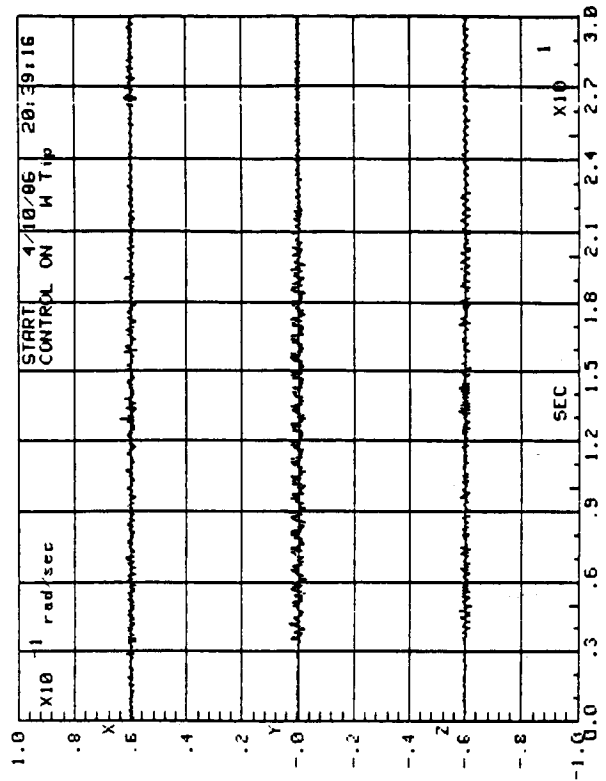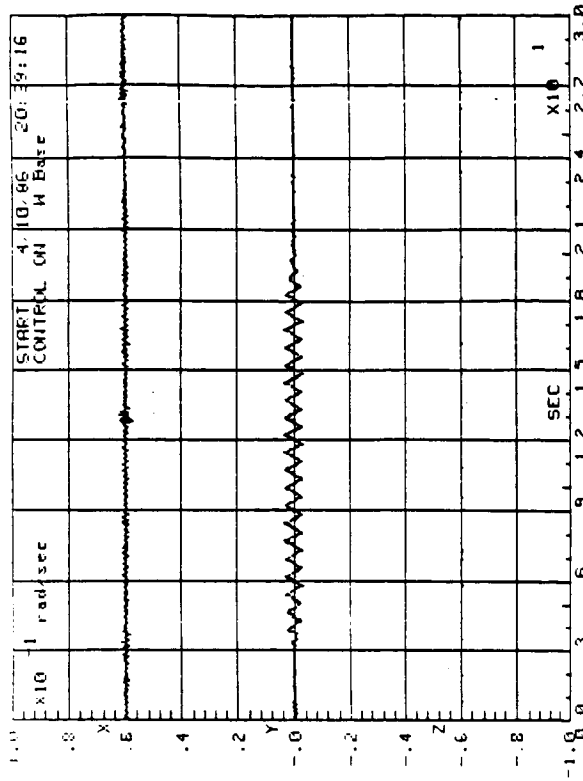
A future configuration change will be the addition of a three meter offset antenna to the ASTROMAST tip and an antenna feed located on the payload mounting plate. In addition, the Vibrational Control of Space Structures (VCOSS)-II Linear Momentum Exchange Devices will be placed on the ASTROMAST at two different locations. These additions will facilitate both decentralized and distributive control methodologies. Also, a bi-directional linear thruster system is planned for location at the ASTROMAST tip so that active vibration suppression can be tested using these thrusters. The integration of the previously mentioned LSS/GTV modifications will provide adequate sensors, effectors, and LSS dynamic pathologies so that the test facility can encompass many facets of dynamics and control verification.

LIGHT PATH

3 METER ANTENNA
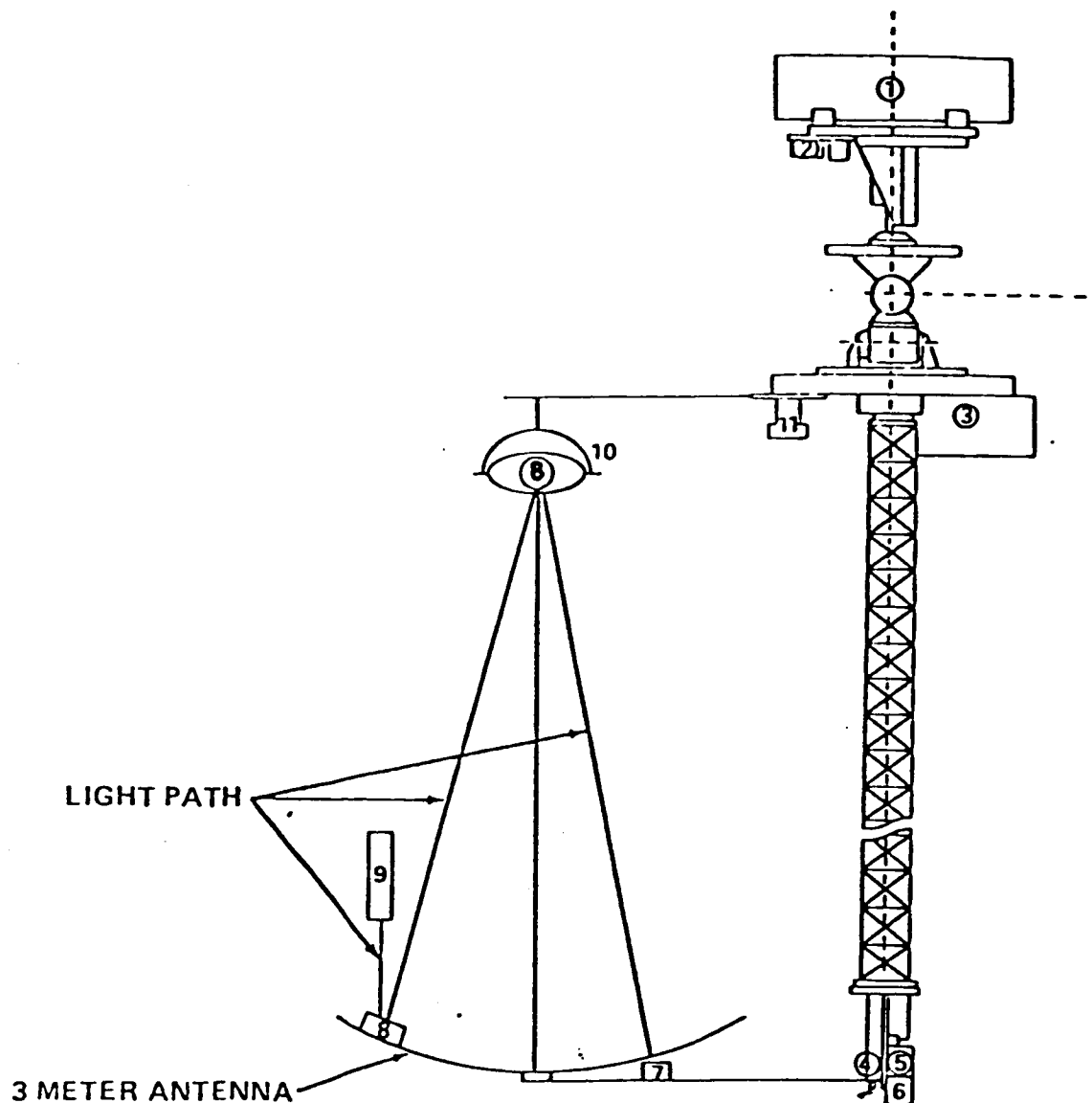
FIGURE   FUTURE LSS/GTV SETUP

1. SHAKE TABLE
2. 3 AXIS BASE ACCELEROMETERS
3. 3 AXIS BASE RATE GYROS
4. 3 AXIS TIP RATE GYROS
5. 3 AXIS TIP ACCELEROMETERS
6. BIDIRECTIONAL THRUSTERS

7. OPTICAL DETECTOR
8. REFLECTORS
9. LASER
10. 2 GIMBAL SYSTEM
11. N_2 BOTTLES

IDENTIFICATION OF LARGE SPACE STRUCTURES:

A STATE-OF-PRACTICE REPORT.

ASCE TASK COMMITTEE ON
IDENTIFICATION OF LARGE STRUCTURES
IN SPACE.

COMMITTEE MEMBERS

Prof. M. Kamat, Ga. Tech., Organizer
Prof. E. D. Denman, U. Houston.
Dr. T. K. Hasselman, Eng. Mech. Assoc.
Dr. J. N. Juang, NASA Langley Res. Ctr.
Prof. J. L. Junkins, Tex. A&M U.
Prof. C. T. Sun, Purdue U.
Prof. F. Udwadia, U. Sou. Cal.
Dr. V. B. Venkayya, USAF., Wright-Patterson AFB.

Lt. E. Dale, USAF., Edwards AFB, Monitor
Mr. E. Kippel, ASCE NY, Monitor

87
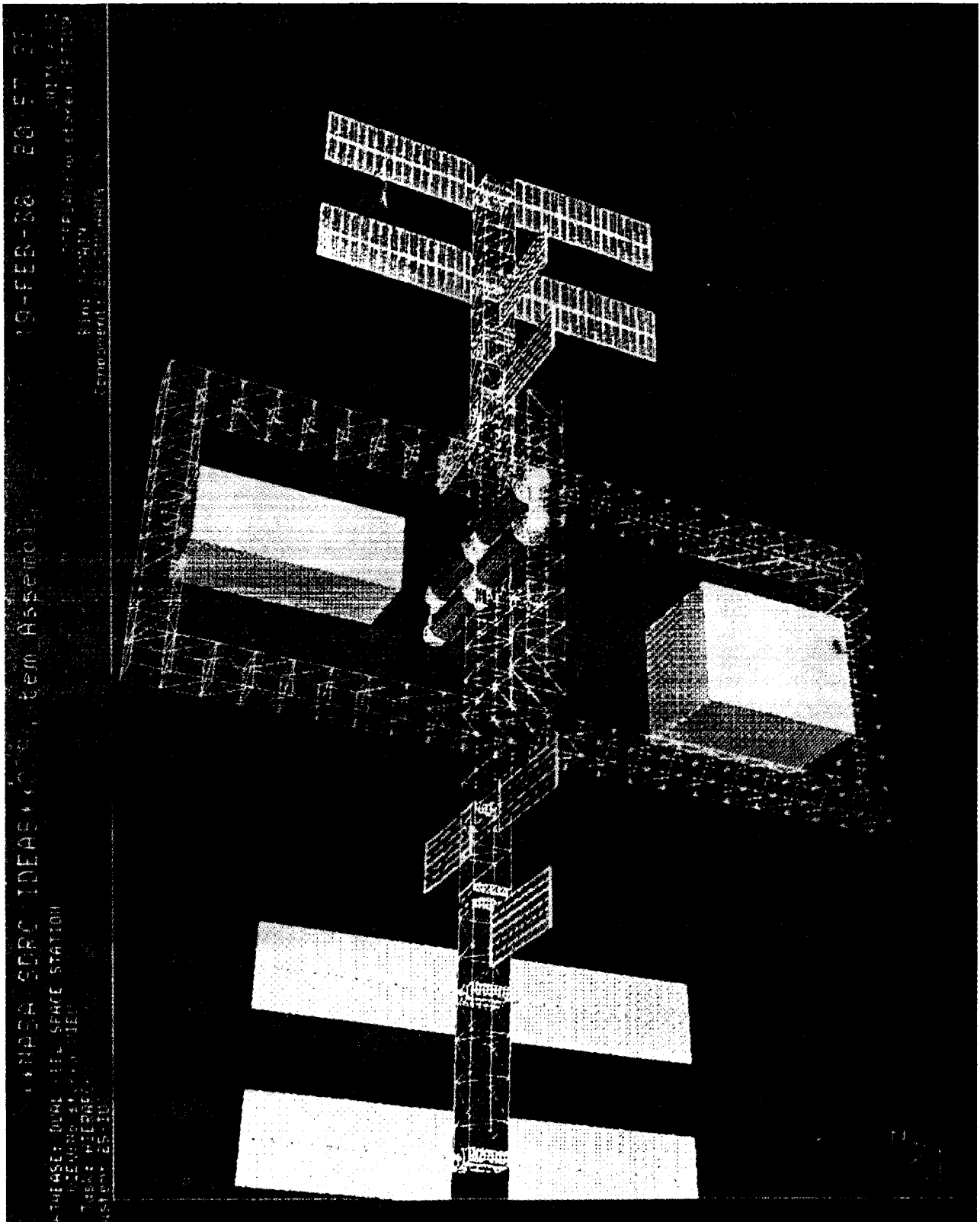
SIMPLIFIED ILLUSTRATION OF THE IDENTIFICATION PROCESS

(A) SCHEMATIC FLOW DIAGRAM

INPUT → SYSTEM → OUTPUT

SYSTEM IDENTIFICATION

(B) LOGICAL FLOW DIAGRAM

PHYSICAL SYSTEM → PHYSICAL EXPERIMENT → SYSTEM IDENT. → IDENT. MODEL
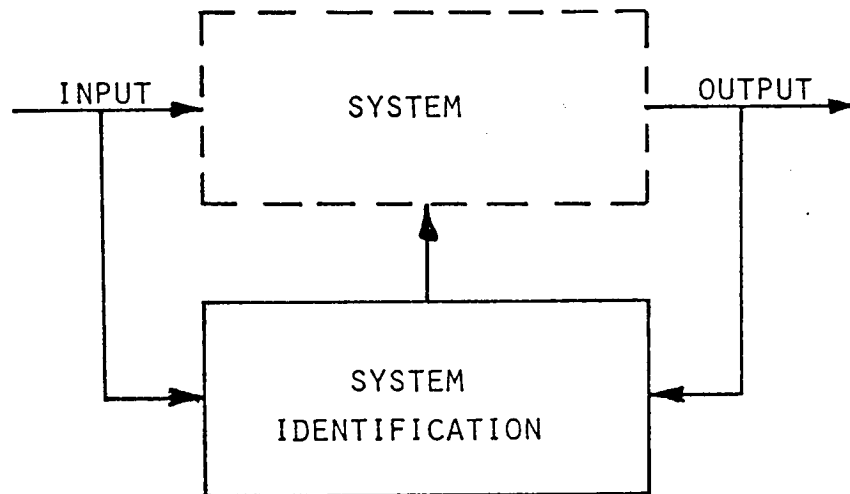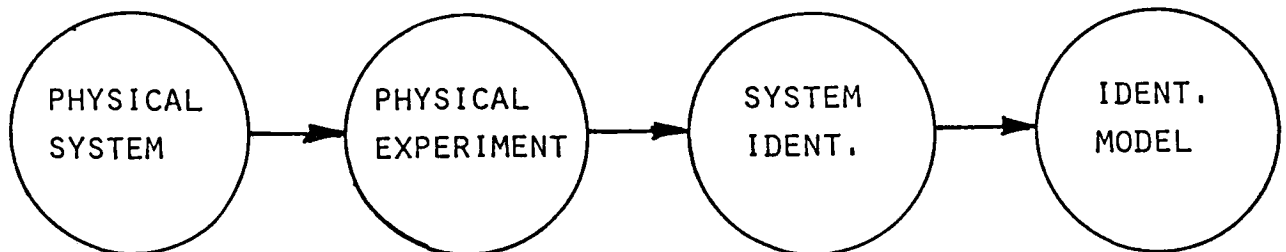
LOGICAL FLOW DIAGRAM ILLUSTRATING
IDENTIFICATION PROCESS FOR LARGE SPACE STRUCTURES
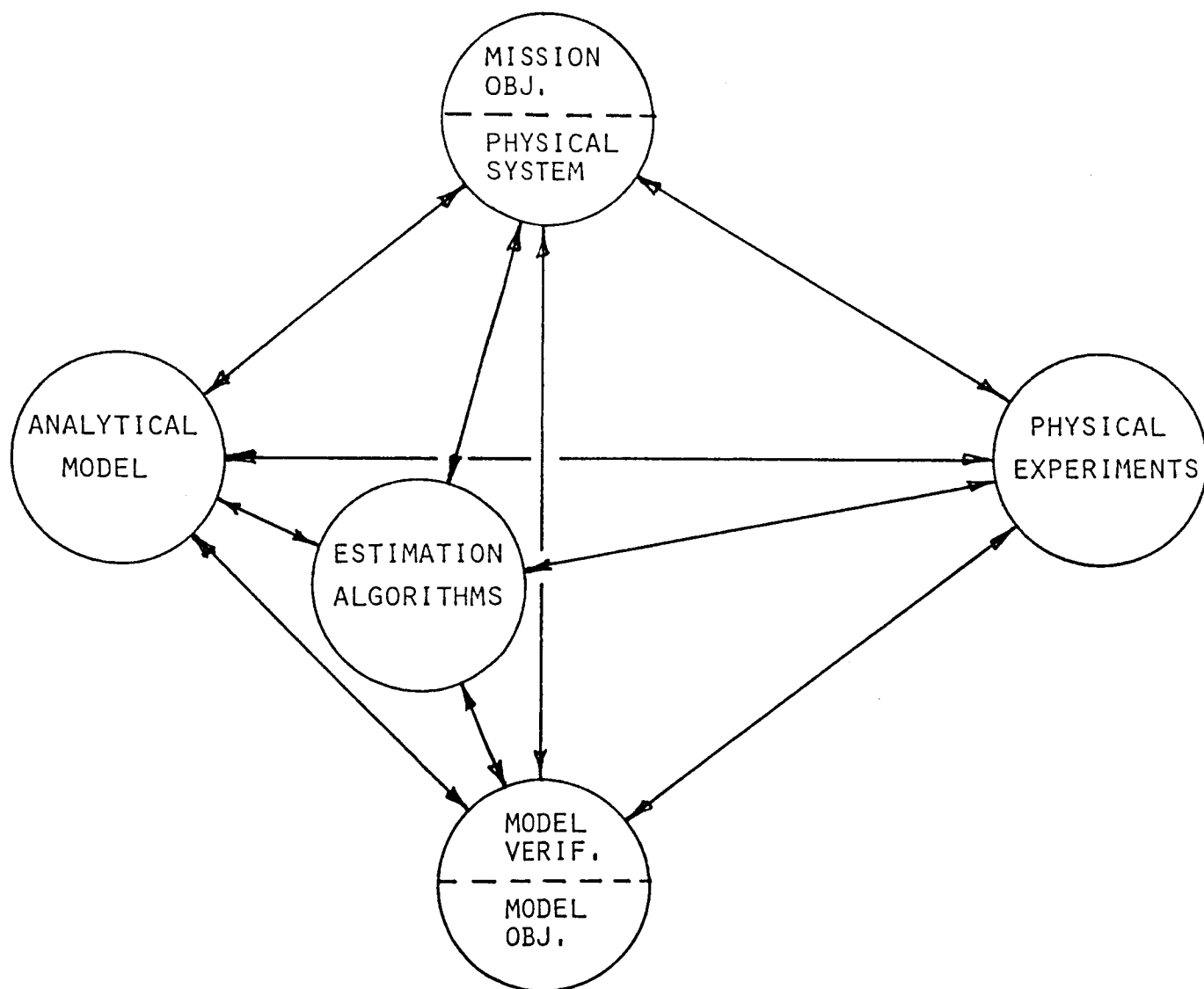
Task Definition:

I. Structure Model Definition.

Discrete Spatial Structure Model Variables.

$x(t)$=Structure node displacement $(n \times 1$ vector$)$

$y(t)$=Measured displacement $(l \times 1$ vector$)$

$f(t)$=Applied force $(m \times 1$ vector$)$

B=Force actuator matrix $(B \in \mathcal{R}^{n \times m})$

C=Displacement sensor matrix $(C \in \mathcal{R}^{l \times n})$

D=Damping matrix $(D \in \mathcal{R}^{n \times n})$

K=Stiffness matrix $(K \in \mathcal{R}^{n \times n})$

M=Mass matrix $(M \in \mathcal{R}^{n \times n})$

A. Matrix polynomial formulation.

Node Displacement Equation.

$$M \frac{d^2 x(t)}{dt^2} + D \frac{dx(t)}{dt} + K\, x(t) \;=\; B\, f(t)$$

Measurement Equation.

$$y(t) \;=\; C\, x(t)$$

B. State variable formulation.

Node displacements and velocities.

$$\begin{bmatrix} \dot{x}(t) \\ \ddot{x}(t) \end{bmatrix} = \begin{bmatrix} 0 & I \\ -M^{-1}K & -M^{-1}D \end{bmatrix} \begin{bmatrix} x(t) \\ \dot{x}(t) \end{bmatrix} + \begin{bmatrix} 0 \\ M^{-1}Bf(t) \end{bmatrix}$$

$$z(t) = \begin{bmatrix} x(t) \\ \dot{x}(t) \end{bmatrix}$$

$$\dot{z}(t) = Az(t) + Bf(t)$$

Measurement equation.

$$y(t) = Cz(t)$$

C-2

92

Controllability and Observability.

Controllability.

System must be controllable for the 2n modes to be excited.

Controllability matrix: $Q_c = \begin{bmatrix} B & AB & A^2B & \ldots \end{bmatrix}$

Q_c must span the 2n algebraic space

Observability.

System must be observable for the 2n modes to be measured.

Observability matrix: $Q_o = \begin{bmatrix} C^T & A^TC^T & (A^T)^2C^T & \ldots \end{bmatrix}$

Q_o must span the 2n algebraic space.

II. Identification of Large Space Structure on Orbit.

    A. Identify mass, damping and stiffness Matrices.

    B. Identify mechanical properties:

        1. Shear rigidity.

        2. Bending rigidity.

        3. Mass per unit length.

        4. Inertia of structure.

III. Verification and Validation of Model.

    A. Comparsion to mathematical model.

    B. Comparsion to ground testing data.

    C. Comparsion of structure dynamics to simulations.

    D. Comparsion of dynamics with structure control.

Modelling Errors, and Uncertainities.

I. Modelling errors.

    A. Exact knowledge of properties of materials.

    B. Order of the structure model.

    C. Joint mechanics.

    D. Nonlinearities.

    E. Lack of full structure ground testing.

II. Environment.

    A. Radiation, thermal effects, etc. on structure.

    B. Change of mechanical properties of materials.

Noise, Computations, and Data Collection.

I. Noise.

 A. Uncertain forces due to environment.

 B. Measurement errors due to finite word length.

 C. Noise in data transmission.

II. Computations.

 A. Limitation of algorithms for identification.

 B. Computational errors, i. e. finite word length.

III. Data Collection.

 A. Frequency response of sensors and actuators.

 B. Inaccurate location of sensors and actuators.

 C. Finite word length of A/D convertors in data collection.

CONTENTS

97

Tuesday, April 22, 1986

SESSION 2

(Concurrent Sessions on Structures and Control)

Structures Session 2A - Tulon Bullock, Chairman

Active Damping Experiments	G. C. Horner, LaRC
A General Method for Dynamic Analysis of Structures	R. C. Engels, UTSI
Dynamic Behavior of a Large Flexible Space Station During Space Shuttle Orbiter Docking	N. G. Fitz-Coy and J. E. Cochran, Jr., Auburn Univ.
Transient Response for Interaction of Two Dynamic Bodies	A. Prabhakar and L. G. Palermo, MMC

Structures Session 2B - Ronald E. Jewell, Chairman

Mover II - A Computer Program for Model Verification of Dynamic Systems	J. D. Chrostowski, T. K. Hasselman, Eng. Mech. Assoc.
Considerations in the Design and Development of a Space Station Scale Model	P. E. McGowan, LaRC
Verification of Large Beam-Type Space Structures	C. G. Shih, J. C. Chen J. A. Garba, JPL
Verification of Flexible Structures by Ground Test	B. K. Wada and C. P. Kuo, JPL

MICROPROCESSOR CONTROLLED PROOF-MASS ACTUATOR

BY

GARNETT C. HORNER
STRUCTURAL DYNAMICS BRANCH
LANGLEY RESEARCH CENTER
HAMPTON, VA 23665

MICROPROCESSOR CONTROLLED PROOF-MASS ACTUATOR

The objective of the microprocessor controlled proof-mass actuator is to develop the capability to mount a small programmable device on laboratory models. This capability will allow research in the active control of flexible structures.

The approach in developing the actuator will be to mount all components as a single unit. All sensors, electronic and control devices will be mounted with the actuator. The goal for the force output capability of the actuator will be one pound force.

MICROPROCESSOR CONTROLLED PROOF-MASS ACTUATOR

OBJECTIVE:

TO DEVELOP A SMALL PROGRAMMABLE ACTUATOR THAT CAN BE MOUNTED ON LABORTORY MODELS FOR THE PURPOSE OF CONDUCTING CONTROL RESEARCH.

APPROACH:

TO MOUNT AS A UNIT:

- A ONE POUND FORCE ACTUATOR

- A MICROCONTROLLER CIRCUIT

- A POWER AMPLIFIER

- COLOCATED ACCELEROMETER

PROOF-MASS ACTUATOR

The proof-mass actuator consists of a cylindrical section
approximately 3 inches in length. Internal to this section is
the proof-mass which is a small cylinder of magnet iron. The
proof-mass rides on linear ball bearings and contains two small
samarium cobalt `donut' magnets. There is also a wound copper
coil that energizes the proof-mass. The electerical leads to the
coil can be seen on the extreme right. The small hub on the
right is the structural attachment point.

The two smaller cylindrical sections protruding to the left of
the actuator are the colocated sensors. The longer of the two is
a linear variable differential transformer (LVDT) that measures
the position of the proof-mass. The smaller cylinder is an
accelerometer that measures acceleration of the structure.

PROOF-MASS ACTUATOR
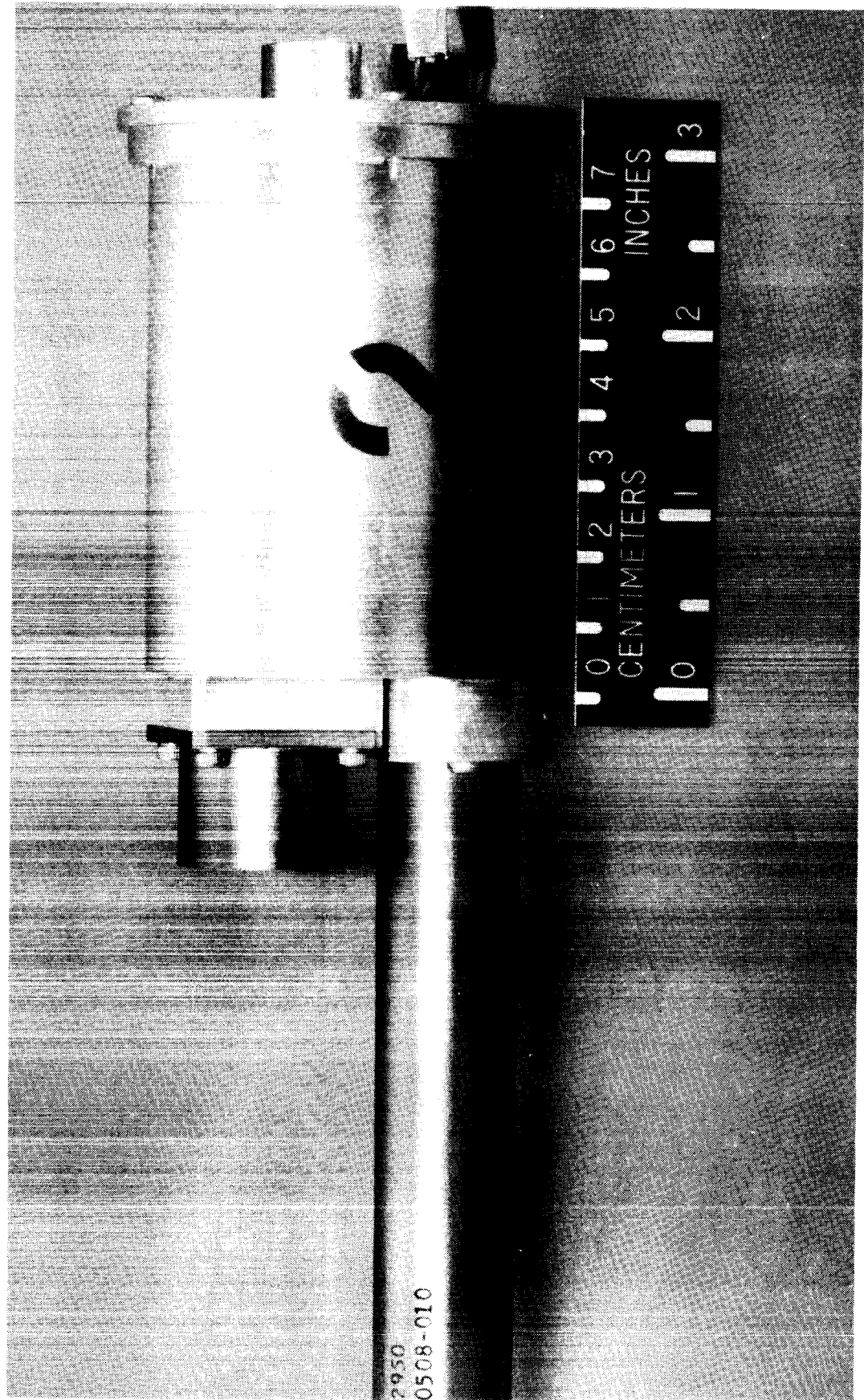
MICROPROCESSOR CONTROLLER BOARD

The microprocessor controller board contains three primary components. The analog-to-digital converter (ADC) and a switching circuit that selects one of three analog inputs. The output of the ADC connects to two of the ports of the microprocessor which is an Intel 8751. The output of the 8751 goes to a digital-to-analog converter (DAC) which in turn connects to the input of the power amplifer.

The 8751 has erasable/programmable memory which contains the program that accepts the analog inputs and constructs the output command. The output command controls the position of the proof-mass to produce a force of a prescribed magnitude and phase.

MICROPROCESSOR CONTROLLER BOARD
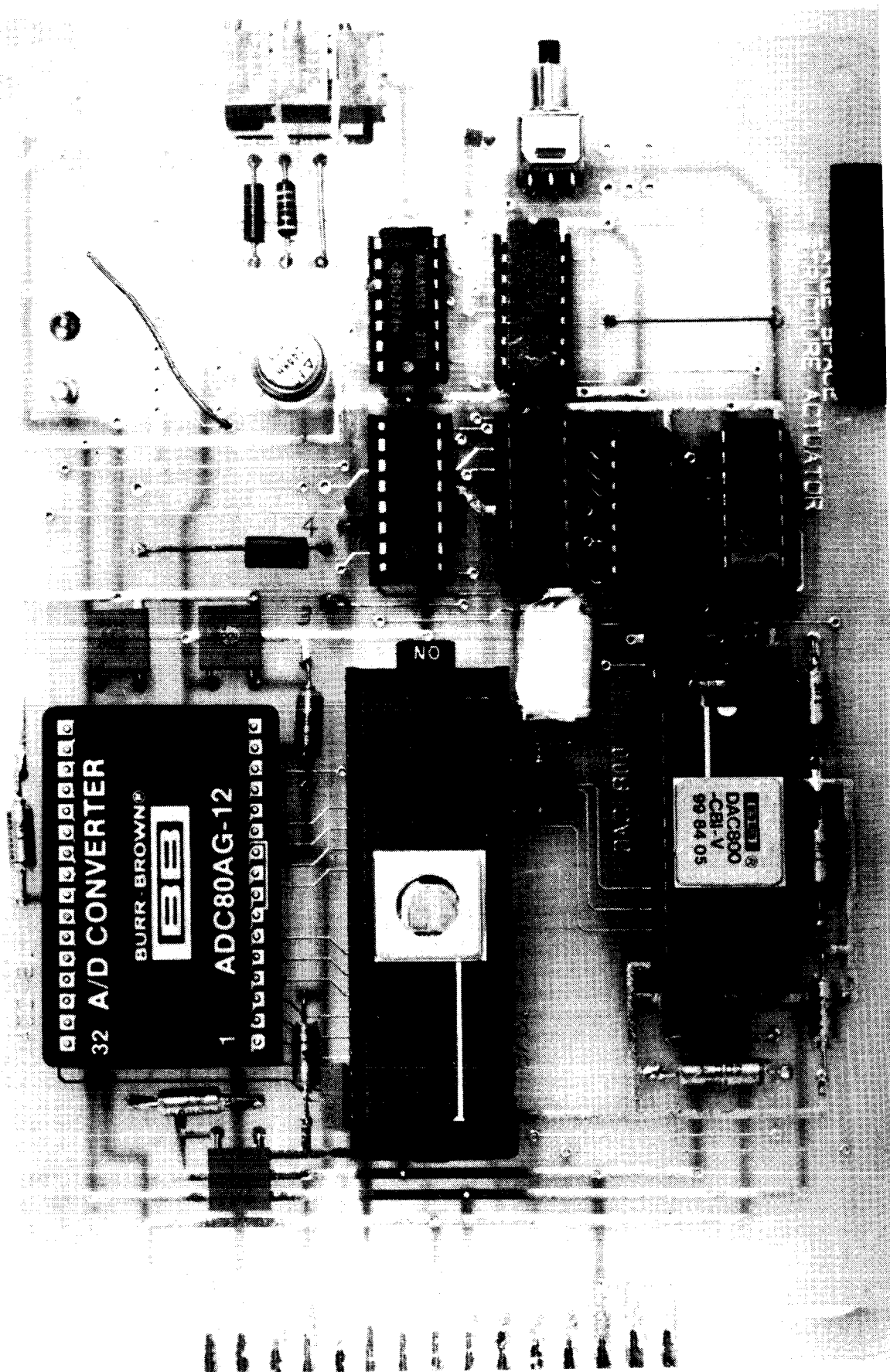
POWER AMPLIFIER BOARD

The power amplifer board is fairly simple in design because
there are few conponents. The main component is the Burr-Brown
operational amplifier. The amplifier accepts a ±10 volt input
and outputs ±1 ampere.

POWER AMPLIFIER BOARD
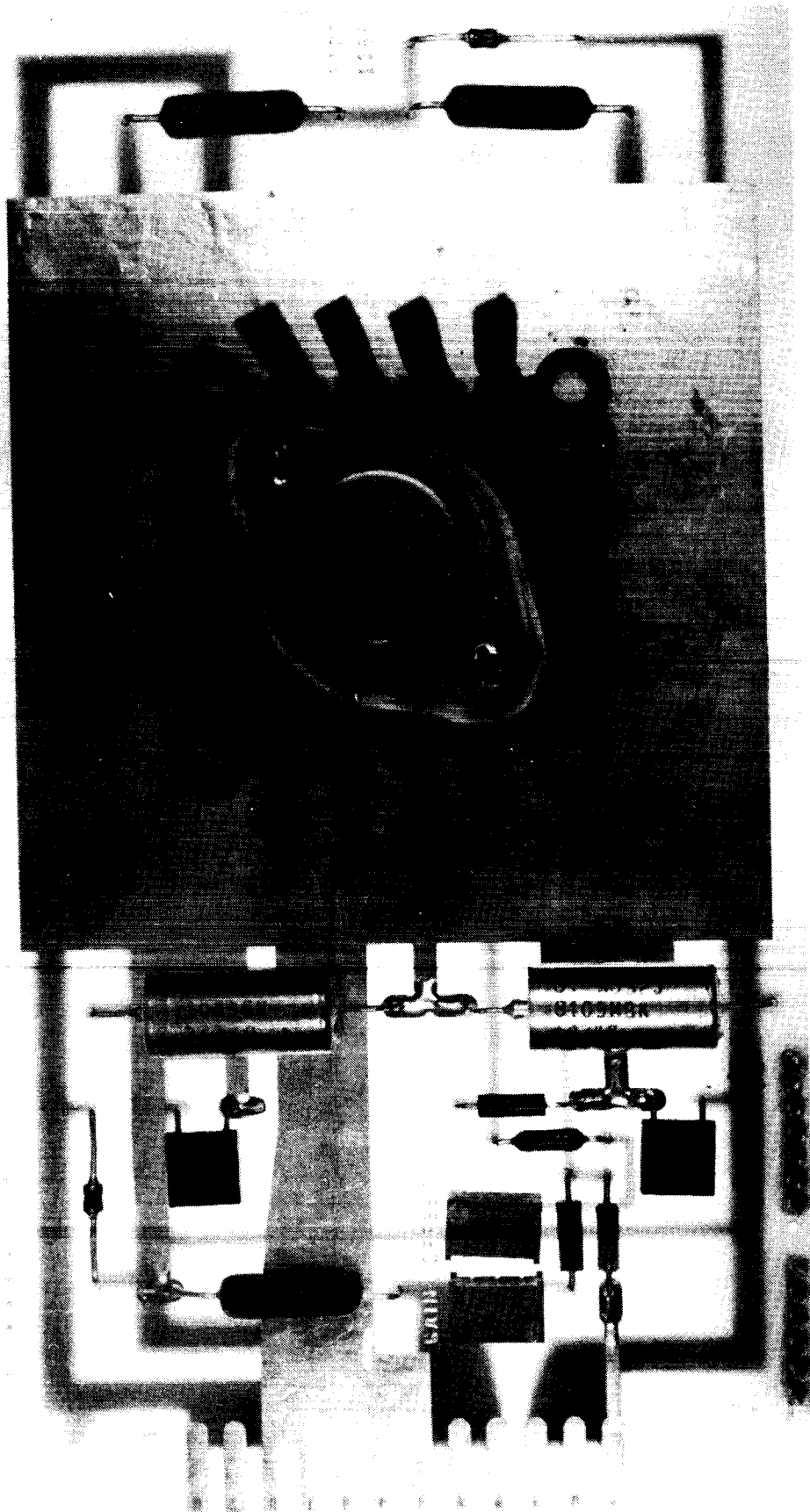
MODEL OF PROOF MASS ACTUATOR

The model of the actuator is assumed to be single degree-of-freedom dynamic system. The mass of the proof-mass is represented by m_p, the stiffness of the actuator is k_p, the back-emf is denoted by c_p, and the control force is f_g. The other spring and mass simply represent a structural mode to be controlled.

MODEL OF PROOF-MASS ACTUATOR
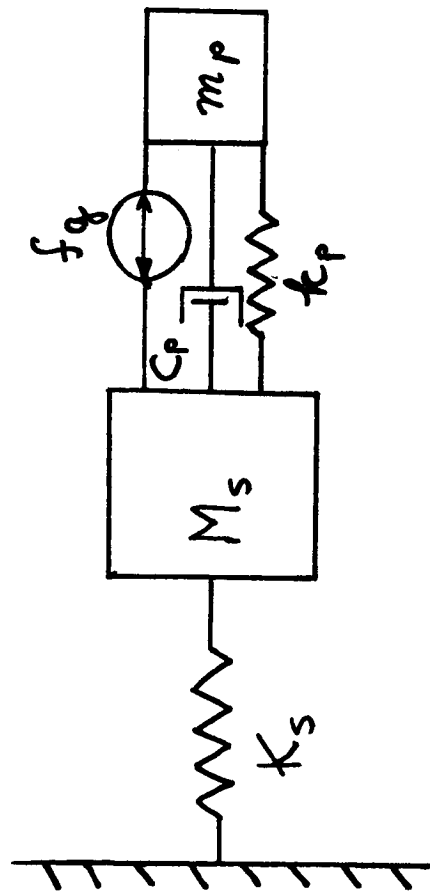
DYNAMIC CHARACTERISTICS

The dynamic characteristics of the proof-mass actuator are
described in the transfer function. Here the transfer function
is defined as the ratio of the output force to the input
voltage as a function frequency. The plot of the magnitude of
the transfer function shows that the usable range of the
actuator is approximately above 2 Hertz. Beyond 4 Hertz the
transfer function is nearly flat.

DYNAMIC CHARACTERISTICS

$$\frac{\text{FORCE}}{\text{VOLTAGE}}$$

113
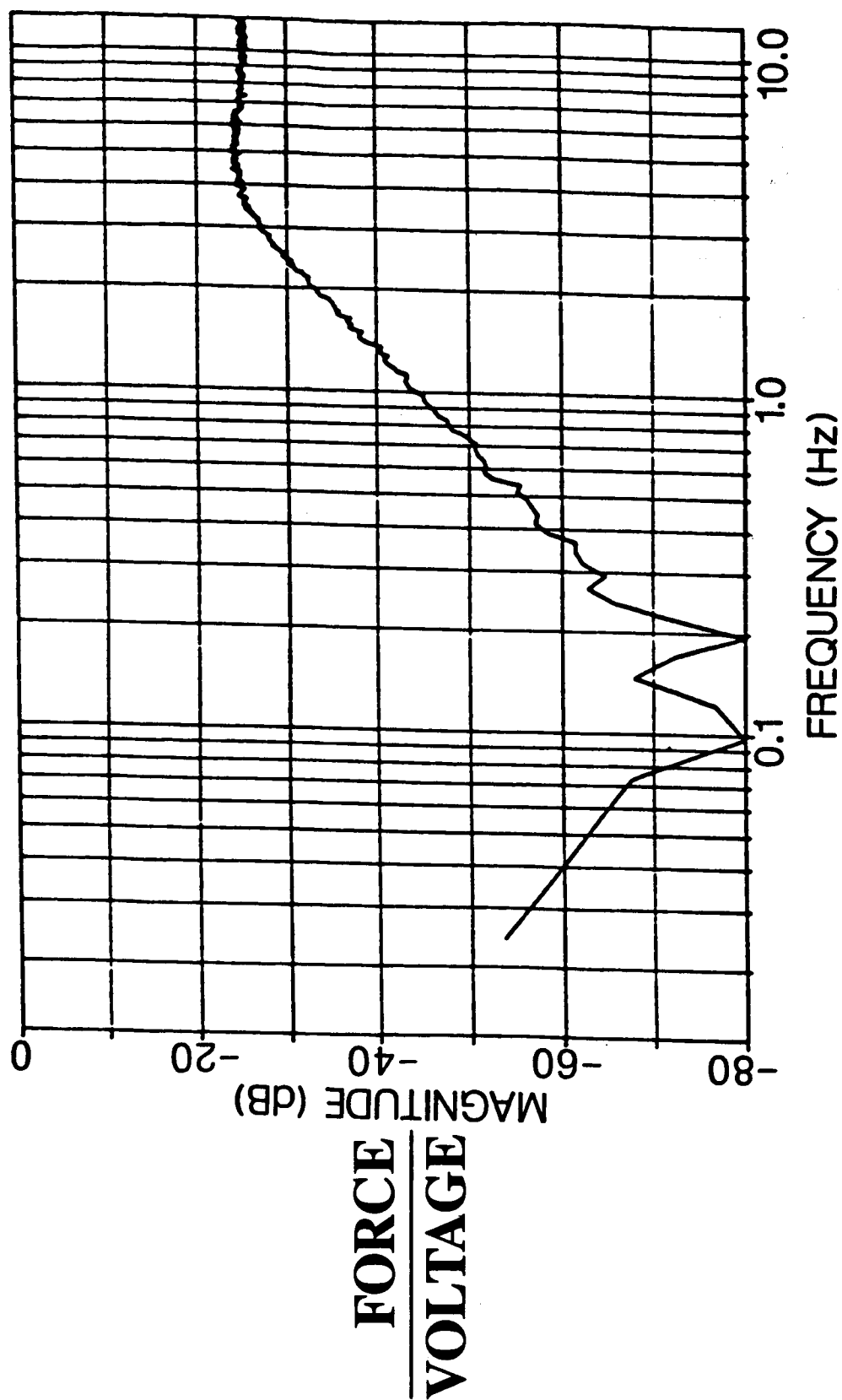
DYNAMIC CHARACTERISTICS - continued

The phase angle of the transfer function is shown is this figure. The erratic response below .4 Hertz is due to the inability of the instrumentation to properly respond to these low frequencies.

DYNAMIC CHARACTERISTICS

$$\frac{\text{FORCE}}{\text{VOLTAGE}}$$

115
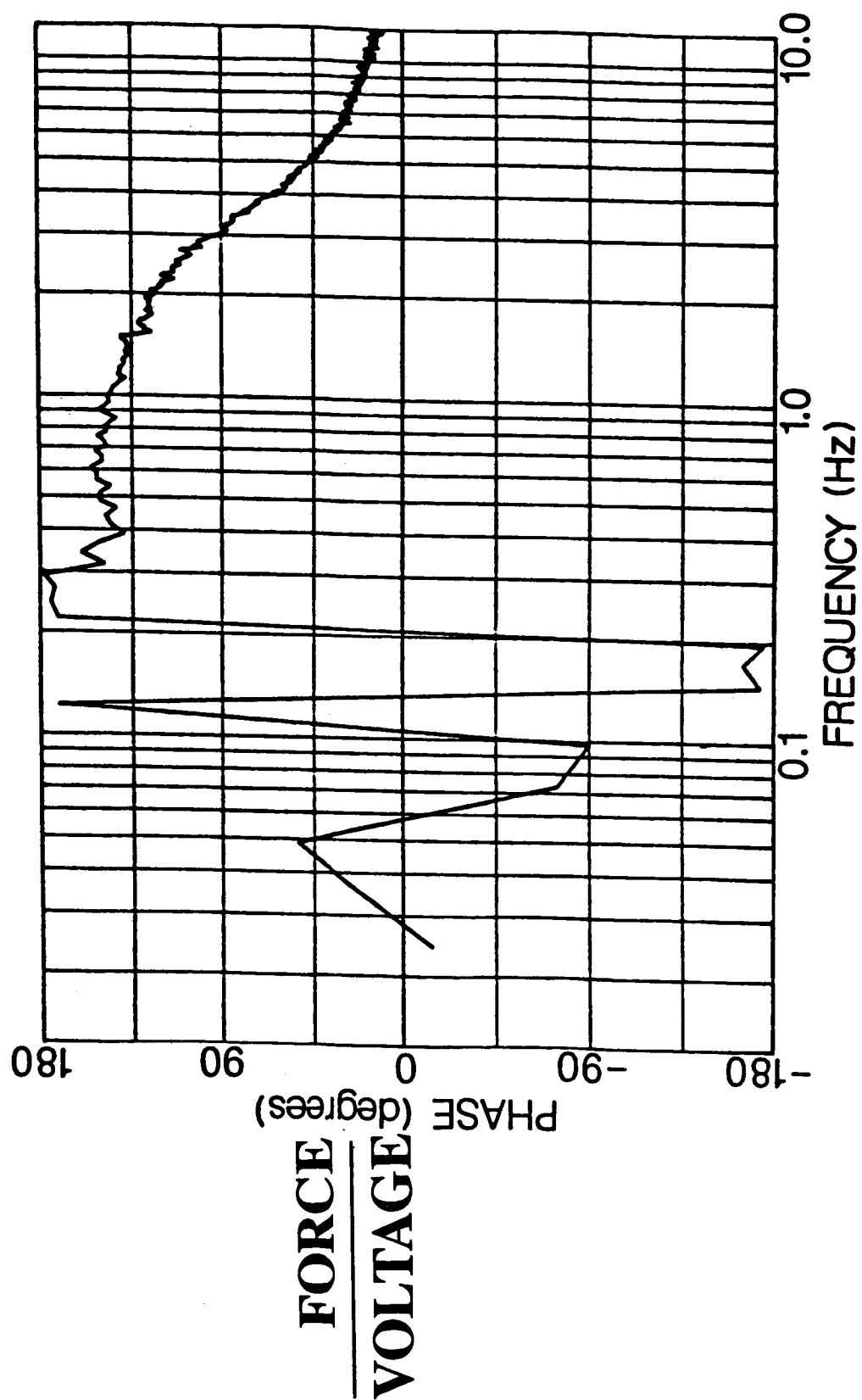
CONCLUSIONS

The major conclusions of the research are that a programmable force actuator has been developed. The actuator has approximately a one pound force capability over the usable frequency range which is above 2 Hertz.

CONCLUSIONS

- **PROGRAMMABLE FORCE ACTUATOR DEVELOPED**

- **ONE POUND CONTROL FORCE CAPABILITY**

- **LOW FREQUENCY RESPONSE LIMIT APPROXIMATELY 2 HERTZ**

- **NEARLY FLAT RESPONSE FROM 2 HERTZ TO 1000 AND ABOVE**

A GENERAL METHOD FOR DYNAMIC ANALYSIS OF STRUCTURES

OVERVIEW

BY

REMI C. ENGELS

THE UNIVERSITY OF TENNESSEE SPACE INSTITUTE

TULLAHOMA, TN

WORKSHOP ON STRUCTURAL DYNAMICS AND CONTROL INTERACTION OF FLEXIBLE STRUCTURES
APRIL 22-24, 1986
MSFC/NASA, ALABAMA

I. Definition of the Term "Element"

An element is defined as any structural unit whose degrees of freedom (DOFS) can be categorized as either interface DOFS or non-interface (internal) DOFS.

Interface DOFS are those DOFS through which the element is connected to one or more neighboring elements. Non-interface DOFS are internal to the element and do not directly couple to neighboring elements.

The term "element" then, has a rather broad meaning. An element could be a fundamental structural unit such as a rod, a beam, a plate, etc. or it could be an entire structural component. Furthermore, the parameters of the element could be distributed or lumped. Figure 1 schematically illustrates the element concept.

Any structural system can now be thought of as a composite of n such elements. The choice of elements is totally arbitrary and is a matter of user convenience. In particular, the user does not have to worry about the "size" of the element as is the case for example when using a standard finite element approach. This means that in general n is relatively small and little bookkeeping is necessary.

Spatial periodicity of structures can be taken into account in a natural manner. These important advantages will be further clarified in the next few sections.

II. Modeling of an Element

Each element will be modeled using a set of assumed modes. In particular, a combination of interface constraint modes (ICM) and a set of interface restrained normal modes (IRNM) can be employed. Note that other types of assumed modes can be selected and should be investigated. The above choice is motivated by the Craig/Bampton approach to component modes synthesis and has several important advantages.

1. Interface Constraint Modes (ICM)

Let us assume the element has $\mathcal{A}$ interface DOFS x_{Ij} $(j=1,2,\cdots,\mathcal{A})$. The ICM corresponding to DOF x_{Ij} is defined as the static deformation pattern of the element for $x_{Ij}=1$ and $x_{Ii}=0$ (for all $i\neq j$). Note that many "shape functions" used in the finite element method are actually ICM.

2. Interface Restrained Normal Modes (IRNM)

IRNM are the regular mass normalized mode shapes for the element with fixed interface DOFS.

3. Displacement of an Element

The displacement vector of a discrete element can be partitioned as:

$$\underset{\sim}{X} = \left\{ \begin{array}{c} \underset{\sim}{X}_I \\ \hdashline \underset{\sim}{X}_N \end{array} \right\} \qquad (1)$$

The non-interface displacement can be written as

$$\underset{\sim}{X}_N = S_{NI}\,\underset{\sim}{X}_I + \underset{\sim}{\bar{X}}_N \qquad (2)$$

where the first term $S_{NI}\underset{\sim}{X}_I$ represents a static deformation due to the interface displacements. The term $\underset{\sim}{\bar{X}}_N$ is best described as the difference

$$\underset{\sim}{\bar{X}}_N = \underset{\sim}{X}_N - S_{NI}\,\underset{\sim}{X}_I \qquad (3)$$

The displacement vector $\underset{\sim}{\bar{X}}_N$ is now written as a linear combination of the IRNM

$$\underset{\sim}{\bar{X}}_N = \Phi_N\,\underset{\sim}{\bar{q}}_N \qquad (4)$$

Structural System
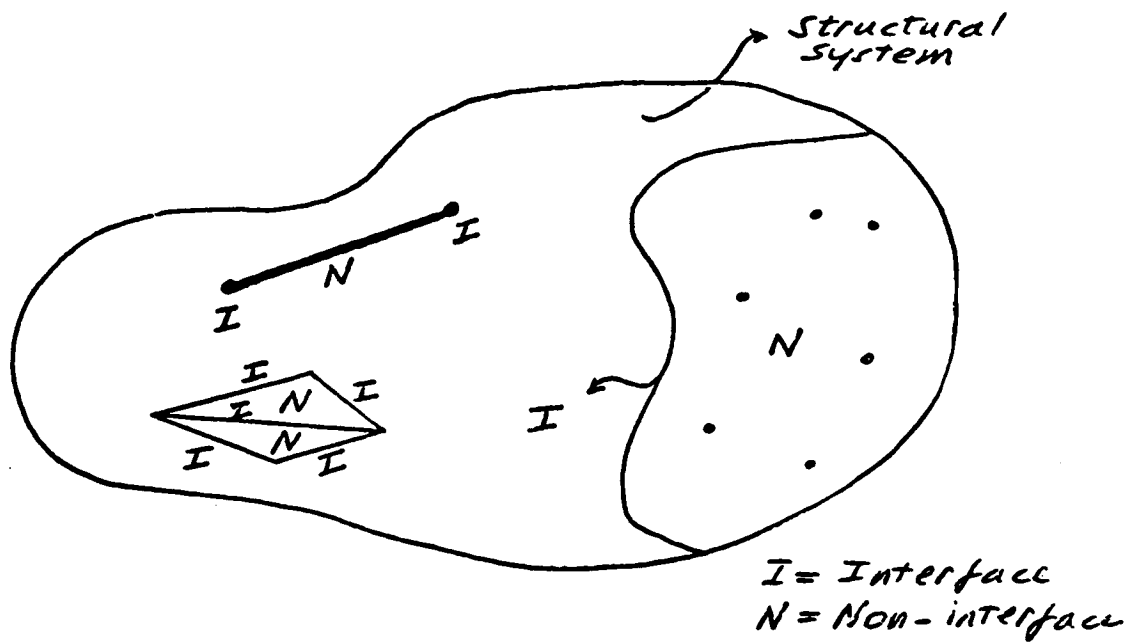
I = Interface
N = Non-interface

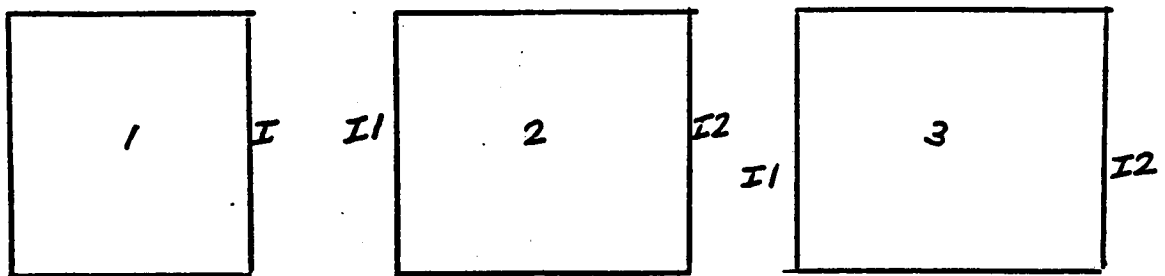**Figure 1:** A Schematic Representation of the Element Concept.

Figure 2: Schematic Representation of Three Elements

where $\bar{q}_N$ is a set of modal coordinates.

The displacement vector $\underset{\sim}{x}$ can now be written as

OF POOR QUALITY

ORIGINAL PAGE IS

$$\underset{\sim}{x} = \begin{bmatrix} t & | & I^e \bar{\Phi}_N \end{bmatrix} \left\{ \frac{\underset{\sim}{x}_I}{\bar{q}_N} \right\} \qquad (5)$$

with

$$t \overset{\Delta}{=} \begin{bmatrix} I \\ S_{NI} \end{bmatrix} \quad , \quad I^e \overset{\Delta}{=} \begin{bmatrix} 0 \\ I \end{bmatrix} \qquad (6)$$

The columns of matrix t clearly represent the ICM of the element. The actual general form of the matrix S_{NI} will be given shortly.

The elements of the vectors $\underset{\sim}{x}_I$ and $\bar{q}_N$ will be the generalized coordinates used to model a structural element. Equation (5) is also valid for distributed parameter elements.

Equation (5) indicates why the elements can be chosen with a large degree of freedom. If the matrices t and $I^e\bar{\Phi}_N$ can be determined with enough accuracy then a legitimate element is found regardless of its size. For example entire beams, rods and plates can be considered as one element. Even large components could be considered as single elements as long as Eq. (5) can be adequately written. As a consequence, a considerable amount of bookkeeping can be avoided, thereby reducing the cost of the analysis.

In the next section we will introduce the element equations of motion.

III. The Element Equations of Motion

From here on we will work with discrete systems because relationships can be shown more explicitly. It should be kept in mind however, that all results are equally valid for distributed-parameter systems.

The most general form of the element displacement vector $\underset{\sim}{x}$ is:

$$\underset{\sim}{x} = \left\{ \begin{array}{c} \underset{\sim}{x}_{I1} \\ \underset{\sim}{x}_{I2} \\ \vdots \\ \underset{\sim}{x}_{I\mathcal{A}} \\ \hline \underset{\sim}{x}_N \end{array} \right\} \qquad (7)$$

$\mathcal{A}$ = number of distinct interfaces of the element
For Example:
$\mathcal{A} = 3$ for element e

with

$$\underset{\sim}{x}_I \overset{\Delta}{=} \left\{ \begin{array}{c} \underset{\sim}{x}_{I1} \\ \underset{\sim}{x}_{I2} \\ \vdots \\ \underset{\sim}{x}_{I\mathcal{A}} \end{array} \right\} \qquad (8)$$
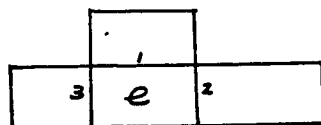
$\underset{\sim}{x}$ can be written as:

$$\underset{\sim}{x} = \left\{ \begin{array}{c} \underset{\sim}{x}_I \\ \hline \underset{\sim}{x}_N \end{array} \right\} \qquad (9)$$

Because distinct interfaces by definition do not connect directly to each other, the element stiffness matrix corresponding to vector $\underset{\sim}{x}$ in Eq. (7) is:

$$K = \begin{bmatrix} K_{I1I1} & 0 & \cdots & 0 & K_{I1N} \\ 0 & K_{I2I2} & \cdots & 0 & K_{I2N} \\ \vdots & \vdots & & \vdots & \vdots \\ 0 & 0 & \cdots & K_{I\mathcal{A}I\mathcal{A}} & K_{I\mathcal{A}N} \\ \hline K_{NI1} & K_{NI2} & \cdots & K_{NI\mathcal{A}} & K_{NN} \end{bmatrix} \quad \longleftrightarrow \quad \left\{ \begin{array}{c} \underset{\sim}{x}_{I1} \\ \underset{\sim}{x}_{I2} \\ \vdots \\ \underset{\sim}{x}_{I\mathcal{A}} \\ \hline \underset{\sim}{x}_N \end{array} \right\} \qquad (10)$$

122

The mass matrix has a similar form. Another form corresponding to vector $\underset{\sim}{x}$ in Eq. (9) is:

$$M = \begin{bmatrix} M_{II} & M_{IN} \\ M_{NI} & M_{NN} \end{bmatrix} \quad , \quad K = \begin{bmatrix} K_{II} & K_{IN} \\ K_{NI} & K_{NN} \end{bmatrix} \tag{11}$$

with partitioning corresponding to Eq. (9).

The form of Eq. (10) suggests that

$$S_{NIj} = - K_{NN}^{-1} K_{NIj} \quad , \quad j = 1, 2, \ldots, d \tag{12}$$

and

$$\underset{\sim}{x} = \begin{bmatrix} I & 0 & \cdots & 0 & 0 \\ 0 & I & \cdots & 0 & 0 \\ \vdots & \vdots & & \vdots & \vdots \\ 0 & 0 & \cdots & I & 0 \\ \hline S_{NI1} & S_{NI2} & \cdots & S_{NId} & \bar{\Phi}_N \end{bmatrix} \begin{Bmatrix} \underset{\sim}{x}_{I1} \\ \underset{\sim}{x}_{I2} \\ \vdots \\ \underset{\sim}{x}_{Id} \\ \bar{q}_N \end{Bmatrix} \tag{13}$$

or,

$$\underset{\sim}{x} = \begin{bmatrix} I & 0 \\ \hline S & \bar{\Phi}_N \end{bmatrix} \begin{Bmatrix} x_I \\ \bar{q}_N \end{Bmatrix} \tag{14}$$

with

$$\bar{X}_N = \bar{\Phi}_N \bar{q}_N \tag{15}$$

where $\bar{\Phi}_N$ are IRNM and the partitions in Eq. (14) correspond to Eq. (13).

Using Eqs. (11), (12) and (14) the mass and stiffness matrices for an element corresponding to coordinates $\underset{\sim}{x}_I, \bar{q}_N$ are:

$$\bar{M} = \begin{bmatrix} M_{11} & M_{12} \\ M_{12}^T & I \end{bmatrix} \leftrightarrow \begin{Bmatrix} \ddot{x}_I \\ \ddot{\bar{q}}_N \end{Bmatrix} \tag{16}$$

$$\bar{K} = \begin{bmatrix} K_{11} & 0 \\ 0 & \bar{\omega}^2 \end{bmatrix} \leftrightarrow \begin{Bmatrix} x_I \\ \bar{q}_N \end{Bmatrix} \tag{17}$$

where

$$M_{11} = M_{II} + M_{IN} S + S^T (M_{IN}^T + M_{NN} S) \tag{18}$$

$$M_{12} = (M_{IN} + S^T M_{NN}) \bar{\Phi}_N \tag{19}$$

$$K_{11} = K_{II} + K_{IN} S \tag{20}$$

and where we made use of the fact that

$$K_{IN} + S^T K_{NN} = 0 \tag{21}$$

$$\left. \begin{array}{l} \bar{\Phi}_N^T M_{NN} \bar{\Phi}_N = I \\ \bar{\Phi}_N^T K_{NN} \bar{\Phi}_N = \bar{\omega}^2 \end{array} \right\} \quad \text{IRNM orthonormality conditions} \tag{22}$$

The approach followed to model the element reveals a unique perspective on a serious shortcoming of the standard finite element techniques when used to construct element mass matrices. Indeed, it is clear that a standard finite element mass matrix (consistent) represents a Guyan reduction in which the internal degrees of freedom (non-interface) are eliminated, i.e. all $\bar{q}_N$ coordinates are neglected. As will be seen later, such an approximation is valid only when the elements are "small" enough so that indeed the coordinates $\bar{q}_N$ have no effect on the response of the structure.

In the next section we will discuss the formation of the system equations.

IV. The System Equations

1. Coupling of Two Elements

In this section we will demonstrate how elements are assembled into global components. As an example, consider the three elements in Figure 2. Equations (16-20) represent the general form of the element equations. The displacement vector for element i can be written as

$$\left\{ \begin{array}{c} \underset{\sim}{x}^i_I \\ \bar{q}^i_N \end{array} \right\} \tag{23}$$

In general, the vector $\underset{\sim}{x}^i_I$ represents a set of local displacement coordinates. In order to enforce displacement compatibility between the element interfaces it is necessary to transform $\underset{\sim}{x}^i_I$ into a set of global coordinates $\underset{\sim}{X}^i_I$,

$$\left\{ \begin{array}{c} \underset{\sim}{x}^i_I \\ \bar{q}^i_N \end{array} \right\} = \left[\begin{array}{cc} Q^i_I & 0 \\ 0 & I \end{array} \right] \left\{ \begin{array}{c} \underset{\sim}{X}^i_I \\ \bar{q}^i_N \end{array} \right\} \tag{24}$$

where Q^i_I is a geometric transformation matrix. Note that no transformation is necessary for $\bar{q}^i_N$ because elements only connect through interfaces. Using equations of the type Eq. (24) we can rewrite Eqs. (16-20) in the following form

$$\bar{M}^i = \left[\begin{array}{cc} M^i_{11} & M^i_{12} \\ M^i_{21} & I \end{array} \right] \longleftrightarrow \left\{ \begin{array}{c} \ddot{\underset{\sim}{X}}^i_I \\ \ddot{\bar{q}}^i_N \end{array} \right\} \tag{25}$$

$$\bar{K}^i = \left[\begin{array}{cc} K^i_{11} & 0 \\ 0 & \bar{\omega}^2_i \end{array} \right] \longleftrightarrow \left\{ \begin{array}{c} \underset{\sim}{X}^i_I \\ \bar{q}^i_N \end{array} \right\} \tag{26}$$

where M^i_{11}, M^i_{12} and K^i_{11} are easily found.

The first step in the assembly process is to connect element 1 to element 2 by requiring that

$$\underset{\sim}{X}^1_I = \underset{\sim}{X}^2_{I1} \ , \qquad \text{for all times} \tag{27}$$

The uncoupled equations of motion for the 1-2 component can be written as follows

$$\left[\begin{array}{cc|ccc} M^1_1 & M^1_{12} & & & \\ M^1_{21} & I & & 0 & \\ \hline & & m^2_{11} & m^2_{12} & m^2_{13} \\ & 0 & m^2_{21} & m^2_{22} & m^2_{23} \\ & & m^2_{31} & m^2_{32} & I \end{array} \right] \left\{ \begin{array}{c} \ddot{\underset{\sim}{X}}^1_I \\ \ddot{\bar{q}}^1_N \\ \ddot{\underset{\sim}{X}}^2_{I1} \\ \ddot{\underset{\sim}{X}}^2_{I2} \\ \ddot{\bar{q}}^2_N \end{array} \right\} + \left[\begin{array}{cc|ccc} K^1_{11} & 0 & & & \\ 0 & \bar{\omega}^2_1 & & 0 & \\ \hline & & k^2_{11} & k^2_{12} & 0 \\ & 0 & k^2_{21} & k^2_{22} & 0 \\ & & 0 & 0 & \bar{\omega}^2_2 \end{array} \right] \left\{ \begin{array}{c} \underset{\sim}{X}^1_I \\ \bar{q}^1_N \\ \underset{\sim}{X}^2_{I1} \\ \underset{\sim}{X}^2_{I2} \\ \bar{q}^2_N \end{array} \right\} = 0 \tag{28}$$

where the damping and forcing terms are omitted since we are only interested in the eigenvalue problem. Note that for element 2 we have two interfaces and we denoted

$$M^2_{11} = \left[\begin{array}{cc} m^2_{11} & m^2_{12} \\ m^2_{21} & m^2_{22} \end{array} \right] , \quad M^2_{12} = \left[\begin{array}{c} m^2_{13} \\ m^2_{23} \end{array} \right] , \quad K^2_{11} = \left[\begin{array}{cc} k^2_{11} & k^2_{12} \\ k^2_{21} & k^2_{22} \end{array} \right] \tag{29}$$

Taking into account Eq. (27) we can write the coupled equations of motion for component 1-2 as

124

$$
\begin{bmatrix}
m_{22}^2 & m_{21}^2 & 0 & m_{23}^2 \\
m_{12}^2 & M_{11}' + m_{11}^2 & M_{12}' & m_{13}^2 \\
0 & M_{21}' & I & 0 \\
m_{32}^2 & m_{31}^2 & 0 & I
\end{bmatrix}
\begin{Bmatrix}
\ddot{\underline{X}}_{I2}^2 \\
\ddot{\underline{X}}_I' \\
\ddot{\underline{q}}_N' \\
\ddot{\underline{q}}_N^2
\end{Bmatrix}
+
\begin{bmatrix}
k_{22}^2 & k_{21}^2 & 0 & 0 \\
k_{12}^2 & K_{11}' + k_{11}^2 & 0 & 0 \\
0 & 0 & \bar{\omega}_1^2 & 0 \\
0 & 0 & 0 & \bar{\omega}_2^2
\end{bmatrix}
\begin{Bmatrix}
\underline{X}_{I2}^2 \\
\underline{X}_I' \\
\underline{q}_N' \\
\underline{q}_N^2
\end{Bmatrix}
\tag{30}
$$

At this point, element 3 should be connected to the 1-2 component. Before doing this, Equation (30) will be manipulated into a form identical to Equations (16-17). This is an important feature of the presented technique. Indeed, it will allow us to consider the 1-2 component as a standard element as defined in Section I. In other words, the resulting equations will represent the dynamics of element 1-2. In addition, the equations will be in a form suitable to apply an escalator type eigensolver to be discussed later.

2. Transformation of the Interface Displacement Vector

The first step in reducing the 1-2 component into a single element is to introduce the following transformation

$$
\underline{X}_I' = S_{II2} \, \underline{X}_{I2}^2 + \bar{\underline{X}}_I'
\tag{31}
$$

with

$$
S_{II2} = -\left[K_{11}' + k_{11}^2 \right]^{-1} k_{12}^2
\tag{32}
$$

This transformation is entirely equivalent to Eq. (2). The term $S_{II2} \underline{X}_{I2}^2$ represents that part of $\underline{X}_I'$ which is due to the displacement of the interface I2. The term $\bar{\underline{X}}_I'$ is the displacement of I with respect to the interface I2 as seen by an absolute observer. Note that the matrix $[K_{11}' + k_{11}^2]$ is never singular because it represents the stiffness matrix of a rigid body restrained system.

The displacement vector $\bar{\underline{X}}_I'$ can be written as a linear combination of IRNM as follows

$$
\bar{\underline{X}}_I' = \bar{\Phi}_I' \, \bar{\underline{q}}_I'
\tag{33}
$$

where the eigenvalue problem solved is

$$
\bar{\omega}_{I1}^2 \left[M_{11}' + m_{11}^2 \right] \bar{\Phi}_I' = \left[K_{11}' + k_{11}^2 \right] \bar{\Phi}_I'
\tag{34}
$$

The following transformation

$$
\begin{Bmatrix}
\underline{X}_{I2}^2 \\
\underline{X}_I' \\
\underline{q}_N' \\
\underline{q}_N^2
\end{Bmatrix}
=
\begin{bmatrix}
I & 0 & 0 & 0 \\
S_{II2} & \bar{\Phi}_I' & 0 & 0 \\
0 & 0 & I & 0 \\
0 & 0 & 0 & I
\end{bmatrix}
\begin{Bmatrix}
\underline{X}_{I2}^2 \\
\bar{q}_I' \\
\underline{q}_N' \\
\underline{q}_N^2
\end{Bmatrix}
\tag{35}
$$

can now be substituted into Eq. (30), yielding

$$
\begin{bmatrix}
m_{11} & m_{12} & m_{13} & m_{14} \\
m_{21} & I & m_{23} & m_{24} \\
m_{31} & m_{32} & I & 0 \\
m_{41} & m_{42} & 0 & I
\end{bmatrix}
\begin{Bmatrix}
\ddot{\underline{X}}_{I2}^2 \\
\ddot{\bar{q}}_I' \\
\ddot{q}_N' \\
\ddot{q}_N^2
\end{Bmatrix}
+
\begin{bmatrix}
k_{11} & 0 & 0 & 0 \\
0 & \bar{\omega}_{I1}^2 & 0 & 0 \\
0 & 0 & \bar{\omega}_1^2 & 0 \\
0 & 0 & 0 & \bar{\omega}_2^2
\end{bmatrix}
\begin{Bmatrix}
\underline{X}_{I2}^2 \\
\bar{q}_I' \\
\bar{q}_N' \\
\bar{q}_N^2
\end{Bmatrix}
\tag{36}
$$

where $m_{11}, m_{12}, \ldots, m_{23}, m_{24}$ and k_{11} can be easily found.

125

3. The IRNM Eigenvalue Problem

The second step in reducing Eq. (30) to a form identical to Eqs. (16-17) is the solution of the eigenvalue problem

$$\bar{\omega}^2 \begin{bmatrix} I & m_{23} & m_{24} \\ M_{32} & I & 0 \\ M_{42} & 0 & I \end{bmatrix} \underset{\sim}{\Phi} = \begin{bmatrix} \bar{\omega}_I^2 & 0 & 0 \\ 0 & \bar{\omega}_1^2 & 0 \\ 0 & 0 & \bar{\omega}_2^2 \end{bmatrix} \underset{\sim}{\Phi} \tag{37}$$

Using the transformation

$$\left\{ \begin{array}{c} \bar{q}'_I \\ \bar{q}'_N \\ \bar{q}^2_N \end{array} \right\} = \bar{\Phi}\, \bar{q} \tag{38}$$

in Eq. (36) yields

$$\begin{bmatrix} \bar{M}_{11} & \tilde{M}_{12} \\ \tilde{M}_{21} & I \end{bmatrix} \left\{ \begin{array}{c} \underset{\sim}{\ddot{X}}^2_{I2} \\ \ddot{\bar{q}} \end{array} \right\} + \begin{bmatrix} \tilde{K}_{11} & 0 \\ 0 & \bar{\omega}^2 \end{bmatrix} \left\{ \begin{array}{c} \underset{\sim}{X}^2_{I2} \\ \bar{q} \end{array} \right\} = \underset{\sim}{0} \tag{39}$$

with

$$\bar{M}_{11} = m_{11} \quad , \quad \bar{M}_{12} = [\, M_{12} \;\; M_{13} \;\; M_{14} \,]\, \bar{\Phi}$$

$$\bar{K}_{11} = k_{11} \tag{40}$$

Equation (39) is now equivalent in form to Eqs. (16-17). It essentially represents the equations of motion for the 1-2 component viewed as one single element. If along the way no modes are truncated then Eq. (39) involves no unusual approximations. In particular, for the continuous equivalent, the equations corresponding to Eq. (39) are still "exact".

The eigenvalue problem (37) has a very special form and an optimum solution will be discussed in Section V.

An important aspect of the present technique is the truncation of the mode set $\bar{\Phi}$ according to a preset frequency. This preset frequency must reflect the frequency content in an element necessary to obtain the desired fidelity in the overall system model. How the "element" cut-off frequency compares to the "system" cut-off frequency is still a matter of research or "experience".

Once the appropriate truncation is performed, a third element can be added through interface 12. Note that the number of degrees of freedom is already reduced. The eigenvalue problem (37) is small and can be solved very efficiently as will be shown.

It is also important to note that because of the transformation (31) we do not loose any accuracy in the rigid body and static properties of the system when modes are truncated.

4. Coupling of Element 1-2 and Element 3.

The next step is to couple element 3 to element 1-2. This process is very similar to the one already described. From Eqs. (25-26) we can obtain for $i = 3$

$$\bar{M}^3 = \begin{bmatrix} M_{11}^3 & M_{12}^3 \\ M_{21}^3 & I \end{bmatrix} \quad , \quad \bar{K}^3 = \begin{bmatrix} K_{11}^3 & 0 \\ 0 & \bar{\omega}_3^2 \end{bmatrix} \longleftrightarrow \left\{ \begin{array}{c} \underset{\sim}{X}_I^3 \\ \bar{q}_N^3 \end{array} \right\} \tag{41}$$

The uncoupled equations of motion for the 12-3 component can be written as

$$
\begin{bmatrix}
\begin{array}{cc|c}
\widetilde{M}_{11} & \widetilde{M}_{12} & 0 \\
\widetilde{M}_{21} & I & \\
\hline
& 0 & \begin{matrix} M_{11}^3 & M_{12}^3 \\ M_{21}^3 & I \end{matrix}
\end{array}
\end{bmatrix}
\left\{
\begin{array}{c}
\ddot{\underset{\sim}{X}}{}^2_{I2} \\
\ddot{\underset{\sim}{q}} \\
\hline
\ddot{\underset{\sim}{X}}{}^3_{I1} \\
\ddot{\underset{\sim}{q}}{}^3_N
\end{array}
\right\}
+
\begin{bmatrix}
\begin{array}{cc|c}
\widetilde{K}_{11} & 0 & 0 \\
0 & \bar{\omega}^2 & \\
\hline
& 0 & \begin{matrix} K_{11}^3 & 0 \\ 0 & \bar{\omega}_3^2 \end{matrix}
\end{array}
\end{bmatrix}
\left\{
\begin{array}{c}
\underset{\sim}{X}{}^2_{I2} \\
\underset{\sim}{q} \\
\hline
\underset{\sim}{X}{}^3_{I1} \\
\underset{\sim}{q}{}^3_N
\end{array}
\right\} = 0
\tag{12}
$$

where we used Eqs. (39) and (41). Note that the interface I2 of element 3 is part of the model if no other elements are to be connected. However, if other elements are to be connected, this interface must be made explicit.

We now must impose the compatibility condition

$$
\underset{\sim I2}{X}{}^2 = \underset{\sim I1}{X}{}^3
\tag{43}
$$

Because this is the last element, no further transformations of the interface displacement vector is necessary. Using Eq. (34) we can write

$$
\begin{bmatrix}
\widetilde{M}_{11}+M_{11}^3 & \widetilde{M}_{12} & M_{12}^3 \\
\widetilde{M}_{21} & I & 0 \\
M_{21}^3 & 0 & I
\end{bmatrix}
\left\{
\begin{array}{c}
\ddot{\underset{\sim}{X}}{}^3_{I1} \\
\ddot{\underset{\sim}{q}} \\
\ddot{\underset{\sim}{q}}{}^3_N
\end{array}
\right\}
+
\begin{bmatrix}
\widetilde{K}_{11}+K_{11}^3 & 0 & 0 \\
0 & \bar{\omega}^2 & 0 \\
0 & 0 & \bar{\omega}_3^2
\end{bmatrix}
\left\{
\begin{array}{c}
\underset{\sim}{X}{}^3_{I1} \\
\underset{\sim}{q} \\
\underset{\sim}{q}{}^3_N
\end{array}
\right\} = \underset{\sim}{0}
\tag{44}
$$

which represent the coupled equations for elements 1-2 and 3.

Next, we can solve the small eigenvalue problem.

$$
\omega_{I2}^2 \left[\widetilde{M}_{11} + M_{11}^3 \right] \underset{\sim I}{\phi}{}^2 = \left[\widetilde{K}_{11} + K_{11}^3 \right] \underset{\sim I}{\phi}{}^2
\tag{45}
$$

so that

$$
\underset{\sim I1}{X}{}^3 = \underset{\sim I}{\phi}{}^2 \, \underset{\sim I}{q}{}^2
\tag{46}
$$

Note that no "bar" is necessary over the above quantities, because if the system is free, the rigid body properties will be incorporated in Eqs. (45) and (46).

Incorporating Eq. (46) into Eq. (44) yields

$$
\begin{bmatrix}
I & \widetilde{m}_{12} & \widetilde{m}_{13} \\
\widetilde{m}_{12}^T & I & 0 \\
\widetilde{m}_{13}^T & 0 & I
\end{bmatrix}
\left\{
\begin{array}{c}
\ddot{\underset{\sim I}{q}}{}^2 \\
\ddot{\underset{\sim}{q}} \\
\ddot{\underset{\sim}{q}}{}^3_N
\end{array}
\right\}
+
\begin{bmatrix}
\omega_{I2}^2 & 0 & 0 \\
0 & \bar{\omega}^2 & 0 \\
0 & 0 & \bar{\omega}_3^2
\end{bmatrix}
\left\{
\begin{array}{c}
\underset{\sim I}{q}{}^2 \\
\underset{\sim}{\bar{q}} \\
\underset{\sim}{q}{}^3_N
\end{array}
\right\} = \underset{\sim}{0}
\tag{47}
$$

with

$$
\widetilde{m}_{12} = \underset{\sim I}{\phi}{}^{2T} \widetilde{M}_{12}, \quad \widetilde{m}_{13} = \underset{\sim I}{\phi}{}^{2T} M_{12}^3
\tag{48}
$$

Finally, note the simple form of this system of equation (47). First, generally truncation will reduce the size significantly. In addition, the specific form will allow for application of the escalator algorithm as discussed in Section V. This eigenvalue solver will yield a set of system frequencies $\bar{\omega}^2$ and system modes $\bar{\phi}$ with a minimum of effort and cost.

Before we discuss the special eigenvalue solver, remarks are in order:

(1) So far, we described how the elements are coupled together. It is a matter of repeating the same procedure for each added element. Each time truncation is used on the element level as well as on the level of the current system. A series of relatively small eigenvalue problems is

127

solved using a very efficient eigenvalue problem solver. The entire system is gradually built up, keeping only the necessary frequency fidelity at each stage. Several interesting questions arise, for example: (a) what is the ideal trade-off between element frequency truncation and current system frequency truncation, and how do both relate to the overall desired fidelity? (b) Which is the optimum way of solving the successive eigenvalue problems? Should we wait until several elements are collected before a current system eigenvalue problem is solved? This is an important question since it affects storage, cost and accuracy.

(2) The manner in which the elements are coupled together makes this technique ideally suited to handle spatial periodicity. Indeed, Eq. (39) shows that each current system can be considered as an "element". If care is taken, it is possible to use the same element over again, without adding significantly to the cost. For example, a periodic truss can be started with one element which is truncated according to a desired frequency. This model can now be doubled and truncated again. This truncated 2-element model can now be doubled again, to yield a 4-element truss, etc.

V. The Eigenvalue Problem Solver

In this section we will describe an eigenvalue problem solution technique which is particularly suited for our purposes.

First, let us consider the following special eigenvalue problem:

$$\lambda \begin{bmatrix} 1 & m_1 & m_2 & \cdots & m_n \\ m_1 & 1 & 0 & \cdots & 0 \\ m_2 & 0 & 1 & \cdots & 0 \\ \vdots & \vdots & \vdots & & \vdots \\ m_n & 0 & 0 & \cdots & 1 \end{bmatrix} \begin{Bmatrix} \phi_0 \\ \phi_1 \\ \vdots \\ \phi_n \end{Bmatrix} = \begin{bmatrix} k_0 & 0 & \cdots & 0 \\ 0 & k_1 & \cdots & 0 \\ \vdots & \vdots & & \vdots \\ 0 & 0 & \cdots & k_n \end{bmatrix} \begin{Bmatrix} \phi_0 \\ \phi_1 \\ \vdots \\ \phi_n \end{Bmatrix} \qquad (49)$$

This problem has a diagonal stiffness matrix and a unit mass matrix except for the first row and column. The m_i values are such that the mass matrix is positive definite.

The characteristic equation of this problem can be written as follows

$$(\lambda - k_0) - \lambda^2 \sum_{i=1}^{n} \frac{m_i^2}{\lambda - k_i} = 0 \qquad (50)$$

This assumes implicitly that $k_i \neq k_j$ (for $i \neq j$ and $i,j = 1,\cdots,n$) and also that $k_0 \neq 0$. If $k_i = k_j$ then it can be shown that there is a root $\lambda = k_i$. It can also be shown that all roots satisfy the inequality

$$\lambda_0 < k_0 < k_1 < \lambda_1 < k_2 < \lambda_2 < \cdots < \lambda_{n-2} < k_{n-1} < \lambda_{n-1} < k_n < \lambda_n \qquad (51)$$

In other words, we have isolated the eigenvalues of the system represented by Eq. (49). Note that property (51) again shows that for $k_i = k_j$, k_i becomes a root of the system. Property (51) allows us to use for example the Newton-Raphson technique to find the actual eigenvalues λ_i. This iteration scheme converges quadratically provided a good initial value is found. Without going into detail, at this point we can say that property (51) allows for a very accurate initial value for each of the eigenvalues. Therefore, convergence is extremely fast, often after two or three iterations.

Once the eigenvalues are determined, it is computationally a trivial matter to obtain the corresponding eigenvectors. Also, multiple roots are no problem. This algorithm was programmed but not yet optimized. Nevertheless, on a VAX/780, it requires only 10 seconds of CPU time to solve a problem with n = 450, which is a size far beyond our needs. As part of the presented dynamic analysis technique this eigenvalue problem must be solved for each interface dof.

VI. Summary and Conclusions

The presented research deals with the development of a dynamic analysis method for structural systems. The modeling approach is essentially a finite element method in the sense that the structure

128

is divided into n "elements". An "element" is defined as any structural unit whose dofs. can be categorized as either interface or non-interface dofs. The term "element" then, has a rather broad meaning. An element could be a fundamental unit such as a rod, a beam, a plate etc. or it could be an entire structural component. Furthermore, the parameters for the element could be distributed or lumped. The choice of elements is totally arbitrary and is a matter of user convenience. In particular, issues of accuracy and convergence do not enter on the level of element choice as is the case in a standard finite element method. This means for example that bookkeeping is reduced to a minimum.

Each element will be modeled using a set of interface constraint modes (ICM) combined with a set of interface restrained normal modes (IRNM). If the ICM and IRNM can be found with enough accuracy, then a legitimate "element" is defined. For example, entire beams, rods and plates can be considered as one element. Entire components can be made into one element in an off-line manner. Moreover, the entire system can be modeled as if it was represented by partial differential equations. Note that standard finite element techniques in general only use ICM ($=$ shape functions) which leads to very interesting and useful insights into important shortcomings of these techniques. In particular, the problem of an accurate mass distribution is addressed by this new approach.

The element assembly process is essentially the same as in the standard finite element method. However, each combination of elements is automatically converted into a single element. This procedure is based on static condensation without loss of accuracy. This feature is very important and allows for each structural unit to be interpreted as an "element". It also allows for the stiffness matrix to remain diagonal.

The next step is the solution of the system eigenvalue problem. The procedure calls for the sequential solution of a number of small eigenvalue problems based on a truncation principle for IRNM. In addition, the form of these eigenvalue problems is very simple such that an escalator type of eigenvalue problem solver can be used which is extremely cost-effective and fast. The response, loads, etc. calculations are rather standard, but also benefit from the approach in terms of accuracy and cost-effectiveness. The groundwork for this technique is in place and is currently supported by the AFWL/ARBH Kirtland AFB, NM. Some of the advantages of the new technique are: (1) The problem of Order Reduction is believed to be solved. The technique implicitly reduces the system order. Whenever an element is added only information necessary to obtain a prescribed fidelity in the system model is retained. (2) Very accurate. In fact, if desired, "exact" solutions in the distributed parameter sense can be obtained for any structure. (3) Fast and cost-effective. This is due to the small number of elements; the solution of a series of small eigenvalue problems instead of one large problem; the special nature of these small eigenvalue problems combined with the cost-effectiveness of the escalator eigenvalue problem solver. (4) Applicable in general. In particular, extremely large structures do not pose a problem. Once a model is agreed upon, any number of modes and frequencies with any degree of accuracy can be computed. (5) It is anticipated that Micro Computers can be used to solve even the largest of problems. This is due to the small bookkeeping effort and the sequential nature of the solution. (6) Spatial periodicity can be taken into account in a natural manner. (7) It is anticipated that this method will be useful in areas like control optimization, identification and possibly non-linear phenomena. The feasibility of this technique as well as several of the above advantages have been demonstrated with several examples.
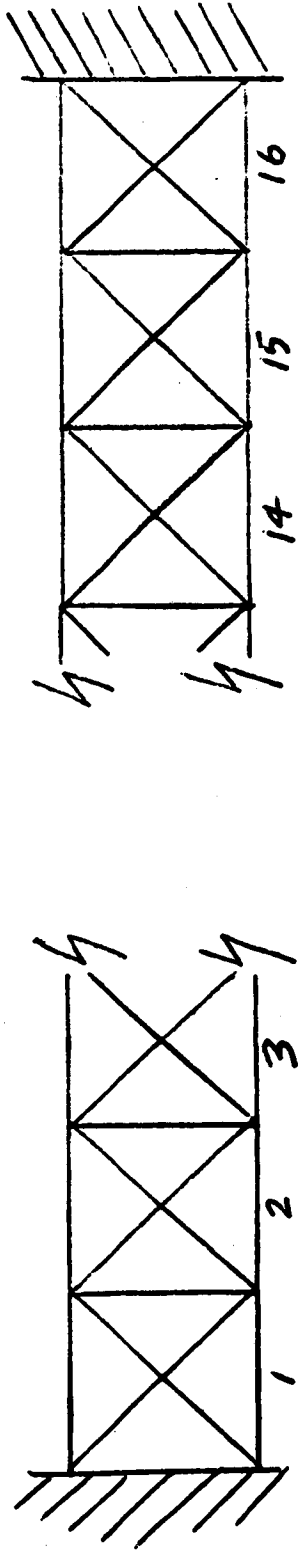
VI. EXAMPLE

FIXED-FIXED TRUSS
16 BAYS
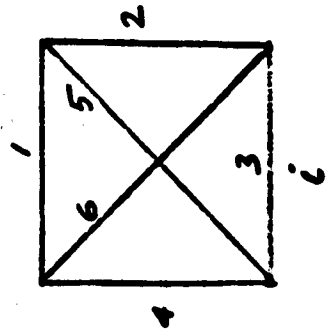
$L_1 = L_2 = L_3 = L_4 = 50$

$L_5 = L_6 = 50\sqrt{2}$

$A = 1$

$E = 10 \times 10^6$

$\rho = 0.1$

$\frac{1}{g} = 0.00259$

VI. EXAMPLE (CONT)

FREQUENCY COMPARISONS

N	EXACT	MSC-NASTRAN	% ERROR	MSC-NASTRAN	% ERROR
1	15.13	15.05	0.5	15.13	-0.002
2	39.28	38.60	1.7	39.28	-0.01
3	72.08	69.72	3.3	72.10	-0.04
4	79.51	79.37	0.2	79.55	-0.06
5	111.2	105.6	5.1	111.3	-0.1
6	155.1	144.2	7	155.4	-0.2
7	159.2	158.1	0.7	159.5	-0.2
8	202.8	184.2	9.1	203.4	-0.3
9	239.1	224.5	6.1	240.3	-0.5
10	253.3	235.4	7.1	254.7	-0.5
40	788.1	691.0	12.3	823.4	-4.5
50	850.9	751.3	11.7	893.4	-5.0

PRESENTED TECHNIQUE

$$M_{LONG} = \rho A L \begin{bmatrix} 5/12 & 1/12 \\ 1/12 & 5/12 \end{bmatrix}$$

$$M_{TRANS} = \rho A L \begin{bmatrix} \frac{1}{2} & 0 \\ 0 & \frac{1}{2} \end{bmatrix}$$

USUAL VERSION

TAKING PINS AS NODES

$$M_{LONG} = \frac{\rho A L}{6} \begin{bmatrix} 2 & 1 \\ 1 & 2 \end{bmatrix}$$

$$M_{TRANS} = \frac{\rho A L}{6} \begin{bmatrix} 2 & 1 \\ 1 & 2 \end{bmatrix}$$

TAKING PINS AS NODES

VI. EXAMPLE (CONT)

FREQUENCY COMPARISONS

N	EXACT	MSC-NASTRAN	% ERROR	MSC-NASTRAN	% ERROR
1	15.13	15.05	0.5	15.12	0.07
2	39.28	38.59	1.8	39.24	0.1
3	72.08	69.67	3.3	71.92	0.2
4	79.51	79.31	0.3	79.49	0.03
5	111.2	105.4	5.2	110.8	0.4
6	155.1	143.7	7.4	154.3	0.5
7	159.2	157.6	1	159.1	0.06
8	202.8	183.2	9.7	201.4	0.7
9	239.1	222.6	8.1	238.8	0.1
10	253.3	233.9	7.7	251.0	0.9
40	788.1	649.4	17.6	777.0	1.4
50	850.9	700.1	17.7	837.1	1.6

PRESENTED TECHNIQUE →

$$M_{LONG} = \rho AL \begin{bmatrix} \frac{1}{2} & 0 \\ 0 & \frac{1}{2} \end{bmatrix}$$

$$M_{TRANS} = \rho AL \begin{bmatrix} \frac{1}{2} & 0 \\ 0 & \frac{1}{2} \end{bmatrix}$$

USE BEAM THEORY TO SIMULATE TRUSS ELEMENTS 277 NODES 534 DOFS (4 SEGMENT-ELEMENT)

NOTE, HAS NOT CONVERGED YET IN HIGH FREQS

SPACE STATION/SHUTTLE ORBITER

DYNAMICS DURING DOCKING

N. G. Fitz-Coy* and J. E. Cochran, Jr.[+]
Auburn University, AL 36849-3501

Mathematical models of a reference Space Station
configuration ("Power Tower") and a Space Shuttle
Orbiter are developed and used to study the dynamic
behavior of the Space Station/Orbiter system just
prior to and subsequent to an impulsive docking of
the two spacecraft. The physical model of the Space
Station is a collection of rigid and flexible bodies.
The orbiter is modeled as a rigid body. An algorhthm
developed for use in digitally simulating the dynamics
of the system is described and results of its applica-
tion are presented.

INTRODUCTION

Placing a permanently manned space station in low earth orbit has
been identified as the next major goal of the United States civilian
space program.[1] This station will serve as a multifunctional base for
scientific and commercial advances in space. It will contain
laboratories for research in such areas as communication, solar system
development, material processing, and astrophysics. The station will
also serve as a platform for satellite repair, thus expanding the life
span of these expensive space assets and reducing repair costs.
In-orbit satellite equipment updating will also be possible, thus
assuring that technological developments are quickly incorporated.
Additionally, the Space Station will serve as a base for the assembly of
other space structures which are too large to be first assembled on
earth and then placed into orbit by the Space Shuttle.

The National Aeronautics and Space Administration (NASA) has been
assigned the task of defining a reference configuration for the Space
Station. From a field of five candidate configurations, NASA has
selected the "Power Tower" arrangement (see Fig. 1) as the reference

---

* Graduate Research Assistant.

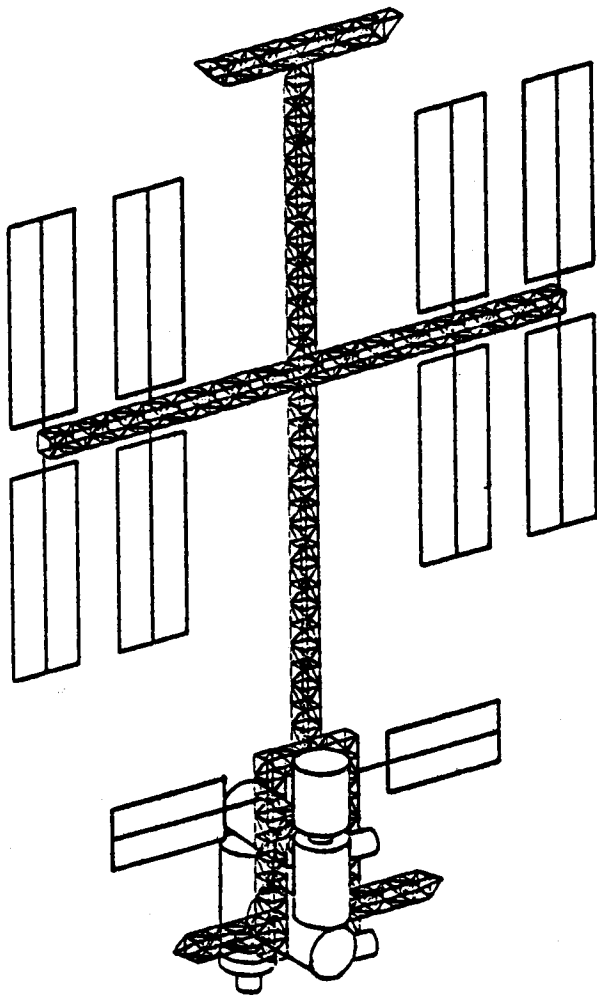+ Professor of Aerospace Engineering.

Fig. 1 "Power Tower" Space Station Configuration
(Without Payload).

configuration.[2] One of the reasons cited by NASA for selecting the
Power Tower configuration is its extraordinary expansion capabilities.
This configuration will consist of pressurized modules for habitation
and work areas, solar arrays for power acquisition, radiators for heat
dispersion, a docking port for the Space Shuttle, and a light-weight
truss constructed of carbon epoxy to which all the above are attached.
Due to the large size and the expected growth of the Space Station, it
is not reasonable to assume that the structure can be analyzed as a
rigid body.

The transfer of crew, supplies, and equipment to the Space Station
will require frequent docking of a Space Shuttle orbiter with the
station. It is therefore important that an understanding of the effects
of docking on the motion of the Space Station/Space Shuttle system be
developed. Estimates of these effects on the motion of the proposed
Space Station configuration are needed to adequately design its attitude
and translational control systems. Careful investigation of the docking
process should result in improvements in the reference configuration.

It is expected that the closing rate of an orbiter with the Space
Station will be small (on the order of 1.0 ft/sec). However, due to the
high degree of flexibility of the station, the docking of the orbiter
may still produce significant deflections of parts of the station. The
rare possibility of a Space Station control systems malfunction requires
that docking of the orbiter with an <u>uncontrolled</u> Space Station be
considered. Furthermore, the dynamic response of an uncontrolled Space
Station/Orbiter system during docking is of considerable importance from
the standpoint of control system design.

Early studies on docking involved investigators such as Williams,[3]
Grubin,[4] Chiarappa,[5] Brayton,[6] and Cochran and Henderson.[7] With the
exception of the work done by Cochran and Henderson, these early studies
were not concerned with the effects of flexibility on docking. In
considering the effects of flexibility, Cochran and Henderson analyzed a
system consisting of a rigid target vehicle to which two point masses
are connected by massless, flexible, extensible rods. A rigid
rendezvous vehicle was allowed to dock with the target vehicle and the
effects of the flexibility of the appendages were then analyzed.

Recently, the problem of spacecraft flexibility has received
renewed attention. In particular, Levinson and Kane,[8,9,10] have
considered the planar docking dynamics of bodies consisting of flexible
and rigid components. Some of the work done by Levinson and Kane
involves the docking dynamics of (1) a spacecraft modeled as a
cantilever beam and a rigid rendezvous vehicle, and (2) a spacecraft
modeled as a free-free beam and a rigid rendezvous vehicle.[9,10] In
these analyses, the deformation of the structure was represented by
unconstrained mode shapes which were obtained using a finite element
approach. It was shown by Hablani[11] that unconstrained mode shapes
portray the deformation of the structure more accurately than
constrained mode shapes. Here, "constrained mode shapes" refers to mode
shapes obtained when one end of the structure is constrained and the

structure is then caused to vibrate at its natural frequencies. On the other hand, unconstrained mode shapes are obtained when the structure is completely free. Many other investigators such as Likins,[12] Hughes and Skelton[13] and Ho and Herber[14] have developed simulation routines and modal truncation methods to analyze the effects of flexibility on large spacecraft.

The docking problem considered in this paper differs from the work done by Levinson and Kane. Herein, the motion is three-dimensional rather than planar and a more complex model of one of the bodies is developed and utilized. Unconstrained mode shapes are used to define the motion of the structure. These mode shapes were obtained from the MacNeal-Schwendler (MSC) Nastran[16] finite-element modal analysis routine. They were incorporated in a computer program developed to simulate the dynamics of the Space Station before and after docking. A particular docking mechanism is not considered; instead, the docking is modeled as an impulsive interaction between the Space Station and an Orbiter.

In the following sections the governing equations of the Space Station/Orbiter system are derived and simulation results are presented. The motions of the Space Station and Space Station plus Orbiter system are considered first. Next, the equations governing the impulsive interaction between the Station and an Orbiter are derived. Use of the complete set of equations to simulate the motion of the Space Station before and after docking with an Orbiter occurs is then discussed. Representative simulation results are presented and interpreted. Finally, conclusions are stated along with suggestions for additional research.

EQUATIONS OF MOTION

The station is modeled as a hybrid of flexible and rigid components in which the base section (lower section containing the modules and the docking port) is modeled as a system of rigid bodies and the remaining structure (upper and lower keels, booms, and solar arrays) is modeled as a collection of flexible bodies. The center of mass of the undeformed station is assumed to move in a circular orbit about the earth. Because impulsive docking is assumed, the presence in the system of the Orbiter after docking is modeled by adding a rigid body to the base section of the original Station model.

As shown in Fig. 2, the inertial position vector $\underline{R}_p$ of a generic mass element, P, of mass, dm, can be written as

$$\underline{R}_p = \underline{R}_s + \underline{r} , \tag{1}$$

where $\underline{r}$ includes vectors for both the deformed and undeformed structure. If the structure is assumed to be flexible, the vector $\underline{r}$ can be expressed as

$$\underline{r} = \underline{r}_u + \underline{u} .$$ (2)

As shown in Fig. 3, $\underline{r}_u$ is the vector locating the point P in the $SX_sY_sZ_s$ system when the structure is undeformed; and $\underline{u}$ defines the deformation of the structure in the $SX_sY_sZ_s$ system. The $SX_sY_sZ_s$ system is tied to the station in such a way that S coincides with the station's mass center when the structure is undeformed. The nominal orientation of this coordinate system is such that the X_s-axis is tangent to the orbit, the Y_s-axis is parallel to the boom and points towards starboard, and the Z_s-axis is parallel to the keel and is directed radially towards the center of the earth. When docking occurs, the $SX_sY_sZ_s$ system rotates with the Space Station. If the deformation is defined in terms of unconstrained mode shape vectors, $\underline{\phi}_k$, then $\underline{u}$ can be written as

$$\underline{u} = \sum_{k=1}^{N} \underline{\phi}_k q_k ,$$ (3)

where $\underline{\phi}_k$ is the mode shape of the kth mode, and q_k is the generalized coordinate associated with the kth mode. Substitution of Eq. (2) into Eq. (1) results in

$$\underline{R}_p = \underline{R}_s + \underline{r}_u + \underline{u}.$$ (4)

The translational equations of motion are obtained from

$$\int_{M_s} \underline{f}\, dm = \int_{M_s} \underline{a}_p\, dm = \int_{M_s} \underline{\ddot{R}}_p\, dm,$$ (5)

where $\underline{f}$ is the force per unit mass acting on the differential element of mass, $\overline{dm}$, and M_s is the total station mass.

From Eq. (4), $\underline{\ddot{R}}_p$ can be expressed as

$$\underline{\ddot{R}}_p = \underline{\ddot{R}}_s + \underline{\dot{\omega}}_s \times (\underline{r}_u + \underline{u}) + \underline{\omega}_s \times [\underline{\omega}_s \times (\underline{r}_u + \underline{u})] + 2\underline{\omega}_s \times \underline{\dot{u}} + \underline{\ddot{u}} ,$$ (6)

where $\underline{\omega}_s$ is the angular velocity of the $SX_sY_sZ_s$ system and a "$\cdot$" over a vector denotes time differentiation of that vector's X_s-, Y_s- and Z_s-components only. Substituting Eqs. (3) and (6) into Eq. (5), the resulting equation can be evaluated to obtain the following matrix form of the translational equations of motion:
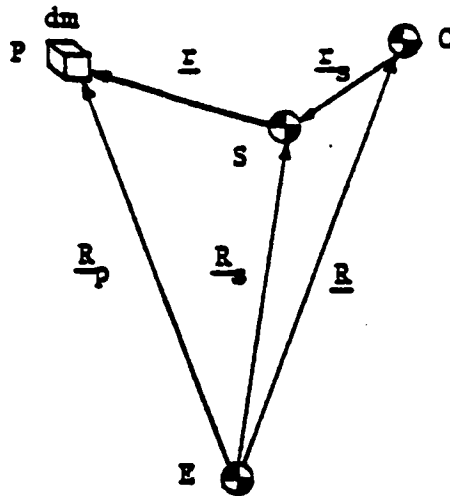
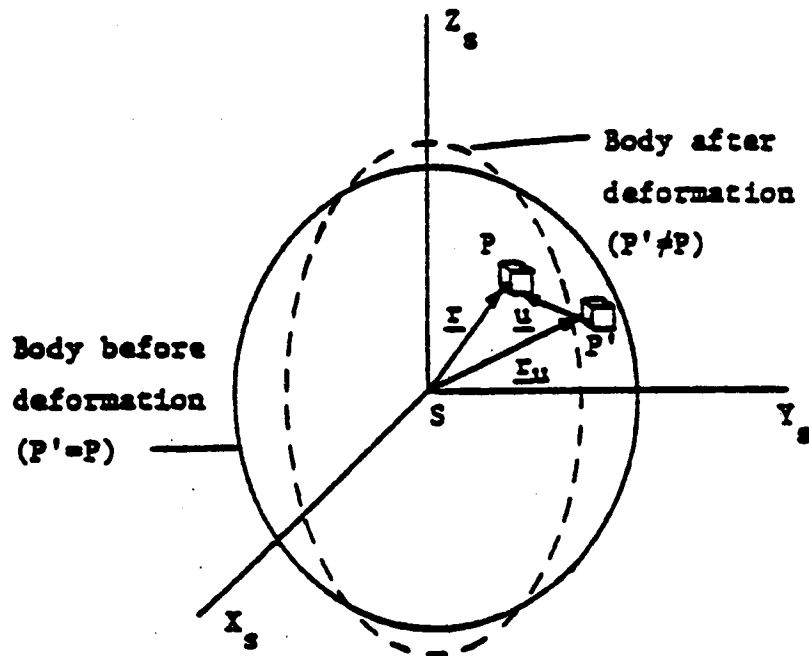**Fig. 2. Inertial Position Vector of Differential Element, dm.**

Fig..3. Description of Space Station's Deformation in the $SX_sY_sZ_s$ System.

$$\underline{F}^{ex} = M_s \, \underline{\ddot{R}}_s + \underline{C}^T \sum_{k=1}^{N} \, [(\underline{\dot{\tilde{\omega}}}_s + \underline{\tilde{\omega}}_s \underline{\tilde{\omega}}_s) \, \underline{m}_k q_k$$

$$+ 2\underline{\tilde{\omega}}_s \underline{m}_k \dot{q}_k + \underline{m}_k \ddot{q}_k] \qquad (7)$$

where $\underline{m}_k$ is the modal momentum coefficient[11] defined as

$$\underline{m}_k = \int_{M_s} \underline{\phi}_k \, dm \, , \qquad (8)$$

and $\underline{F}^{ex}$ is the total external force. The direction cosine matrix, $\underline{C}^T$, is also introduced to accommodate the different coordinate systems used in writing Eq. (6). Here, $\underline{C}^T$ transforms vector components in $SX_sY_sZ_s$ system to corresponding components in the EXYZ system. Thus, Eq. (7) represents the translational equations of motion written in the EXYZ system.

The rotational equations of motion about the station's mass center are obtained from

$$\int_{M_s} \underline{\tau} \, dm = \int_{M_s} \underline{r} \times \underline{a}_p dm, \qquad (9)$$

where $\underline{\tau}$ is the torque per unit mass about S due to the force per unit mass $\underline{f}$. The left side of Eq. (12) is the total external torque about the station's mass center; that is,

$$\int_{M_s} \underline{\tau} \, dm = \underline{T}^{ex} \, . \qquad (10)$$

By substituting Eqs. (2), (6), and (10) into Eq. (9), and evaluating the integrals which appear in the resulting equation, one may rewrite Eq. (9) in the matrix form,

$$\underline{T}^{ex} = \sum_{k=1}^{N} \, [q_k \underline{\tilde{m}}_k \underline{C}\underline{\ddot{R}}_s + \underline{I}\underline{\dot{\omega}}_s + \underline{\tilde{\omega}}_s \underline{I}\underline{\omega}_s$$

$$+ 2\underline{A}_k \underline{\phi}_k q_k + 2\underline{D}_k \underline{\phi}_k \dot{q}_k + (\underline{\mu}_k + \sum_{j=1}^{N} \underline{\beta}_{kj} q_j)\ddot{q}_k] \, , \qquad (11)$$

where $\underline{I}$ is the inertia dyadic of the station. The flexibility coefficient,[11] $\underline{\mu}_k$, of Eq. (11) is defined as

$$\underline{\mu}_k \stackrel{\Delta}{=} \int_{M_s} \tilde{\underline{r}}_u \underline{\phi}_k \, dm \qquad (12)$$

and

$$\underline{\beta}_{kj} \stackrel{\Delta}{=} \int_{M_s} \tilde{\underline{\phi}}_j \underline{\phi}_k \, dm \ .$$

Again, the direction cosine matrix, $\underline{\underline{C}}$, has been used to transform the components of vectors to a common reference coordinate system (i.e., the $SX_sY_sZ_s$ system in this case).

Equations (7) and (11) constitute six of the six plus N (6+N) equations needed to define the motion. The remaining N equations are obtained from the equations

$$\int_{M_s} \underline{\phi}_j \cdot \underline{f} \, dm = \int_{M_s} \underline{\phi}_j \cdot \underline{a}_p \, dm \qquad , \ j=1,2,\ldots,N, \qquad (13)$$

where $\underline{a}_p$ is given by Eq. (6). Generalized forces, Q_j, $j=1,2,3,\ldots,N$, may be defined by

$$Q_j = \int_{M_s} \underline{\phi}_j \cdot \underline{f} \, dm = \int_{M_s} \underline{\phi}_j \cdot \underline{f}^{ex} \, dm + \int_{M_s} \underline{\phi}_j \cdot \underline{f}^{in} \, dm \ , \qquad (14)$$

where $\underline{f}^{ex}$ and $\underline{f}^{in}$ are the "external" and "internal" parts of $\underline{f}$. Thus, Eq. (13) can be rewritten as

$$Q_j = \int_{M_s} [\underline{\phi}_j \cdot \ddot{\underline{R}}_s + \underline{\phi}_j \cdot \dot{\underline{\omega}}_s \times (\underline{r}_u + \underline{u}) + \underline{\phi}_j \cdot \underline{\omega}_s \times \{\underline{\omega}_s \times (\underline{r}_u + \underline{u})\}$$

$$+ \ 2\underline{\phi}_j \cdot \underline{\omega}_s \times \dot{\underline{u}} + \underline{\phi}_j \cdot \ddot{\underline{u}}] \, dm \ . \qquad (15)$$

The integrals on the right-hand side of Eq. (15) may be evaluated to obtain the following matrix form for Eq. (15):

$$Q_j = \underline{m}_j^T \underline{\underline{C}} \ddot{\underline{R}}_s + (\underline{\mu}_k^T + \sum_{j=1}^{N} \underline{\beta}_{kj}^T q_j) \dot{\underline{\omega}}_s + \underline{\omega}_s^T \underline{\underline{R}}_j \underline{\omega}_s$$

$$+ \sum_{k=1}^{N} \underline{\omega}_s^T \underline{\underline{P}}_{jk} \underline{\omega}_s q_k + 2 \sum_{k=1}^{N} \underline{\omega}_s^T \underline{\beta}_{jk} \dot{q}_k + \sum_{k=1}^{N} m_{jk} \ddot{q}_k, \qquad (16)$$

where

$$\underset{=}{R}_j \triangleq \int_{M_s} \tilde{\phi}_j \tilde{r}_u \, dm , \tag{17a}$$

$$\underset{=}{P}_{jk} \triangleq \int_{M_s} \tilde{\phi}_j \tilde{\phi}_k \, dm , \tag{17b}$$

$$m_{jk} \triangleq \int_{M_s} \phi_j^T \phi_k \, dm . \tag{17c}$$

Since the elastic deformations are assumed small (i.e., less than 10% of the structural length), then all terms second-order and higher-order in q_k are dropped from Eqs. (7), (11), and (16). Similar action is taken regarding the angular velocity, $\underline{\omega}_s$, of the station. Also, all products of q_k and $\underline{\omega}_s$ are neglected.

By dropping the appropriate terms from Eqs. (7), (11), and (16), one may rewrite these equations as follows:

$$\underline{F}^{ex} = M_s \underline{\ddot{R}}_s + \underset{=}{C}^T \sum_{k=1}^{N} [-\underset{=}{\tilde{m}}_k q_k \underline{\dot{\omega}}_s + \underline{m}_k \ddot{q}_k], \tag{18}$$

$$\underline{T}^{ex} = \sum_{k=1}^{N} [q_k \underset{=}{\tilde{m}}_k \underset{=}{C} \underline{\ddot{R}}_s + \underset{=}{I} \underline{\dot{\omega}}_s + \underline{\mu}_k \ddot{q}_k], \tag{19}$$

$$Q_j = \underline{m}_j^T \underset{=}{C} \underline{\ddot{R}}_s + \underline{\mu}_k^T \underline{\dot{\omega}}_s + \sum_{k=1}^{N} m_{jk} \ddot{q}_k . \tag{20}$$

Explicit expressions for the forces and torques expressed in Eqs. (18), (19), and (20) are now developed.

Forces and Torques

A satellite in a low earth orbit (nominally 300 km altitude) is affected by several forces. For example, the important external forces and torques may include those due to gravity, the atmosphere, thrusters, other control devices, and solar radiation. In this paper, gravitational forces and gravity-gradient torques are the only external forces and torques considered.

The gravitational force acting on a differential element of mass, dm, is expressed as

$$\underline{f}^g = -\frac{\mu_o}{R_p^3} \underline{R}_p \ , \tag{21}$$

where μ_o is the gravitational constant of the earth and $\underline{R}_p$ is the vector shown in Fig. 4.

By recalling Eq. (1), one can approximate R_p^{-3} by (Ref. 17)

$$R_p^{-3} = \frac{1}{R_s^3} [1 - \frac{3}{R_s^2} \underline{r} \cdot \underline{R}_s + H.O.T.] \tag{22}$$

By substituting Eqs. (1) and (22) into Eq. (21), and then integrating, one may show that

$$\underline{F}^{ex} = \underline{F}^g = -\frac{\mu_o}{R_s^3} M_s \underline{R}_s - \frac{\mu_o}{R_s^3} \underline{\underline{C}}^T \sum_{k=1}^{N} \underline{m}_k q_k$$

$$+ \frac{3\mu_o}{R_s^5} \sum_{k=1}^{N} (q_k \underline{\underline{C}}^T \underline{m}_k \underline{R}_s) \underline{R}_s$$

$$+ \frac{3}{2} \frac{\mu_o}{R_s^5} \underline{\underline{C}}^T t_r (\underline{\underline{I}}) \underline{R}_s - 3 \frac{\mu}{R_s^5} \underline{R}_s \underline{\underline{C}}^T \underline{\underline{I}} + H.O.T. \tag{23}$$

Next, the contribution by terms containing R_s^{-5} may be neglected and the external force expressed (in the EXYZ system) as

$$\underline{F}^{ex} = -\frac{\mu_o}{R_s^3} [M_s \underline{R}_s + \underline{\underline{C}}^T \sum_{k=1}^{N} \underline{m}_k q_k] \ . \tag{24}$$

It was noted by Kaplan[18] that gravity-gradient torques provide excellent directional stability for spacecraft in eccentric orbits. Thus, in considering a circular orbit (eccentricity equals zero), it is reasonable to assume that gravity-gradient torques may be used to provide stabilization for the Space Station. The gravity-gradient torque can be obtained by crossing the vector $\underline{r}$ with the external forces defined in Eq. (21) (Ref. 17, pp. 112-119) and is presented here as

$$\underline{T}^{ex} = \frac{\mu_o}{R_s^3} [\underline{\underline{\tilde{C}R}}_s \sum_{k=1}^{N} \underline{m}_k q_k + \frac{3}{R_s^2} \underline{\underline{\tilde{C}R}}_s \underline{\underline{I}} \underline{\underline{C}} \underline{R}_s] \ . \tag{25}$$

Equation (25) represents a set of differential equations, written in the $SX_sY_sZ_s$ system, that governs the rotational motion of the Space Station.
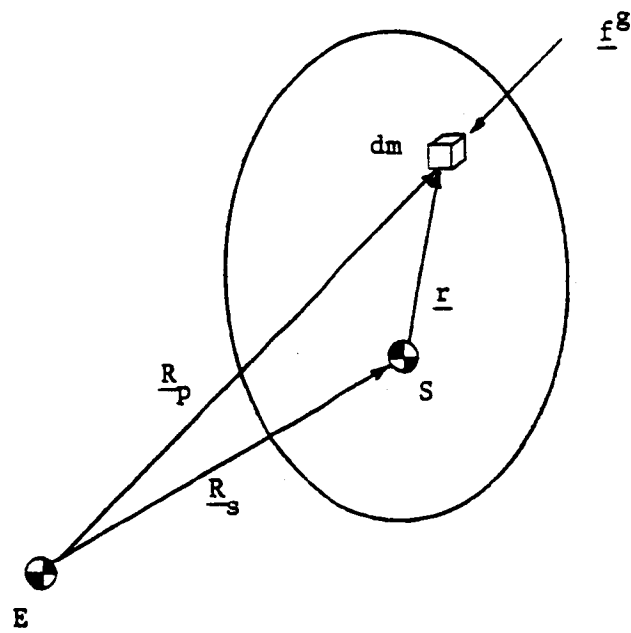
Fig. 4 Gravitational Force Acting on dm.

The generalized force, Q_j, associated with the jth mode of vibration can be decomposed into two parts. One part contains the contribution due to internal forces, and the other contains the contribution due to external forces. Each contribution can be formulated as shown in the following set of equations.

$$Q_j = Q_j^{in} + Q_j^{ex} \qquad (26a)$$

$$Q_j^{in} = \sum_{k=1}^{N} m_{jk}\ddot{q}_k + \sum_{k=1}^{N} c_{jk}\dot{q}_k + \sum_{k=1}^{N} k_{jk}q_k \qquad (26b)$$

$$Q_j^{ex} = -\frac{\mu_o}{R_s^3} [\underline{R}_s^T \underline{\underline{C}}^T \underline{m}_j + \gamma_j + \sum_{k=1}^{N} m_{jk}q_k] \qquad (26c)$$

In Eqs. (26), c_{jk} and k_{jk} represent the jk^{th} element of the structural damping and stiffness matrices. The quantity γ_j in Eq. (26) is defined as follows:

$$\gamma_j \overset{\Delta}{=} \int_{M_s} \underline{\phi}_j^T (\underline{r}_u)dm. \qquad (27)$$

The complete linearized equations of motion are obtained by combining Eqs. (18), (19), and (20) with Eqs. (24), (25), and (26). From these expressions, one may show that the equations that govern the translation motion may be expressed as

$$-\frac{\mu_o}{R_s^3} [M_s\underline{R}_s + \underline{\underline{C}}^T \sum_{k=1}^{N} \underline{m}_k q_k]$$

$$= M_s\ddot{\underline{R}}_s + \underline{\underline{C}}^T \sum_{k=1}^{N} [-\tilde{\underline{m}}_k q_k \underline{\omega}_s + \underline{m}_k \ddot{q}_k] , \qquad (28)$$

whereas, the rotational motion is governed by

$$\frac{\mu_o}{R_s^3} [\widetilde{\underline{\underline{CR}}}_s \sum_{k=1}^{N} \underline{m}_k q_k + \frac{3}{R_s^2} \widetilde{\underline{\underline{CR}}}_s \underline{\underline{I}} \underline{\underline{CR}}_s]$$

$$= \sum_{k=1}^{N} [q_k \tilde{\underline{m}}_k \underline{\underline{CR}}_s + \underline{\underline{I}}\dot{\underline{\omega}}_s + \underline{\mu}_k \ddot{q}_k] . \qquad (29)$$

The generalized coordinates are governed by the following expression:

$$-\frac{\mu_o}{R_s^3}\left[\sum_{k=1}^{N} m_{jk}q_k + \underline{R}_s^T \underline{C}^T \underline{m}_j + \gamma_j\right] + \sum_{k=1}^{N} m_{jk}\ddot{q}_k + \sum_{k=1}^{N} c_{jk}\dot{q}_k + \sum_{k=1}^{N} k_{jk}q_k$$

$$= \underline{m}_j^T \underline{C} \ddot{\underline{R}}_s + \underline{\mu}_j^T \dot{\underline{\omega}}_s + \sum_{k=1}^{N} m_{jk}\ddot{q}_k \quad . \tag{30}$$

The 6+N linearized differential equations expressed in Eqs. (28), (29), and (30) are sufficient to simulate the motion of the station before and after docking. To simulate motion after docking, M_s and $\underline{\underline{I}}$ must be adjusted to account for the presence of the orbiter that is now attached to the station.

DOCKING

As stated previously, a particular docking mechanism is not considered in this paper. Instead, the docking of the orbiter with the Space Station is assumed to produce impulsive changes in the kinematical variables. In what follows, the docking of the orbiter with the Space Station is modeled as rigid body docking with a cantilever beam/rigid body assembly. A similar problem was addressed by Levinson and Kane in Ref. 10 where they analyzed the planar case of a rigid body docking with a free beam.

The system to be analyzed (see Fig. 5) consists of a single rigid body (orbiter) and a cantilever beam/rigid body assembly (Station). The system of Fig. 5 can be subdivided into the systems of Fig. 6.

The Space Station (bodies A and B) is assumed to have linear and angular velocities, $\underline{u}_s$ and $\underline{\omega}_s$, before docking occurs. After docking, these velocities become $\underline{v}_s$ and $\underline{\Omega}_s$, respectively. The orbiter's linear velocity will change from $\underline{u}_o$ to $\underline{v}_o$ due to docking. Also, the angular velocity of the orbiter will change from $\underline{\omega}_o$ to $\underline{\Omega}_s$. As stated above, the orbiter and the Space Station are assumed to couple rigidly during docking, and then to rotate together.

Equations for Docking

The law of conservation of linear momentum for body A can be expressed as

$$\int_{m_A} (\underline{v}_a - \underline{u}_a)dm = \int_{t_1}^{t_2}(\int \underline{f}\, dm)dt , \tag{31}$$

where m_A is the mass of body A. The quantities $\underline{u}_a$ and $\underline{v}_a$ are the "before" and "after" velocities of a differential element of mass, dm, and are defined here as
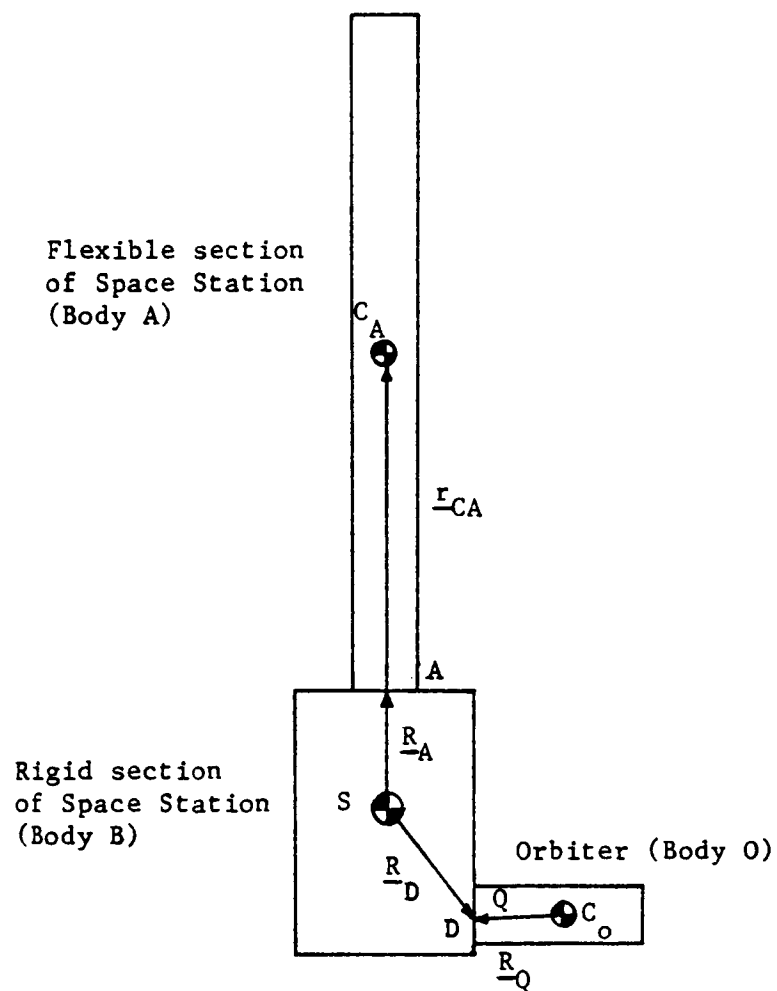
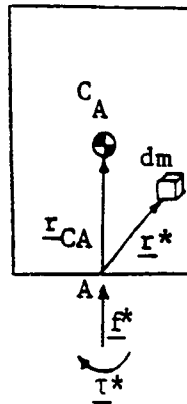Fig. 5. Schematic of Orbiter/Space Station Assembly.

Fig. 6(a). Free-Body Diagram for Flexible Section of
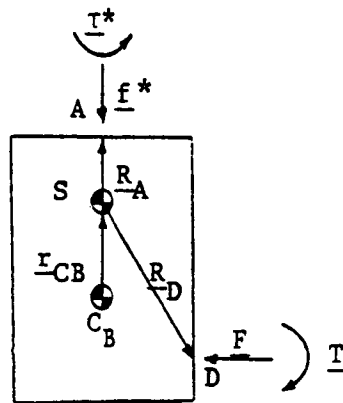the Space Station (Body A).

Fig. 6(b). Free-Body Diagram for Rigid Section of
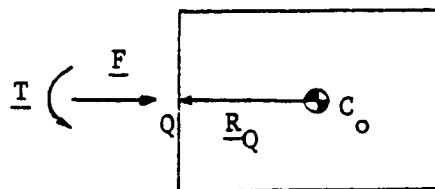the Space Station (Body B).

Fig. 6(c). Free-Body Diagram for the Orbiter (Body O).

$$\underline{u}_a = \underline{u}_s + \underline{\omega}_s \times \underline{R}_A + \underline{\omega}_s \times \underline{r}^* + \sum_{k=1}^{N} \underline{\phi}_k \dot{q}_k^- \qquad (32a)$$

and

$$\underline{v}_a = \underline{v}_s + \underline{\Omega}_s \times \underline{R}_A + \underline{\Omega}_s \times \underline{r}^* + \sum_{k=1}^{N} \underline{\phi}_k \dot{q}_k^+ \qquad (32b)$$

where $\dot{q}_k^-$ and $\dot{q}_k^+$ are the "before" and "after" time rate of change of the generalized coordinates. Equation (32) may be substituted into Eq. (31), and the result integrated to obtain the following form of the statement of the law of conservation of linear momentum for body A:

$$m_A (\underline{v}_s - \underline{u}_s) + m_A (\underline{\Omega}_s - \underline{\omega}_s) \times (\underline{R}_A + \underline{r}_{CA}) + \sum_{k=1}^{N} \underline{P}_k (\dot{q}_k^+ - \dot{q}_k^-)$$

$$= - \int_{t_1}^{t_2} \underline{f}^* \, dt \quad . \qquad (33)$$

The quantity $\underline{P}_k$ shown in Eq. (33) represents the momentum flexibility coefficient[11] for body A and is defined as

$$\underline{P}_k \triangleq \int_{m_A} \underline{\phi}_k \, dm \quad .$$

The law of conservation of linear momentum may also be applied to bodies B and O. For body B, one has

$$m_B (\underline{v}_s - \underline{u}_s) = \int_{t_1}^{t_2} (\underline{F} + \underline{f}^*) dt, \qquad (34)$$

and for body O,

$$m_o (\underline{v}_o - \underline{u}_o) = - \int_{t_1}^{t_2} \underline{F} \, dt \qquad (35)$$

Equations (33), (34), and (35) may be combined to give

$$m_A (\underline{v}_s - \underline{u}_s) + m_A (\underline{\Omega}_s - \underline{\omega}_s) \times (\underline{R}_A + \underline{r}_{CA}) + \sum_{k=1}^{N} \underline{P}_k (\dot{q}_k^+ - \dot{q}_k^-)$$

$$+ m_B (\underline{v}_s - \underline{u}_s) + m_o (\underline{v}_o - \underline{u}_o) = \underline{0} \qquad (36)$$

148

The dot product of $\underline{\phi}_j$ with Eqs. (31) and (32) combined provides an expression for $\overset{\circ}{q}_k^+ - \overset{\circ}{q}_k^-$.

$$\int_m [(\underline{v}_s - \underline{u}_s) \cdot \underline{\phi}_j + (\underline{\Omega}_s - \underline{\omega}_s) \times (\underline{R}_A + \underline{r}^*) \cdot \underline{\phi}_j$$

$$+ \sum_{k=1}^{N} \underline{\phi}_j \cdot \underline{\phi}_k (\overset{\circ}{q}_k^+ - \overset{\circ}{q}_k^-)] \, dm = - \int_{t_1}^{t_2} \underline{\phi}_j \cdot \underline{f}^* \, dt \qquad (37)$$

The right-hand side of Eq. (37) is zero because at the point at which $\underline{f}^*$ is applied, the deformation is zero. Thus, Eq. (37) can be rewritten in matrix form as

$$\underline{P}_j^T(\underline{v}_s - \underline{u}_s) - \underline{P}_j^T \tilde{\underline{R}}_A(\underline{\Omega}_s - \underline{\omega}_s) + \underline{G}_j^T(\underline{\Omega}_s - \underline{\omega}_s)$$

$$= - \sum_{k=1}^{N} m_{jk}(\overset{\circ}{q}_k^+ - \overset{\circ}{q}_k^-) \qquad (38)$$

where

$$\underline{G}_j = \int_{m_A} \tilde{\underline{r}}^* \, \underline{\phi}_j \qquad (39a)$$

and

$$m_{jk} = \int_{m_A} \underline{\phi}_j^T \underline{\phi}_k \, dm \ . \qquad (39b)$$

To account for the N modes of vibration, Eq. (38) can be rewritten in the following form:

$$\underline{\underline{P}}^T(\underline{v}_s - \underline{u}_s) - \underline{\underline{P}}^T \tilde{\underline{R}}_A(\underline{\Omega}_s - \underline{\omega}_s) + \underline{\underline{G}}^T(\underline{\Omega}_s - \underline{\omega}_s) = \underline{\underline{M}} \overset{\circ}{\underline{q}} \ , \qquad (40)$$

The Nx3 matrices, $\underline{\underline{P}}^T$ and $\underline{\underline{G}}^T$, are defined as:

$$\underline{\underline{P}}^T = \begin{bmatrix} \underline{P}_1^T \\ \underline{P}_2^T \\ \vdots \\ \underline{P}_N^T \end{bmatrix} , \qquad \underline{\underline{G}}^T = \begin{bmatrix} \underline{G}_1^T \\ \underline{G}_2^T \\ \vdots \\ \underline{G}_N^T \end{bmatrix} \ . \qquad (41a)$$

$$\underset{=}{M} = - \begin{bmatrix} m_{11} & m_{12} & \cdots & m_{1N} \\ m_{21} & & & \\ \vdots & & & \\ m_{N1} & \cdots & & m_{NN} \end{bmatrix} \quad ; \quad \underset{.}{\dot{q}} = \begin{bmatrix} \dot{q}_1^+ - \dot{q}_1^- \\ \dot{q}_2^+ - \dot{q}_2^- \\ \vdots \\ \dot{q}_N^+ - \dot{q}_N^- \end{bmatrix} \qquad (41b)$$

The law of conservation of angular momentum yields three additional expressions. These expressions are obtained from the following equations by applying the law of conservation of angular momentum to bodies A and B combined (Space Station), and to body O (Orbiter). Equation (42) is obtained when the law of conservation is applied to the Space Station.

$$(\underset{=}{I}_s + \underset{=}{I}_A^*) \cdot (\underline{\Omega}_s - \underline{\omega}_s) + [m_A(\underline{R}_A + \underline{r}_{CA}) + \sum_{k=1}^{N} \underline{P}_k q_k] \times (\underline{v}_s - \underline{u}_s)$$

$$+ \underline{R}_A \times \sum_{k=1}^{N} \underline{P}_k \dot{q}_k + \sum_{k=1}^{N} \underline{G}_k \dot{q}_k = \int_{t_1}^{t_2} [\underline{T} + \underline{R}_D \times \underline{F}] dt \qquad (42)$$

A similar expression is obtained for body O (Orbiter).

$$\underset{=}{I}_o \cdot (\underline{\Omega}_s - \underline{\omega}_s) = - \int_{t_1}^{t_2} [\underline{T} + \underline{R}_Q \times \underline{F}] \, dt \qquad (43)$$

If one combines Eqs. (35), (42) and (43), then the statement of conservation of angular momentum can be expressed in the following matrix form:

$$(\underset{=}{I}_s + \underset{=}{I}_A^* + \underset{=}{I}_D) \underline{\Omega}_s + [m_A(\tilde{\underline{R}}_A + \tilde{\underline{r}}_{CA}) + \underset{=}{P}q](\underline{v}_s - \underline{u}_s) + [\tilde{\underline{R}}_A \underset{=}{P} + \underset{=}{G}] \underset{.}{\dot{q}}$$

$$+ m_o(\tilde{\underline{R}}_D - \tilde{\underline{R}}_Q)(\underline{v}_o - \underline{u}_o) = (\underset{=}{I}_s + \underset{=}{I}_A^*) \underline{\omega}_s + \underset{=}{I}_o \underline{\omega}_o \qquad (44)$$

Equations (36), (40), and (44) represent six plus N (6+N) equations in nine plus N (9+N) unknowns. The relationship between $\underline{v}_s$ and $\underline{v}_o$ accounts for the remaining three equations. This relationship is written here as

$$\underline{v}_o = \underline{v}_s - (\tilde{\underline{R}}_D - \tilde{\underline{R}}_Q) \underline{\Omega}_s. \qquad (45)$$

It can be shown that Eqs. (36), (40), (44), and (45), when combined, yield the following equations that govern the impulsive interaction between the Station and the Orbiter.

$$[\underline{PM}^{-1} (\underline{G}^T - \underline{P}^T \tilde{\underline{R}}_A) - m_A (\tilde{\underline{R}}_A + \tilde{\underline{r}}_{CA}) - m_o (\tilde{\underline{R}}_D - \tilde{\underline{R}}_Q)] \; \underline{\Omega}_s$$

$$+ [(m_A + m_B + m_o) \underline{E} + \underline{PM}^{-1}\underline{P}^T] \; \underline{v}_s$$

$$= [(m_A + m_B) \underline{E} + \underline{PM}^{-1}\underline{P}^T] \; \underline{u}_s + m_o \underline{u}_o$$

$$+ [\underline{PM}^{-1} (\underline{G}^T - \underline{P}^T \tilde{\underline{R}}_A) - m_A (\tilde{\underline{R}}_A + \tilde{\underline{r}}_{CA})] \; \underline{\omega}_s \qquad (46)$$

$$[\underline{I}_s + \underline{I}_A^* + \underline{I}_o - m_o (\tilde{\underline{R}}_D - \tilde{\underline{R}}_Q)(\tilde{\underline{R}}_D - \tilde{\underline{R}}_Q)$$

$$+ (\tilde{\underline{R}}_A\underline{P} + \underline{G}) \; \underline{M}^{-1} (\underline{G}^T - \underline{P}^T \tilde{\underline{R}}_A)] \; \underline{\Omega}_s$$

$$+ [m_A(\tilde{\underline{R}}_A + \tilde{\underline{r}}_{CA}) + \widetilde{\underline{Pq}} + m_o (\tilde{\underline{R}}_D - \tilde{\underline{R}}_Q) + (\tilde{\underline{R}}_A\underline{P} + \underline{G})\underline{M}^{-1}\underline{P}^T] \; \underline{v}_s$$

$$= [m_A (\tilde{\underline{R}}_A + \tilde{\underline{r}}_{CA}) + \widetilde{\underline{Pq}} + (\tilde{\underline{R}}_A\underline{P} + \underline{G})\underline{M}^{-1}\underline{P}^T] \; \underline{u}_s + m_o (\tilde{\underline{R}}_D - \tilde{\underline{R}}_Q)\underline{u}_o$$

$$+ [\underline{I}_s + \underline{I}_A^* + (\tilde{\underline{R}}_A\underline{P} + \underline{G}) \; \underline{M}^{-1} (\underline{G}^T - \underline{P}^T \tilde{\underline{R}}_A)] \; \underline{\omega}_s + \underline{I}_o \underline{\omega}_o \qquad (47)$$

$$\dot{\underline{q}} = \underline{M}^{-1}\underline{P}^T (\underline{v}_s - \underline{u}_s) + \underline{M}^{-1} [\underline{G}^T - \underline{P}^T \tilde{\underline{R}}_A](\underline{\Omega}_s - \underline{\omega}_s) \qquad (48)$$

One may obtain from Eqs. (46), (47) and (48) the changes in the state variables which occur during docking. Consideration is now given to the simulation of the motion of the Space Station before and after docking occurs.

SOLUTION TECHNIQUES

Computer programs were developed and used in conjunction with the Harris H-800 minicomputer at Auburn University to simulate the motion of the Space Station. The computer programs consist of three steps, the first of which simulates the motion of the station prior to docking. The second step encompasses the determination of the changes in the kinematical variables due to the docking of an Orbiter with the Space Station. Finally, the third step simulates the motion of the Space Station/Orbiter system after docking has occurred.

In the following sections, the details of the numerical simulation of the Space Station before and after docking are discussed.

Mode Shapes

To describe the deformations of the flexible structure, unconstrained mode shape vectors (eigenvectors) were obtained from a MSC Finite Element program available at Auburn University on the IBM 3033 computer. These mode shape vectors were obtained using the Givens (tridiagonal) method, and were normalized with respect to the mass of the Station.

The truss structure of Fig. 1 was modeled as a structure consisting of "equivalent" beam elements (see Fig. 7). The equivalence was obtained by modeling a section of the truss structure and subjecting it to known forces and torques. With the deformations (both linear and angular) obtained from this model, the stiffness of an equivalent beam was computed using standard beam theory equations.

Using the equivalent beam model for the station, two sets of eigenvectors were obtained. One set contains the eigenvectors for the station without the Orbiter and the other set contains the eigenvectors for the Space Station/Orbiter system. To obtain the eigenvectors for the Space Station/Orbiter system, the Orbiter was modeled as a rigid body attached to the rigid base of the Station.

Numerical Simulation

Equations (28), (29), and (30) represent a set of six plus N (6+N) coupled, second-order differential equations. In the simulation process, these equations are numerically integrated using a fourth-order Runge-Kutta scheme. In order to efficiently utilize the Runge-Kutta scheme, Eqs. (28), (29), and (30) were manipulated to give the following expressions. The expression associated with the generalized coordinates is shown here as

$$[M]\ddot{q} + [C]\dot{q} + [K]\, q = F \tag{49}$$

where

$$[M] = -\frac{1}{M_s}\, \underline{\underline{X}}^T \underline{\underline{X}}$$

$$+ [\frac{1}{M_s}\, \underline{\underline{X}}^T \underline{\underline{X}} q + \underline{\underline{u}}^T]\, \underline{\underline{I}}^{-1} \{-\underline{\underline{u}} + \frac{1}{M_s}\, \widetilde{\underline{\underline{X}}q}\underline{\underline{X}}\} \; , \tag{50a}$$

$$[C] = -2\zeta[\omega_n]\underline{\underline{M}} \tag{50b}$$
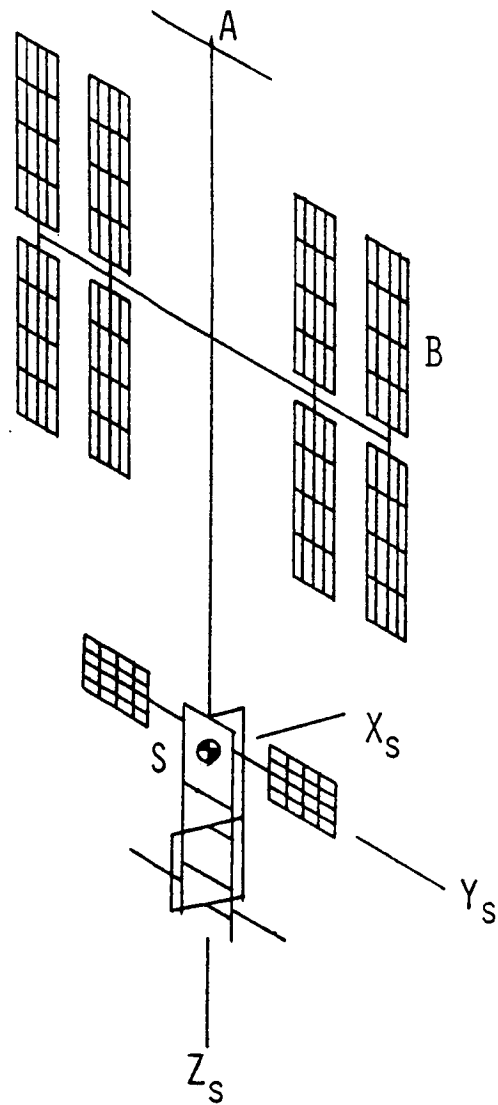
Fig. 7 NASTRAN Equivalent Beam Model.

$$[K] = \frac{1}{M_s} \frac{\mu_o}{R_s^3} \underset{=}{X}^T \underset{=}{X} - [\omega_n^2] \underset{=}{M} + \frac{\mu_o}{R_s^3} \underset{=}{M}$$

$$+ [\frac{1}{M_s} \underset{=}{X}^T \underset{=}{\widetilde{Xg}} + \underset{=}{\mu}^T] \underset{=}{I}^{-1} \{\frac{1}{M_s} \frac{\mu_o}{R_s^3} \underset{=}{\widetilde{Xg}} \underset{=}{X}\} , \qquad (50c)$$

and

$$\underline{F} = - \frac{\mu_o}{R_s^3} \underline{\Gamma} - [\frac{1}{M_s} \underset{=}{X}^T \underset{=}{\widetilde{Xg}} + \underset{=}{\mu}^T] \underset{=}{I}^{-1} \{3 \frac{\mu_o}{R_s^5} \underset{=}{\widetilde{CR}}_s \underset{=}{I} \underset{=}{CR}_s\} \qquad (51d)$$

The angular acceleration of the Station is obtained from

$$\dot{\underline{\omega}}_s = \underset{=}{I}^{-1} \{3 \frac{\mu_o}{R_s^5} \underset{=}{\widetilde{CR}}_s \underset{=}{I} \underset{=}{CR}_s + \frac{1}{M_s} \frac{\mu_o}{R_s^3} \underset{=}{\widetilde{Xg}} \underset{=}{Xg}$$

$$+ (-\underset{=}{\mu} + \frac{1}{M_s} \underset{=}{\widetilde{Xg}} \underset{=}{X}) \ddot{\underline{q}}\} , \qquad (52)$$

and the linear acceleration of the center of mass of the station is obtained from

$$\ddot{\underline{R}}_s = - \frac{\mu_o}{R_s^3} \underline{R}_s - \frac{1}{M_s} \frac{\mu_o}{R_s^3} \underset{=}{C}^T \underset{=}{Xg} + \frac{1}{M_s} \underset{=}{C}^T \underset{=}{\widetilde{Xg}} \dot{\underline{\omega}}_s - \frac{1}{M_s} \underset{=}{C}^T \underset{=}{Xg} \ddot{\underline{q}} \qquad (53)$$

In Eqs. (51), (52), and (53),

$$\underset{=}{X} = [\underline{m}_1 \ \underline{m}_2 \ \underline{m}_3 \ \cdots \ \underline{m}_N] \qquad (54a)$$

$$\underset{=}{\mu} = [\underline{\mu}_1 \ \underline{\mu}_2 \ \underline{\mu}_3 \ \cdots \ \underline{\mu}_N] , \qquad (54b)$$

$$\underset{=}{M} = \begin{bmatrix} m_{11} & m_{12} & \cdots & m_{1n} \\ m_{21} & m_{22} & \cdots & m_{2n} \\ \vdots & \vdots & & \vdots \\ \ddot{m}_{N1} & \ddot{m}_{N2} & \cdots & \ddot{m}_{NN} \end{bmatrix} , \quad \underline{g} = \begin{bmatrix} q_1 \\ q_2 \\ \vdots \\ \dot{q}_N \end{bmatrix} , \qquad (54c,d)$$

$$\underline{\Gamma} = \begin{bmatrix} \gamma_1 \\ \gamma_2 \\ \vdots \\ \gamma_N \end{bmatrix} , \quad \underset{=}{X}^T = \begin{bmatrix} \underline{m}_1^T \\ \underline{m}_2^T \\ \vdots \\ \underline{m}_N^T \end{bmatrix} , \quad \underset{=}{\mu}^T = \begin{bmatrix} \underline{\mu}_1^T \\ \underline{\mu}_2^T \\ \vdots \\ \underline{\mu}_N^T \end{bmatrix} \qquad (59e,f,g)$$

154

During the simulation, Eq. (49) is solved for the highest derivative, $\ddot{q}$, and then integrated to obtain the time rate of change of the generalized coordinates, $\dot{q}$. During each time increment, the calculated values of q are substituted into Eq. (51), which is integrated numerically to obtain the angular velocity and angular displacements. A similar process is applied to Eq. (52) to obtain the linear velocity components and linear displacements of the station's mass center.

The process described above is continued until docking occurs. At the instant of "docking," the changes in kinematical variables are obtained by solving Eqs. (46) and (47) simultaneously for the angular velocity, $\underline{\Omega}_s$, and the linear velocity, $\underline{v}_s$, of the station's mass center. These results are then substituted into Eq. (48) to obtain the time rate of change of the generalized coordinates.

Motion after docking is simulated exactly as that before docking, with the exception of accounting for the presence of the Orbiter.

Before any simulation may be accomplished, the initial conditions on $\underline{\omega}_s$, $\underline{R}_s$, q_k, $\dot{q}_k$ and the Orbiter's linear and angular velocity must be given or calculated. This process is considered in the next section.

Initial Conditions

The Space Station's center of mass is assumed to be initially in a 500 km circular orbit inclined at 28.5° (see Fig. 8). Initially, the Station rotates at the mean motion for that orbit. For simplicity, the angle of the ascending node, Ω, was assumed to be zero, and simulation began when the Station occupies the ascending node position. The initial conditions of the generalized coordinate were obtained by assuming a state of dynamic equilibrium for the Space Station. Using these assumptions, the initial conditions on the Space Station state variables were calculated and are shown here in Table 1.

The results discussed in the following sections were obtained using these initial conditions.

RESULTS AND DISCUSSION

An algorithm was developed to numerically integrate the equations of motion of the Space Station and the Space Station/Orbiter system. In this algorithm, a fourth-order Runge-Kutta integration scheme with an integration time increment of 0.01 seconds was used. The motion was simulated over a real time interval of 200 seconds during which docking occurred. A separate algorithm was developed to compute changes that occur in the kinematical variables of the Station due to impulsive docking with the Orbiter. In both algorithms, the structural deformations were calculated using the first eight vibrational modes. A
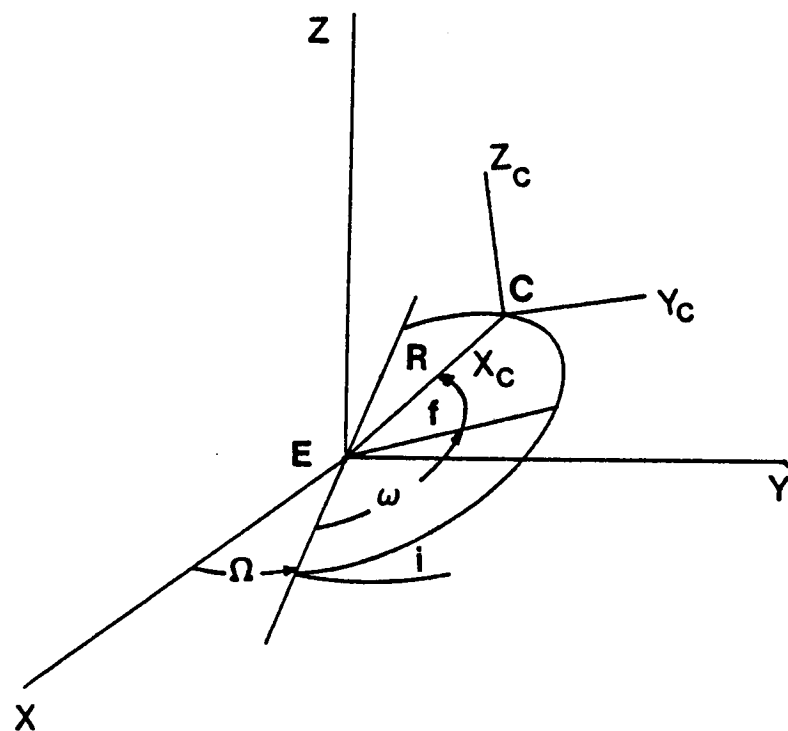
Fig. 8 Orbit Description.

TABLE 1

INITIAL CONDITIONS

Parameter	Initial Value
$\underline{R}_s$ (EXYZ system)	
x-component	6878 km
y-component	0 km
z-component	0 km
$\dot{\underline{R}}_s$ (EXYZ system)	
x-component	0
y-component	7.6127 km/s
z-component	0 km/s
$\underline{\omega}_s$ ($SX_sY_sZ_s$ system)	
x-component	0 rad/s
y-component	0 rad/s
z-component	1.1068×10^{-3} rad/s
q_j, $j=1,2,\ldots,N$	-0.19623, -0.41874
	0.25247, -0.52811
	0.23838, -0.13866
	0.10141, 0.22680
$\dot{q}_j$, $j=1,2,\ldots,N$	0, 0, 0,..., 0

157

third algorithm was developed to compute the mass properties of the Space Station, which are shown in Table 2.

To investigate the effects of docking on motion of the Space Station, three approach orientations of the Orbiter were considered. These are as follows: (1) An approach along the X-axis in the positive X-direction, (2) an approach at 45° to the X-axis in the XY-plane (see Fig. 9), and (3) an approach at 45° to the X-axis in the XZ-plane (see Fig. 9). For each approach orientation, the closing rate of the Orbiter was varied between 0.5 ft/sec and 1.5 ft/sec.

A comparison was made of the changes that occur in the magnitude of the Station's angular velocity when the Station is modeled as a hybrid of flexible and rigid bodies to that of the Station when modeled as a single rigid body. Figures 10 through 14 show this comparison for various approach orientations. It can be observed from these figures that flexibility does affect the angular motion of the Station. The primary effect is due to the time required for the flexible bodies to respond to the impact of the Orbiter with the rigid body to which they are attached. This can be called an "inertia" contribution. Although the cases of Y-axis or Z-axis approach are probably not realistic, it is observed that with either approach the "inertia" contribution of the flexible bodies does not produce significant changes in the angular velocity of the Station's mass center. Thus, for these approaches, the rigid body model yields the larger changes in angular velocity. However, for an approach along the X-axis it is observed that the inertia contribution of the flexible bodies does significantly affect the angular velocity of the Station. Thus, with an X-axis approach, the hybrid model predicts a greater change in angular velocity.

Figure 15 shows the changes in the magnitude of the angular velocity of the hybrid model for approaches (1) along the X-axis, (2) at 45° to the X-axis in the XY-plane, and (3) at 45° to the X-axis in the XZ-plane. It can be observed that the XZ-plane approach produces the smallest changes in the Station's angular velocity.

The simulation results of Figs. 16 through 18 were obtained by numerically integrating the equations of motion of the Station and the Station/Orbiter system. In Eq. (50b), a proportional damping coefficient of 0.01 was assumed. Simulation began when the Station occupied the ascending node position (see Fig. 8); fifty seconds later, docking of the Orbiter occurs. The motion of the Station/Orbiter system after docking is simulated for an additional 150 seconds. The results represented in these figures are the total displacements of the tip of the upper keel (point A) and the center of mass of an upper outboard panel (point B). The deformations of points A and B after docking are observed to be in-phase when the Orbiter approaches along either X-axis or at 45° to the X-axis in the XZ-plane. However, when the the Orbiter's approach is at 45° to the X-axis in the XY-plane, the motion after docking is no longer in-phase. This is probably due to the combined transverse and longitudinal motion of the panels when the approach is in the XY-plane.

158

TABLE 2

STATION MASS PROPERTIES

WEIGHT 2.6612×10^5 lbs

MOMENTS AND PRODUCTS
OF INERTIA

IXX	2.0318×10^9	lb-ft^2
IYY	1.8704×10^9	lb-ft^2
IZZ	2.5434×10^8	lb-ft^2
IXY	≈ 0	lb-ft^2
IXZ	7.4644×10^6	lb-ft^2
IYZ	≈ 0	lb-ft^2

XY-PLANE
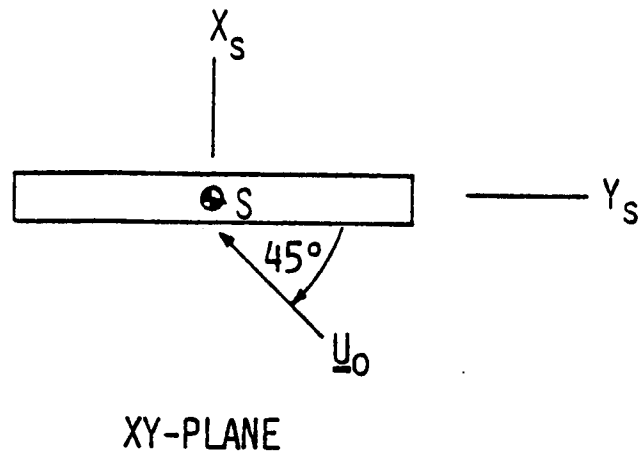
XZ-PLANE

Fig. 9 Approach Orientations for the
XY- and XZ-Planes.

Fig. 10 Change in Angular Velocity Magnitude vs.
Closing Rate for an Approach Along the
X-axis.

Fig. 11 Change in Angular Velocity Magnitude vs.
Closing Rate for an Approach at 45 deg.
to the X-axis in the XZ-plane.

Fig. 12 Change in Angular Velocity Magnitude vs.
Closing Rate for an Approach at 45 deg.
to the X-axis in the XY-plane.

Fig. 13 Change in Angular Velocity Magnitude vs.
        Closing Rate for an Approach along the
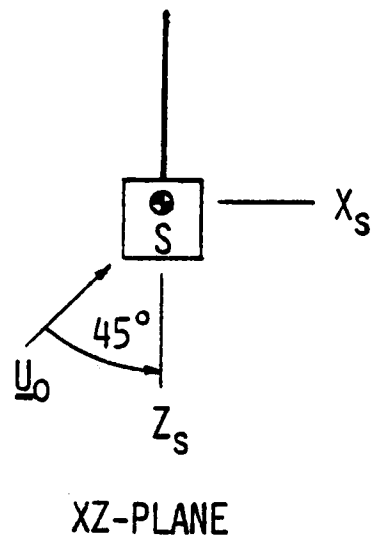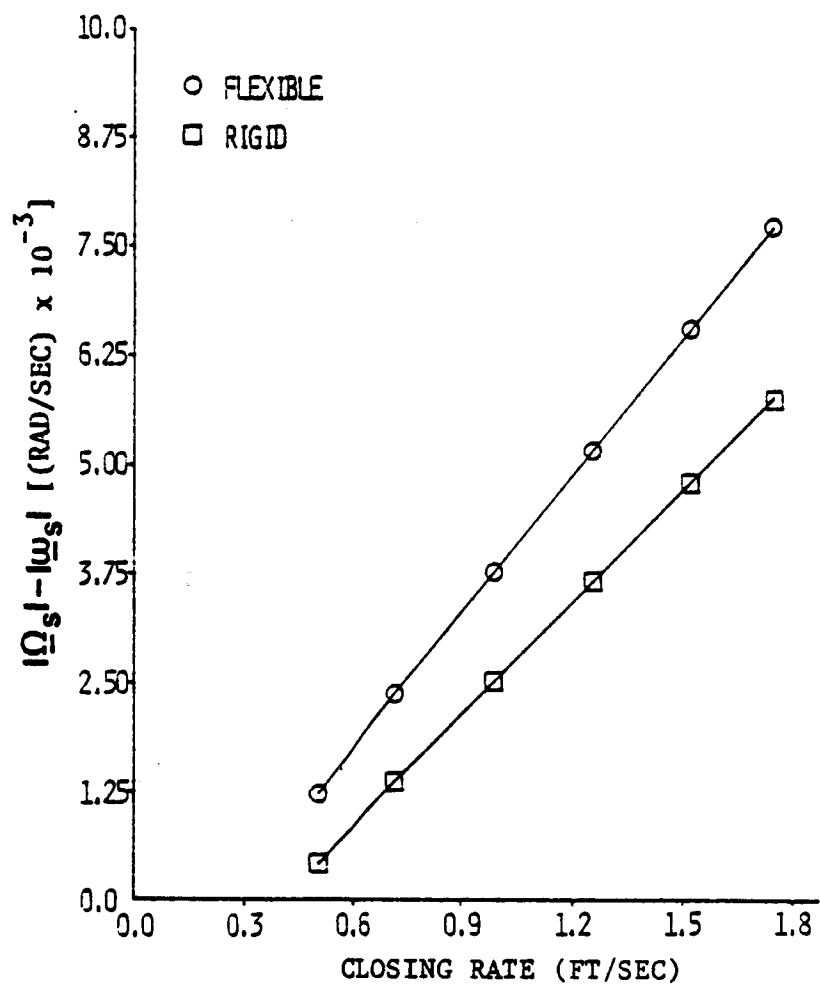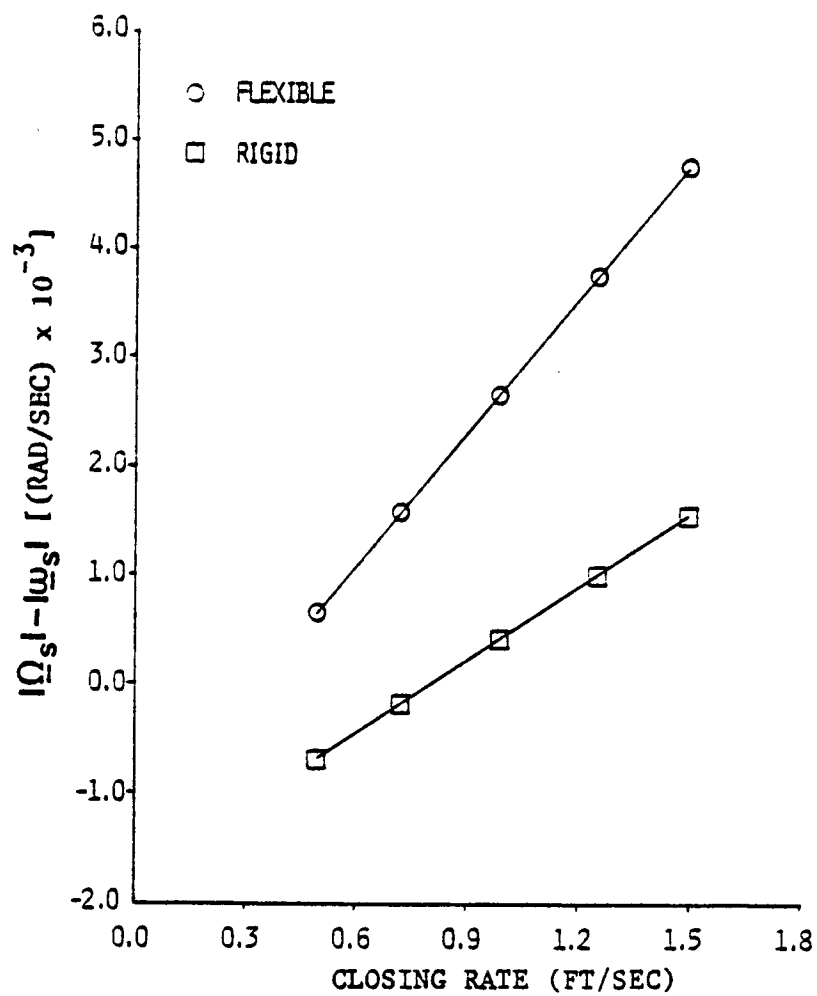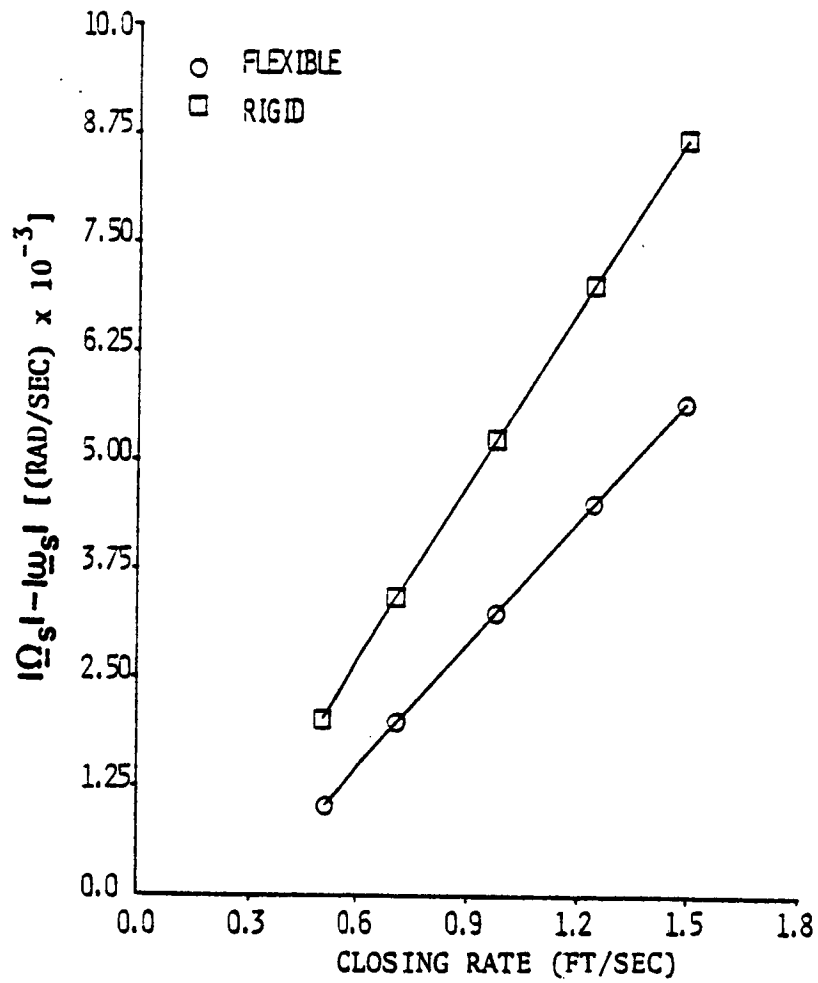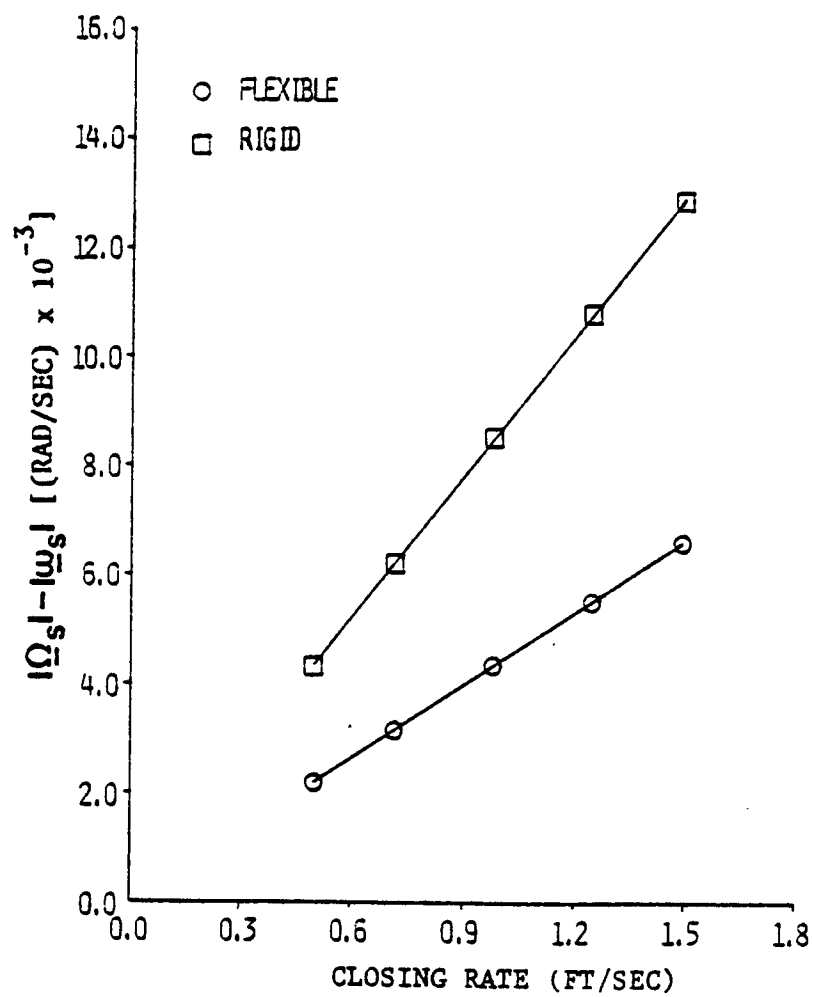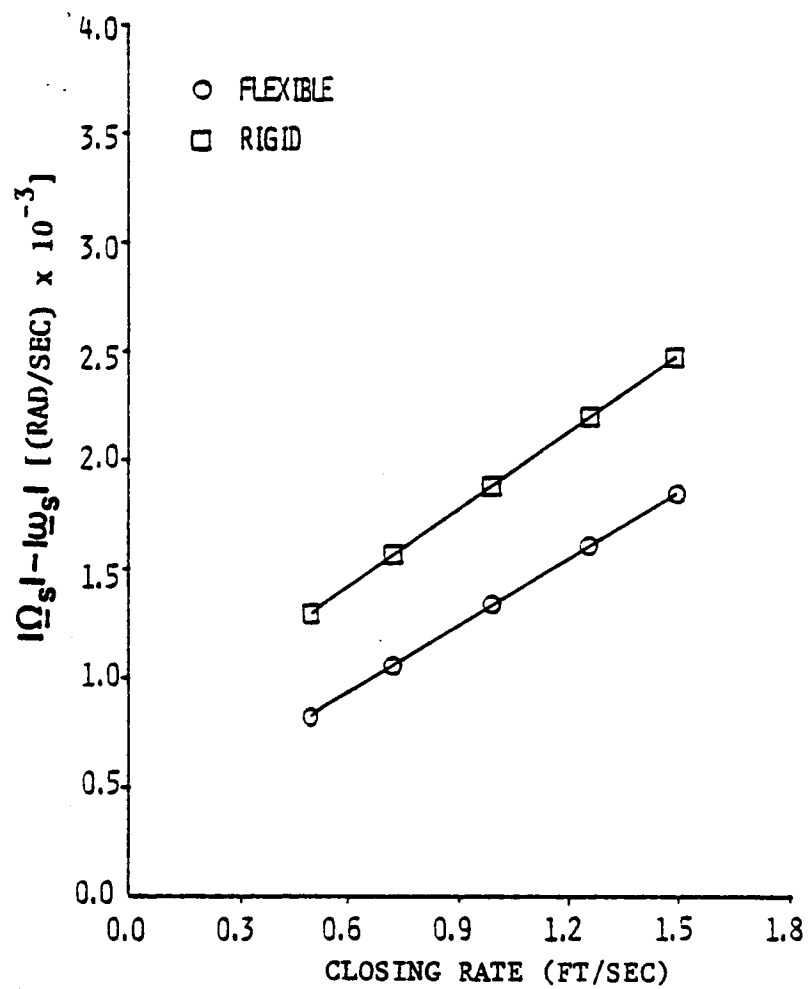   Y-axis.

Fig. 14 Change in Angular Velocity Magnitude vs.
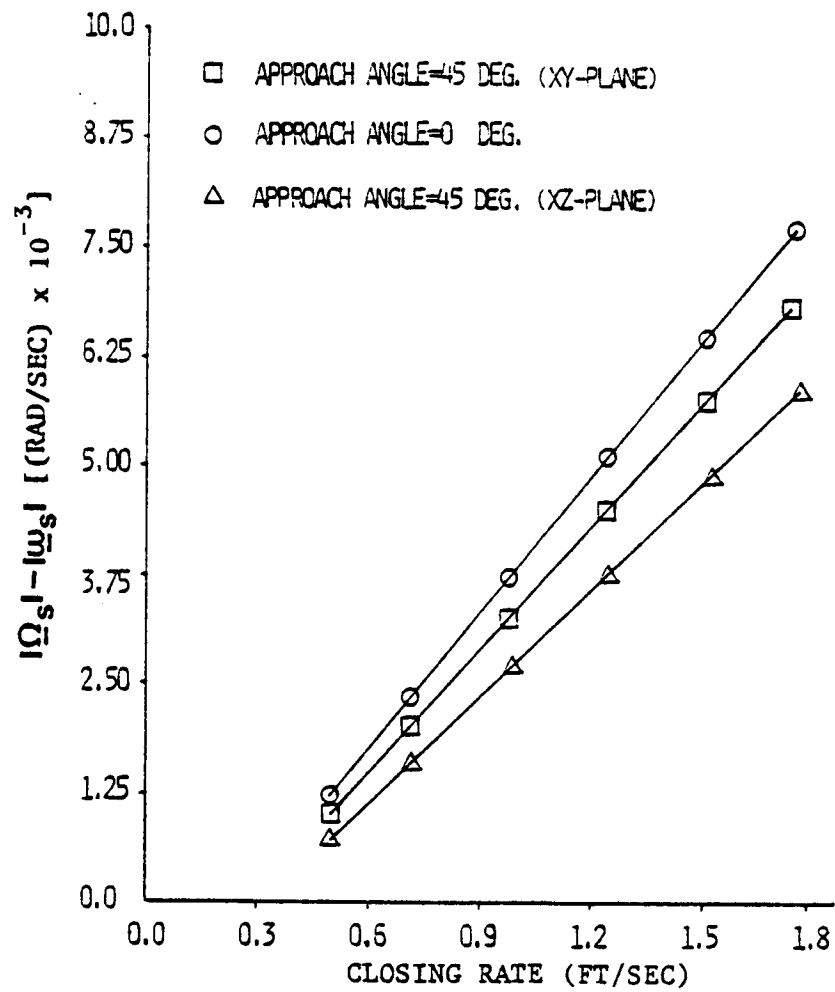Closing Rate for an Approach Along the
Z-axis.

Fig. 15 Comparison of the Change in Angular Velocity
Magnitude vs. Closing Rate for the Space
Station Modeled as a Hybrid of Flexible and
Rigid Bodies.

Figures 16 through 18 also indicate that the maximum deformation of point B is substantially greater than the deformation of point A (approximately twice as large). Figures 19 and 20 show the maximum deformations of points A and B for the various approach orientations and closing rates. An approach along the X-axis produces the greatest maximum deformations, whereas an approach in the XY-plane produces the smallest maximum deformation.

CONCLUSIONS AND RECOMMENDATIONS

The results obtained reveal that flexibility is a significant factor in the dynamics of the docking of an Orbiter with the proposed Space Station. In particular, the changes in the angular velocity of the more rigid part of the Station are greatly affected by flexibility.

Only the first eight modes of vibration were modeled in this analysis. Additional modes of vibrations should be considered in further studies. However, increasing the number of vibrational modes will result in increased computational requirements.

More general results could have been obtained if the Station's payload was considered. In addition, the motion of the crew may have a significant effect on the docking dynamics of the Space Station/Orbiter system.

Finally, a suitable control system must be designed to stabilize the rotational motion of the Station/Orbiter system. Realistically, this can only be done after, or during, a dynamic analysis of a Station model that incorporates payload and crew motion.

ACKNOWLEDGEMENT

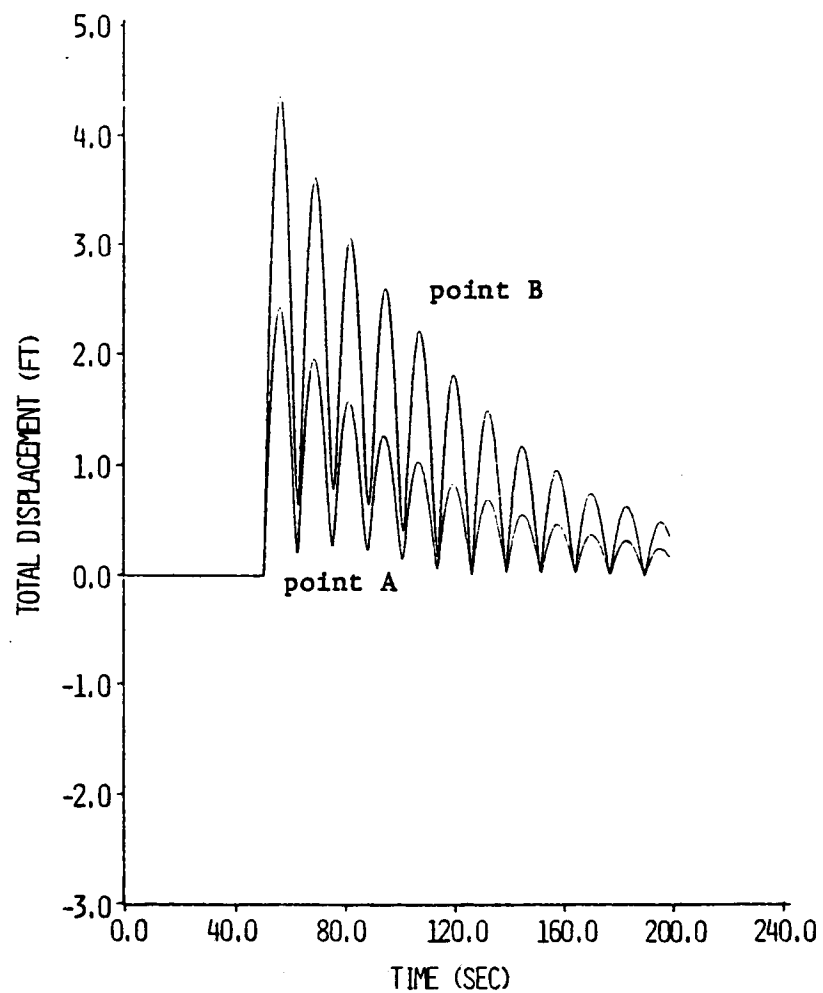Fig. 16 Displacement Simulation for an Approach
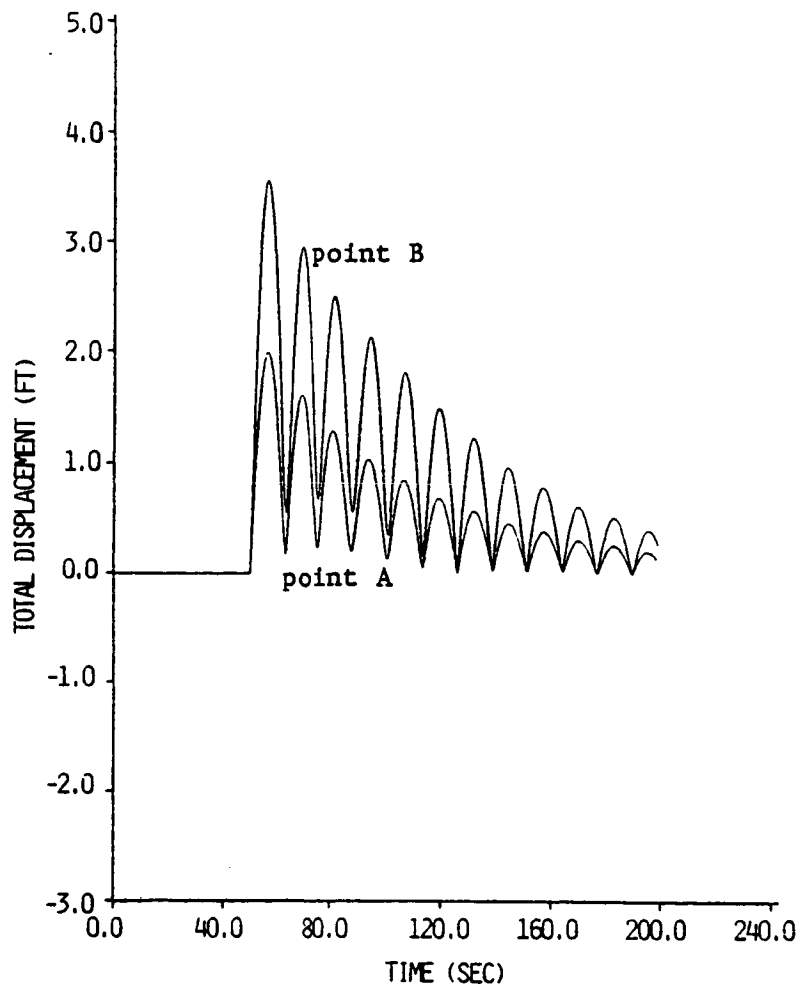Along the X-Axis. (Docking Occurs at T=50 sec.)

Fig. 17 Displacement Simulation for an Approach at 45^0 to the X-Axis in the XZ-Plane. (Docking Occurs at T=50 sec.)
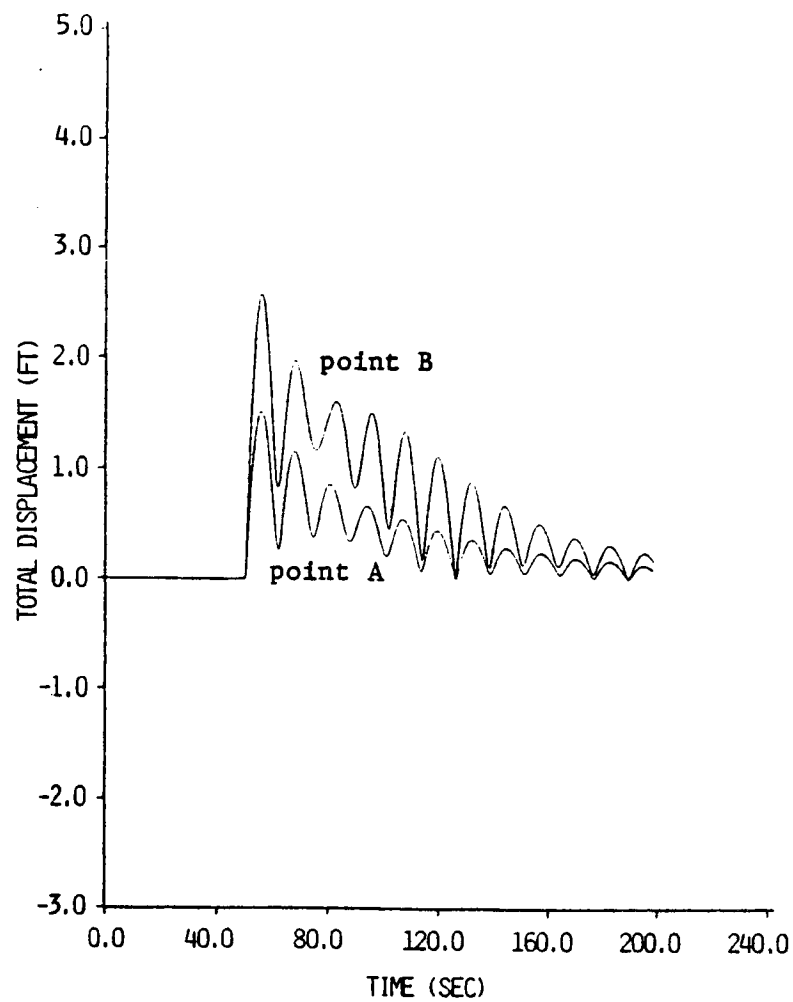
169

Fig. 18 Displacement Simulation for an Approach at 45°
to the X-Axis in the XY-Plane. (Docking Occurs
at T=50 sec.)
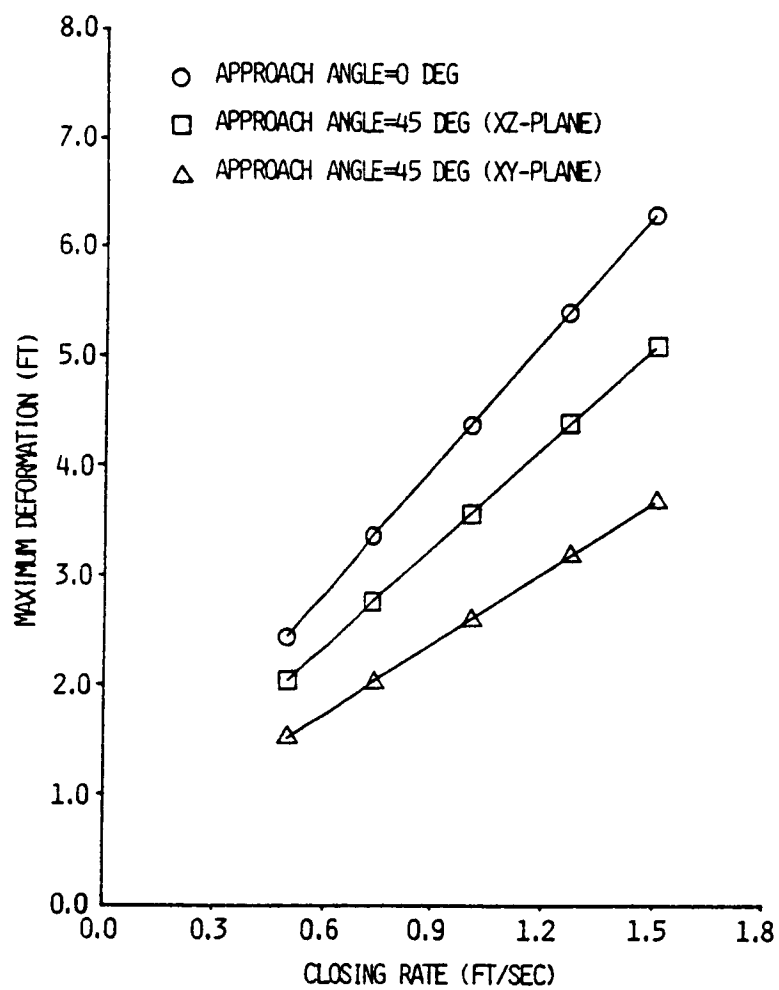
Fig. 19 Maximum Deformation of Point B
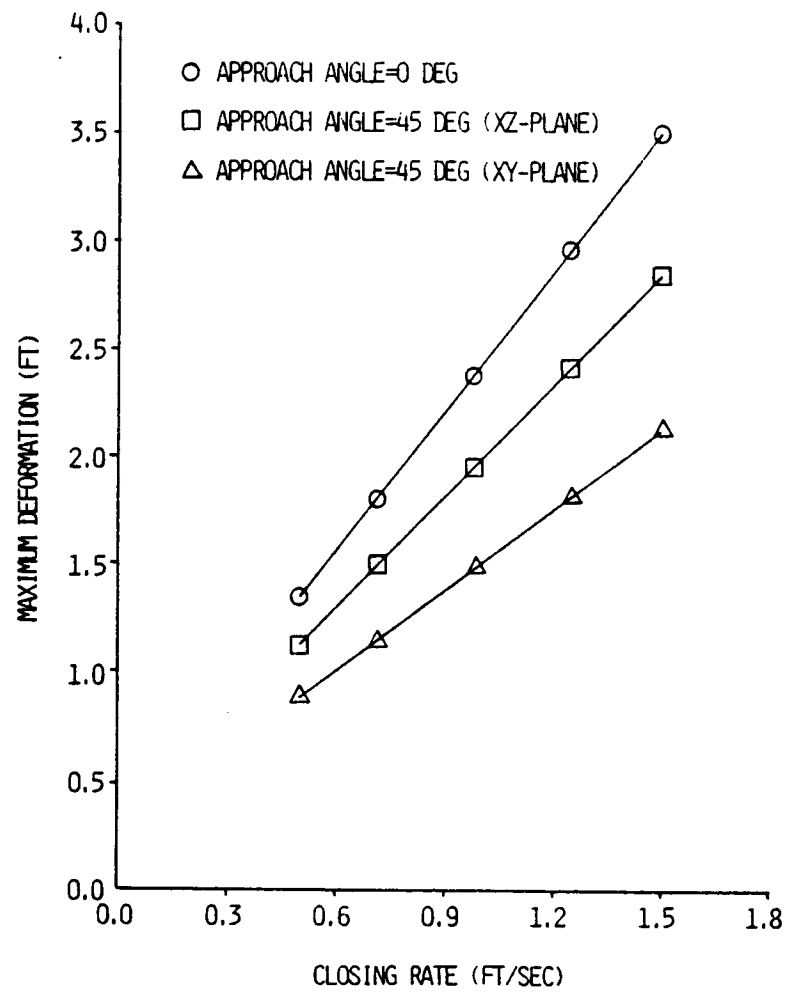
Fig. 20 Maximum Deformation of Point A.

REFERENCES

1. Haggerty, James., Spinoff 1984, National Aeronautics and Space Administration, Office of External Relations, Technology Utilization and Industry Affairs Division, Washington, DC, July 1984, pp. 16-17.

2. JSC-19989, Space Station Reference configuration Description, August 1984.

3. Williams, H. M., and Ward, J. W., "Orbital Docking Dynamics," AIAA Journal, Vol. 1, No. 6, June 1963, pp. 1360-1364.

4. Grubin, C., "Docking Dynamics for Rigid Body Spacecraft," AIAA Journal, Vol. 2, No. 1, January 1964, pp. 5-12.

5. Chiarappa, D., "Rendezvous and Docking," Analysis and Design of Space Vehicle Flight Control System, Vol. VIII, NASA-CR-827, July 1967.

6. Brayton, W. D., "Dynamic Analysis of the Probe and Drogue Docking Mechanism," Journal of Spacecraft and Rockets, Vol. 3, No. 5, May 1966, pp. 700-706.

7. Cochran, J. E., Jr., and Henderson, G. L., Jr, "Docking Dynamics of Spacecraft with Flexible Appendages," Dynamic Analysis of and Synthesis of an Attitude Control System for a Spacecraft to Rendezvous with Comets and Asteroids, Vol. IV, Final Report, contract NAS8-28110, Auburn University, Auburn, Alabama, July 31, 1973.

8. Kane, T. R., and Levinson, D. A., "Simulation of Large Motions of Nonuniform Beams in Orbit, Part II - The Unrestrained Beam," Journal of the Astronautical Sciences, Vol. XXIX, No. 3, July-September 1981, pp. 245-275.

9. Levinson, D. A., and Kane, T. R., "Simulaiton of Large Motions of Nonuniform Beams in Orbit, Part I - The Cantilever Beam," Journal of the Astronautical Sciences, Vol. XXIX, No. 3, July-September 1981, pp. 213-244.

10. Levinson, D. A., and Kane, T. R., "Docking of a Spacecraft with an Unrestrained Orbiting Structure," Journal of Astronautical Sciences, Vol. XXXI, No. 1, January-March 1983, pp. 23-48.

11. Hablani, Hari B., "Constrained and Unconstrained Modes: Some Modeling Aspects of Flexible Spacecraft," Journal of Guidance, Control, and Dynamics, Vol. 5, No. 2, March-April 1982.

12. Likins, P. W., "Analytical Dynamics and Nonrigid Spacecraft Simulation," Technical Report 32-1593, Jet Propulsion Laboratory, Pasadena, California, July 15, 1974.

13. Hughes, P. C., and Skelton, R. E., "Modal Truncation for Flexible Spacecraft," Journal of Guidance and Control, Vol. 4, No. 3, May-June 1981.

14. Ho, J. Y. L., and Herber, D. R., "Development of Dynamics and Control Simulation of Large Flexible space systems," Journal of Guidance, Control, and Dynamics, Vol. 8, No. 3, May-June 1985.

15. Kane, T. R., and Levinson, D. A., "Formulation of Equations of Motion for Complex Spacecraft," Journal of Guidance and Control, Vol. 3, No. 2, March-April 1980.

16. Schaeffer, Harry G., MSC/NASTRAN Primer: Static and Normal Modes Analysis, Schaeffer Analysis, Inc., 1982.

17. Kane, T. R., Dynamics, Second Edition, Stanford University, 1972.

18. Kaplan, M. H., Modern Spacecraft Dynamics and Control, John Wiley & Sons, 1976.

TRANSIENT RESPONSE FOR INTERACTION OF TWO DYNAMIC BODIES

by

A. Prabhakar & L.G. Palermo

Martin Marietta Michoud Aerospace, New Orleans, Louisiana

ABSTRACT

During the launch sequence of any space vehicle complicated boundary interactions occur between the vehicle and the launch stand. At the start of the sequence large forces exist between the two; contact is then broken in a short but finite time which depends on the release mechanism. The resulting vehicle response produces loads which are very high and often form the design case. It is known that the treatment of the launch pad as a second dynamic body is significant for an accurate prediction of launch response.

A technique has been developed for obtaining loads generated by the launch transient with the effect of pad dynamics included. The method solves uncoupled vehicle and pad equations of motion. The use of uncoupled models allows the simulation of vehicle launch in a single computer run. There is no need for a second computer run to introduce compensating forces that are required to simulate detachment for coupled models. Modal formulation allows a closed-form solution to be written, eliminating any need for a numerical integration algorithm.

When the vehicle is on the pad the uncoupled pad and vehicle equations have to be modified to account for the constraints they impose on each other. This necessitates the use of an iterative procedure to converge to a solution, using Lagrange multipliers to apply the required constraints . As the vehicle lifts off the pad the coupling between the vehicle and the pad is eliminated point by point until the vehicle flies free.

Results obtained by this method have been shown to be in good agreement with observed loads and other analysis methods.

The resulting computer program is general, and has been used without modification to solve a variety of contact problems. The contact point description could be made more elaborate to include effects of friction, geometry, etc. By allowing the second body (it need not be a pad) to have rigid body free-free modes other problems, such as berthing/docking dynamics, could be tackled.

TRANSIENT RESPONSE FOR INTERACTION OF TWO DYNAMIC BODIES

by

A. Prabhakar & L.G. Palermo

Martin Marietta Michoud Aerospace, New Orleans, Louisiana

1.0 INTRODUCTION

This paper describes a method of obtaining the transient response of two interacting dynamic bodies. The technique was developed originally to obtain the response during the launch sequence of the Space Shuttle Vehicle (SSV) from a dynamic launch pad. Because of the historical association with the SSV launch problem this paper presents the development from that particular viewpoint but it must be ·emphasised that the method is generally applicable, and the resulting computer code has been used in solving a variety of contact problems.

The launch event of any space vehicle causes complicated boundary interactions between the vehicle and the launch stand. At the start of the sequence large forces exist between the two; contact is then broken in a short but finite time which depends on the release mechanism. During this time the two may recontact as the loads are redistributed in the system. The vehicle response resulting from this non-linear transient phenomenon produces loads which often form the design case. It is known from experience that the use of a non-dynamic launch pad predicts loads that are too high. Therefore the treatment of the launch pad as a second dynamic body is significant for an accurate prediction of launch response.

A technique has been developed for obtaining loads generated by the launch transient with the effect of pad dynamics included (ref. 1). The method solves uncoupled vehicle and pad equations of motion. The use of uncoupled models allows the simulation of vehicle launch in a single computer run. There is no need for a second computer run to introduce compensating forces that are required to simulate detachment for coupled models. Modal formulation allows a closed-form solution to be written, eliminating any need for a numerical integration algorithm. However, an iterative procedure is required to solve the equations of motion when the two bodies are in contact.

Several other factors influence the response from the launch transient. A control system maintains a vertical vehicle attitude, zeroing out angular accelerations, by changing the direction of the thrust vector of the Solid Rocket Boosters (SRBs). Another source of large loads is from the constraints imposed on the cryogenic shrinkage of the External Tank (ET); these loads are relieved as the vehicle separates from the launch pad. Also important is a second order effect resulting from the offset centre of gravity of the vehicle. This offset c.g. would tend to induce greater structural deflection than can be obtained normally; we have termed this effect "gravity softening". Techniques for the proper simulation of these effects are discussed in the paper. An area for further development is to make the contact point description more elaborate to include the effects of friction, geometry, misalignment, etc.

Although in the development presented in this paper the pad is a grounded body, it could be made more general and have rigid body modes allowed. This would enable the technique to be used in calculating the berthing/docking dynamic response for the Space Station.

NOMENCLATURE

C_M Coupling mass term in Craig-Bampton formulation of analysis models.

F   Generalised force.

F(t)   Discrete time variant applied force.

g   Gravitational acceleration.

h   Integration interval.

I   Identity matrix

K   Stiffness matrix.

M   Mass matrix.

M_B, K_B Boundary mass and stiffness terms in Craig-Bampton formulation.

q   Modal freedoms.

RB   Geometric rigid body modeshape.

x   Discrete freedoms.

x_g Freedoms of the centre of gravity of the vehicle.

Φ Modeshapes matrix.

η Error between successive iterations.

τ Time variation during an integration interval.

ω_n Natural frequency (radians/sec).

ζ Ratio of critical damping.

Subscripts

A   Applied

v   Vehicle

s   Launch stand

C   Contact

0   Values at time zero (initial values)

Superscripts

T   Transpose

-1   Inverse

2.0   THEORETICAL DEVELOPMENT

The development presented in this paper uses equations of motion of the two bodies (vehicle and pad) which are uncoupled from one another. The use of such uncoupled equations is more natural conceptually as it allows the two bodies to be treated independently. The free-free vehicle can thus fly off the pad without inducing the compensating forces that are required when a coupled system model is used, and the solution can be obtained in one computer run. However, when the vehicle is on the pad the uncoupled pad and vehicle equations have to be modified to account for the constraints they impose on each other. This necessitates the use of an iterative procedure to converge to a solution, effectively using Lagrange multipliers to apply the required constraints . As the vehicle lifts off the pad the coupling between the vehicle and the pad is eliminated point by point until the vehicle flies free.

2.1   EQUATIONS OF MOTION

Write the uncoupled vehicle and stand equations as

$$
\begin{bmatrix} M_v & 0 \\ 0 & M_s \end{bmatrix} \begin{Bmatrix} \ddot{x}_v \\ \ddot{x}_s \end{Bmatrix} + \begin{bmatrix} K_v & 0 \\ 0 & K_s \end{bmatrix} \begin{Bmatrix} x_v \\ x_s \end{Bmatrix} = \begin{Bmatrix} F(t) \\ 0 \end{Bmatrix} \tag{1}
$$

Assume that the coupling between the vehicle and the main launch pad (MLP) equations is a pure stiffness i.e. the coupling is massless. This coupling stiffness K_C would overlay the relevant vehicle and stand degrees of freedom when the two are in contact. Equations of motion can now be written as

$$
\begin{bmatrix} M_v & 0 \\ 0 & M_s \end{bmatrix} \begin{Bmatrix} \ddot{x}_v \\ \ddot{x}_s \end{Bmatrix} + \left[\begin{bmatrix} K_v & 0 \\ 0 & K_s \end{bmatrix} + \begin{bmatrix} K_C \\ & \end{bmatrix} \right] \begin{Bmatrix} x_v \\ x_s \end{Bmatrix} = \begin{Bmatrix} F(t) \\ 0 \end{Bmatrix} \tag{2}
$$

The coupling matrix K_C can be partitioned out and taken to the right hand side of (2) giving

$$
\begin{bmatrix} M_v & 0 \\ 0 & M_s \end{bmatrix} \begin{Bmatrix} \ddot{x}_v \\ \ddot{x}_s \end{Bmatrix} + \begin{bmatrix} K_v & 0 \\ 0 & K_s \end{bmatrix} \begin{Bmatrix} x_v \\ x_s \end{Bmatrix} = \begin{Bmatrix} F(t) \\ 0 \end{Bmatrix} - \begin{bmatrix} K_C \\ & \end{bmatrix} \begin{Bmatrix} x_v \\ x_s \end{Bmatrix} \tag{3}
$$

i.e. the coupled system equations have been written in terms of the uncoupled degrees of freedom with a correction term (force) for the effect of interaction between vehicle and stand. This constraint imposed by the interaction of the pad and vehicle now makes the problem suitable for an iterative procedure such as Lagrange multipliers (ref. 2). Application of Lagrange multipliers to the lift-off problem was developed in ref. 3. In the development presented here, because of the very simple assumed nature of K_C (see section 2.2) Lagrange multipliers do not occur explicitly.

If Φ and q are defined such that

$$
x = \Phi q \tag{4}
$$

where $\Phi^T M \Phi = I$

178

and $\quad \Phi^T K \Phi = \omega_n^2$

then the modal form of the equations of motion (3) can be written as

$$\begin{bmatrix} I & 0 \\ 0 & I \end{bmatrix}\begin{Bmatrix} \ddot{q}_v \\ \ddot{q}_s \end{Bmatrix} + \begin{bmatrix} \omega_{nv}^2 & 0 \\ 0 & \omega_{ns}^2 \end{bmatrix}\begin{Bmatrix} q_v \\ q_s \end{Bmatrix} = \begin{bmatrix} \Phi_v^T & 0 \\ 0 & \Phi_s^T \end{bmatrix}\begin{Bmatrix} F(t) \\ 0 \end{Bmatrix} \qquad (5)$$

$$-\begin{bmatrix} \Phi_v^T & 0 \\ 0 & \Phi_s^T \end{bmatrix}\begin{bmatrix} K_C \end{bmatrix}\begin{bmatrix} \Phi_v & 0 \\ 0 & \Phi_s \end{bmatrix}\begin{Bmatrix} q_v \\ q_s \end{Bmatrix}$$

The second term on the right hand side of the above equation is the contact force term F_C. Assuming a modal damping ratio of ζ the equations can thus be written as

$$\ddot{q} + 2\zeta\omega_n\dot{q} + \omega_n^2 q = F_A + F_C \qquad (6)$$

If the two bodies are allowed free body motions then the values of ω_n corresponding to the rigid body modes are obviously zero. This formulation allows computer core savings because of the diagonalisation of the mass and stiffness matrices. Only small partitions of Φ_v and Φ_s corresponding to the coupling points are retained in core.

As the vehicle lifts off from the stand and contact is broken point by point, the coupling stiffness K_C is reduced until, finally, it becomes zero and the vehicle flies free.

2.2   COUPLING STIFFNESS MATRIX K_C

When the two bodies (vehicle and pad) are in contact they impose constraints on their coupled motion which may be stated as :

a)   Vehicle and pad displacements at the points of contact are equal.
b)   Contact forces have values only at points which are in contact.

These constraints are most easily applied using Lagrange multipliers (refs. 1,3). Their application becomes straightforward if a simple coupling stiffness K_C is assumed.

Contact points between the vehicle and the pad are shown in figure 1. The function of the coupling stiffness K_C is merely to constrain the degrees of freedom in contact to move together. A 6 DoF stiffness matrix (3 freedoms each for the SRB and MLP ends of the contact) can serve to provide the required constraints for each contact point. Greater simplification of K_C is possible if no cross-coupling between the x,y,z freedoms at each end is allowed.

An uncoupled stiffness matrix K_C automatically satisfies the constraint requirements stated above, and Lagrange multipliers do not occur explicitly in the formulation. Values of K_C must be chosen to be high relative to the local stiffness values of the two bodies, but yet not so high as to induce spurious responses. The use of an uncoupled stiffness matrix K_C has an additional advantage in that the reduction of K_C, as the vehicle lifts off the pad, simply involves zeroing the relevant stiffness terms.

2.3 ITERATIVE SOLUTION OF EQUATIONS OF MOTION

Suppose at a given time $t = t_0$ the solution has been obtained i.e. we know $q_0, \dot{q}_0$ and the contact force F_{C0} for a given applied force F_{A0} .

If h is the integration interval then at time $t = t_0 + h$ the new value of applied force F_A is known. Suppose the stand force needed to satisfy the equations of motion at time $t = t_0 + h$ is F_C. Over the interval h we may approximate the forcing function to $A + B\tau$, and the equations of motion become

$$\ddot{q} + 2\zeta\omega_n\dot{q} + \omega_n^2 q = A + B\tau \tag{7}$$

The coefficients A and B can be obtained by comparing the above to (6).

At time $\tau = 0$ the forcing function is F_{A0} and the contact force is F_{C0} .

Hence $\quad A = F_{A0} + F_{C0} \tag{8a}$

Similarly at $\tau = h$, for the assumed contact force F_C we can obtain B as

$$B = \frac{F_A - F_{A0}}{h} + \frac{F_C - F_{C0}}{h} \tag{8b}$$

Closed form solution of equations (7) can be obtained easily in terms of constants A and B. For the rigid body modes ($\omega_n = 0$) the equations of motion simply are

$$\ddot{q} = A + B\tau \tag{9}$$

Successive integration gives $\dot{q}$ and q.

For the vibration modes of the vehicle the general solution is more complicated; it can be written as

$$q = e^{-\zeta\omega_n\tau} [K_1 \cos\omega_d\tau + K_2 \sin\omega_d\tau] + C + D\tau \tag{10}$$

where $\quad \omega_d = \omega_n\sqrt{1 - \zeta^2}$

$D = B / \omega_n^2$

$C = (A - 2\zeta\omega_n D) / \omega_n^2$

$K_1 = q_0 - C$

$K_2 = (\dot{q}_0 + \zeta\omega_n K_1 - D) / \omega_d$

Modal velocity and acceleration can be obtained from (10).

The iterative solution procedure, therefore, is to estimate a value for the contact force at the end of the

integration interval $\tau = h$. Coefficients A, B can then be calculated from (8). These coefficients are used in (9) and (10) to obtain estimated values of q. Forces and displacements at vehicle-stand interface can then be calculated. Separation of vehicle from the stand is tested for, and a modified coupling stiffness matrix generated. Contact force consistent with the modified coupling stiffness matrix and vehicle displacements is used to obtain new values for constants B which in turn yield improved estimates for q ; the process is repeated until the stand force obtained between successive iterations is within a specified tolerance, indicating that the solution has converged to the required accuracy.

2.4   TEST FOR CONVERGENCE

If the solution has converged, the right hand side of equation (6) has to be equal to its left side. If the two are not equal then the error is

$$\eta = F_A + F_C - \ddot{q} - 2\zeta\omega_n\dot{q} - \omega_n^2 q$$

If F_{Ci} denotes the stand force estimate from the previous iteration, and F_{Cj} the stand force from the current iteration then, substituting for $\ddot{q}, \dot{q}$, and q in terms of A and B gives the error between successive iterations as

$$\eta = F_{Cj} - F_{Ci} \tag{11}$$

i.e the error in successive iterations is simply the difference in the contact force. The solution may be said to be converged if the value of the error becomes sufficiently small; for our purposes a satisfactory error criterion was a difference of less than 1 lbf. between successive iterations.

2.5   DETERMINATION OF INTEGRATION STEP SIZE

Because the error between successive iterations is in the stand force the integration step size need only be small enough to track the highest frequency in the contact force. An estimate of the oscillatory behaviour of the vehicle on the pad is obtained by reducing the mass and stiffness properties of the two bodies to the stand interface points and coupling the two appropriately. The highest frequency from the resulting eigensolution governs the integration step size :

$$h \leq 0.25 / f_h \tag{12}$$

where f_h is the highest frequency so obtained.

2.6   INITIAL CONDITIONS

Initial conditions are most easily obtained by solving the static problem of the vehicle resting on the pad. They can be compared to the response obtained from the method itself by allowing the vehicle to settle under the action of applied static loads; mean values of the resulting oscillations should be the same as obtained statically, providing a good check on the computer code and the models.

2.7   SEPARATION AND RECONTACT CRITERIA

Conditions governing the behaviour of the contact points between the pad and the vehicle are easily established when using the uncoupled stiffness matrix K_C.

When the vehicle is bolted to the pad the contact point can sustain both tensile and compressive loads. Once the SRB bolts have been fired, the contact point becomes non-linear in that no tensile loads can be sustained. Contact between the vehicle and the pad is thus assumed broken as soon as the bolt goes into tension.

The condition for reattachment is similarly simple. Because of the assumed nature of K_C (no cross coupling) a check of relative displacements between the two bodies shows when recontact takes place. However on recontact, to simulate the sliding joint beteen the vehicle and the pad, only axial (normal) loads were permitted because otherwise any lateral drift would induce spurious forces.

3.0   GENERATION OF LAUNCH ANALYSIS MODELS

Each component of the launch vehicle was modeled mass coupled in mixed modal and discrete coordinates using the Craig-Bampton method (ref. 4). Using this method a set of freedoms, called the boundary freedoms, are grounded and an eigensolution obtained of the remaining DoFs. From this eigen a number of significant modes are retained. A dynamics model is then constructed using the retained modes and the boundary set of retained freedoms. The resulting mass and stifffness matrices are of the form

$$M = \begin{bmatrix} I & C_M \\ C_M^T & M_B \end{bmatrix} \qquad K = \begin{bmatrix} \omega_n^2 & 0 \\ 0 & K_B \end{bmatrix} \qquad (13)$$

Some very important points need to be noted in the generation of such models. Any freedoms which have large concentrated loads (e.g. SSV major interfaces) must be retained as discrete. Contact points, which require high fidelity results to properly simulate separation and recontact, must also be kept explicitly. A reduction of the remaining degrees of freedom is permissible as indicated above using the Craig-Bampton method, with an eigensolution and the retention of only the important modes. This mode selection is often by simple frequency bandpass, but other criteria can be employed. Finally, since the launch vehicle will have large rigid body motions, the stiffness of each component must be truly free-free to inhibit the build-up of spurious forces.

Component models are assembled into a launch vehicle model by overlaying the common boundary freedoms. The launch vehicle model is then eigensolved with properties as in equation (4) to diagonalise the mass and stiffness matrices. All modes from this final eigensolution are retained for further analysis.

4.0 EXTERNAL FORCING FUNCTIONS

Any dynamic system is subject to forcing functions which can be constant or time varying. The determination of these forcing functions is usually the most difficult part of any dynamics problem. The launch vehicle is subject to a number of external influences most of which have been refined over the years and are well known. How these various forces are dealt with is described in this section.

4.1 DATABASE FORCING FUNCTIONS

A computer tape containing the NASA launch analysis forcing functions was obtained from MSFC. There was data for 11 lift-off cases, comprising engine forcing functions, winds and gusts.

This forcing function data, which is standard for SSV launch analysis, was converted to generalised forcing functions using the final free-free vehicle modal matrix. The data was read as required during the execution of the computer program.

4.2 GRAVITY LOADS

Gravity loads can be obtained easily for the mass coupled models as generated using the Craig-Bampton method. A geometric rigid body modeshape of the model can be constructed, bearing in mind that, since the modes are obtained for zero boundary motion, the geometric modeshape corresponding to the modal freedoms is zero. The gravity loads are then obtained from the mass matrix as

$$FG = \begin{bmatrix} I & C_M \\ C_M^T & M_B \end{bmatrix} \begin{Bmatrix} 0 \\ RB \end{Bmatrix} \{g\} = \begin{bmatrix} C_M \\ M_B \end{bmatrix} [RB] \{g\} \qquad (14)$$

Thus the discrete mass of the vehicle, which causes gravity loads, is inherent in the column partition of the mass matrix corresponding to the boundary freedoms. This method allows very easy calculation of vehicle gravity loads.

4.3 CRYOGENIC LOADS

Cryo loads are generated at the SRB to MLP boundary because of the restraints imposed on shrinkage of the ET as the cold propellents are loaded. As the vehicle lifts off these restraints are removed and the SRBs twang inwards. Any technique for cryo load application should properly simulate this behaviour. This was achieved simply by applying the cryo loads to the ET itself such as to shrink the tank. Structural flexibility allows the loads to be distributed properly through the vehicle, and produces the required cryo reaction loads at the SRB base.

Since the cryo loads are a function of the structural stiffness, and are not related to the mass matrix, they must be applied only at the discrete freedoms of the mass-coupled component modal model. Otherwise, spurious modal distortions are obtained.

Cryo loads were assumed to be steady state and were added to the gravity force vector to give the total constant force on the vehicle.

183

4.4 CONTROL SYSTEM

The vehicle control system directs SRB gimballing to zero out any net moments about the vehicle centre of gravity. The formulation given in this section was developed to simulate the effect of the control system in maintaining a vertical attitude of the launch vehicle during the first few seconds of flight.

Using the geometric rigid body modeshape RB the resultant force vector P_R at the c.g. of the vehicle is obtained from the physical applied forces P_A as

$$P_R = RB^T P_A \qquad (15)$$

This vector may be written in terms of its three force and three moment components as

$$P_R = \begin{pmatrix} F_R \\ M_R \end{pmatrix} \qquad (16)$$

The control system action is such that the resultant moments M_R vanish subject to the constraint that the corrective forces are applied only at the lateral (y,z) freedoms at the SRB gimbals. Forces required to produce a moment of $- M_R$ are obtained by relating x_{sl}, the SRB lateral gimbal freedoms, to the freedoms at the c.g. of the vehicle with the geometric rigid body modeshape as

$$x_{sl} = RBL \; x_g$$

where RBL is the appropriate partition of RB. Hence we can write

$$x_g = (RBL^T \; RBL)^{-1} \; RBL^T \; x_{sl}$$

$$= T1 \; x_{sl} \qquad (17)$$

As only the partition of T1 corresponding to the rotational degrees of freedom (T1R) is needed to zero out the net moments about vehicle c.g. the above can be written as

$$x_{gr} = T1R \; x_{sl} \qquad (18)$$

Using the corrective moment required we can obtain FSL, the SRB lateral forces, as

$$FSL = -T1R^T \; M_R$$

$$= -T1R^T \; RBL^T \; P_A \qquad (19)$$

However, during computation, the forcing functions are known as generalised quantities. Using the final free-free modes discrete forces can be obtained from generalised as

$$P_A = \Phi^{-1T} \; F_A \qquad (20)$$

The inverse of the modal matrix Φ can be obtained easily from its properties. For mass normalised modes

we have

$$\Phi^T M \Phi = I$$

Hence $\quad \Phi^{-1} = \Phi^T M$

thus reducing the process of inversion to that of multiplication. Now we can write the discrete SRB corrective forces as

$$FSL = - T1R^T RBL^T \Phi^{-1T} F_A \tag{21}$$

The corrective forces FSL in equation (21) are converted to generalised forces for use in the lift-off program.

4.5 GRAVITY SOFTENING

Because of the offset c.g. of the vehicle, deflection of the c.g. from its null position will induce a further bending moment in the structure, which in turn will lead to extra deflection. This effect may be viewed as a softening of the structure under gravity loading and could be important as the vehicle rocks on the pad when the Space Shuttle main engines (SSMEs) are lit.

Implementation of the gravity softening effect was as for the control system. As before we can relate the motion of the vehicle c.g. to the motion of the boundary freedoms x_b using the rigid body mode shape

$$x_b = RB \; x_g$$

Hence $\quad x_g = (RB^T \; RB)^{-1} \; RB^T \; x_b$

$$= T2 \; x_b \tag{22}$$

This relationship is assumed to hold even for the deformed vehicle i.e. for small deflections.

Using the final free-free modes of the vehicle the boundary freedoms are related to the modes as

$$x_b = \Phi_b \; q$$

where Φ_b is the partition of the modal matrix corresponding to the boundary freedoms. Hence the motion of the c.g. is obtained in terms of modal freedoms as

$$x_g = T2 \; \Phi_b \; q$$

$$= ERV \; q \tag{23}$$

The translational and rotational components of c.g. motion can be written as

$$\begin{Bmatrix} x_{gt} \\ x_{gr} \end{Bmatrix} = \begin{bmatrix} ERVt \\ ERVr \end{bmatrix} \{q\} \tag{24}$$

The translational deflection x_{gt} obtained from the above equation causes an additional moment because of the motion of the centre of gravity (gravity force application point). This moment may be written in matrix form as

$$M_G = - \begin{bmatrix} 0 & -FGZ & FGY \\ FGZ & 0 & -FGX \\ -FGY & FGX & 0 \end{bmatrix} \{x_{gt}\}$$

$$= FGM \ x_{gt} \tag{25}$$

Using the relationships developed in (24) and (25) the generalised moment due to deflection of the c.g. is given by

$$FSOF = ERVr^T \ M_G$$

$$= ERVr^T \ FGM \ ERVt \ q \tag{26}$$

The "softening stiffness" is thus obtained as

$$KSOF = ERVr^T \ FGM \ ERVt \tag{27}$$

For static calculation of initial conditions KSOF is used in conjunction with the linear elastic stiffness of the vehicle to obtain extra deflection because of its off-set centre of gravity. The effect of gravity softening on the deflection of the vehicle c.g. is shown in table 1.

In the response calculations the softening effect is considered to be an extra applied force and is carried on the right hand side of the equations of motion. This force is obtained from equation (26) above; if the matrix multiplications are carried out from the right the process is very quick and requires just the small amount of core needed by ERV and FGM.To avoid numerical stability problems FSOF was considered to be constant over an integration interval (typically 0.0001 sec.).

The gravity softening effect was turned off at SRB ignition.

5.0 APPLICATIONS AND RESULTS

The computer code generated with this methodology has been used in a number of diverse applications. The main effort was in obtaining launch loads for a SSV with an Aft Cargo Carrier attached to the aft frame of the ET; the payload in the ACC was an Orbital Transfer Vehicle (OTV). Figure 2 is an illustartion of the ACC-OTV concept. Figure 3 shows one of the loads responses between the ET and the aft SRB attachment. Loads generated on an OTV propellent tank are shown in figure 4. The hydroelastic volume change in the ullage space of the liquid oxygen tank of the ET due to the lift-off transient is shown in figure 5; the oscillation in the tank bottom pressure is shown in figure 6. The primary mode in both these phenomenon is the 4Hz first bulge mode of the tank. Figures 3-6 illustrate the severity of response when

186

the SRBs are lit (6.6 sec in the plots). These responses correlate well with the results obtained by other independent analyses.

The program was used to calculate barge impact loads and ET response during docking procedures in the harbour at VAFB. A sketch of the barge and the dock is shown in figures 7 and 8. It was assumed that the barge had an initial velocity imparted by a wave. The barge was then allowed to impact a dock of various stiffness values. It was found that the loads generated at the ET transporter interfaces were acceptable even for severe impact cases. The dock impact loads were governed by the barge stiffness for a stiff dock, and by the dock stiffness for a soft dock.The impact wave as it travels through the deck of the barge is shown in figure 9.

6.0   CONCLUDING REMARKS

Results obtained by the method developed in this paper have been shown to be in good agreement with observed loads and other analysis methods.

The resulting computer program has general applicability, and has been used without modification to solve a variety of contact problems. The contact point description could be made more elaborate to include effects of friction, geometry, etc. By allowing the second body (it need not be a pad) to have rigid body free-free modes other problems, such as berthing/docking dynamics, could be tackled.

7.0   REFERENCES

1)   Prabhakar, A   " Development of a lift-off response program to obtain launch loads for ACC-OTV ", MMC Michoud IOM 3524-85-260

2)   Halfman,R L   "DYNAMICS VOL II ", Addison-Wesley 1962

3)   White,C W   and   Bodley,C   " Boundary interchanges between redundantly connected complex structures ", MMC Denver R78-48628

4)   Craig,R R   and   Bampton,M C C   "Coupling of substructures for dynamic analyses", AIAA Journal Vol. 6 No. 7   July 1968

TABLE 1

VEHICLE C.G. MOTIONS UNDER STATIC LOADS

		X (in)	Y (in)	Z (in)
1)	GRAVITY ONLY ①	-1.174	-0.053	-1.531
2)	① + G-SOFTENING	-1.179	-0.058	-1.726
3)	① + CRYO	0.184	-0.050	-0.923
4)	① + G-SOFTENING + CRYO	0.181	-0.057	-1.060

C-3

188
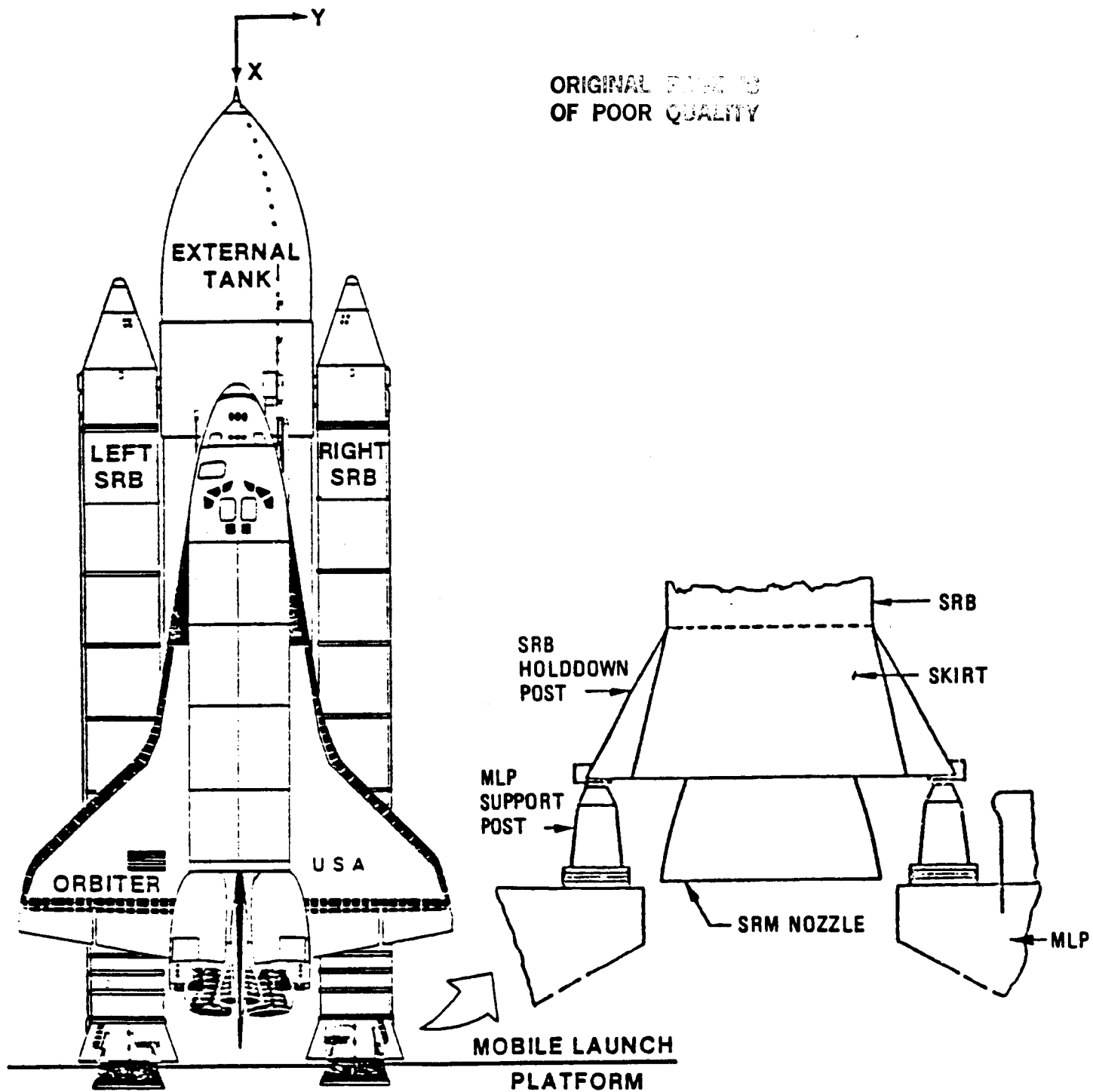
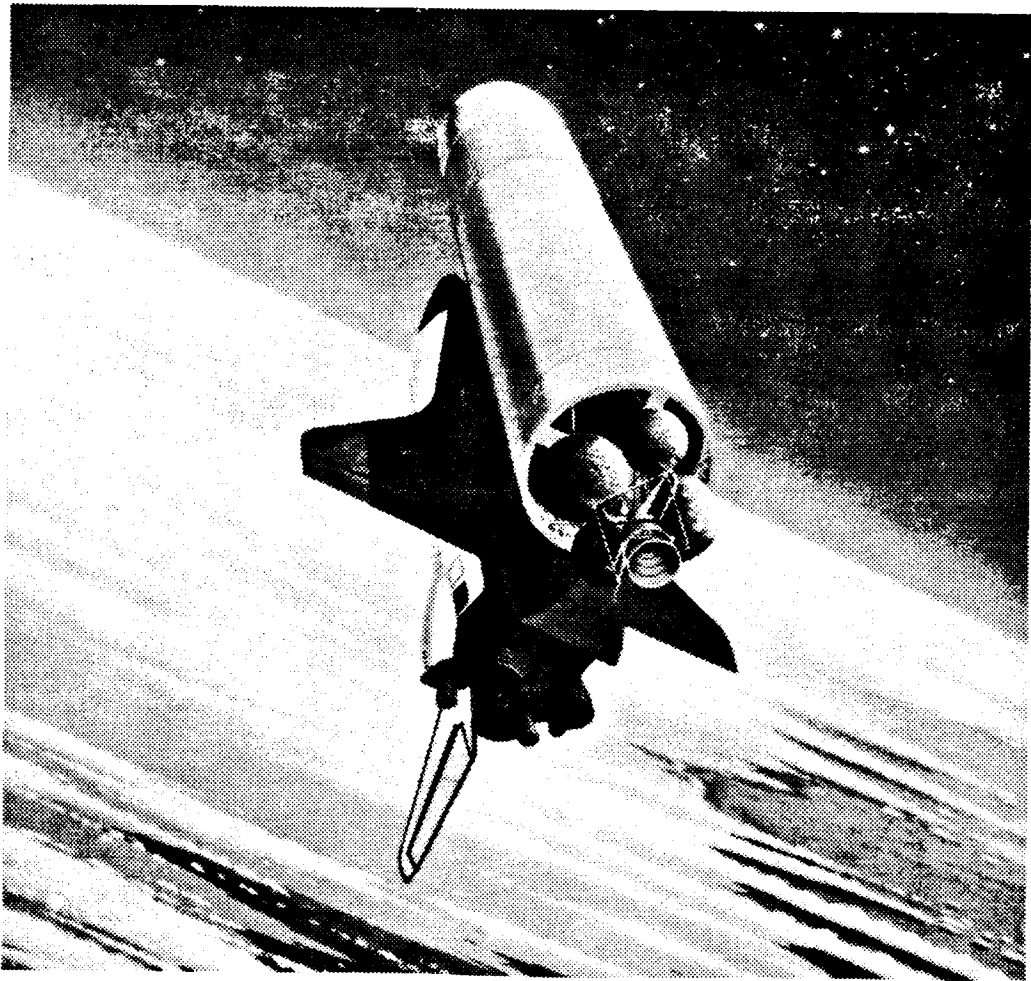FIGURE 1   TOP SIDE VIEW OF THE SPACE SHUTTLE VEHICLE
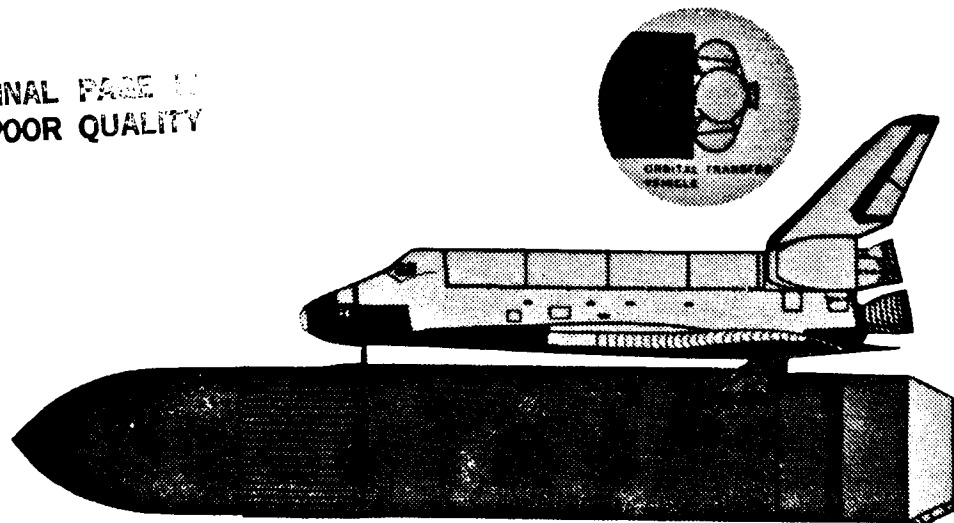
FIGURE 2

ACC-OTV LAUNCH TRANSIENT ANALYSIS

ET/SRB UPPER Y FORCE

FIGURE 3

191
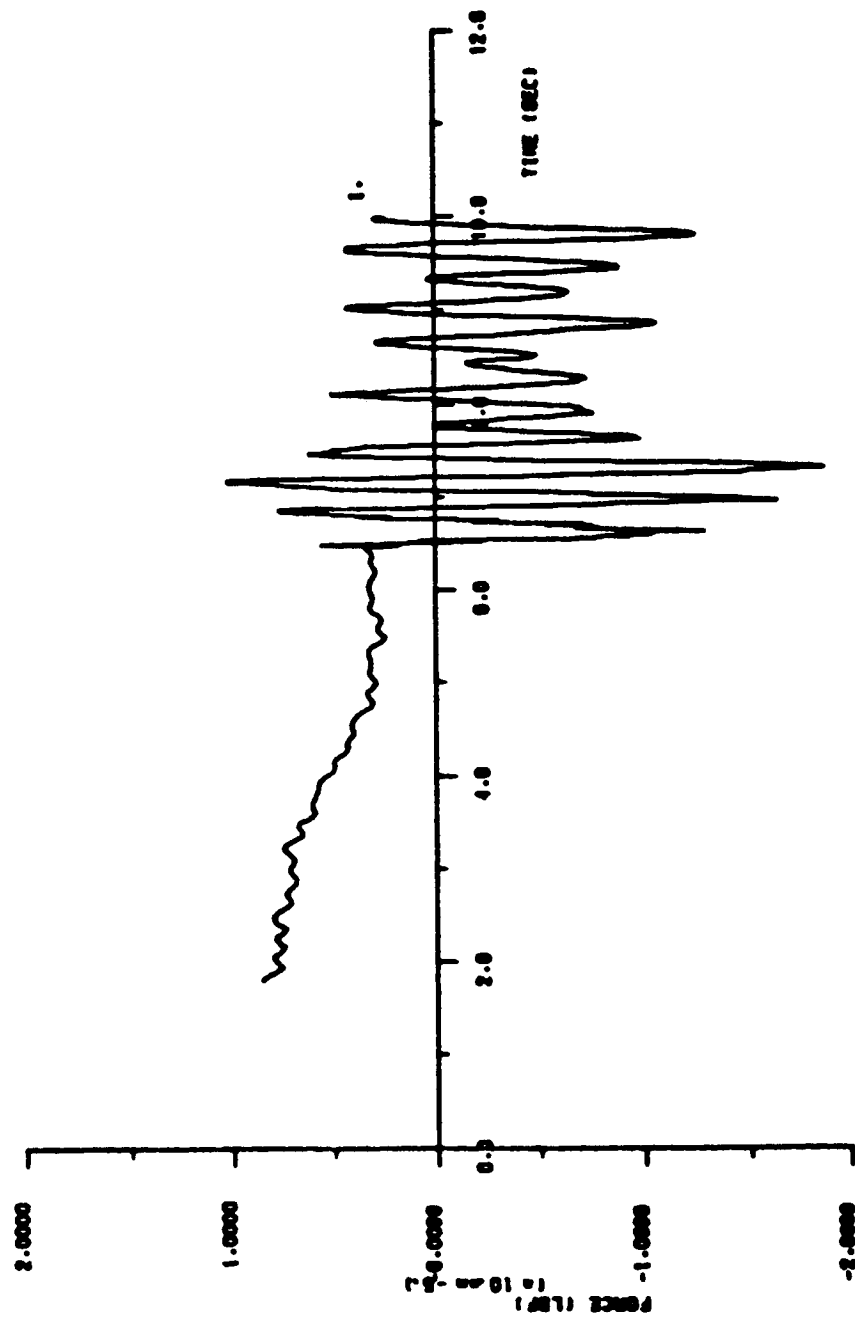
ACC-OTV LAUNCH TRANSIENT RESPONSE ANALYSIS

OTV UPPER LOX TANK X FORCE
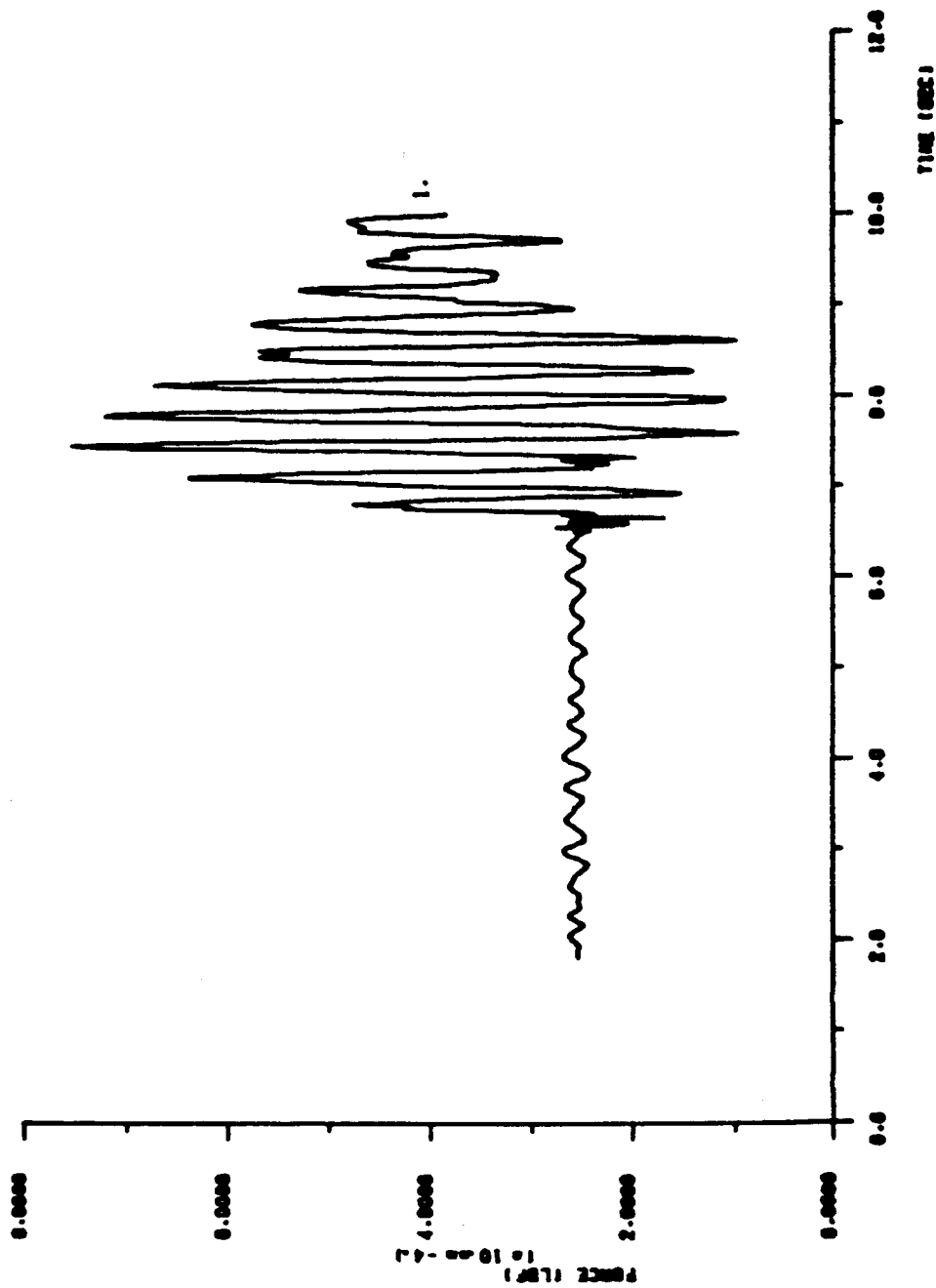
FIGURE 4

192

LOX TANK PRESSURE SLUMP ANALYSIS - LIFT-OFF TRANSIENT

ULLAGE SPACE VOLUME OSCILLATION

FIGURE 5

193
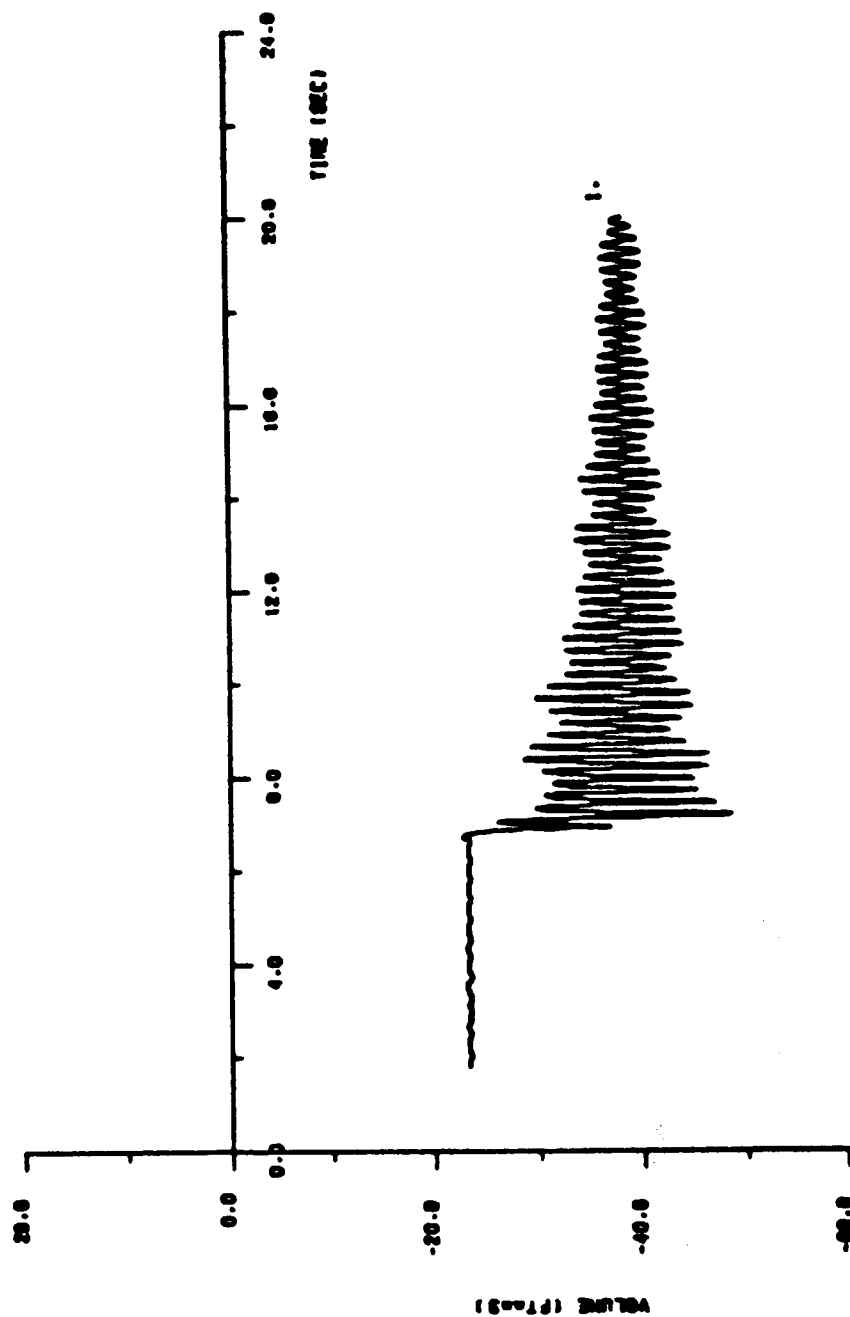
LOX TANK PRESSURE SLUMP ANALYSIS - LIFT-OFF TRANSIENT

TANK BOTTOM PRESSURE
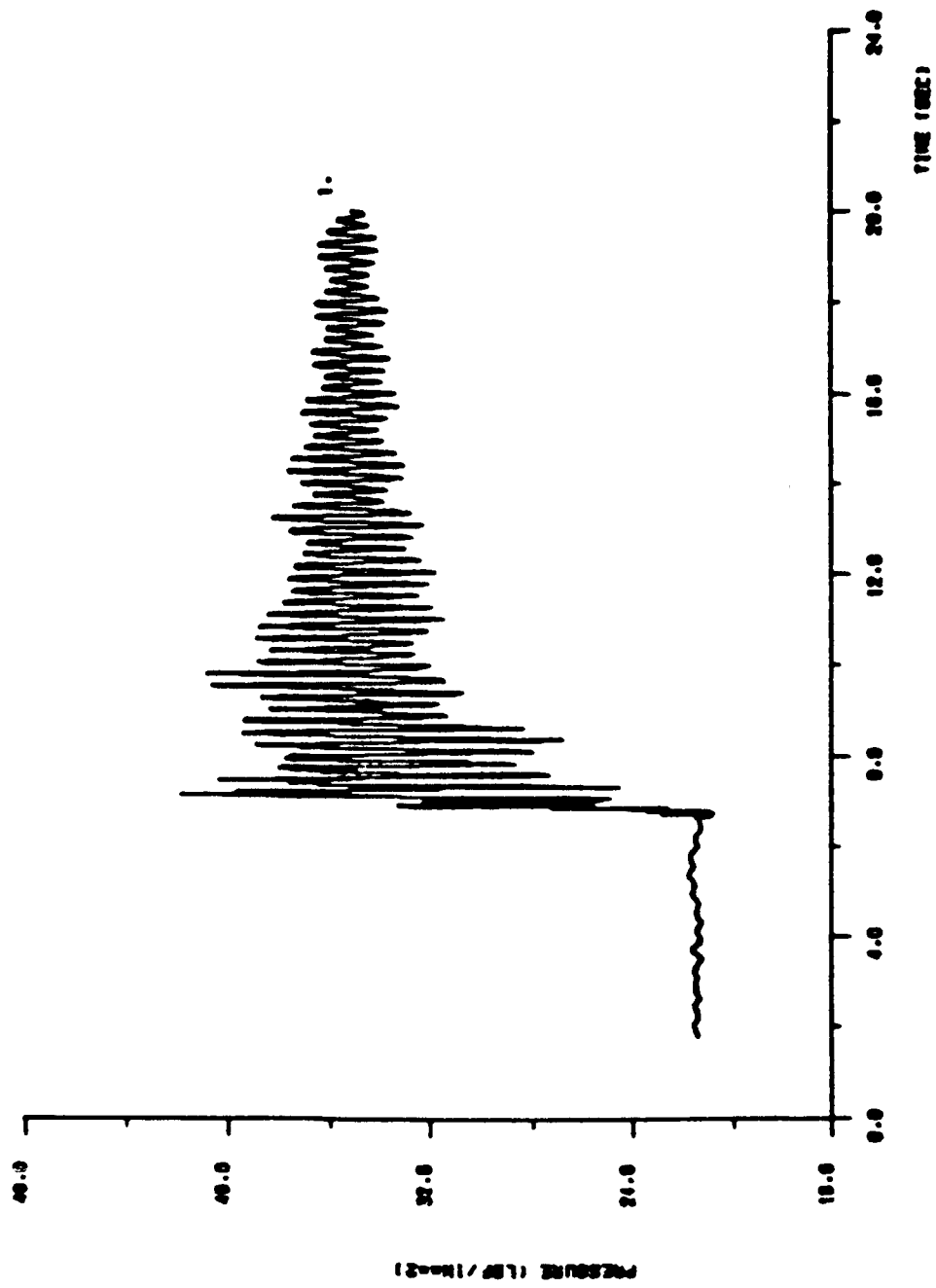
FIGURE 6
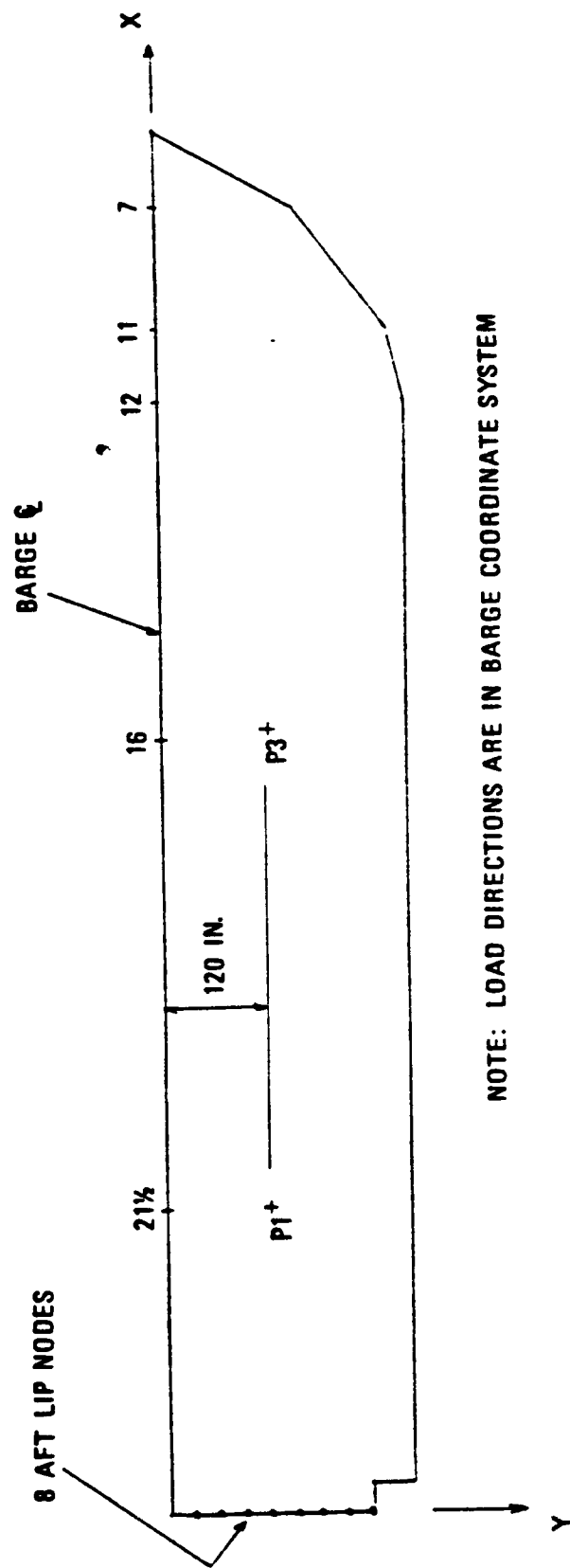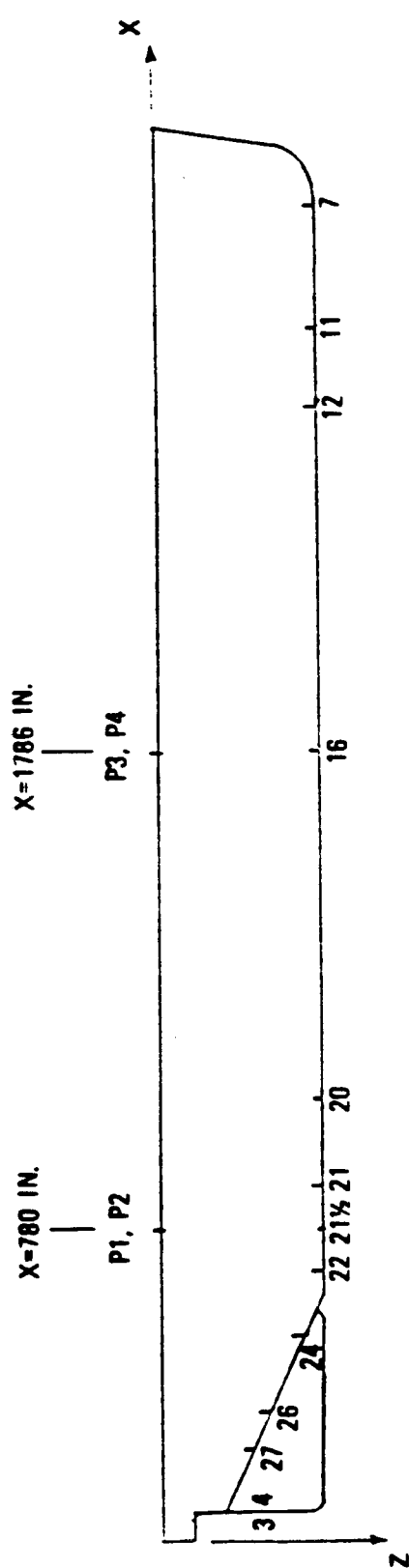
NOTE: LOAD DIRECTIONS ARE IN BARGE COORDINATE SYSTEM

FIGURE 7: BARGE RESPONSE LOCATIONS

FIGURE 8: VAFB DOCK CROSS SECTION

Labels on figure:
RUBBER BUMPERS
FIR TIMBERS
CONCRETE
MEAN WATER LEVEL
UNDISTURBED SHALE ROCK

BARGE DECK RESPONSE FOR A 12 IN./SEC Z IMPACT
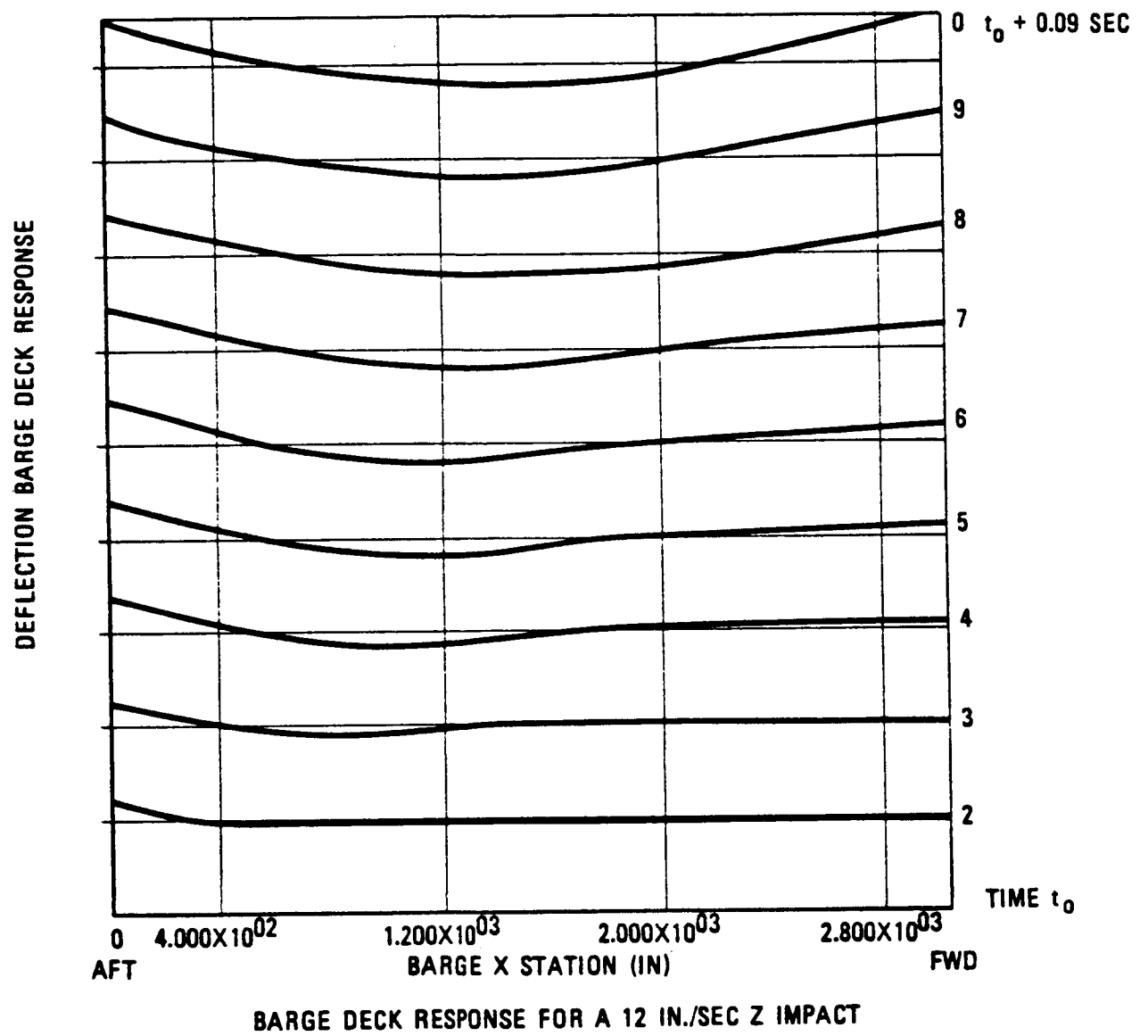
FIGURE 9

- MOVER II -

A COMPUTER PROGRAM
FOR
MODEL VERIFICATION OF DYNAMIC SYSTEMS

J.D. Chrostowski and T.K. Hasselman
Engineering Mechanics Associates, Inc.
Torrance, California

Workshop on Structural Dynamics
and
Control Interaction of Flexible Structures

Marshall Space Flight Center

April 22-24, 1986

DYNAMIC MODEL VERIFICATION

Dynamic model verification is the process whereby an analytical model of a dynamic system is compared with experimental data, adjusted if necessary to bring it into agreement with the data, and then qualified for future use in predicting system response in a different dynamic environment. There are various ways to conduct model verification. The approach adopted in MOVER II employs Bayesian statistical parameter estimation. Unlike "curve fitting" whose objective is to minimize the difference between some analytical function and a given quantity of test data (or "curve"), Bayesian estimation attempts also to minimize the difference between the parameter values of that function (the model) and their initial estimates, in a least squares sense. The objectives of dynamic model verification, therefore, are to produce a model which (1) is in agreement with test data, (2) will assist in the i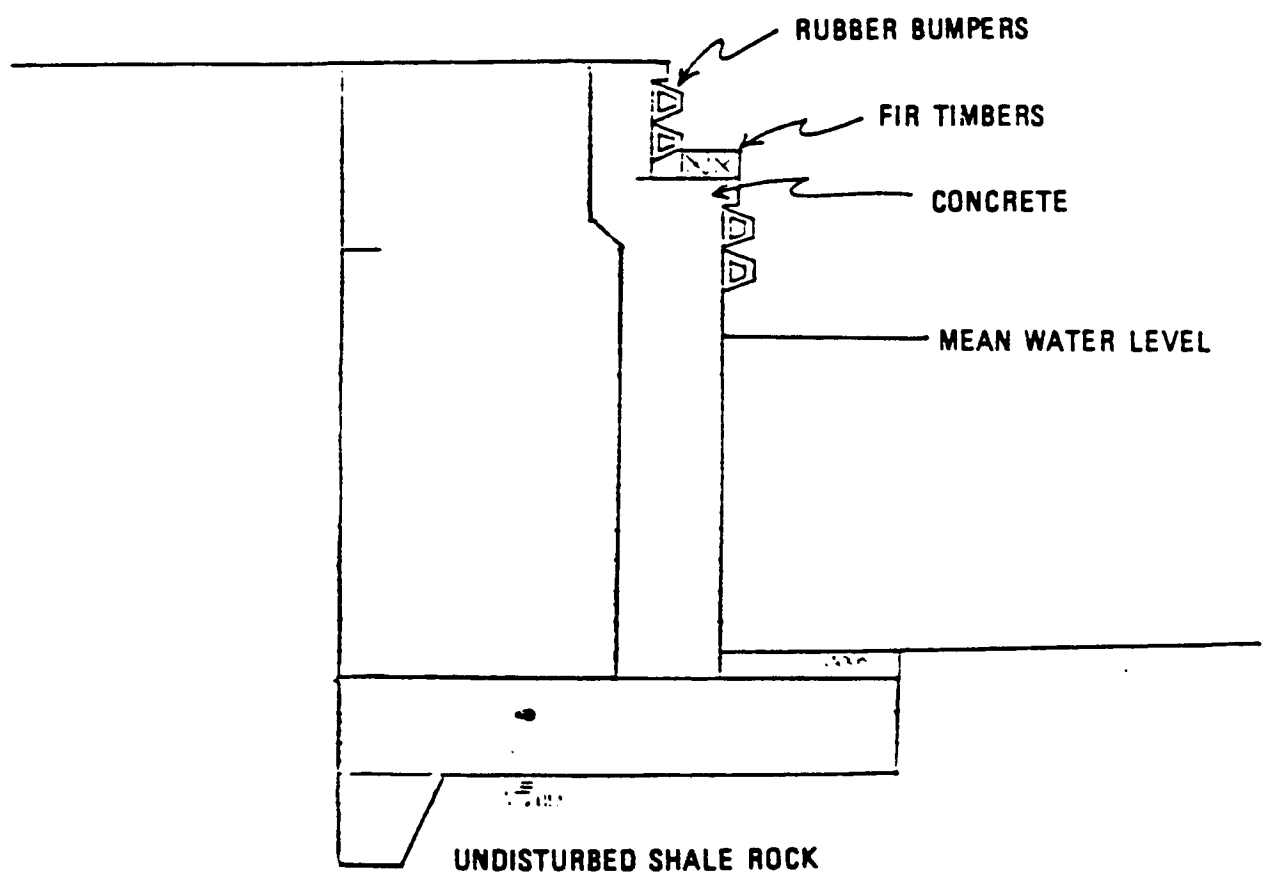nterpretation of test data, (3) can be used to help verify a design, (4) will reliably predict performance, and (5) in the case of space structures, facilitate dynamic control.
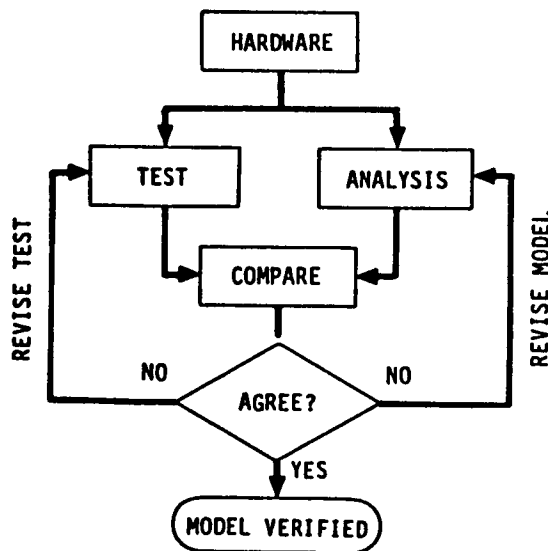
OBJECTIVES

● MATCH ANALYSIS AND TEST

● INTERPRET DATA

● VERIFY DESIGN

● PREDICT PERFORMANCE
  - IMPEDANCE
  - DISPLACEMENT
  - LOADS
  - FATIGUE
  - ETC.

● FACILITATE CONTROL

200

HISTORY OF DEVELOPMENT

One of the earliest attempts in automating the Bayesian parameter estimation procedures was begun in 1972. Under Contract to NASA, a computer code called MOUSE was developed and demonstrated on the Saturn V launch vehicle. Although the methodology used in developing MOUSE was quite general, it was only applicable to one-dimensional shear beam models. In 1976, two efforts funded by NASA were begun in parallel to further develop the MOUSE concept. The first effort was directed towards general dynamic systems, i.e., models which might be constructed from lumped parameter, finite elements, modal coordinates, or some combination of the three, and which might also contain heavy damping. The computer code MOVER was developed to automate the verification of such systems, and won a NASA New Technology award in 1982. The second effort was geared towards efficient model verification of large, lightly damped systems typified by aerospace structures, with specific application to the Space Shuttle Orbiter finite element model; the computer code CATELAST was developed to automate this procedure. Over the past several years, an advanced version of MOVER has evolved. Called MOVER II, it incorporates modal synthesis and substructuring techniques for modeling large multi-component systems and provides a variety of graphic outputs to facilitate interpretation of results. MOVER II has been used to verify models of turbo-pumps rail vehicles, launch vehicles and high-speed rotating machinery.

- 1973 - MOUSE (Model Optimization Using Statistical Estimation)

- 1977 - MOVER (Model Verification)

- 1978 - CATELAST (Correlation of Analysis and Test for Large Structures)

- 1984 - MOVER II

201

MOTIVATION

Compared with the state-of-the-art of model generation and analysis, which has matured considerably over the past decade or so, the state-of-the-art in experimental model verification is still very much in its infancy. Structural testing, particularly dynamic testing and data processing, has also progressed significantly in recent years, but the proven ability to assimilate experimental data systematically into a specified model configuration to obtain an improved set of model parameters values, has not experienced the same steady growth. The original objectives for the MOUSE code were (1) to revise the mass and stiffness parameters of a finite element model using a Bayesian statistical estimator, (2) impose no limits on the amount of test data required, and (3) provide a quantitative measure of the significance of the revised parameter values based on the quantity, quality and suitability of the data. Practical experience with MOUSE, however, indicated the need to satisfy several additional objectives: (4) incorporate a modeling capability applicable to general structural models, regardless of configuration or size; (5) estimate damping, as well as mass and stiffness parameters, even for structures with closely spaced modes; (6) eliminate the requirement for "pure" modal data; (7) require that the program resolve experimental data (to obtain natural frequencies, orthogonal mode shapes and modal damping) from sinusoidal response which may contain contributions of several closely spaced modes; and (8) require that the program be compatible with conventional analytical and experimental data.

1) RETAIN STATE-SPACE/FREQUENCY DOMAIN FORMULATION FOR LINEAR TIME-INVARIANT SYSTEMS

2) REPLACE NETWORK MODELING CAPABILITY IN MOVER WITH ADDITIONAL CAPABILITY FOR MODELING STRUCTURAL/MECHANICAL SYSTEMS

3) INCORPORATE SUBSTRUCTURING

4) ADD PARAMETER SENSITIVITY ANALYSIS IN THE FORM OF RESPONSE DERIVATIVES TO FACILITATE PARAMETER SELECTION

5) ADD INTERPRETIVE/DIAGNOSTIC OUTPUT AND GRAPHICS

- CONVERGENCE HISTORY OF OBJECTIVE FUNCTION AND PARAMETER ESTIMATES

- COMPARISON OF PRIOR MODEL AND REVISED MODEL TO DATA USED IN ESTIMATION

- SIGNIFICANCE INDICATOR FOR PARAMETER ESTIMATES

- CORRELATION MATRIX OF REVISED PARAMETER ESTIMATES

- MOVER II -

MODELING AND PARAMETER ESTIMATION CAPABILITIES

MOVER II has been structured to allow the verification of general dynamic systems. Lumped parameter models can be input by providing the equation(s) of motion for simple elements and/or components; this facilitates the analysis of discrete springs, dampers and simple components. Complex structural/mechanical models can be verified by inputting either a finite element representation (i.e., mass, damping, stiffness matrices) or by a modal representation (i.e., generalized mass, damping, stiffness). Finally, complex dynamic systems can be synthesized from combinations of lumped, finite element and modal models through the application of displacement constraints between individual components and subassemblies.

MOVER II has the capability of updating initial parameter estimates associated with lumped, modal and finite element models. In addition, submatrix scaling parameters can be estimated rather than individual finite element parameters. The submatrix scaling parameters are capable of increasing or decreasing the overall mass and stiffness of selected components and/or subassemblies. This step makes the analysis of large problems more tractable by reducing the number of variable parameters, while at the same time avoiding numerical difficulties associated with estimation of the individual parameters of small structural elements.

MODELING -

- LUMPED PARAMETER MODELS
- FINITE ELEMENT MODELS
- SUBSTRUCTURING

PARAMETER ESTIMATION -

- DISCRETE PARAMETERS
  - LINEARIZED FINITE ELEMENT PARAMETERS
  - LUMPED STIFFNESS, MASS AND DAMPING
- DISTRIBUTED PARAMETERS
  - LINEARIZED LINKED FINITE ELEMENT PARAMETERS
  - SUBMATRIX SCALING COEFFICIENTS
  - MODAL MATRIX PARAMETERS

203

LUMPED PARAMETER MODELS

The figure below shows an example of a damper component that was successfully verified using MOVER II. The damper component was modeled as an axi-symmetric, lumped parameter system with two rotational degrees of freedom in- and out-of-plane of the paper. The mass of the weight assembly was accurately measured, and its value was fixed during the verification process. The rotational damping, C_R, and the translational damping, C_L, were then estimated using load cell data acquired from random input shake tests. The results of the verification process showed that the prior model was grossly in error and that MOVER II adjusted the damping parameters to bring the revised model into good agreement with experimental response measurements.
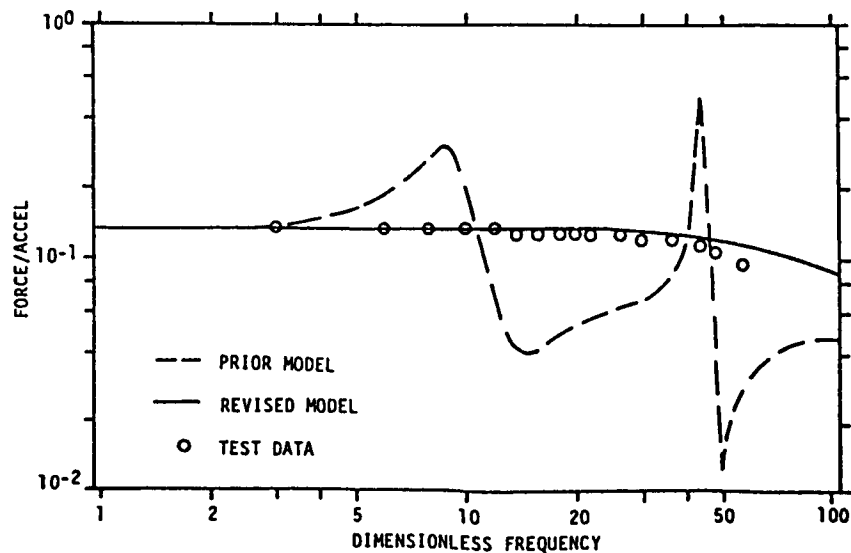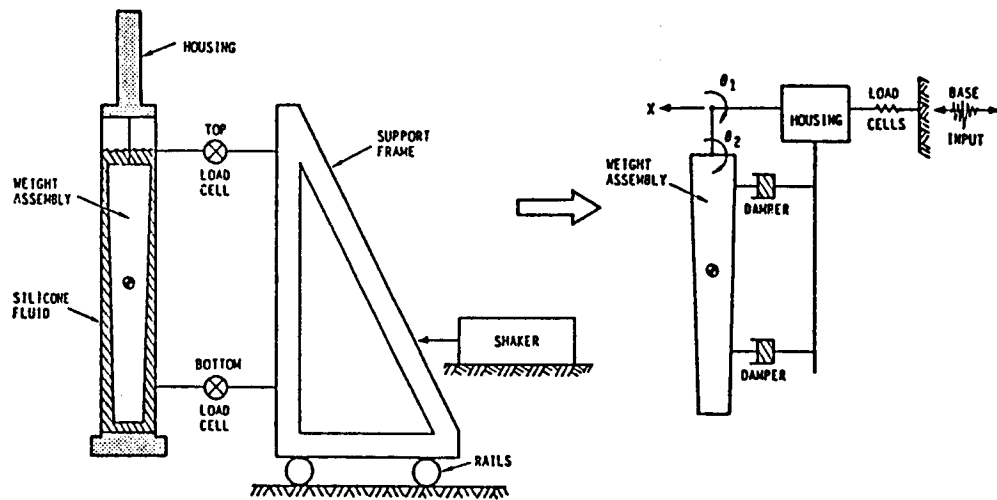
FINITE ELEMENT/MODAL MODELS

The figure below shows a cantilevered column, fixed at one end,
constrained by a spring at the opposite end, with a pendulum damper
assembly (previously verified).   Transfer function data acquired during
single-point random and sine testing were used to verify both a finite
element and modal representation of the column assembly.   Submatrix
scaling parameters were used to update prior estimates of stiffness and
mass properties of three distinct sections of the assembly, as well as the
generalized mass and stiffness of the first two column bending modes.   The
results of this verification effort were successful at both the finite
element and modal level as demonstrated by the improved correlation
between revised model frequency response and experimental test response.

205
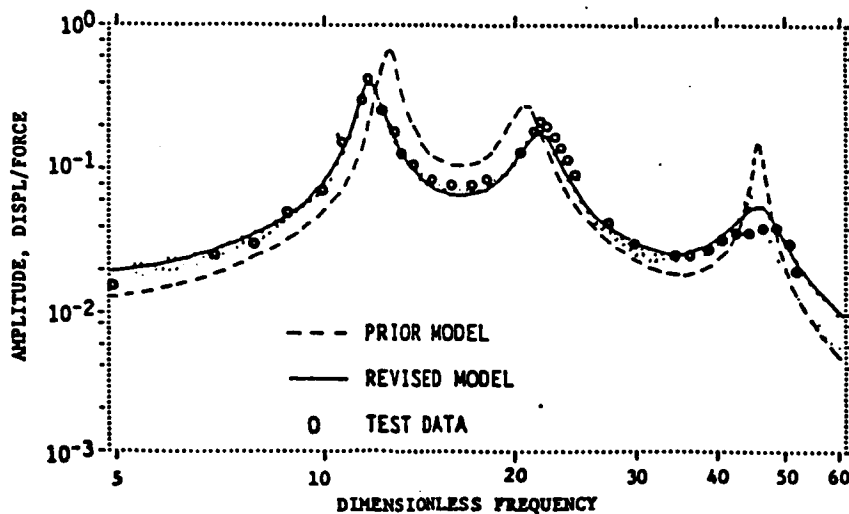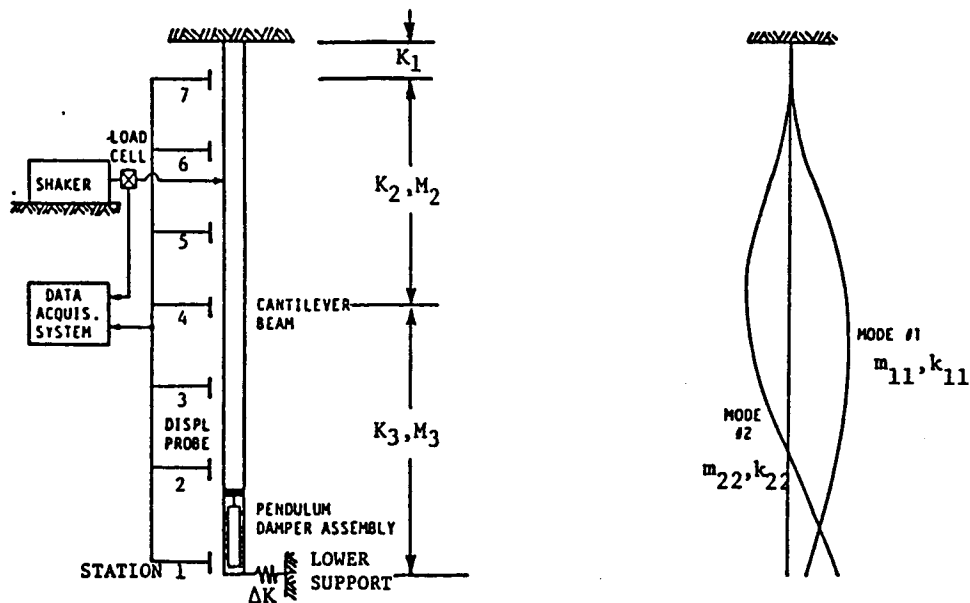
SUBSTRUCTURED MODELS

MOVER II's real strength lies in its ability to synthesize complex dynamic systems from component and subassembly models. As demonstrated in the figure below, a complex model of rotating machinery can be synthesized by combining lumped, modal and finite element models. In terms of model verification, MOVER II can first be used to verify component and subassembly models, thereby reducing verification efforts at the system level. Note that the damper component and column assembly were previously verified, allowing their parameters to be fixed during verification of the system. To construct the system dynamic model, the spinning rotor is attached to a modal representative of the case by lumped parameter models of the upper and lower suspensions. The column assembly is attached to the top of the casing, and a modal model of the case is attached to ground by a lumped model representing the support mount. This synthesis is accomplished through application of displacement constraints. Once constructed, system parameters (including lumped, modal, and/or finite element parameters) may be updated using the submatrix scaling option.
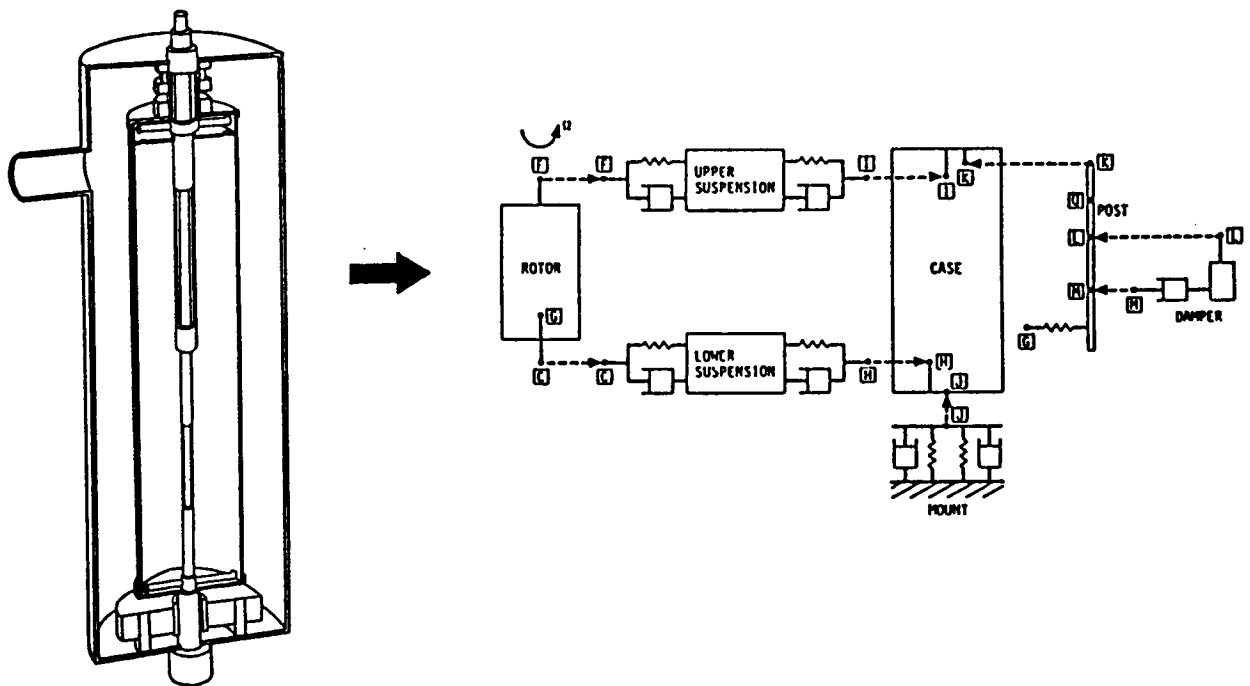
DATA REQUIREMENTS

MOVER II requires the mass, damping and stiffness matrices for component and subassembly models. These can be derived from finite element models, lumped models, or from reduced modal models. The user can then synthesize the complete dynamic system by defining physical coordinates and supplying appropriate displacement constraints between components and subassemblies. To perform Bayesian parameter estimation, submatrix scaling parameters to be updated must be defined and initial estimates of their values assigned, along with confidence in those estimates. In addition, the force distribution used during testing must also be reflected in the model.

MOVER II updates parameter estimates based on experimentally obtained Frequency Response Functions (FRF). The user must therefore supply amplitude and phase data at discrete test frequencies for comparison with model estimates. In addition, the user must input the confidence associated with the FRF; these can be estimated from coherence data obtained from time series analysis of the vibration data.

MODEL -

- SUBSTRUCTURE MASS, DAMPING, STIFFNESS MATRICES
- FORCE DISTRIBUTION
- SUBSTRUCTURE CONNECTIVITY
- INITIAL PARAMETER VALUES AND CONFIDENCE ESTIMATES

TEST -

- COMPLEX FREQUENCY RESPONSE FUNCTIONS (AMPL/PHASE)
- CONFIDENCE LEVEL ON FRF (COHERENCE)

COMPUTATIONAL TOOLS

MOVER II incorporates several features which facilitate the analysis and model verification of complex structural/mechanical dynamic systems. To accommodate dynamic systems that may contain heavy damping or asymmetric damping matrices, the equations of motion are handled internally in first-order form. A complex eigensolver is then used to extract the complex modes; the problem size can then be reduced by using MOVER II's modal truncation option. During the parameter estimation phase of the analysis, sensitivity calculations (response changes due to parameter perturbations) are performed closed-form using eignevalue/eigenvector derivatives calculated internally. These sensitivity calculations feed into a Bayesian estimator which compares analytical FRF response/parameter confidence with experimental FRF response/confidence to update critical modeling parameter estimates. The Bayesian estimator allows quantitative confidence levels to be assigned to revised parameter estimates and experimental data to be processed sequentially.

- FIRST-ORDER EQUATION FORMULATION
  (ASYMMETRIC M, C, K)

- COMPLEX EIGENSOLVER

- CLOSED-FORM SENSITIVITY CALCULATIONS

- MODAL TRUNCATION

- BAYESIAN ESTIMATOR

- SEQUENTIAL DATA PROCESSING

208

PRINTED OUTPUT

MOVER II allows the user to obtain various types of printed output. To aid during initial problem setup, intermediate calculations are available to the user for assessing (1) Model generation, (2) Modal extraction, (3) Sensitivity calculation, (4) Response calculations, and (5) Bayesian estimation. During normal execution, MOVER II outputs during each estimation cycle updated (1) Eigenvalues/Eigenvectors, (2) Complex frequency response, (3) RMS response variation (model vs. data), (4) Original, prior and revised parameter estimates. When MOVER II has converged on a solution, a revised parameter convariance matrix is printed which allows the user to assess the confidence in the updated parameter values.

INITIAL OUTPUT { ● ECHO PRINT OF INPUT DATA

OUTPUT FOR
EACH ITERATION

● EIGENVALUES/EIGENVECTORS

● COMPLEX FREQUENCY RESPONSE

● RMS RESPONSE VARIATION
(CALC'D VS. MEAS'D)

● ORIGINAL, PRIOR, REVISED
PARAMETER ESTIMATES

FINAL OUTPUT { ● REVISED PARAMETER COVARIANCE
MATRIX

GRAPHICAL OUTPUT

MOVER II includes a graphics package to facilitate the model verification process. The package allows the user to obtain the following x-y plots:

- Amplitude and phase of complex frequency response as functions of frequency; plots of both prior model and revised model frequency response as well as measured frequency response, are overlaid on the same graph.

FREQUENCY RESPONSE COMPARISONS

DIMENSIONLESS FREQUENCY
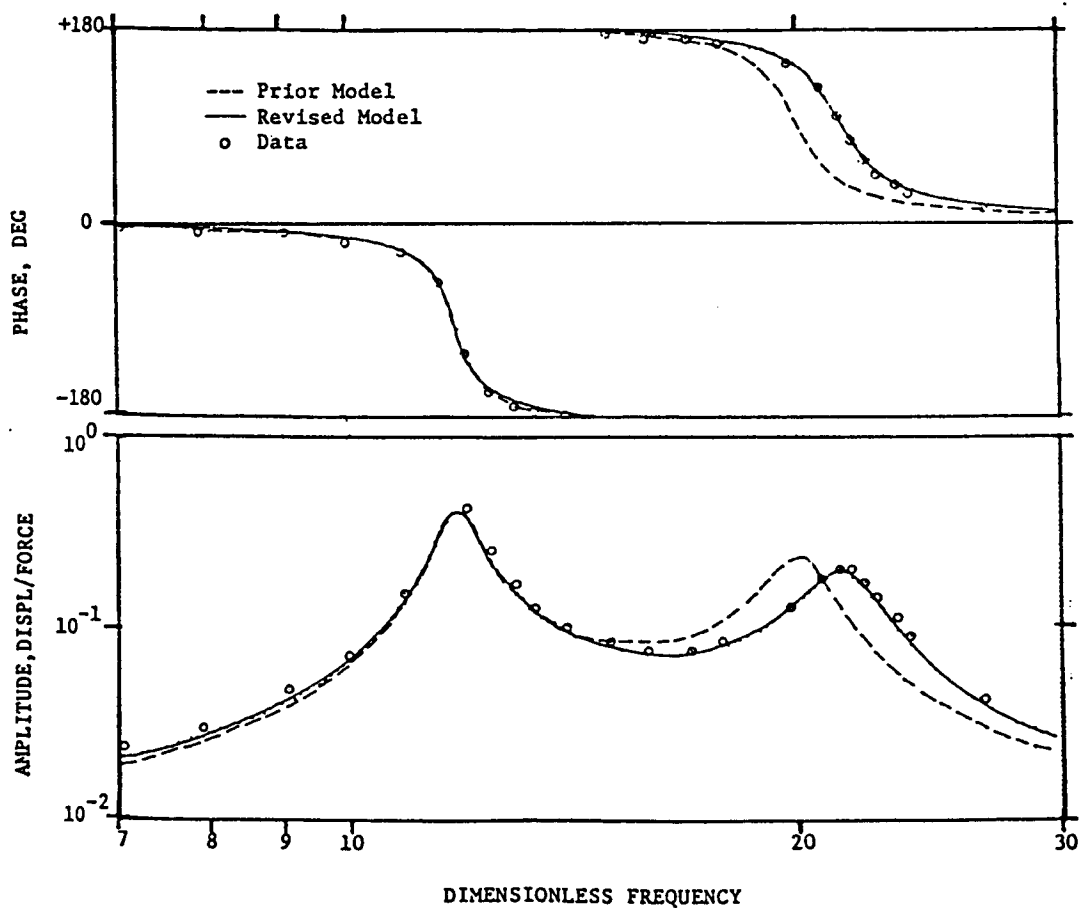
GRAPHICAL OUTPUT (CONTINUED)

MOVER II also plots -

- Sensitivity of response to selected parameters; plots of perturbed frequency response amplitudes as a function of frequency for individually varied parameters, showing comparisons with nominal frequency response amplitude and measured data.

SENSITIVITY PLOTS
(Ampl w.r.t. Parameters $\dot{M}_3$ and ΔK)

(a) Parameter M_3

(b) Parameter ΔK

GRAPHICAL OUTPUT (CONTINUED)

Additional x-y plots provided by MOVER II include:

- History of parameter adjustments as a function of iterative Bayesian estimation cycle showing convergence characteristics of each estimated parameter.

- Statistical significance of individual parameter estimates as a function of their variation from intial parameter estimates.

These graphics greatly facilitate the model verification procedure and are particularly useful during the initial and intermediate phases of ground testing, model verification and structural modification.

```
                          ***    MODE NO. 2 GENERALIZED MASS (GAMMA2)    ***

                     0.0                         1.0                        2.0
CYCLE #    PARM VALUE  |.........|.........|.........|.........|.........|.........|.........|.........|
   1       1.00000E+00  .                                   *                                       .
   2       7.68081E-01  .                                *                                          .
   3       7.98866E-01  .                               *                                           .
   4       8.57914E-01  .                               *                                           .
   5       8.46938E-01  .                               *                                           .
   6       8.52537E-01  .                               |                                           .
                        ..............................................................................
                     |       |       |       |       |       |       |       |       |
                     0.0                         1.0                        2.0
```
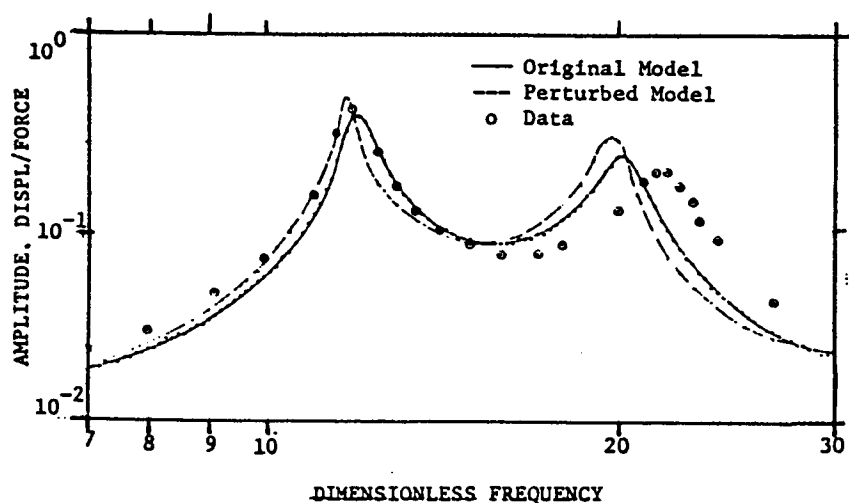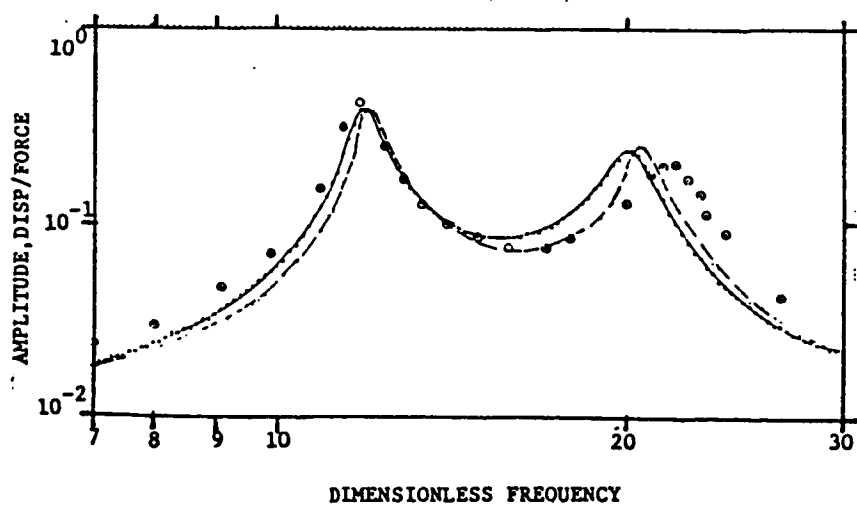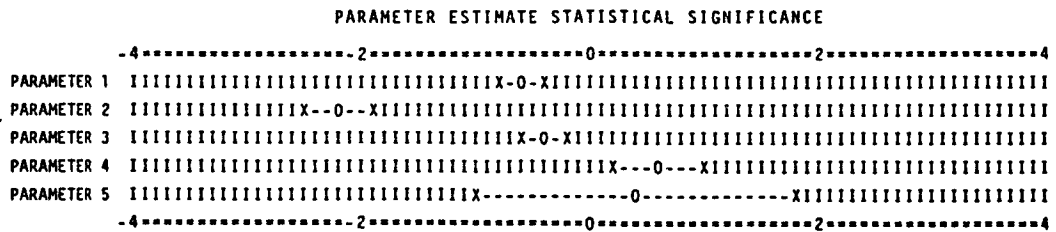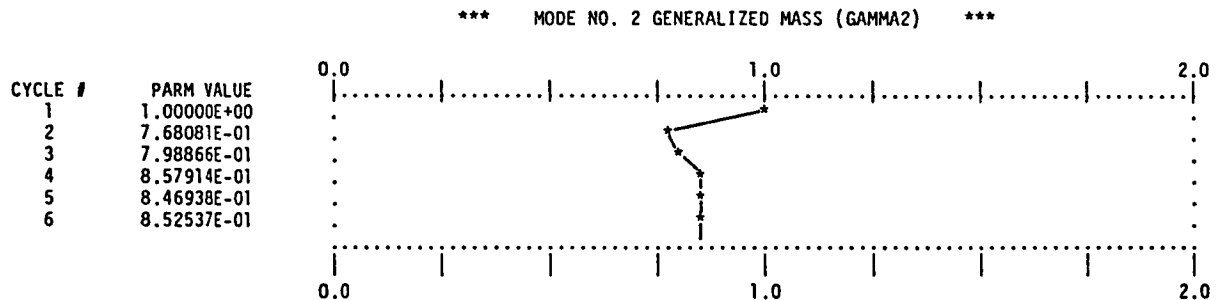
```
                              PARAMETER ESTIMATE STATISTICAL SIGNIFICANCE
                  -4-------------------2-------------------0-------------------2-------------------4
   PARAMETER 1  IIIIIIIIIIIIIIIIIIIIIIIIIIIIIIIIIIIIIX-0-XIIIIIIIIIIIIIIIIIIIIIIIIIIIIIIIIIIIIIIIIIIIII
   PARAMETER 2  IIIIIIIIIIIIIIIX--0--XIIIIIIIIIIIIIIIIIIIIIIIIIIIIIIIIIIIIIIIIIIIIIIIIIIIIIIIIIIIIIIIIIII
   PARAMETER 3  IIIIIIIIIIIIIIIIIIIIIIIIIIIIIIIIIIIIIIX-0-XIIIIIIIIIIIIIIIIIIIIIIIIIIIIIIIIIIIIIIIIIIIIIII
   PARAMETER 4  IIIIIIIIIIIIIIIIIIIIIIIIIIIIIIIIIIIIIIIIIIIX---0---XIIIIIIIIIIIIIIIIIIIIIIIIIIIIIIIIIIIIIII
   PARAMETER 5  IIIIIIIIIIIIIIIIIIIIIIIIIIIIIIIIIIX-------------0-------------XIIIIIIIIIIIIIIIIIIIIIIIIIIII
                  -4-------------------2-------------------0-------------------2-------------------4
```

CONCLUSIONS

MOVER II has been used extensively and successfully over a period of several years to verify the structural/mechanical models of civil, mechanical and aerospace systems. Experience has shown the importance of using both component and system level test data in a structured verification effort. The techniques utilized in MOVER II should find further application in the space program. The control of large structures in space will require accurate structural models for maneuvering, pointing, and shape maintenance. These models will be verified to the maximum extent possible prior to launch, but will most likely require final adjustment to reflect as-built conditions in a zero-g environment. It is apparent that some form of model verification techniques will play an important role in the successful deployment of these large systems.

1) MOVER II IS AN OUTGROWTH OF A SERIES OF MODEL VERIFICATION COMPUTER PROGRAMS ORIGINALLY FUNDED BY NASA/MSFC BEGINNING IN 1971

2) MOVER II HAS BEEN USED EXTENSIVELY TO VERIFY HIGH-SPEED ROTATING MACHINERY USING A SUBSTRUCTURING APPROACH FOR MODEL VERIFICATION AS WELL AS MODELLING ITSELF

3) A SIMILAR SUBSTRUCTURE MODELING AND MODEL VERIFICATION APPROACH IS ENVISIONED FOR LARGE SPACE STRUCTURES

CONSIDERATIONS IN THE DESIGN AND DEVELOPMENT OF A SPACE STATION SCALE MODEL

Paul E. McGowan
NASA Langley Research Center
Hampton, VA 23665

Presented at the
Workshop on Structural Dynamics and Control Interaction
of Flexible Structures

April 22–24, 1986
Marshall Space Flight Center

INTRODUCTION

The paper reviews preliminary work at the Langley Research Center (LaRC) related to the design, analysis and testing of a Space Station scale model. Included are some rationale for focusing the scale model program on Space Station and the utilization of the model to achieve the program objectives. In adddition, some considerations involved in designing a dynamics scale model, such as ground test facilities, sub-scale component fabrication and model replication vs. simulation are presented. Finally, some related research areas currently ongoing at LaRC in support of scale model development are discussed.

TALK OUTLINE

- OVERVIEW OF LaRC SCALE MODEL PROGRAM

- UTILIZATION OF SCALE MODEL

- SCALING CONSIDERATIONS

- RELATED RESEARCH

LaRC SPACE STATION MODEL PROGRAM

The major objective of the LaRC scale model program is to develop technology to improve our ability to predict the on-orbit structural dynamics of large, flexible, multi-bodied, and articulated spacecraft. The approach taken is to develop the technologies for using properly scaled structural models to provide confidence for verification and control of full scale structures which are too large to be tested in the earth's 1-g environment. To this end, the project will fabricate a near replica scale model of Space Station and conduct a comprehensive ground test/analysis program to characterize the structural dynamics of the model. The resulting analysis will then be used to predict the in-orbit behavior of the full scale structure. Finally, via a correlation of the model results with flight data obtained during on-orbit assembly and testing of Space Station, verified analysis and ground test methodologies for other structutres of this class will be developed.

LaRC SPACE STATION SCALE MODEL PROGRAM

OBJECTIVES:

Develop technology which provides a verified capability to predict on–orbit structural dynamics of large, multi–bodied spacecraft.

APPROACH:

Fabricate a near–replica scale model of Space Station.

Conduct comprehensive ground test–analysis technology program.

Correlate results with full scale flight data from on–orbit testing.

219

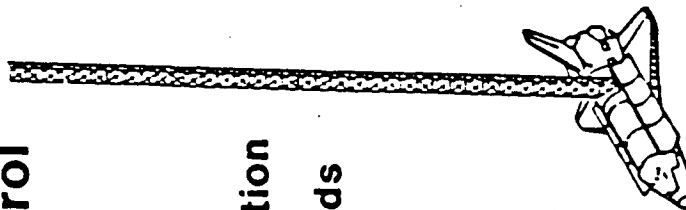## THE CONTROL OF FLEXIBLE STRUCTURES (COFS) PROGRAM

The development of the scale model resides under the COFS III project at LaRC. COFS III is the third in a series of three major projects under the Control of Flexible Structures (COFS) Program. The COFS program consists of a series of detailed ground and flight test/analysis projects on a variety of large space strucrures. COFS III emphasizes multi-body dynamics and control and focuses on a class of structures which are too large to be properly tested beyond the component/subassembly level in the earth's 1-g environment. Technology derived from COFS I and II will transfer directly to COFS III, especially in the areas of developing testing techniques and characterizing multi-jointed structures.

CONTROL OF FLEXIBLE STRUCTURES

COFS III
Multi-Body Dynamics & Control

- Test Methods
- Systems Identification
- Model Sensitivities
- Analysis Validation
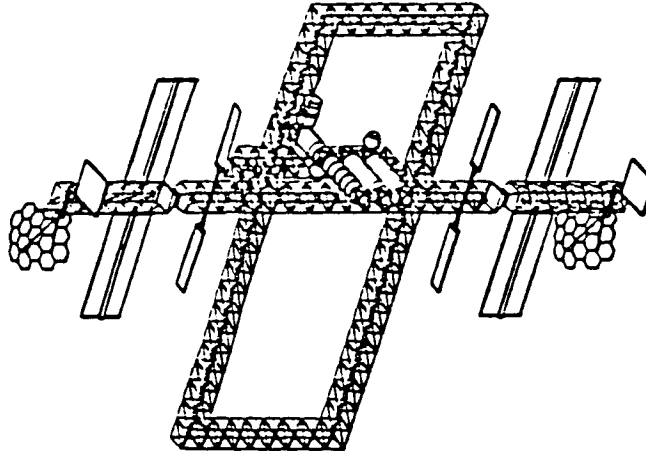- Space Station Supporting Technology

COFS II
Three-Dimensional Dynamics & Control

- Systems Identification
- Shape Definition
- Distributed Controls
- Adaptive Controls

COFS I
Beam Dynamics & Control

- Systems Identification
- Test Methods
- Distributed Controls

221

MOTIVATION FOR SPACE STATION AS COFS III FOCUS

The Space Station is an excellent example of future generation multi-bodied structures requiring validated structural dynamics and control analyses, thus it serves as a natural focus for the COFS III project. A scale model ground test/analysis program addresses the key technologies of the COFS Program including development of verified analyses, ground test methods, and spacecraft vibration suppression methods. Unlike COFS I and II, COFS III does not contain an orbital test as part of the project; however, the expected availability of flight test data from the full scale station in orbit will allow the correlation between ground and flight tests necessary to verify analyses. Furthermore, the scale model provides a means for conducting technology development tests and examining the response of evolutionary configurations and/or alternative component combinations prior to flight.

MOTIVATION FOR SPACE STATION AS COFS III FOCUS

- SS is large, flexible, joint-dominated, <u>multi-bodied</u>, and <u>articulated</u> → provides great challenges in structural dynamics and control.

- Addresses key COFS technology goals
  - Development of verified analyses for multi-bodied spacecraft
  - Extend current ground test methods
  - Development of vibration suppression and control methods

- Availibility of full scale test data to correlate model ground test results and analytical predictions on complex structure.
  - Ground tests of key subassemblies
  - On-orbit flight test data

- Follow-on COFS activities through support of evolutionary SS configurations and technology development tests.

JUSTIFICATION FOR SCALE MODEL DYNAMIC GROUND TESTS

A major justification for ground tests of scale model hardware is the reduction of the effects of gravity and size on full-scale ground tests. For many large space structures, scale models offer the only opportunity to achieve fully mated test data prior to flight, which could help uncover potential problems or verify designs and mathematical models. Scale models can also be useful in determining instrumentation requirements and optimum placement on the full scale vehicle and for studying anticipated flight maneuvers and investigating flight anomalies. Finally, as specifically related to Space Station, the model provides a test bed for robotics experiments and for studying potential growth configurations.

JUSTIFICATION FOR SCALE MODEL DYNAMIC GROUND TESTS

- Fully mated full scale ground tests are desirable but not possible due to gravity and large size.

- Significant improvements in analysis capability possible through:
  - Hands–on experience with realistic hardware
  - Acquisition of mated vehicle data prior to flight

- Uncover potential problems which influence design.

- Pilot for examining instrumentation requirements of orbiting station.

- Tool for studying anticipated flight maneuvers and investigating flight anomalies.

- Test bed for MRMS and robotics operations.

225

APPROACH FOR OBTAINING QUALIFICATION OF MATH MODELS

An approach for obtaining verified analytical models is shown in the adjoining chart. The scale models are used to develop methods for correlating analyses with tests of model components and mated configurations. The full scale hardware is limited to component and element testing and perhaps flight tests of some hardware. Once the full scale vehicle is in orbit, flight data can be used for the final adjustments to the scale-model-verified analyses to obtain a fine-tuned representation of the full-scale vehicle on-orbit behavior.

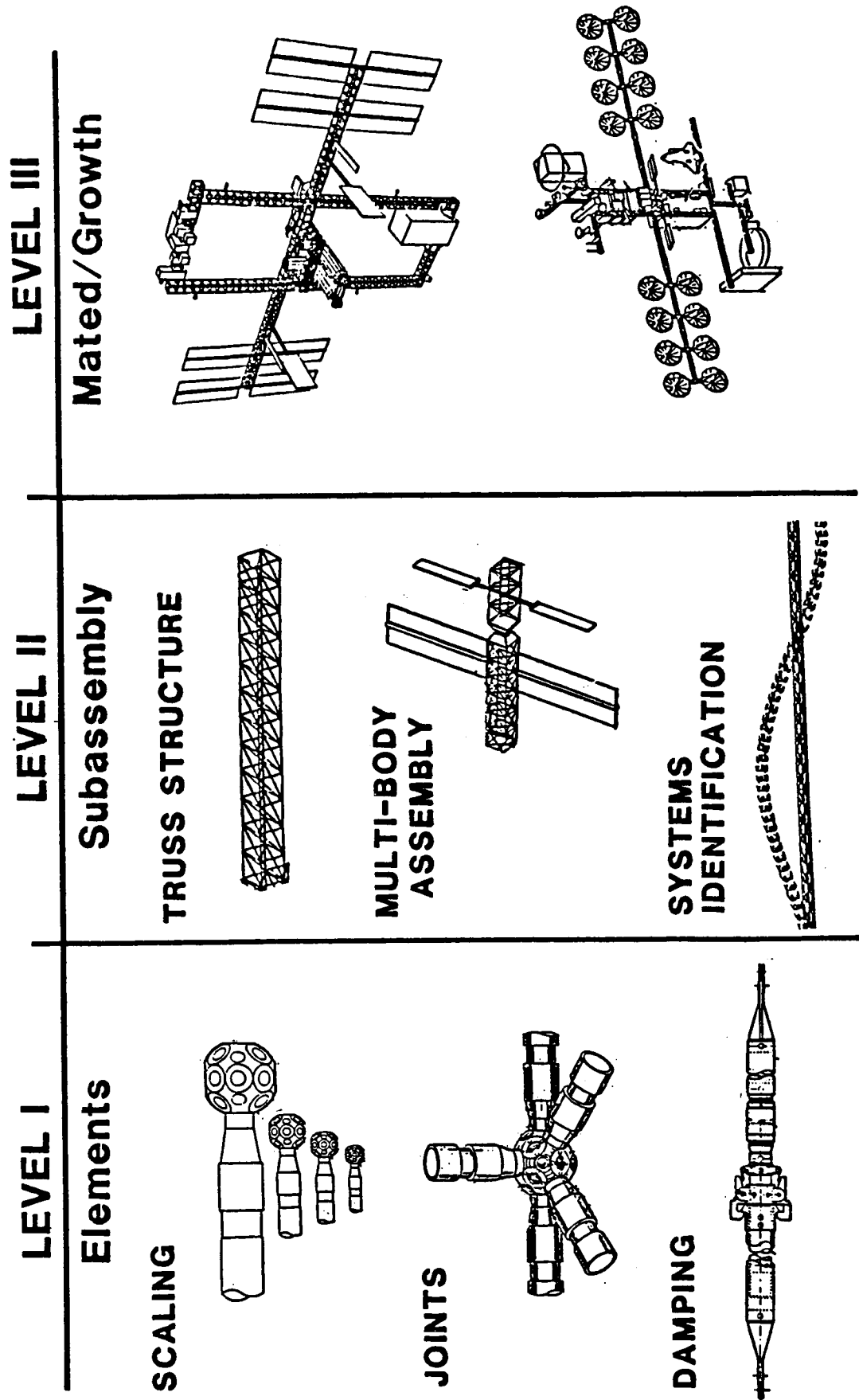# APPROACH FOR OBTAINING QUALIFICATION OF MATH MODELS
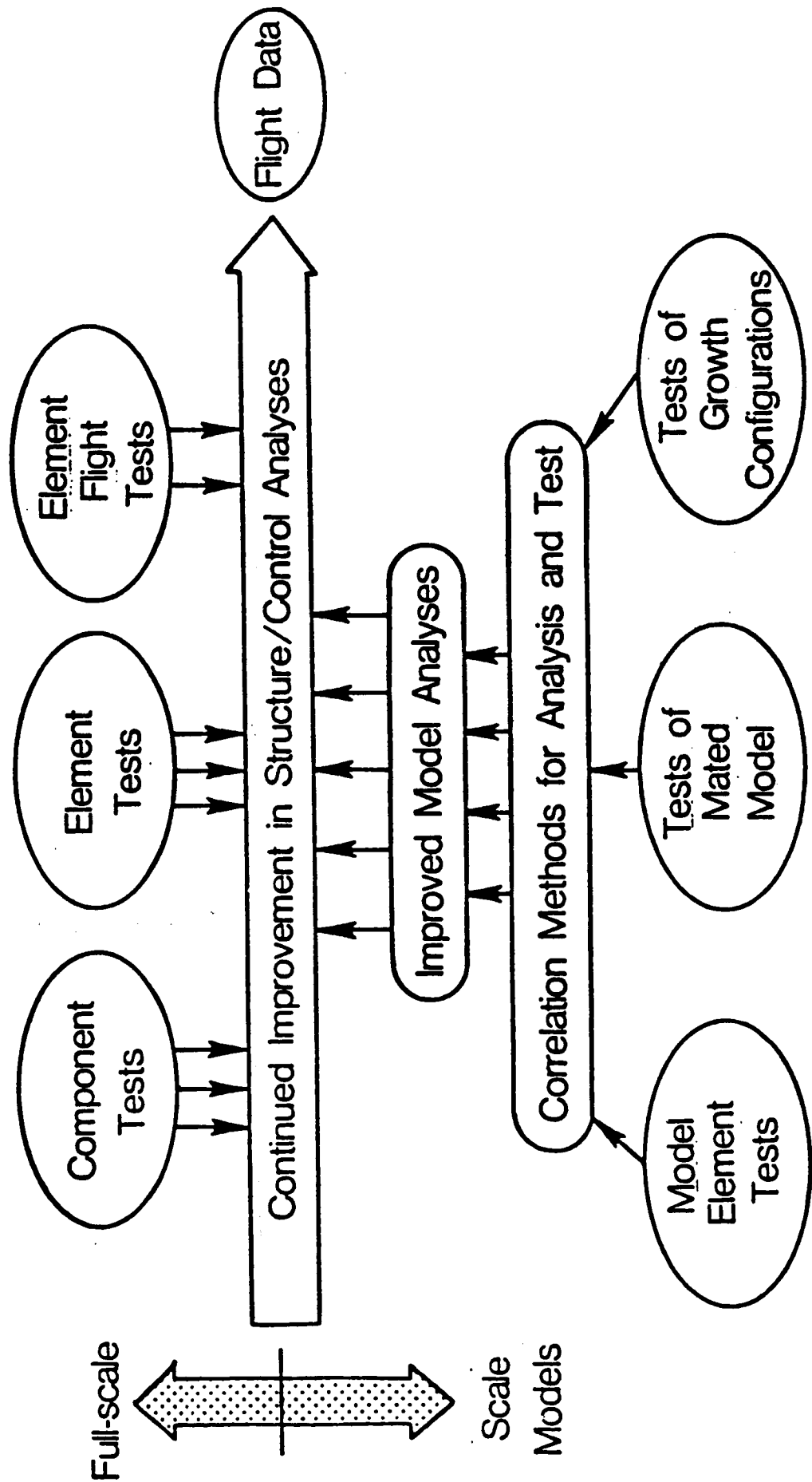
COFS III GROUND TEST SCENARIO

The ground test scenario for the COFS III project includes three levels. First, the scaling of elements such as structural joints and truss members along with analytical characterization of these elements. Second, major subassemblies of the full structure will be tested and systems identification performed to identify the characteristics of those subassemblies and make adjustments of analyses. The scale model will be modular in design such that all anticipated full scale assembly scenarios can be duplicated on the ground prior to flight. In addition, the scale model will undergo the same types of tests anticipated for the full-scale structure (i.e., static/dynamic tests of major subassemblies) in order to obtain as many comparisons between model and full-scale test data as possible. Third, fully-mated scale model ground tests will be performed on both IOC and any growth versions.

COFS III GROUND TEST SCENARIO

SCALE MODEL TECHNOLOGY

LEVEL I	LEVEL II	LEVEL III
Elements	Subassembly	Mated/Growth

LEVEL I — Elements: SCALING, JOINTS, DAMPING

LEVEL II — Subassembly: TRUSS STRUCTURE, MULTI-BODY ASSEMBLY, SYSTEMS IDENTIFICATION

LEVEL III — Mated/Growth

DYNAMIC MODEL SCALING

The optimum scale factor for a dynamics model is a trade-off between how well the individual model components can be manufactured at sub-scale and how large a model can be tested inside the available test facility. Manufacturing limitations would tend to increase the model size (provides lower bound) while simultaneously the limited size of conventional test facilities tend to decrease the model size (provides upper bound). Another major factor in dynamic model scaling is the identification of components which require replication and those for which only require mass and inertia simulation. For the COFS III model, components such as the joints, truss members as well as interfaces between major subsystems or payloads and the structure will likely require replication: however, model cost and complexity can be reduced by simulating modules, major subsystems, and payloads.

DYNAMIC MODEL SCALING

● Optimum model scale factor is a trade-off.

  – Advantages of decreasing model size
    o Gravity effects reduced
    o Eases facility, suspension, and instrumentation reqmts.
    o Improves model handling (weight)
  – Disadvantages of decreasing model size
    o Fabrication process more difficult
    o Component replication more critical (tolerances)
    o Creates handling problems (fragility)

● Ground test facility crucial to achieve meaningful test data.

  – Facility size provides upper bound on model size.
  – LSL satisfies volume and suspension requirements

● Component Replication vs. Simulation

  – Replication desirable for stiffness/damping properties
    Joints
    Tubular Members
    Interfaces
  – Reduce model cost and complexity thru simulation
    Modules
    Subsystems
    Payloads

EFFECT OF SCALE FACTOR ON MODEL FREQUENCY TO

PENDULUM FREQUENCY RATION

Pendulum suspensions on long cables are the most likely technology for supporting models during tests, especially in complete system configurations. Examining the effect of scale factor on the model-frequency-to-suspension-pendulum-frequency ratio provides a means for identifying a reasonable range for the scale factor. Shown on the adjoining chart is the variation of frequency ratio with model scale factor for an initial and a growth configuration of the scale model tested verticallly. The acceptable design region is the upper right quadrant such that the scale factor is above the assumed manufacturing limitation of .25 and the frequency ratio is above the desired value of 5.

232

EFFECT OF SCALE FACTOR ON MODEL FREQUENCY TO PENDULUM FREQUENCY RATIO
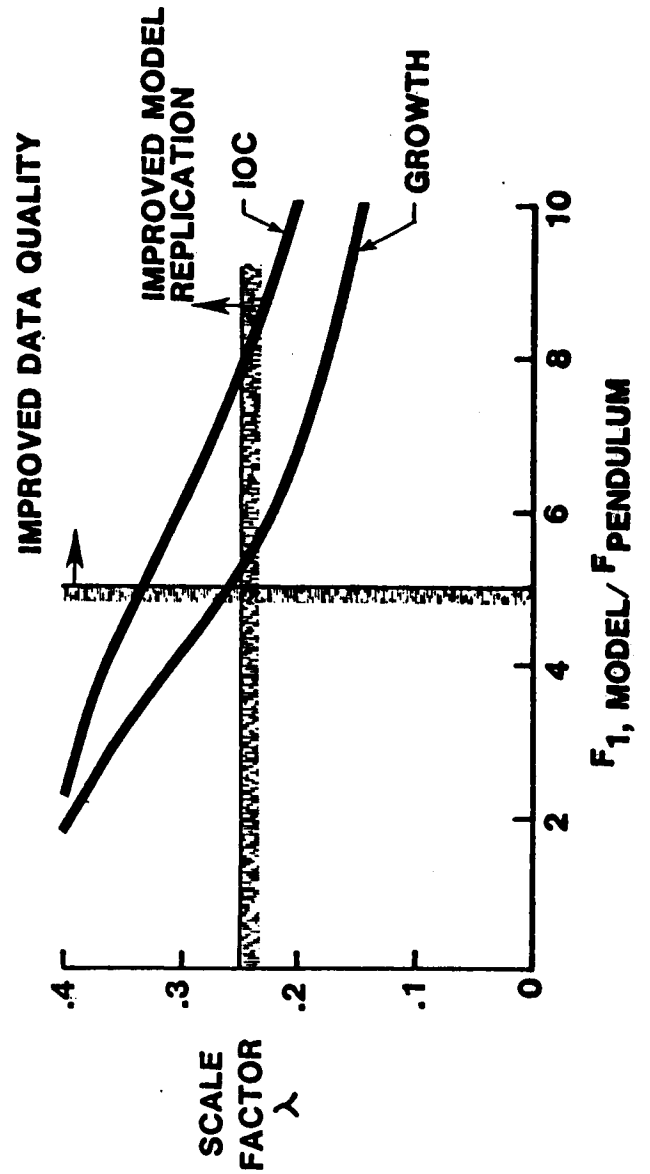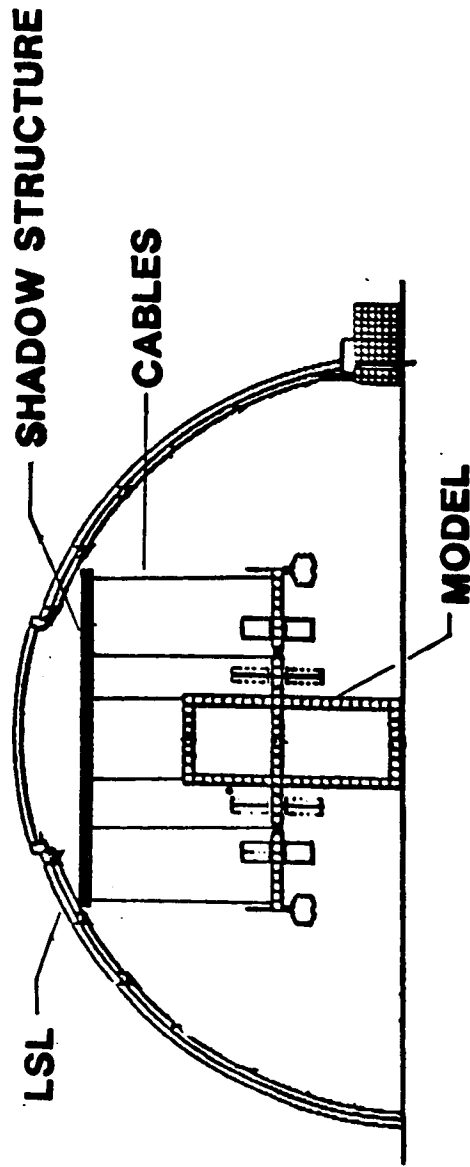
ASSESSMENT OF SUSPENSION CABLES ON

SCALE MODEL TESTING

A key issue in the area of ground test methods was addressed in a study of the interaction of the scale model with a candidate suspension system and proposed test facility. Depicted in the adjoining chart are the 3 steps used to study these effects. Note this study was initially performed on a single keel configuration; however, the conclusions reached are expected to be similar for the dual keel station. A first step is to suspend the model from cables which connect directly to the top of the test facility (assumed to be rigid). Next, a shadow structure concept is used whereby the model is suspended from the rigid shadow structure, which covers the model planform, and the shadow structure is in turn suspended from the test facility (also assumed to be rigid). This concept provides maximum versatility in locating cable attachment points. Finally, step 3 involves accounting for the flexibility of the dome in the analysis procedure. Initial analyses have shown the effects of the dome flexibility on the model dynamics to be negligible, thus most analyses to date have focused around step 2.
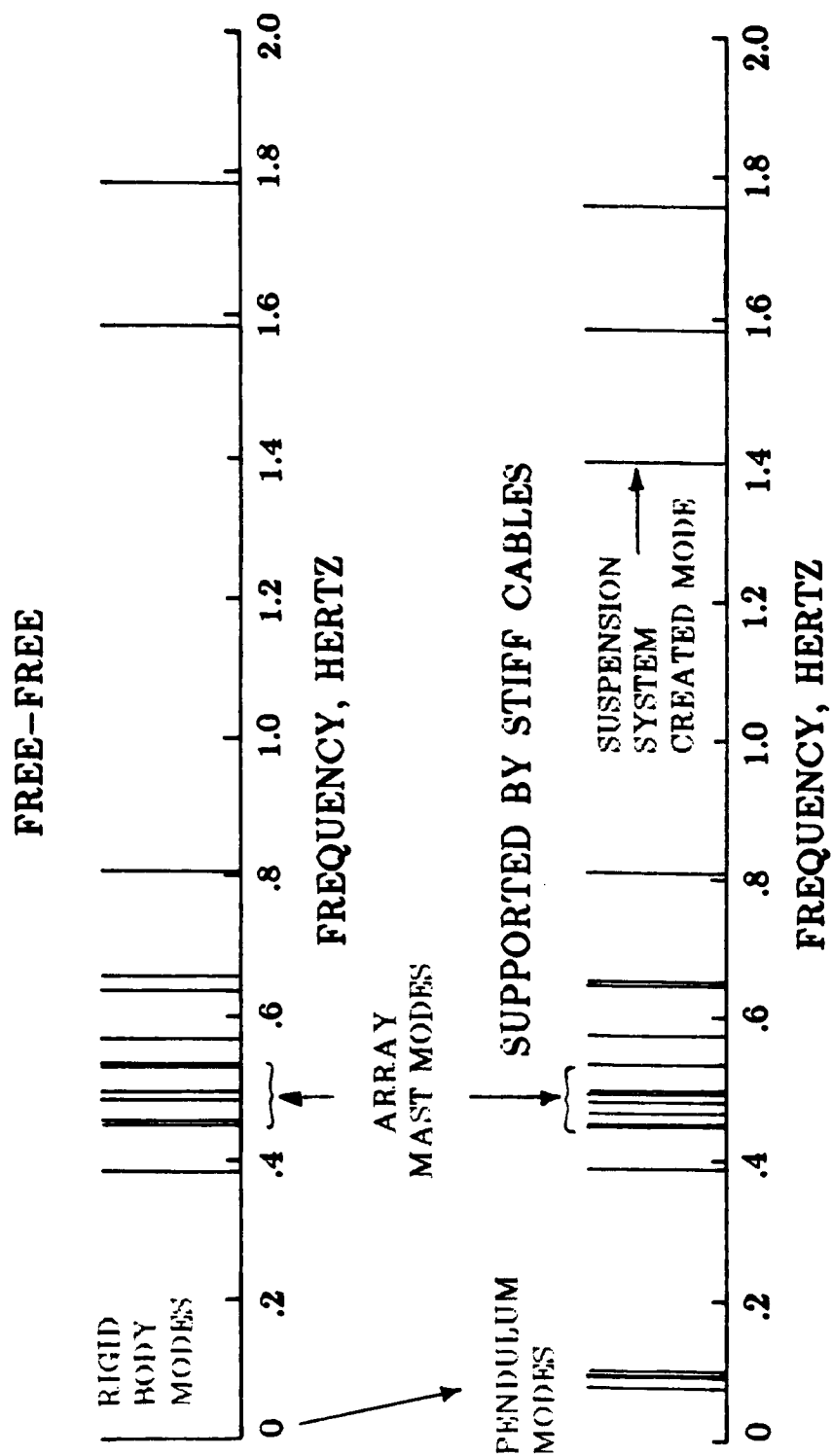
ASSESSMENT OF SUSPENSION CABLES ON
SCALE MODEL TESTING

RIGID
DOME

STEP 1

RIGID
DOME

SHADOW
STRUCTURE

STEP 2

FLEX
DOME

SHADOW
STRUCTURE

STEP 3
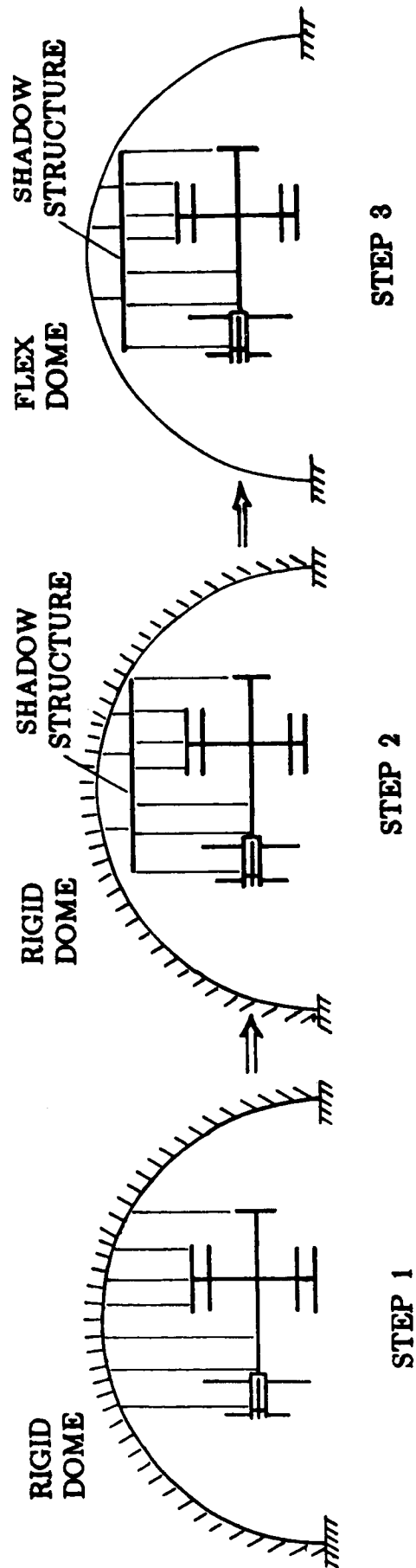
MODAL DENSITY OF 1/3 SCALE SPACE STATION MODEL

A comparison between the modal density of a 1/3 scale model analyzed in a free-free condition and the same model analyzed as suspended in a pendulum configuration is shown in the adjoining chart. The results of the supported case represent a superposition of suspending the model both vertically and horizontally in order to extract both in-plane and out-of-plane modes. The free-free rigid body modes become pendulum modes in the supported case. The natural frequencies of these models are well separated from those of the structural modes, thus there were no interactions evident. Furthermore, there were no significant changes in structural frequencies due to the suspension system and all free-free modes were identifiable.

MODAL DENSITY OF 1/3 SCALE SPACE STATION MODEL

FREE–FREE

RIGID
BODY
MODES

FREQUENCY, HERTZ

| 0 | .2 | .4 | .6 | .8 | 1.0 | 1.2 | 1.4 | 1.6 | 1.8 | 2.0 |

ARRAY
MAST MODES

SUPPORTED BY STIFF CABLES

PENDULUM
MODES

SUSPENSION
SYSTEM
CREATED MODE

FREQUENCY, HERTZ

| 0 | .2 | .4 | .6 | .8 | 1.0 | 1.2 | 1.4 | 1.6 | 1.8 | 2.0 |

NOTE – FULL SCALE FREQUENCIES = MODEL FREQUENCIES / 3

RELATED RESEARCH AREAS

The Structural Dynamics Branch, Structures and Dynamics Division, of
the Langley Research Center is involved in a variety of research areas
directly applicable to the scale model program. One such area is the study
of active member dampers which could be placed in the truss members of a
truss structure to provide vibration suppression. This is one concept
currently envisioned for introducing a vibration suppression mechanism into
the scale model. Another effort is an on-going evaluation of in-house
capability to manufacture model components such as structural joints and
graphite/epoxy tubular members. In addition, ground test methods for large
multi-jointed structures are being developed by conducting tests (static and
dynamic) of prototype Space Station hardware.

RELATED RESEARCH AREAS

- **Application of active member dampers for vibration suppression of truss structures**

- **Evaluate model fabrication capabilities**
  - Structural joints
  - Gr/Ep tubular members

- **Improve ground test methods**

- **Examine suspension system effects on scale model**

SPACE STATION SCALE MODEL RESEARCH HARDWARE

Some of the research hardware used in LaRC's in-house scale model efforts are shown in the adjoining photo. Two seven-bay erectable truss structural models have been built under contract, one at full scale (15-foot bays) and one at 1/4 scale. These models have been assembled in various configurations to demonstrate the versatility of the erectable concept. Currently these structures are undergoing testing at LaRC. These tests include static tests of the joint components to characterize joint stiffness and modal testing to characterize frequencies and mode shapes.
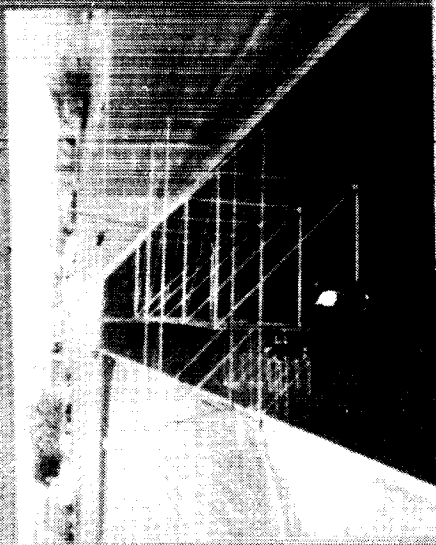
240

SPACE STATION SCALE MODEL
RESEARCH HARDWARE
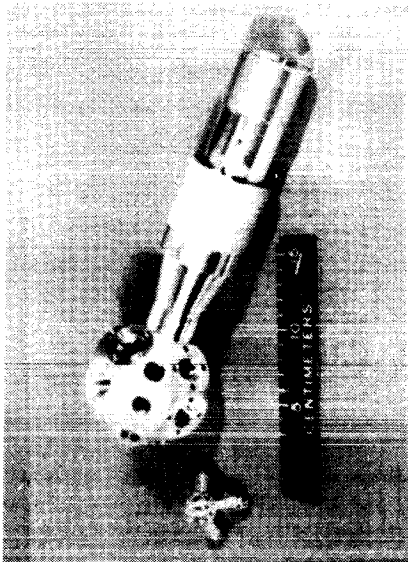
Prototype erectable joints
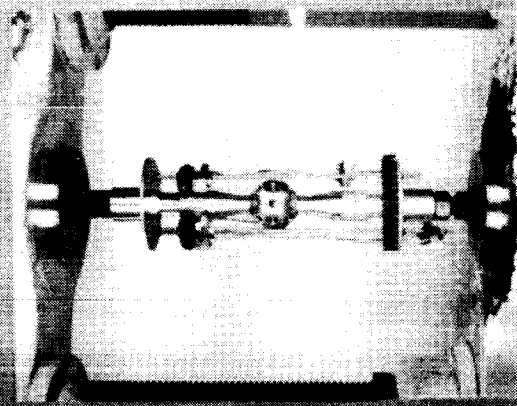
Static tests on joint components

Full and quarter scale erectable truss structures

Dynamic tests on quarter scale hardware

SCALING OF GRAPHITE/EPOXY TUBES

In addition to fabricating subscale joint components, recent efforts have focused on studying the manufacturability and scalability of graphite/epoxy (gr/ep) tubes currently proposed for Space Station truss members. The photo shows a series of gr/ep tubes fabricated at full (2 in. O.D., .060 in. wall), 1/2, 1/3, and 1/4 scales such that the aspect ratio of each tube remains constant. The tubes will undergo a series of static and dynamic tests to examine the degree of replication provided by the manufacturing process at each scale.

SCALING OF GRAPHITE/EPOXY TUBES

Full Scale

1/2 Scale

1/3 Scale

1/4 Scale

NASA
L-86-5757
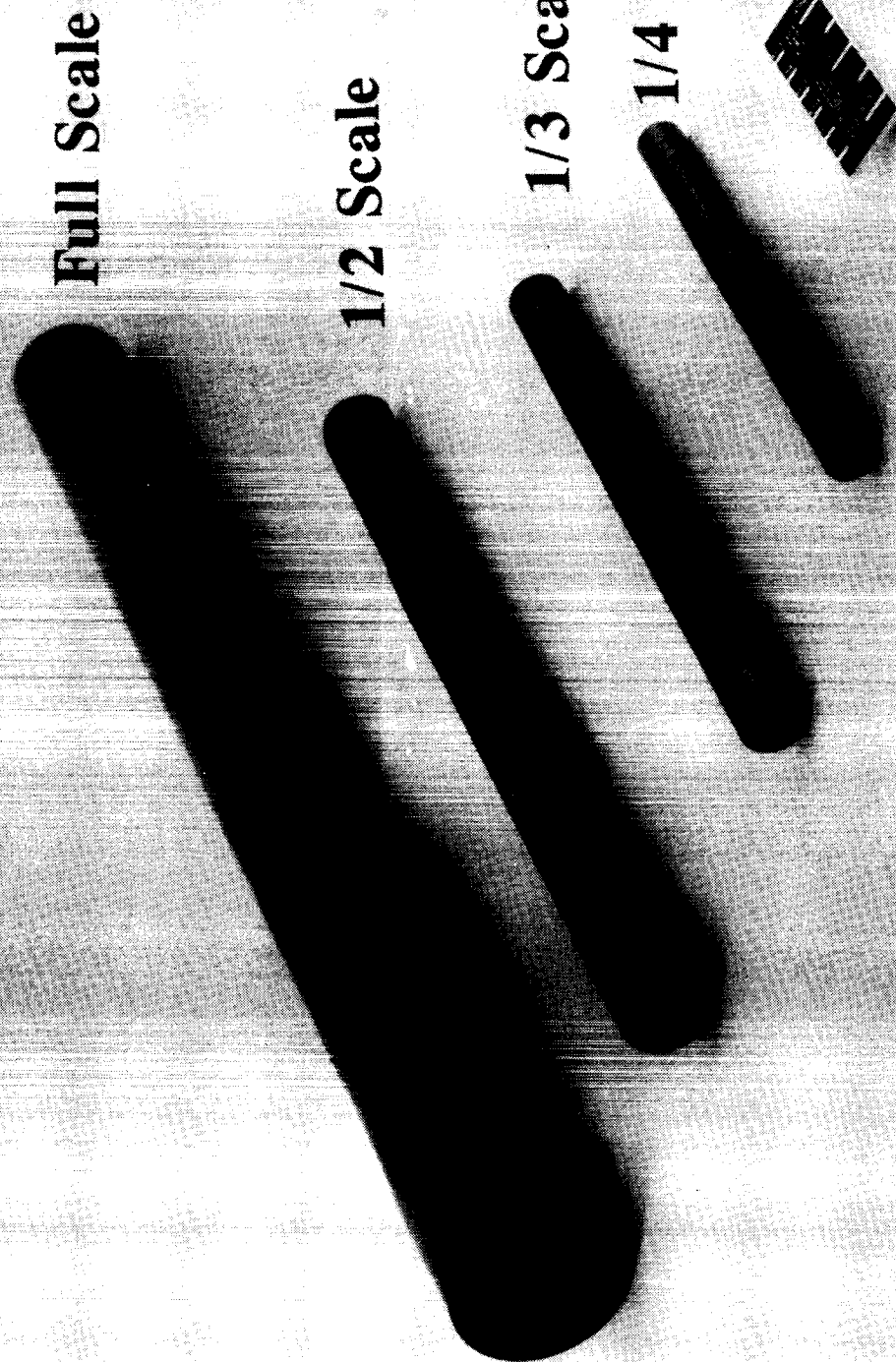
A summary of LaRC's plans for the development of a Space Station scale model has been presented. The purpose of this program is to develop technology for better predicting the structural dynamics and control of large multi-bodied spacecraft. The focus, Space Station, provides an opportunity for comparing the ground test/analysis results with full-scale orbital data which will be obtained for other purposes in the Space Station development effort. Several issues which affect the scale factor determination were discussed along with research aimed at each of those issues.

CONCLUDING REMARKS

- Focus problem addresses COFS goals with opportunity to support Space Station, IOC and beyond.

- Scale model viable method to achieve validated full–scale analysis.

- Scale factor determination a trade–off between fabrication and facility/suspension limitations.

- Greatest fabrication challenges in areas of structural joints and tubular members.

- Preliminary studies indicate suspension system/model interactions can be analytically extracted.

VERIFICATION OF LARGE BEAM-TYPE SPACE STRUCTURES

Choon-Foo Shih, Jay C. Chen, and John A.Garba

Applied Technologies Section
Jet Propulsion Laboratory
California Institute of Technology
Pasadena, California

Abstract

This paper describes the verification approach of large beam type space structures. The proposed verification approach consists of two parts. The first part is to remove the gravity effect on the tested substructure and to identify the on-orbit dynamic characteristics of the substructure by using the measurements of the ground test. A scaling law is also established to define the critical length of the structure which can be tested in 1-g field without incurring a buckling problem. The second part is to develop an adequate scaling law to extrapolate the dynamic characteristics of the prototype structure by using results from the substructure. The verification approaches are demonstrated on two typical structural configurations, the feed support structure of a wrap-rip antenna and a candidate Shuttle flight experiment. The results indicate that it is practical to verify the on-orbit dynamic characteristics of these structures by using the proposed approach.

Introduction

Structures to be used for future space application will be very large in size, such as space station or large deployable antenna systems [1]. These space structures may have dimensions on the order of 30 to 200M. The major technical problem which must be overcome before large flexible structures can be utilized for future missions is to develop confidence in predicting their on orbit dynamic characteristics. Current test methods are inadequate for such structures because of their service configurations and the effect of ground test environments. Methods must be developed to accurately predict on-orbit dynamic characteristics of large very flexible structures by utilizing ground test data obtained from either multiple supports, scale model testing, or substructure testing. A possible approach to this problem is addressed in this paper.

Since many large flexible space structures can be modeled as beams [2], the generic structural element chosen for this investigation is a large space beam. The results obtained from

analyzing a large space beam are applied to large multi-dimensional beam type space structures, such as a typical feed support structure for a wrap-rib antenna [3] and the MAST, a deployable beam shuttle flight experiment which is being planned by NASA as part of the Control of Flexible Structure (COFS) program [4]. The approach of this work is to perform a series of analytical investigations to examine the applicability of scale model ground testing for the determination of structural dynamic characteristics and to examine the applicability of testing a full scale substructure in a 1-g environment. These analyses establish dimensionless parameters for verifying structural characteristics of large beam type space structures and establish the limitations of these test methods for structural verification.

The verification approach presented in this paper consists of two parts. The first part is to investigate the gravity effect on the dynamic characteristics of a large space beam. A closed form solution for the dynamic response of a large space beam subjected to its own weight has been derived previously [5]. The results provide a better understanding of structural characteristics of a large space beam under gravity. In addition, the relationships for the natural frequencies in a 1-g field and a 0-g field are formulated. This allows the identification of the on-orbit dynamic characteristics of large beam type structures by utilizing the ground test data of such structures.

The second part of the verification approach is to develop scaling laws. A scaling law for the critical buckling length of large laced columns is established. This allows the selection of an adequate length of the structures for ground test. Another scaling law for the bay number of the structure with replicable bays is also developed. The results can be applied to extrapolate the dynamic characteristics of a large prototype structure by using the testing data of a substructure. In order to obtain more representative results, the shear effect is accounted for in developing this scaling law. Alternate approaches, such as suspending the system vertically, is also discussed in this work. Finally,

the approaches developed in this work are demonstrated on both a typical feed support structure of a wrap-rib antenna and the MAST configuration. Numerical results from the NASTRAN code as well as the closed form solution are presented.

Gravity Effect

The free vibration of a large space beam with simply supported ends subjected to its own weight (Figure 1) has been investigated in Reference 5. The results established the relationship of the natural frequencies in the 1-g field to those in a 0-g field. They are expressed by

$$\frac{\omega_{gm}}{\omega_{om}} = \left[1 + \frac{NL^2}{m^4\pi^2 EI} + \frac{AW_i^2}{2I} \right]^{1/2} ;$$

for $i = m = 1, 3, 5, \dots$ (1.a)

$$\frac{\omega_{gm}}{\omega_{om}} = \left[1 + \frac{NL^2}{m^4\pi^2 EI} \right]^{1/2} ;$$

for $m = 2, 4, 6, \dots$ (1.b)

where ω_{gm} is the natural frequency of the mth mode due to gravity effect, ω_{om} is the natural frequency of the mth mode in the 0-g environment, N is the axial stretching force, L is the beam length, E is the Young's Modulus, I is the cross sectional moment of inertial, A is the cross sectional area and W_i is the series coefficient determined form the static deformation, W(x), due to its own weight

$$W(x) = \sum_{i=1,3,5,\dots} W_i \sin \frac{i\pi x}{L} \qquad (2)$$

Equation (1) indicates that the natural frequencies of the symmetric modes (m=1,3,5...) depend on not only the axial stretching force but also the static deformation due to its own weight. However, the natural frequencies of the asymmetric modes (m=2,4,6...) are not affected by the static deformation. It should be pointed out that the results shown in Equation (1) are based on the linearized approach of the governing equation. The vibration amplitude is assumed to be relatively small compared to the static deformation due to its own weight in a 1-g field. For a large vibration amplitude, the nonlinear behavior of free vibration can be obtained from Reference 5. The present paper will consider only small amplitude vibration.

The dynamic characteristics of a vertically hanging beam (Figure 2) subjected to gravity effect can be derived by using the energy method. The normalized frequency equation can be expressed by

$$\frac{\omega_{gm}}{\omega_{om}} = \left[1 + \frac{MgL^3}{2\pi^2 m^2 EI} \right]^{1/2} \text{ for all m} \quad (3)$$

where M is the mass per unit length. It should be pointed out that for the laced columns the mass M in Equation (3) is the total mass of the structure divided by the total length of the structure.

Limitations of Ground Tests

The results discussed above allow the verification of structural characteristics of large beam type structures in space by utilizing the ground test data of such structures. However, one of the limitations of the ground test for a very large flexible structure is the buckling of the structure due to its own weight. This kind of buckling problem will restrict the length of the structure tested in a 1-g environment. In order to define the critical buckling length of the structure in 1-g field, a scaling law must be established.

Generally, the results of buckling analyses provide the eigenvalues and their corresponding buckling modes. The eigenvalue is the factor by which the pre-buckling stresses are multiplied to produce buckling. Since the loading environment is designated as 1-g, the relationship between the structure length and the critical gravity multiplier (eigenvalue) must be established in order to define the critical buckling length of the structure in the designated 1-g field.

A typical buckling mode of a 20-bay structure subjected to a field 7.2 times earth gravity is shown in Figure 3. The geometric dimensions and material properties of this structure are obtained from Reference 3 and are also shown in Figure 4. The buckling mode shown in Figure 3 is a local type buckling mode of the top longerons. This occurs because the compressive stresses in the top longerons exceed the critical buckling stresses. Numerical results based on NASTRAN results, shown in Table 1, indicate that the critical buckling stress of the longeron (N_{cr}) is not significantly affected by the structural length. Based on the assumption that the critical buckling stress of the longerons remains constant, it can be derived that the critical gravity multiplier is inversely proportional to

the square of the bay number if each bay of the structure is replicable. This can be expressed by

$$\lambda = \left(\frac{n_{cr}}{n}\right)^2 \qquad (4)$$

where λ is the critical gravity multiplier of a n-bay structure and n_{cr} is the critical buckling bay number of the structure in a 1-g field. Table 2 shows the critical gravity multiplier, based on NASTRAN results, as a function of the bay number. Applying the Equation (4), the critical bay number of this structure can be predicted. These are also listed in Table 2. Satisfactory results are observed. In addition, it is noted that the lowest buckling mode of a 2-D 20-bay structure is a global lateral buckling (Figure 5). Table 3 indicates that Equation (4) is valid for this kind of lateral buckling mode also.

Scaling Law

Since the buckling problem limits the length of the structure tested on the ground and each bay of the structure is replicable, a proper approach to successfully conduct a ground test is to test the structure with a number of bays less than the critical number of bays. Therefore, a scaling law must be established in order to extrapolate nature frequencies of the full size structure by using results from substructure testing.

It is known that the natural frequency of a uniform beam is inversely proportional to the square of the beam length. This is based on the assumption that the shear effect is negligible. However, Reference 6 indicates that the effect of shear on the deflection is much greater for a laced column than for a solid beam. Hence, this kind of shear effect must be considered in large beam type space structures, such as the typical feed support structure of a large antenna or the MAST.

It is noted that the effect of the shearing force reduces the critical buckling load of a laced column. This must be considered as the stiffness of the structure is decreased due to the action of shearing forces. In order to account for this effect in the vibration problem, the stiffness term in the frequency equation should be modified. This modified stiffness can be approximated from the buckling strength of a laced column. Following a similar approach as that used in Reference 7, the modified stiffness (EI_e) of a triangular laced column as shown in Figure 4 can be expressed by

$$EI_e = \frac{EI}{1 + \frac{c}{n^2}} \qquad (5.1)$$

where EI is the bending stiffness of the laced column which can be approximately expressed by $EA_\ell b^2/2$, the c/n^2 is the correction term due to the shear effect, the constant c depends upon the structural geometry and the vibration modes. For a triangular laced column, the constant c for the bending modes can be expressed by

$$c = \frac{2m^2\pi^2 EI}{3\ell^3 b^2}\left(\frac{d^3}{EA_d} + \frac{b^3}{EA_b}\right) \qquad (5.2a)$$

where ℓ is the length of the longerons, d is the length of the diagonals, b is the length of the battens, EA_d and EA_b are the axial stiffnesses of the diagonals and the battens, respectively. Equation (5.2a) can be rewritten as

$$c = \frac{\pi^2 m^2 A_\ell}{3\ell^3}\left(\frac{d^3}{A_d} + \frac{b^3}{A_b}\right) \qquad (5.2b)$$

Substituting the modified stiffness into the frequency equation of a beam subjected to lateral vibration, the scaling law can be expressed as

$$\frac{\omega_P}{\omega_{sb}} = \frac{n_{sb}^2}{n_P^2}\left(\frac{1 + \frac{c}{n_{sb}^2}}{1 + \frac{c}{n_P^2}}\right)^{1/2} \qquad (6)$$

where ω_P is the natural frequency of the full size structure, ω_{sb} is the natural frequency of the substructure, n_P is the bay number of the full size structure and n_{sb} is the bay number of the substructure. It should be noted that the first part of the righthand side of Equation (6) accounts for pure bending and the second part accounts for the shear effect.

The scaling law of Equation (6) is verified by using a 2-dimensional feed support structure. The geometric dimensions and material properties of this structure are the same as those shown in Figure 4. The constant c in Equation (6) for a 2-D laced column can be obtained directly from Reference 6. Both 20-bay and 40-bay laced columns are used to predict the natural frequencies of a 60-bay structure. Note that the structure will exhibit lateral buckling if the bay number exceeds 47, as shown in Table 3. The natural frequencies of these structures are calculated by using NASTRAN and are also listed in Table 4. The comparison between the predicted natural

249

frequencies of a 60-bay structure and those from NASTRAN results are also shown in Table 4. The results indicate that the effect of shear plays a significant role on extrapolating the natural frequencies of a longer laced column. It also shows that the scaling law based on Equation (6) provides satisfactory results.

Verification Process

The results discussed above can be applied to verify the on-orbit dynamic characteristics of large beam type space structures. The verification process can be summarized in the following steps:

1. Implementation of the buckling analysis for the structure subjected to its own weight provides the critical gravity multiplier (eigenvalue) and its corresponding buckling mode.

2. Application of the scaling law for the critical buckling length, as shown in Equation (4), determines the critical buckling bay number of the structure in a 1-g field.

3. Selection of a structure with bay number less than the critical bay number for ground test to provide substructure testing measurements in 1-g environment, such as the static deformation, axial stresses and natural frequencies.

4. Application of the frequency equation, as shown in Equation (1) or (3), removes the gravity effect and determines the natural frequencies of the selected substructure in a 0-g field.

5. Application of the scaling law for bay number, as shown in Equation (6), verifies the on-orbit natural frequencies of the prototype structure.

Applications

Two large beam type space structures are examined. The first one is a typical feed support structure of a wrap-rib antenna, shown in Figure 4. The results from the buckling analysis associated with the scaling law indicate that the structure will buckle due to its own weight if the bay number of this structure exceeds 54. In order to prevent the buckling problem, a 40-bay structure is proposed for the ground test. Since no real ground testing is anticipated in the example problem, the measurements of this 40-bay structure are assumed to be those obtained from NASTRAN results as listed in Table 5. Following Steps 4 and 5 as discussed in the verification process, the on-orbit natural frequencies of a

longer structure (such as 60-bay) can be determined and these are listed in Table 6 together with the direct NASTRAN results for comparison. A good agreement is observed.

The second space structure examined in this work is based on the MAST configuration which is being considered by NASA for a future flight experiment [4]. The material properties and geometric dimensions of the MAST are listed in Table 7. The full length of the prototype MAST is approximately 60 meters (54 bays). However, a 10-bay MAST is proposed for the ground test because of the buckling limitation of the structure subjected to the gravitational environment. The ground test data of this 10-bay MAST, based on NASTRAN results, are also shown in Table 5. Following the verification process as discussed previously, the natural frequencies of this 54-bay MAST can be predicted and the results are also shown in Table 6. The higher discrepancy shown in this case is believed to be due to the smaller number of bays used in the ground test. The scaling factor due to shear effect is more accurate for a laced column with a large number of panels. For instance, if a 20-bay MAST could be tested in the 1-g field, better results could be achieved.

An alternate approach of verifying on-orbit dynamic characteristics of this MAST configuration is to test MAST substructure suspended vertically. The restriction of the MAST length, due to buckling caused by its own weight, is no longer a major concern in the vertical suspension test. A 20-bay MAST is chosen for the vertical suspension approach. Results, as shown in Table 8, indicate that the gravity effect on the natural frequencies of a 20-bay MAST hanging vertically is insignificant. The predicted natural frequencies of the prototype MAST, based on a vertical suspended approach, are shown in Table 9. Better results are observed in this case.

Conclusions

An approach for the verification of a beam type space structure has been described. The effect of gravity on the dynamic characteristics of both horizontally and vertically supported beams has been studied and the results are applied to identify the on-orbit dynamic characteristics of the structure tested on the ground. The natural frequencies of the full size structure are extrapolated from those of the substructure by using scaling laws. The results indicate that, in order to accurately predict the natural frequencies of a laced column, the shear effect should be considered in this scaling law. NASTRAN analyses are

implemented to verify the results based on the proposed verification approaches. Satisfactory results are observed in verifying the on-orbit natural frequencies of both the typical feed support structure of a wrap-rib antenna and the MAST configuration.

References

1. NASA Conference Publication, "Large Space System Technology - 1981", Part 1 and Part 2, NASA CP-2215, November 1981.

2. Renton, J. D., "The Beam-Like Behavior of Space Trusses", AIAA Journal, Vol. 22, No. 2, February 1984, pp. 273-280.

3. Lockheed Missiles and Space Company, Inc., "Interim Report for Study of Wrap-Rib Antenna Design", LMSC-D714653, July 1981.

4. NASA Langley Research Center, "COFS, Control of Flexible Structures Workshop", August 27-28, 1985.

5. Shih, C. F., Chen, J. C., and Garba, J. A., "Vibration of a Large Space Beam Under Gravity Effect", to be published in the June 1986 issue of the AIAA Journal.

6. Timoshenko, S. P. and Gere, J. M., "Theory of Elastic Stability", McGraw-Hill, Inc., 2nd Edition, 1961, pp. 132-142.

7. Bleich, F., "Buckling Strength of Metal Structures", Mc-Graw Hill Inc., 1952, pp. 169-175.

Acknowledgement

Table 1 Critical Buckling Stress of Longeron vs. Bay Number

Bay No.	20	40	60	80	100
N_{cr}(ksi)	1.44	1.41	1.40	1.39	1.39

Table 2 Predicted Critical Bay Number of the Feed Support Structure with Different Bay Number

Bay No.	20	40	53	60	80
λ	7.20	1.75	0.992	0.772	0.432
n_{cr}	54	53	53	53	53

Table 3 Critical Buckling Bay Number of a 2-D Feed Support Structure

Bay No.	10	20	40
λ	21.70	5.20	1.28
n_{cr}	47	46	46

Table 4 Comparison of Predicted Natural Frequencies for a 60-bay Structure

m	n	ω_m (NASTRAN)(HZ)	ω^b/ω_m^*	ω^s/ω_m^*
1	20	4.10	0.785	1.051
1	40	1.24	0.950	1.007
1	60	0.58		
2	20	10.67	0.577	1.070
2	40	4.00	0.864	1.016
2	60	2.05		
3	20	17.04	0.477	1.065
3	40	7.14	0.800	1.018
3	60	3.97		

ω^b: Predicted natural frequency based on the assumption that the shear effect is negligible.

ω^s: Predicted natural frequency based on the scaling law which includes the shear effect.

ω_m^*: Natural frequency of the mth mode for the 60-bay structure (NASTRAN Results).

Table 5 Measurements Based on NASTRAN Results

Measurements	Feed Support Structure (40-bay)	MAST (10-bay)
Max. Deformation (in.)	14.64	0.0406
Max. Compressive Stress(PSI)	8054	344
Max. Tensile Stress (PSI)	4043	192
Natural Frequencies in 1-g field (Hz):		
m = 1	0.953	17.23
m = 2	3.086	47.91

Table 6 Comparison of Natural Frequency of Large Beam Type Space Structures

Structure	Mode No.	ω_p(Hz)	ω_e(Hz)
Feed Support Structure (60-bay)	1	0.418	0.415
	2	1.554	1.523
Mast (54-bay)	1	0.767	0.715
	2	3.097	2.749

ω_p: Predicted natural frequencies from verification approach.

ω_e: NASTRAN results

251

Table 7   Geometric Dimensions and Material
Properties of the MAST

Overall Geometry

Total Length (L)	2380.86 in
Length of Each Bay (ℓ)	44.09 in.
Diameter enclosing the MAST (D)	55.12 in.
Bay Number	54

Cross-Section

Longerons: (3)
Length (ℓ)	44.09 in.
Inside Diameter of all Longerons	0.55 in.
Outside Diameter of Top Longerons	0.812 in.
Outside Diameter of Bottom Longerons	0.763 in.

Diagonals: (3)
Length (d)	64.91 in.
Outside Diameter (Solid)	0.287 in.

Battens: (3)
Length (b)	47.64 in.
Inside Diameter	0.25 in.
Outside Diameter	0.328 in.

Material

Graphite Epoxy
Young's Modulus (E)	9.62×10^6 psi
Poisson's Ratio (ν)	0.3

Mass

Joints	0.787 lb
Specific Weight Density	
Longeron	0.07814 lb/in^3
Diagonal	0.1604 lb/in^3
Batten	0.05954 lb/in^3

Table 8   Comparison of Natural Frequencies of a 20-bay
MAST Structure Hanging Vertically

Mode No.	ω_0(Hz)	ω_E^1(Hz)	ω_E^2 (Hz)
1	4.883	4.888	4.887
2	16.524	16.531	16.528

ω_0: Natural frequencies in 0-g field (NASTRAN)
ω_E^1: Natural frequencies in 1-g field (NASTRAN)
ω_E^2: Natural frequencies in 1-g field (Equ. (3))

Table 9   Comparison of Natural Frequencies
of the Prototype MAST

Mode No.	ω_p(Hz)	ω_e(Hz)	ω_p/ω_e
1	0.719	0.715	1.005
2	2.841	2.749	1.033

ω_p: Predicted natural frequencies from verification approach
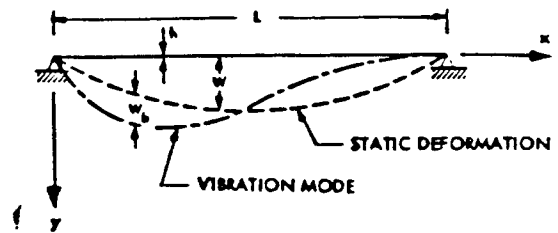ω_e: NASTRAN results
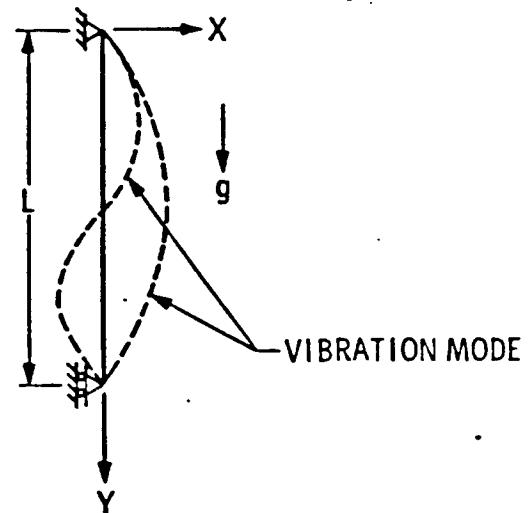

Figure 1   Simply-Supported Beam
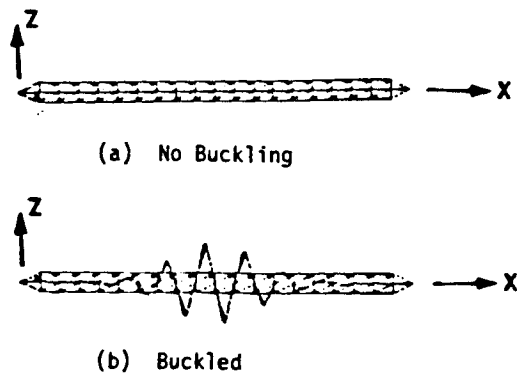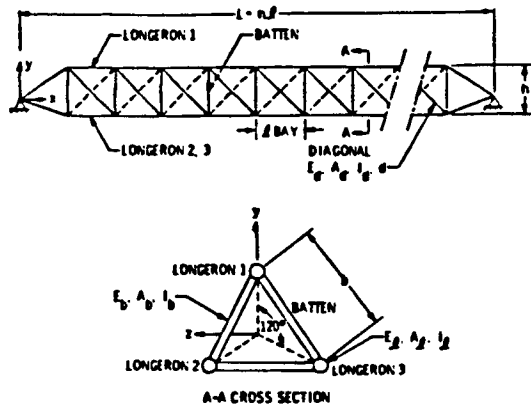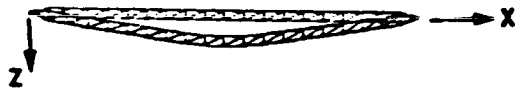

Figure 2   Vertically Hanging System

(a)   No Buckling

(b)   Buckled

Figure 3   Buckling Mode of a 20-bay
Feed Support Structure (Top
View)

252

Figure 4 Geometric Dimensions and Material
           Properties of the Feed Support
           Structure

Side View (45° w.r.t. y-axis and z-axis)

Figure 5 Lateral Buckling Mode of a
           2-D Feed Support Structure

253

VERIFICATION OF FLEXIBLE STRUCTURES BY GROUND TEST

BEN K. WADA

C. P. KUO

Jet Propulsion Laboratory
California Institute of Technology

Presented at

Workshop on Structural Dynamics and Control
Interaction of Flexible Structures

Sponsor
NASA OAST/MSFC
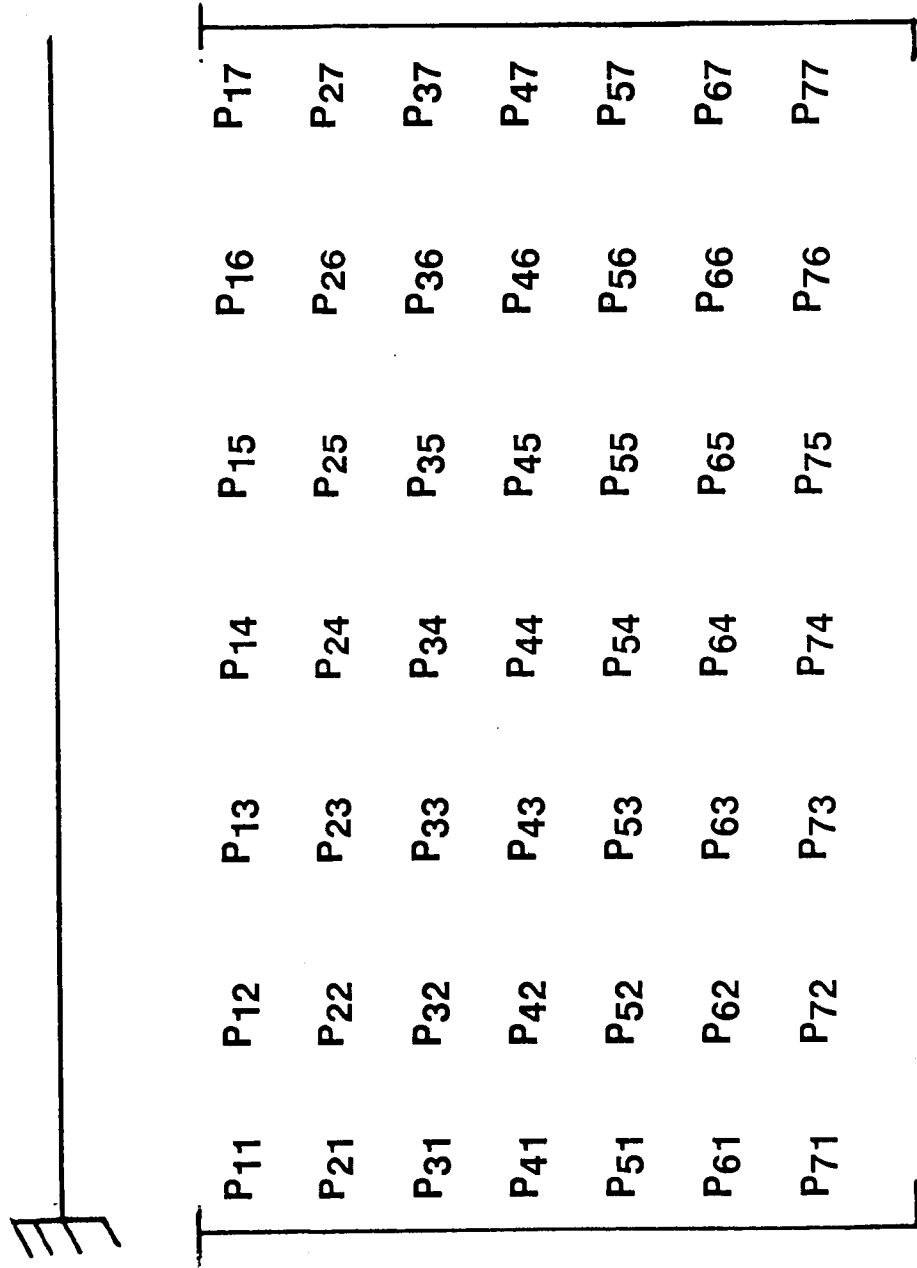April 22-24, 1986
Marshall Space Flight Center, Alabama

JPL

JPL

OBJECTIVE

- Validate Math Models of Large Space Structures by Ground Tests.

- Present Concepts for Two Types
  - Continuous Type
  - Linded Subsystems

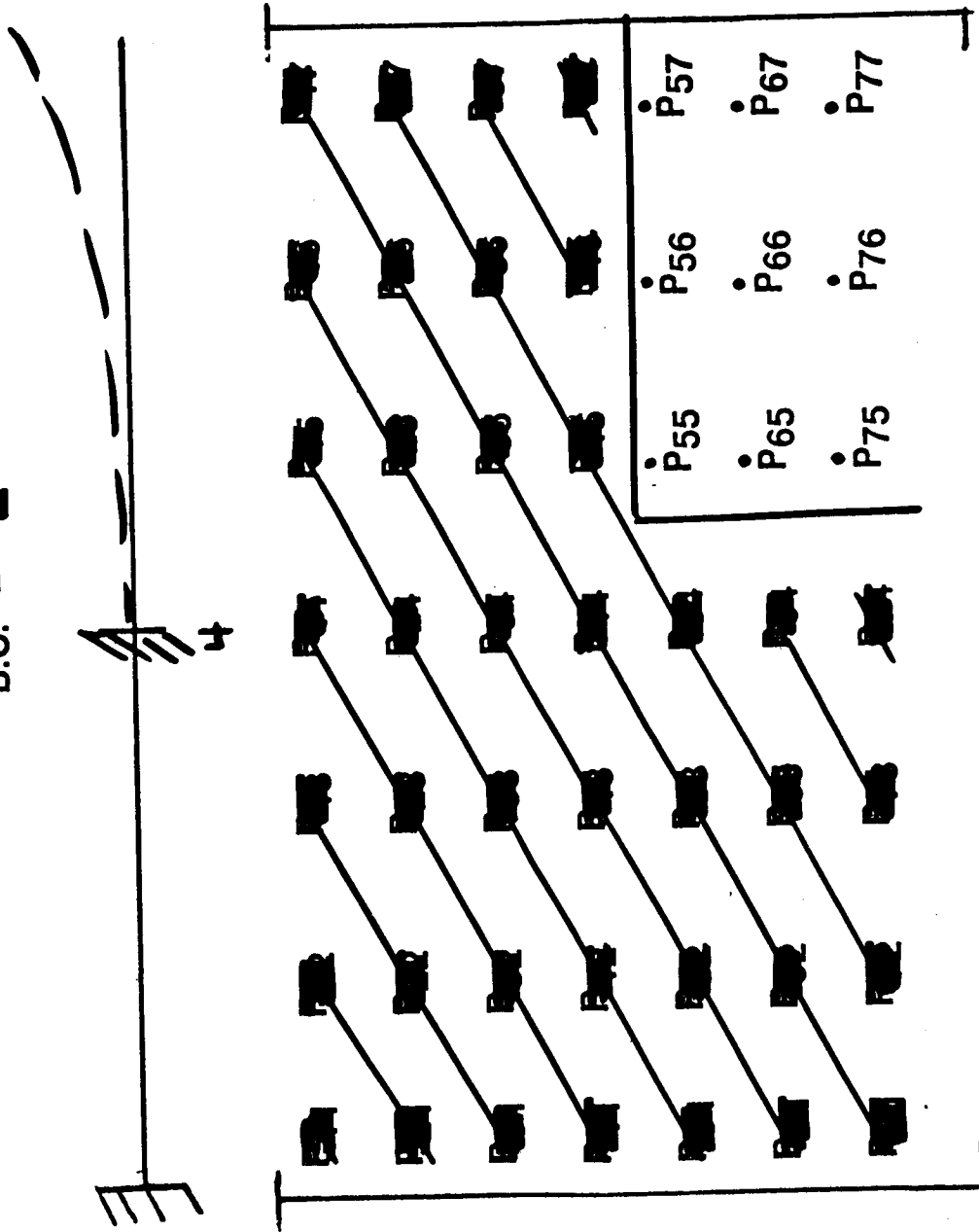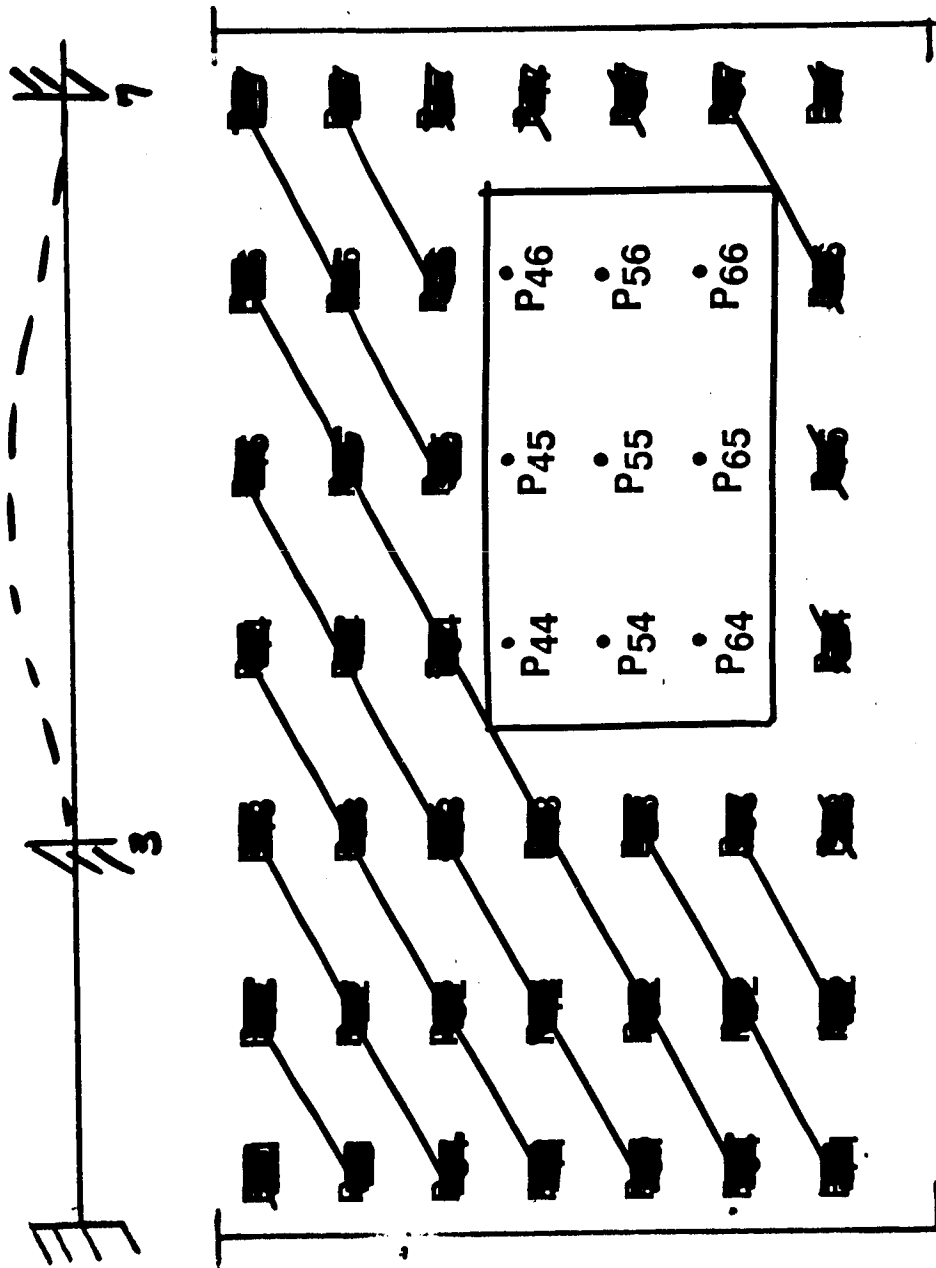CONTINUOUS TYPE STRUCTURE

B.C. = -

JPL

P_{11}	P_{12}	P_{13}	P_{14}	P_{15}	P_{16}	P_{17}
P_{21}	P_{22}	P_{23}	P_{24}	P_{25}	P_{26}	P_{27}
P_{31}	P_{32}	P_{33}	P_{34}	P_{35}	P_{36}	P_{37}
P_{41}	P_{42}	P_{43}	P_{44}	P_{45}	P_{46}	P_{47}
P_{51}	P_{52}	P_{53}	P_{54}	P_{55}	P_{56}	P_{57}
P_{61}	P_{62}	P_{63}	P_{64}	P_{65}	P_{66}	P_{67}
P_{71}	P_{72}	P_{73}	P_{74}	P_{75}	P_{76}	P_{77}

CONTINUOUS TYPE STRUCTURE

B.C. = -1

JPL

258

P55 P56 P57
P65 P66 P67
P75 P76 P77

CONTINUOUS TYPE STRUCTURE

B.C. = -2

JPL

P46   P45   P44
P56   P55   P54
P66   P65   P64

259

CONTINUOUS TYPE STRUCTURE

B.C. = -3

JPL
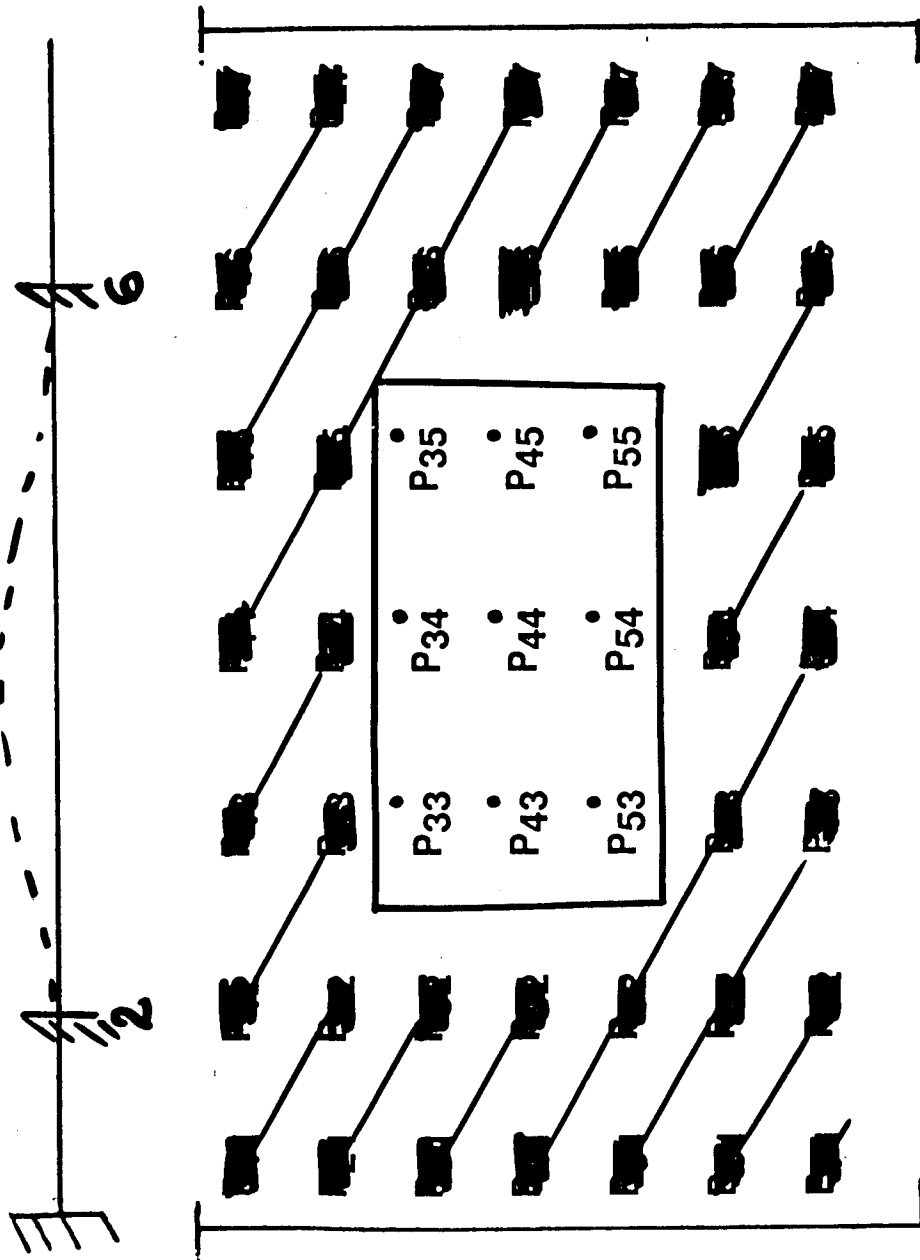
JPL

SIMULATED TEST CONFIGURATION

CURRENT APPROACH

MBCT TEST CONFIGURATIONS

JPL

BC#1
BC#2
BC#3
BC#4
BC#5
BC#6

JPL
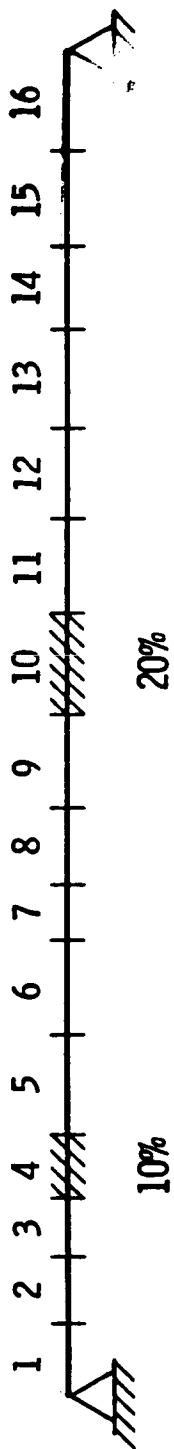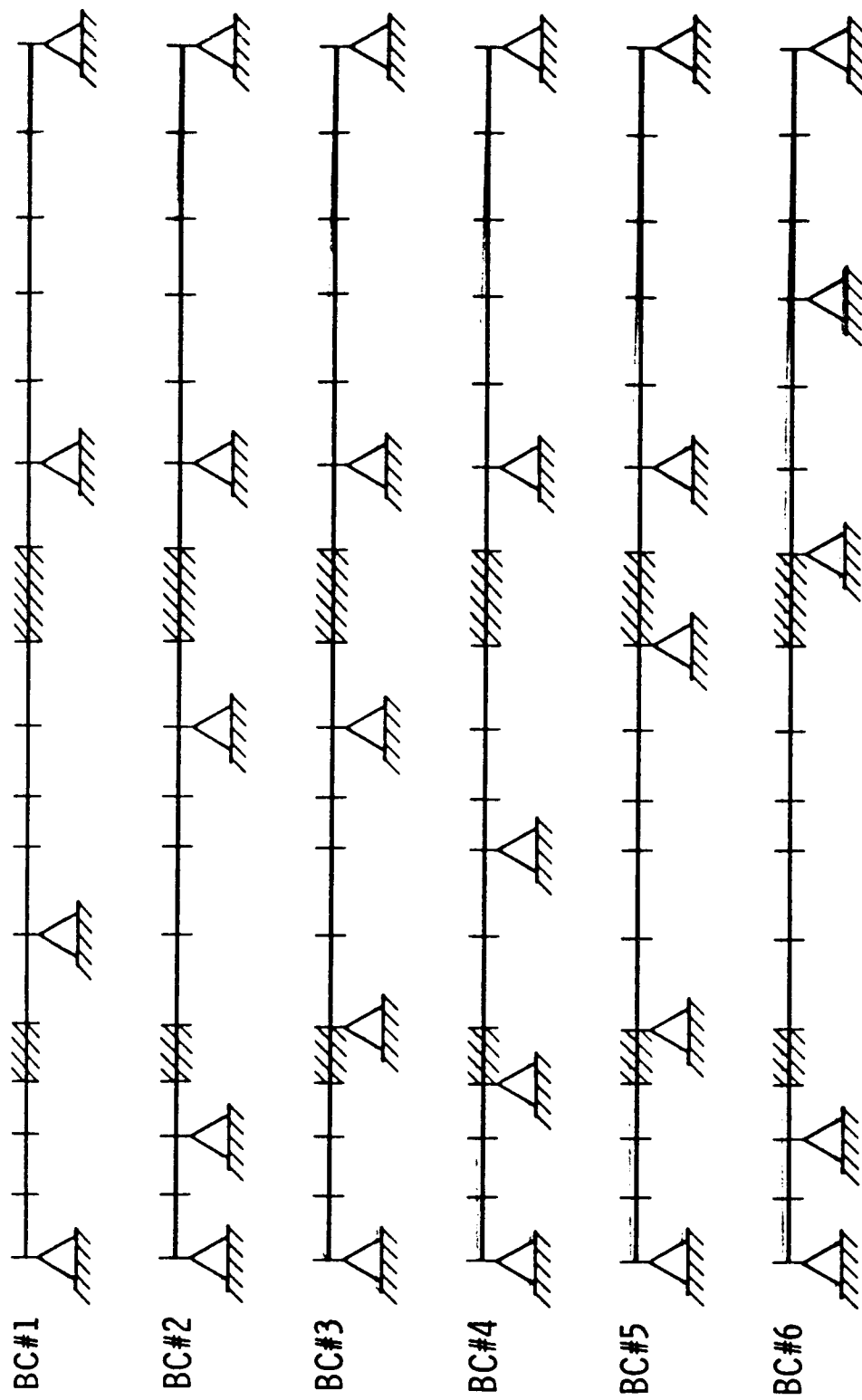
RESULTS OF ESTIMATED PARAMETERS, ITERATIONS 1 AND 2
ΔI_4 AND ΔI_{10} (THEORETICAL VALUES, (ΔI_4 = 0.00834, ΔI_{10} = 0.01667)

CASE	ITERATION 1		ITERATION 2		CONFIGURATION
a ΔI_4	0.005884	70%	0.008121	97.38%	CONVENTIONAL MODAL TEST,
ΔI_{10}	0.015499	93%	0.016722	100.31%	10 FREQUENCIES TOTAL
b ΔI_4	0.007084	85%	0.008330	99.88%	MBCT CONFIGURATION 1-2,
ΔI_{10}	0.015291	92%	0.016640	99.82%	10 FREQUENCIES TOTAL
c ΔI_4	0.007849	94%	0.008339	99.99%	MBCT CONFIGURATION 1-2,
ΔI_{10}	0.014891	89%	0.016636	99.80%	8 FREQUENCIES TOTAL
d ΔI_4	0.007716	93%	0.008338	99.98%	MBCT CONFIGURATION 1-2,
ΔI_{10}	0.014683	88%	0.016630	99.76%	6 FREQUENCIES TOTAL
e ΔI_4	0.007544	91%	0.008336	99.95%	MBCT CONFIGURATION 1-2,
ΔI_{10}	0.014360	86%	0.016625	99.73%	4 FREQUENCIES TOTAL

JPL — THE MOMENT OF INERTIA OF EVERY ELEMENT OF THE SIMPLY SUPPORTED BEAM

ELEMENT NO.	USED IN THEORETICAL MODELLING I	REAL I	DIFF %	IDENTIFIED I BY MBCT METHOD (CONFIGURATIONS x MODES)					
				12 x 3	12 x 2	12 x 6	12 x 10	5 x 4	6 x 3
1	.08333	.08333	0	.08286	.08300	.08389	.08339	.08328	.08302
2	.08333	.08750	5	.08767	.08741	.08729	.08766	.08753	.08757
3	.08333	.09166	10	.09162	.09187	.09149	.09128	.09163	.09167
4	.08333	.08750	5	.08747	.08736	.08743	.08779	.08747	.08744
5	.08333	.08333	0	.08329	.08336	.08342	.08320	.08333	.08330
6	.08333	.07916	-5	.07915	.07910	.07911	.07971	.07916	.07917
7	.08333	.04167	-50	.04168	.04169	.04162	.04149	.04167	.04167
8	.08333	.08750	5	.08747	.08737	.08767	.08731	.08751	.08760
9	.08333	.12500	50	.12505	.12530	.12495	.12595	.12501	.12483
10	.08333	.07916	-5	.07910	.07911	.07933	.07900	.07913	.07919
11	.08333	.08750	5	.08755	.08752	.08754	.08696	.08751	.08745
12	.08333	.07916	-5	.07910	.07912	.07840	.08084	.07917	.07916
13	.08333	.08750	5	.08719	.08738	.08831.	.08069	.08753	.08761
14	.08333	.15000	80	.14861	.14973	.15237	.16862	.15009	.15006
15	.08333	.07916	-5	.08132	.08058	.08058	.08225	.07900	.07799
16	.08333	.08333	0	.07608	.07626	.07909	.07331	.08369	.08969

LINKED SUBSYSTEMS
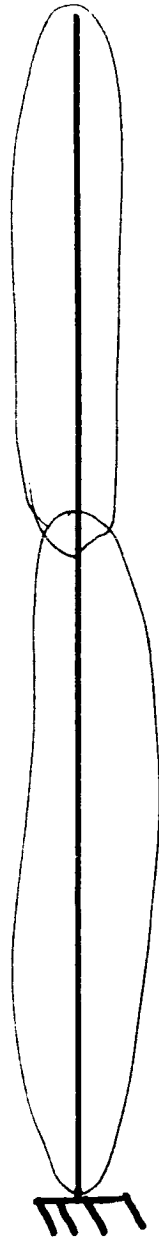
$$
\begin{matrix}
P_{11} & P_{12} & P_{13} & P_{14} & P_{15} & P_{16} & P_{17} \\
P_{21} & P_{22} & P_{23} & P_{24} & P_{25} & P_{26} & P_{27} \\
P_{31} & P_{32} & P_{33} & P_{34} & P_{35} & P_{36} & P_{37} \\
P_{41} & P_{42} & P_{43} & P_{44} & P_{45} & P_{46} & P_{47} \\
P_{51} & P_{52} & P_{53} & P_{54} & P_{55} & P_{56} & P_{57} \\
P_{61} & P_{62} & P_{63} & P_{64} & P_{65} & P_{66} & P_{67} \\
P_{71} & P_{72} & P_{73} & P_{74} & P_{75} & P_{76} & P_{77}
\end{matrix}
$$

265

JPL

MODAL SYNTHESIS

$$\{u\}^i = q_R^i\{\phi\}_R^i + q_C^i\{\phi\}_C^i + q_N^i\{\phi\}_N^i + q_A^i\{\phi\}_A^i$$

$$+ q_Q^i\{\phi\}_Q^i + q_I^i\{\phi\}_I^i + q_{RE}^i\{\phi\}_{RE}^i + \cdots + q_u^i\{\phi\}_u^i$$
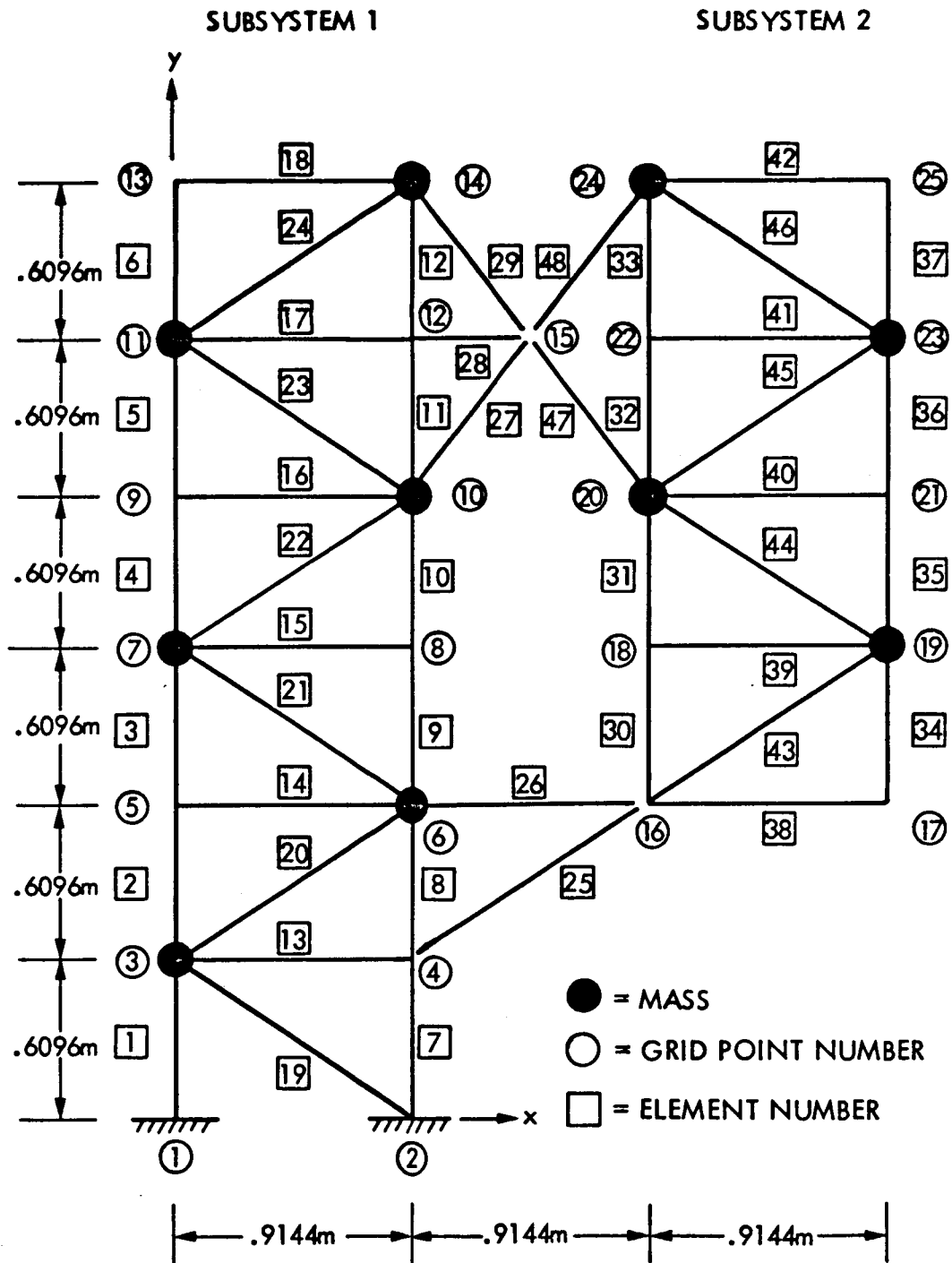
FIGURE 3. SAMPLE PROBLEM TOTAL SYSTEM
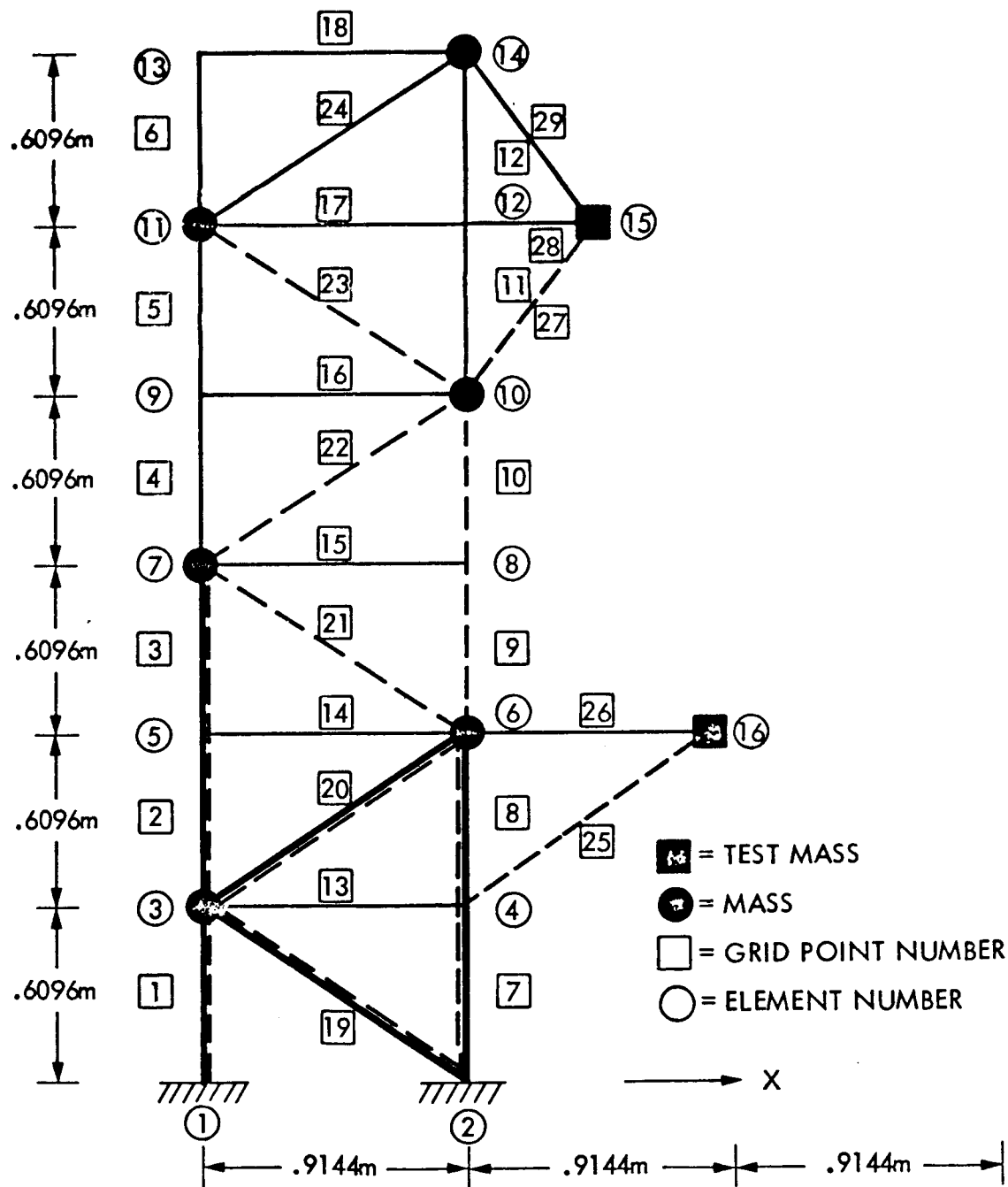
FIGURE 4. SUBSYSTEM 1

LOADS CONDITION

JPL

- MODAL TEST "TEST MASS" AT (15)

- MODAL TEST "TEST MASS" AT (16)

- FORCE AT (15) , X & Y-DIR.

- FORCE AT (16) , X & Y-DIR.

- FORCE AT (10) , X & Y-DIR.

JPL

LOAD CONDITION vs SE IN MEMBERS
>10% SE

MEMBERS / LOAD COND →	1	2	3	4	5
21, 22, 23	X				X
9, 10			X		X
25		X		X	
27			X		

JPL

COMPARISON

MODE NO.	CORRECT (Hz)	ESTIMATED (Hz)
1	4. 044	4. 041
2	15. 209	15. 015
3	27. 054	26. 814
4	30. 077	30. 097
5	35. 832	36. 222

MEMBER 25 & 27 - ERROR BY 100%

JPL

SUMMARY

- Not Rely on Ground Test Which Simulates Space Conditions.

- Integrated - Test/Analysis

- Developing Concepts

- Validate on Laboratory and Flight Experiments.

April 22, 1986   (Concurrent Sessions on Structures and Control)

Control Session 2A - Leonard Meirovitch, Chairman

Optimum Mix of Passive and Active   L. Rogers, W-P AFB
Control for Space Structures

1-CAT: A MIMO Design Methodology   J. R. Mitchell,
                                                 J. C. Lucas,
                                                 Control Dynamics

Inter-Stable Control Systems   G. von Pragenau, MSFC

Status Report and Preliminary Results of   J. P. Williams, LaRC
the Spacecraft Control Laboratory

Control Session 2B - J. L. Junkins, Chairman

Flexible Spacecraft Control Simulation   J. Bossi, Boeing

Improving Stability Margins in   B. T. Oranc and
Discrete-Time LQG Controllers   C. L. Phillips, Auburn

An Overview of Research Conducted by   R. C. Montgomery,
the Spacecraft Control Branch on the   LaRC
NASA LaRC Grid

Space Station Structural/Control   C. R. Larson
Interaction (Payload Pointing and Micro-G)   Rockwell/SD

OPTIMUM MIX OF PASSIVE AND ACTIVE CONTROL OF SPACE STRUCTURES

FOR

WORKSHOP ON STRUCTURAL DYNAMICS AND CONTROL INTERACTION OF FLEXIBLE STRUCTURES

AT
NASA MARSHALL
22 - 24 APR 1986

DR LYNN ROGERS
AFWAL / FIBA
WPAFB OH
(513) 255-5664

DR KEN RICHARDS
MARTIN MARIETTA DENVER AEROSPACE
(303) 977-8745
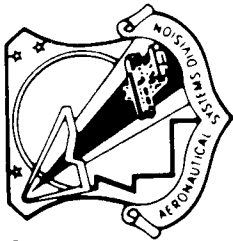
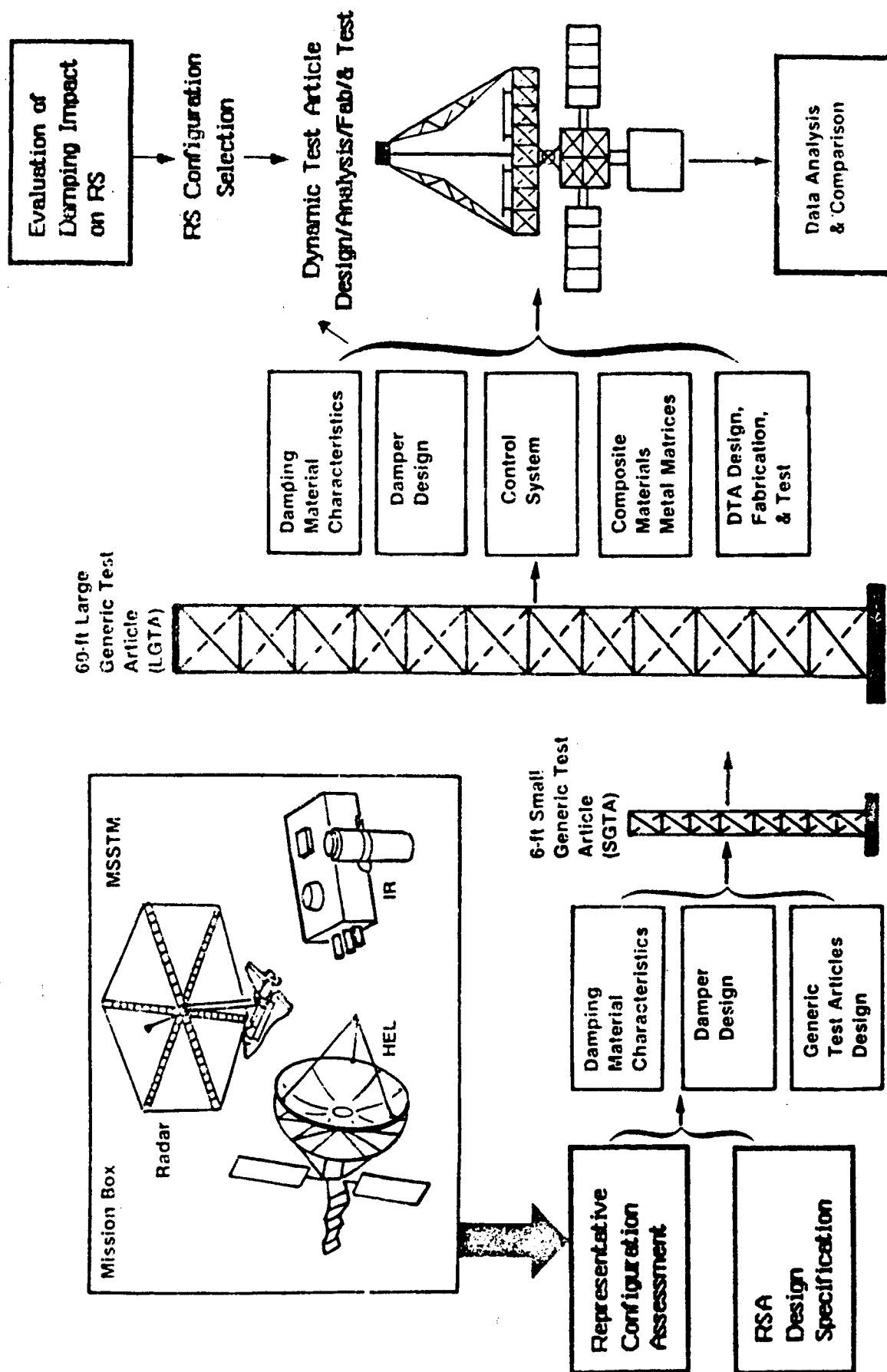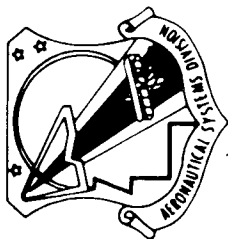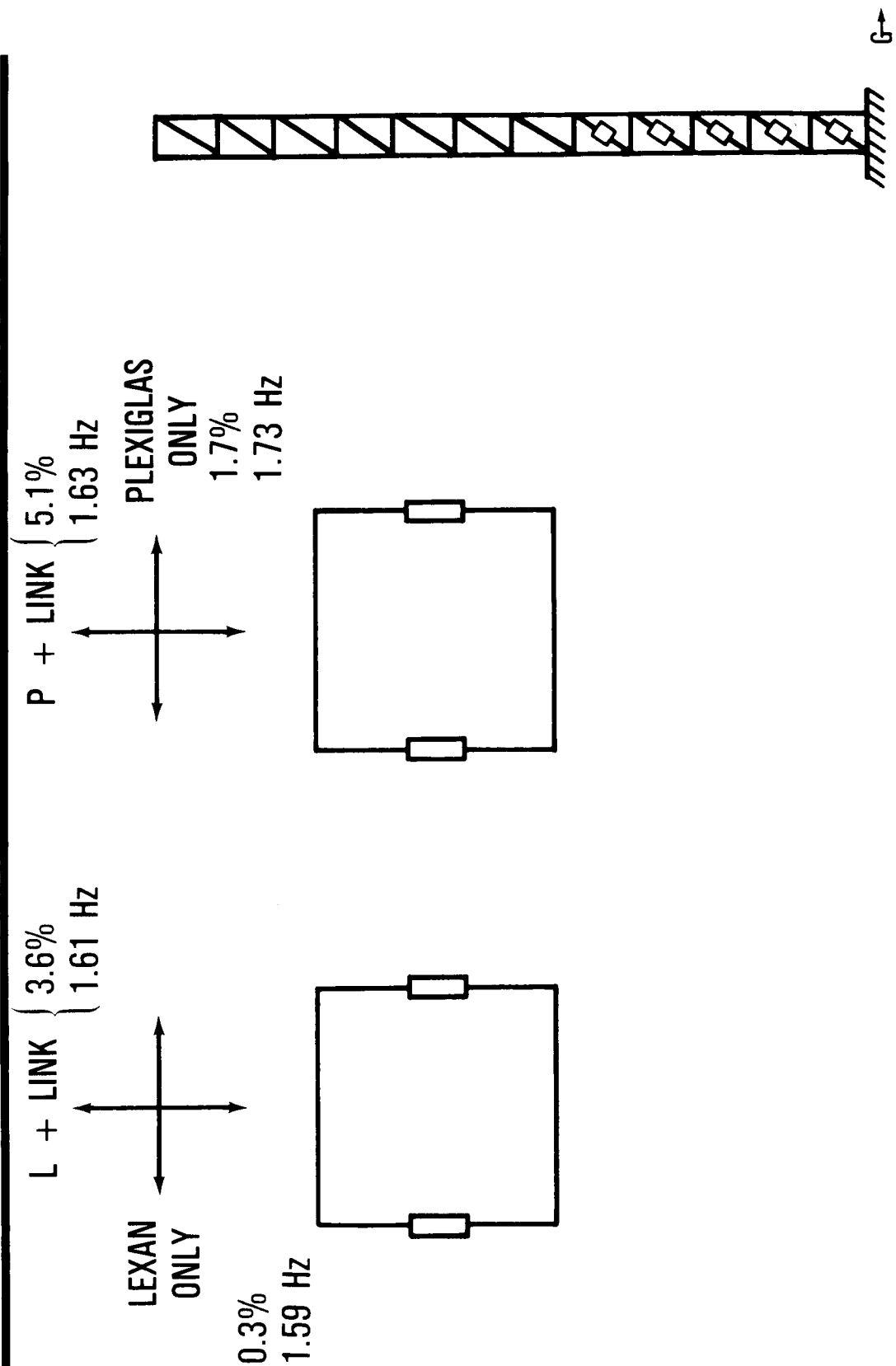# PACOSS-RELSAT FUNDING PROFILE ($K)

	FY83	FY84	FY85	FY86	FY87	FY88	TOT.
PACOSS	390	421	518	1349	640	154	3472
RELSAT-GE	75	325	450	310	30	–	1190
RELSAT-BOEING	74	375	194	433	30	–	1106
							5768

PACOSS – SIMPLIFIED FLOW DIAGRAM

LARGE GENERIC TEST ARTICLE

L + LINK $\left\{ \begin{array}{l} 3.6\% \\ 1.61 \text{ Hz} \end{array} \right.$

LEXAN
ONLY
0.3%
1.59 Hz

P + LINK $\left\{ \begin{array}{l} 5.1\% \\ 1.63 \text{ Hz} \end{array} \right.$

PLEXIGLAS
ONLY
1.7%
1.73 Hz

G

278

PACOSS - DISCRETE DAMPER CONFIGURATION

Plexiglas Tube

Plexiglas Tube

3-M Acrylic Core Foam

$R_1 = 1. \text{ in.}$
$R_2 = 0.75 \text{ in.}$
$W = 1. \text{ in.}$

R_2 R_1

L_2

W

8 in.

L_1

Bonded Joint

PAYOFF OF DAMPING

L-O-S ANGLE

DAMPED

UNDAMPED

JITTER: TIME / RANGE

TIME ON TARGET

FASTER RETARGET

SETTLING TIME

RETARGET TIME

READY

LINE-OF-SIGHT ANGLE
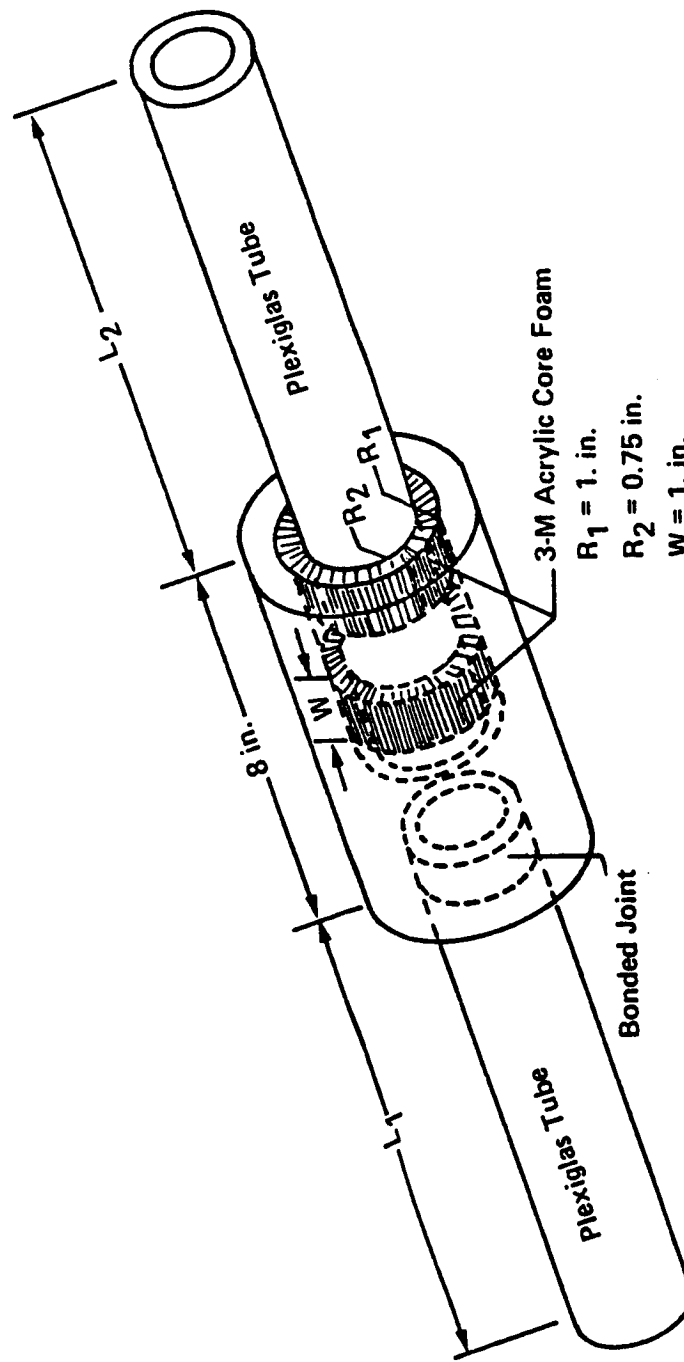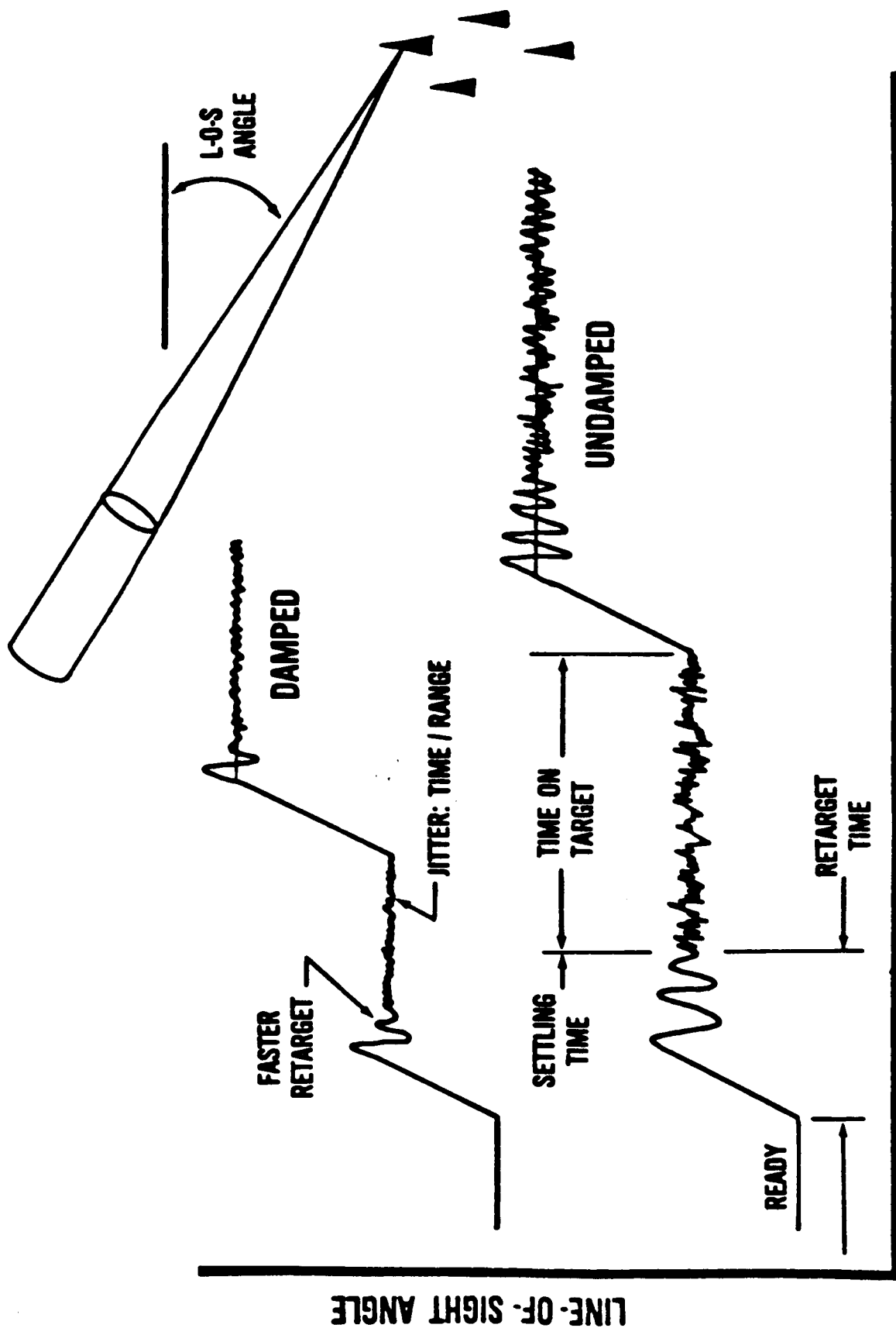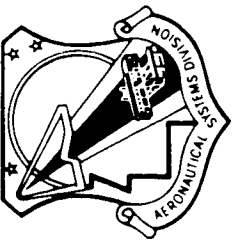
TIME

- THE CHALLENGE: VIBRATION SUPPRESSION (SETTLING TIME AND JITTER) OF A STRUCTURE CHARACTERIZED BY LOW FREQUENCY HIGH GLOBAL MODAL DENSITY
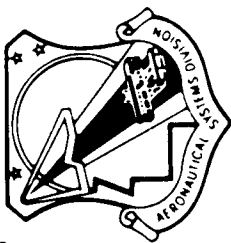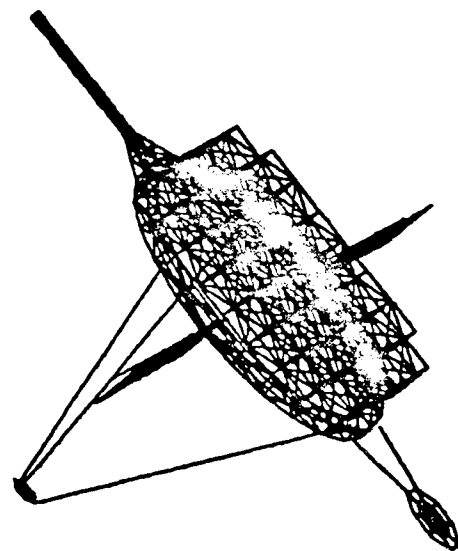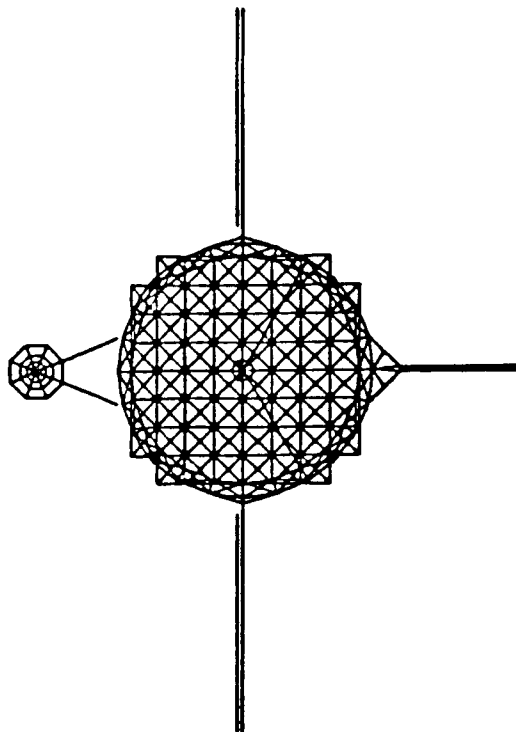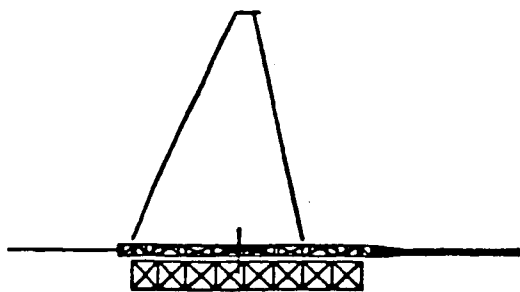
DEFINITION

- FLEXIBLE STRUCTURE: STRUCTURES WHICH HAS NATURAL VIBRATION FREQUENCIES IN THE PASSBAND OF THE CONTROL SYSTEM
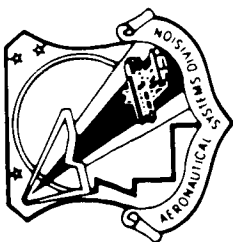
DEFINITION

- PRECISION STRUCTURE: STRUCTURE CARRYING OBJECTS WHICH MUST FLY IN PRECISE FORMATION
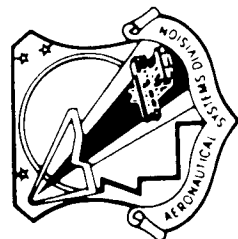
DTA PRELIMINARY FINITE ELEMENT MODEL
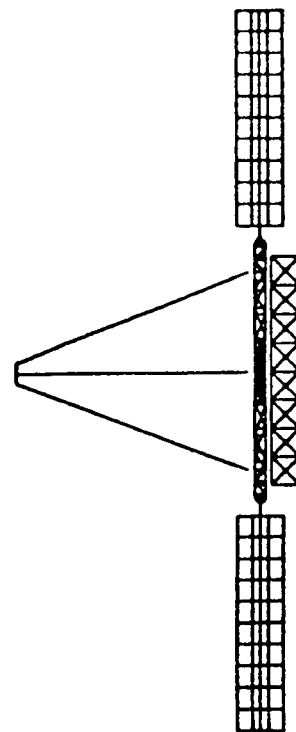
MARTIN MARIETTA

SUMMARY OF FINAL DTA DIMENSIONS

COMPONENT	DIMENSION (M)	MASS (KG)
1) BOX TRUSS	2.59 x 2.59 x 0.324	146
2) RING TRUSS	DIAMETER: 2.9	59.7
3) TRIPOD	DIAMETER AT BASE: 2.59 HEIGHT: 2.59	29.4
4) EQUIPMENT PLATFORM	LENGTH: 1.295	7.00
5) ANTENNA	DIAMETER: 0.648	4.52
6,7) SOLAR ARRAYS	LENGTH: 2.59	12.0

C-4

PACOSS DAMPING CONCEPTS

DAMPING CONCEPT	APPLICATION COMPONENTS
CONSTRAINED LAYER TREATMENT	ANTENNA SUPPORT TUBES TRIPOD LEGS
JOINT DAMPING	BOX TRUSS CORNER JOINTS BOX TRUSS / RING TRUSS INTERFACE
ELONGATIONAL DAMPING ELEMENT	TENSION MEMBERS
EXTENSIONAL SHEAR DAMPER	EQUIPMENT PLATFORMS SUPPORT TRUSS
TUNED MASS DAMPER	SOLAR ARRAYS

Active Control Energy Expenditure

vs.

Passive Damping Augmentation

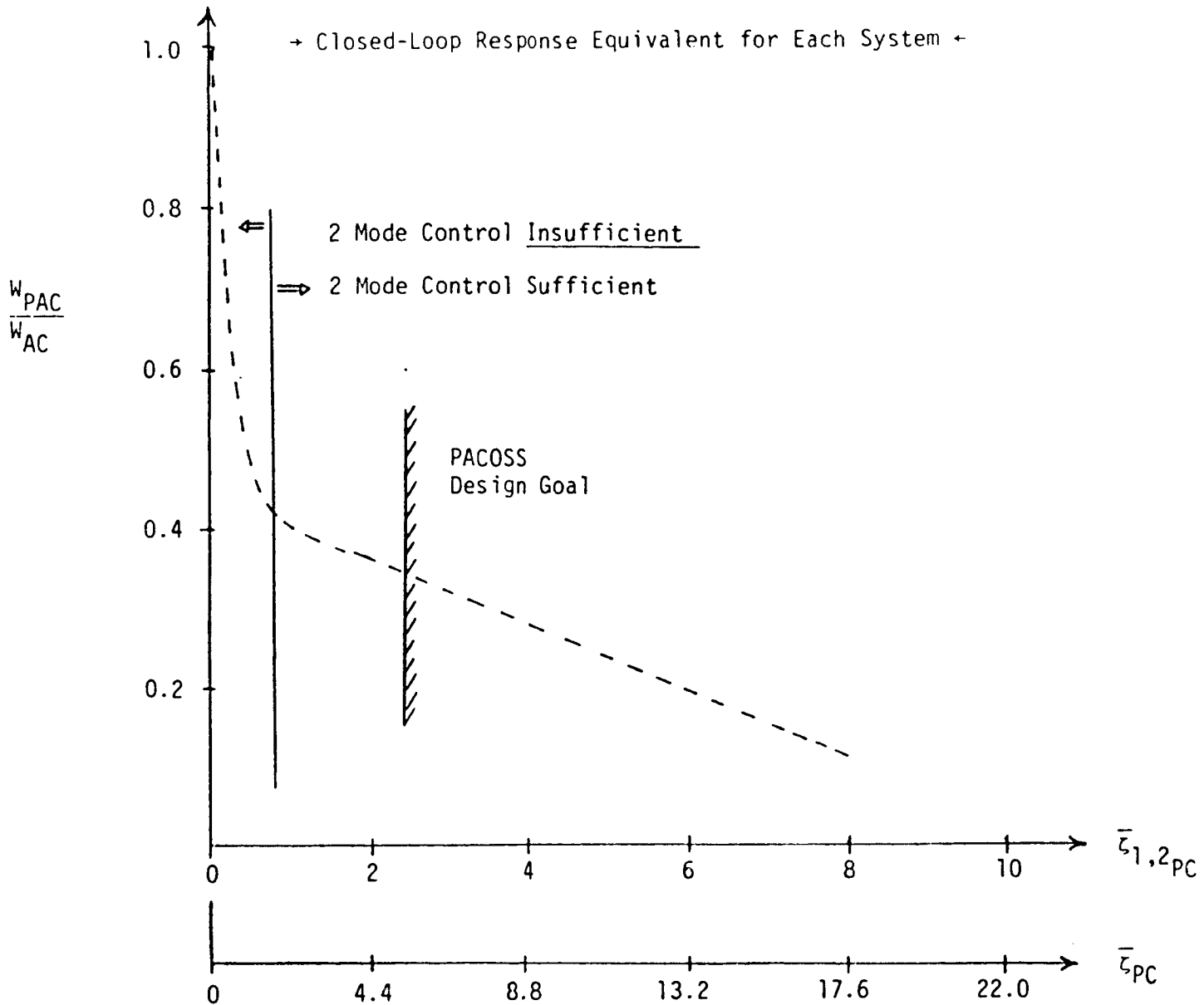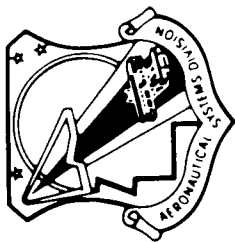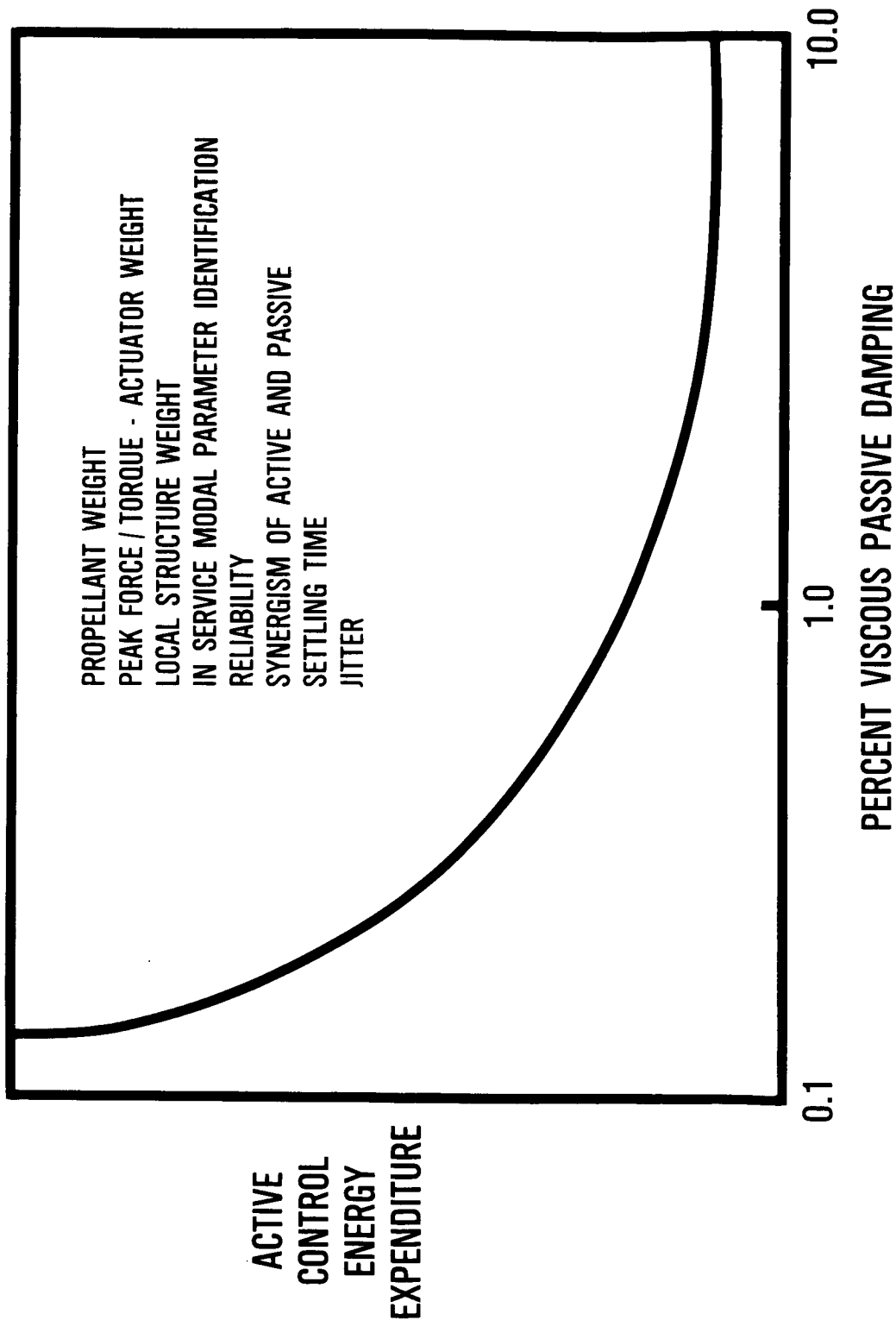→ Closed-Loop Response Equivalent for Each System ←

1.0

$\dfrac{W_{PAC}}{W_{AC}}$

0.8 ⟸ 2 Mode Control Insufficient

⟹ 2 Mode Control Sufficient

0.6

PACOSS
Design Goal

0.4

0.2

$\bar{\zeta}_{1,2_{PC}}$

0   2   4   6   8   10

$\bar{\zeta}_{PC}$

0   4.4   8.8   13.2   17.6   22.0

Figure 3 Active Control Energy Expenditure

SYSTEM LIFE CYCLE OPTIMUM

PROPELLANT WEIGHT
PEAK FORCE / TORQUE - ACTUATOR WEIGHT
LOCAL STRUCTURE WEIGHT
IN SERVICE MODAL PARAMETER IDENTIFICATION
RELIABILITY
SYNERGISM OF ACTIVE AND PASSIVE
SETTLING TIME
JITTER

ACTIVE CONTROL ENERGY EXPENDITURE

PERCENT VISCOUS PASSIVE DAMPING

0.1   1.0   10.0

288
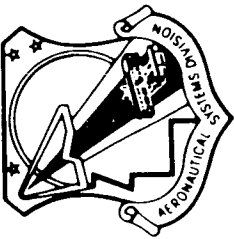
SUMMARY

- ANALYZED, TESTED AND CORRELATED 5% PASSIVE DAMPING IN LARGE TRUSS

- RSA RE-TARGET ANALYSIS SHOWS PAYOFF OF PASSIVE DAMPING

- LSS MUST INCORPORATE PASSIVE DAMPING FROM THE OUTSET (RELATIVE STIFFNESSES MUST BE TAILORED)

- SYSTEM PERFORMANCE WILL NOT BE MET BY EITHER ACTIVE OR PASSIVE ALONE

2. In 1983, the Flight Dynamics Laboratory at Wright-Patterson AFB initiated three contracts in passive damping in space. The two RELSAT (Reliability for Satellite Equipment Under Vibration) contracts (GE Valley Forge and Boeing Aerospace) use integrally damped equipment support structure to suppress vibratory disturbances on equipment. Vibration levels have been reduced 50-70%. RELSAT technology would be useful to design passive damping into local modes, which may or may not be significant. A contract with LTV has designed, built, tested, and qualified for flight, damped laminated skin for an A7 aircraft leading edge flap, three of which are now flying.

3. The PACOSS contract examined future Air Force missions and systems for needed passive damping technology. The truss type construction is typical and a pair of free standing 60 foot tall truss towers were built and tested early in the contract. These tests established that five per cent viscous damping was very practical for these proper size of space type truss construction. High global modal density interacting with active control is judged to be the challenge. PACOSS will design, build, and test a Dynamic Test Article (DTA) which incorporates an active control system.

4. The Twin Towers were designed to have close natural frequencies and a range of modal damping for various modes.

5. The link dampers were carefully designed to have the correct stiffness relative to the rest of the structure. The design process is based on modal strain energy. The damping results from energy dissipation in the viscoelastic material (VEM).

6. Qualatively, the payoff of damping, whether passive or active, is self evident. Damping reduces settling time and jitter, which results in less system time per target.

7. The challenge is vibration suppression/settling time and line-of-sight [JOS] jitter) of a space structure which possesses low frequency, high density of global vibration modes.

8. "Flexible structure" is defined as any structure which has natural vibration frequencies in the passband of the control system. This includes all satellites, because low frequency appendage (solar arrays, antennas, equipment booms) modes interact with the "rigid borly" attitude control system.

9. "Precision structure" is defined as any structure carrying objects (e.g., mirrors) which must fly in precise formation. Note that the structure itself is not necessarily precise.

10. The Dynamic Test Article (DTA) has been carefully designed to have high density of global vibration modes appropriate to the vibration properties of a broad class of system. The ring truss, the box truss, the tripod, the solar arrays, the equipment boom, and the antenna have been sized. Sensors, actuators, and other control system components will be included.

11. The DTA dimensions and weights are carefully selected to fit the shuttle cargo bay. Launch of this particular DTA is not appropriate.

12. Five types of damping concepts, including the link of the 60' Twin Towers, will be integrally designed into the DTA.

13. Analysis of the Representative System Article (RSA), which is dynamically similar to the DTA, for a retargeting maneuver has shown that modest levels of passive damping dramatically reduce the control energy required.

14. More trade studies are needed for specific retargeting and/or LOS jitter due to dynamic disturbances. These studies should investigate control energy required as a function of percent of viscous passive damping over a range of 0.1 - 10.%. Ideally, a system level like cycle merit function could be developed, which properly weights all related effects.

15. In summary, the payoffs of passive damping and its synergism with active control is beginning to be understood.

REFERENCES

1. Rogers, L. C. et al, "Passive Damping in Large Precision Space Structures," AIAA Paper 80-0677, presented at the AIAA/ASME/ASCE/AHS 21st Structures, Structural Dynamics and Materials Conference, Seattle WA, May 1980.

2. White, C. W., Martin Marietta Denver Aerospace, Denver CO, "Analysis of Damped Twin Towers," The Shock and Vibration Bulletin, No. 55-Part 1, June 1985, pp. 119-130.

3. Gehling, R. N., and Morgenthaler, D. R., "Representative System Report," MCR-84-541, Martin Marietta Denver Aerospace, Denver CO, November 1985.

4. Gehling, R. N., and Harcrow, H. W., "Effects of Passive Damping on Active Control Design," Presented at 26th AIAA/ASME/ASCE/AHS Structures, Structural Dynamics, and Materials Conference, Orlando FL, 15-17 April 1985. AIAA-85-0776-CP.

1-CAT: A MIMO DESIGN METHODOLOGY

J. R. Mitchell
J. C. Lucas

Control Dynamics Company
Office Park South
600 Boulevard South, Suite 304
Huntsville, AL 35802

ABSTRACT

The main thrust of this paper is the introduction and illustration of the One Controller at a Time (1-CAT) methodology for designing digital controllers for Large Space Structures (LSS's). In the introduction the flexible mode problem is first discussed. Next, desirable features of an LSS control system design methodology are delineated. The 1-CAT approach is presented, along with an analytical technique for carrying out the 1-CAT process. Next, 1-CAT is used to design digital controllers for the proposed Space Based Laser (SBL). Finally, the SBL design is evaluated for dynamical performance, noise rejection, and robustness.

INTRODUCTION

The design of attitude and vibration suppression control systems for future, large space structures (LSS's) is a difficult problem because the performance specifications are expected to be very stringent and accurate dynamical models are not anticipated before the structure is actually placed in orbit. LSS's of the future will exhibit many lightly damped flexible modes and are expected to require many actuators and sensors for adequate control authority and sensitivity. Such LSS's will comprise true, coupled multiple input, multiple output (MIMO) systems. The final design of the control system will have to be done after the structure has been tested (on orbit) and the models have been updated.

The Flexible Mode Problem

In the design of high performance attitude control systems for LSS's, flexible modes pose two distinct problems. First, they provide paths through which disturbances can be propagated throughout the structure. As a consequence, performance in attitude control can be greatly degraded. For example, in proposed high energy laser beam pointing systems, a source of disturbances will be coolant flow in mirrors used to guide the laser beam along the optical path. The effects of coolant flow on beam pointing and beam quality is modeled as disturbance signals propagating through flexible modes. The second problem is that of flexible modes being excited by command signals from the attitude control system. This is especially true in performing large angle maneuvers. For example, in a high energy laser beam pointing system, in order to change pointing directions (e.g., retargeting) a large physical element such as a mirror or a beam expander may have to be slewed. In such a

case flexibile modes of the system can be significantly excited, and the settling time for the initiation of high precision pointing can become unacceptable.

Historically, the design of control systems in which flexible modes were problems has been accomplished by either attempting to gain stabilize or by notching the modes. The effects of both these are essentially the same, i.e., they tend to reduce the level that a mode can be excited, and neither approach significantly effects the modal damping in the closed loop from that of the open loop. The major drawback with gain stabilization and/or notching is that the effects of disturbances on performance is, in general, not improved and, in fact, can be worsened. Hence, gain stabilization and/or notching are only effective when disturbances are not a problem and the bandwidths of the loops are expected to be well below the first flexible mode.

In order to meet the stringent performance requirements of many LSS's it is anticipated that the control bandwidth must include a frequency range that covers the first several modes. In this case the control system must be designed so that these modes are damped, at least to the degree of the rigid body modes, and the higher frequency modes are notched or gain stabilized. Then, even though the response of the system to a standard input, such as a step, will be a multi-modal response, all the modes will decay at a minimum rate or will not be excited significantly. Modal damping is very desirable because it has a global effect over a structure, i.e., the damping of the modes will be reflected in any transfer function between arbitrary points.

Desirable Features of LSS Control System Design Methodology

Study of the digital controller design problem for Large Space Structures (LSS) has identified several objectives on which attention must be

focused when selecting a design technique. These include not only performance with respect to system behavior but also practical implementation, check-out, and operation in an orbiting space structure. The design technique desirable features are as follows:

- Simplicity of Controller

A digital controller design technique for LSS must lead to controllers of reasonable order for the very high order system models defined by flexible spacecraft. This is to minimize the computational burden of the onboard computer when the controller is implemented.

- Straightforward and Traceable Design Procedure

A design technique should be readily understandable and the design process should trace effects of closed loop control upon the system behavior throughout the design process. In this way a designer can see how the system is evolving during the design process, and therefore, have insight into problems and/or causes of problems should they arise.

- Stability of Closed Loop System

The technique should inherently provide stability of the closed loop system resulting from the combination of the digital controller and the LSS model. In fact, a reasonable amount of relative stability should be inherent.

- Inherent Robustness Checks

Robustness is of particular concern to the LSS control system designer because accurate models are not anticipated. Hence, the technique should produce designs with reasonable robustness with respect to model inaccuracies and plant variation. In addition, the design technique should provide built-in checks for robustness at stages in the design process. This is also a part of an easily traceable design procedure.

- Disturbance Rejection

Disturbance rejection is a major concern in control system design for LSS's and should inherently be achieved through the design process.

- Digital Design Accomplished in Digital Domain

Design of digital control systems should be accomplished in the digital domain so that the effects of sampling and computational transport lags can be accounted for during the design phase rather than designing a continuous controller and then attempting to implement a digital equivalent which, at best, is an approximation to the desired controller.

- Efficiency of Design

The design technique should be reasonably efficient with respect to computer processing and storage requirements and should be algorithmic in nature so that the design process can be easily repeated as model updates are obtained.

- Applicable to High Order Systems

The design technique should be capable of handling high order systems. It is anticipated that LSS models will be of order one hundred or more; hence, the numerical techniques used to implement the design methodology should be tried and proven for systems with orders in excess of one hundred.

- Incorporation of Experimental Model Data

As mentioned above, it is anticipated that the final design of an LSS cannot be completed until data from on-orbit testing is obtained. The design process should be able to easily utilize this data to generate model updates so that the control system design can be fine-tuned for increasing system performance.

Recent technological advances in the development of control system design philosophies for LSS's include Lockheed's Low Authority Control/High Authority Control (LAC/HAC),[1] TRW's Positivity,[2,3] and General Dynamics' Model Error Sensitivity Suppression (MESS).[4] Each of these techniques has been developed under the ACOSS Program, sponsored by the Defense Advanced Research Projects Agency (DARPA). Although the techniques take different approaches, they are common in the respect that each is carried out by following a very complex design procedure, which can even be iterative. In addition, none of these techniques possesses all the desirable features listed above.

In this paper, an alternate LSS design philosophy, called 1-CAT, is presented. When properly carried out the 1-CAT philosophy produces viable solutions to the flexible mode problem and inherently possesses the desirable features delineated above.

Theoretical Background of 1-CAT

The multi-input/multi-output (MIMO) digital controller design technique, 1-CAT, finds its basis in the fundamental principals of classical analysis and design control theory. It springs from the fact that the marriage of a MIMO system (plant) and controller can be viewed as a coupled multiloop system. The controllers for the loops cannot be designed independently, but they can be designed one at a time; this is the thesis of 1-CAT: "One Controller At a Time".

To delineate the process, consider a system having three inputs and three outputs. With all possible feedback paths open, the transfer characteristic between a particular input-output pair may be analyzed and a controller designed to stabilize the loop to satisfactory specifications. With

this loop closed, another input-output pair may be analyzed and a controller likewise designed. The second controller is not designed independently, because the effects of the first controller are taken into account when the first loop is closed. A third controller can then be designed with the first two loops closed and so on until all desired feedback paths are closed through the appropriate controller. Of course, it is doubtful that a designer would desire to close all nine possible feedback paths of this system; however, the 1-CAT technique does not preclude this possibility.

Three pertinent facts regarding the 1-CAT technique bear mention at this point.

- If the plant is stabilizable, the resulting closed loop system will be stable.

Stabilizability simply implies that if there are uncontrollable modes, i.e., modes whose eigenvalues cannot be changed by feedback, their eigenvalues must have negative real parts. In this case the uncontrollable modes cannot result in instability, but the controllable modes can. However, the 1-CAT approach can be applied so that no controllable mode can cause a stability problem and, in fact, can produce a design that will ensure a specified amount of relative stability.

For example, suppose that the 1-CAT approach is applied to a three loop example. With all loops open, assume that a controller is designed for the first loop so that all controllable modes have closed loop eigenvalues with real parts less than $-\alpha$. Now with the first loop closed a controller is designed for the second loop so that all controllable modes have closed loop eigenvalues with real parts less than $-\alpha$. Then with the first two loops closed a controller is designed for the third loop so that all controllable

modes have closed loop eigenvalues with real parts less than $-\alpha$. Now suppose a root locus study is performed on the first loop with the second and third loops closed and with the controllers designed for each loop included. The controllable modes in this loop can be separated into those modes only controllable from loop one and those modes that are also controllable from loops two and/or three. Using the gain factor for which loop one was designed, those modes only controllable from loop one must have eigenvalues with real parts less than $-\alpha$, since these modes are not affected by the designs in loop two and/or three and loop one was designed to achieve this specification. The other controllable modes in loop one must have eigenvalues with real parts less than $-\alpha$ since these eigenvalues are controllable from loop two and/or three which were also designed to meet this specification.

The bottom line is that as subsequent loop closures are made eigenvalues of preceding loops cannot have real parts greater than $-\alpha$. However, it should be noted that if a subsequent loop is designed with a more relaxed specification, the relative stability of the preceding loops can relax, too.

Although the above arguments have been made for the first loop of a three loop example, they obviously can be extended to the design of a system with many loops and to other loops rather than the first. In addition, other measurements of relative stability can be used, e.g., gain margins and phase margins. In order to ensure no degradation in the relative stability of loops previously closed, subsequent loops should be designed so that relative stability is improved or as a minimum not allowed to degrade.

Implementation of the 1-CAT Philosophy

If carried-out properly, the 1-CAT philosophy is a sound approach for designing MIMO control systems. It is obvious that, at least from a

300

theoretical point of view, root locus techniques could be used to carry out the design process. However, this would require transfer functions of all the elements of the transfer function matrix. Since LSS's are anticipated to be high order, e.g., one hundred or more, these transfer functions will be difficult to obtain and cumbersome to handle with root locus techniques.

An alternative approach is frequency response techniques. One frequency response approach that could be used, is one in which the frequency response data is generated along the line $-\alpha + j\omega$, where α is the stability margin in which it is desirable that all poles be to the left. Then as loops are closed, all those modes lying to the right of the $-\alpha$ line are forced to produce counter clockwise encirclements of the $-1.0 + j0.0$ point on the Nyquist plot. When the design is completed, the compensation can be easily frequency shifted, back to $\alpha = 0$. This is a theoretically sound approach; however, it does not easily accommodate experimental data, since frequency response data along the line $-\alpha + j\omega$ is difficult to generate experimentally or to compute from experimental results.

Another frequency domain approach is to use classical frequency response data, i.e., $\alpha = 0$ data, and design each loop to specified gain margins, phase margins, etc. There are two questions that must be answered in regard to this approach:

(1) How can these designs be achieved, and added modal damping be assured?

(2) As subsequent loops are closed, how can degradation in the performance of the closure of previously closed loops be avoided?

The answer to the first question is that modal damping can be added to flexible modes by properly phase stabilizing the modes. Phase stabilization

of a mode is achieved by designing compensation so that on an open loop polar frequency response, the peak of the mode occurs when the phase is near $0°$.

The amount of damping added to a mode is a function of the amount of peaking of the mode. From root locus techniques it is well known that when a loop is closed and the loop gain factor is increased, the poles migrate from the open loop pole locations toward the open loop zero locations. Interpreting this in terms of phase stabilization means that the higher a phase stabilized mode is made to peak in the open loop, the closure it will approach a left-half plane open loop zero in the closed loop. If the zero is well in the left half plane, significant damping to the mode can be added with significant modal peaking. If the damping of the zero is small, e.g., it may even be less than that of the pole, there are two routes that can be taken. First, compensation can be designed that has a pole that migrates to the zero with small damping. The compensation zero can be selected further in the left half plane with an acceptable damping. Then, the mode can be forced to have significant peaking and consequently approach the damping of the compensation zero.

The second route is to design for maximum modal damping. It is a fact that when a mode is phase stabilized and the loop gain is increased, its initial break is into the left half plane. However, if the peaking is increased, the damping can reach a maximum value and then decrease. Such a case occurs when the zero, toward which the mode is migrating, has damping on the same order or less than the corresponding mode. For lightly damped modes, such as occur in LSS's, this is indicated on an open loop frequency response plots by deep troughs in the magnitude characteristics. For such

situations, maximum damping can be approximately achieved by phase stabilizing the mode and selecting the loop gain so that the peak of the mode is above 0 dB and the trough of the zero, toward which the mode is migrating, is below 0 dB. If several modes are to be handled in this fashion, then frequency shaping of the loop gain will be required so that each mode satisfies this condition.

Now returning to the second question. In order that subsequent loop closures will not degrade the open loop performance of previous closed loops, the dominant frequency ranges of modes controlled in previous loops, i.e., designed for increased damping, must be precluded from the interior of the unit disk centered at -1 +j0 point in the GH(jω) - plane for each subsequent loop closure. In essence this means that if a dominant mode of a previously closed loop is dominant in a subsequent loop it must still be phase stabilized to assure that damping is not lost. It should be noted that rigid body modes are included here.

Loop Closure in MIMO Systems

The 1-CAT design philosophy dictates that feedback loops are sequentially designed and closed. A frequency response approach was selected because either continuous or sampled-data frequency responses are numerically easy to compute (even for high order systems) and frequency response data are easily obtained from experimental results. By following the rules of the previous section degradation in loop performance by subsequent loop closures can be assured. In this section, an analytical technique for taking into account a loop closure in a MIMO system is presented. It should be noted that the presentation is made using continuous transfer function notation but

interpretation in terms of standard frequency responses or sampled-data frequency responses simply requires a change in the function notation; hence, no generality is lost.

A block diagram representation of a multiple input, multiple output (MIMO) system is shown in Figure 1. One approach for mathematically representing this is through the transfer function matrix, i.e.,
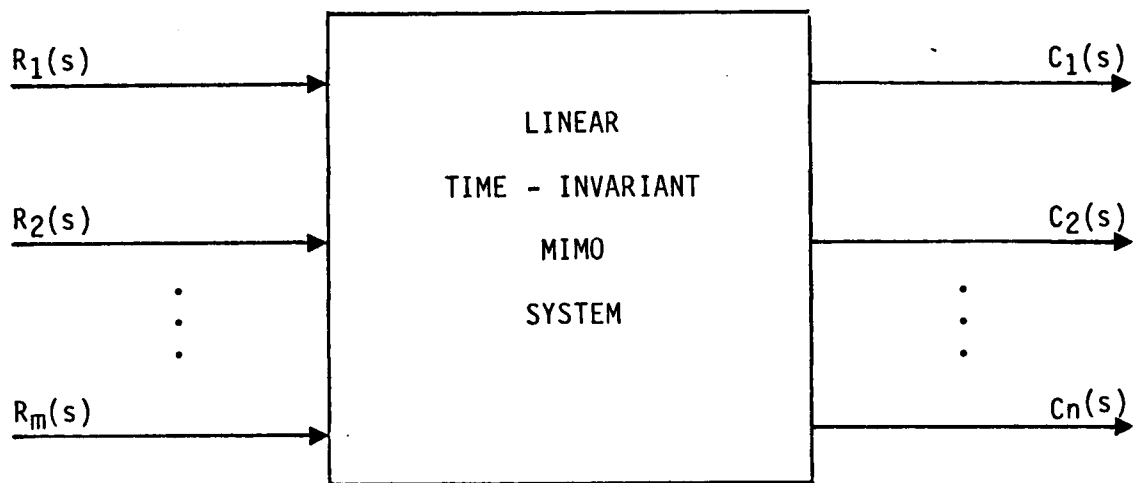
$R_1(s)$ LINEAR TIME - INVARIANT MIMO SYSTEM $C_1(s)$

$R_2(s)$ $C_2(s)$

$R_m(s)$ $C_n(s)$

Figure 1. Block Diagram of a MIMO System.

$$[G(s)] = \begin{bmatrix} G_{11}(s) & G_{12}(s) & \cdots & G_{1m}(s) \\ G_{21}(s) & G_{22}(s) & \cdots & G_{2m}(s) \\ \cdot & & & \\ \cdot & & & \\ G_{n}(s) & G_{n2}(s) & \cdots & G_{nm}(s) \end{bmatrix} \tag{1}$$

in which

$$\frac{C_i(s)}{R_j(s)} = G_{ij}(s). \tag{2}$$

304

The transfer function matrix description given by (1) can be used to represent either closed loop or open loop systems. All that is required is that when a loop is closed the matrix must be recomputed to reflect the loop closure.

In fact, the computation of the elements of the matrix can be done in a straight forward manner. A loop closure from output p to input k through a feedback compensator $K_2(s)$ and forward path compensator $K_1(s)$ is shown in Figure 2. This system can be represented in the form of Figure 1 by recomputing the elements of the new system matrix as follows:

$$G'_{ij}(s) = G_{ij}(s) - \frac{K_1(s) \, K_2(s) \, G_{ik}(s) \, G_{pj}(s)}{1 + K_1(s) \, K_2(s) \, G_{pk}(s)}, \quad \begin{array}{l} i \neq p \\ j \neq k \end{array} \tag{3}$$

$$G'_{pj}(s) = \frac{G_{pj}(s)}{1 + K_1(s) K_2(s) G_{pk}(s)}, \quad j \neq k, \tag{4}$$

$$G'_{ik}(s) = \frac{K_1(s) G_{ik}(s)}{1 + K_1(s) K_2(s) G_{pk}(s)}, \tag{5}$$

where $i = 1, 2, \ldots, n$ and $j = 1, 2, \ldots, m$ and the prime notation represents the elements of the new matrix. In summary, equation (3) is used to compute all the elements of the matrix except those in the pth row and k^{th} column; equation (4) is used to compute all the elements in the pth row except the kth element; equation (5) is used to compute the elements of the kth column.

By investigating the frequency responses of equations (3), (4) and (5) several observations on closing loops in MIMO systems can be made. First, from (4) it is seen that in the frequency range where $| 1 + K_1 K_2 G_{pk}(j\omega) |$ is larger than unity the pth output becomes less affected by all inputs except $R_k(s)$. The implications are that as loops are closed, the pth output tends
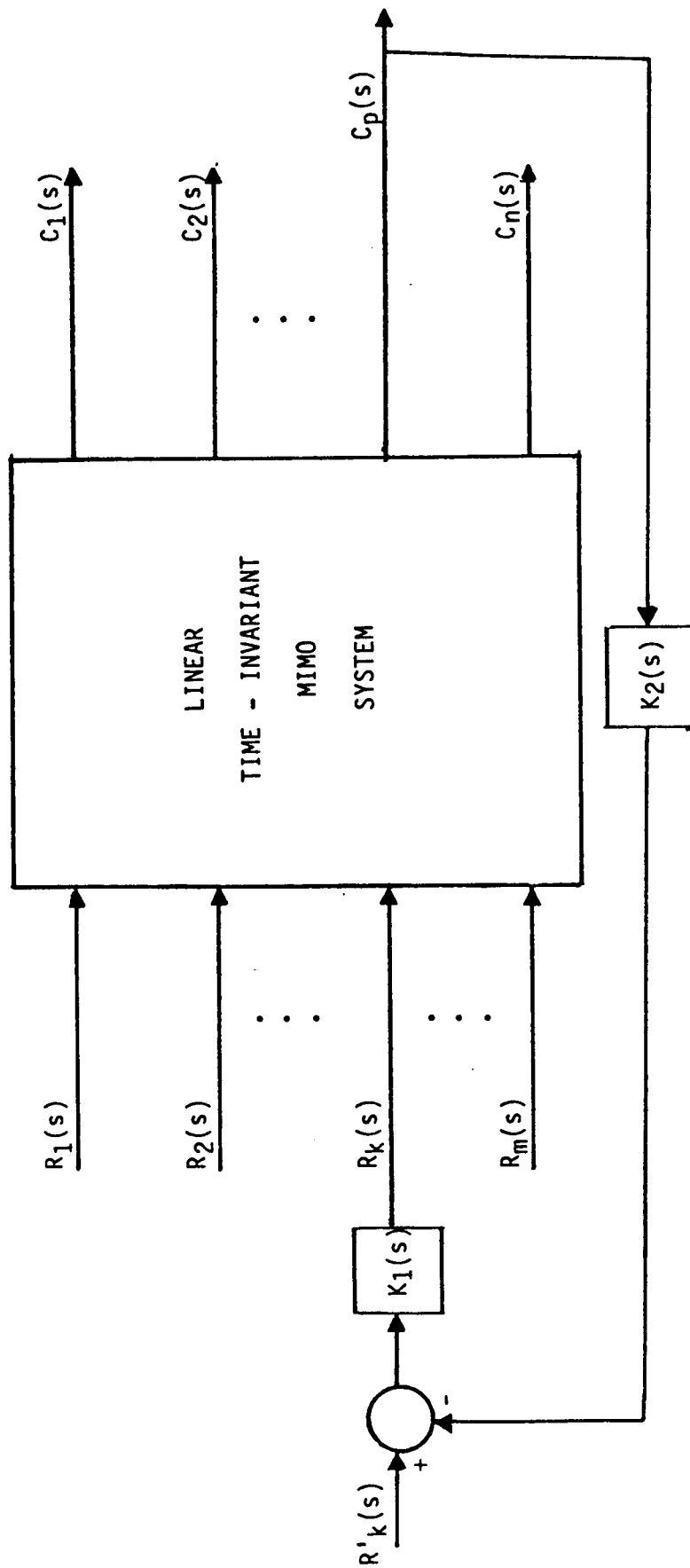
Figure 2. MIMO System with Feedback from Output p to Input k.

to be decoupled from the other inputs in the frequency range where $|K_1 K_2 G_{pk}(j\omega)| >> 1$, which is roughly the control frequency range. In fact, if in the control frequency range the product of the compensators $K_1(j\omega)$ $K_2(j\omega)$ is selected so that the polar frequency response of $K_1 K_2 G_{pk}(j\omega)$ does not violate the unity disk centered at $-1.0 + j0.0$ in the $K_1 K_2 G_{pk}(j\omega)$ plane decoupling from the other inputs over the whole control frequency range is assured. The amount of decoupling on a frequency by frequency basis is easily seen by reviewing the amount that the frequency response of $|1 + K_1 K_2 G_{pk}(j\omega)|$ is above 0 dB.

In the cases where loops are closed with a unity forward transfer function, e.g., vibration suppression loops for LSS's, a decoupling effect over the control frequency range is not only realized between the other inputs and the $p\underline{th}$ output but between the $k\underline{th}$ input and the other outputs. Investigating equation (4) in a similar fashion as done for (3) above easily validates this statement.

Another observation from equation (3) is that by closing a loop between the $k\underline{th}$ input and $p\underline{th}$ output the transmission zeros between the other inputs and other outputs are affected. In face, from (3) a designer can see exactly what the product $K_1 K_2$ needs to be in order to place zeros in desirable locations. For example, to generate a notch at $\omega = \omega_1$ in $G_{ij}(s)$ where $i \neq p$ and $j \neq k$, then

$$K_1 K_2 (j\omega_1) = \frac{- G_{ij}(j\omega_1)}{G_{ij}(j\omega_1)G_{pk}(j\omega_1) - G_{ik}(j\omega_1)G_{pj}(j\omega_1)} \qquad (6)$$

With the frequency response of the elements of the transfer function matrix available, a designer can easily carry-out the 1-CAT process by

sequentially using equations (3), (4), and (5). A check on the effects of a loop closure on any element of the transfer matrix can be made by simply comparing "before" and "after" frequency responses. System robustness can be determined by opening individual loops, with the other loops closed, and looking at closest approach points to the -1.0 + j0.0 point.

Design of Space Based Laser Attitude Control System Using 1-CAT

In order to demonstrate the application of 1-CAT on a reasonable order LSS control problem, an attitude and vibration suppression control system is designed for a planar model of the Space Based Laser (SBL). Figure 3 shows the structural model of the SBL. As indicated by the figure the structure containing the mirrors is attached to ground through an isolator. While in reality the mirror structure is actually attached to the Aft section of the orbiting platform, the approximation is reasonable for the differences in mass of the two sections.

The goal is to design a beam tilt angle control system with acceptable dynamic performance and disturbance rejection. The tilt angle of the beam can be controlled by torquing the primary support structure of the beam expander about its gimbal point, assumed centered at the connection of the isolation system and the beam expander, by torquing the secondary mirror (SM), and by independently torquing any or all of the primary mirror segments (PM1, PM2, PM3). The secondary mirror angular rate is sensed inertially, whereas the angular rate of each segment of the primary mirror is sensed relative to the primary support structure. The tilt angular error is sensed in inertial space by the Outgoing Wavefront Sensor (OWS).

Table 1 and 2 contain the data used in constructing the model of the SBL. Included in this model are twenty-six degrees of freedom containing many flexible modes which are insignificant to the design effort. Modal truncation can be used to reduce the order of the system in order that (1) unnecessary calculations are eliminated and (2) some significant modes be eliminated so post analysis can establish the effects of unmodeled modes on

TABLE 1. OSBL MODAL DATA

	Modal frequencies		Tilt error gains	Gimbal point inertial rotation gain	1st Segment of the primary mirror gain	2nd Segment of the primary mirror gain
	Hertz	RAD/SEC				
1	0.0	0.0	0.1420E-02	0.1000E-02	0.0000E+00	0.0000E+00
2	0.0	0.0	-0.0000E+00	0.0000E+00	0.0000E+00	0.0000E+00
3	0.0	0.0	-0.3724E-03	-0.4694E-03	0.0000E-00	0.0000E+00
1	4.473337	20.10601	0.1774E-01	0.6057E-03	0.2390E-03	0.2304E-03
5	6.592096	41.42439	-0.5440E-07	-0.1409E-08	0.9075E-07	-0.5427E-07
6	7.061209	44.36600	-0.1360E-00	0.1972E-09	0.5392E-05	0.2103E-09
7	7.414550	46.50699	-0.1050E-01	-0.1006E-02	-0.1450E-02	-0.1434E-02
8	9.251732	50.13035	-0.6094E-04	0.7369E-05	-0.0577E-02	0.1707E-01
9	9.252620	50.13593	-0.3199E-05	0.5606E-07	0.1470E-01	0.2726E-04
10	9.530362	59.00103	0.2332E-01	-0.1059E-03	0.1200E-01	0.1210E-01
11	9.001935	62.09003	-0.3449E-02	0.3062E-04	-0.3277E-03	-0.3724E-03
12	9.997501	62.01615	-0.3121E-07	-0.9670E-10	0.7530E-05	-0.1446E-07
13	10.00001	62.83193	-0.1301E-07	0.1214E-09	-0.0045E-00	-0.4094E-08
14	10.46396	65.74702	-0.2377E-01	0.4017E-04	0.1210E-01	0.1216E-01
15	10.80504	67.09510	-0.2290E-06	0.3015E-05	-0.9200E-02	0.1045E-01
16	10.00673	67.90071	0.4034E-05	-0.9050E-07	0.1593E-01	0.4263E-04
17	11.94206	75.03420	0.2414E-02	0.1402E-02	-0.3779E-02	-0.3563E-02
18	12.85439	80.76653	0.1425E-00	0.4536E-09	-0.2093E-04	-0.0901E-09
19	15.49392	97.35114	-0.0032E-02	0.2171E-03	-0.2314E-02	-0.2495E-02
20	17.50351	109.9770	0.5707E-02	0.1370E-02	-0.3002E-02	-0.2771E-02
21	17.94535	112.7540	-0.7000E-09	-0.3152E-09	0.1692E-04	0.7516E-09
22	23.47099	147.5228	-0.2010E-01	0.1405E-02	-0.1573E-02	-0.1608E-02
23	29.26876	183.9010	0.2309E-10	-0.5097E-11	-0.2007E-04	0.3235E-11
24	77.00790	404.3576	-0.1010E-00	0.3061E-09	-0.2495E-02	-0.3615E-09
25	09.34500	561.3762	-0.6393E-02	0.5500E-02	0.2331E-02	-0.5641E-02
26	145.0540	911.4013	-0.2000E+00	-0.1416E-03	-0.5057E-04	0.1422E-03

TABLE 1. OSBL MODAL DATA (continued)

	Modal frequencies Hertz	Modal frequencies RAD/SEC	3rd Segment of the primary mirror gain	Secondary mirror inertial rotational gain	Gimbal point inertial Y translation gain	Secondary mirror inertial Y translation gain
1	0.0	0.0	0.0000E+00	0.1000E-02	0.0000E+00	0.2524E-01
2	0.0	0.0	0.0000E+00	0.0000E+00	0.0000E+00	0.0000E+00
3	0.0	0.0	0.0000E+00	-0.4694E-03	0.1034E-01	0.3757E-02
4	4.473337	28.10601	0.2390E-03	-0.4000E-01	0.7600E-03	0.5439E-03
5	6.592096	41.42439	-0.7709E-07	0.7500E-07	-0.3749E-00	-0.5502E-00
6	7.061209	44.36608	-0.5392E-05	-0.2026E-00	-0.1636E-09	0.1491E-00
7	7.414550	46.50699	-0.1440E-02	0.1566E-01	0.0142E-03	-0.1260E-01
8	9.251732	58.13035	-0.0513E-02	0.1461E-03	0.1790E-05	-0.1404E-03
9	9.252620	58.13593	-0.1401E-01	-0.5420E-06	0.1104E-06	0.5019E-06
10	9.530362	59.80103	0.1200E-01	0.3111E-02	-0.9767E-03	-0.3107E-02
11	9.801935	62.09003	-0.3376E-03	0.8371E-02	0.3223E-04	-0.0530E-02
12	9.997501	62.81615	-0.7564E-05	-0.5596E-00	0.1276E-00	0.6074E-00
13	10.00001	62.83193	-0.0074E-08	0.2265E-09	-0.4624E-09	-0.1340E-09
14	10.46396	65.74702	0.1210E-01	0.4413E-03	-0.1211E-02	-0.4615E-03
15	10.80504	67.09510	-0.9144E-02	0.1797E-03	-0.4270E-05	-0.1062E-03
16	10.80673	67.90071	-0.1597E-01	0.2118E-05	-0.1055E-06	-0.2015E-05
17	11.94206	75.03420	-0.3779E-02	-0.2110E-01	0.4754E-03	0.2322E-01
18	12.85439	80.76653	0.2093E-04	-0.7007E-00	0.1600E-09	0.0127E-08
19	15.49392	97.35114	-0.2314E-02	-0.1250E-01	-0.1054E-01	-0.1430E-01
20	17.50351	109.9778	-0.3002E-02	-0.2626E-01	-0.7049E-02	0.3105E-01
21	17.94535	112.7540	-0.1601E-04	0.4559E-00	0.1433E-00	-0.5104E-08
22	23.47099	147.5220	-0.1573E-02	0.0570E-01	-0.1631E-03	-0.1025E+00
23	29.26076	183.9010	0.2007E-04	-0.1217E-09	-0.3312E-11	0.1199E-09
24	77.00790	404.3576	0.2495E-02	0.9256E-09	0.3040E-09	0.2961E-09
25	89.34500	561.3762	0.2331E-02	0.1501E-01	0.3206E-02	0.2503E-02
26	145.0540	911.4013	-0.5057E-04	0.7271E+00	-0.7452E-04	0.1443E-01

TABLE 2

ACTUATOR AND SENSOR DYNAMICS

GIMBAL TORQUE ACTUATORS

$$G_{GT}(s) = \frac{(200)^2}{s^2 + 2(.707)200\ s + (200)^2}$$

TILT ANGLE SENSOR

$$G_{TA}(s) = \frac{125}{s + 125}$$

MINOR ACTUATORS

$$G_{sm}(s) = \frac{500}{s + 500}$$

RATE SENSORS

$$G_{RS}(s) = \frac{250s}{s + 250}$$

ISOLATOR

$$I(s) = 628.3s + 3948$$

the final design. It should be noted that modal truncation is not a prerequisite for the application of 1-CAT. By using the frequency response techniques mentioned earlier model order does not pose a significant constraint on the design process.

Modal truncation is easily accomplished in the frequency domain by examining the relative peaking of each mode. A step-by-step process of modal selection can be achieved by examining the DC gain and resonant peak gain of each mode. The gains defined by the relations in equation 7 and 8 provide a basis of comparison between each flexible mode and the rigid body modes.

$$\text{DC GAIN} = \frac{G_{pi} \, T_{ai}}{\omega_i^2} \tag{7}$$

$$\text{RESONANT PEAK GAIN} = \frac{G_{pi} \, T_{ai}}{2\zeta \, \omega_i^2} \tag{8}$$

where

G_{pi} is the gimbal point torque modal gain at the i-th mode

T_{ai} is the tilt angle angular sensor modal gain at the i-th mode

ω_i is the i-th modal frequency.

The process begins by computing the rigid body gain at each flexible modal frequency. This gain is compared to the DC gain for the particular mode of interest. The largest DC gain that exceeds both the rigid body gain for that frequency and all other modal DC gains is labeled a dominant mode, W_{d1}. The process continues with the dominant mode W_{d1} replacing the rigid body modes as a basis of comparison. The DC gain of each mode lying at a

higher frequency than W_{d1} is compared to the gain of the mode W_{d1} at each succeeding mode frequency. If a mode's DC gain dominates the gain of the mode W_{d1} at that frequency W_i and is larger than all other remaining DC gains then it is chosen as W_{d2}. This process continues until all modes have been compared in this fashion. The resulting selection would appear somewhat as the solid line of Figure 4. This solid line is actually the straight line approximation of the magnitude frequency response. Once this has been achieved, the selection criterion proceeds to check the resonant peak of each mode defined by (8). If the resonant gain is such that it exceeds the value of the straight line approximation at that mode frequency W_i then it can be included in the model. This step must be tempered with practicality since the resonant peak may exceed the curve with a only small value of epsilon. Technically its effects are noticable but it is inconsequential to the design. A reasonable and easily implemented solution is to choose only those modes whose resonant gain exceeds the DC gain curve by a tolerance which is defined by the designer.

Relations (7) and (8) were applied to the modal data in Table 1 with the resulting selection of modes being listed in Table 3. Modes 25 and 26 are ignored for this design even though they would have been considered by this process. The validity of modes at frequencies this high is questionable.

In addition to the dynamics of the modes presented in Table 1, sensor and actuator dynamics were included in the model in order that the design problem be more realistic. The bandwidth for all sensors and actuators except for the tilt angle sensor is just outside the range of the modal frequencies selected for the model. This provides a phase shift in the modal frequency range without gaining any gain stablilizton from the actuator and sensor dynamics.
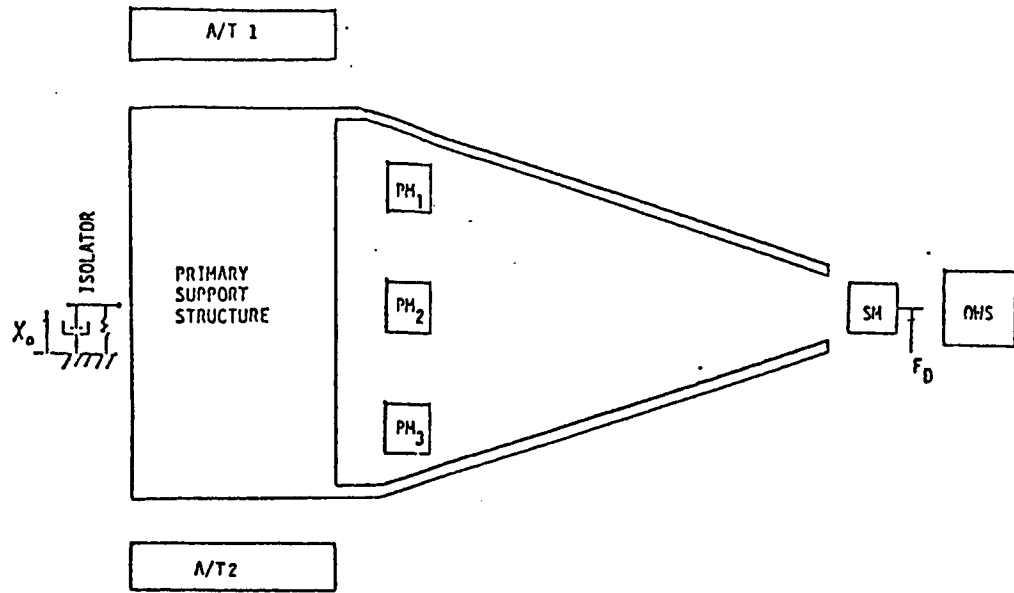
Figure 3.   SBL Beam Expander Structual Model.
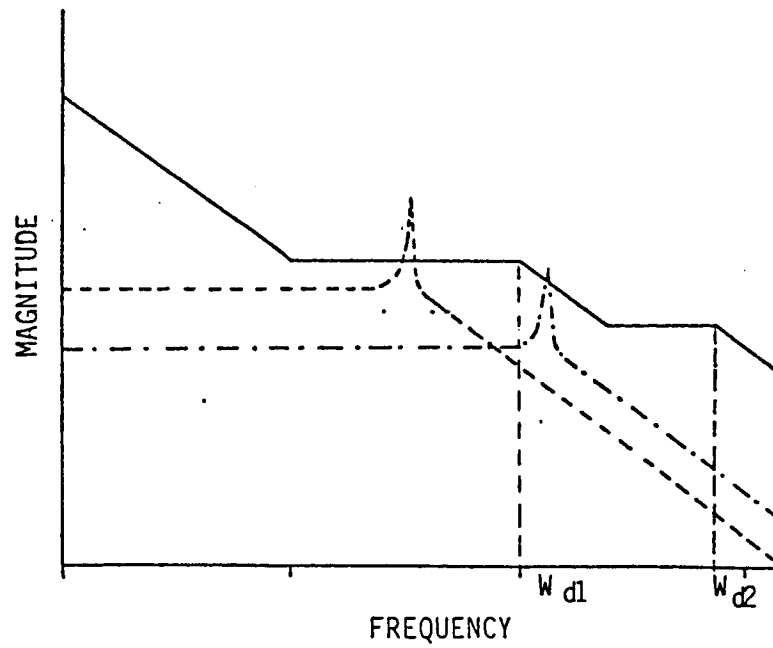
Figure 4.   Modal Selection Criterion

TABLE 3

SELECTED MODES AND FREQUENCIES

Mode No.	Frequency rad/sec
1	0
3	0
4	28.10681
7	46.58699
10	59.88103
14	65.74702
17	75.0342
19	97.35114
20	109.9778
22	147.5228

Since the isolation system is assumed attached to ground, it provides a path for AFT disturbances to be propagated to the tilt error. This is illustrated in the system model shown in Figure 5. In this figure $\underline{K}_{pm1}$, $\underline{K}_{pm2}$, $\underline{K}_{pm3}$, $\underline{K}_{sm}$, and $\underline{K}_g$ are, respectively, the torque modal gain vectors of the three primary mirror segments, the secondary mirror and the gimbal. K_i is a disturbance force error modal gain vector, $\underline{1}_T{}^T$ is the transpose of the tilt angle modal gain vector, and $\underline{1}_I{}^T$ is the transpose of the modal displacement vector at the gimbal point. The other modal gain vectors denoted by the symbol $\underline{1}$ with the appropriate subscripts are the sensor modal gain vectors at the designated structural points. The transfer function matrix $G(s)$ is the modal transfer function previously defined. $I(s)$ represents the isolator whose transfer function is listed in Table 2.

The design problem for the SBL can now be restated as the determination of a digital feedback control law for commanding torques at the secondary mirror, the gimbal, and each segment of the primary mirror so that: (1) commanded tilt angle is accurately achieveable with a reasonable dynamic reponse and (2) disturbances have minimum effect on tilt angle.

SBL Control Law Design and Analysis

Figure 6 shows the digital feedback control law selected to accomplish the goals of the design. The basic operation is that of closing a negative feedback path around each mirror by sampling the sensed rate of each mirror and operating on the signal with a digital controller to obtain a commanded torque signal which is converted to an analog signal for each mirror actuator.
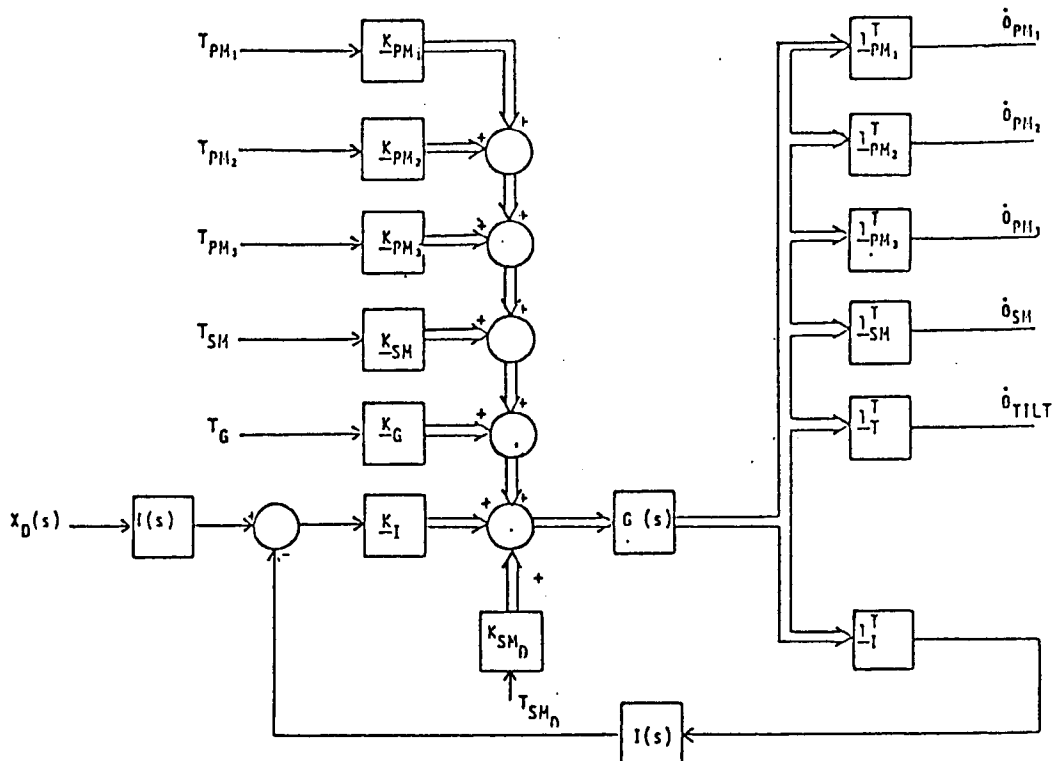
Figure 5. Vector-matrix block diagram showing the feedback path around the system dynamics due to the isolation system.
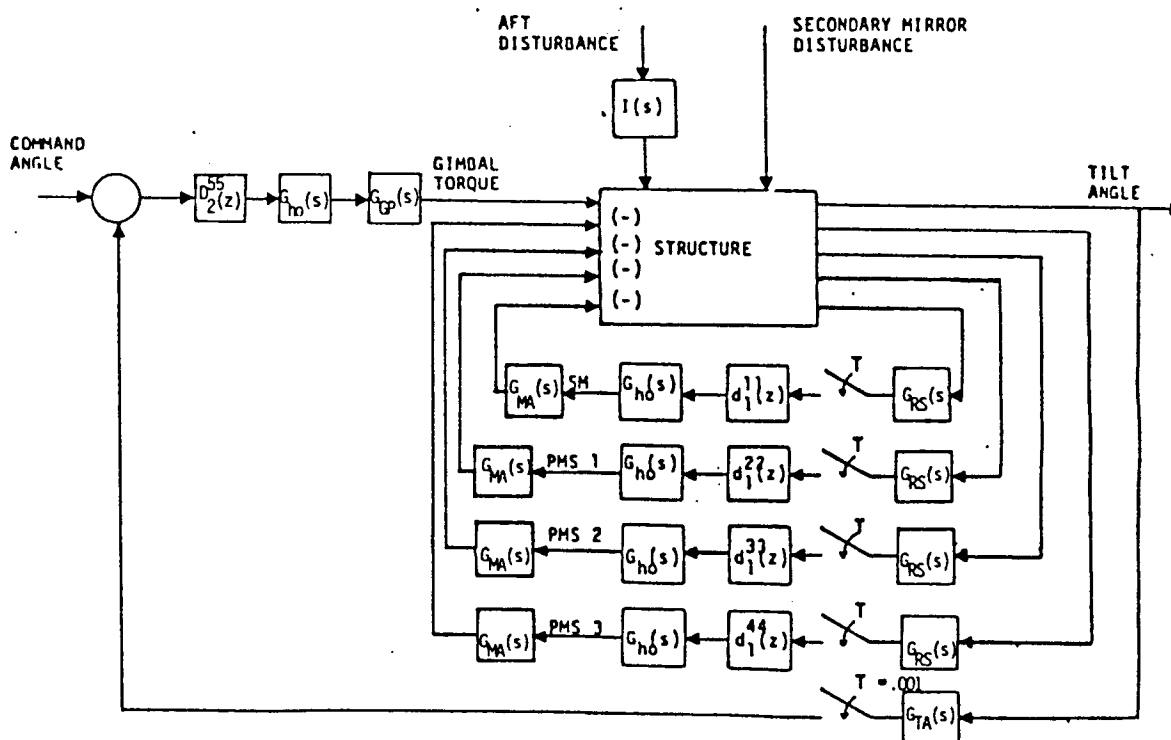
Figure 6. Block Diagram For OSBL

The effect of closing the loops is to obtain damping in the tilt angle loop. The negative sign in the block labeled STRUCTURE indicates the differencing to obtain an error signal. For these rate loops the desired rate is always zero; hence, the error signal is simply the negated value of the each digital controller. Simarily a negative feedback loop is formed for the attitude signal by differencing the commanded angle with the sampled value of the sensed tilt angle and then operating on the error with a digital controller in the forward path. The digital controller is placed in the forward path to insure zero steady state error as well as closed loop stability. The block labeled STRUCTURE is essentially the block diagram shown in Figure 5 with the exception of the minus sign discussed earlier. Each loop is to be design with as high a bandwidth as possible, which for this particular design implies that the digital controllers should be designed with as high a gain as possible. This will insure disturbance rejection as well as achieved the dynamic response required.

The 1-CAT approach can be readily applied to this designed. The order in which the loops are closed will be first the secondary mirror loop, the three primary mirror segment loops in numerical order, and then the tilt angle loop.

In order to better see the effects of the design and the closure of each loop on the tilt angle loop, the open loop frequency responses of the SM, PM1, PM2, and Tilt angle loops are shown in Figures 7-10. The frequency response of PM3 has been ignored because it like the response of the PM2 loop is very much the same as the response of PM1. This is due to the structure of the SBL being primarily symmetric about the line of sight. The response of the Tilt angle loop shows very clearly eight flexible modes. The dynamical

319

effect occurring at .6 rad/sec is due to the isolation system. The reponse of the SM loop indicates that six flexible modes of the model are significant in this loop while the responses of PM1 and PM2 indicate that only two modes show a large dynamical response in the two rate loops.

As stated earlier the design begins with the secondary mirror loop, and on close examination of the frequency response of the loop, the modes are found to be near perfectly phase stabilized. With this in mind, the loop is closed with a simple gain factor of 70 dB. This produces a gain margin of 22 dB with a phase margin of 40 degrees. Closing this loop with a gain factor of this magnitude will produce naturally tracking notches in the remaining loops at the frequencies of the dominant modes of this loop.[5] The resulting tilt angle loop response with the SM loop closed is shown in Figure 11. By comparing Figure 11 to Figure 10, the effects of the loop closure are obvious. Each mode that was phase stabilized and amplified in the SM loop is reduced in the tilt angle loop. In addition, by comparing the phases for each mode it is seen that the modes have been damped. The primary mirror segment loops were not appreciably affected since neither of the dominant modes of those loops are significant in the secondary mirror loop.

With the secondary mirror loop closed, the design proceeds with the first primary mirror segment loop in a similar manner. Close examination of the PM1 frequency response with the SM loop closed indicates the dominant modes to be near perfectly phase stabilized, however, the other flexible modes present are not phase stabilized and adding gain to these modes will result in the lowering of the damping of those modes in other loops containing modes of similar frequencies. A gain factor of 100 dB is chosen for compensation in this loop since dynamical compensation for the other modes would

320

not significantly enhance the design due to their low gain. The resulting gain margin is 24 dB. The results of the loop closure is very evident in the remaining primary mirror loops as well as the tilt angle loop. The dominant modes of PM1 have been completely eliminated in the remaining open loops as indicated by Figures 12 and 13. The damping of the flexible mode at 75 rad/sec has been decreased due to slightly to much gain in PM1, but comparison to Figure 11 shows that the overall response is now improved. Due to the similarity of the primary mirror loops nothing is to be gained by changing the design of 100 dB, and hence those loops are closed with 100 dB gain factors and similar gain margins results.

The effects of the closing of the rate loops on the tilt angle loop are easily seen by comparing Figures 10 and 14. The tilt angle loop now has the low frequency phase approaching from -90 degrees as opposed to it approaching from -180 degrees. In addition, the flexible modes have been damped by the rate loops automatically increasing the bandwidth. These improvements greatly aid in achieving a reasonable closed loop bandwidth and dynamic response for the tilt angle loop. The compensators used to achieve a high bandwidth and reasonable stability margins are listed as follows:

Gain Factor of 130 dB

First Order Lead Compensator that produces 55 degrees at 7 rad/sec.

$$D_1(z) = \frac{9.9595566\, z - 9.937599}{z - .09789425}$$

Second Order Dominant Pole Compensator with a break frequency of 11.3 rad/sec and a damping ratio of .1.

$$D_2(z) = \frac{3.19262\ z^2 + 6.38524\ z + 3.19262}{10000(1.00116\ z^2 - 1.99994\ z + .9989)}$$

First Order Lag Compensator that produces -10 dB and -30 degrees at 200 rad/sec.

$$D_3(z) = \frac{.2556939\ z - .2129331}{z - .9572393}$$

The compensated open loop tilt angle frequency response is shown in Figure 15. The stability margins of this response are

phase margin = 41 degrees

gain margin = 12 dB.

A closed loop frequency response of the tilt angle loop with all other loops closed is shown in Figure 16. From this plot of the response, the closed loop bandwidth is found to be 1.3 Hz. The resonant peak of the response is 3.9 dB occuring at .52 Hz, and no flexible modal peak is greater than -10 db.

Figures 17 and 18 show the frequency response of the secondary mirror loop and the first primary mirror segment loop respectively. Each response shown is an open loop response with all other loops closed. The purpose of this action is to examine the stability margins of each loop with all other loops closed. The original stability margin of the secondary mirror loop was a gain margin of 22 dB and a phase margin of 40 degrees. The original margins are relatively unchanged but an additional gain margin of 15 dB is now added due to the cancelation of the rigid body response in the loop. The first primary mirror loop has a gain margin that is relatively unchanged from its original value as well as the other two primary mirror rate loops.

322

Figure 21 shows the results of a step response of the SBL tilt angle control system. The response is clearly dominated by a pair of complex conjugate poles with an undamped natural frequency of approximately .5 Hz (as is suggested by the frequency domain analysis). The percent overshoot is approximately 48% while the settling time is 2.3 seconds.

In addition to a reasonable dynamical response, it is desirable to have a robust design. Figures 19 and 20 indicate that the design is indeed robust. Figure 19 is an open loop response of the tilt angle loop with the first two flexible modes reduced in frequency by 20%. The gain margin and phase margin are now 3 dB and 42 degrees respectively. Although the gain margin is reduced, the system is still closed loop stable. The closed loop response of the tilt angle loop shows an unchanged bandwidth and resonant peak with a modal peak of 7 dB.

A step response of this perturbed model is shown in Figure 22. The response clearly shows the undamped pair of complex conjugate poles at 15 rad/sec. Although the step response has a high frequency component added to it, both pair of poles "die" out at approximately the same rate. The percent overshoot has increased to 75% while the settling time has remained relatively unchanged.

Disturbance rejection is a requirement of the SBL design for the line of sight or tilt angle. Figures 23 and 24 show the open and closed loop for both an aft disturbance and secondary mirror coolant disturbance respectively. The closed loop response is reduced in comparison to the open loop response in both figures and indicates good disturbance rejection by the designed system.

In addition, the disturbance rejection properties of the system is illustrated by the application of the Aft Disturbance PSD of Figure 25 and the Coolant Disturbance PSD of Figure 27. Again it is seen by Figures 26 and 28 that the closed loop response shows a marked improvement over the open loop response of the tilt angle loop.

1ST PRIMARY SEGMENT 00000

1loop22

Figure 8. 1st Primary Mirror Rate (rad/sec)/1st Primary Mirror Applied Torque (N-m) all Feedback Paths Open.

Sat Mar 20

SECONDARY MIRROR LOOP 00000

openlp11
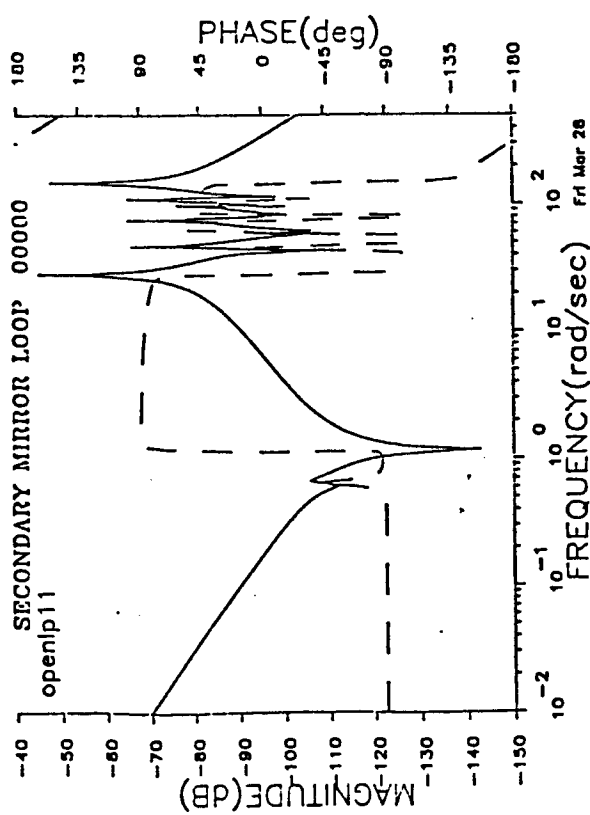
Figure 7. Secondary Mirror Angular Rate (rad/sec)/Secondary Mirror Applied Torque (N-m) all Feedback Paths Open.

Fri Mar 20

ATTITUDE LOOP 00000

openlp55

Figure 10. Tilt Angle (Rad)/Gimbal Point Torque (N-m), all Feedback Paths Open.

Fri Mar 20

2ND PRIMARY SEGMENT 00000

1loop33
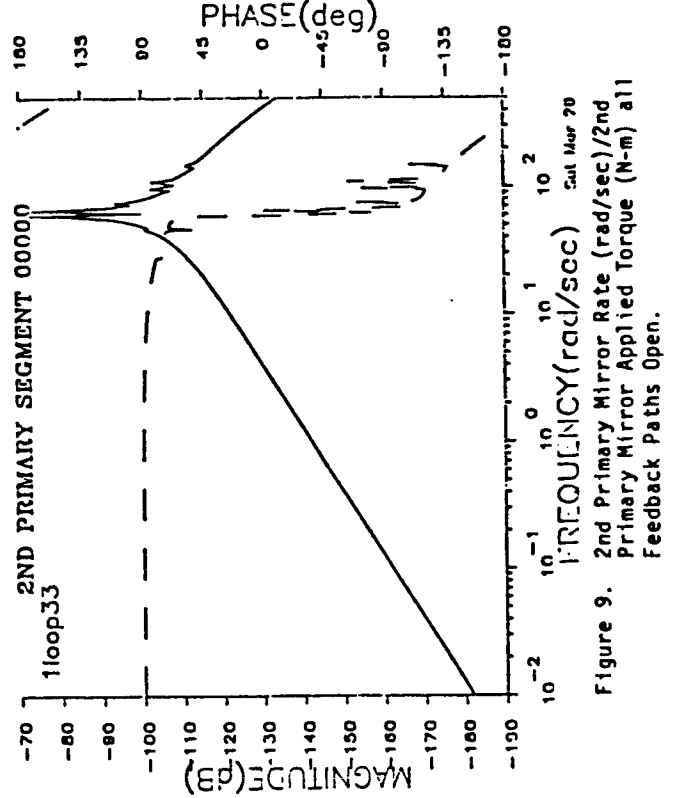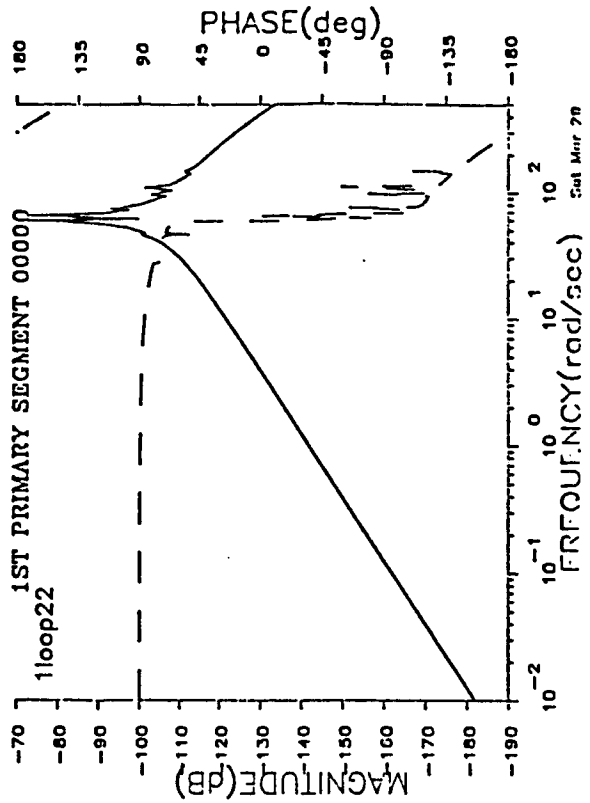
Figure 9. 2nd Primary Mirror Rate (rad/sec)/2nd Primary Mirror Applied Torque (N-m) all Feedback Paths Open.

Sat Mar 20

Figure 12. 2nd Primary Mirror Rate (rad/sec)/2nd Primary Mirror Applied Torque (N-m) SM, and 1st PM Loops Closed.

Figure 14. Tilt Angle (rad)/Gimbal Point Torque (N-m) All Mirror Rate Loops Closed.
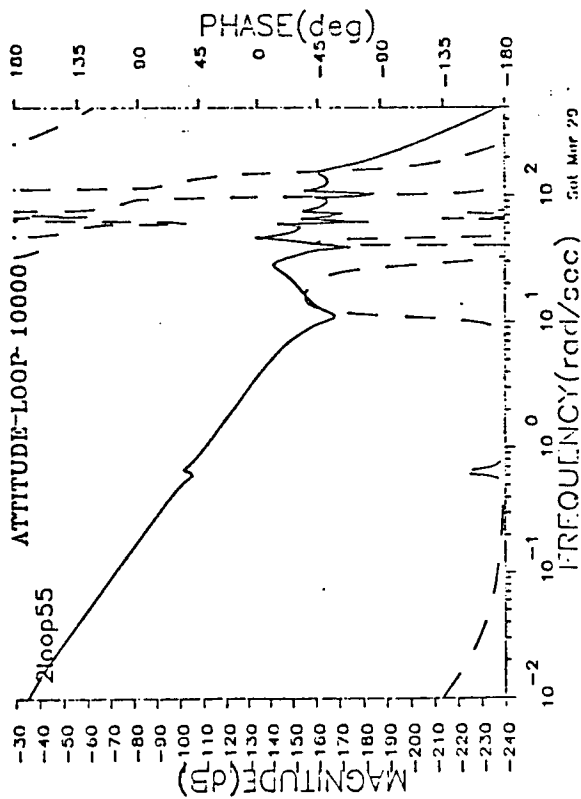
Figure 11. Tilt Angle (Rad)/Gimbal Point Torque (N-m), Secondary Mirror Loop Closed.
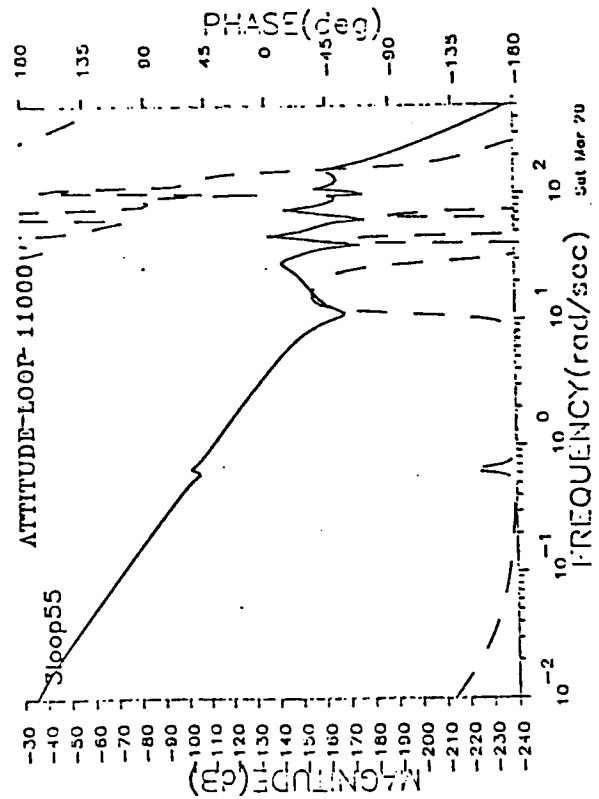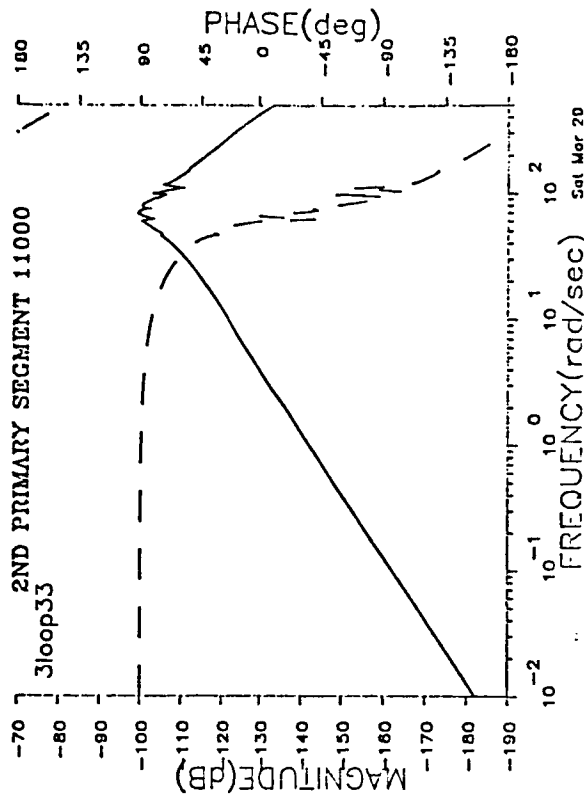
Figure 13. Tilt Angle (Rad)/Gimbal Point Torque (N-m), SM and 1st PM Loops Closed.

326
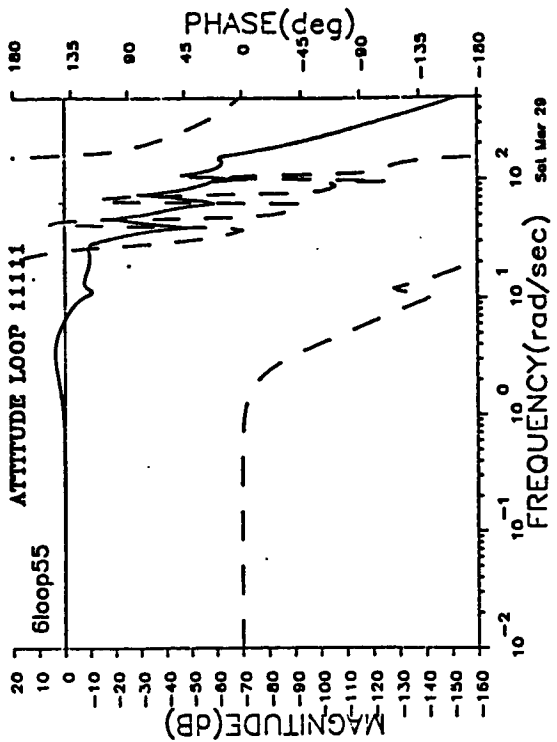
Figure 16. Tilt Angle (rad)/Gimbal Point Torque (N-m)
All Loops Closed.
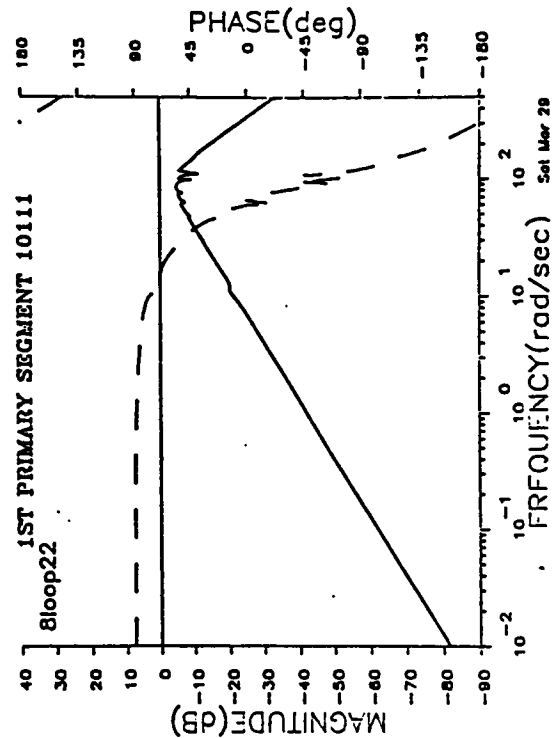
Figure 18. 1st Primary Mirror Rate (rad/sec)/1st Primary
Mirror Applied Torque (N-m), 1st Primary Loop
Open.
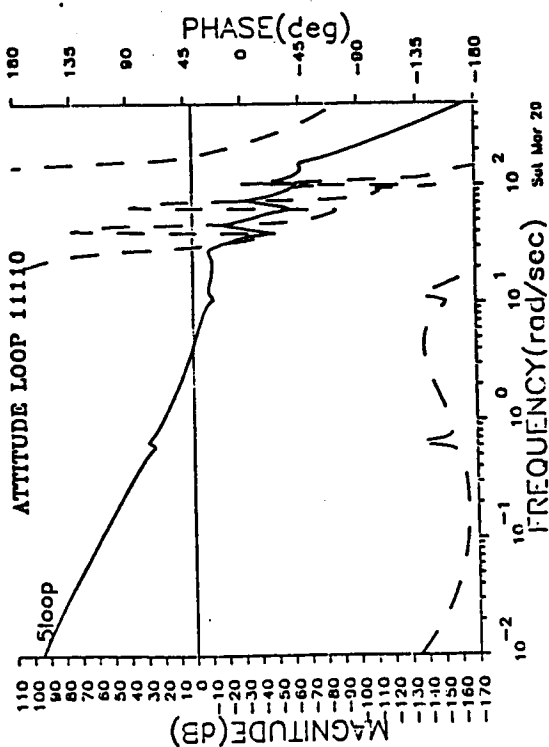
Figure 15. Tilt Angle (rad)/Gimbal Point Torque (N-m)
All Mirror Rate Loops Closed, $D_2(z)^{55}$ Included.
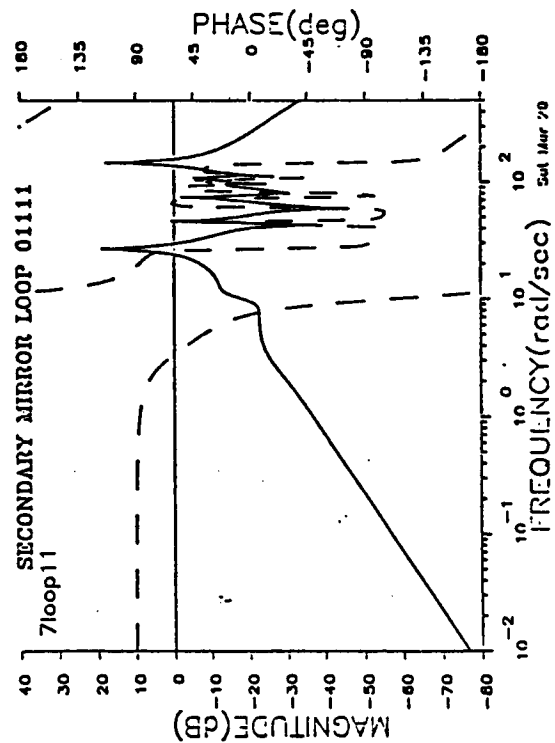
Figure 17. Secondary Mirror Rate (rad/sec)/Secondary Mirror
Applied Torque (N-m), SM Loop Open.

327

Figure 20. Tilt Angle (rad)/Gimbal Point Torque (N-m) All Loops Closed. First 2 Modes Reduced in Frequency by 20%.
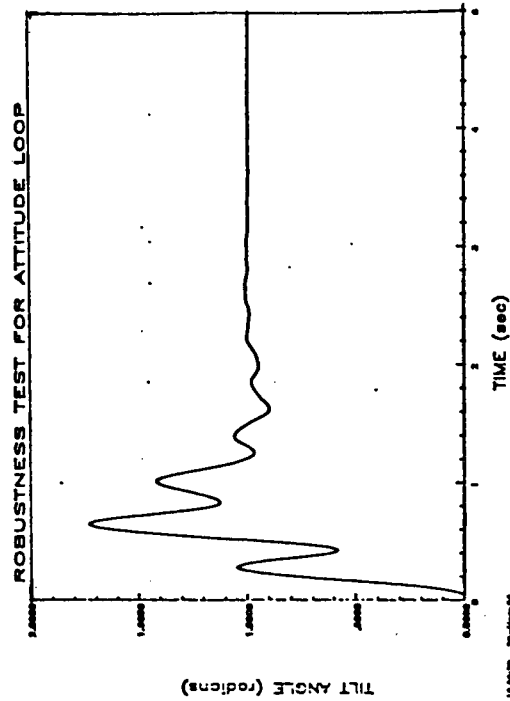
Figure 22. Tilt Angle Response to a Unit Step Command Input with the First 2 Modes Reduced in Frequency by 20%.

Figure 19. Tilt Angle (rad)/Gimbal Point Torque (N-m) Tilt Loop Open First 2 Modes Reduced in Frequency by 20%.

Figure 21. Tilt Angle Response to a Unit Step Command Input.

328
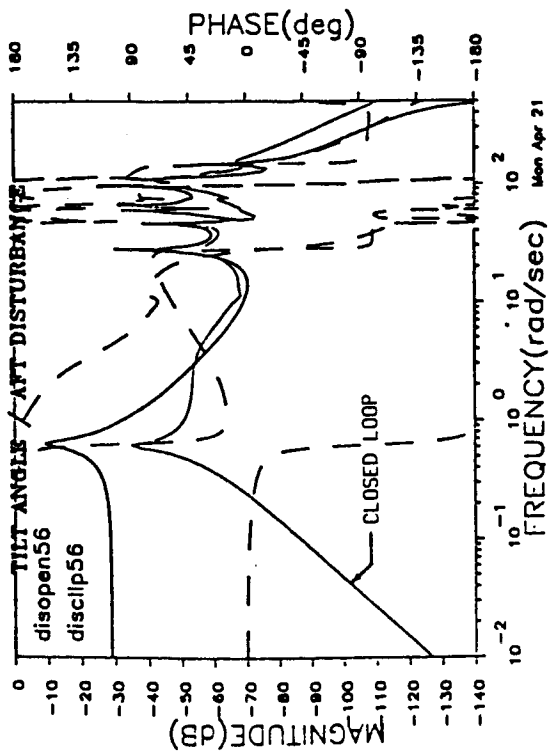
Figure 23 Tilt Angle (Rad)/AFT Disturbance Displacement Open Loop and with all Loops Closed.
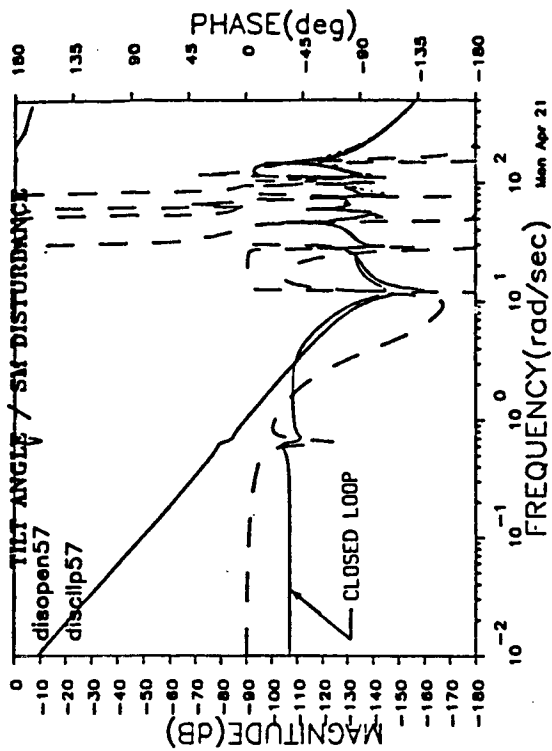
Figure 24 Tilt Angle (Rad)/SM Coolant Disturbance, Open Loop and with all Loops Closed.
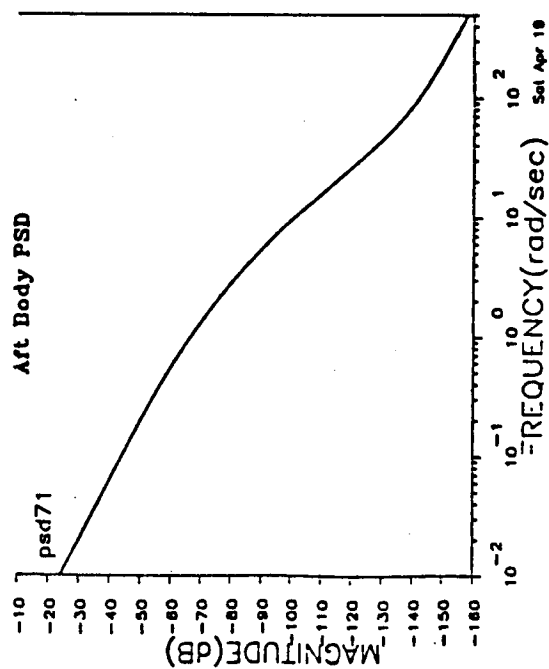
Figure 25 AFT Body Disturbance PSD dB=10 Log₁₀ (Mag)
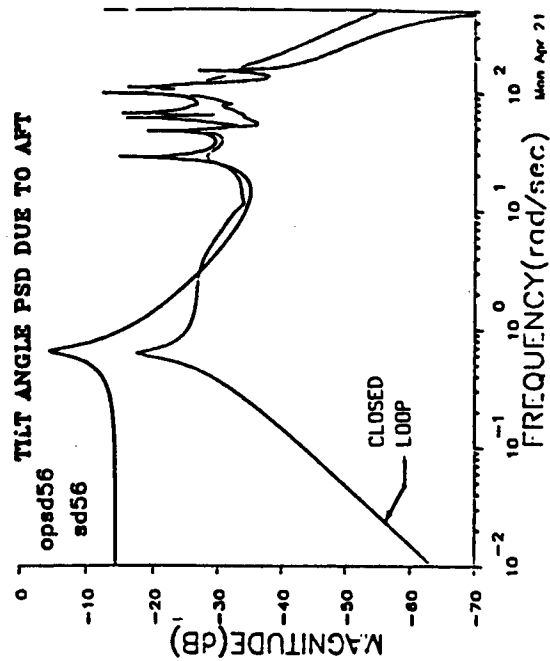
Figure 26 Tilt Angle PSD Due to AFT Body Disturbance, Open Loop and with all Loops Closed dB=10 Log₁₀ (Mag).
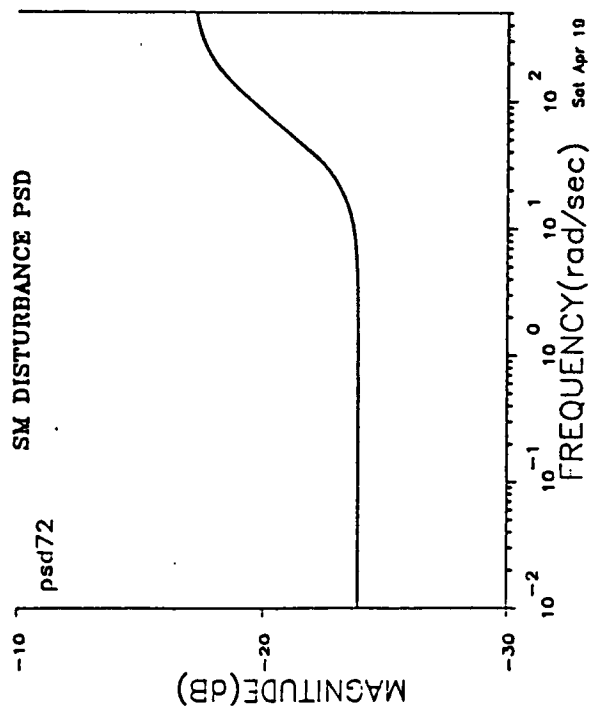
329

TILT ANGLE PSD DUE TO SM

opsd57
psd57

CLOSED
LOOP

MAGNITUDE(dB)

FREQUENCY(rad/sec) Mon Apr 21

Figure 28 Tilt Angle PSD Due to SM Disturbance, Open Loop
and with all Loops Closed dB=10 Log$_{10}$ (Mag).

SM DISTURBANCE PSD

psd72

MAGNITUDE(dB)

FREQUENCY(rad/sec) Sat Apr 10

Figure 27 SM Coolant Flow Disturbance PSD dB=10 Log$_{10}$ (Mag).

Conclusion

In this paper the 1-CAT technique for designing multivariable control systems has been presented. The 1-CAT approach, within itself, does not dictate any particular design domain, although in the work presented here, frequency response techniques have been emphasized. Frequency domain techniques were selected in order that large order systems could be handled as easily as low order systems. In particular, after the frequency responses describing the plant are generated, system order is completely transparent in the 1CAT approach. The salient features of 1-CAT are as follows:

1. Provided the system is stabilizable, 1-CAT will produce a closed loop stable system.

2. The overall controller is relatively simple in comparison to those generated by modern control techniques, which typically produce controllers on the same order as the system model used.

3. By designing for a specified amount of relative stability and using phase stabilization of significant modes,[5] robustness is an inherent part of the design.

4. 1-CAT is a straightforward, step-by-step procedure.

The 1-CAT approach was illustrated by designing a tilt angle control system for a planar model of the SBL. Although the design was for a single axis of the SBL, this is not a limitation of the 1-CAT technique. Design for a multiple axis model could have been done in a similar straightforward manner. A three axis design would be achieved by first designing all of the rate loops and then designing the position loops.

This paper has shown that the 1-CAT approach is a viable candidate for designing controllers for multiple input, multiple output systems. 1-CAT

assures a stable system. Since 1-CAT is straigntforward, it appears feasible that it could be used as the basis of a self-tuning control algorithm. It is also feasible that 1-CAT could provide a baseline design that could then be optimized by other design approaches, e.g., a modified MIMO CIP,[6] in order to maximize disturbance rejection while maintaining reasonable stability and robustness.

References

1. "ACOSS Five (Active Control of Space Structures) Phase II," Lockheed Missiles and Space Company, Inc., Sponsored by Defense Advanced Research Projects Agency, Report No. RADC-TR-82-21, March 1982.

2. "ACOSS Eight (Active Control of Space Structures) Phase II," TRW, Sponsored by Defense Ad-vanced Research Projects Agency, Report No. RADC-TR-81-242, September 1981.

3. "ACOSS Fourteen (Active Control of Space Structures)," TRW, Sponsored by Defense Advanced Research Projects Agency, Contract No. F30602-81-0194, November 1982.

4. "ACOSS One (Active Control of Space Structures) Phase I," General Dynamics, Sponsored by Defense Advanced Research Projects Agency, Report No. RADC-TR-80-79, March 1980.

5. J. R. Mitchell, H. Eugene Worley, and Sherman M. Seltzer, "Digital Control System Design for a Precision Pointing System," Annual Rocky Mountain Guidance and Control Conference, Keystone, Colo-rado, February 5-9, 1983.

6. L. L. Gresham, J. R. Mitchell, and W. L. McDaniel, Jr., "A Multivariable Control System De-sign Algorithm," AIAA Journal of Guidance and Control, Vol. 3, No. 4, July August 1980.

Acknowledgement

COMMIT YOUR WORKS TO THE LORD, AND YOUR THOUGHTS SHALL BE ESTABLISHED
PROV. 16:3

INTER—STABLE CONTROL SYSTEMS

BY

GEORGE L. VON PRAGENAU
SYSTEMS DYNAMICS LABORATORY
NASA MARSHALL SPACE FLIGHT CENTER
HUNTSVILLE, AL 35812
APRIL 22, 1986

WORKSHOP ON STRUCTURAL DYNAMICS AND CONTROL
INTERACTION OF FLEXIBLE STRUCTURES

850108

INTER-STABLE CONTROL SYSTEMS

by

George L. von Pragenau

NASA Marshall Space Flight Center
Huntsville , Al. 35812

Algebraic structures are discussed for control systems that maintain stability in the presence of resonance uncertainties. Dual algebraic operations serve as elementary connections that propagate the stability of inter-stable subsystems. Frequency responses within complex half-planes define different types of inter-stability. Dominance between incompatible types is discussed. Inter-stability produces sufficient but unnecessary stability conditions, except for conservative systems where the conditions become also necessary. Multivariable systems, colocation of actuator and sensor, and virtual colocation are treated. Instead of passivity, inter-stability relates stability to the mapping of poles and zeros by transfer functions and transfer matrices. Inter-stability determines stability on the subsystem level, is less complex even for multivariable systems, adds design flexibility, and relaxes the dynamic data problem of large systems such as space stations.

1   INTER-STABILITY IS THE PROPAGATION OF STABILITY THROUGH ALGEBRAICALLY DEFINED CONNECTIONS OF COMPATIBLE SUBSYSTEMS.

2   COMPATIBLE SUBSYSTEMS ARE STABLE AND SHARE A COMPLEX HALF-PLANE FOR ALL MAPPINGS OF THE 1st QUADRANT FROM THE COMPLEX FREQUENCY PLANE.

3   ONLY LINEAR AND CONSTANT SYSTEMS ARE CONSIDERED IN THE FORM OF TRANSFER FUNCTIONS AND TRANSFER MATRICES.

4   ADDITION, REDUCTION (I.E. INVERSE ADDITION), AND MATRIX COUPLING (E.G. INCIDENCE MATRICES) SPECIFY THE CONNECTIONS.

5   INTER-STABILITY IS DIRECTLY BASED ON THE EIGENVALUE MAPPING OF PROPERLY CONNECTED SUBSYSTEMS INSTEAD OF A PASSIVITY CONCEPT.

6   INTER-STABILITY YIELDS RESONANCE-INERT (ROBUST) CONTROL SYSTEMS WITH THE ADDED BENEFIT OF ANALYZING LOW ORDER SUBSYSTEMS.

PHYSICAL CONNECTIONS ARE DEFINED BY THE ALGEBRAIC OPERATIONS OF ADDITION, RE-
DUCTION, AND MATRIX COUPLING. THE OPERATIONS KEEP VECTORS IN A SEMIPLANE.

1   ADDITION + WITH THE UNIT ELEMENT 0 HAS THE DOMINANCE ELEMENT @.
     A+0=A, @+A=@, A-A=0, A+B=B+A, (A+C)c=Ac+Bc, @c=@

2   REDUCTION x WITH THE UNIT ELEMENT @ HAS THE DOMINANCE ELEMENT 0.
     Ax@=A, 0xA=0, A\A=@, AxB=BxA, (AxB)c=AcxBc, 0c=0

3   ADDITION AND REDUCTION ARE PARALLEL AND SERIES CONNECTIONS WITH A DUALITY.
     (AxA)+(AxA)=A, (A+A)x(A+A)=A, 1/(A+B)=(1/A)x(1/B), 1/(AxB)=(1/A)+(1/B)

4   SUBDUCTION \ IS THE DUAL OF SUBTRACTION AND CONNECTS NEGATIVE SUBSYSTEMS.
     NEGATIVE SUBSYSTEMS ARE INCOMPATIBLE, BUT CAN BE DOMINATED.

5   MATRIX COUPLING IS THE TRANSFORMATION OF A DIAGONAL MATRIX D OF SUBSYSTEM
     ELEMENTS BY INCIDENCE, MODAL, AND ROTATION MATRICES T. M=T',D·T

SYSTEMS DYNAMICS

INTER-STABILITY EXPERIENCE

NASA MSFC GLvP

LABORATORY ED14

APRIL 22, 1986

==

1965 INTER-STABILITY CRITERIA FROM HALF-PLANE IMAGES AND ALGEBRAIC CONNECTIONS
WERE DEFINED AND APPLIED TO STABILIZE THE SATURN-V HYDRAULIC SUPPORT.

1970 INTER-STABILITY CRITERIA FOR SPACE VEHICLE ATTITUDE CONTROL WERE DOCU-
MENTED IN A SECRET REPORT (NOW DECLASSIFIED).

1972 INTER-STABILITY WAS PROPOSED FOR RESONANCE-INERT STABILITY OF SPACE
STATIONS (NASA TN D-6731, JUNE 1972).

1974 FEASIBILITY OF INTER-STABLILITY FOR THE SPACE SHUTTLE WAS SHOWN AND
PROPOSED TO JSC.

1976 RECEIVED A PATENT ON COLOCATED RATE GYROS FOR ATTITUDE REFERENCE WITH
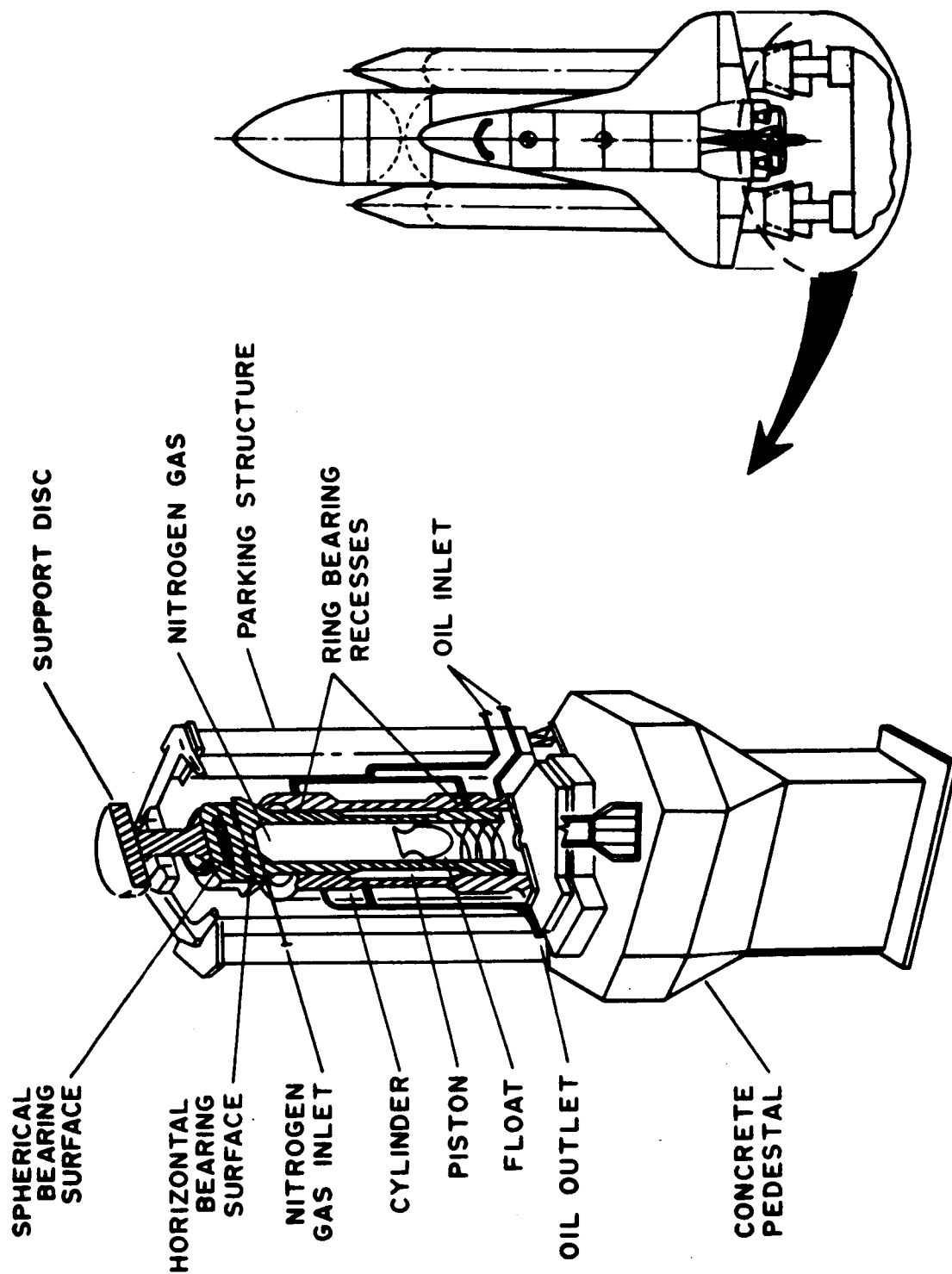PLATFORM UPDATING AND ANOTHER PATENT ON VIBRATION ATTENUATION.

SYSTEMS DYNAMICS   SPACE SHUTTLE 6-DEGREES OF FREEDOM SUPPORT   NASA MSFC GLvP

LABORATORY ED14   APRIL 22, 1986

FOUR SUPPORTS HELD THE SATURN-V AND SPACE SHUTTLE DURING GROUND VIBRATION TESTS AS IN FREE FLIGHT WITHOUT FRICTION. HYDRAULIC BEARINGS AND PNEUMATIC PISTONS PROVIDED FRICTIONLESS LOW MASS SUPPORT. THE VEHICLES WERE TESTED FULL SIZE.

SUPPORT DISC

NITROGEN GAS

PARKING STRUCTURE

RING BEARING RECESSES

OIL INLET

SPHERICAL BEARING SURFACE

HORIZONTAL BEARING SURFACE

NITROGEN GAS INLET

CYLINDER

PISTON

FLOAT

OIL OUTLET

CONCRETE PEDESTAL

SYSTEMS DYNAMICS   INTER-STABLY DESIGNED HYDRAULIC SUPPORT UNIT   NASA MSFC GLvP

LABORATORY ED14   APRIL 22, 1986

THE HYDROSTATIC BEARINGS AND THE PNEUMATIC PISTON WERE DESIGNED INTER-STABLY.
THE PISTON MODEL, A 2nd/2nd ORDER QUOTIENT TRANSFER FUNCTION, WAS KEPT POSITIVE
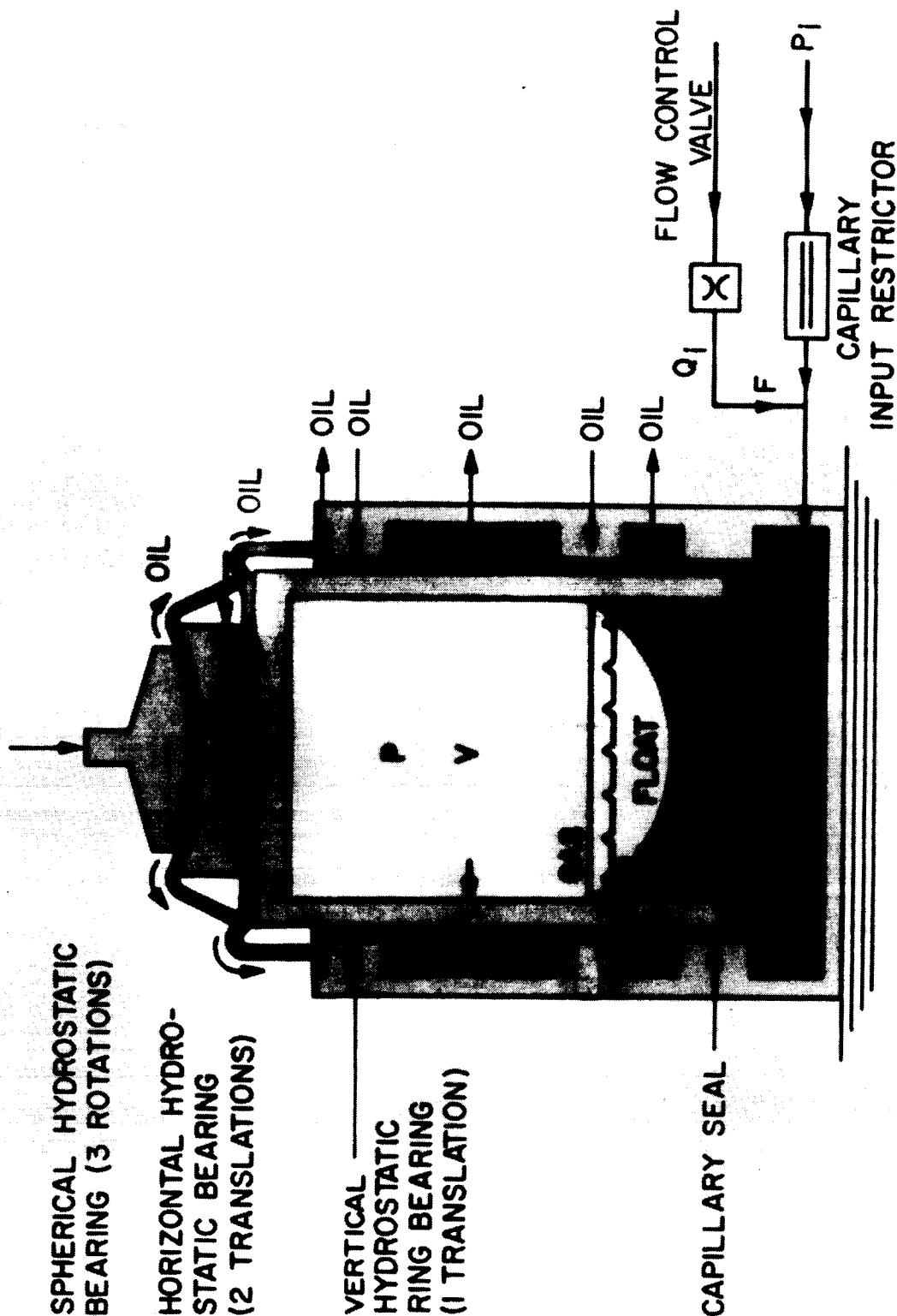IMAGINARY LIKE THE TEST ARTICLE WHICH IS ADDITIVELY CONNECTED.

SPACE VEHICLE's LOAD

OIL

OIL
OIL

OIL

OIL

OIL

OIL

FLOW CONTROL VALVE

Q_1

F

P_1

CAPILLARY INPUT RESTRICTOR

FLOAT

SPHERICAL HYDROSTATIC BEARING (3 ROTATIONS)

HORIZONTAL HYDRO-STATIC BEARING (2 TRANSLATIONS)

VERTICAL HYDROSTATIC RING BEARING (I TRANSLATION)

CAPILLARY SEAL

SCHEMATIC OF HYDRAULIC SUPPORT UNIT

341

SYSTEMS DYNAMICS   NASA MSFC GLvp

              POSITIVE IMAGINARY INTER-STABLE MAPPING EXAMPLE

LABORATORY ED14   APRIL 22, 1986

INTER-STABLE TRANSFER FUNCTIONS MAP FROM THE 1st QUADRANT OF THE COMPLEX FRE-
QUENCY PLANE INTO A COMPLEX HALF-PLANE. THE HALF-PLANE's ORIGIN IS THE IMAGE OF
THE ZEROS AND INFINITY THE IMAGE OF THE POLES. THE FIRST QUADRANT EXCLUDES THE
ORIGIN AND THE IMAGINARY AXIS, BUT INCLUDES THE POSITIVE REAL AXIS. POSITIVE
IMAGINARY SYSTEMS MAP INTO THE UPPER HALF-PLANE AND ONTO THE POSITIVE REAL AXIS
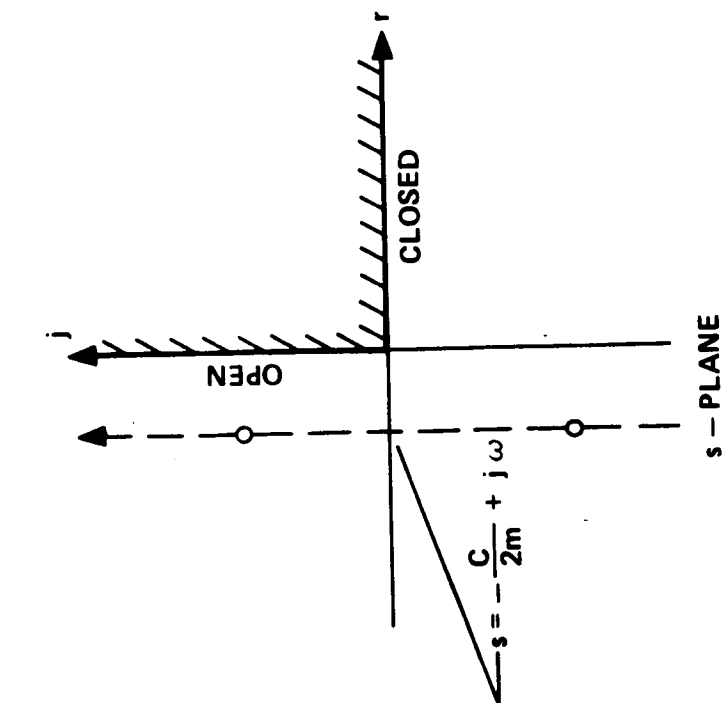WITHOUT THE ORIGIN. THE NEGATIVE REAL AXIS IS EXCLUDED.
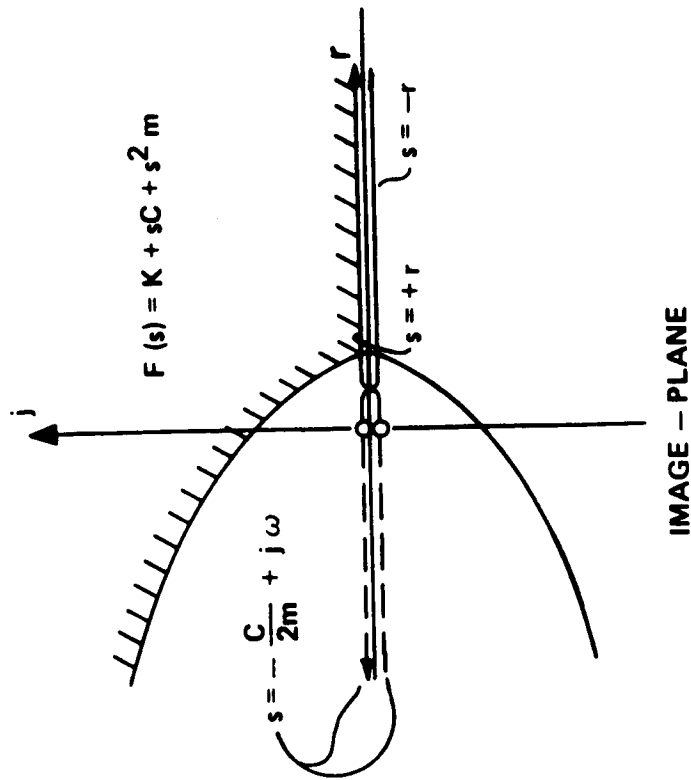
$$F(s) = K + sC + s^2 m$$

$s = +r$

$s = -r$

$s = -\dfrac{C}{2m} + j\omega$

IMAGE – PLANE

$s = -\dfrac{C}{2m} + j\omega$

OPEN

CLOSED

s – PLANE

SYSTEMS DYNAMICS

NASA MSFC GLvP

SUBSYSTEM TRANSFER FUNCTIONS ARE STABLE AND MAP THE COMPLEX FREQUENCY PLANE'S 1ST QUADRANT INTO A COMPLEX HALF–PLANE. THE ORIGIN IS THUS NOT ENCIRCLED.

1   THE 1ST QUADRANT INCLUDES THE POSITIVE REAL AXIS, BUT EXCLUDES THE IMAGINARY AXIS. CONSERVATIVE SYSTEMS ARE THUS CONSIDERED AS INTER–STABLE.

2   POSITIVE REAL SYSTEMS MAP INTO THE RIGHT HALF–PLANE OUTSIDE THE IMAGINARY AXIS, e.g., $a_1 b_1 > [SQR(a_0 b_2) - SQR(a_2 b_0)]$ FOR 2ND/2ND ORDER QUOTIENTS.

3   POSITIVE IMAGINARY SYSTEMS MAP INTO THE UPPER HALF–PLANE OUTSIDE THE NEGATIVE REAL AXIS AND ORIGIN, e.g., $a_0/b_0 < a_1/b_1 < a_2/b_2$ FOR 2ND/2ND ORDER.

4   NEGATIVE IMAGINARY SYSTEMS MAP INTO THE LOWER HALF–PLANE OUTSIDE THE NEGATIVE REAL AXIS AND ORIGIN, e.g., $a_0/b_0 > a_1/b_1 > a_2/b_2$ FOR 2ND/2ND ORDER.

5   NEGATIVE IMAGINARY SYSTEMS BECOME POSITIVE IMAGINARY SYSTEMS BY INVERSION AND VICE VERSA.

6   POSITIVE REAL SYSTEMS BECOME POSITIVE (NEGATIVE) IMAGINARY WHEN MULTIPLIED (DIVIDED) BY THE COMPLEX FREQUENCY s AND VICE VERSA.

7   NEGATIVE IMAGINARY SYSTEMS BECOME POSITIVE IMAGINARY WHEN MULTIPLED WITH THE COMPLEX FREQUENCY SQUARE s^2 AND VICE VERSA WHEN DIVIDING WITH s^2.

CONSTANT GAIN SYSTEMS ARE STABLE WHEN THE BELOW CRITERIA ARE MET. INTER-STABIL-
ITY IS MORE RESTRICTIVE, BUT UNRESTRICTED IN RESONANCES AND HIGH SYSTEM ORDERS
DUE TO THE BUILDING BLOCK APPROACH.

STABLE OPERATIONS & INVERSION

Ω SET OF CONSTANT GAIN SYSTEMS

Σ SET OF STABLE SYSTEMS, $\left\{ S, S_1, S_2 \right\} \subset \Sigma \subset \Omega$

ADDITION	$S_1 + S_2 \in \Sigma$
MATRIX PRODUCT	$S_1 S_2 \in \Sigma$
ADJOINT	adj $S \in \Sigma$
DETERMINANT	$|S| \in \Sigma$
MATRIX INVERSION S^{-1} = adj $S / |S| \in \Omega$	

NECESSARY & SUFFICIENT FOR STABILITY: CONSIDER ZEROS OF $|S|$ ONLY

SYSTEMS DYNAMICS   NASA MSFC GLvP

LABORATORY ED14   SATURN-V POGO STABILITY CASE   APRIL 22, 1986

POGO IS AN AXIAL VEHICLE OSCILLATION DUE TO MECHANICAL VECTOR FEEDBACK FROM THE
TANK PRESSURES OVER THE ENGINE THRUSTS TO THE AXIAL VEHICLE RESONANCES.

INTERFACE OF PROPULSION & VEHICLE STRUCTURE

SYSTEMS DYNAMICS

NASA MSFC GLvP

LABORATORY ED14

SATURN-V POGO VECTOR FEEDBACK LOOP

APRIL 22, 1986

==

THE FEEDBACK VECTOR HAS FOUR P-COMPONENTS THAT REPRESENT PROPULSION GAINS FROM TANK PRESSURES TO TWO ENGINE GROUPS. THE D's ARE DISTURBANCES. OMEGA INVERSE IS A DIAGONAL MATRIX OF RIGID VEHICLE MASS AND STRUCTURAL RESONANCES. THE DIAGONAL MATRIX CLOSES THE FEEDBACK LOOP THROUGH RECTANGULAR COUPLING (MODAL) MATRICES.
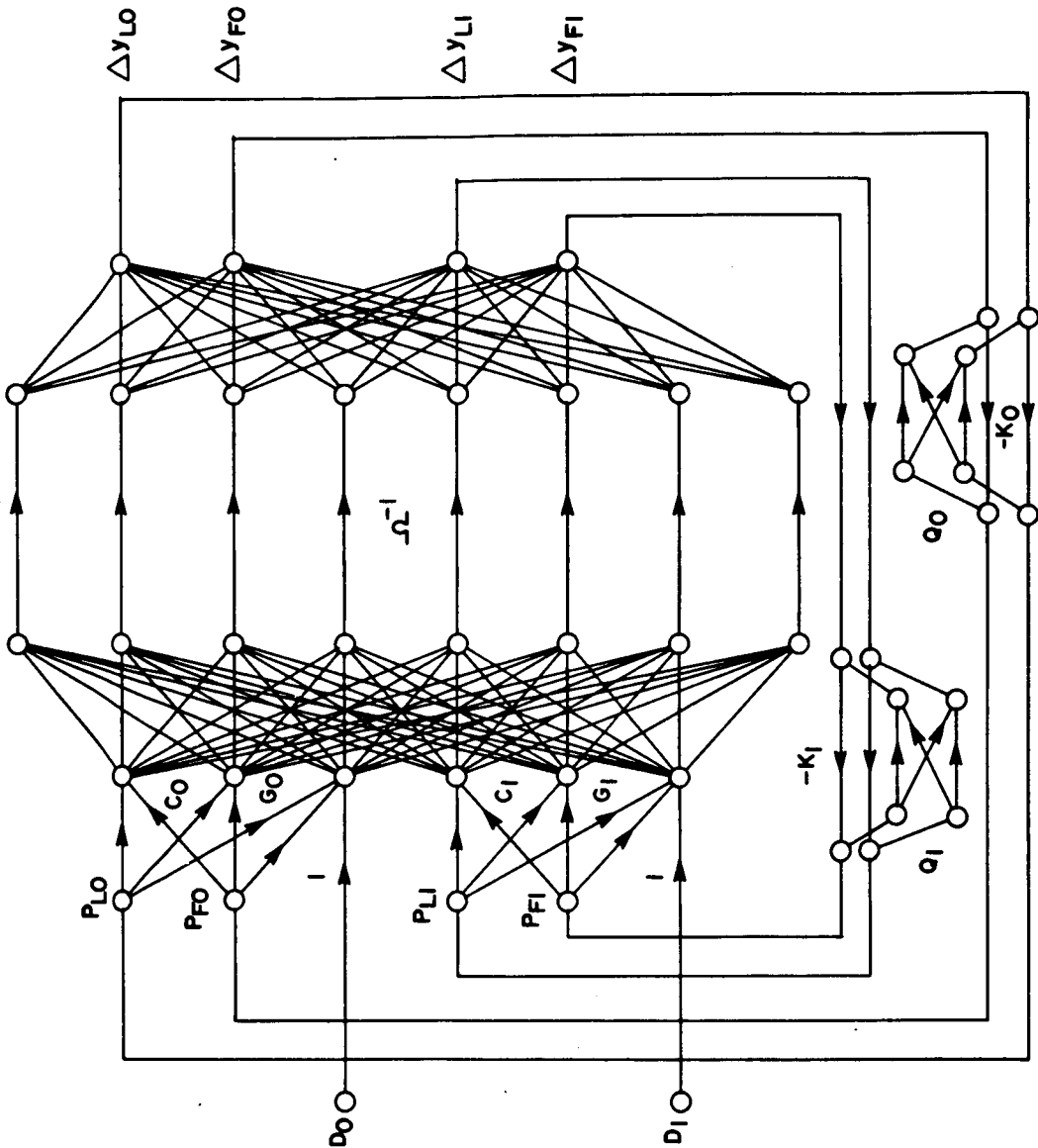
FREQUENCY RESPONSE OF POGO SYSTEM MATRIX DETERMINANT SHOWS SYSTEM INSTABILITY BY
ENCIRCLING THE ORIGIN. A STABLE TRANSFER MATRIX FORMULATION WAS USED, REQUIRING
A FINAL MATRIX INVERSION. THE METHOD GENERALIZES THE NIQUIST CRITERION.

SCALE
MAX. AMPL X 10^{-17}
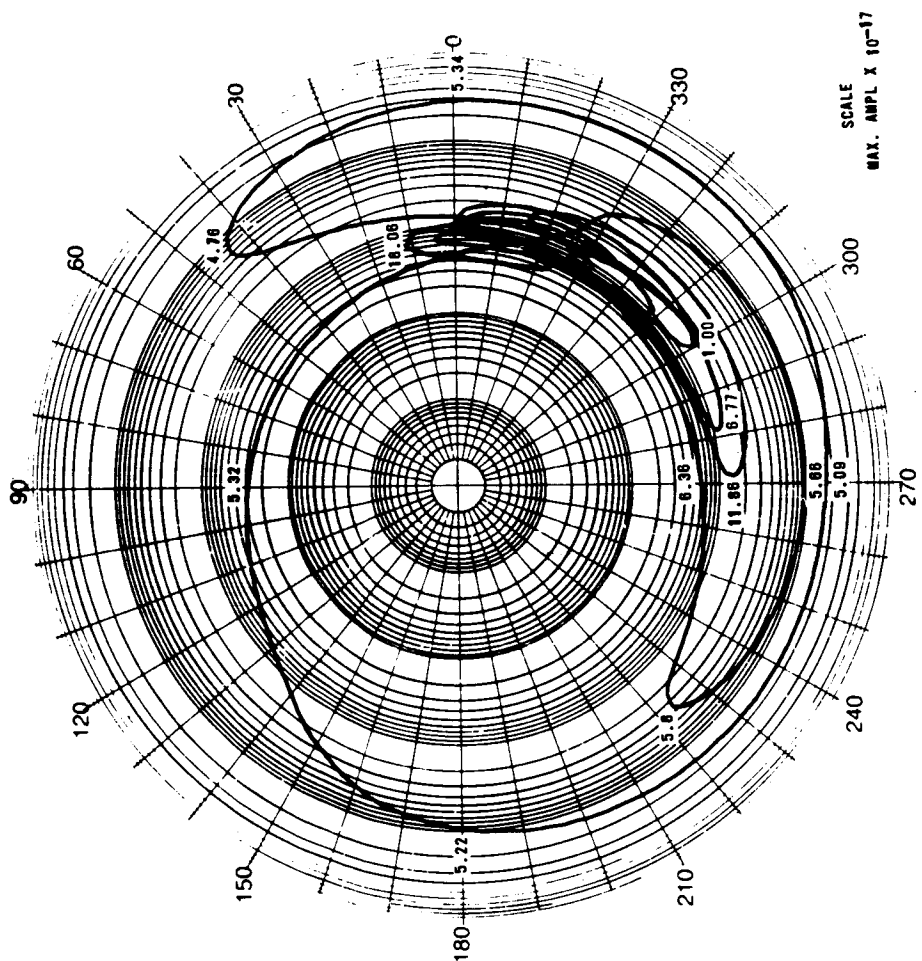
SATURN V FIRST FLIGHT STAGE OF AS–502 MISSION
AT 120 SEC FLIGHT TIME

NASA MSFC GLvP

LABORATORY ED14 STABLE DETERMINANT PLOT OUTSIDE OF ORIGIN APRIL 22, 1986

==

FREQUENCY RESPONSE OF POGO SYSTEM MATRIX DETERMINANT SHOWS SYSTEM STABILITY BY
NOT ENCIRCLING THE ORIGIN. A STABLE TRANSFER MATRIX FORMULATION WAS USED,
REQUIRING A FINAL MATRIX INVERSION. PLOT SHOWS SUCCESSFUL ELIMINATION OF POGO.
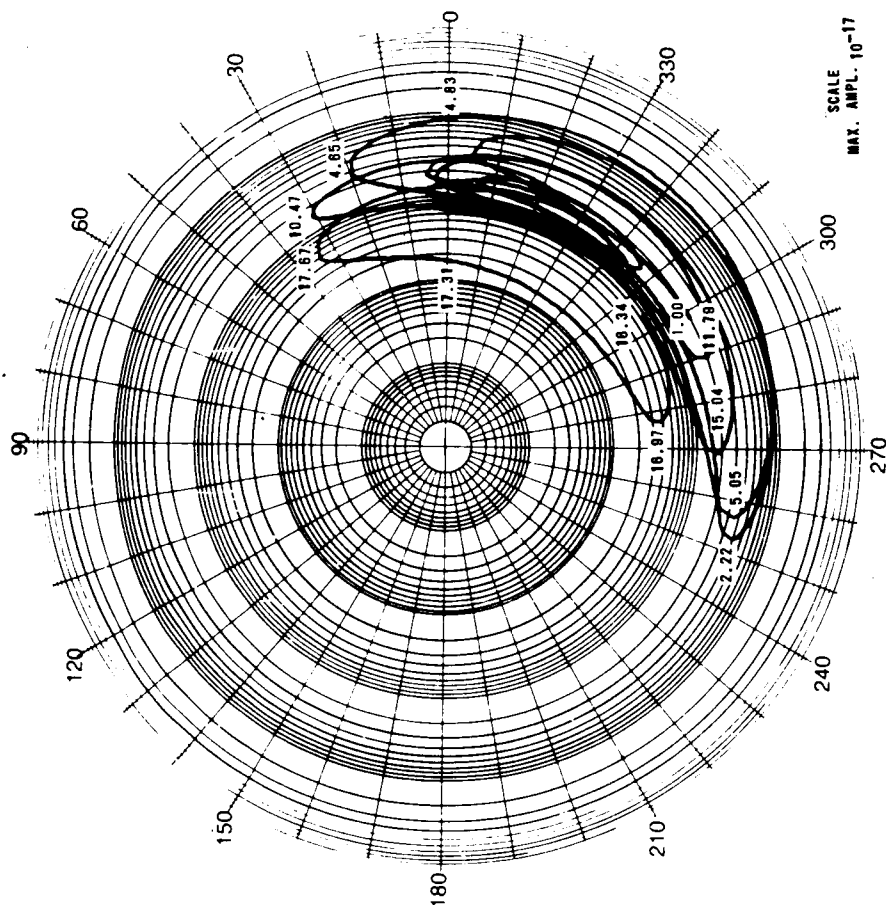
**SATURN V FIRST FLIGHT STAGE OF AS-504 MISSION
AT 120 SEC FLIGHT TIME**

SCALE
MAX. AMPL. 10^{-17}

SYSTEMS DYNAMICS

INTER-STABLE TRANSFER MATRICES

NASA MSFC GLvP

LABORATORY ED14

APRIL 22, 1986
===

INTER-STABLE TRANSFER MATRICES ARE COMPLEX DEFINITE, HAVE INTER-STABLE TRANSFER FUNCTIONS AS ELEMENTS, AND ARE INTER-STABLE UNDER ADDITION AND REDUCTION.

1 THE TRANSFER MATRIX M IS COMPLEX DEFINITE IF THE QUADRATIC FORM $Q = u'M u$ MAPS INTO THE ELEMENTS' HALF-PLANE FOR ALL COMPLEX VECTORS u.

2 MATRIX INVERSION HAS A COMPLEX CONJUGATE (DENOTED BY ') QUADRATIC FORM $P = v'M^{-1} v = u'M'u = Q'$ FOR $v = M u$ AND THUS IS INTER-STABLE.

3 MATRIX ADDITION PRESERVES THE INTER-STABILITY OF THE ELEMENTS AS SEEN FROM $Q = u' (M + N) u = u'M u + u'N u$.

4 THE INVERSION OF A MATRIX SUM PRESERVES INTER-STABILITY AS SEEN FROM $Q = v' (M + N)^{-1} v = u' (M' + N') u = u'M'u + u'N'u$ FOR $v = (M + N) u$.

5 MATRIX REDUCTION PRESERVES INTER-STABILITY AS SEEN FROM $Q = u' (M x N) u = v' (M'^{-1} + N'^{-1}) v = v'M'^{-1} v + v'N'^{-1} v$ FOR $v = (M x N) u$.

6 MATRIX REDUCTION IS COMMUTATIVE LIKE ADDITION AND IS DEFINED AS FOLLOWS $M x N = (M^{-1} + N^{-1})^{-1} = (N^{-1} + M^{-1})^{-1} = N x M$.
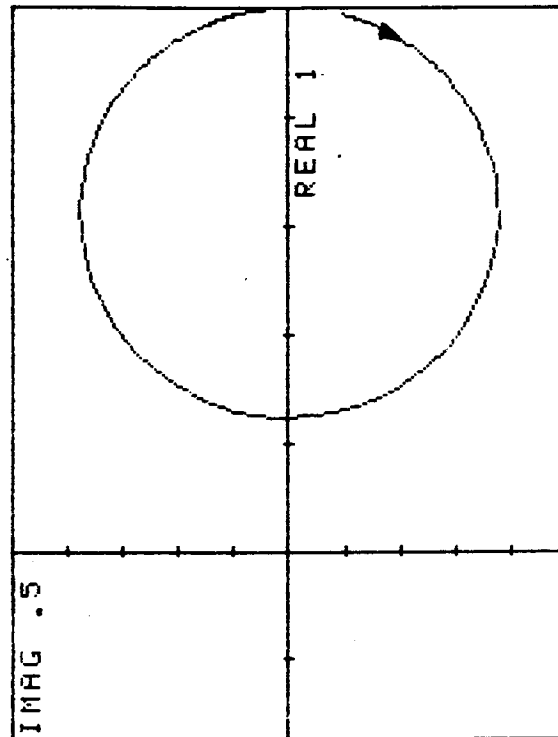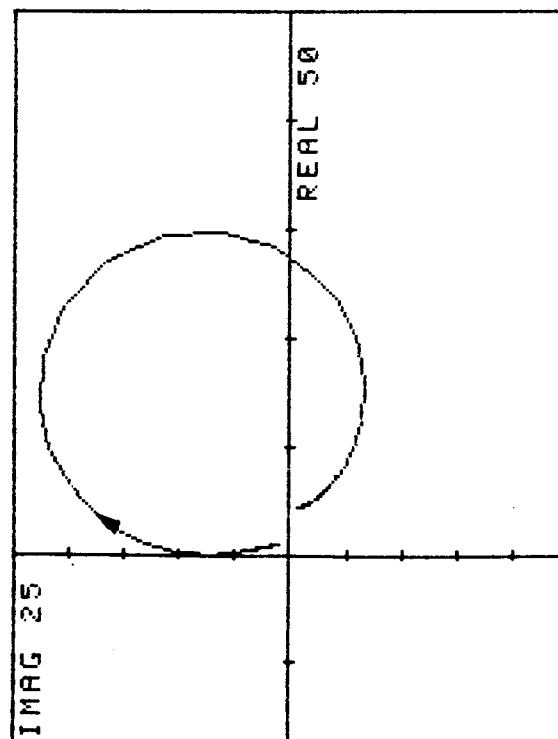
349

SYSTEMS DYNAMICS   POSITIVE REAL TRANSFER FUNCTION   NASA MSFC GLvP

LABORATORY ED14   APRIL 22, 1986
===
POSITIVE REAL TRANSFER FUNCTIONS FOR A LEAD NETWORK ON THE LEFT AND A NOTCH
(LAG/LEAD) FILTER ON THE RIGHT.

IMAG .5

REAL 1

IMAG 25

REAL 50

SYSTEMS DYNAMICS   NASA MSFC GLvP

LABORATORY ED14   POSITIVE IMAGINARY DOMINANCE   APRIL 22, 1986
==
POSITIVE IMAGINARY ADDED TO A NEGATIVE IMAGINARY TRANSFER FUNCTION RESULTS IN A
POSITIVE IMAGINARY TRANSFER FUNCTION. COMPONENTS ARE 2nd/2nd ORDER QUOTIENTS.
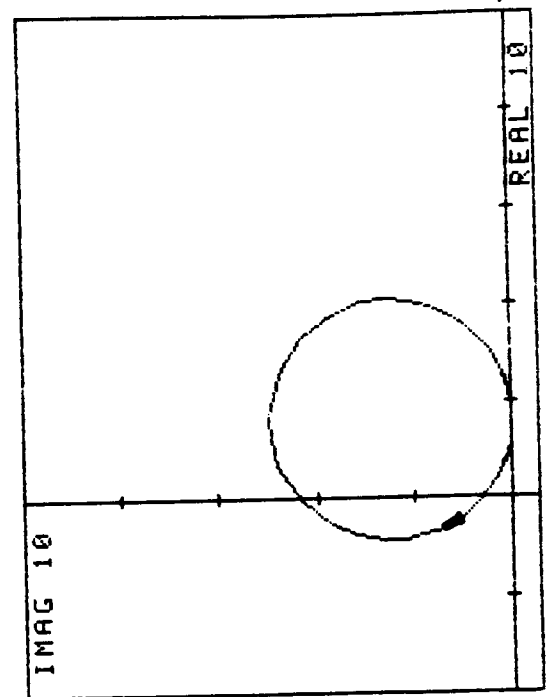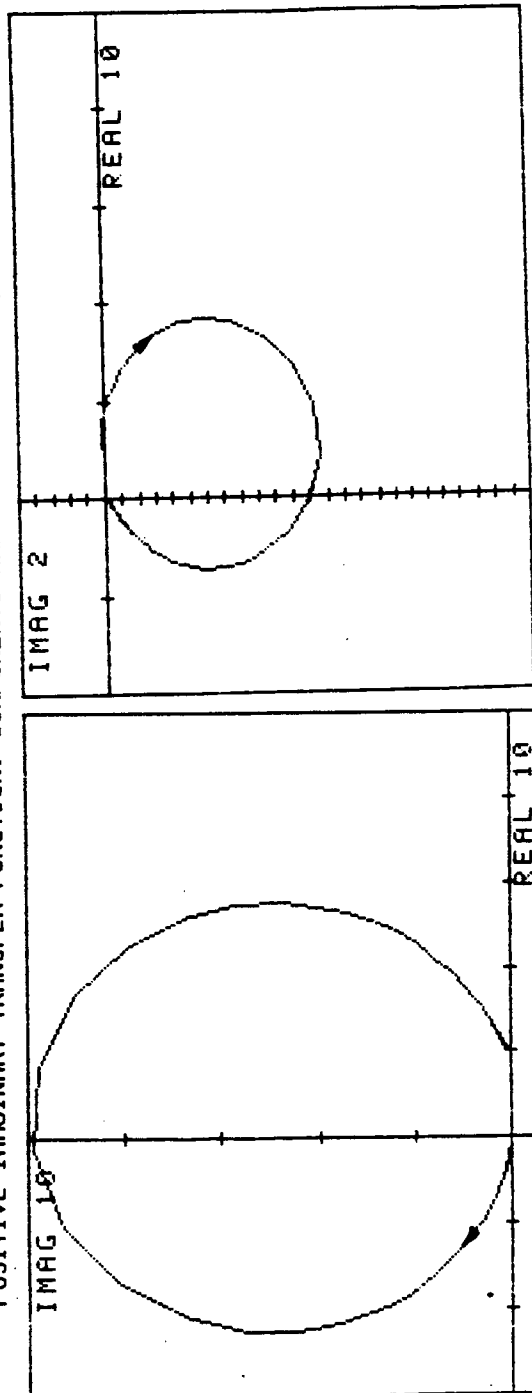
INTER-STABLE CONTROL EXAMPLE

$V = G(U - HV)$

$U = (1/G + H)V$

$V = U/(1/G + H)$

$V = (G \times 1/H)U$

$\Sigma \, 1/(K_j + sC_j + s^2 M_j)$ (G)

$\dfrac{a_0 + sa_1 + s^2 a_2}{b_0 + sb_1 + s^2 b_2}$ (H)

$V = \left[\displaystyle\sum_i 1/(K_i + sC_i + s^2 M_i) \right] \times \dfrac{b_0 + sb_1 + s^2 b_2}{a_0 + sa_1 + s^2 a_2} \; U$

COMPLEX IMAGE PLANE

REAL

IMAG.

H^{-1}

G
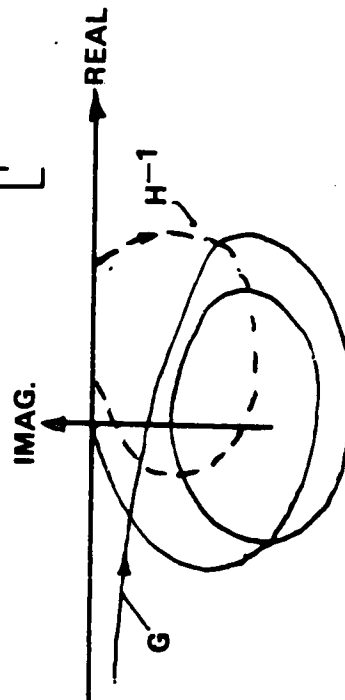
INTER-STABILITY:

$b_0/a_0 > b_1/a_1 > b_2/a_2$

352

SYSTEMS DYNAMICS   RATE GYRO COLOCATION RANGE FOR SPACE SHUTTLE   NASA MSFC GLvP
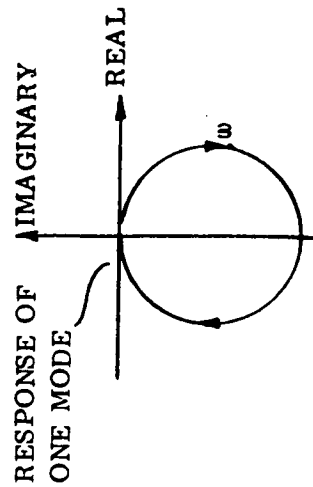
LABORATORY ED14   APRIL 22, 1986

ESTIMATED FORWARD LIMIT FOR
RATE GYRO LOCATIONS ON ORBITER

ESTIMATED FORWARD LIMIT FOR
RATE GYRO LOCATIONS ON SOLID ROCKET MOTOR

353

SYSTEMS DYNAMICS   RATE GYRO COLOCATION RANGE FEASIBILITY STUDY   NASA MSFC GLvP

LABORATORY ED14   APRIL 22, 1986

SIDE — S
FORCE

ODD MODES

EVEN MODES

1
3
2

GIMBAL

ALLOWABLE RANGE OF RATE GYRO LOCATIONS

RESPONSE OF ONE MODE

IMAGINARY

REAL

ω

MODAL RESPONSE:
$$\frac{-\sigma}{S} = \sum_{i=1}^{\infty} \frac{-Y_i Y_i'}{m_i(\omega_i^2 + s^2 2\zeta\omega_i + s^2)}$$

GIMBAL RELATION: $y = -\sigma n$, $n > 0$

RATE GYRO CONDITION: $\dfrac{\text{SENSOR ROTATION}}{\text{GIMBAL TRANSLATION}} < 0$ below of $\sim$ 5 Hz

ALLOWABLE RATE GYRO LOCATION RANGE: SA-V 12m, ORB. $\sim$ 4m, SRM $\sim$ 8 m

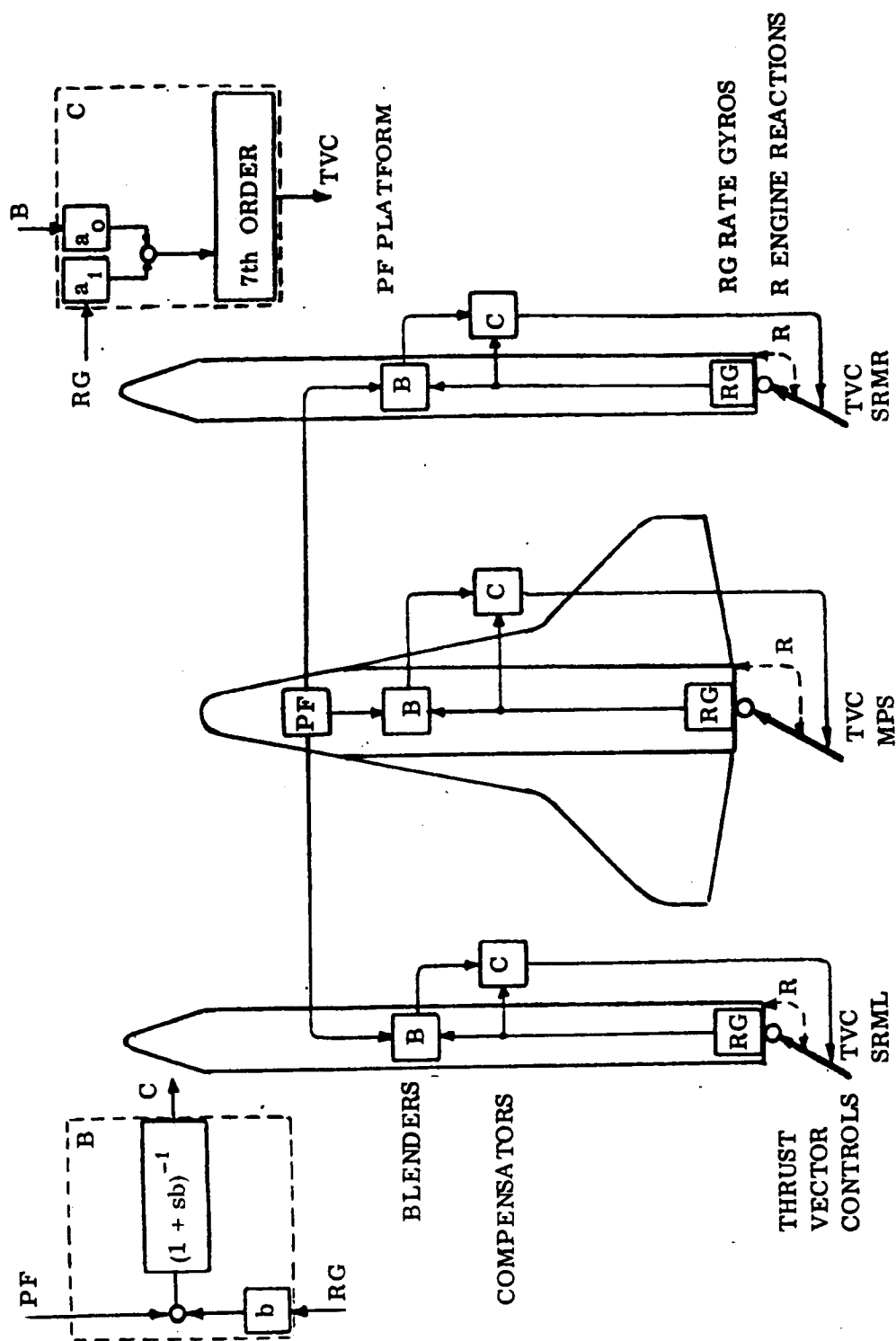SYSTEMS DYNAMICS   INTER-STABLE SPACE SHUTTLE ATTITUDE CONTROL

LABORATORY ED14

NASA MSFC GLvP   APRIL 22, 1986

PF PLATFORM

RG RATE GYROS

R ENGINE REACTIONS

7th ORDER

TVC

BLENDERS

COMPENSATORS

THRUST VECTOR CONTROLS

NOTE: BLENDERS AND COMPENSATORS ARE NOT PHYSICALLY SEPARATED, ONLY THEIR SIGNALS ARE SEPARATED.

$(1 + sb)^{-1}$

355

SYSTEMS DYNAMICS   DECOMPOSITION OF A 2nd/2nd ORDER QUOTIENT   NASA MSFC GLvP

LABORATORY ED14   APRIL 22, 1986
===

A POSITIVE IMAGINARY TRANSFER FUNCTION QUOTIENT IS DECOMPOSED INTO ADDITIVE AND
REDUCTIVE BRANCHES THAT RESEMBLE MECHANICAL COMPONENTS. THE ALGORITHM DELIVERS
NECESSARY AND SUFFICIENT CONDITIONS FOR INTER-STABILITY. CONTINUOUS FRACTIONS
CAN BE USED, BUT YIELD ONLY SUFFICIENT CONDITIONS, EXCEPT FOR CONSERVATIVE
SYSTEMS. GENERALLY, TRANSFER FUNCTION PLOTS ALWAYS YIELD NECESSARY AND SUFFI-
CIENT INTER-STABILITY CONDITIONS.

$$F(s) = \frac{a_0 + s a_1 + s^2 a_2}{b_0 + s b_1 + s\, b_2} = K_0 + [(sC_1 + s\,M) \times (K_1 + [K_2 \times sC_2])]$$
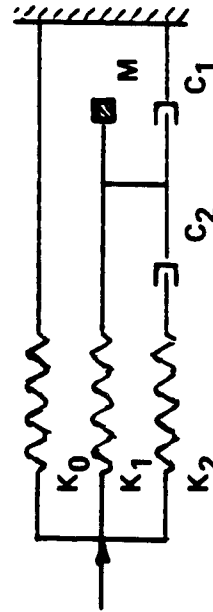
$$K_0 = a_0/b_0 \qquad C_1 = (a_1 - b_1\, a_0/b_0)/b_0 \qquad M = (a_2 - b_2\, a_0/b_0)/b_0 \qquad K_1 = a_1/b_1 - a_0/b_0$$

$$K_2 = a_2/b_2 - a_1/b_1 \qquad C_2 = (a_2 - b_2\, a_1/b_1)/b_1$$

SYSTEMS DYNAMICS   INTER-STABILITY PROSPECT   NASA MSFC GLvP

LABORATORY ED14   APRIL 22, 1986
==

1   INTER-STABLE CONTROL SYSTEMS ARE INHERENTLY INSENSITIVE TO RESONANCES WHICH
     RELAXES THE DYNAMIC DATA PROBLEM.

2   DOCKING AND UNDOCKING CANNOT UPSET STABILITY FOR SUBSYSTEMS OF THE SAME
     INTER-STABILITY TYPE. THREE TYPES ARE IDENTIFIED.

3   BUILDING BLOCK FEATURE REDUCES THE DIMENSION OF ANALYSES BY MAGNITUDE,
     HELPS THE UNDERSTANDING, AND GUIDES THE DESIGN.

4   INTER-STABILITY UNCOUPLES DIVERSE DESIGN AREAS AND DEFINES THE INTERFACES.
     CRITERIA ARE WELL DEFINED AND READY FOR THE SPACE STATION DEVELOPMENT.

STATUS REPORT AND PRELIMINARY RESULTS OF THE SPACECRAFT CONTROL LABORATORY EXPERIMENT

By Jeffrey P. Williams

Spacecraft Control Branch
NASA Langley Research Center
Hampton, VA.   23665

Marshall Workshop on Structural Dynamics and Control
of Large Flexible Structures

April 22-24, 1986

INTRODUCTION

The Spacecraft Control Laboratory Experiment (SCOLE) has been conceived to provide a physical test bed for investigation of control techniques for large flexible spacecraft. The SCOLE problem is defined as two design challenges. The first challenge is to design control laws for a mathematical model of a large antenna attached to the space shuttle by a long flexible mast. The second challenge is to design and implement a control scheme on a laboratory representation of the structure modelled in the first part. Control sensors and actuators are typical of those which the control designer would have to deal with on an actual spacecraft. The primary control processing computer is representative of the capacity and speed which may be expected in actual flight computers. This paper gives a brief description of the laboratory apparatus and some preliminary results of structural dynamics tests and actuator effectiveness tests.

INTRODUCTION

* EXPERIMENT CONCEIVED TO PROVIDE A COMMON "DESIGN CHALLENGE" FOR INTERESTED INVESTIGATORS

* SLEWING AND POINTING CONTROL PROBLEM

* USES ANTENNA LIKE STRUCTURAL CONFIGURATION AND INERTIAL SENSORS AND ACTUATORS

* VARIETY OF SENSOR AND ACTUATOR TYPES
  - Accelerometers, rate sensors, optical position
  - Thrusters, cmg, reaction wheel

* MULTI-MICROPROCESSOR BASED COMPUTING

361

CONTROL PROBLEM

The control problems to be studied are slewing and pointing maneuvers. The slew is defined as a minimum time maneuver to bring the antenna line-of-sight (LOS) pointing to within an error limit delta of the pointing target. The second control objective is to rotate about the line of sight and stabilize about the new attitude while keeping the LOS error within the bound delta.

CONTROL PROBLEM:

* PRIMARY — SLEW 20 DEGREES ABOUT MINIMUM AXIS OF INERTIA
  LINE-OF-SIGHT (LOS)POINTING WITHIN .02 DEGREES RMS

* SECONDARY — ROTATE ABOUT LOS WHILE MAINTAINING POINTING
  ACCURACY

LABORATORY APPARATUS

The laboratory experiment shown in the slide attempts to implement the definition of the math model design challenge within reasonable limits of the 1g, atmospheric environment. The experimental facility exhibits the essential SCOLE characteristics of a large mass/inertia connected to a small mass/inertia by a flexible beam. Some trades are made in terms of structure, sensors, actuators, and computational capability in order to develop the experiment in a timely and cost effective manner. To this end, the basic structure is made of homogeneous continuous elements. It is suspended from a steel cable with the positive z-axis of the shuttle pointing up, thus minimizing the static bending of the antenna mast. The suspension point is a two-degree-of-freedom gimbal for pitch and roll with yaw freedom supplied by the suspension cable. The sensors are aircraft quality rate sensors and servo acclerometers. An optical sensor is available for attitude determination. The shuttle based control moments are provided by a pair of 2-axis control moment gyros. The mast mounted control torques are provided by two-axis reaction wheels. Reflector based forces are provided by solenoid actuated cold air jets. Computational facilities consist of mico-computer based cpu's with appropriate analog interfaces, and a hybrid computer for control of the control moment gyros. The elements which make up the SCOLE experiment are described in detail in the following text.
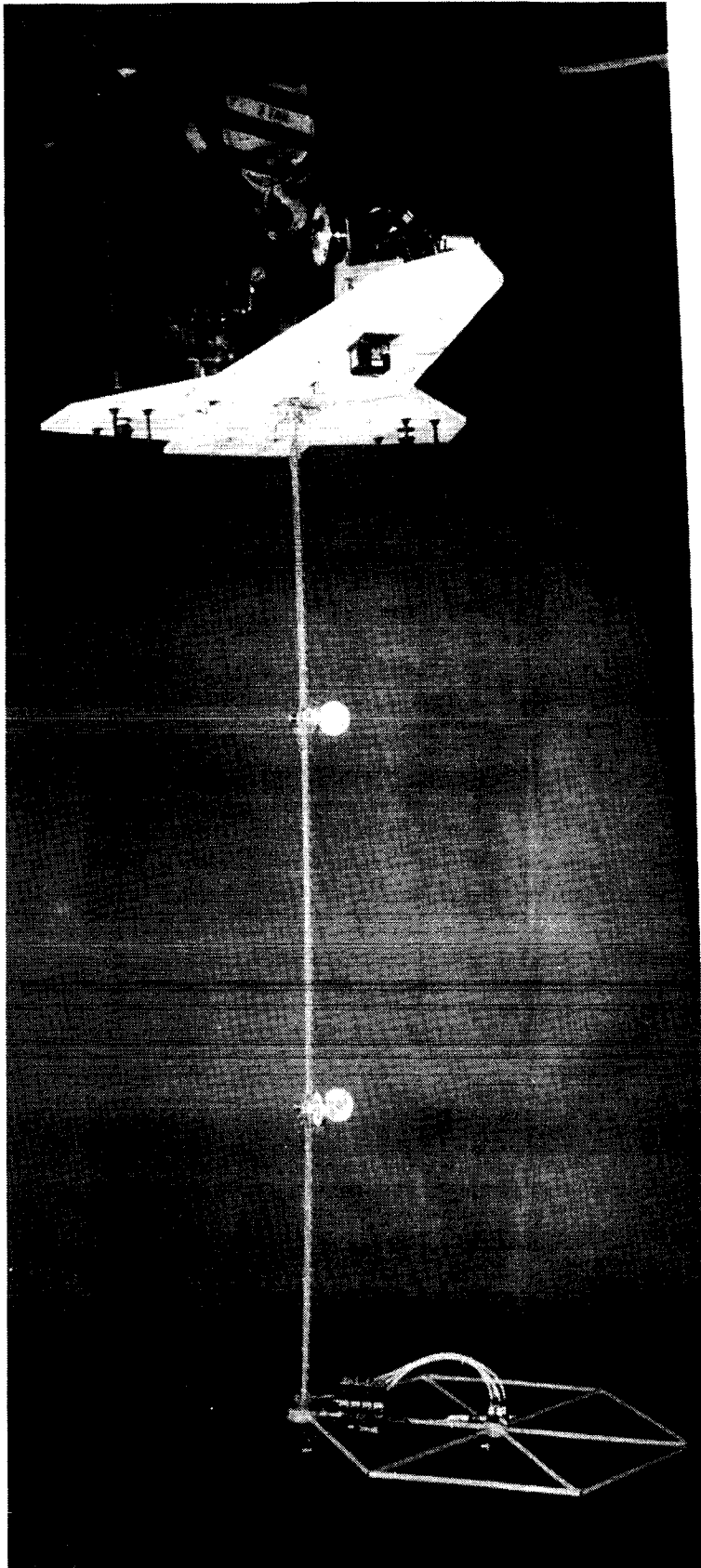
STRUCTURES

The Spacecraft Control Laboratory Experiment is comprised of three basic structures: the shuttle, the mast, and the reflector panel. The assembly of these individual components is shown in the slide.

The shuttle planform is made from a 13/16 inch steel plate and has overall dimensions of 83.8 by 54.0 inches. Its total weight is 501.7 pounds. The shuttle's center of mass is located 3.4 inches below the experiment's point of suspension, and 26.8 inches forward of the tail edge.

The mast is 120 inches long. It is made from stainless steel tubing and weighs 4.48 pounds. One-inch thick manifolds are mounted to the mast at each end.

The reflector panel is hexagonal in shape, made from welded aluminum tubing, and weighs 4.76 pounds. It is located 126.6 inches below the SCOLE's point of suspension. The center of the reflector is located at 12.0 inches in the x direction and 20.8 inches in the y direction from the base of the mast.

STRUCTURAL DETAILS

- ESSENTIAL CHARACTERISTICS

  SHUTTLE $\Longrightarrow$ LARGE MASS/INERTIA

  MAST $\Longrightarrow$ FLEXIBLE, CONTINUOUS BEAM

  REFLECTOR $\Longrightarrow$ SMALL MASS/INERTIA

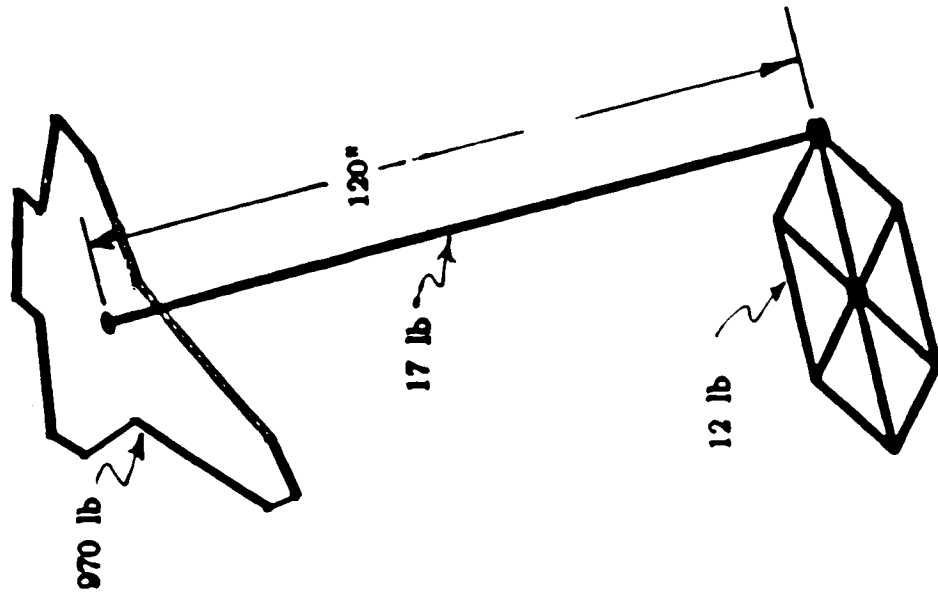 FREE BOUNDARY CONDITIONS

- SATISFIED BY:

  SHUTTLE $\Longrightarrow$ 3/4" STEEL PLATE WITH
  WEIGHTS ADDED TO
  INCREASE MASS/INERTIA

  MAST $\Longrightarrow$ 3/4" x .049" STEEL TUBE

 REFLECTOR $\Longrightarrow$ ALUMINUM TUBE FRAME

  PENDULUMN WITH UNIVERSAL JOINT
  (5 DOF)

367

SUSPENSION

The complete system is suspended from an 11-foot cable attached at the system center of gravity via a universal joint. Roll and pitch rotational freedom is provided by pillow block ball bearings which have an estimated break-out torque of .1 ft-lb. The universal joint is fixed to the shuttle plate and the center of gravity is made to coincide with the center of rotation by means of an adustable counter balance system.

368

SENSORS

The sensors for the experiment consist of nine servo-accelerometers and two, three-axis rotational rate sensing units. The power supplies for the sensors are mounted on the shuttle plate to minimize the number of large gage wires which must cross the universal joint suspension point. Only a single 115 VAC wsource and the signal wires cross the universal joint. The wires for the sensors are routed on the shuttle and along the mast.
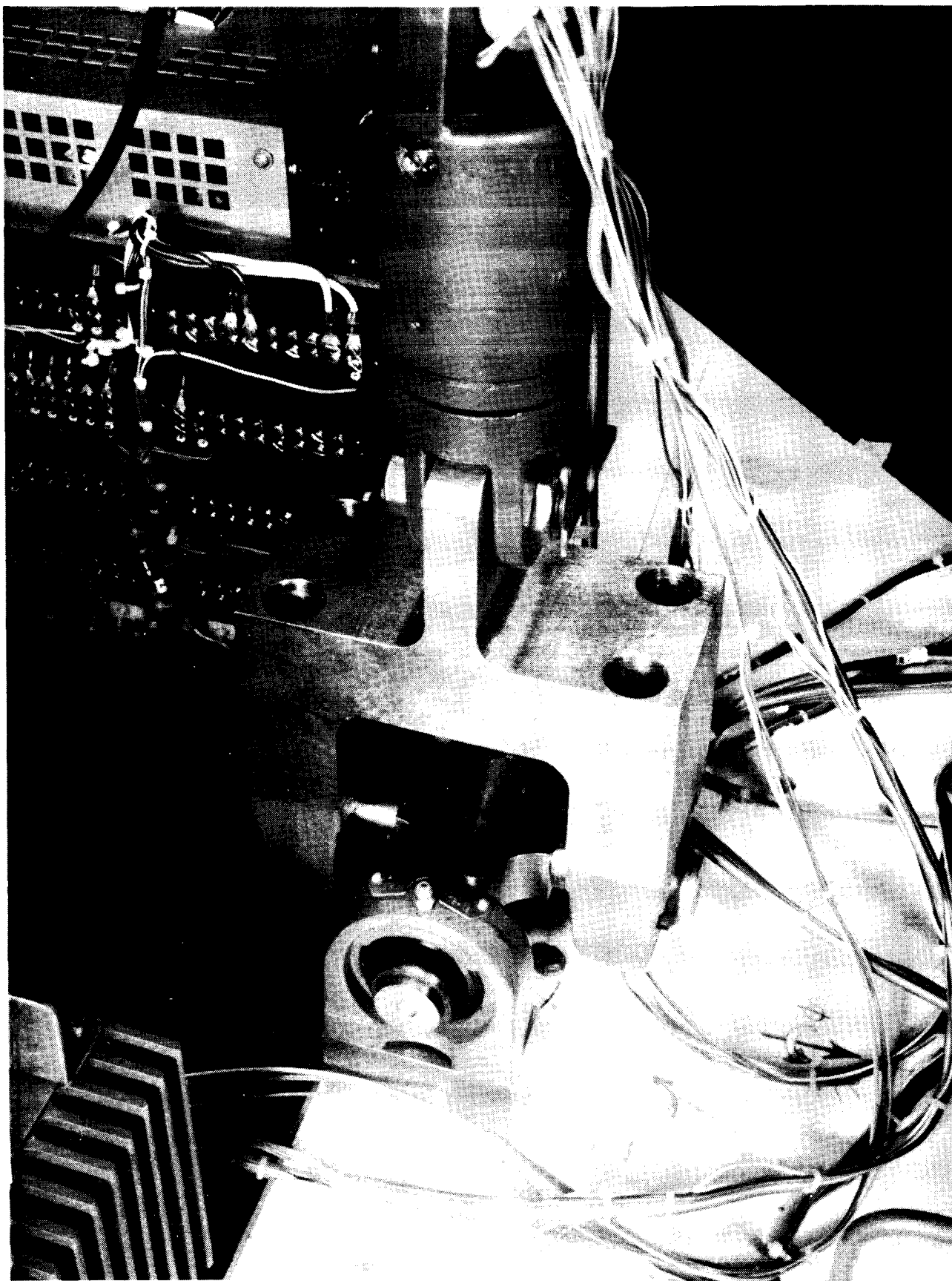
SENSORS

TYPE LOC.	3 AXIS RATE GYRO	2 AXIS ACCELERATION	3 AXIS ACCELERATION
SHUTTLE	X		X
MAST	X	2 places	
REFLECTOR		X	

* Rate gyros   60 and 360 deg/sec range
                    flat response to 10 Hz
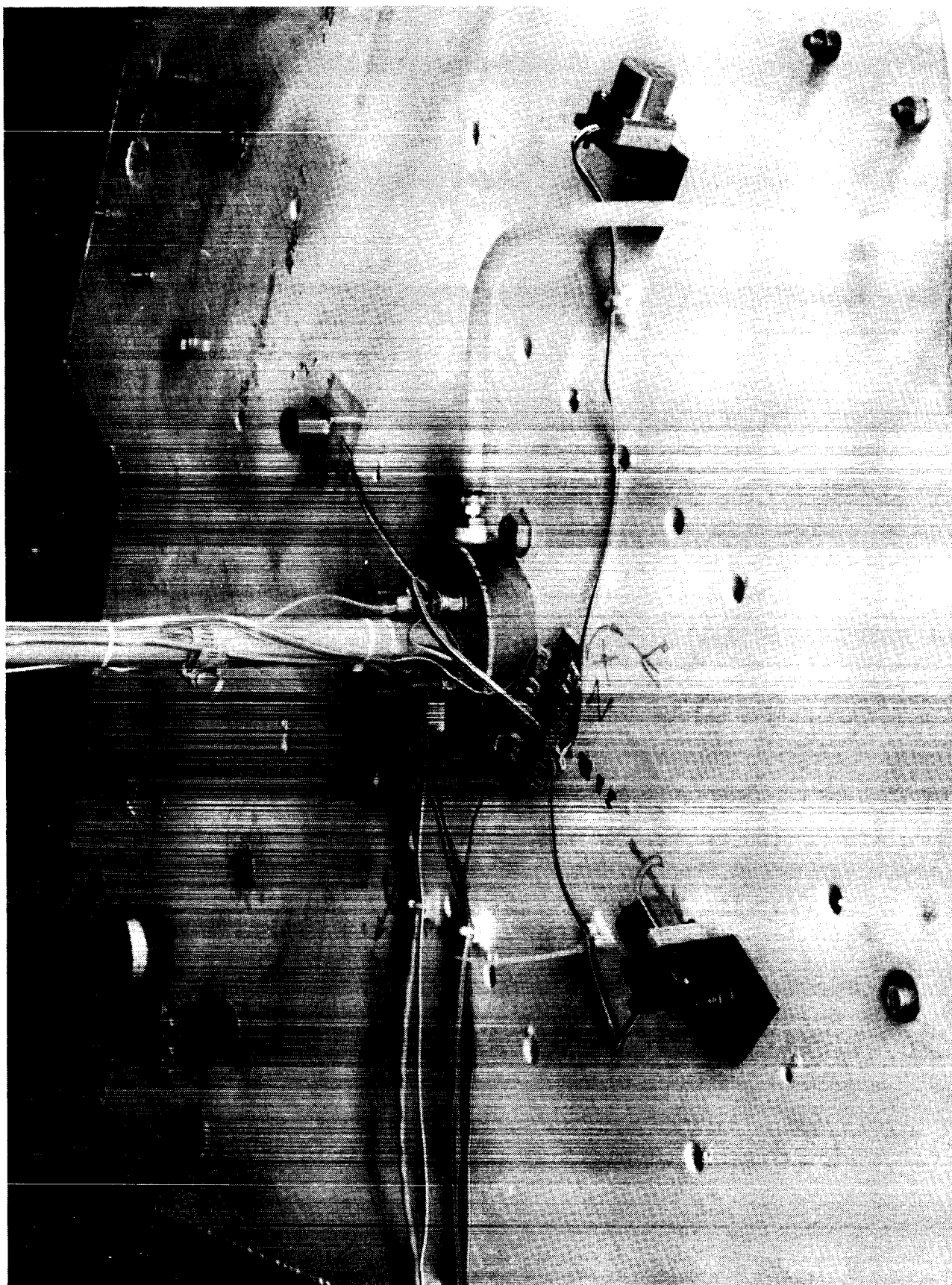
* Accelerometers +/-20 g range, 5 micro-g threshold
                      flat response to 50 Hz

ACCELEROMETERS

The shuttle-mounted accelerometers shown in the slide sense the x, y, and z acceleration. They are distributed away from the suspension point to aid inertial attitude estimation. All nine accelerometers have a frequency response which is nearly flat up to 350 Hz.

NASA
L-85-9852

RATE SENSORS

The shuttle-mounted rate sensor package shown in the slide senses three axis rigid body angular rates of the shuttle plate. The rotational rate sensors are three axis aircraft quality instruments. The frequency response is approximately flat to 1 Hz and -6 db at 10 Hz. Linearity is about .6 percent full scale. The range is 60 deg/sec for the yaw and pitch axes and 360 deg/sec for roll. A rate sensor package mounted at the end of the mast senses three axis angular rates at the reflector end of the mast.
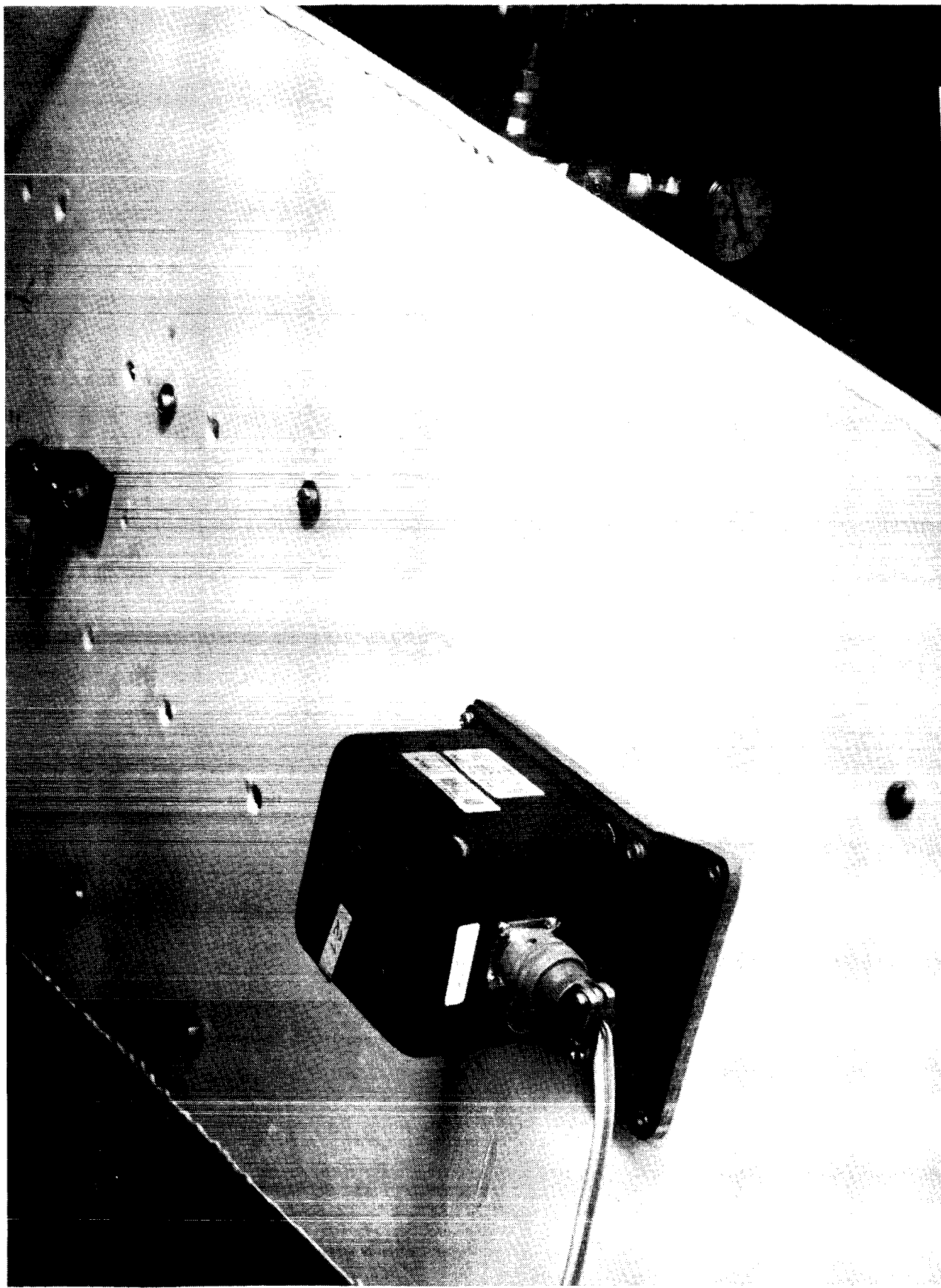
OPTICAL SENSOR

An optical sensor based on an optically sensitve 65-kbit dynamic memory chip has been developed. It is capable of measuring two-dimensional position with about 0.5 percent resolution and can communicate the position data to the host computer over a serial data link. An Intel 8751 micro-controller is used to program the refresh rate of the memory cell and detect the optical image. A point of light is sensed by first filling the memory with ones. Then the refresh is disabled for a pre-determined amount of time so that the cells exposed to the light will change to a zero state. The 8751 then scans the entire array to determine the location of the point of light. It then transmits the position and rescans a sixteen by sixteen square area around the last position and again transmits the detected position.
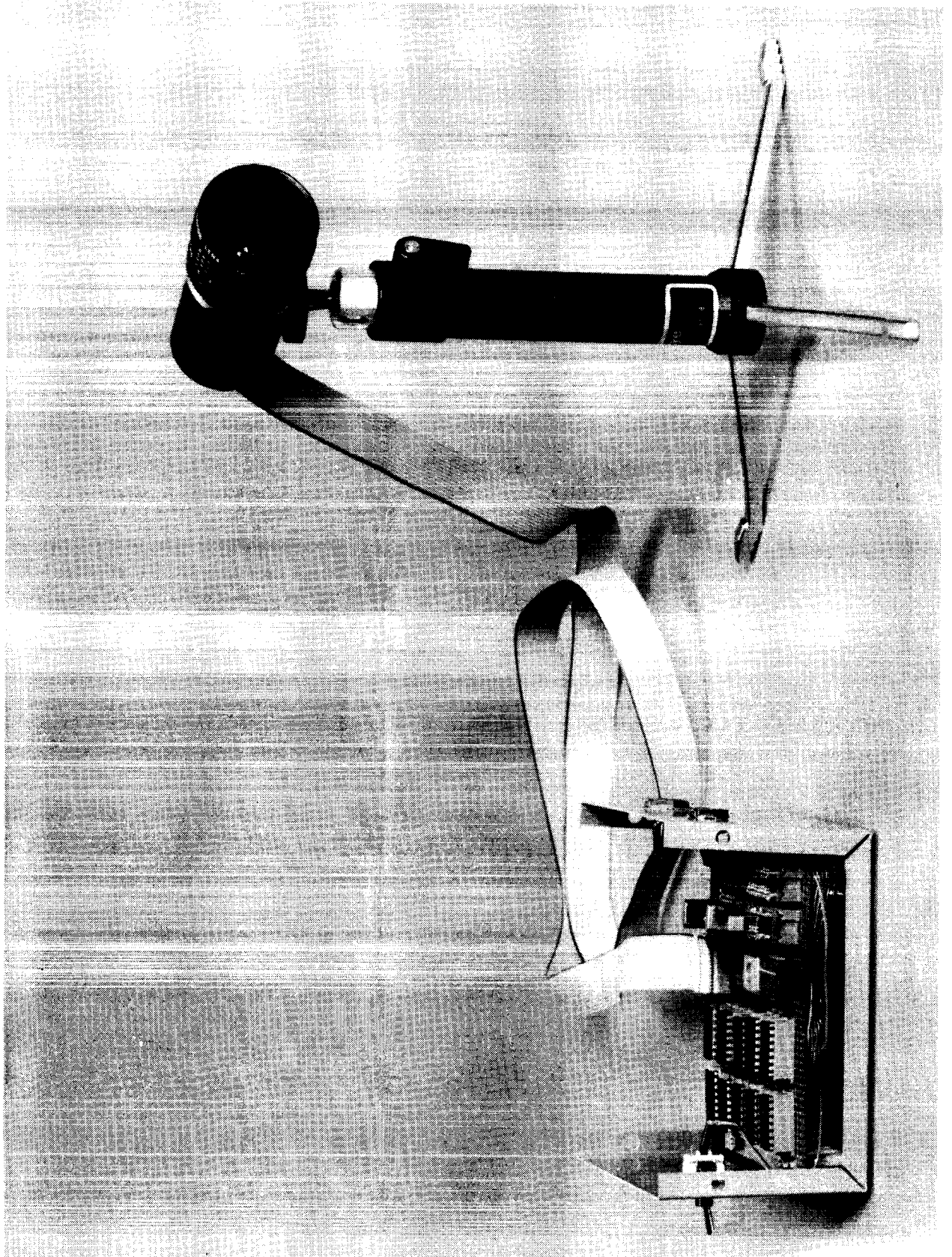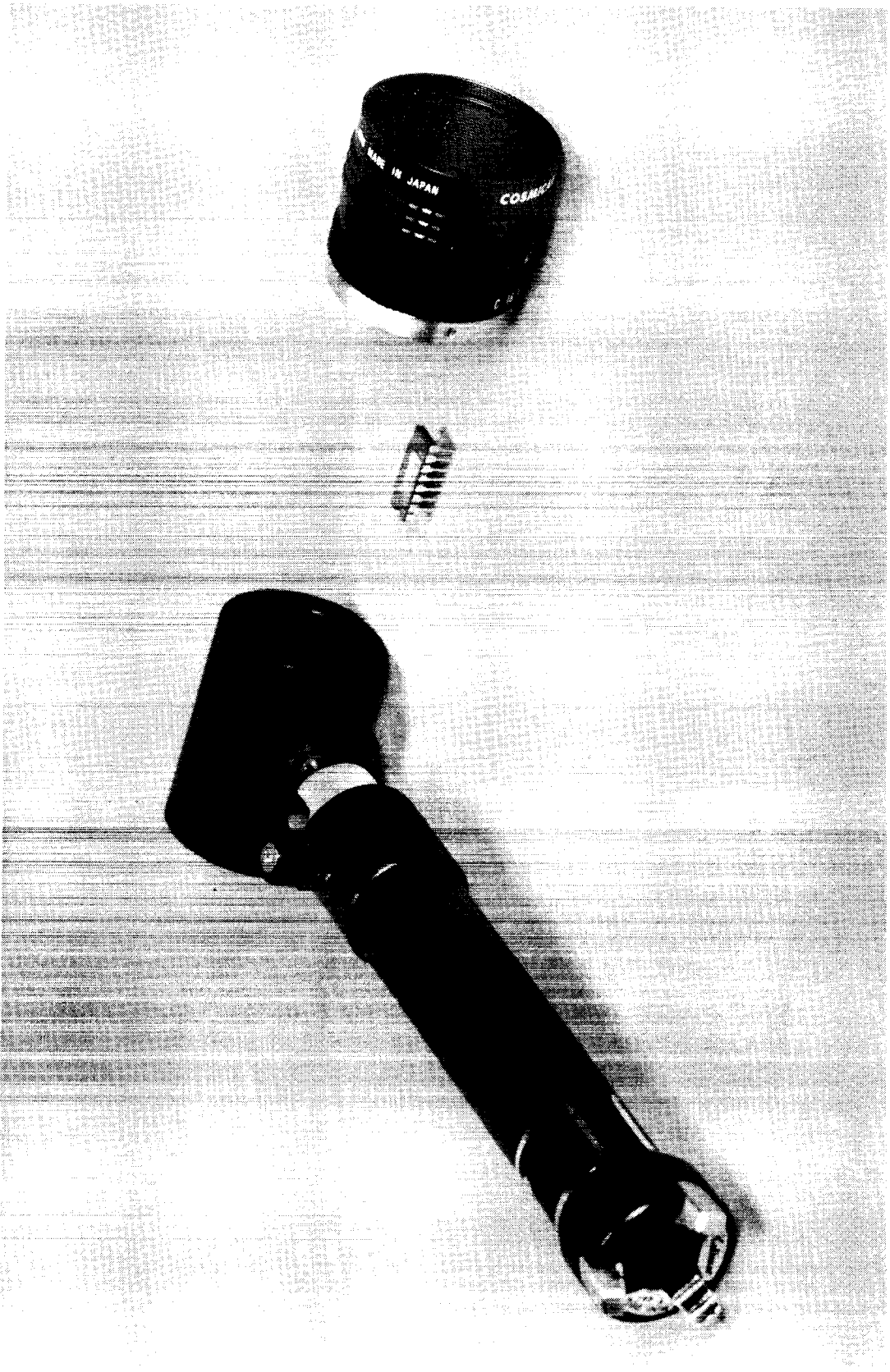
DYNAMIC MEMORY CHIP

The memory chip shown in the center of the slide is not without disadvantages. The map of the memory cells is not uniform there are a number of dead zones around each memory cell and the address map is interlaced rather than one-to-one. Also the image plane is divided into two halves by a dead zone of about 20 percent of the total imaging width.

ACTUATORS

The actuators consist of both proportional and on-off controllers. Shuttle attitude control is provided by a pair of two-axis control moment gyros (CMG). Mast vibration suppression is provided by a pair of two-axis reaction wheels. Reflector forces are provided by four cold gas jets. As with the sensors, all devices are inertial, and the power supplies and amplifiers are mounted on the shuttle. All actuators were manufactured in house.

ACTUATORS

TYPE / LOC.	2 AXIS CMG	2 AXIS REACTION WHEEL	2 AXIS THRUST
SHUTTLE	2 places		
MAST		2 places	
REFLECTOR			X

* CMG
  - 1.8 ft–lb gimbal torque
  - .337 in–lb–sec momentum
  - flat frequency response to 1kHz (est.)
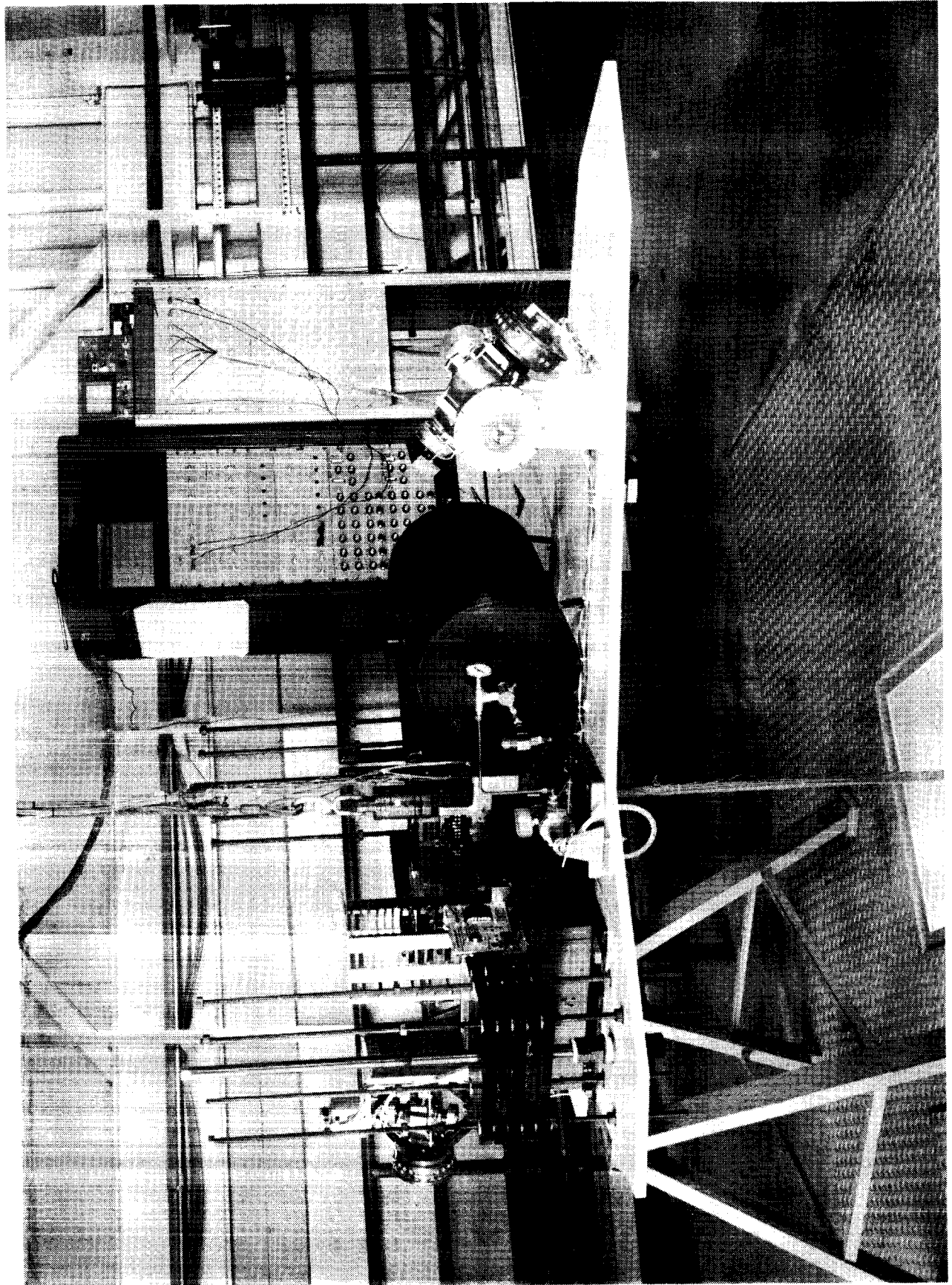
* Reaction wheel
  - 20 oz–in torque
  - flat frequency response to 1kHz (est.)

* Thrust
  - .5 lb for 15 seconds
  - .023 second rise time

CONTROL MOMENT GYROS

A pair of two-axis control moment gyros (cmg's) are mounted on the shuttle plate to provide three axis torques. The CMG's each have two gimbals which are direct driven by individual DC torque motors. The momentum wheel is mounted in the inner gimbal and is driven by two permanent magnet DC motors. The nominal momentum is about 2.5 ft-lb-sec. The gimbal torque motors are driven by current amplifiers so the output torque will be proportional to the command voltage sent to the power amplifier. The gimbal torquers will produce +/- 1.5 ft-lb at frequencies up to 1 kHz. The gimbals are instrumented with tachometers and sine-cosine pots to allow decoupled control of the shuttle attitude angles in a precision command mode.
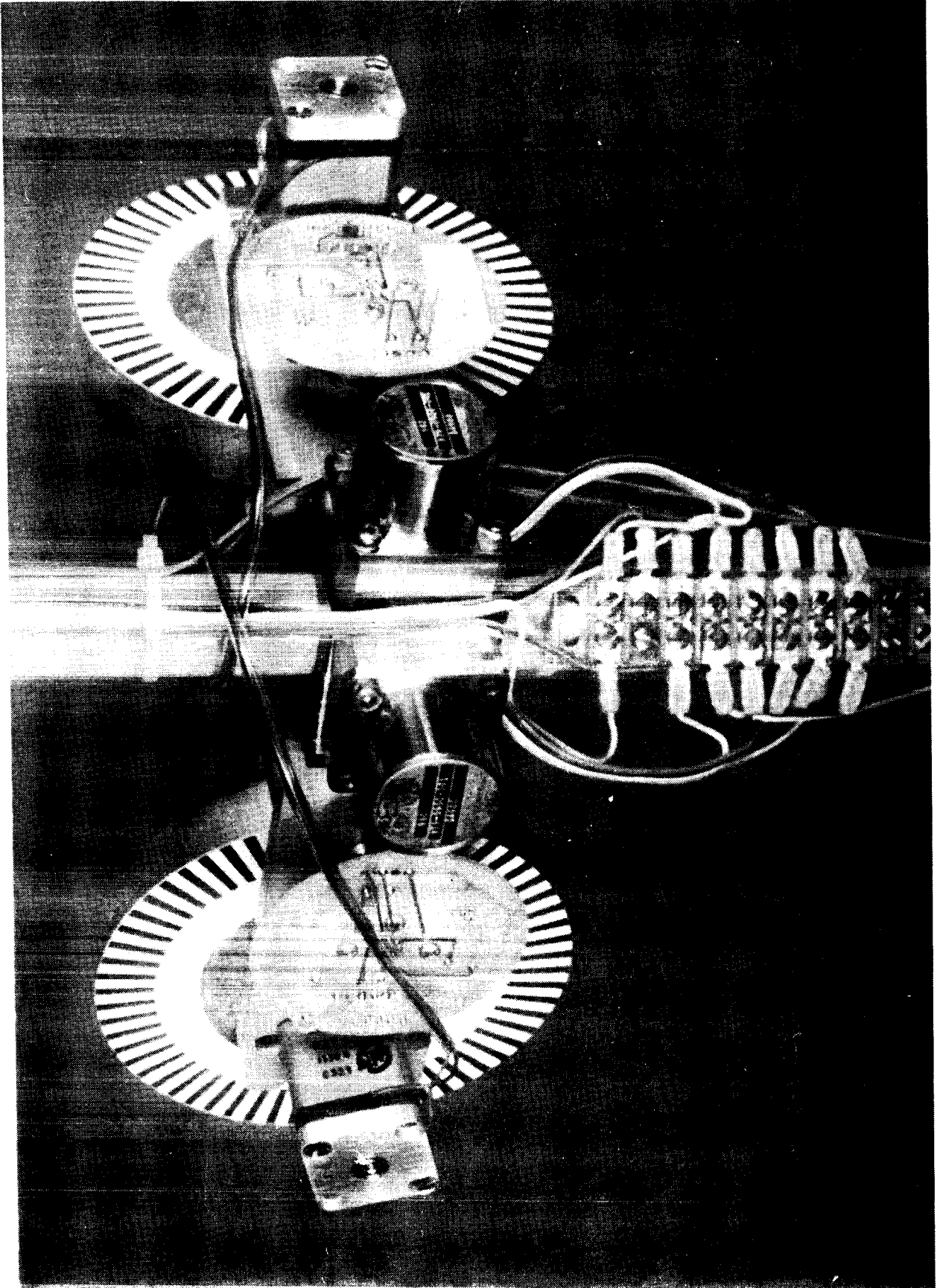
NASA
L-85-9854

C-5

383

REACTION WHEELS

The mast-mounted reaction wheels consist of aluminum disks with inertia of about .00027 lb-ft-sec2 mounted directly on the drive shaft of a 20 oz-in permanent magnet DC motor. The motors are powered by high bandwidth current amplifiers.

THRUSTERS

The control forces on the reflector are provided by solenoid actuated cold gas jets. The thrusters are mounted in the center of the reflector and act in the x-y plane. The jets are supplied by a compressed air tank mounted on the shuttle. The pressurized air travels through the mast to the solenoid manifold which gates the air flow between the regulated supply tank and the thrusters. Thrust is initiated by opening the solenoid with a discrete command. The rise time of the thrust to 90 percent is about 20 milli-seconds.

NASA
L-85-9859

387
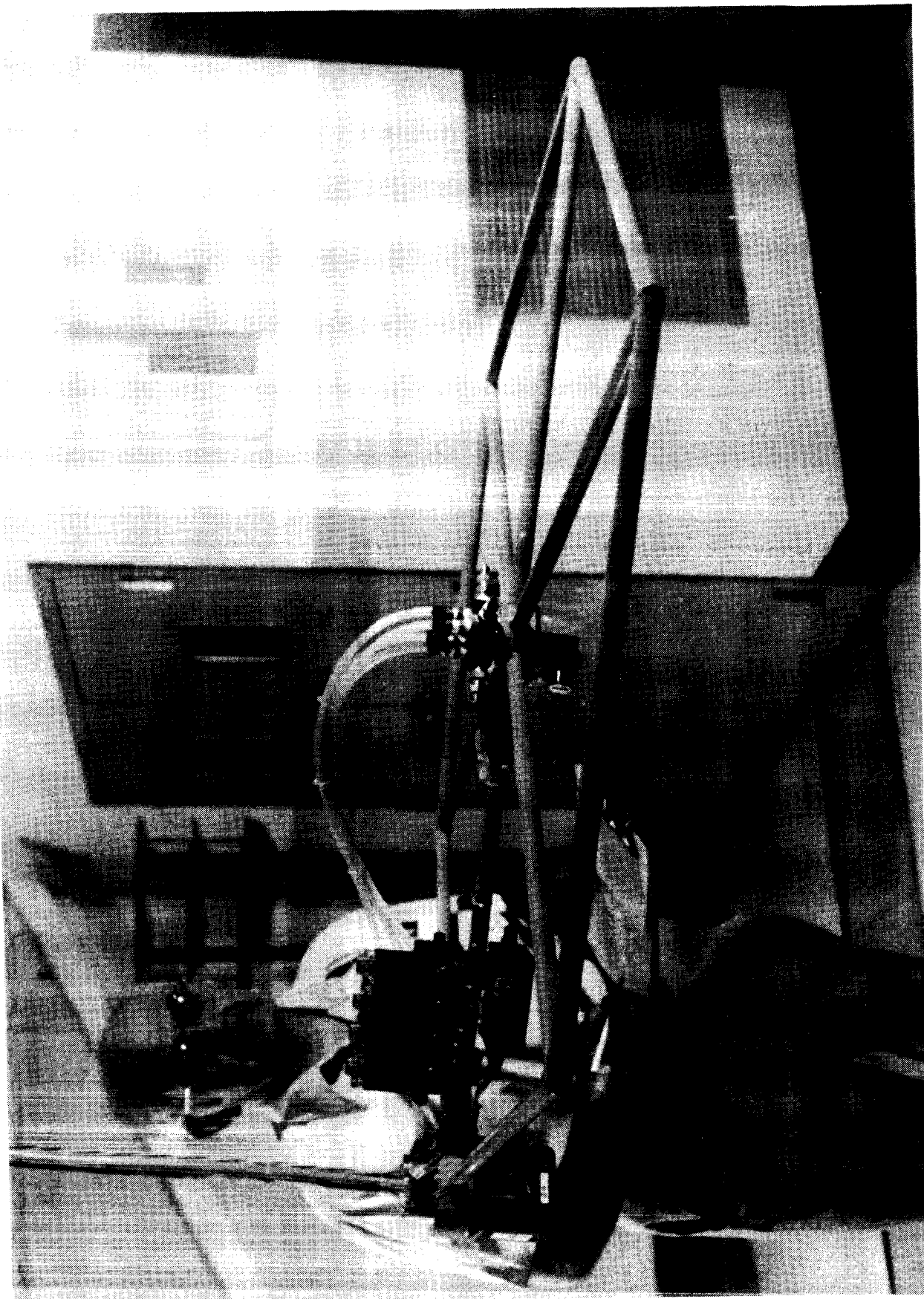
COMPUTER SYSTEM

The main computer for control law implementation will be a
micro-computer based on the Motorola M68000 microprocessor. The computer
has 0.5 mbyte of random access memory and a 40 M-byte hard disk. The
operating system is based on UNIX with C, Fortran and Pascal compilers
available for applications programming. The computer has 12 serial ports
and one parallel port. Terminals are connected on two of the ports and an
answer-only modem is attached to another. One port is used for an orignate-
only modem. A line printer is attached to another port.

Analog interfaces consist of a 4 bit output-only discrete channel,
8 digital-to-analog converters and 64 analog-to-digital converters. All
converters are 12 bit devices with a range of +/-10v. Subroutines for
accessing the analog interfaces and setting the digital sampling interval
are provided.

SCOLE COMPUTER INTERFACES
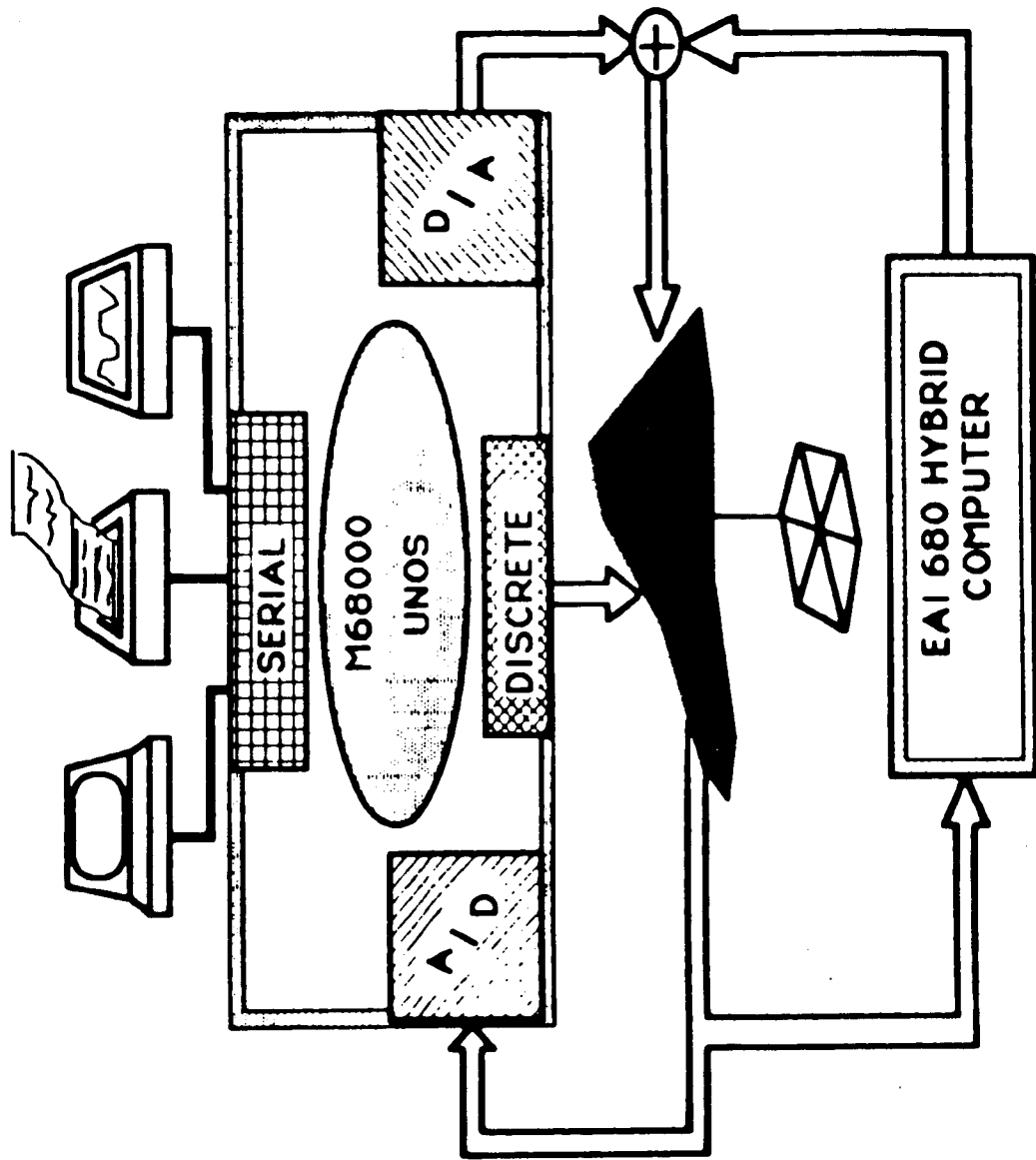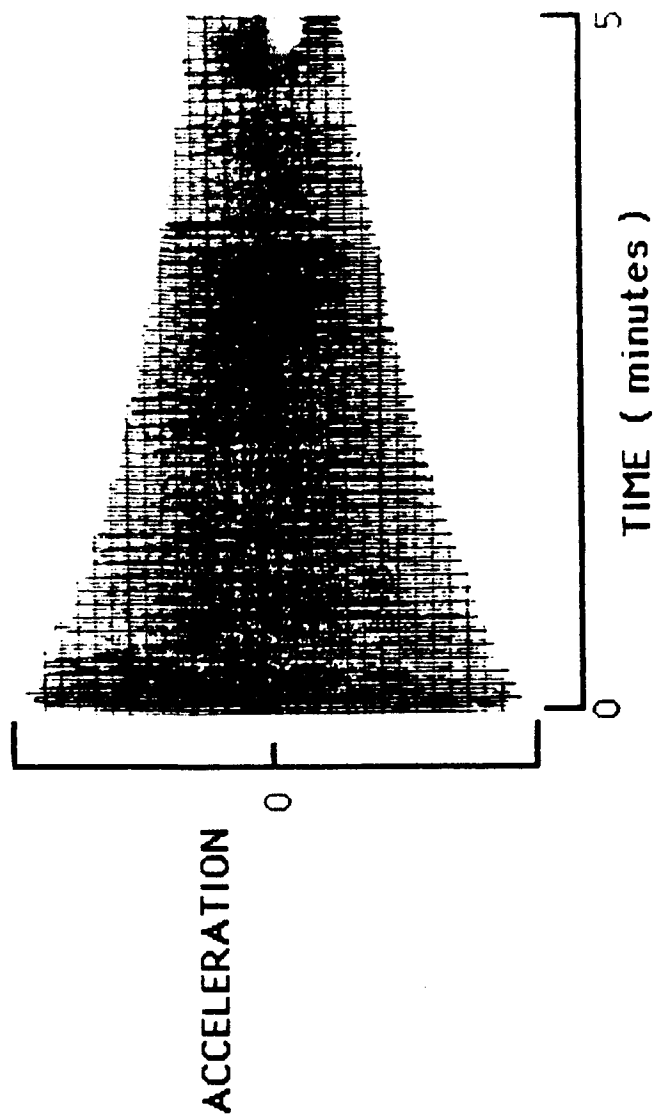
SCOLE DAMPING

The structure is very lightly damped. The slide shows a finite element model of the second flexible mode for a vertical cantilever configuration. The time history of a reflector-mounted accelerometer shows less than 0.1 percent natural damping.

TYPICAL SCOLE DAMPING

CANTILEVERED MAST - MODE 2

.516 Hz   1% damping

ACCELERATION

0

TIME (minutes)

0   5
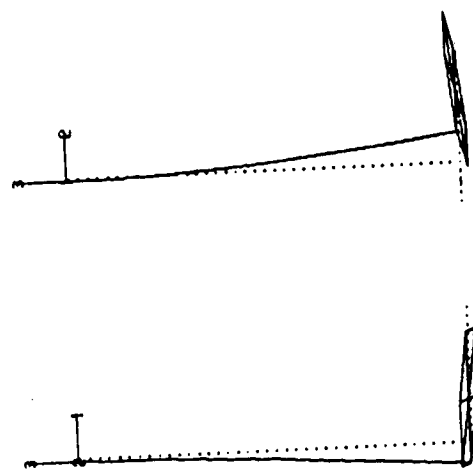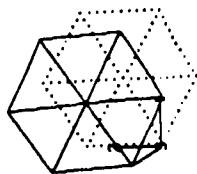
MAST MODES

Experimentally determined frequency and damping for the first five cantilever modes are shown in the slide. The difficulty in modelling the system damping is apparent.

CANTILEVERED MAST ROOTS

IMAGINARY

REAL
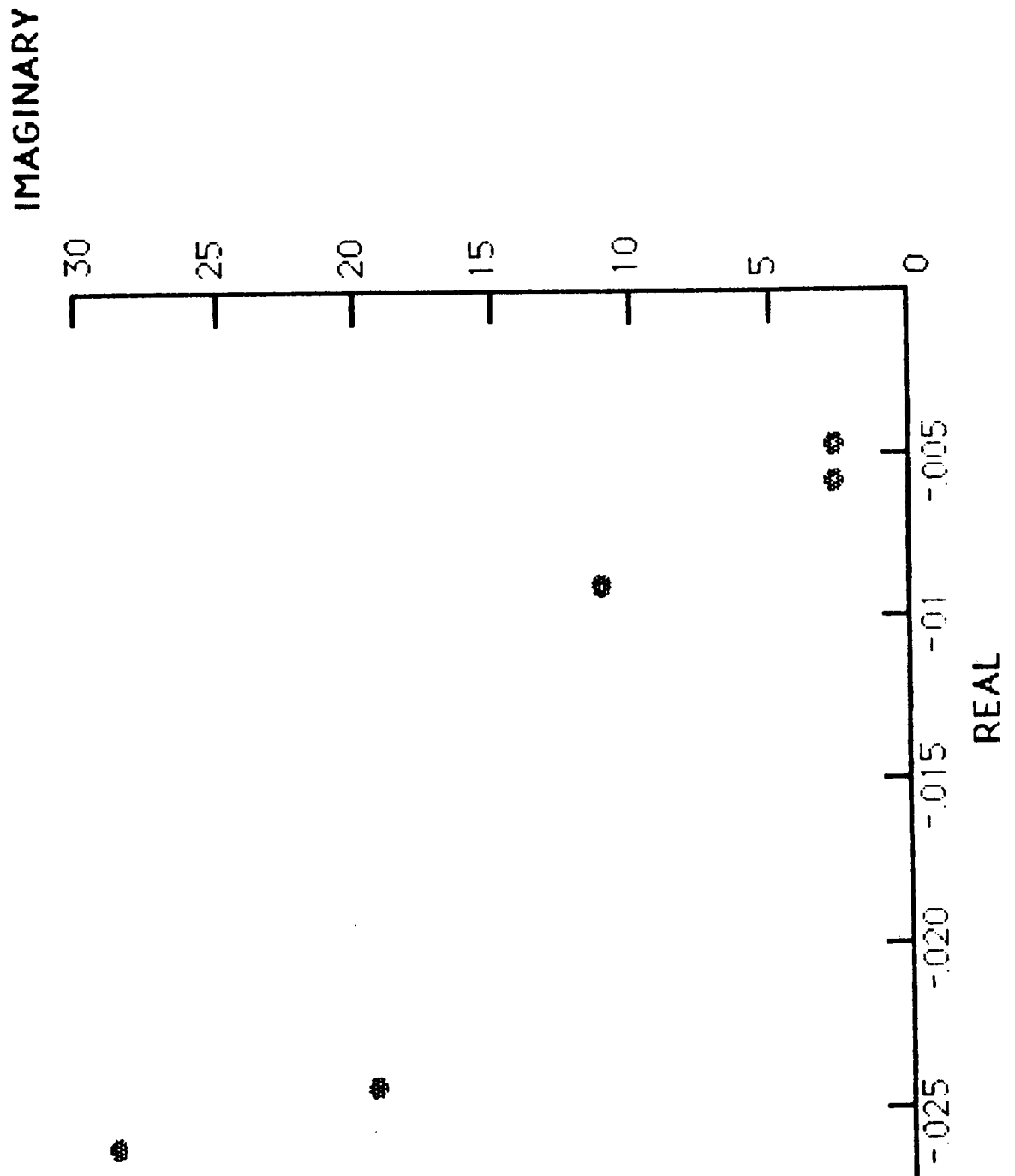
VIBRATION SUPPRESSION

Effectiveness of the thrusters for vibration suppression is demonstrated by the time histories of a reflector-mounted accelerometer, its integral and the thruster command signal. An Euler integration was used to estimate the velocity so the motion started by manually exciting the antenna so the reflector moves along the x-axis. The lower trace shows the command to the +/- x thruster. No compensation is made to stop the limit cycle at the end of the experiment.

SCOLE VIBRATION SUPPRESION
USING ON-OFF THRUSTERS

CANTILEVERED MAST – FIRST MODE
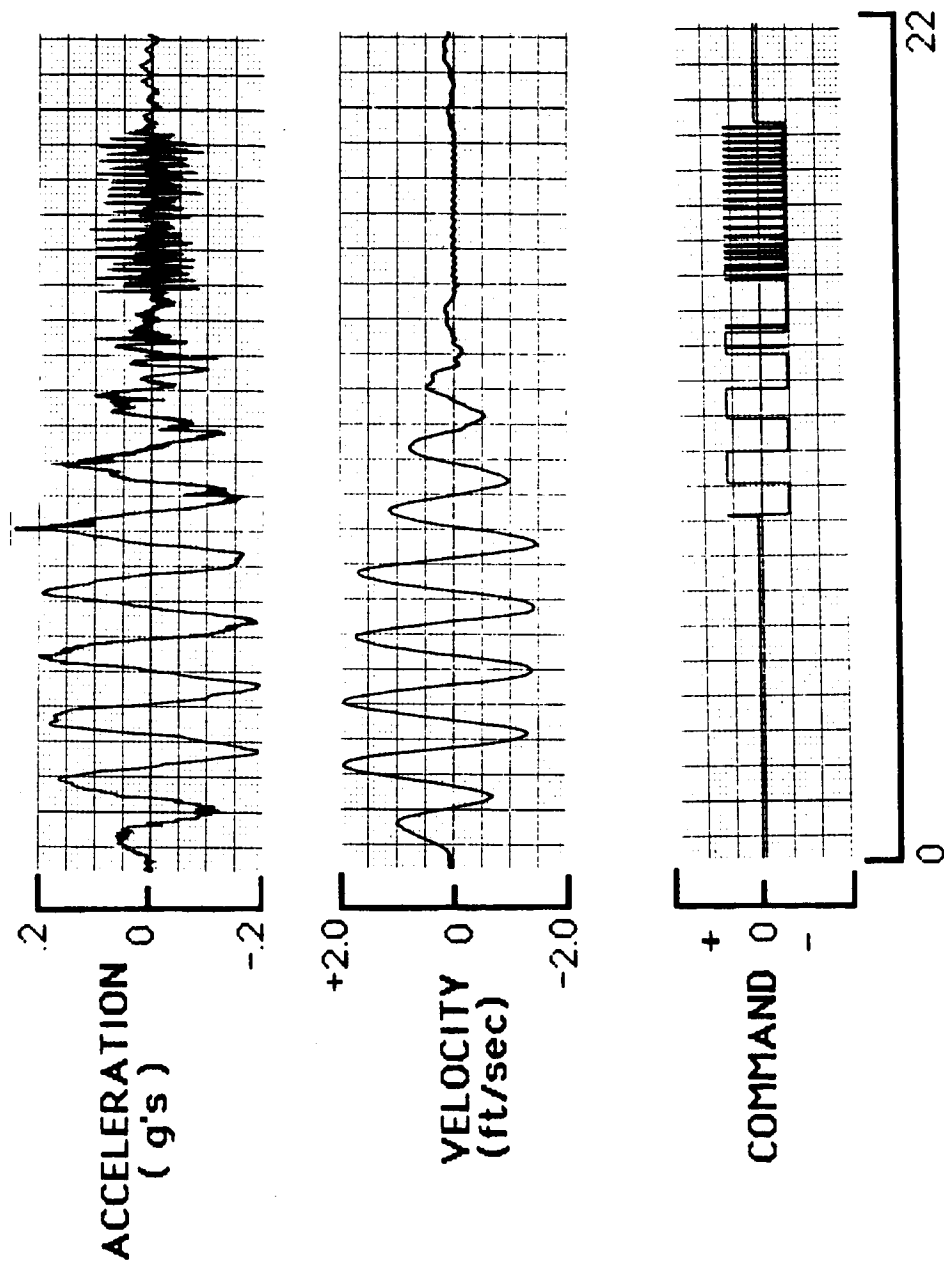
SUMMARY

The SCOLE design challenge was conceived as a common dynamics and control and test-bed for the testing and validation of a variety of control schemes for large flexible structures. The structural configuration and the statement of the control objective are representative of the problems presented by the design concepts of future large satellites.

The laboratory apparatus addresses many of the practical implementation questions and will provide valuable experience with a variety of sensor and actuator types. The experimental hardware is available to interested researchers.

396

SUMMARY

* THE SCOLE EXPERIMENT HAS A REALISTIC CONTROL OBJECTIVE

* THE SCOLE HARDWARE PRESENTS MANY OF THE PRACTICAL IMPLEMENTATION PROBLEMS WHICH WE EXPECT FORM LARGE SPACE STRUCTURES

* A WIDE VARIETY OF SENSOR AND ACTUATORS ARE AVAILABLE FOR MANEUVER CONTROL AND VIBRATION SUPPRESSION

* THE EXPERIMENT IS AVAILABLE TO INTERESTED RESEARCHERS

Boeing Aerospace Company

ENGINEERING
TECHNOLOGY

FLEXIBLE SPACECRAFT SIMULATOR

(860-7A202)

PROBLEM

• Verification of control algorithms for flexible spacecraft can be done only through simulation and test; these are necessary to understand control/structure interaction sufficiently to design robust controllers for future spacecraft.

OBJECTIVE

• To develop a low-cost facility which simulates the fundamental problem of C/SI.

• To provide accessibility for designs so that experience can be gained in applying various multivariable control design methods to an actual structure.

SIMULATOR HARDWARE

The simulator facility and test structure are shown in the figures. The structure consists of a rigid core to which six weighted arms are attached by short, flexible pins. This attachment provides rigidity in the vertical plane to support the weight of the arms, but flexibility in the horizontal plane. Thus, depending on tip weight, the arms display a first bending mode between 0.4 and 1.4 Hz. The structure rests on a plexiglass support disk which floats on a flat air-bearing table with no discernable friction. This gives the test structure three rigid-body modes (in the horizontal plane) and permits coupling of the bending modes to produce six lightly damped flexible modes with predicted frequencies below about 3 Hz. Symmetry of the arms results in several modes having nearly identical frequencies. The test structure weighs about 16 lbs; the short arms are about 30 in. in length, and the long arms are about 40 in. in length.

An available laboratory digital computer, an Apple-II+, is used as the controller and test data collection device. This machine turns out to be relatively slow (having a 1 MHz clock), so that careful coding was needed to get efficient calculation. Another reason for using this machine was the availability of an optical imaging device which has a direct digital interface with the computer through a plug-in board.

This device, called the Micron Eye*, is mounted above the center of the core and looks down on an X-shaped pattern. The image is transferred directly to the memory of the computer (in about 0.1 sec), where it is analyzed to determine translation and rotation of the core. Due to the pixel arrangement in the array, the field of view and quantization levels are different for the x-direction (i.e., the long direction of the pattern) and the y-direction.

In the current configuration, the x-axis field of view is about 7 in. and the resolution is 0.057 in., while the y-axis field of view is about 1.4 in. and the resolution is 0.022 in. The processing of the image produces an angle resolution of about 0.012 rad.

*Manufactured by Micron Technology, Inc., Boise, Idaho.

SIMULATOR HARDWARE (Contd)

To minimize cost, the test structure has been designed to require no on-board power or external connections. Control force actuation is accomplished by air jets which are fixed to the support table and directed toward fins attached to the support disk of the floated element. The jets are placed to permit about 4 in. of free motion, so that the forces generated on the fins will be equivalent to the reaction forces that would occur if the jets were mounted on the floated element. Air pressure for the jets is provided by a shop air supply through solenoid valves. To maintain subsonic flow in the system, a maximum pressure of about 15 psig is used, and the valve and nozzle orifices are 5/16 in. Tests show a jet thrust of about 0.2 lbs.

The valves are driven by a pulse-width, pulse-frequency (PWPF) modulator circuit which permits the use of a proportional control law with the on-off valves. The PWPF circuit has been designed to accept commands from a digital computer (through an 8-bit D/A converter) such that a command of 1-bit produces a minimum pulse-frequency of about one pulse per second. The maximum pulse frequency is about 30 pulses per second, which occurs at 50% modulation factor (i.e., 50% 'on' time).

FLEXIBLE SPACECRAFT SIMULATOR
(860-7A202)

APPROACH

- Test facility is being constructed at U.W.

- Test element provides 3 rigid body and 6 flexible modes, all in the horizontal plane, with frequencies below about 2.5Hz.

- Control force actuation will be on/off air jets; sensing by optical displacement sensors.

- Loop closure will be accomplished using an Apple-II digital computer; control algorithms will be designed using the IAC, and MATRIX-X.

STRUCTURAL ANALYSIS

A NASTRAN model of the test structure displays the six flexible mode frequencies and mode shapes. The three lowest frequency modes have shapes as shown. The first two involve translation of the core while the third is a pure rotation mode. The higher frequency modes have similar shapes but involve short arm motion.

With 0.2 kg weights on the arm tips, some tests were made by manually applying periodic inputs and timing the resulting oscillations. The results show modes at 0.40, 0.43, 0.54, 0.57, and 2.5 Hz.

STRUCTURAL ANALYSIS

FIRST 3 FLEXIBLE MODE SHAPES

Boeing Aerospace Company

ENGINEERING
TECHNOLOGY
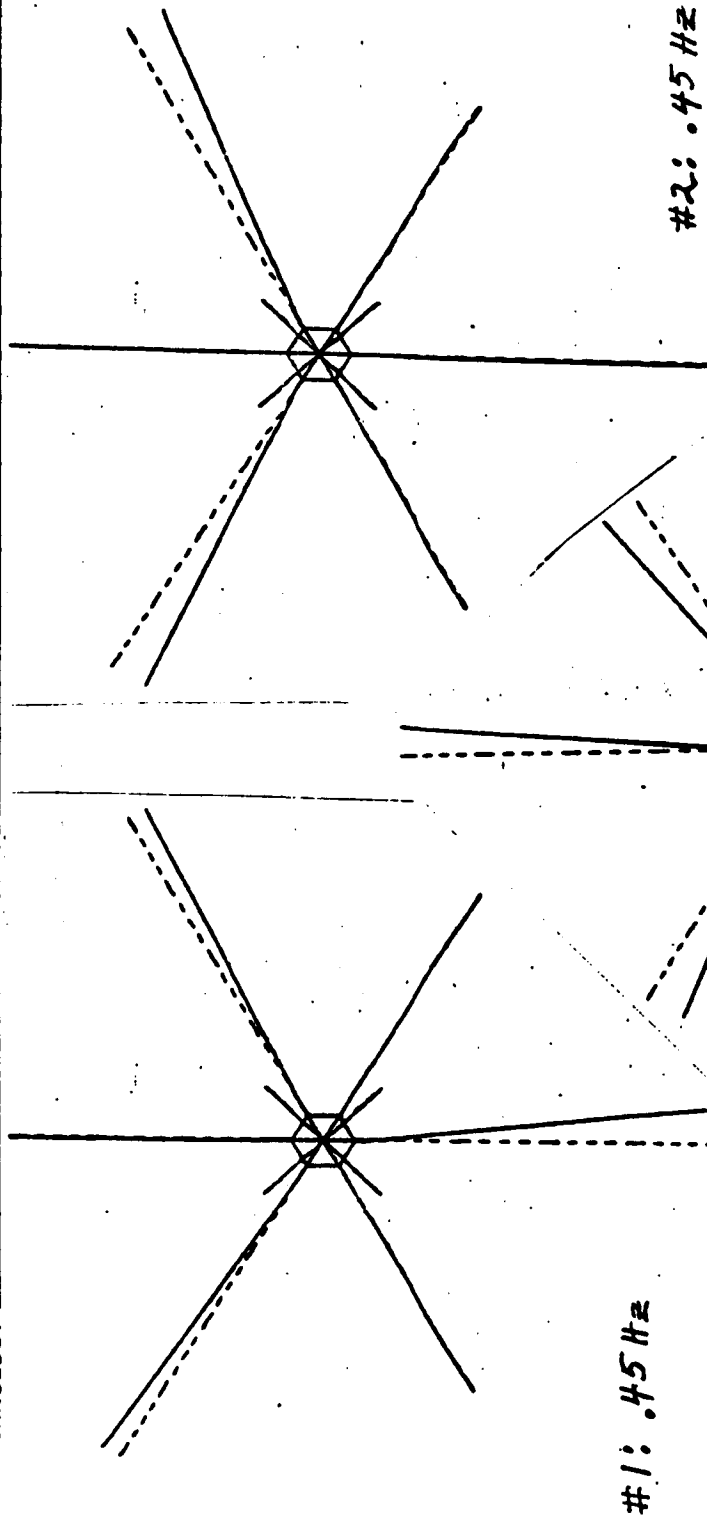
#2: .45 Hz

#3: .52 Hz

#1: .45 Hz

INITIAL CONTROL ALGORITHM TESTS

Following careful calibration and adjustment to minimize the effects of nonlinearities (e.g., quantization), a series of closed-loop tests have been conducted with a control law which treats the test structure as a rigid body. The x-, y-, and angle channels are assumed to be independent for this case. Since the sensor provdides only displacement measurements, rate information must be derived.

The design utilizes a 2nd-order observer and state feedback regulator on each channel. The low sample frequency prompts the use of a direct digital design. The control law software includes an initialization routine whereby the estimator and regulator pole locations in the z-plane can be input and the gains are calculated for the rigid body model.

INITIAL CONTROL ALGORITHM TESTS

RIGID-BODY CONTROL LAW DESIGNS

- x-, y-, and θ- channels are independent
- 2nd order observer and state feedback regulator are used on each channel
- Sample Interval: 0.23 sec
- Designed Closed-Loop Pole Locations:

		Z-plane	S-plane
Case 1:	reg.:	$0.57 \pm 0.30J$	$-1.9 \pm 2.1J$
	est.: x,y:	$0.50 \pm 0.30J$	$-2.3 \pm 2.35J$
	θ:	$0.41 \pm 0.32J$	$-2.8 \pm 2.9J$
Case 2:		Same as Case 1	
Case 3:	reg.:	$0.77 \pm 0.19J$	$-1.0 \pm 1.0J$
	est.:	Same as Case 1	

CASE 1:

This case involves fixing the arms to produce a rigid body. With the regulator and estimator poles as shown previously, the closed-loop response for the 100 samples (23 sec) is well-behaved. Note the control activity in θ; this appears to arise from angular quantization effects on the rate estimate.

CASE 1: RIGID BODY DISPLACEMENT RESPONSE

ENGINEERING
TECHNOLOGY

Boeing Aerospace Company

DY (in)

0.2174
0
-0.2174

50   100   Time step
(0.25 sec/unit)

DTH (rad)

0.1226
0
-0.1226

50   100   Time step

409

CASE 1: RIGID BODY CONTROL INPUTS

UY (bit)

0

100

50

100

Time step

(0.23 sec/unit)

UT (bit)

0

100

50

100

Time step

ENGINEERING

TECHNOLOGY

410
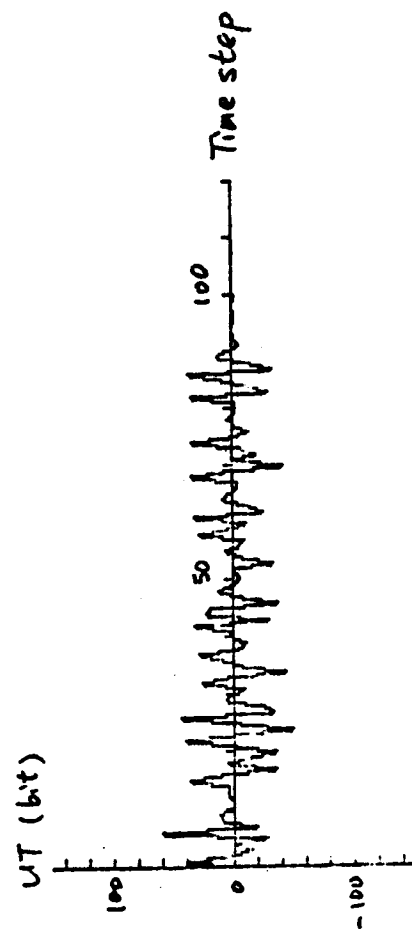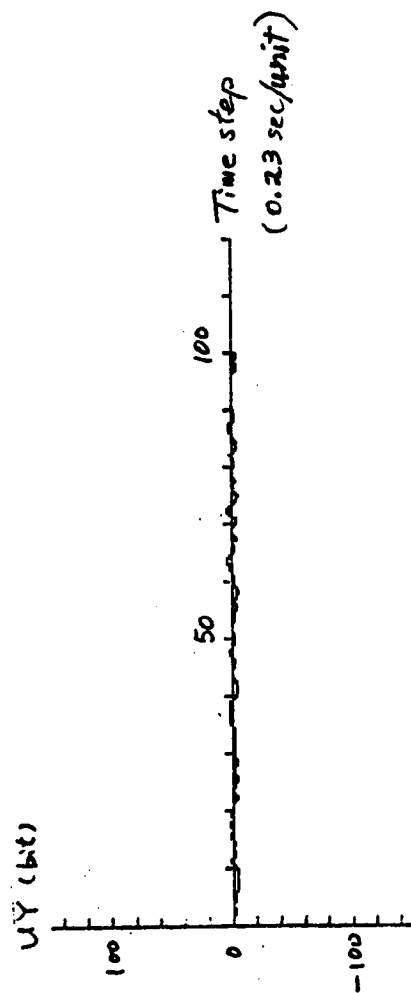
CASE 2:

This involves the same control gains as Case 1, but with the flexible modes present. The structure is held still for about 2 sec, then released (by turning the air-bearing floatation on). Both Y and θ diverge very quickly and the θ commands reach saturation levels (of 125 bits). When y-displacement reaches the limit of the sensor field of view, control is lost and the structure bounces between its stops.

This demonstrates an instability induced by interaction of the control bandwidth with the structural modes which are not included in the control law. Analysis is in progress to identify which modes are involved.

411

CASE 2: FLEXIBLE BODY DISPLACEMENT RESPONSE

Boeing Aerospace Company

DY (in)

Time step
(0.23 sec/unit)

DTH (rad)

Time step

412

CASE 3:

In this case, the flexible modes are present, but the regulator gain has been reduced. A lightly damped oscillation is observed in the x-displacement at about .58 Hz, but the system is stable with bounded control commands.

This demonstrates that narrowing the control bandwidth reduces interaction with the structural modes, thus restoring stability. The next step will be to include the flexible modes in the control law and again widen the control bandwidth to find the limit of stability.

CASE 3: FLEXIBLE BODY CONTROL INPUTS

415

CASE 3: FLEXIBLE BODY DISPLACEMENT RESPONSE

ENGINEERING
TECHNOLOGY

Boeing Aerospace Company

UX (bit)

Time step

(0.23 sec/unit)

UY (bit)

Time step

UT (bit)

Time step

IMPROVING STABILITY MARGINS

IN DISCRETE-TIME LQG CONTROLLERS

B. Tarik Oranc and Charles L. Phillips

Electrical Engineering Department

Auburn University

Auburn, AL 36849

ABSTRACT

This paper discusses some of the problems encountered in the design of discrete-time stochastic controllers for problems that may adequately be described by the "LQG" assumptions; namely, the problems of obtaining acceptable relative stability, robustness, and disturbance rejection properties. The paper proposes a dynamic compensator to replace the optimal full state feedback regulator gains at steady state, provided that all states are measurable. The compensator increases the stability margins at the plant input, which may possibly be inadequate in practical applications. Though the optimal regulator has desirable properties the observer based controller as implemented with a Kalman filter, in a noisy environment, has inadequate stability margins. The proposed compensator is designed to match the return difference matrix at the plant input to that of the optimal regulator while maintaining the optimality of the state estimates as dictated by the measurement noise characteristics.

I. INTRODUCTION

The design of robust stochastic controllers for problems adequately described by the "LQG" assumptions has been a field of active research in recent years. Since Doyle's [1] and Doyle and Stein's [2] introductory papers different approaches have been taken in order to design various robust LQG controllers. It can be stated generally that the approaches taken were to increase the stability margins, namely the gain and phase margins at the plant input, sufficiently so that the closed loop system remained stable under large parameter changes in the plant and/or sensor failures. It is important to note at this point that most research has been on continuous time systems. The robustness problem may be more pronounced in discrete time controllers due to sampling rate limitations and the phase lag associated with sampling.

In order to have a better understanding of the problem it is necessary to briefly review the respective parts of the stochastic controller. The stochastic LQG controller is comprised of the LQ optimal feedback controller and the Kalman filter based current full state observer. It has been well established that the continuous time LQ controller based system has excellent guaranteed stability margins, namely a phase margin of at least 60^0 and an infinite gain margin. Unfortunately the discrete time equivalent doesn't have these guaranteed margins. However as the sampling period approaches zero the stability margins approach those that of the continuous time LQ controller. The Kalman filter will

show an excellent performance in estimating states and will also be stable. However when the Kalman filter is used to estimate the state variables for feedback to the LQ controller the robustness properties of the system will not be guaranteed. Doyle has given a simple example where a LQG controller-filter combination has very small gain margins, and hence is not robust. An investigation of the paper by Johnson [3] explains this behavior of the LQG controllers.

Consider the state space representation of a plant for which a LQG controller is to be designed.

$$x(k+1) = Ax(k) + Bu(k) + Gw(k)$$

$$y(k) = Cx(k) + v(k)$$

(1)

where

$$x(k) \epsilon R^n \ , \ u(k) \epsilon R^r \ , \ y(k) \epsilon R^m$$

and $w(k)$ and $v(k)$ are uncorrelated, zero mean white gaussian noise processes.

Denoting the constant Kalman filter gains by K_f and the constant LQ gains by K_c we consider the discrete time equivalent of Theorem 8.3 as stated in the monograph by O'Reilly [4].

Theorem : There exists a class of linear systems (1) such that one or more eigenvalues of $(I - K_fC)(A - BK_c)$ of the observer based feedback controller may lie outside of the unit circle in the complex plane though all eigenvalues of $(A - BK_c)$ and all the eigenvalues of $(A - K_fCA)$ are designed to lie within the unit circle, and even though the system pairs (A,B) , (A,C) are, respectively completely controllable and completely observable.

The significance of this theorem lies in the fact that although the closed loop eigenvalues of the LQG system are the union of the observer eigenvalues and optimal regulator eigenvalues, and hence result in a stable closed loop system, the eigenvalues of the controller may lie outside the unit circle, therefore causing the controller to be unstable. It may therefore be concluded that the LQG control system may not be robust.

There have been three major approaches in alleviating the robustness problem that may occur in LQG systems. In light of the theorem all three methods will be investigated in the same frame work. The first approach is that of Doyle and Stein [2]. They developed a robustness recovery procedure in which they added fictitious process noise at the plant input. By controlling the way the fictitious noise entered the plant input they recovered the loop transfer function (LTR) at the plant input asymptotically as the noise intensity is increased. This method has the drawback that the system has to be square. A recent paper by Madiwale and Williams [5] has extended the LTR procedure to minimum phase, non-square and left-invertable systems with full or reduced order observer based LQG designs. It is observed that the LTR method actually results in the Kalman filter gains being forced asymptotically into a region where all eigenvalues of the controller lie within the unit circle. The major problem in this method is that the Kalman filter is no longer optimal with respect to the true disturbances on the plant as its eigenvalues have been shifted via the effective adjustment on

the process noise . Another disadvantage is that the 40 dB/decade roll-off associated with the LQG design is pushed out into the high frequency range where unmodelled high frequency modes might be excited and cause instability.

The second approach which was initiated by Gupta [6], and by Moore et al [7] in separate papers was to achieve robustness in frequency bands where the problems occurred without changing the closed-loop characteristics outside those frequency bands. Gupta used frequency-shaped cost functionals to achieve robustness by reducing filter gain outside the model bandwidth. On the other hand Moore et al [7] essentially improvised on Doyle and Stein's LTR method by adding fictitious colored noise instead of white noise to the process input, thereby relocating both the Kalman filter eigenvalues and the controller eigenvalues. Recently Anderson et al [8] have investigated the relations between frequency dependent control and state weighting in LQG problems. Both of these procedures result in controller eigenvalues that lie within the unit circle, thereby overcoming the problems stated in the theorem.

The last approach is due to Okada et al [9]. Their approach is drastically different from the previous approaches. They have changed the structure of the LQG controller by introducing a feed-forward path from the controller input to the controller output. This is equivalent to introducing an additional feedback loop from the output to the input of the plant. The criteria for the selection of the gains in this path is to force the

controller to satisfy the circle criterion. This additional loop results in a robust controller with poor response properties. Therefore the response is improved by synthesizing an extended perfect model-following (EMPF) system [9]. This approach has the disadvantage that its statistical properties haven't been established. Furthermore it is not always applicable theoretically. However, in practice it outperforms Doyle and Stein's LTR method with some approximations as described in [9].

The approach taken in this paper is an extension of the LTR procedure. A dynamic compensator is proposed to replace the optimal feedback gains so as to recover the open loop transfer function at the plant input.

II. DERIVATION OF THE DYNAMIC COMPENSATOR

The LQ optimal controller can be designed for a system as described by equations (1) provided that all states are available for measurement. The resulting steady state controller which is depicted in Figure 1 will have excellent properties as mentioned previously.
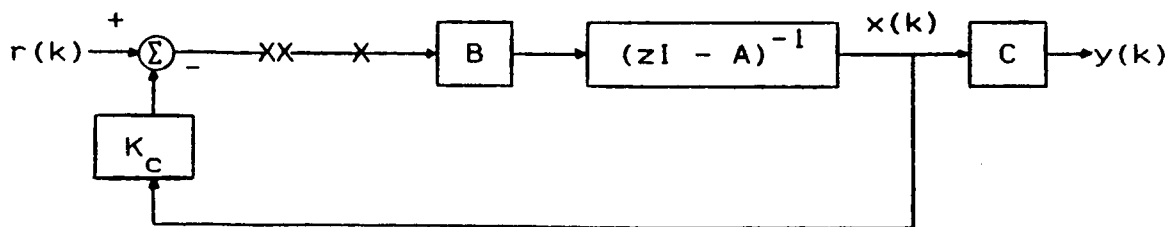
FIGURE 1. The LQ Based Optimal Controller

The optimal control for this system is described by the following equation.

$$u(k) = -K_c x(k) \qquad (2)$$

In the case that the state measurements are corrupted by white gaussian noise an LQG controller can be designed in which the Kalman filter is used to estimate the states. The LQG design results in the following controller equations for the infinite horizon problem.

The Kalman filter is described by

$$\hat{x}(k+1) = A\hat{x}(k)+Bu(k)+K_f[y(k+1)-CA\hat{x}(k)-CBu(k)] \qquad (3)$$

and the optimal control is described by

$$u(k) = -K_c\hat{x}(k) \qquad (4)$$

Figure 2 depicts the LQG system.
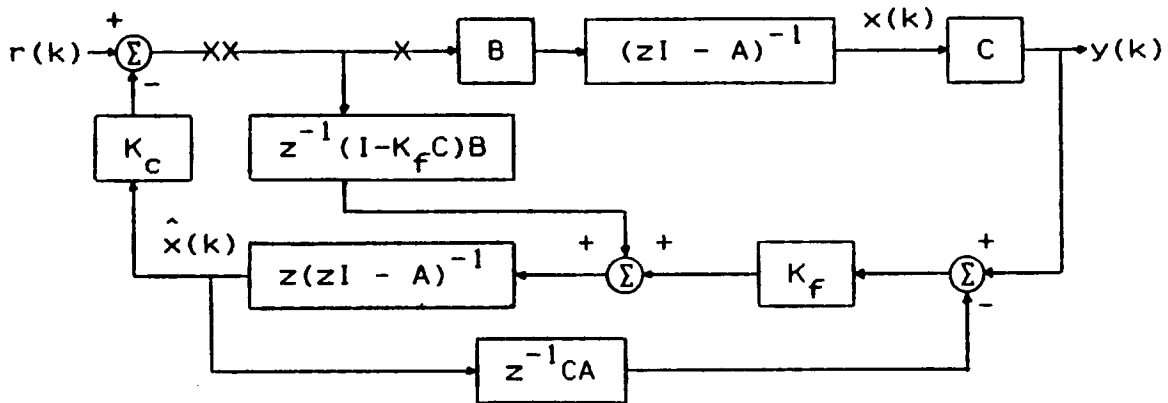
FIGURE 2. The LQG Based Optimal Controller/Observer

The following three properties of the system have been established :

P1: The closed loop transfer function matrices from r(k) to x(k) are identical in both the LQG and LQ systems.

P2: The loop transfer function matrices with the loops broken at XX are identical in both implementations.

P3: The loop transfer function matrices with the loops broken at X are generally different. Furthermore the LQG open-loop system might possibly have unstable poles.

423

The return difference ratios of the LQG and LQ systems are given by the following expressions.

$$T_{lqg}(z) = zK_c[zI-(I-K_fC)A+(I-K_fC)BK_c]^{-1}K_fC(zI-A)^{-1}B \qquad (5)$$

$$T_{lq}(z) = K_c(zI-A)^{-1}B \qquad (6)$$

Now define

$$\Delta(z) = T_{lqg}(z) - T_{lq}(z) \qquad (7)$$

It is now proposed to replace the constant optimal feedback gains K_c by a dynamic system $\Psi(z)$ in the LQG system and solve for it as $\Delta(z)$ approaches zero pointwise in z.

$$\Delta(z) = T_{lqg}(z)\Big|_{K_c=\Psi(z)} - T_{lq}(z) = 0 \qquad (8)$$

$$\Delta(z) = z\Psi(z)[zI-(I-K_fC)A+(I-K_fC)B\Psi(z)]^{-1}K_fC(zI-A)^{-1}B$$
$$- K_c(zI-A)^{-1}B = 0 \qquad (9)$$

$$\{z\Psi(z)[zI-(I-K_fC)A+(I-K_fC)B\Psi(z)]^{-1}K_fC-K_c\}(zI-A)^{-1}B = 0 \qquad (10)$$

Since $(zI-A)^{-1}B \neq 0$ equation (9) becomes

$$z\Psi(z)[zI-(I-K_fC)A+(I-K_fC)B\Psi(z)]^{-1}K_fC-K_c = 0 \qquad (11)$$

To solve for $\Psi(z)$ it is necessary to assume that $\det(K_fC)\neq 0$. This implies that the number of outputs should be equal to the number of states i.e. m = n. Equation (10) then becomes

$$\{z\Psi(z)[zI-(I-K_fC)A+(I-K_fC)B\Psi(z)]^{-1}-K_c(K_fC)^{-1}\}K_fC = 0 \qquad (12)$$

or

$$z\Psi(z)[zI-(I-K_fC)A+(I-K_fC)B\Psi(z)]^{-1} - K_c(K_fC)^{-1} = 0 \qquad (13)$$

$$\{z\Psi(z)-K_c(K_fC)^{-1}[zI-(I-K_fC)A+(I-K_fC)B\Psi(z)]\} *$$
$$[zI-(I-K_fC)A+(I-K_fC)B\Psi(z)]^{-1} = 0 \qquad (14)$$

424

$$\{z\Psi(z)-K_c(K_fC)^{-1}[zI-(I-K_fC)A]-K_c(K_fC)^{-1}(I-K_fC)B\Psi(z)\} *$$

$$[zI-(I-K_fC)A+(I-K_fC)B\Psi(z)]^{-1} = 0 \qquad (15)$$

$$\Delta(z) = \{[zI-K_c(K_fC)^{-1}(I-K_fC)B]\Psi(z)$$

$$- K_c(K_fC)^{-1}[zI-(I-K_fC)A]\} *$$

$$\{(zI-(I-K_fC)A+(I-K_fC)B\Psi(z)]^{-1}K_fC\} *$$

$$(zI-A)^{-1}b = 0 \qquad (16)$$

Therefore, if

$$\Psi(z) = [zI-K_c(K_fC)^{-1}(I-K_fC)B]^{-1}K_c(K_fC)^{-1}[zI-(I-K_fC)A] \qquad (17)$$

Then $\Delta(z) = 0$.

III. OBSERVATIONS

Before an example can be presented to demonstrate the effect of the dynamic compensator the following observations must be stated. Several problems are encountered in the design of the dynamic compensator. The major problem is the dependence of the compensator coefficients on the Kalman filter gains. Many of the problematic systems that were investigated, i.e. those with unstable controllers, result in extremely high compensator gains, and large, hence unstable, compensator poles. The reason for this behavior is observed to be the high condition numbers associated with K_f and K_fC. Because of this high condition number the matrix $(K_fC)^{-1}$ has extremely large entries, which in turn result in large poles and compensator gains.

A system similar to the one investigated by Doyle and Stein [2], chosen specifically to illustrate the unstable controller poles, resulted in extremely high compensator gains, and large unstable poles. Although the compensator

recovered the stability margins at the plant input of the LQG system it is not an acceptable compensator. In an attempt to find a physically realizable compensator several systems have been tested. Those that result in a realizable compensator have the properties that, the matrices mentioned previously have low condition numbers, and the controller eigenvalues are all within the unit circle. Since the controller is stable the low phase and gain margins associated with the problematic LQG systems are not observed, and the dynamic compensator does not have a pronounced effect to validate its use in practical systems.

IV. AN EXAMPLE

To illustrate the effects of the dynamic compensator on the stability margins of the open loop frequency response the following example was considered.

Let the plant be described by the following state equation :

$$x(k+1) = \begin{bmatrix} 1.0 & 0.005 \\ -0.015 & 0.98 \end{bmatrix} x(k) + \begin{bmatrix} 1.25E-5 \\ 0.005 \end{bmatrix} u(k)$$

$$+ \begin{bmatrix} 0.18 \\ -0.3 \end{bmatrix} w(k) \quad (18)$$

$$y(k) = \begin{bmatrix} 2.0 & 1.0 \\ 0.0 & 0.3648 \end{bmatrix} x(k) + \begin{bmatrix} 1.0 & 0.0 \\ 0.0 & 1.0 \end{bmatrix} v(k)$$

With $E\{w(k)\}=E\{v(k)\}=0$; $E\{w(i)w(j)\}=E\{v(i)v(j)\}=200\delta_{ij}$

The controller is :

$$u(k)= - [50.0 \quad 10.0] \hat{x}(k)$$

The state estimates are described by equation (3), where the

Kalman filter gains are given by,

$$K_f = \begin{bmatrix} 0.0827901406 & -0.13645879 \\ -0.13430101 & 0.223924574 \end{bmatrix} \quad (19)$$

The compensator as obtained from equation (17) is

$$\Psi(z) = \left[357.546 \frac{(z - 0.85914)}{(z - 0.125149)} \right.$$

$$\left. 34.2609 \frac{(z - 0.73884)}{(z - 0.125149)} \right] \quad (20)$$

To investigate the effect of the compensator on the system, the open loop frequency responses of the system are determined at both of the breakpoints defined previously. In Figure 3 the Nyquist plots of the system with the constant LQ gains are depicted. The Nyquist plots of Figure 4 are those of the system with the dynamic compensator. As seen, even though there is a slight increase in the phase margin the difference is not significant. Also the system exhibits an unexpected behavior at high frequencies which decreases the gain margin.

To observe the effect of the compensator on system robustness the plant was perturbed to be

$$x(k+1) = \begin{bmatrix} 1.0 & 0.1 \\ -0.2 & 0.9 \end{bmatrix} x(k) + \begin{bmatrix} 1.25E-5 \\ 0.005 \end{bmatrix} u(k)$$

$$+ \begin{bmatrix} 0.18 \\ -0.3 \end{bmatrix} w(k) \quad (21)$$

$$y(k) = \begin{bmatrix} 2.0 & 1.0 \\ 0.0 & 0.3648 \end{bmatrix} x(k) + \begin{bmatrix} 1.0 & 0.0 \\ 0.0 & 1.0 \end{bmatrix} v(k)$$

427

The Nyquist plots of Figures 5 and 6 as obtained for the open loop responses of the system with and without the dynamic compensator indicate that the effect is not significant, but that there is definitely an improvement. As seen from Figure 6 there is an improvement in both the gain and phase margins,at the plant input, i.e., the loop breaking point XX. However at point X there is a decrease in the gain margin while a slight increase in the phase margin was noted.

The following example demonstrates the fact that although the compensator designed for the system is not practically acceptable it recovers the stability margins at the plant input of the LQG system. The plant is the same as the one given in (18) with the C matrix chosen to result in an unstable controller. The plant output is decribed by the following equation :

$$y(k) = \begin{bmatrix} 2.0 & 1.0 \\ 0.0 & 0.1 \end{bmatrix} x(k) + \begin{bmatrix} 1.0 & 0.0 \\ 0.0 & 1.0 \end{bmatrix} v(k) \qquad (22)$$

The Kalman filter gains for this system are given by,

$$K_f = \begin{bmatrix} 0.143435809 & -0.0624081382 \\ -0.23095458 & 0.10172081836 \end{bmatrix} \qquad (23)$$

The compensator is described by,

$$\Psi(z) = \left[-181195.7489 \ \frac{(z - 0.99095002)}{(z + 565.52065)} \right.$$

$$\left. -112641.206 \ \frac{(z - 0.98813697)}{(z + 565.52065)} \right] \qquad (20)$$

The Nyquist plots of the system, with and without the compensator are depicted in Figures 7 and 8. As seen from

Figure 8 the LQ open-loop frequency response is recovered at the plant input,i.e. at point X, when the compensator is used. However the extremely large gains of the compensator drastically change the frequency response of the system with the loop opened within the controller,at point XX.

V. CONCLUSION

As seen from the results described above, the dynamic compensator that was designed to mimic the return difference of the LQ system at the plant input of the LQG system did result in the anticipated improvement in the stability margins at the plant input. An appreciable improvement is observed for the LQG system with the unstable controller, though there is no longer any guaranteed stability margins at the loop opening point within the controller,i.e. at point XX. The same magnitude of improvement is not seen for systems with stable controllers. However, an increase in the phase margins is observed when the plant model is perturbed. Further research may be directed towards investigating why a realizable compensator can not be obtained for all systems which have unstable controllers,and hence low stability margins, especially for systems that do not have the same number of states and outputs. Also an investigation of the effects of the compensator on the time response of the system must be performed.

REFERENCES

[1] Doyle,J.C., "Guaranteed Margins for LQG Regulators," IEEE Trans. Auto. Cont., Aug. 1978.

[2] Doyle,J.C., Stein,G., "Robustness with Observers," IEEE Trans. Auto. Cont., Aug. 1979.

[3] Johnson,C.D., "State-variable Design Methods May Produce Unstable Feedback Controllers," Int. Jour. Cont., April 1979.

[4] O'Reilly,J., Observers for Linear Systems , Academic Press, N.Y. 1983.

[5] Madiwale,A.N., Williams,D.E., "Some Extensions of Loop Transfer Recovery ,", ACC ,1985, pp 790-795.

[6] Gupta,N.K., "Robust Control/Estimator Design by Frequency-shaped Functionals," IEEE Conf. on Dec. and Control (CDC), 1981, pp 1167-1172.

[7] Moore,J.B., Gangsaas,D., Blight,J.D., "Performance and Robustness Trades in LQG Regulator Design," IEEE CDC, 1981, pp 1191-1200.

[8] Anderson,B.D.O., Moore,J.B., Mingori,D.L. "Relations Between Frequency Dependent Control and State Weighting in LQG Problems," IEEE CDC, 1983, pp 612-617.

[9] Okada,T., Kihara,M., Furihata,H., "Robust Control System with Observer," Int. Jour. Cont., May 1985.
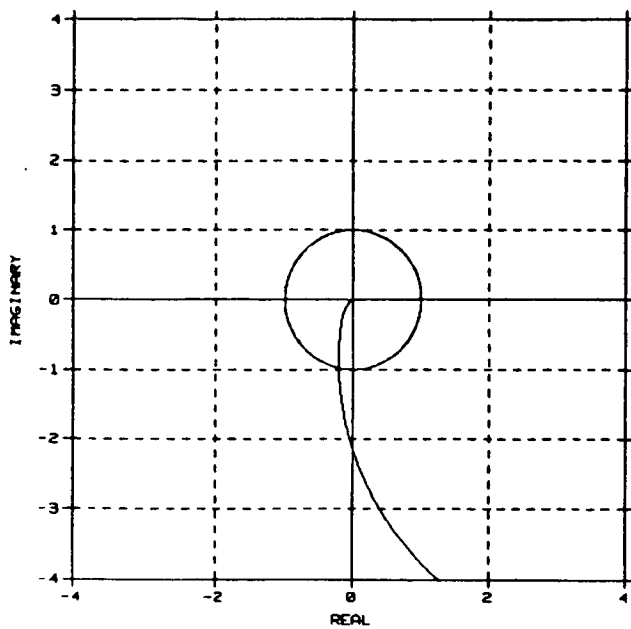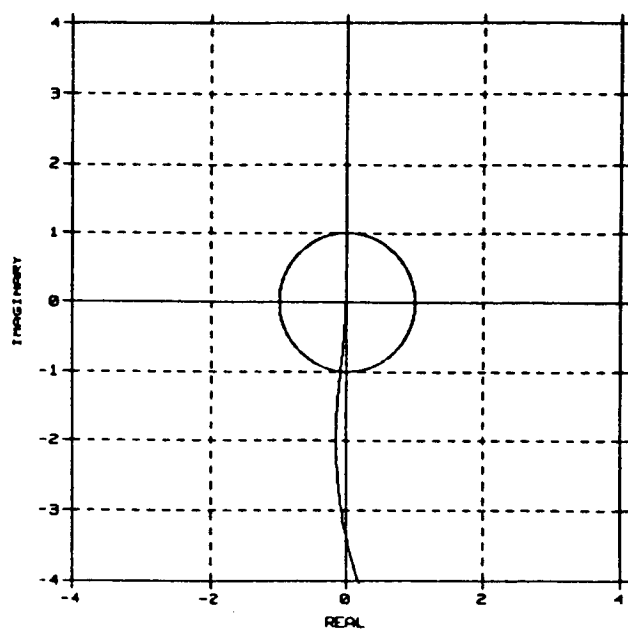
a)Loop point X   b)Loop point XX

Figure 3. LQG System Frequency Response With Constant
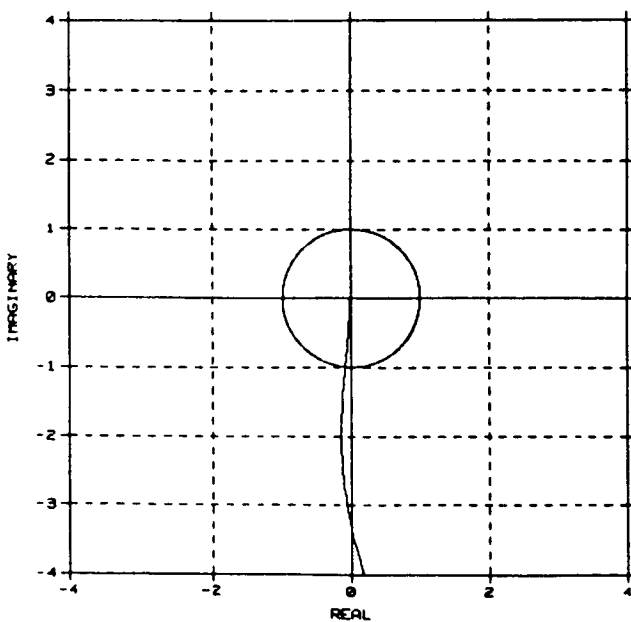
Optimal LQ Gains
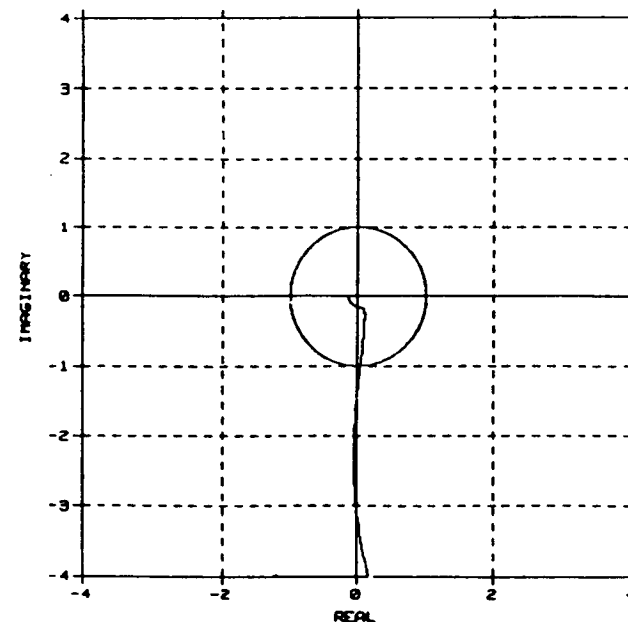
a)Loop point X   b)Loop point XX

Figure 4. LQG System Frequency Response With Dynamic

Compensator

431
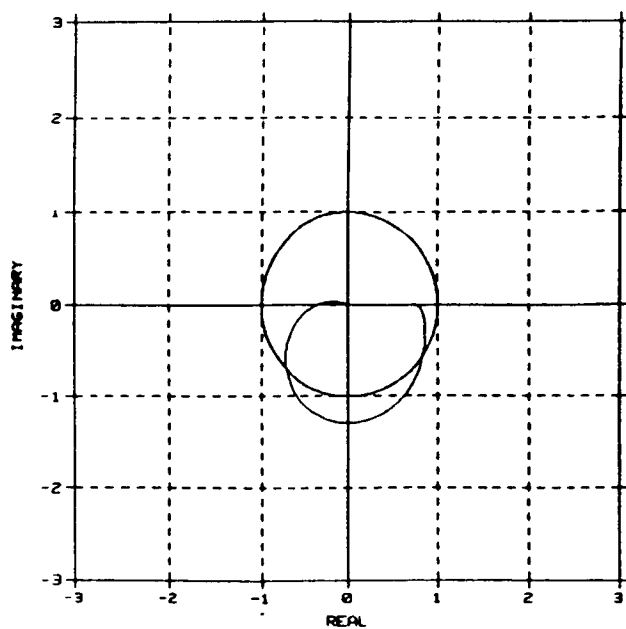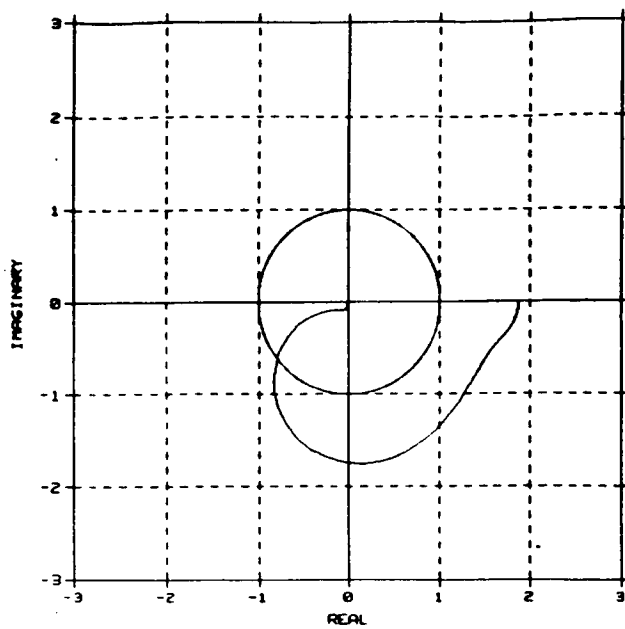
a)Loop point X

b)Loop point XX

Figure 5.   Perturbed LQG System Frequency Response

With Constant Optimal LQ Gains
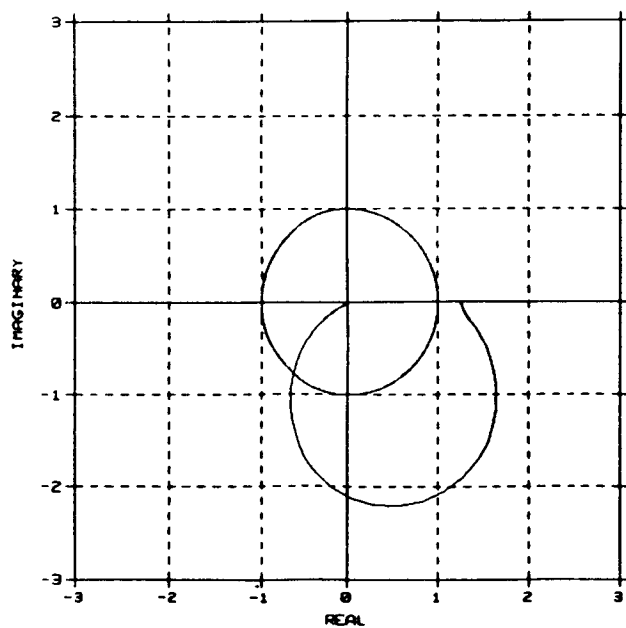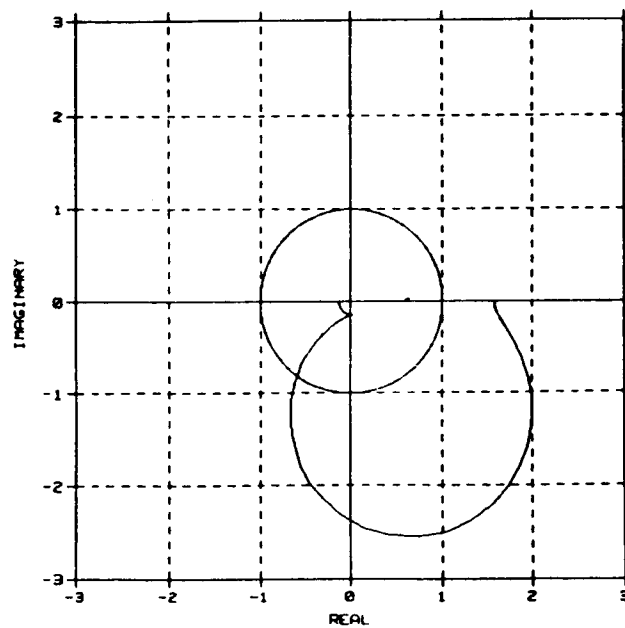
a)Loop point X

b)Loop point XX

Figure 6. Perturbed LQG System Frequency Response

With Dynamic Compensator

432
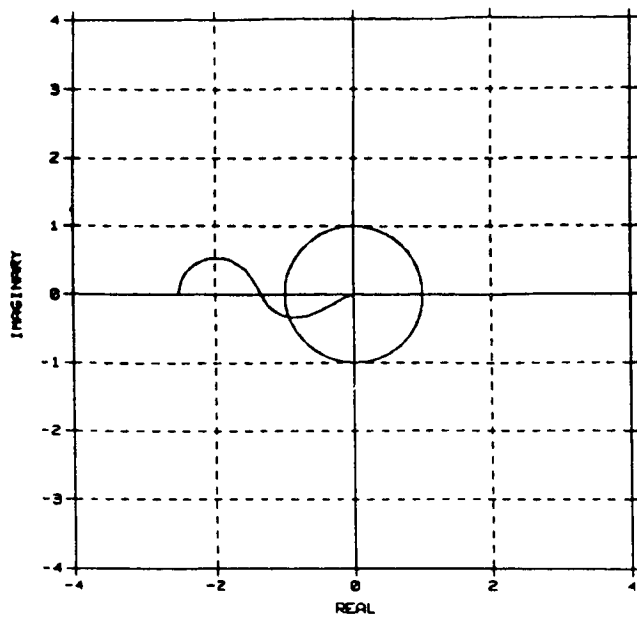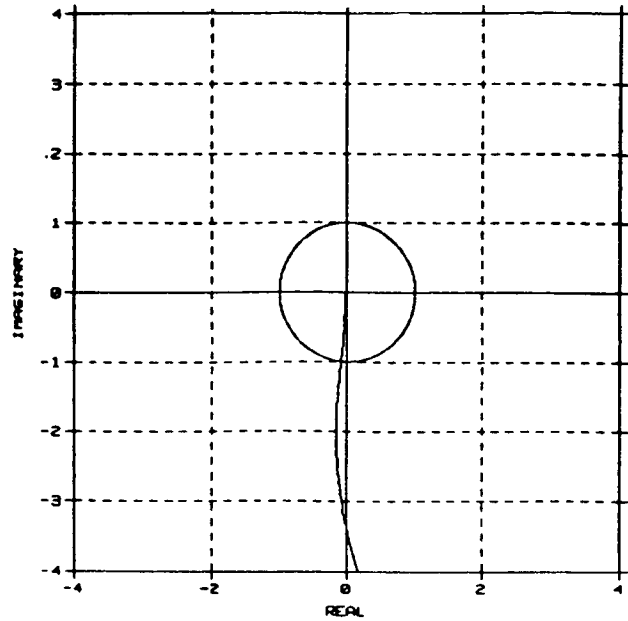
a)Loop point X   b)Loop point XX

Figure 7.   LQG System Frequency Response With Constant

Optimal LQ Gains. (Unstable Controller)
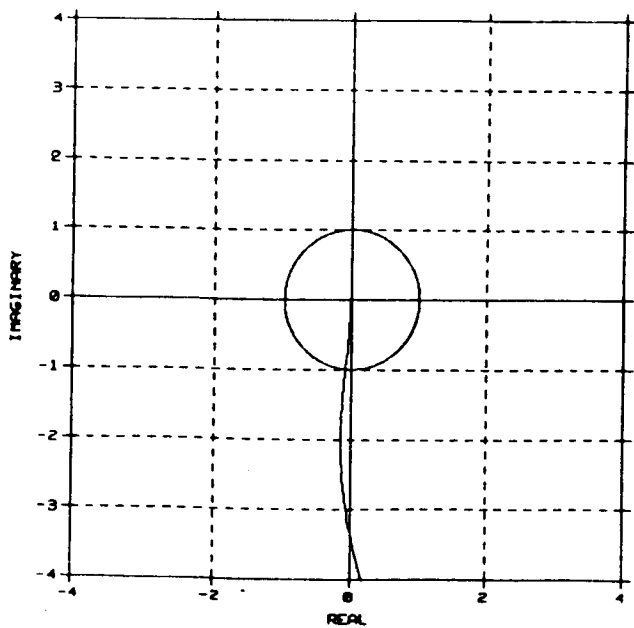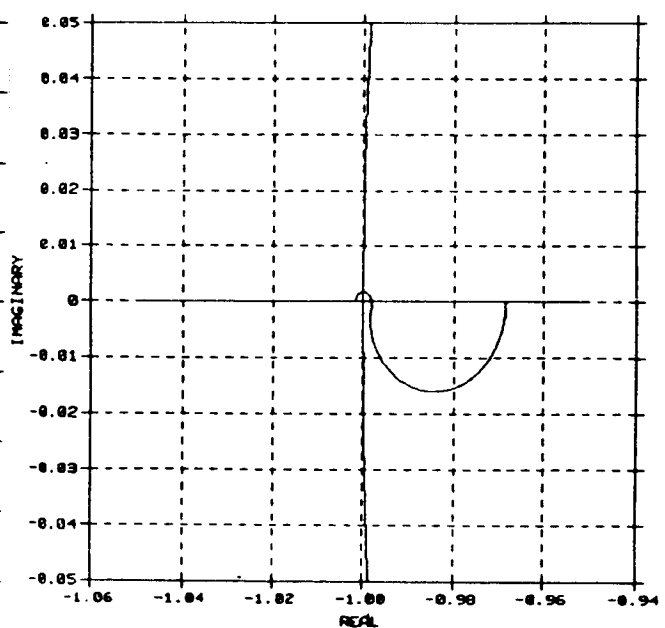
a)Loop point X   b)Loop point XX

Figure 8.   LQG System Frequency Response With Dynamic

Compensator. (Unstable Controller)

An Overview of Controls Research
on the NASA LaRC Grid

by
Raymond C. Montgomery
Spacecraft Control Branch
NASA Langley Research Center
Hampton, VA 23665

Presented at the
Workshop on Structural Dynamics and Control
Interaction of Flexible Structures
NASA Marshall Space Flight Center
Alabama 35812

April 22-24, 1986

OVERVIEW

ORIGINAL PAGE IS
OF POOR QUALITY

The NASA Langley Research Center has assembled a flexible grid on which
control systems research can be accomplished on a two-dimensional
structure that has many physically distributed sensors and actuators.
The grid is a rectangular planar structure that is suspended by two
cables attached to one edge so that out of plane vibrations are normal
to gravity. There are six torque wheel actuators mounted to it so that
torque is produced in the grid plane. Also, there are six rate gyros
mounted to sense angular motion in the grid plane and eight
accelerometers that measure linear acceleration normal to the grid
plane. All components can be relocated to meet specific control system
test requirements. Digital, analog , and hybrid control systems
capability is provided in the apparatus.

To date, research on this grid has been conducted in the areas of system
and parameter identification, modal estimation, distributed modal
control, heirarchial adaptive control, and advanced redundancy
management algorithms. The presentation overviews each technique
and will present the most significant results generated for each area.

436

AN OVERVIEW OF CONTROLS RESEARCH ON THE NASA LaRC GRID

by
Raymond C. Montgomery
Spacecraft Control Branch
NASA Langley Research Center
Hampton, Va. 23665

22 April, 1986

GRID SIMULATOR MODEL

A simulator is available for interested researchers to use in the development of algorithms to be tested on the grid. Finite element modelling is used to generate mode shapes and frequencies for use in the simulator and in control system design models. The grid is modelled with 68 node points and the cable support with 8. Only out of plane motion is considered.

GRID SIMULATOR MODEL

The finite element analysis is carried out with a software package
called SPAR which is available on the LaRC mainframe computer complex.
This package generates printed and graphical output as well files
resident on the computer complex used to transfer data efficiently to
the batch simulator. The batch simulator is used both in the simulation
mode and in control-system design, e.g. to calculate optimal feedback
gains and filter constants for a design.

The simulator has printed and graphical output as well as output
files reflecting control system design constants. These files can be
transferred to the laboratory via high speed serial communication where
the control law can be tested with the laboratory apparatus. The
laboratory computer is a Charles River Data Computer with a UNIX
lookalike operating system called UNOS.

All operations on the simulator and the laboratory apparatus can be
carried out from remote sites. As an example, guest researchers at Ohio
State University have successfully tested a heirarchial control law from
their campus at Columbus, OH.

Some significant algorithms and results will now be described.

**ORIGINAL PAGE IS
OF POOR QUALITY**

ARCHITECTURE OF THE GRID SIMULATOR

441
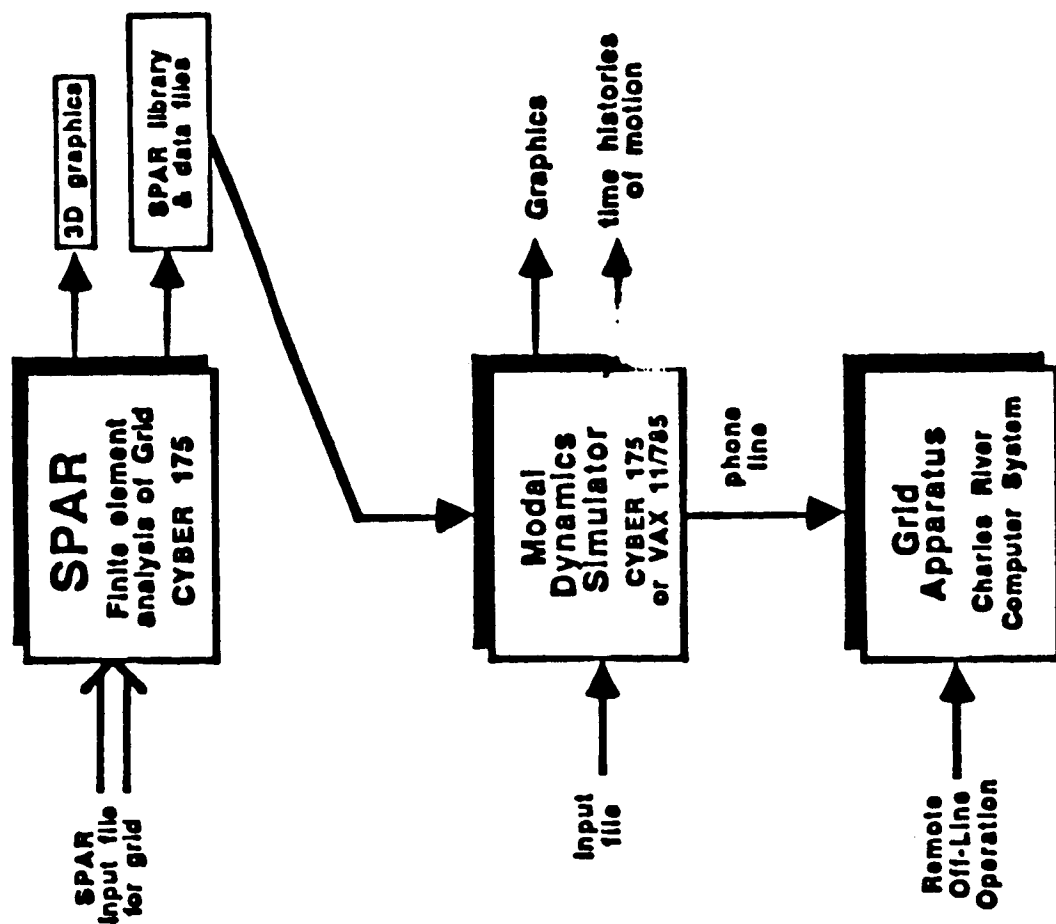
SYSTEM IDENTIFICATION USING
LEAST SQUARE LATTICE FILTERS

The least square lattice filter has been used to determine mode shapes and frequencies of the grid apparatus. Records of the unforced response of the grid at several frequencies were made and frequency and damping and mode shape information was empirically determined by post-processing the records using the lattice filter. The filter is an exact, order recursive, least square solution of the linear least square estimation problem. Although the form of the filter is not linear, there is a simple method of extracting the coefficients of the linear ARMA model form from the lattice filter model. This is done by obtaing the response of the identified lattice filter to the input sequence (1,0,0,...,0). Deciding the proper order of the model given the input data is also required. This has been done by graphing the norm of the model error and selecting the model order as the lowest whose error norm is less than a given threshold. The application of the lattice filter to the grid is presented in:

Montgomery, R. C. and N. Sundararajan: The Application of Least Square Lattice Filters for Identifying the Dynamics of a Two-Dimensional Grid Structure. Journal of Astronautical Sciences, Vol. 33, No. 1, January-March 1985, pp. 35-47.

LSL IN VARIABLE ORDER SYSTEMS ID

Order Determination
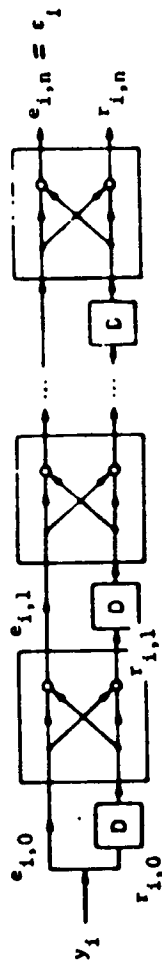
Structural Dynamics Models $y_k = \Phi_k \theta_k + \eta_k$

Relation to LSL $y_i = \phi_i^t \theta_{L_i} + \epsilon_i$

$$\phi_L = [r_{i-1,0} , \cdots , r_{i-1,n-1}]$$

$$\theta_L^t = (k_{i,1} , \cdots , k_{i,u})$$

AR Parameter Extraction
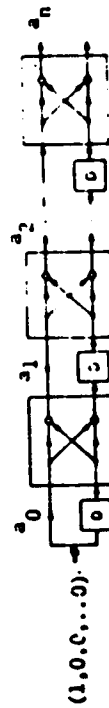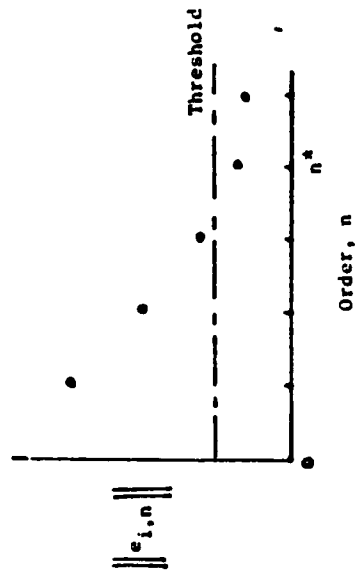
FAILURE DETECTION AND CONTROL SYSTEM RECONFIGURATION

Research on advanced failure detection and system reconfiguration methods has also been accomplished on the grid apparatus. Because of the computational limitations parallel optimal decision theory methods (e.g. banks of Kalman filters operating in parallel using different sets of input data) could not be investigated and a scheme employing sequential testing was developed. In this scheme a bank of Kalman filters is used, however, only one is on-line at a time. The decision to switch to another filter is made by examining the residuals of the operating filter using the sequential probability ratio test (SPRT). Which filter to switch to is determined by the SPRT interpreter. This research is reported in:

Williams, J. P. and R. C. Montgomery: Failure Detection and Accommodation in Structural Dynamics Systems Using Analytic Redundancy. 24th IEEE Conference on Decision and Control. Ft. Lauderdale, FL, December 11-13, 1985, pp. 906-910.

FAILURE HYPOTHESIS TESTING
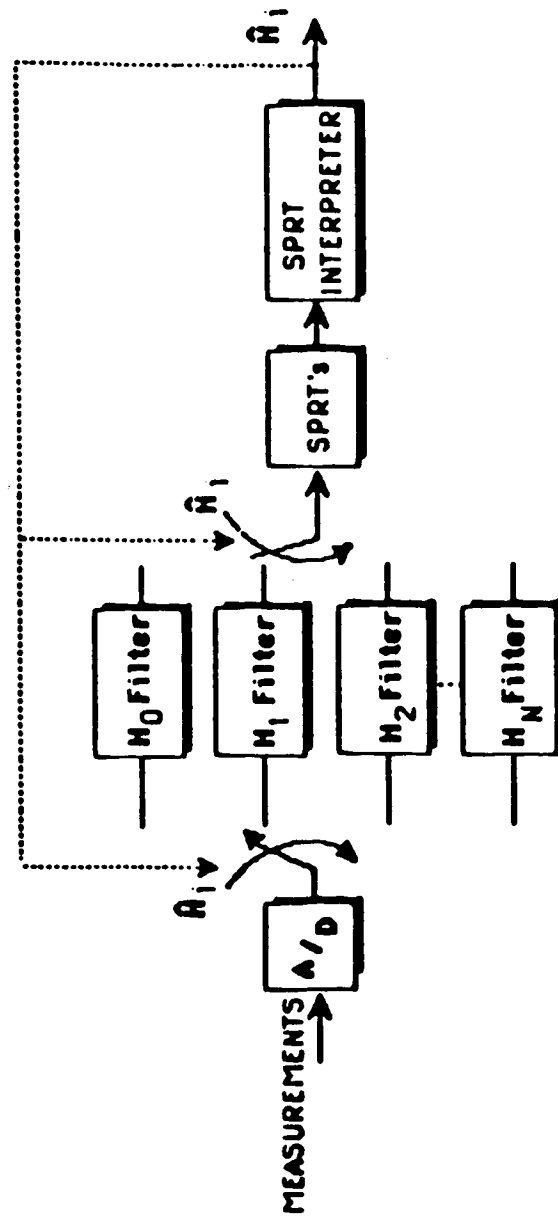
SEQUENTIAL PROBABILITY RATIO TEST (SPRT)

The sequential probability ratio test (SPRT) makes a selection of one from two possible decisions. It is an optimal binary decision test that makes the decision in the least number of observations. It is used with the innovations sequence of the active Kalman filter to decide between the two decisions: the sequence is Gaussian with zero mean and given variance or, the sequence is Gaussian with mean m and given variance. The former case corresponds to the hypothesis of no failures whereas the later corresponds to a failure being present in the system. When a failure is detected the innovation sequence is examined to isolate the failed component.

SEQUENTIAL PROBABILITY RATIO TEST
(SPRT)

* **BINARY HYPOTHESIS TEST**

* **ECONOMIZES ON THE NUMBER OF OBSERVATIONS REQUIRED TO MAKE A DECISION ON THE STATISTICS OF A SAMPLE**

* **USED HERE TO DECIDE WHICH HYPOTHESIS ON THE KALMAN FILTER RESIDUAL SEQUENCE IS MOST PROBABLY TRUE:**

H0: K-F INNOVATIONS SEQUENCE IS GAUSSIAN WITH MEAN 0 AND VARIANCE σ^2
(NO FAILURE HYPOTHESIS)

H1: K-F INNOVATIONS SEQUENCE IS GAUSSIAN WITH MEAN m AND VARIANCE σ^2
(FAILURE HYPOTHESIS)

FAILURE DETECTION AND RECONFIGURATION

The figure shows time histories of on-line failure detection using the
SPRT algorithm to detect a failure. Depending on the input data, each
time a SPRT is started the decision variable will drift from its initial
value of zero towards the decision thresholds. The time required to
reach and cross one of the thresholds is the decision time. This is a
theoretical minimum for the SPRT algorithm. A tendancy of the decision
variable to drift to the failure threshold can be caused by modelling
errors or other events that make the residual (or innovations sequence)
non-white. In application to structural dynamics systems one obvious
cause is spillover of unmodelled structural modes into the residuals.
The assumption here is that the cause is a failure of a sensor or
actuator. Each time a "no failure" decision is made a new SPRT is
started. Following a "failure" decision the residuals are examined to
determine which failure, if any, caused the alarm. After successful
isolation of the failure, a new filter, designed to operate without the
failed component, is used.

For the example of this histogram only sensor failures are considered.
Also, the "no failure" threshold is positive and the "failure" threshold
is negative. At the start of the histograms there are no failures.
Note that the residuals are non-white and that they cause a delay in the
decision time since the decision variable drifts toward the "failure"
threshold. As time progresses the effects of initializing the Kalman
filter decay and the non-white nature of the residual is smaller. The
SPRT in this case makes the decision rapidly without a tendancy of the
decision variable to move toward the "failure" decision. In the later
phase of the histogram a failure is injected into the system. It is
detected and isolated and a new filter is initialized that is designed
without the failed sensor. The sawtooth wave near the end of the
histogram indicates successful recovery of the system from the failure.

FAILURE DETECTION AND RECONFIGURATION

449
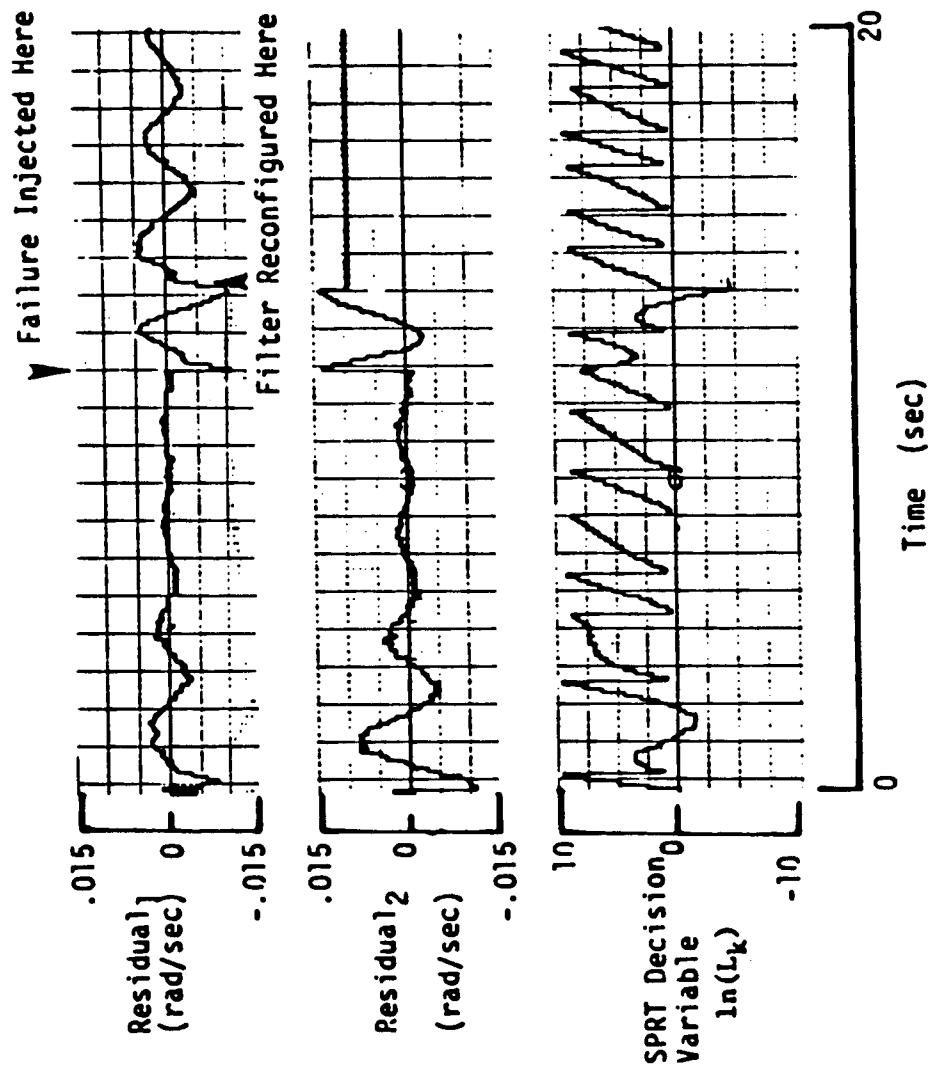
DECENTRALIZED ADAPTIVE CONTROL STRUCTURE

A decentralized adaptive control scheme was remotely tested on the
Langley grid apparatus from the Ohio State University. The adaptive
control scheme investigated considers a group of linear subsystems
consisting of linear state dynamics with coupling to the other
subsystems, a measurement, and an actuator. Each subsystem has a linear
controller with a gain on its measured subsystem state, on the input,
and on the error between the actual subsystem state and its reference
state as generated by a reference model in response to the input. The
gains are driven by adaptation logic that is the subject of the
research.

A more complete description of this research is reported in:

Ozguner, U., Yurkovitch, S., Martin, J., III, and F. Al-Abbass:
Decentralized Control Experiments on NASA's Flexible Grid. Proceedings
of the 1986 American Control Conference, Volume II, pp. 1045-1051.
Seattle, WA.   June 19,1986.

DECENTRALIZED ADAPTIVE CONTROL STRUCTURE
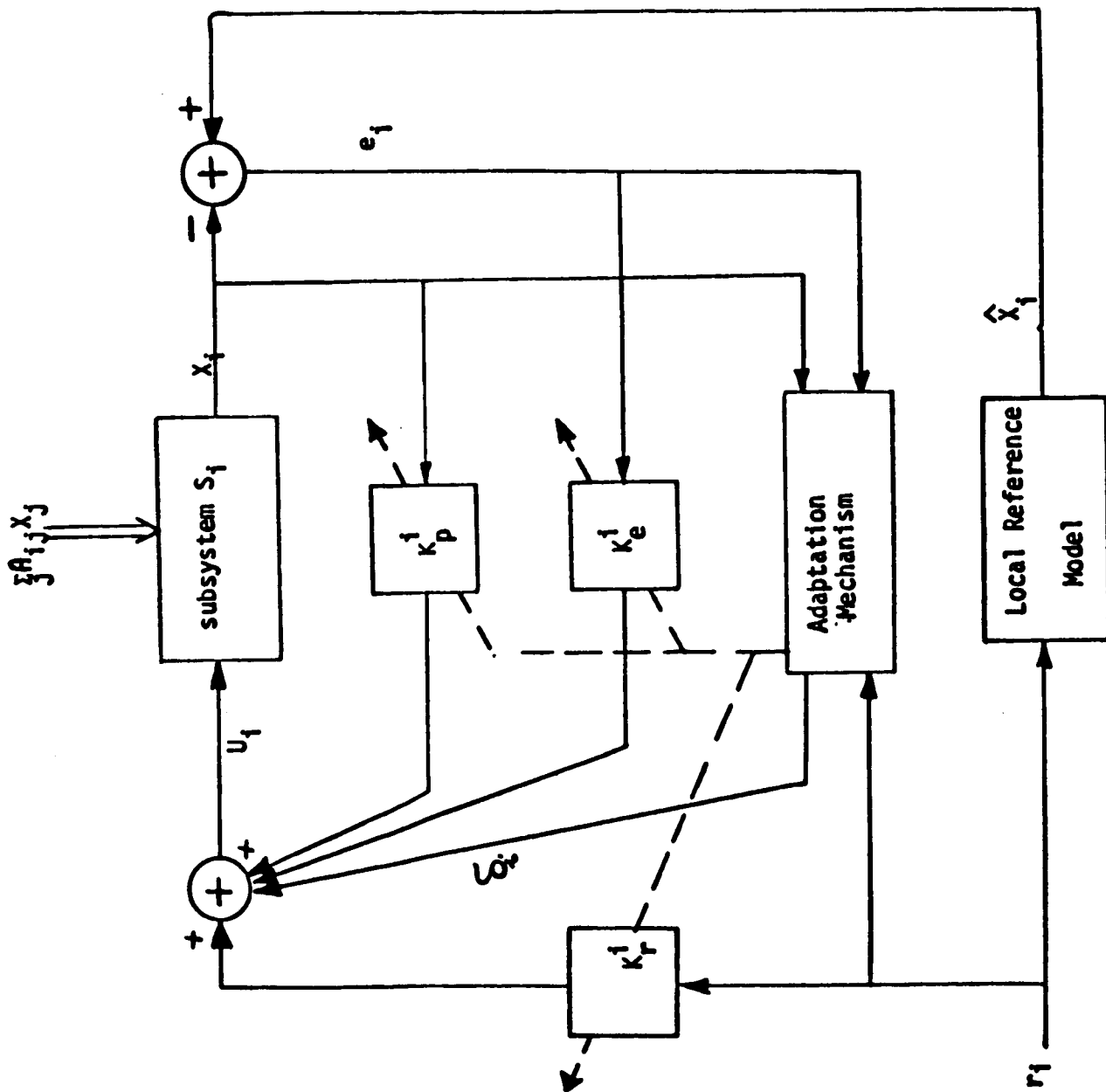
DECENTRALIZED ADAPTIVE CONTROL OF THE GRID

This chart shows simulation time histories of the rate gyro outputs and
the angle estimates on the Langley grid. The controller is the
decentralized adaptive controller previously described wherein each mode
was considered as a separate subsystem. The controller is stable and
produces damping in all simulated modes.

ORIGINAL PAGE IS
OF POOR QUALITY

452

DECENTRALIZED ADAPTIVE
CONTROL OF THE GRID

453
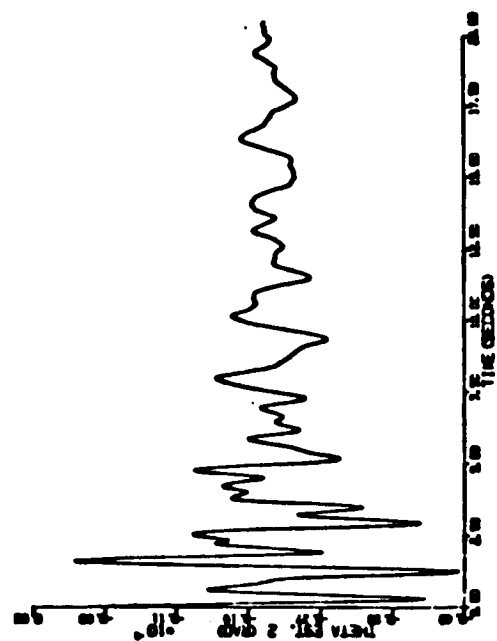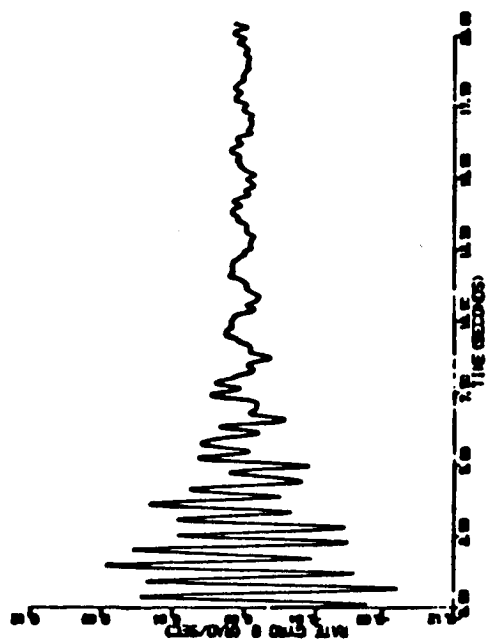
SUMMARY

The Langley grid apparatus has been used in the conduct of research in
several areas of interest in the control of large flexible spacecraft.
These include system identification, modal estimation, distributed modal
control, heirarchial adaptive control, and advanced redundancy
management techniques. Some of these research areas have been described
herein. The grid will continue to be available over the next several
years providing the academic community oportunities for research that
are not available at most universities.   The remote testing capability
of the facility allows researchers the use of realistic hardware to
validate their theories from their own remote site.

SUMMARY

* THE GRID APPARATUS HAS BEEN USED TO CONDUCT RESEARCH IN A NUMBER OF AREAS IMPORTANT TO THE CONTROL OF LARGE FLEXIBLE SPACE STRUCTURES. SOME OF THE AREAS ARE:

  - SYSTEM AND PARAMETER IDENTIFICATION
  - MODAL ESTIMATION
  - DISTRIBUTED MODAL CONTROL
  - HIEARCHIAL ADAPTIVE CONTROL
  - ADVANCED REDUNDANCY MANAGEMENT

* THE GRID AND THE CONTROL PROCESSING COMPUTER ARE A GOOD TEST-BED FOR THE NEW ESTIMATION, CONTROL, AND REDUNDANCEY MANAGEMENT TECHNIQUES

* IT IS POSSIBLE TO RUN CLOSED LOOP EXPERIMENTS FROM REMOTE SITES

455

SPACE
STATION
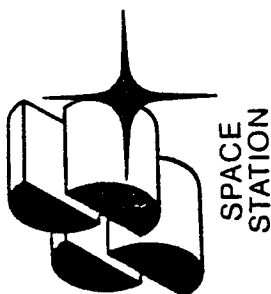
Structural/Control Interaction (Payload Pointing and Micro-g)

Presented to

NASA / MSFC

Workshop on Structural Dynamics

and

Control Interaction of Flexible Structures

April 22, 1986

Presented by C. R. Larson
(213) 922-2031

CHART 1.

On Space Station there are two important customer accommodation requirements: payload pointing and migro-g. A simulation model was developed to evaluate the system capability to meet the requirements. The pointing requirement of a payload is not defined but is expected to be around one arc second. The acceleration requirement for a material processing or life science experiment is 1×10^{-5} G's.

Structural/Control Interaction Objectives

- EVALUATE THE CAPABILITY OF A TYPICAL SPACE STATION PAYLOAD TO MEET ITS POINTING REQUIREMENT (POINTING REQUIREMENT MAY BE ONE ARC SEC)

- DETERMINE IF THE G-LEVEL REQUIREMENT OF 1×10^{-5} G CAN BE PROVIDED FOR MATERIAL PROCESSING EXPERIMENTS

36SS177036

459

CHART 2

Two simulation models were developed. One with a coarse pointing control system and one with a fine pointing control system. The agenda will address both simulations. The coarse simulation is running and the results from the simulation will be discussed. The fine is in the beginning stage of development and will only be briefly mentioned.

Structural/Control Interaction Agenda

- **SIMULATION MODEL**

- **COARSE CONTROLLER**
  - DEFINITION
    - CONFIGURATION
    - CONTROL SYSTEMS
  - PROBLEMS
  - EQUATIONS OF MOTION
  - COARSE CONTROLLER
  - C.G. OFFSET EFFECT
  - RESULTS
    - PAYLOAD POINTING
    - MICRO-G
    - REBOOST
    - MRMS

- **FINE CONTROLLER**
  - METHODS
  - CONTROL SYSTEM DEFINITION
  - STATUS & FUTURE ACTIVITIES

- **CONCLUSIONS**

SPACE STATION

Rockwell International

Space Station Systems Division

36SSS177037

461

CHART 3

A 9000 lb telescope with a 0.05 ft cg offset was chosen to represent a typical payload. The Space Station simulation model is shown in the figure. The telescope is attached to the top of the keel and its mass properties are listed. The model includes the control systems of the payload, alpha controller, the CMG controller, and the migrogravity isolation controller.

Telescope Used to Evaluate Pointing Problem
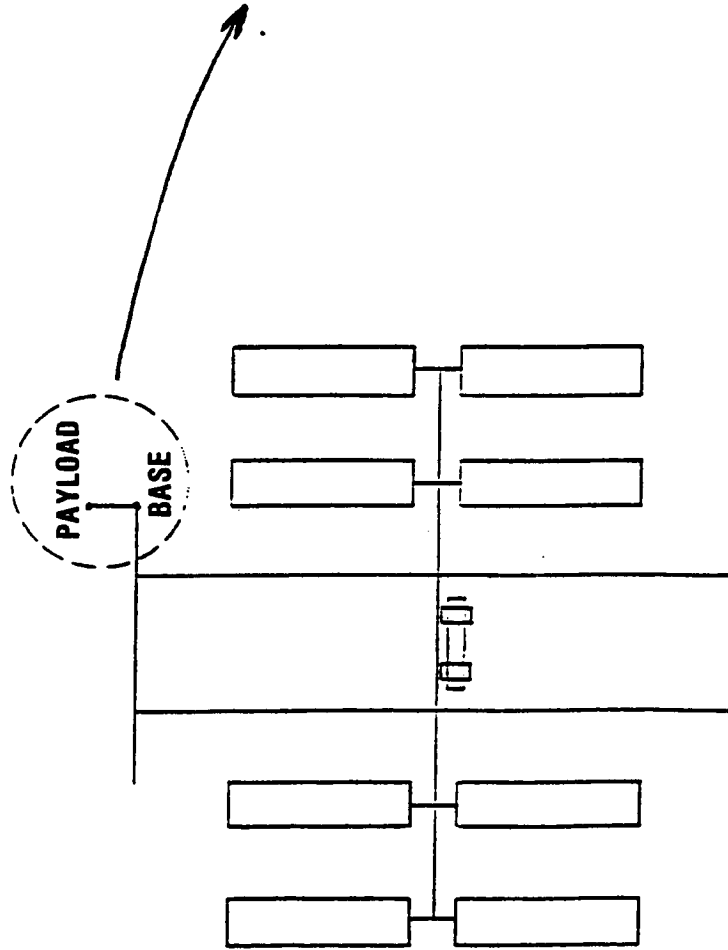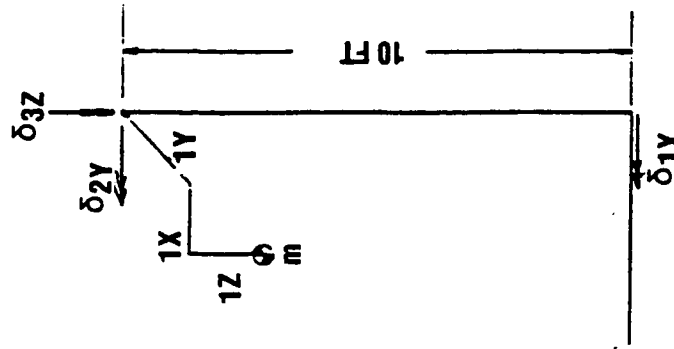
$$IX = 1Y = 1Z = .346 \text{ M}$$
$$M = 275 \text{ slug}$$
$$IX = 1 \times 10^6 \text{ slug - M}^2$$
$$I_Y = I_Z = 1.44 \times 10^7 \text{ slug - IN.}^2$$

SPACE STATION

36SSS177038

Rockwell International
Space Station Systems Division

463

CHART 4

The simulation model contains the listed modes. The 85 structural modes include 6 rigid body modes and 79 flexible modes. The other 8 control system modes are added to remove the locked constraint of the control surfaces (this constraint was used in the structural mode development). The 8 control surface modes are coupled with the structural modes so that the mass matrix is not diagonal.

The four control systems in the model are listed. The solar array pointing system and the CMG attitude pointing system have been modeled with position and rate feedback control. The magnetic isolation system for the migro-g experiment is one developed by Sperry and is a fifth order system for each of the translational degrees of freedom. The control system for the Coarse Pointing System (C.P.S) consists of a position and rate feedback system for the azimuth gimbal control, and position, rate and integral control for the elevation and cross elevation gimbal control.

Simulation Model Contains Coarse Pointing, Solar Array Control, Isolation and Vehicle Flexibility

SPACE STATION

SSS177039

- SIMULATION MODEL CONTAINS

  - MODES

    - 85 STRUCTURAL MODES WITH LOCKED CONTROL JOINTS

    - 3 ROTATIONAL COARSE POINTING MODES (C.P.S.)

    - 2 ROTATIONAL SOLAR ARRAY MODES

    - 3 TRANSLATIONAL MODES IN ISOLATION SYSTEM

  - CONTROLS

    - SOLAR ARRAY POINTING SYSTEM

    - ISOLATION CONTROL SYSTEM

    - CMG CONTROL SYSTEM

    - COARSE POINTING CONTROL SYSTEM

Rockwell International
Space Station Systems Division

465

CHART 5

With the simulation model, the system stability is determined with the closed loop roots. Then the time response was calculated for the list of disturbances shown.

Simulation Determines Stability and Transient Response

SPACE STATION

- **RESULTS**

  - **CLOSED-LOOP ROOTS**

  - **TIME RESPONSE**

    - **ALPHA COMMANDS**

    - **CREW DISTURBANCE**

    - **REBOOST**

    - **MRMS**

36SS6177040

467

CHART 6

The number of modes was limited to 85 because the mass matrix became ill-conditioned when more modes were used. The ill-conditioned mass matrix was caused by the rigid body modes that were added to remove the constraint at the alpha joints. Two potential solutions to solve this problem are: start with modes where the alpha joints have a spring instead of a lock or reduce the total degrees of freedom in the model.

Numerical Problem May be Avoided by Modeling Alpha Joint Flexibility

- **PROBLEM**

  - NUMERICAL INSTABILITY WHEN USING OVER 85 MODES DUE TO ILL-CONDITIONED MASS MATRIX

- **SOLUTION**

  - OBTAIN MODES WITH SPRING AT ALPHA JOINT—THIS WILL RESULT IN RATE COUPLING & SHOULD REMOVE NUMERICAL PROBLEM

  - REDUCE THE NUMBER OF SOLAR ARRAY DEGREES OF FREEDOM, THUS OBTAINING FEWER MODES FOR A GIVEN FREQUENCY RANGE

SPACE STATION

36SSS177041

CHART 7

The system equations are written in first order form. The first coefficient matrix shows the coupling between the rigid body modes for the control surfaces and the structural modes of the system. The coupling exist because these modes are not orthogonal to the structural modes of the system.

System Equations Have Static, Rate, and Inertia Coupling

q_s = RIGID + FLEXIBLE MODAL COORDINATES

q_p = GAP IN ISOLATION SYSTEM

α = ALPHA ROTATION

δ = THREE ROTATIONAL D.O.F. ASSOCIATED WITH THE C.P.S.

X_p = STATE VARIABLES ASSOCIATED WITH ISOLATION SYSTEM

$X\delta$ = STATE VARIABLES ASSOCIATED WITH C.P.S.

Rockwell International
Space Station Systems Division

4CSSV177042
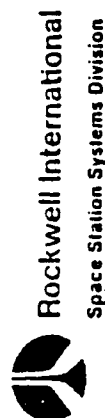
CHART 8

The equations of motion are different when the modes are generated with a spring for the alpha joint. The alpha variable no longer appears explicitly in the equations. The coupling in the first coefficient matrix decreases but additional coupling appears in the second coefficient matrix. The new coupling results because alpha is a function of the modal coordinates.

472

System Equations With Alpha Spring in Modal Data

WHERE

δ = THREE ROTATIONAL D.O.F. ASSOCIATED WITH THE C.P.S.

X_p = STATE VARIABLES ASSOCIATED WITH ISOLATION SYSTEM

X_δ = STATE VARIABLES ASSOCIATED WITH C.P.S.

q_s = RIGID + FLEXIBLE MODAL COORDINATES

q_p = GAP IN ISOLATION SYSTEM

CHART 9

The payload C.G. could have a significant effect on the payload pointing error. The effect of this parameter may be evaluated without generating new modes. The mass matrix for a payload with a different C.G. offset is determined with the new sectionalized mass matrix and the previous set of modes.

Effect of C.G. Offset May Be Obtained Without Generating New Modes

- A SIMULATION MODEL FOR PERFORMING PARAMETRIC STUDIES ON THE EFFECT OF C.G. OFFSET TERMS IN THE C.P.S. IS REQUIRED

- GENERATE NEW MASS MATRIX USING ASSUMED MODE METHOD

  - DEFINE NEW PAYLOAD C.G. OFFSET

  - GENERATE NASTRAN SECTIONALIZED MASS MATRIX [M]

  - ASSUME OLD MODES, $[\phi]$ = MODAL MATRIX

  - MULTIPLY $[\phi]^T$ [M] $[\phi]$ = $[M]_{NEW}$

Rockwell International
Space Station Systems Division

475

46SSS177045A

CHART 10

The angular disturbance at the base of the payload has a maximum value of 60 arc-seconds. The disturbance in this case was a 2 degree command to the alpha controller. The command resulted in a torque near its capability. The response on the telescope is a maximum of 0.02 arc-seconds.

476

Coarse-Pointing System Minimizes Pointing Error Due to Alpha Joint Rotation

TRANSIENT RESPONSE

Y-ROTATION AT BASE
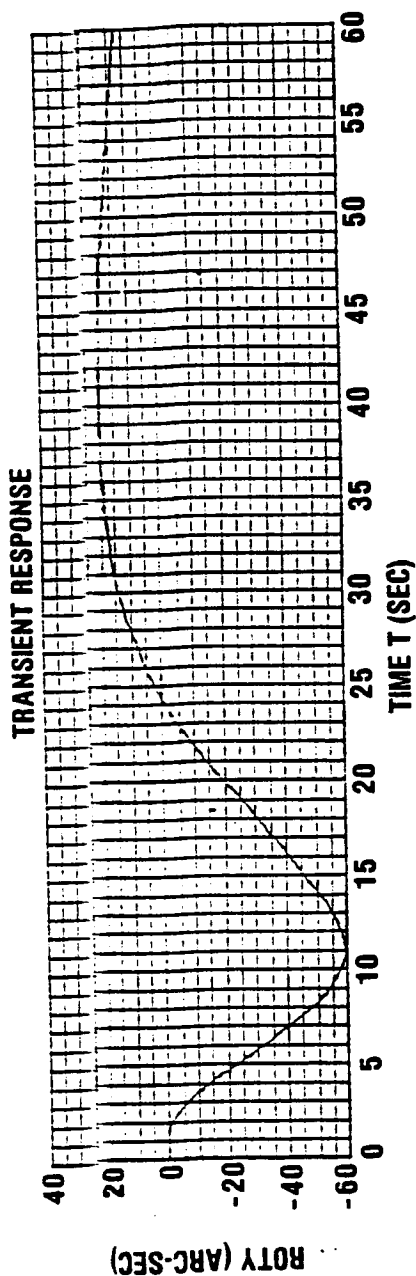
TRANSIENT RESPONSE
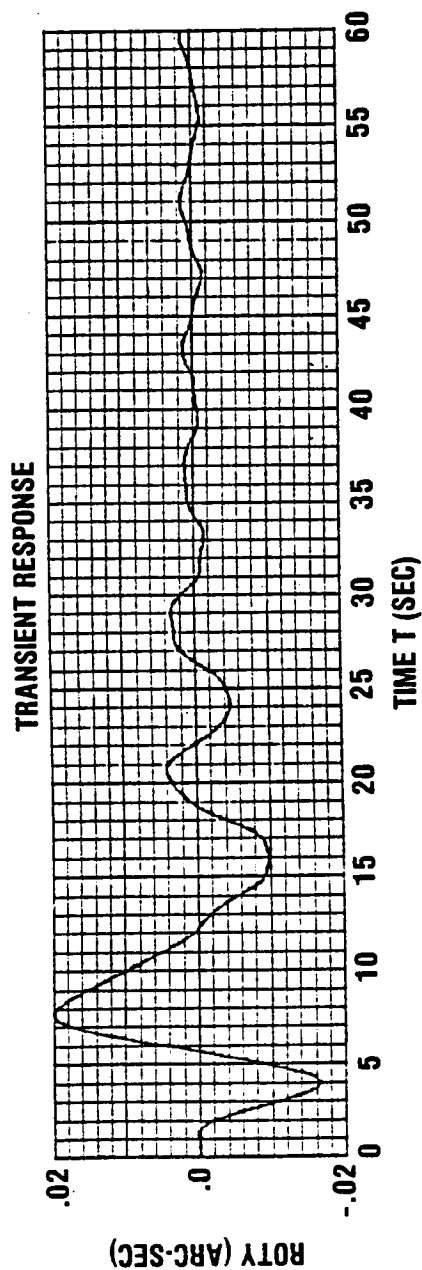
Y-ROTATION AT PAYLOAD

$$\frac{\theta_p}{\theta_B} = \frac{.04}{59} = 7 \times 10^{-4}$$

Rockwell International
Space Station Systems Division

36SSS177047

477

CHART 11

The maximum acceleration at the base of the material processing experiment is 6×10^{-5}. The crew caused the disturbance by pushing off on one side of a module and stopping on the other side. The acceleration is reduced by the Sperry magnetic isolator to 0.3×10^{-5}.

Isolator Reduces Crew Disturbance G-Level

SPACE
STATION

TRANSIENT RESPONSE

9×10^5

TIME T (SEC)

ACCELERATION LEVEL AT BASE

TRANSIENT RESPONSE

9×10^5

TIME T (SEC)

ACCELERATION LEVEL AT PAYLOAD

Rockwell International
Space Station Systems Division
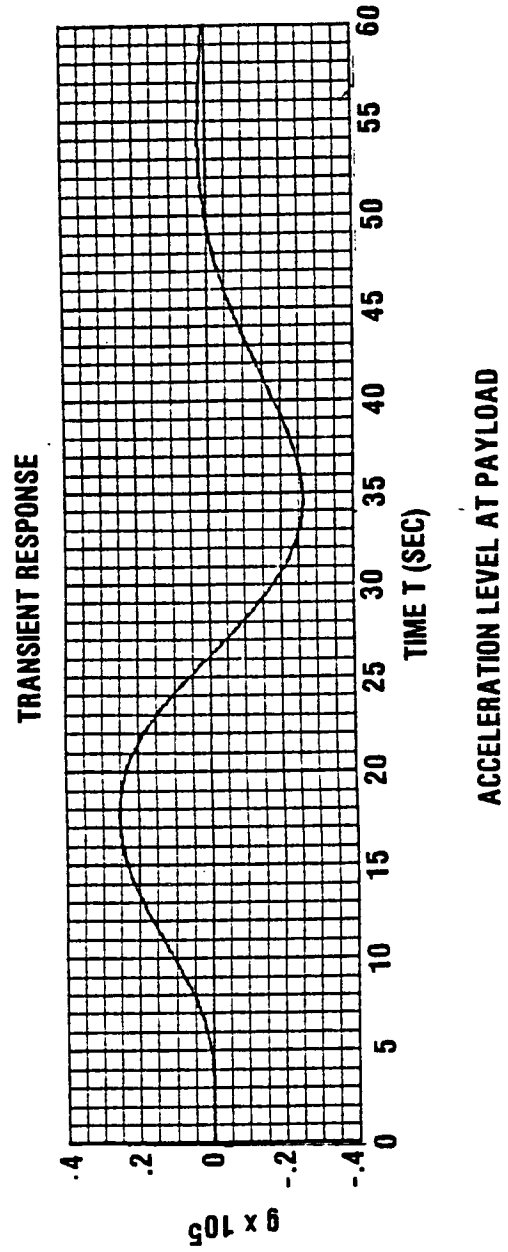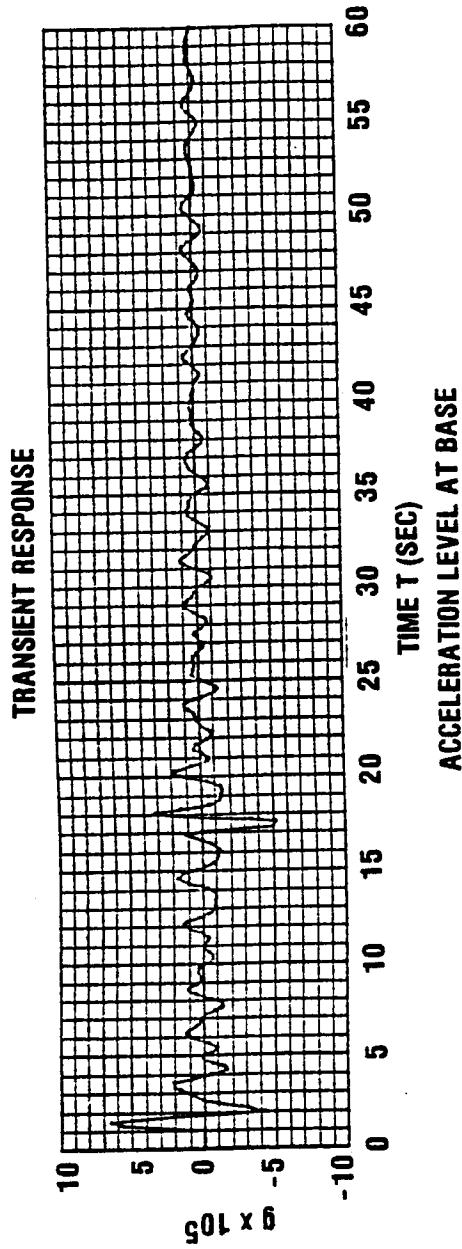
CHART 12

The Sperry fine pointing control system being examined has 40 state variables. The translational and rotational isolation system is a electro magnetic isolation system and is mathematically similar to the micro-g isolation system.

C-6

Fine-Pointing System Contains 40 State Variables

SPACE STATION

δ_{1yc} +

δ_{1y}

$$K_1 + C_1 s$$

T_{1y}

AZIMUTH CONTROL

δ_{2z}

$$\frac{K_2 (s + a_1)^2}{s (s + b_1)}$$

T_{2z}

ELEVATION CONTROL

(gap)

g_1, g_2, g_3

$$\frac{K (s - a_2) (s - a_3)}{s (s^2 + 2 \zeta \omega s + \omega^2)^2}$$

$T\Delta x, T\Delta y, T\Delta z$

x, y, z TRANSLATIONAL ISOLATION

δ_{3x}

$$\frac{\tilde{K} (s - a_2) (s - a_3)}{s (s^2 + 2 \zeta \omega s + \omega^2)^2}$$

T_{3x}

x ROTATIONAL ISOLATION

$\delta_{1yc}, \delta_{1zc}$ +

δ_{1y}

$$\frac{C_3 s^2 + K_3 s + K_{l3}}{s}$$

T_{3y}, T_{3z}

$$\delta_{ly} = \delta_{1y} + \delta_{2y} + \delta_{By}$$
$$(\delta_{lz} = \delta_{2z} + \delta_{3z} + \delta_{Bz})$$

INERTIAL POINTING (y & z DIRECTION)

Rockwell International

Space Station Systems Division

46SSS177052

481

CHART 13

A 203rd order simulation model was developed to evaluate the Space Station customer accommodation payload pointing and micro-g requirements. The simulation shows the pointing errors on the telescope are significantly smaller than at the base of the telescope. The pointing results could change when the parametric studies are performed. The results show the micro-g requirement is met with an active isolation system.

482

Conclusions Payload Pointing and Microgravity

SPACE
STATION

- SPACE STATION COARSE POINTING PROGRAM WITH 203rd ORDER SYSTEM & WITH 85 MODES (MAX. FREQ = 1.1 HZ) IS WORKING

- COARSE POINTING SYSTEM REDUCED ALPHA COMMAND DISTURBANCE FROM 60 ARC SEC AT BASE TO 0.02 ARC SEC

- MICRO-G REQUIREMENTS SATISFIED FOR CREW DISTURBANCE

- PARAMETRIC STUDY FOR DETERMINING C.G. OFFSET EFFECT MAY BE OBTAINED FROM CURRENT SIMULATION WITH MINOR MODIFICATIONS

Rockwell International

Space Station Systems Division

46SSS177054

483

Wednesday, April 23, 1986

SESSION 3

(Concurrent Sessions on Structures and Control)

Structures Session 3A - T. K. Hasselman, Chairman

SAFE Dynamic Flight Experiment	R. W. Schock, MSFC
Application of Robust Projection Operators to the Control of Flexible Structures with Uncertain Parameters	M. H. Bantell, Jr. Boeing
Dynamics of Trusses Having Nonlinear Joints	J. M. Chapman Boeing
Equivalent Beam Modeling Using Numerical Reduction Techniques	J. M. Chapman Boeing

Structures Session 3B - Wayne B. Holland, Chairman

Dynamic Characterization of a Vibrating Beam with Periodic Variation in Bending Stiffness	J. S. Townsend, MSFC
Structural Dynamic System Model Reduction	J. C. Chen, T. L. Rose, B. K. Wada, JPL
Space Telescope Reaction Wheel Assembly Vibration Damping System	R. E. Jewell, MSFC, P. Davis and J. Wilson, Sperry

SOLAR ARRAY FLIGHT DYNAMIC EXPERIMENT

RICHARD W. SCHOCK

NASA/MARSHALL SPACE FLIGHT CENTER

Presented at

WORKSHOP ON STRUCTURAL DYNAMICS AND CONTROL
INTERACTION OF FLEXIBLE STRUCTURES

MARSHALL SPACE FLIGHT CENTER, ALABAMA

APRIL 22-24, 1986

SOLAR ARRAY FLIGHT DYNAMIC EXPERIMENT

Richard W. Schock

ABSTRACT

The purpose of the Solar Array Flight Dynamic Exper-
iment (SAFDE) is to demonstrate the feasibility of
on-orbit measurement and ground processing of large
space structures' dynamic characteristics. Test def-
inition or verification provides the dynamic char-
acteristic accuracy required for control systems
use. An illumination/measurement system was devel-
oped to fly on space shuttle flight STS-41D. The
system was designed to dynamically evaluate a large
solar array called the Solar Array Flight Experiment
(SAFE) that had been scheduled for this flight. The
SAFDE system consisted of a set of laser diode
illuminators, retroreflective targets, an "intelli-
gent" star tracker receiver and the associated
equipment to power, condition, and record the re-
sults. In six tests on STS-41D, data was success-
fully acquired from 18 retroreflector targets and
ground processed, post flight, to define the solar
array's dynamic characteristic. The flight experi-
ment proved the viability of on-orbit test
definition of large space structures dynamic
characteristics. Future large space structures
controllability should be greatly enhanced by this
capability.

SOLAR ARRAY FLIGHT DYNAMIC EXPERIMENT

Richard W. Schock
NASA Marshall Space Flight Center
Huntsville, Alabama

INTRODUCTION

In September of 1984, NASA flight tested the Solar Array Flight Dynamic Experiment (SAFDE) on STS-41D. The purpose of this experiment was to demonstrate the feasibility of on-orbit measurement and ground processing of large space structure dynamic characteristics. The dynamic character- istics are structural natural frequencies, mode shapes, and damping. Ac- curate definition of these characteristics are necessary for large space structures with active control systems to prevent structure/control system interaction. In past vehicles and on-orbit structures, the struc- tural natural frequencies were significantly higher than the control sys- tem frequencies. However, with large space structures, the structural natural frequencies are so low that the control natural frequency will either be very close to the first natural structural frequency or nested between a pair of the lower natural structural frequencies. This problem, coupled with the dense rate of structural frequencies, requires a very accurate definition of the structural characteristics. Unfortunately, large space structures are designed for zero-g use and cannot be adequate- ly tested in one-g environments. On-orbit test, therefore, is the remain- ing alternative to verify analysis results or define correct values where analysis results are inacurate.

To investigate the feasibility of on-orbit large space structure dynamic testing, a dynamic augmentation experiment (SAFDE) was added to an exist- ing flight test called the Solar Array Flight Experiment, SAFE (Fig. 1). The SAFE was indeed an unprecedented opportunity since it flew early and has the characteristics of a large space structure. These characteristics are shown in Table 1.

Table 1

SOLAR ARRAY STRUCTURAL CHARACTERISTICS

o Array Wt

o Blanket	225 kg
o Mast	132 kg
o Container	40 kg
o Cover Assembly	40 kg

o Natural Frequencies	0.033-0.4 Hz
o Array Length	3100 cm
o Array Width	400 cm

As noted, the array has extremely large area to weight ratios and low natural frequencies (0.03 Hz). In atmospheric conditions, air damping dominates over the structural damping, and the array cannot be dynamically tested in one-g. A dynamic augmentation to the SAFE was authorized, and an experiment was developed and integrated into the shuttle orbiter.

MEASUREMENT SYSTEM DEVELOPMENT

In order to measure the solar array dynamic motion, an illumination, remote sensing and recording system had to be developed. The general requirements for the measurement system are to illuminate and track a set of 23 retroreflective targets. The displacement of the targets are measured, converted to engineering units, multiplexed, and stored on a digital tape recorder. Post flight, the data is ground processed to obtain dynamic characteristics of the array.

The specific measurement system requirements are as follows:

1. Simultaneously track 23 retroreflective targets on the solar array.

2. Accuracy requirement, 19 arc seconds.

3. Update rate, 2 Hz.

4. Total target displacement, ±45 cm.

5. Target speed, 6.28 cm/sec.

6. Field of view, 19 x 19 degrees.

7. Survive launch environments.

8. Operate in on-orbit environments, with no active cooling.

The measurement system to accomplish these objectives was developed by the Marshall Space Flight Center and is shown in flow diagram form on Fig. 2. The system consists of the following:

1. Retroreflector field tracker (RFT) containing-

    a. Laser diode illuminators.

    b. Solid state sensor.

    c. Microprocessor.

2. Twenty-three retroreflector targets mounted on the array.

3. Multiplexer (PCM).

4. Digital tape recorder (TR).

5. Power control and distribution assembly (PCDA).

As shown on Fig. 2, the PCDA receives and distributes power, commands and talk back, and experiment health information. The RFT was the major development item, and was designed and built by Ball Aerospace Systems Division[1]. It consists of two hardware items, the illuminator/sensor assembly and the microprocessor. The illuminator sensor assembly is mounted 1.9 meters (75 in.) from the base of the array blanket on the mast side of the blanket. Basically, it has a circular cross section 24 cm (9.45 in.) in diameter by 56.4 cm (22.2 in.) in length, and weighs 7.5 kg (16.8 lbs). The microcomputer is a part of the main electronics box (MEB) which sets on the mission peculiar support structure (MPSS) remote from the sensor. This package is 24.6 x 21.6 x 39.4 cm (9.7 x 8.5 x 15.5 in.) in size and weighs 16.1 kg (35.4 lbs.)

During operations the RFT illuminates the solar array with five laser diode sources which are independently projected onto the solar array. The lasers are 30-milliwatt diodes operating at 820 nanometers. The source illumination is lensed so that the maximum intensity is at the top of the array. The illumination is returned by retroreflector targets to the illumination source. The targets are of varying sizes, from 14 mm (0.55 in.) to 42 mm (1.6 in.), and arranged proportionately to the distance from the sensor. The combination of illumination intensity and reflector size provided a near uniform image intensity to the sensor focal plane. The retroreflector targets were small aluminum standoffs, attached over a solar array hinge. These were designed to stand off perpendicular to the solar array blanket when the blanket was deployed and fold neatly into the blanket folds when the blanket was stowed. Additional rigid targets were attached to the mast, topcover, and tip fitting. The retroreflective surface was a high gain commercially produced retroreflective tape. The retroreflectors are shown in Fig. 3.

The reflector images are focused on a solid state, charge injection device (CID) detector. The detector consists of a 256 x 256 pixel array, each 0.02 millimeters square in an active area of 5 x 5 mm. The detector interrogation is controlled by the microprocessor. The tracking rate is defined by the track algorithm and the target velocity. The track algorithm requires the target motion of the detector to be limited to one pixel per update period. The maximum required velocity of the array is 6.28 cm/sec at the closest target (790 cm or 311 in.). This rate becomes 5.1 pixels/sec. A track rate of 6 Hz was selected to meet this requirement even though the output rate is 2 Hz. The accuracy requirement of 19 arc seconds translates into approximately 1/4000 of the field of view (FOV). This necessitates interpolation to approximately 6.4 percent of a pixel. This interpolation accuracy was met using a star tracker interpolation algorithm.

When the RFT is powered, after an internal self test and initialization, it begins a search and acquisition routine. In each data cycle, the laser illuminator is pulsed to "freeze" the target motion, and the return signal is integrated on the detectors. A 12 x 12 pixel search block is read out and compared to a threshold to determine if a target is present. If one is found, its position is compared to the stored map for identification, a track loop locks onto its position, and it is added to the list of targets being tracked. This function takes approximately 80 seconds.

After the initial search, the same sequence is continually performed, except that the sensor also tracks the target positions. The continued search performs a scavenger function to find targets that may have been missed initially or lost after acquisition. Each target is read out twice per track sequence, once after the laser diodes have been strobed, and once after the CID is injected and the background is accumulated for a time equal to the laser pulse. The difference resulting from the double read is generated on a per pixel basis, and the background noise is thus eliminated.

The software system must provide for simultaneous tracking and acquisition, since tracking of early acquired targets must continue while later targets are acquired. Once all targets are acquired, if a target is lost, the acquisition routine reverts from its normal fixed pattern routine, to a search routine initiated at the last known position of the target. This allows reacquisition of a "lost" target to occur in a maximum of 324 msec.

The numbering of each target was a challenging problem. The array was to be at either 100 percent or 70 percent of full deployment. At 100 percent, 23 targets were visible; at 70 percent, 18 targets were visible. The microprocessor was, therefore, given an expected map of both arrays, and the acquisition system had to be manually "cued" prior to flight test to tell it which set of algorithms to use. If, because of some unforeseen problem, the targets did not appear in their prescribed "areas," then target numbering was done on a first-come-first-served basis until all 18 or 23 assignments were filled. The prescribed geometric algorithms to change angular deviations to engineering displacement would obviously be incorrect. However, the sensor output also included the raw angular deviations which, post test, would allow data evaluators to reconstruct the locations and displacements. Since the solar array "warped" significantly during test, this is, in fact, what happened and will be discussed later in data evaluation.

The RFT successfully completed full flight performance and qualification tests as a unit at the contractor and later as a complete system at Marshall Space Flight Center. Actual tracking accuracy of 10 arc seconds proved better than specification of 19 arc seconds.

EXPERIMENT INTEGRATION AND MISSION OPERATIONS

The SAFDE was physically integrated with the remainder of the OAST-1 mission as shown in Fig. 4. The illuminator/sensor was positioned on a stiff support system 1.9 m (75 in.) in the x-direction from the array blanket. The optic axis is tilted 14.8 degrees from the z-axis to optimize the field of view. This provides a target pattern which is very wide at the base and narrow at the top. The 14.8 degrees was chosen to minimize deflection errors, yet ensure that under maximum deflection conditions, no target was obstructed by solar array structure. Accurate alignment accuracies obtained were ±5 arc minutes.

The SAFDE was a part of a multimission payload called OAST-1. OAST-1 consisted of the Solar Array Flight Experiment, the SAFDE, a photogrammetric experiment with similar objectives but different techniques[2] from

the SAFDE, and a solar cell calibration experiment. Although, the SAFDE and the photogrammetric experiment both measured solar array dynamic deflections, the SAFDE could only operate during orbital night, and the photogrammetric experiment required good sunlight illumination. Adequate operational time was available to do one each on an orbit, so the dynamic tests were run back-to-back. To ensure uniformity of initial conditions, the SAFDE experiment required 10 minutes of "orbiter quiescence" prior to solar array excitation. The SAFDE could not operate with the bright moon in the field of view. Since the orbiter was under attitude control prior to the "quiescent period," and the last Vernier control reaction system (VCRS) pulse was a random process, and since relatively high rates of drift occurred with the solar array extended, the exclusion of the moon from the field of view could not be guaranteed. The severity of the problem changed with the time of the month the flight was to occur. At the final mission time, the moon relationship was such that it set shortly after orbital midnight, which allowed sufficient time to test prior to sunrise with no "moonshine" problem. This operational constraint can be "cured" by more powerful illuminators. Typically, an operational sequence would be the following scenario.

1. Initiate "quiescence" 10 minutes prior to moonset.

2. Perform illumination/sensing system setup and checking functions.

3. At moonset, turn illumination/sensor system on.

4. Excite array with orbiter VRCS.

5. Take data for 12 minutes.

6. Turn off sensor system and terminate test.

Due to safety concerns about exciting the 100-percent-deployed array on the dark side, only 70-percent-deployment tests were performed on the SAFDE. Six excitations were applied to the solar array for the SAFDE test. They included out-of-plane, in-plane, and multimodal tests. The out-of-plane test was a pitch maneuver of the orbiter. The in-plane test was an attempt at a roll maneuver. The orbiter could not perform a pure roll maneuver with the Vernier rate control system; therefore, an incremental maneuver was used. The multimodal maneuver was basically pitching the diagonal corners of the orbiter as to obtain as many modal responses as possible. A further orbiter mission requirement was that the residual rates, after the excitation, be minimized. Therefore, if a positive rotation was placed on the orbiter, it would have to be countered by an equal and opposite impulse to bring the rotation to zero. This requirement resulted in impulse couplets being applied as shown in Fig. 5. The integration and flight operations proved not only adequate but conservative, since additional tests were able to be performed.

FLIGHT RESULTS

Data was obtained on all targets, on all tests, even though some targets were outside of the sensor design range due to the array's darkside

curvature. The array excitations and data take started near orbital midnight and continued for 12 minutes. The blanket curvature shown on Fig. 7 was measured just prior to array excitation or near orbital midnight. The maximum measured curvature was 40 cm in depth.

The 18 targets for the six 70-percent tests each provided x- and y-displacement data for a total or 36 data samples per test. All 36 data samples were simultaneously evaluated by two different response analysis techniques. Both techniques utilize a time-domain curve fit of the data to obtain the modal damping information, and a fast Fourier transform technique to obtain modal amplitude and phase relationships.

The solar array was dynamically evaluated both at orbital midnight by the Marshall Space Flight Center (SAFDE) and at high noon by a Langley Research Center Photogrammetric Experiment[2]. An unexpected curvature formed on the dark side. The result was that the high noon test evaluation closely matched the pretest analytical model, whereas, the SAFDE experiment tested a different structural configuration and did not match pretest analyses. Subsequent post test analyses, using a model which had been modified to account for the previously described mast twist and blanket curvature, improved the analysis/test match but still retained differences.

The structural dynamic natural frequencies and mode shapes, both analytical and measured, are compared in Figs. 8 through 12 and in Table 2.

Table 2

SOLAR ARRAY DYNAMIC CHARACTERISTICS

Analytical Frequency Hz	Mode Shape	Test Frequency	Damping (%)
0.064	Out-of-Plane Bending	0.059 - 0.072	2 - 8
0.067	In-Plane Bending	Not Identified	
0.115	1st Torsion	0.089 - 0.092	1 - 2
0.179	2nd Out-of-Plane Bending	0.121	2 - 4
0.213	2nd Torsion	0.172	2

Neither the photogrammetric nor the SAFDE experiment were able to extract the analytical second mode. This mode is a lateral response, and significant effort was expended to excite it with an in-plane and multimodal test. Mode shapes tended to match well, but natural frequencies not only differed but changed with different test excitations and during decay from each individual excitation. This phenomenom is characteristic of nonlinear structures. The nonlinearity of the structure is illustrated in Figs. 13 and 14. Fig. 13 is a plot of the first mode (out-of-plane deflection) natural frequency versus tip displacement for DAE test No. 1. This test is illustrated because it obtained the maximum tip response of

all tests, therefore providing the largest range of frequency and damping change. The damping change for the same mode, same test is illustrated in Fig. 14. From a tip displacement of 11 cm single amplitude (SA) to 2 cm SA, the damping factor averages about 0.08. Less than 2 cm SA, the factor averages approximately 0.02.

CONCLUSIONS

1. The SAFDE experiment successfully measured the SAFE solar array dynamic response, even under out-of-design conditions.

2. Four of the first five solar array modal characteristics were successfully test determined.

The Solar Array Flight Dynamic Experiment also illustrated a number of points significant to control/structure interaction of large space structures. The solar array was more than just an advance solar array; it was, in fact, representative of a generic class of future large space structures (LSS). The type of construction, strength to weight ratios, natural frequencies, and, most importantly, the inability to adequately dynamic test on the ground are all synonymous with future LSS. Like the LSS, the solar array had very low natural frequencies (0.035 Hz, first mode) and densely spaced modes, greater than 33 modes per Hz. In order to maintain control authority of an LSS with similar characteristics, the control frequency would probably have to be nested among the structural natural frequencies. With the characteristic modal density of LSS, very little frequency "window" would be available to insert the control frequency. This, in turn, would require a highly accurate knowledge of the structural frequencies to avoid control/structure interaction. That accuracy is normally obtained by test verification of the math model, which in the case of large space structures, must be done on-orbit. As previously noted, an unexpected curvature formed on the dark side. The SAFDE experiment, therefore, tested a different configuration than was analyzed pretest and did not match pretest analyses. Model update was required for correlation and verification. Although normal care was taken in design to prepare the solar array for on-orbit use, this anomaly did occur. As such, it may well be representative of "surprises" which occur with any pioneering venture like LSS. With a combination of probable forthcoming surprises, a requirement for highly accurate structural dynamic characteristics, and an inability to ground test to resolve anomalies, on-orbit dynamic tests appear to be a mandatory LSS requirement. This requirement is further supported by the nonlinear behavior illustrated in the preceeding report. The control implication of the nonlinearity is that the already narrow frequency window in which to place a control frequency is further narrowed if the structural frequencies are a function of amplitude. One very favorable indication from the experiment was that the damping of the structure was significantly higher than previous launch or space vehicle experience. And finally, the SAFDE program did demonstrate and confirm the viability of on-orbit test definition of LSS dynamic characteristics.

REFERENCES

1. F. Wargocki, A. Ray, and G. Hall, "Retroreflector Field Tracker
    (State-of-the-Art Imaging Arrays and Their Application),"
    Keith N. Prettyjohns, Editor, Proc. SPIE 501, 1984, p. 283.

2. L. Brumfield, R. Pappa, J. Miller, and R. Adams, "Orbital Dynamics
    of the OAST-1 Solar Array Using Video Measurements," AIAA paper,
    85-0758-CP, 1985.

NASA Solar Array Flight Experiment

FIGURE 1.
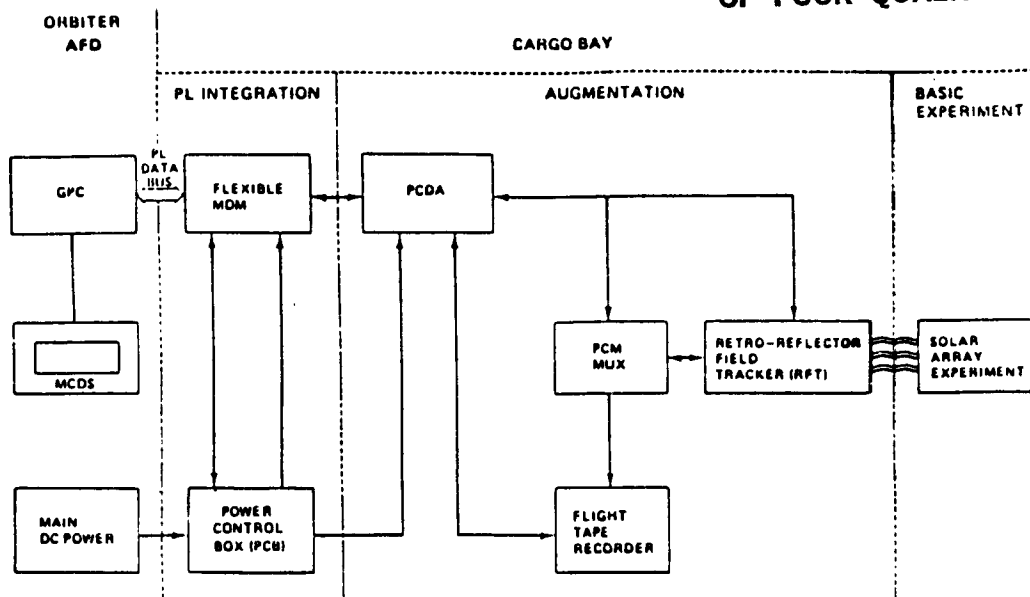
FIGURE 2. SAFDE FUNCTION FLOW

FIGURE 3. SAFDE RETROREFLECTOR TARGET

498

FIGURE 5. 1ST SAFDE ORBITER IMPULSE INPUT AND SOLAR ARRAY TIP RESPONSE
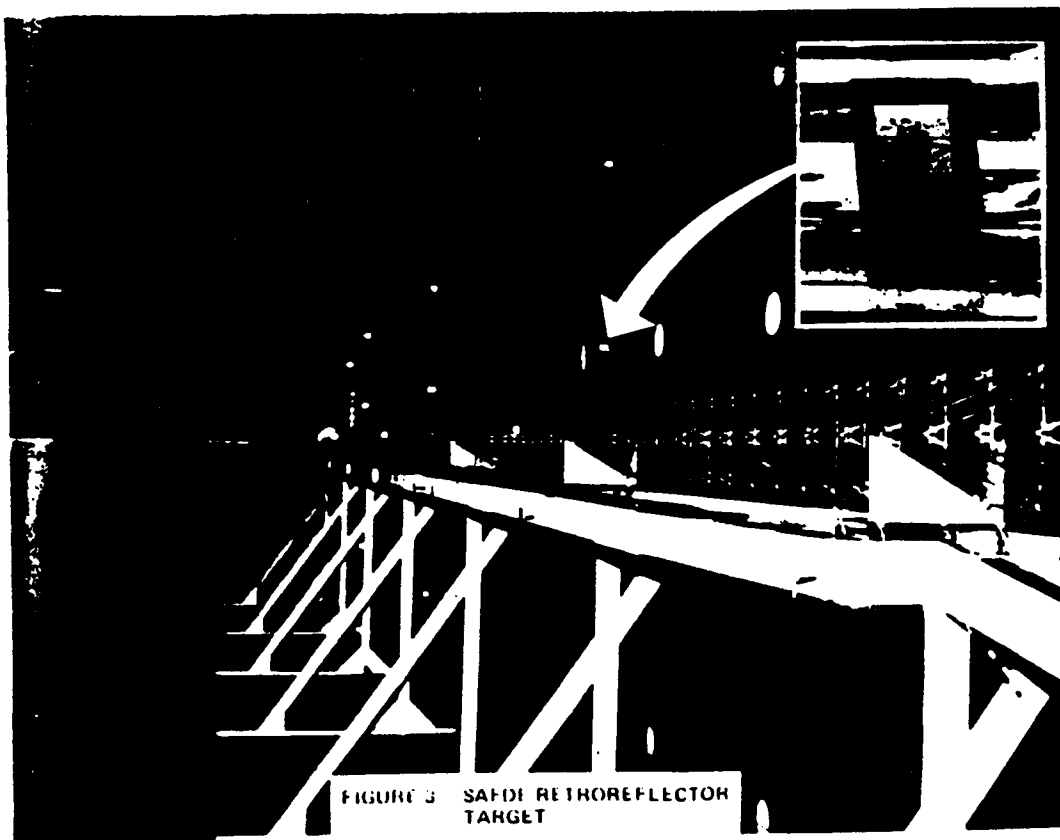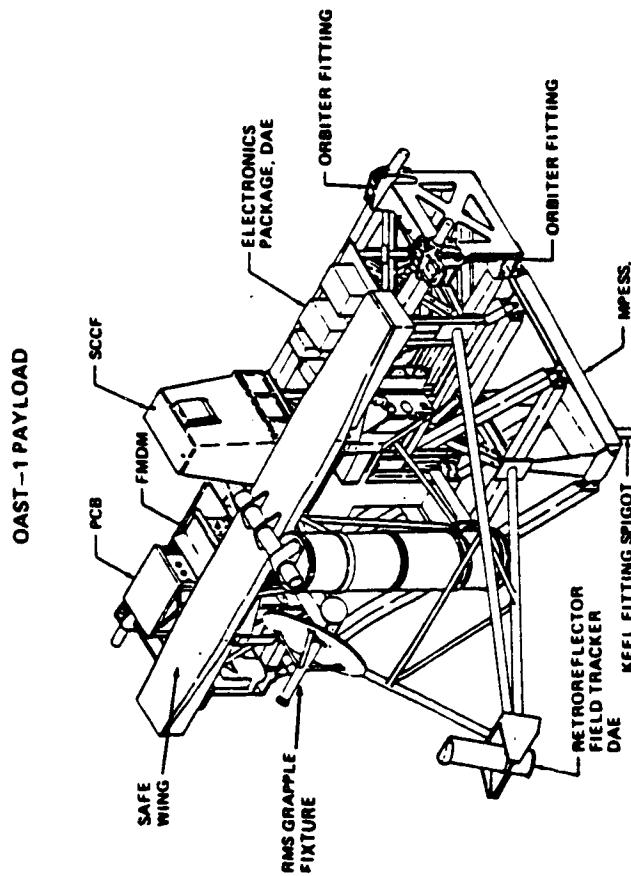
FIGURE 4 OAST-1 SAFE/DAE FLIGHT CONFIGURATION

499

SCALE: 10 cm/div

VIEW AA/BB

SCALE: 10 cm/div

VIEW AA/CC

SCALE: 10 cm/div

VIEW AA/DD

NOTE: X'S ARE TARGET LOCATIONS

FIGURE 7. BLANKET CURVATURE FIRST SAFDE TEST

ELEVATIONS
(cm)

A   2361

B   2124

C   1462

D   799

70% DEPLOYMENT

FIGURE 6. WING CROSS SECTIONAL
VIEW Y-Z PLANE

TEST FREQ. 0.059—0.070

ANALYSIS FREQ. 0.064
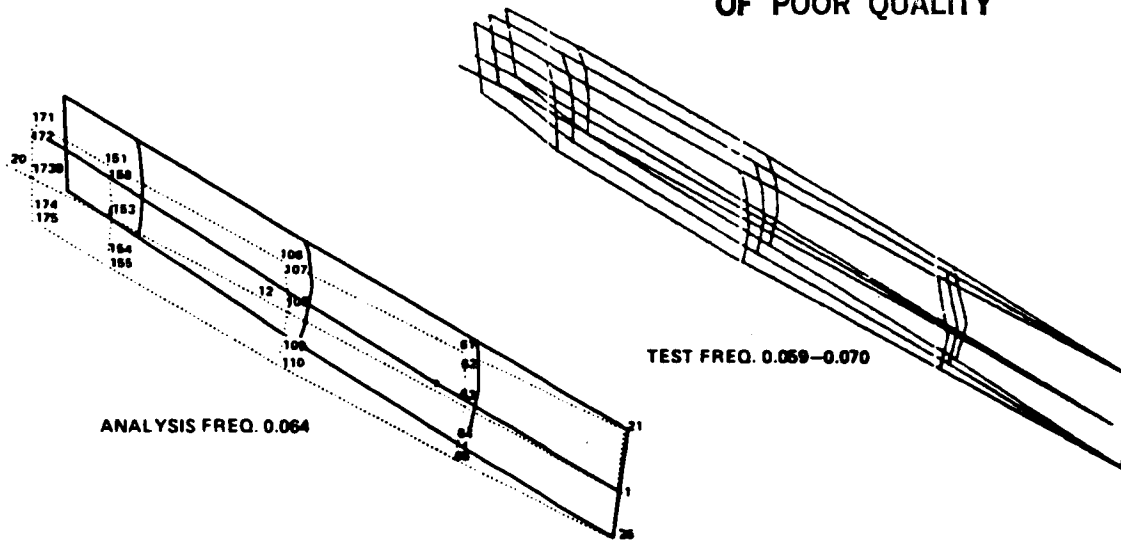
1ST MODE OUT OF PLANE BENDING

FIGURE 8. SOLAR ARRAY DYNAMICS
ANALYSIS/TEST COMPARISON

ANALYSIS FREQ. = 0.067

NO
2ND MODE
IDENTIFIED
IN TEST
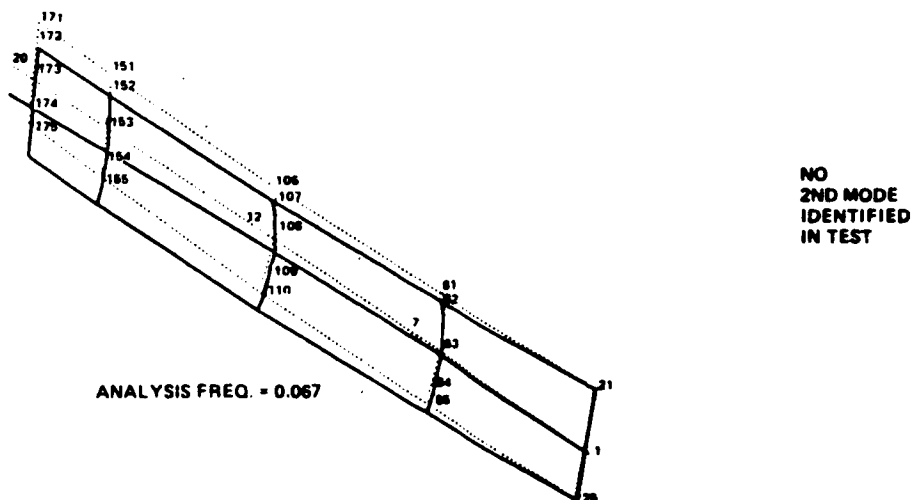
2ND MODE LATERAL BENDING

FIGURE 9. SOLAR ARRAY DYNAMICS
ANALYSIS/TEST COMPARISON

501

ANALYSIS FREQ. = 0.115 HZ.

TEST FREQ. = 0.089 – 0.094

3RD MODE 1ST TORSION
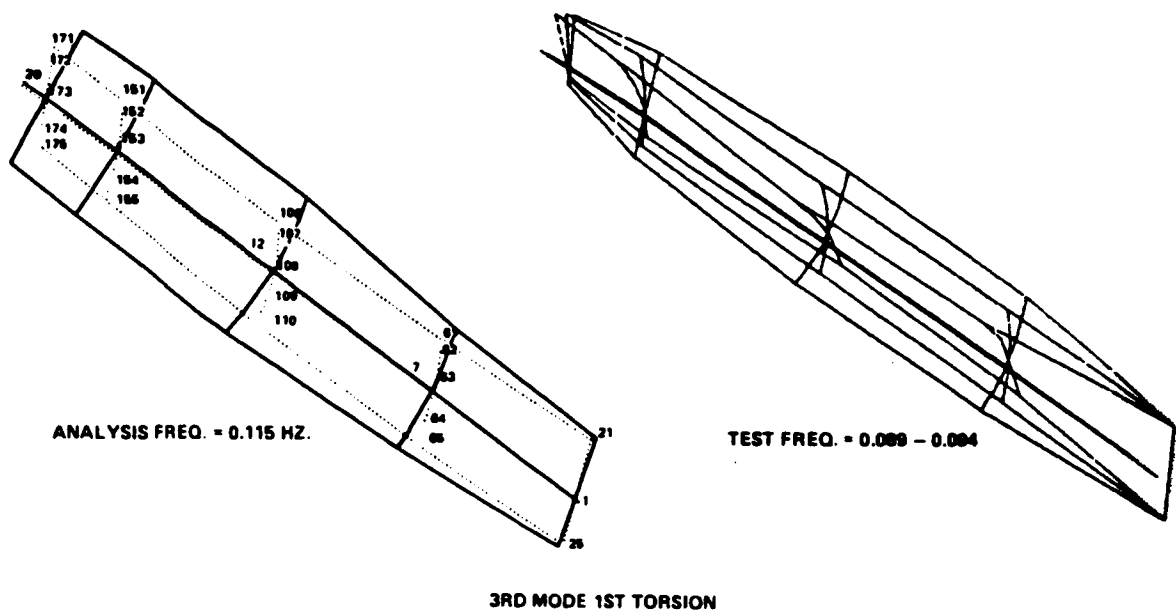
FIGURE 10. SOLAR ARRAY DYNAMICS
ANALYSIS/TEST COMPARISON

ANALYSIS FREQ. = 0.179 HZ

TEST FREQ. = 0.121 HZ

4TH MODE 2ND OUT OF PLANE BENDING
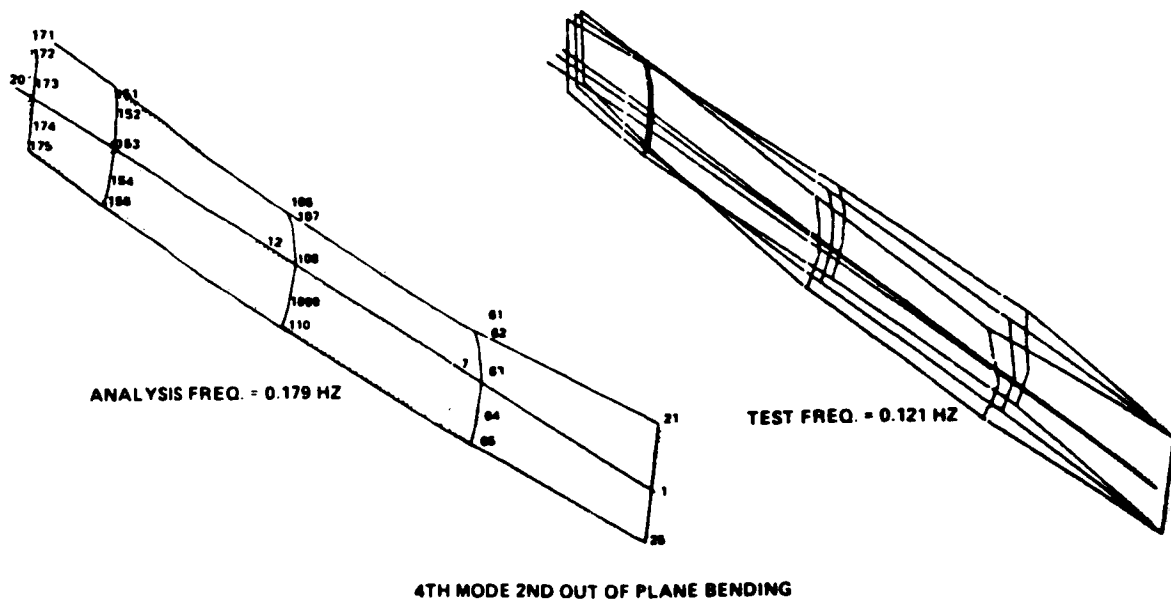
FIGURE 11. SOLAR ARRAY DYNAMICS
ANALYSIS/TEST COMPARISON

ANALYSIS FREQ. = 0.213

TEST FREQ. = 0.172

5TH MODE 2ND TORSION
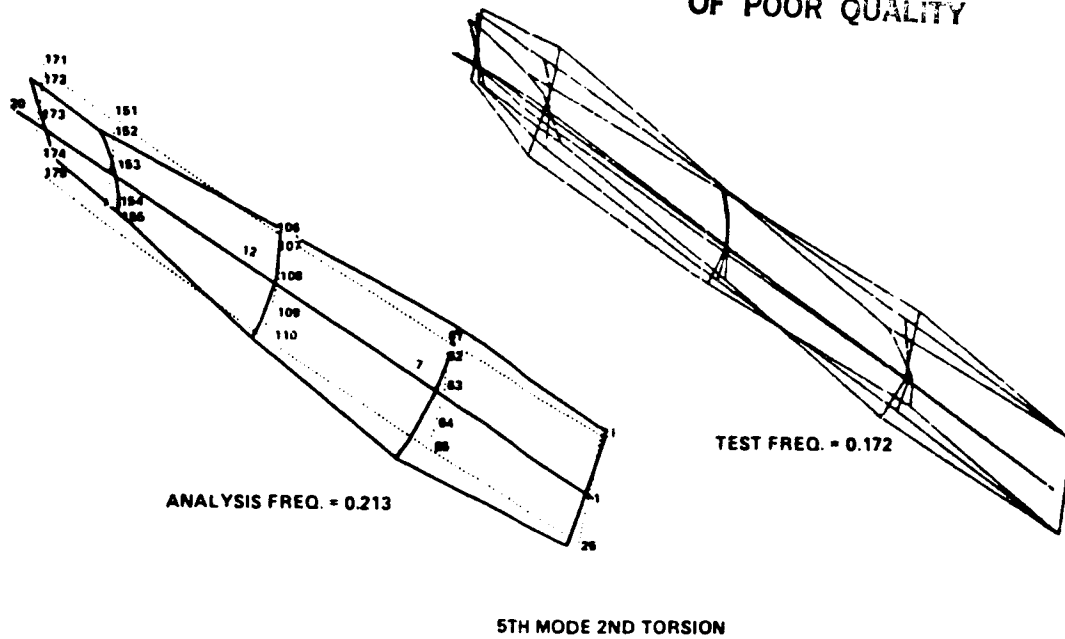
FIGURE 12. SOLAR ARRAY DYNAMICS
ANALYSIS/TEST
COMPARISON
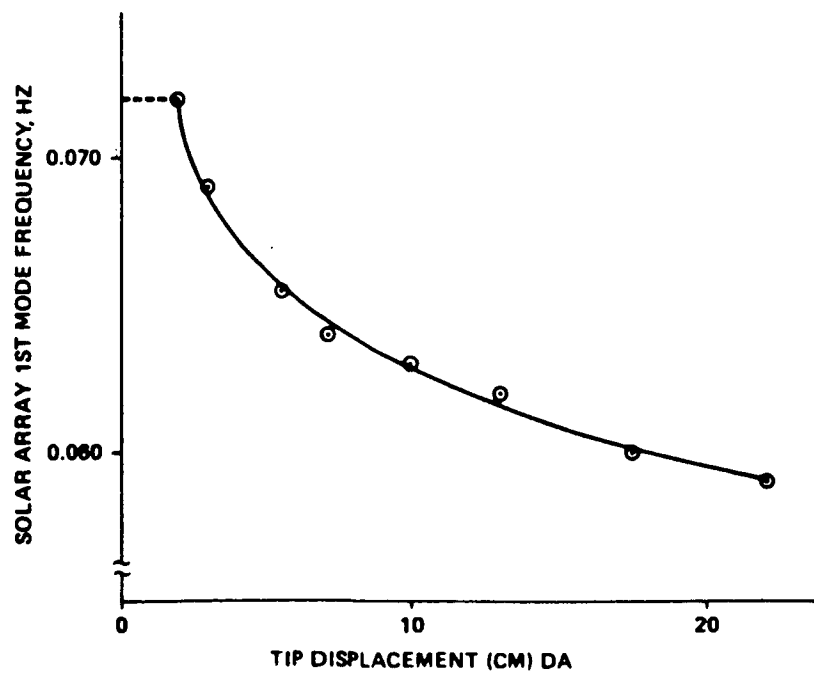
FIGURE 13 1ST MODE NATURAL FREQUENCY VRS
TIP RESPONSE DISPLACEMENT

503
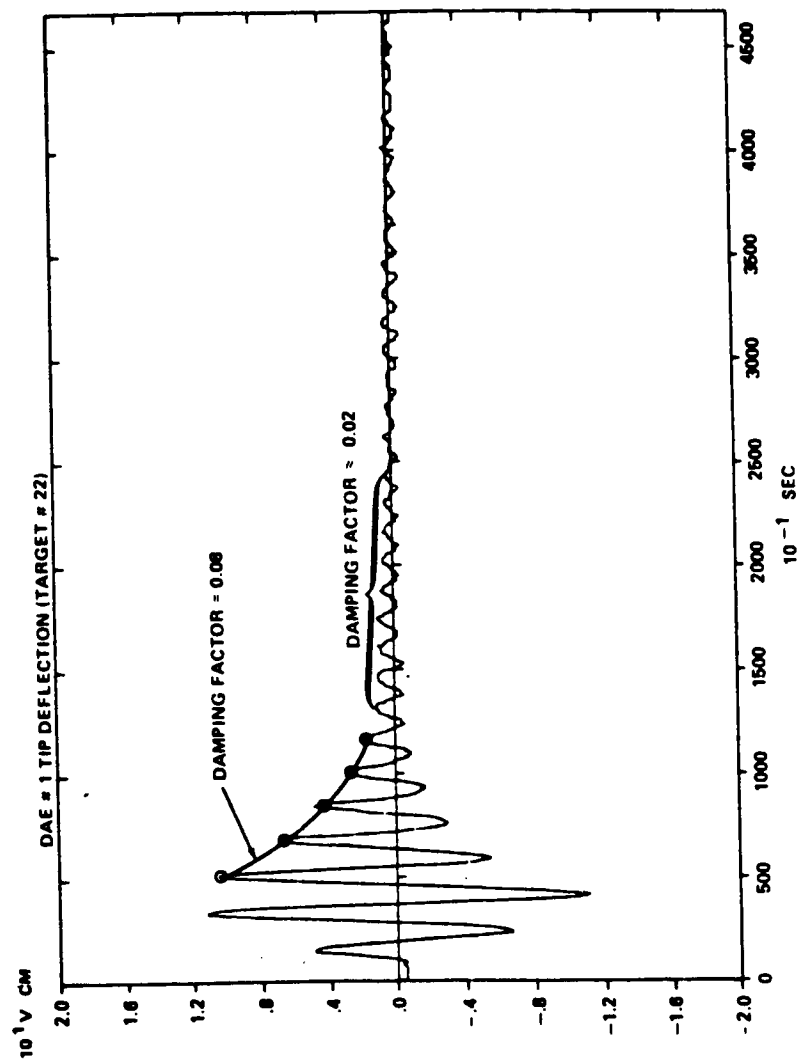
FIGURE 14   SOLAR ARRAY TIP DISPLACEMENT
VRS TIME

PRECISION POINTING AND CONTROL

OF FLEXIBLE SPACECRAFT

M. H. Bantell, Jr.

BOEING AEROSPACE COMPANY

Large Space Structure Control

Precision Pointing and Control of Flexible Spacecraft

The problem and long term objectives for the precision pointing and control of flexible spacecraft are shown on the facing page. The four basic objectives are stated in terms of two principle tasks. Under Task 1, robust low order controllers, improved structural modeling methods for control applications and identification methods for structural dynamics are being developed. Under Task 2, a lab test experiment for verification of control laws and system identification algorithms is being developed. The following presentation highlights work in the following areas. For Task 1, work has focused on robust low order controller design and some initial considerations for structural modeling in control applications. For Task 2, work has focused on experiment design and fabrication, along with sensor selection and initial digital controller implementation.

Precision Pointing and Control of Flexible Spacecraft

Boeing Aerospace Company

- Problem

- Current NASA and DoD plans call for large multiply connected flexible space structures (LSS) with requirements for unprecedented vibration and figure regulation accuracy

- Resulting LSS control problems are multivariable, highly coupled with large model uncertainty

- Controllers must be of relatively low order for implementation

Objectives

Task 1: Large Space Structure Control

- Develop low order robust, high performance controllers using modern techniques

○ Develop improved structural modeling methods for control applications

○ Develop methods for identification of structural dyanamics

Task 2: Flexible Spacecraft Control Simulator

- Develop lab test experiment for verification of control laws and systems identification algorithms

Large Space Structure Control
Fixed Order Controller Design

A flow diagram for comparing fixed order controller synthesis techniques is shown in the facing page. All methods begin with the definition of a continuum structure of theoretically infinite dimension. An evaluation model is derived by finite element methods of order N which is too large for controller design purposes. Model reduction methods are then employed to reduce the structure to various dimensions compatible with the chosen controller design scheme. Four fundamental approaches are discussed as follows. In each case, the objective is to provide a low order controller of dimension $r << N$.

In the first case (path Ⓐ), the structure is reduced directly to dimension r and LQG methods derive a controller which is optimal for the r order structure. In the second case (path Ⓑ), the structure is reduced to order s which is somewhat greater than r but much less than N. Parameter optimization using a nonlinear programming technique is used to synthesize the controller of dimension r. In the third case (path Ⓒ), the structure is reduced to a large dimension n such that LQG controllers can be synthesized without exceeding the available computing capability viz., to "Riccati solvable" dimension. The resulting large order controller is reduced to dimension r by projection methods. In the fourth case (path Ⓓ), a structure of dimension n is employed and the projection is calculated from the solution of coupled sets of Lynapunov and Riccati matrices of dimension n. The resulting projection is optimal because it is derived from a direct optimization of steady state quadratic performance index for the closed loop system equations including the controller. The resulting nonlinear matrix forms solve the first order necessary conditions of optimality but convergence is not guaranteed and the resulting solution is not guaranteed to be globally optimizing.

Large Space Structure Control
Fixed Order Controller Design

509
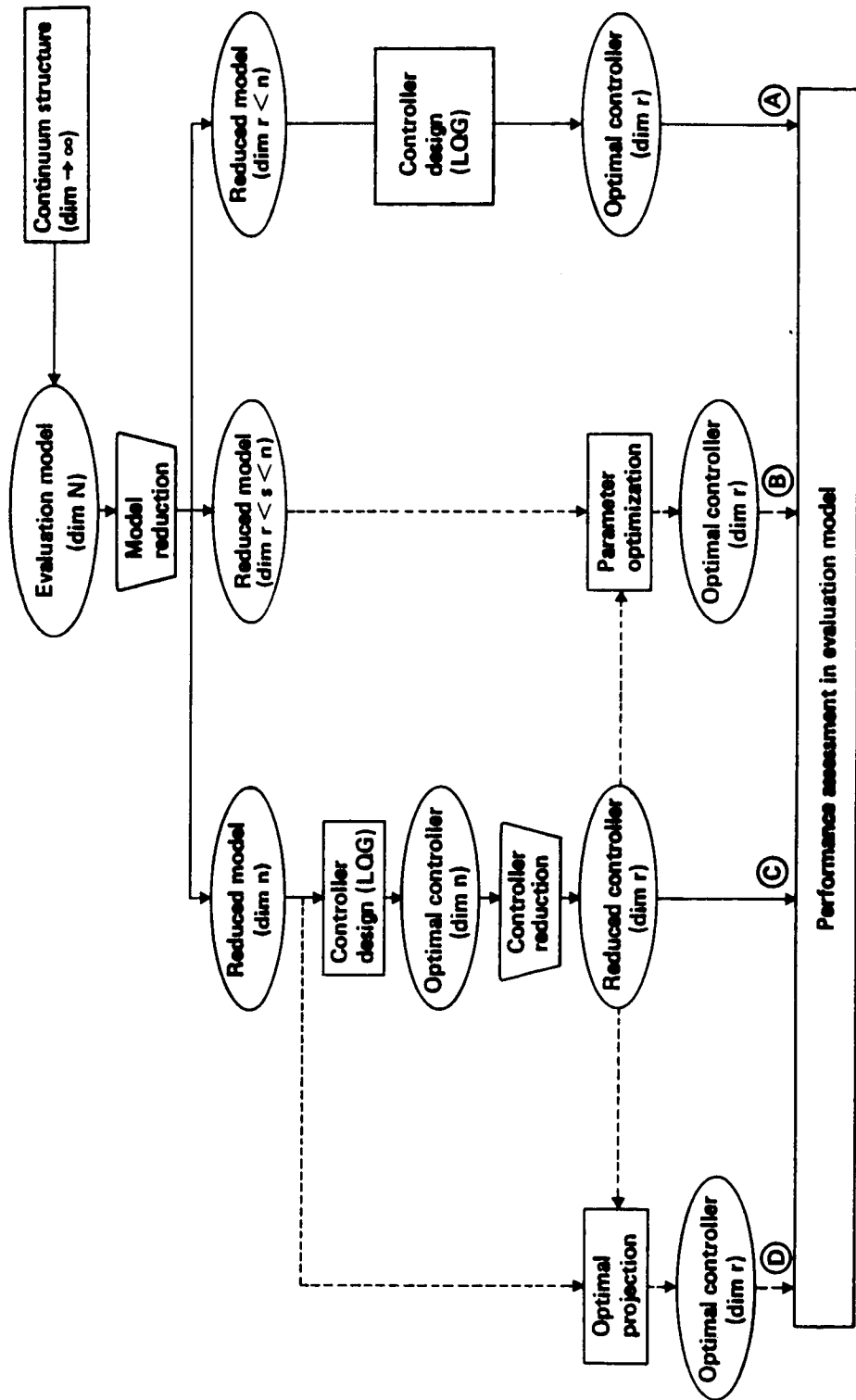
Large Space Structure Control

Low Order Controller Methods/Attributes Comparison

The methods and attributes comparison for the controller synthesis techniques of the previous chart is shown on the facing page. This chart should be viewed and discussed in juxtaposition with the previous chart. The key points for each of the attributes are highlighted as follows.

Model Order

Model order refers to the order of the structural model used in controller design. The model order should be high enough to accommodate the dynamics which significantly impact the control objectives. This usually implicates a model of very high dimension when the controller pass band has strong interaction with the structure over a wide range of frequency.

Controller Structure

Controller structure refers to the various dynamic functions the controller will accommodate viz., integral control, proportional plus derivative, direct output feed back, etc. In a parameter optimization scheme, virtually any controller structure can be realized. In a standard LQG structure, additional variety is best obtained by frequency shaping the quadratic criteria in the integral expression for the cost index.

Controller Stability

The controller is stable if all of its poles are in the left half of the s plane. This criterion is important because it is generally observed that systems with unstable controllers do not exhibit good robustness properties and are particularly sensitive to parameter variations.

Computing Burden

In the synthesis of a controller, it is desirable that the algorithm not utilize numerical search procedures that require special expertise. This is tantamount to the requirement for user friendliness. If the control problem is difficult (because of coupling and ill conditioning) and the initializing guess is poor, numerical procedures do not represent a viable cost effective tool.

Large Space Structures Control
Low Order Controller Methods/
Attributes Comparison
Boeing Aerospace Company

ENGINEERING
TECHNOLOGY

Methods / Attributes	Closed loop			Open loop
	Ⓓ Optimal projection	Ⓒ Sub-optimal projection	Ⓑ Parameter optimization	Ⓐ Low order LQG
Model order	High	High	Low	Low
Controller structure	Limited	Wide range with frequent shaping	Unlimited	Wide range with frequent shaping
Closed loop stability guaranteed	Yes	No	Yes	No
Controller stability guaranteed	Yes	Yes	No	No
Computing burden	Medium	Low	Very high	Low

Large Space Structure Control

Fixed Order Robust Controller Design Techniques

The diagram on the facing page shows various methods for introducing uncertainty into the controller synthesis procedure. The methods are succinctly stated in the comments accompanying the diagram. The competing methods are also identified as closed loop or open loop. Methods B, C, D include uncertainty as part of controller synthesis and therefore constitute closed loop methods. Robustness analysis after controller synthesis (Method A) is an open loop procedure.

The design procedure described in this discussion is summarized as follows. Structure model reduction is accomplished by the method of component cost analysis with white noise introduced at the inputs. The noisey inputs may constitute either disturbance or actuator forcing terms. Model surveys should be performed with both types of inputs to properly identify the important modes with respect to disturbability, controllability, and observability. Internal balancing with respect to the "abilities" is also effective and should be used in conjunction with component cost analysis to give a comprehensive model survey.

Controller synthesis is accomplished by the method of suboptimal projection. The preferred method is q-COVER which is an acronym for Covariance Equivalent Realization of order q. This method will be highlighted in the presentation to follow.

Controller design with uncertainty is most effectively accomplished by introducing the variation of parameters into the reduced order model. This is accomplished by deriving additional states which model state trajectory perturbations or state sensitivities with respect to the set of parameter variations. The objective is to design a controller using quadratic synthesis which is "desensitized" with respect to the parameter variations. The resulting controller should give the best tradeoff between performance degradation and sensitivity to uncertainty.

Large Space Structure Control
Robust Controller Design Techniques

ENGINEERING
TECHNOLOGY

? = uncertainty
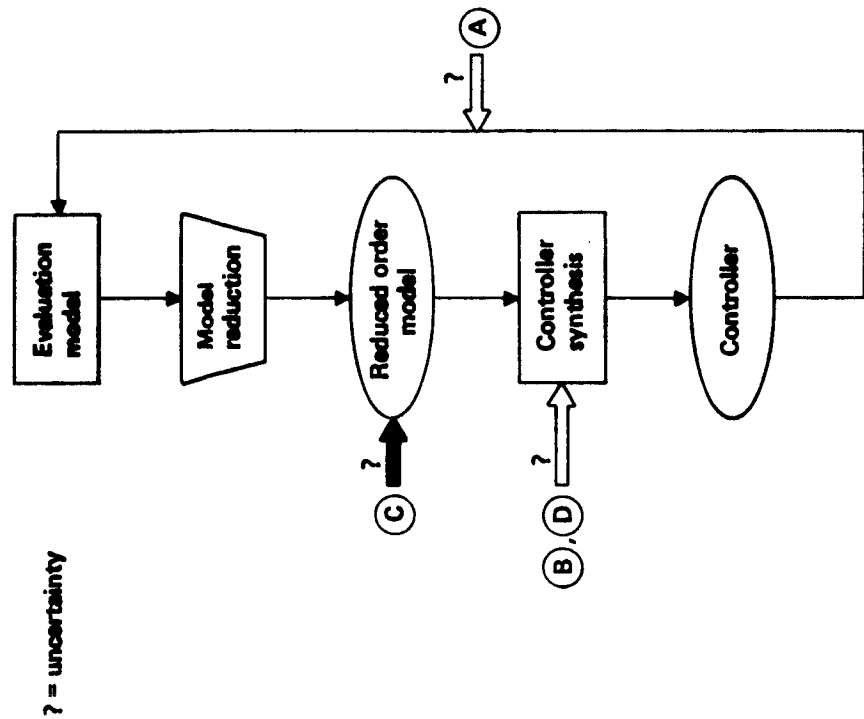
Open loop	(A)	Robustness analysis after nominal controller derived
Closed loop	(B)	Weight discrete cost function with probability of a given plant state
	(C)	Introduce trajectory sensitivity (parameter gradient states) and standard LQG format along with nominal control and state variables
	(D)	Introduce probability density of parameter variations in LQG format

Evaluation model → Model reduction → Reduced order model → Controller synthesis → Controller

? (A)

? (C)

? (B, D)

513

Large Space Structure Control

Generalized LQG Compensator Design

The diagram on the facing page shows a generic configuration for the flexible structure with compensator along with the dynamics of the compensator. Also shown are the realization equations for the flexible structure and the compensator along with generalized quadratic criteria used to synthesize the regulator and filter. The LQG design methodology exploits the separation principle which states that the regulator and filter can be designed as independent elements in the event that process and measurement noises w and n are additive. The key matrices emerging from the synthesis are the Riccati matrices for the regulator and filter designated P_r and P_f, respectively.

Large Space Structure Control
Generalized LQG Compensator Design

Boeing Aerospace Company

ENGINEERING TECHNOLOGY

Regulator design

$$J_r = \min_u \int_0^\infty (y^T Q_r y + u^T R_r u)\, dt$$

Filter design

$$J_f = \min_w \int_0^\infty (z-Hx)^T Q_f (z-Hx) + w^T R_f w\, dt$$

$\dot{x} = Ax + Bu + \Gamma w$
$y = Cx$
$z = Hx + n$

$\dot{\hat{x}} = A_c \hat{x} + K_f e$
$u = -K_r \hat{x}$
$A_c = A - BK_r$
$e = z - H\hat{x}$

Filter: $P_f H^T R_f^{-1}$ $K_f(s)$

Regulator: $R_r^{-1} B^T P_r$ $K_r(s)$

Compensator structure

Large Space Structure Control

Projection Defined

The method of controller reduction by projection is outlined on the facing page. The objective is to compute matrics T_L (qxn) and T_R (nxq) such that the full order compensator $[A_c, K_f, K_r]$ of order n is reduced to $[A_{cq}, K_{fq}, K_{rq}]$ of order q by the transformation indicated. The matrix $H = T_R T_L$ is called a projection matrix, and is such that its rank i.e., the number of independent rows (columns) is exactly q, the order of the reduced compensator.

Large Space Structure Control
Projection Defined

Boeing Aerospace Company

Purpose
- Distill maximal performance from the full order and project into a space of smaller dimension

Projections
- Given the compensator realization $\left\{ A_c, K_f, K_r \right\}$ order n

$$T_L \in R^{q \times n} \quad T_R \in R^{n \times q}$$

$$A_{cq} = T_L A_c T_R$$

$$K_{fq} = T_R K_f$$

$$K_{rq} = K_r T_L$$

$$T_L T_R = I_q$$

$$\text{Rank} \left\{ T_R T_L \right\} = q$$

- Realization $\left\{ A_{cq}, K_{fq}, K_{rq} \right\}$ is of order $q < n$

$$H = T_R T_L \text{ the "projection" matrix}$$

517

Large Space Structure Control

Projection Methods

The selection of a projection algorithm is required in order to compute matrics T_R, T_L. In projection theory, it is desired that the reduced system preserve certain attributes of the full order system. The two methods outlined on the facing page are excellent examples of what is considered to be the most efficient open and closed loop model reduction algorithms. The Riccati balancing method derives a transformation S which balances disturbability and observability measures P_f and P_r to the extent that the singular values in the transformed coordinates are equal. The transformation then isolates those states which are most difficult to control and observe. The method is open loop because the states retained may not contribute to the closed loop control objectives.

The q-COVER method derives a transformation S that renders (A_c, K_f) and (A_c, K_r) disturbable and observable. The reduced order system resulting from this process guarantees to match q covariance derivatives and the first q Markov parameters of the full order system. Thus, both the steady state covariance response and the high frequency system response are preserved up to order q. The method is closed loop because the matching process is performed on the entire controller as an entity, which was derived from closed loop objectives.

518

Large Space Structure Control Projection Methods

Boeing Aerospace Company

Ricatti balancing (open loop)

- Derive a transformation S such that

$$S^{-1} P_f S^T = S^T P_r S = \Sigma$$

$$\Sigma = \text{diag} [\sigma_1, \ldots, \sigma_n]$$

- Compensator is balanced with respect to disturbability (P_f) and observability (P_r)

- Construct T_L, T_R from S corresponding to largest σ's

- Open loop because states retained may not contribute to closed loop control objectives

q-COVER (closed loop)

- Derive a transformation S that renders (A_c, K_f), (A_c, K_r) controllable and observable

- Derive T_L, T_R such that (A_{cq}, K_{fq}, K_{rq}) matches q steady state covariance derivatives and the first q Markov parameters of the full order system

Large Space Structure Control

Tetrahedron Open Loop Frequency Response

The goal in the design of this model was to emulate the characteristics of a typical space structure while keeping the order of the problem small (less than 20 modes). The performance criterion for this system is the transverse (x,y) motion of node 1 at the apex of the tetrahedron. This is analogous to the line-of-sight error performance measure of typical large space structure optical systems. The tetrahedron is supported by six legs, which are pinned to the ground. Masses are lumped at nodes 1 through 4, and the truss elements are capable of supporting only axial loads.

The resulting structure has 12 modes of vibration. The open-loop disturbance response at the apex, to transverse forces F_x, F_y is shown for the first eight modes on the facing page. The last four modes were considered unknown so that robustness to neglected high-frequency dynamics could be evaluated. Control and observation were limited to placement of linear force actuators and rate and position sensing in the supporting legs.

This is a difficult control problem because the vibration modes dominating apex motion are only weakly controllable and observable from the base structure. The modes which dominate apex transverse vibration are the first, second and fourth as shown.

Large Space Structures Control
Tetrahedron Open Loop Frequency Response

ENGINEERING

TECHNOLOGY

Mode	W_n
1	1.342
2	1.666
3	2.891
4	2.957
5	3.398
6	4.204
7	4.662
8	4.755
9	8.539
10	9.251
11	10.285
12	12.905

Tetrahedron structure
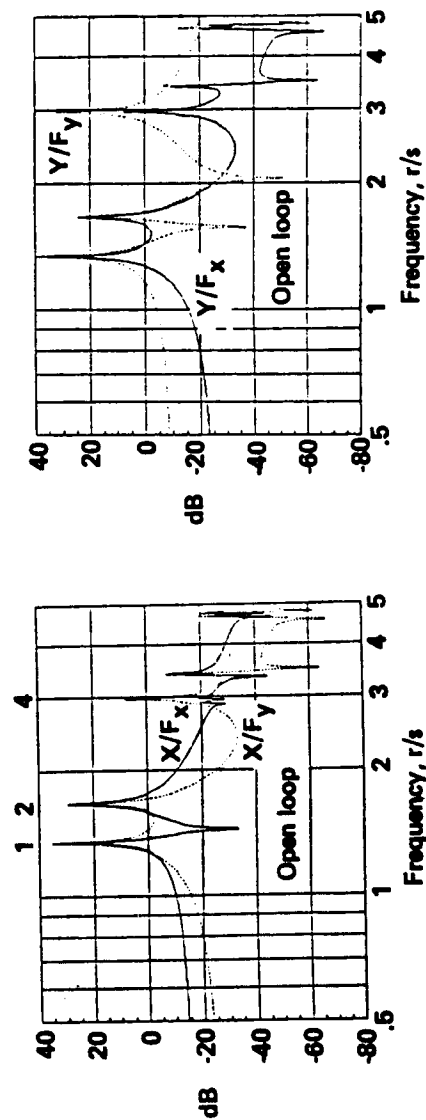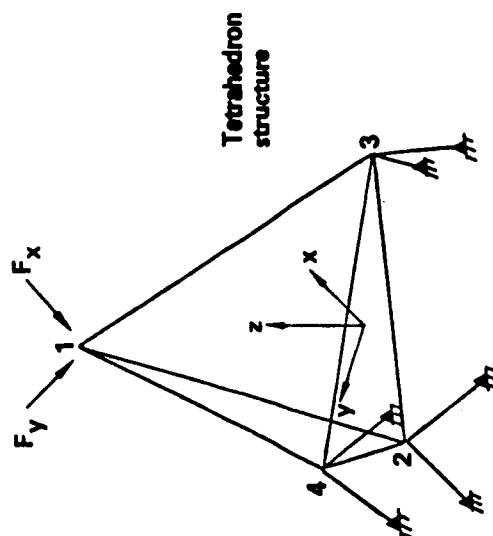
Large Space Structures Control

Tetrahedron Component Cost Analysis

Modal rankings as a function of mode number for V_n and V_δ are drawn on the facing page. Sensors (position + rate) and actuators are colocated in all cases. It is noted that with the exception of Mode 4, the impulsive and white noise evaluations give similar results for observation and control in two legs. For control and observation in multiple legs, cancellations in the row elements of the B matrix induce dropouts in the modal rankings of V_δ. Modal rankings for white noise measure V_n clearly give the correct indication of controllability and observability and analysis of Mode 7 shows that V_δ gives erroneous conclusions regarding these measures. The modal matrix in conjunction with the B matrix shows that Mode 7 is highly controllable and is dominated by z translations of masses 3 and 4 in opposite directions. Therefore to induce the presence of Mode 7 in V_δ for control at nodes 2, 3 and 4, the impulses would require appropriate scaling. For a complex structure with multiple controls, choice of the weights on the delta functions is not straight-forward.

Large Space Structures Control
Tetrahedron Component Cost Analysis

Boeing Aerospace Company

Sensor and actuators colocated in all legs

V_n (white noise)

V_δ (impulsive)

Mode number

Tetrahedron
structure
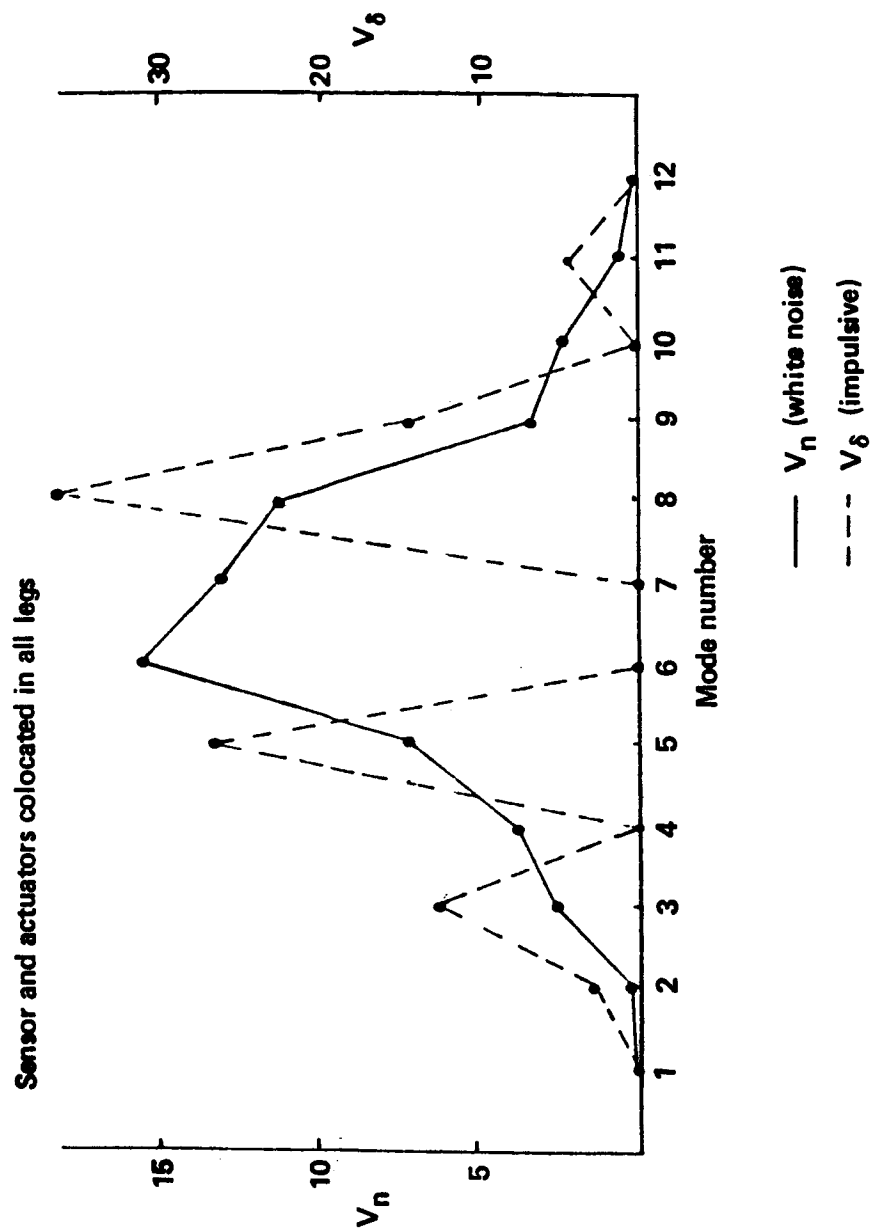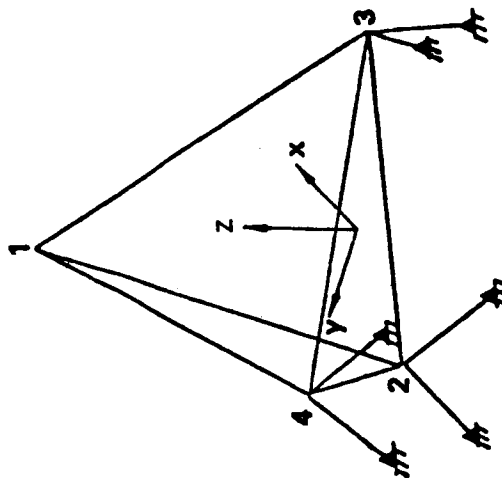
Large Space Structures Control

RMS Comparison of Low Order Controllers

The rms performance comparison for the balancing technique (RB) developed from the separat theorem (certainty equivalence principle) and COVER theory is shown on the facing page. Performance is quantified in terms of rms output at the apex of the structure vs. rms control effort. The plot on the left shows the performance of RB relative to the full 16th order LQG controller, for RB controller orders of 6 and 4. The 6th order controller closely matches the full order LQG. However, the performance 4th order controller is poor and closed loop response was unstable for gain slightly greater than 10. The plot on the right shows the performance of RB relative to COVER with LQG as the standard for absolute comparison. This data is very revealing and the following conclusions are highlighted. It is noted that closed loop response for both the 4th and 6th order COVER controllers is stable even for high gains where there is essentially no improvement in output performance for additional expenditure of controller effort. Additionally, for high gains the 6th order controller requires more control effort than the 4th order controller to achieve essentially the same rms performance. Clearly the 6th RB gives superior performance for this particular application. Comparing the 6th order COVER results with that of the 6th order RB shows that the COVER controller performed poorly for low gain. However, near the knee of the curves the 6th order COVER performance is comparable with the 6th order RB and the 4th order COVER closely matches the 6th order COVER performance.

RMS Comparison of
Low Order Controllers
Large Space Structures Control   Boeing Aerospace Company

525
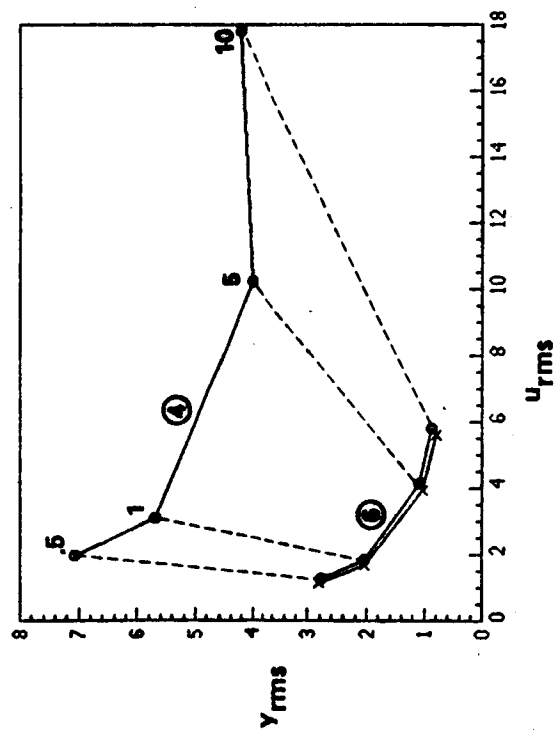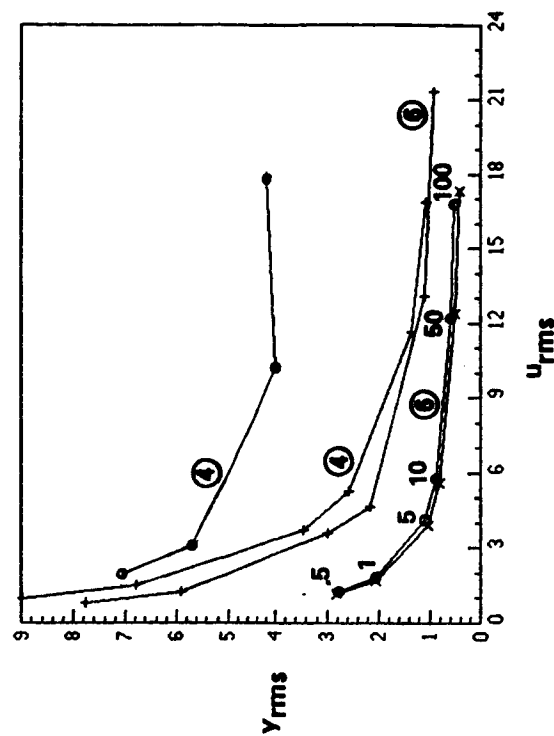
Large Space Structures Control

Comparison of Low Order Controllers

The closed loop frequency response of 6th order RB and 4th order COVER for a gain of 10 is shown on the facing page. Again the comparison is made with respect to the 16th order LQG controller. The data indicates that the 6th order RB controller matches the 16th order LQG very closely. However, the 4th order COVER controller exhibits considerable residual with respect to the controlled modes.

Comparison of Low Order Controllers
Large Space Structures Control

Boeing Aerospace Company

ENGINEERING
TECHNOLOGY

Legend:
—— 16th order LQG
----- Low order

Gain = 10

6th order
RB

Y Axis

Y/F$_Y$

Frequency, r/sec

4th order
COVER

Y/F$_Y$

Frequency, r/sec

X Axis

X/F$_X$

Frequency, r/sec

X/F$_X$

Frequency, r/sec

527

Large Space Structures Control

Comparison of Low Order Controllers

The closed loop frequency response of 6th order RB and 4th order COVER for a gain of 100 is shown on the facing page. The comparison is made with respect to the 16th order LQG controller. It is noted that as the gain increases the COVER controller is improving relative to 16th order performance; the 6th order RB is correspondingly degrading.

Comparison of Low Order Controllers
Large Space Structures Control Boeing Aerospace Company

Legend:
——— 16th order LQG
----- Low order

Y Axis

Y/F_Y

6th order
RB

Gain = 100

X Axis

X/F_X

Y Axis

Y/F_Y

4th order
COVER

X/F_X

ENGINEERING
TECHNOLOGY

529
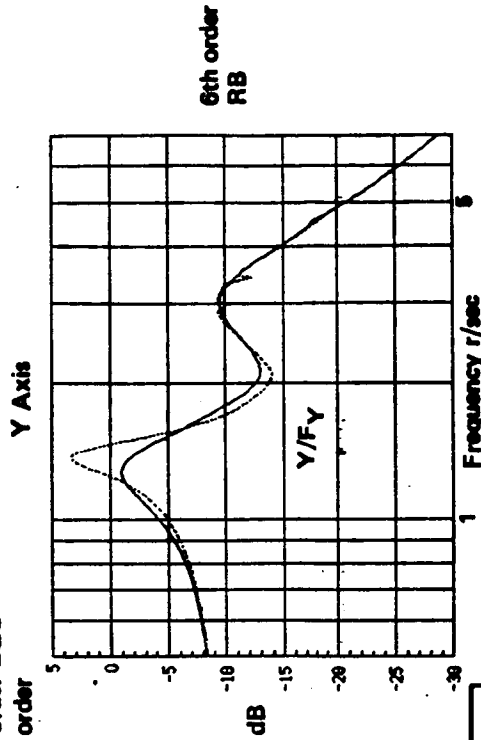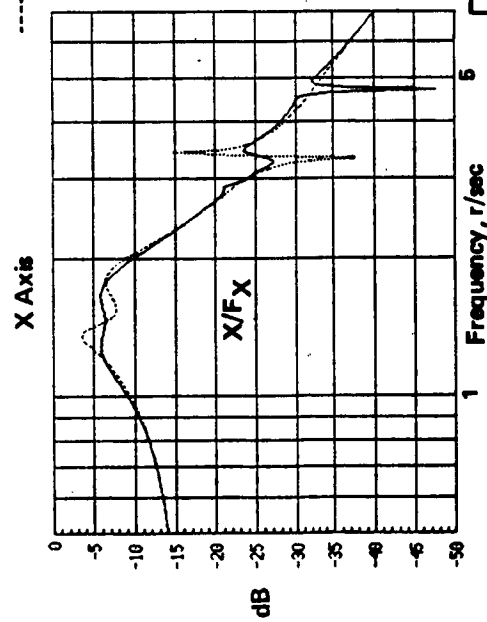
Large Space Structures Control

Comparison of Low Order Controller

A singular value comparison of the 4th order COVER and 6th order RB controllers with respect to the 16th order LQG is shown on the facing page. Singular values of $I + (KG)^{-1}$ give a sufficient condition for stability for multiplicative uncertainty. In particular, the proximity of the minimum singular value (σ) of $I + (KG)^{-1}$ to zero gives an indication of impending instability. This measure is extremely conservative. However, controller design comparison can be made with meaningful results. The comparitive results indicate in a general sense that over the range of frequency fcr which the controllers were designed, the low order controller is more robust to multiplicative uncertainty than the full order controller. The exception is the large peaks at frequencies indicated in the frequency response plots. These are modes that do not contribute to the motion of the apex. However, the data indicates a significant degradation in robustness at these frequencies.

Comparison of Low Order Controllers
Large Space Structures Control

ENGINEERING
TECHNOLOGY

Boeing Aerospace Company

Gain = 100

$$\underline{\sigma} = \min_{sv} [\ I + (KG)^{-1}\ ]$$

531
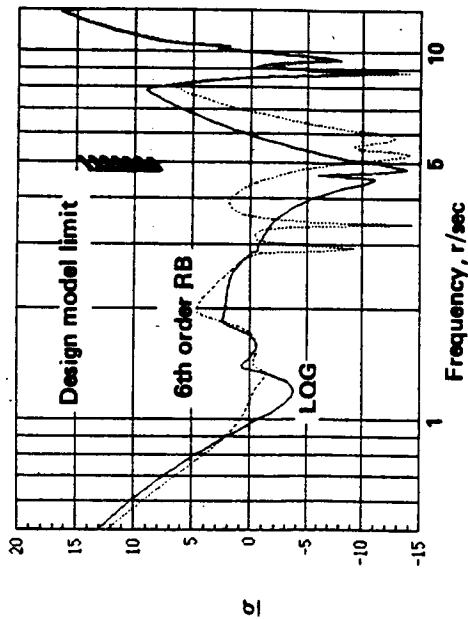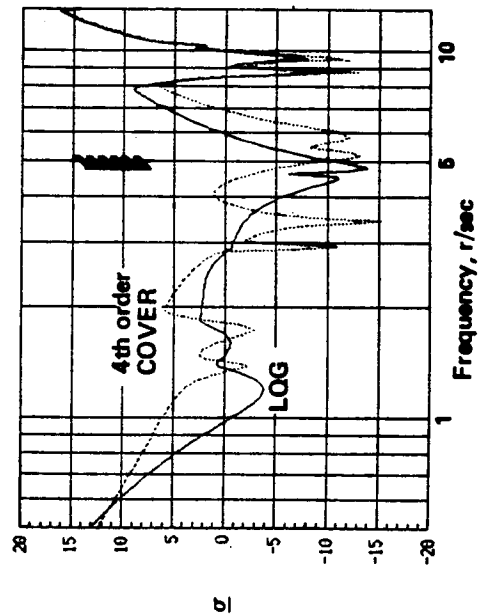
Large Space Structures Control

Time Response Comparison

A time response comparison for the low order controllers of interest are shown on the facing page. The key item to note is that increasing the gain from 10 to 100 brought no increase in rms performance. However, the settling time is significantly improved. It is noted however, that the disturbance environment for structures that require CSI technology is usually wide band and random in nature. Thus rms performance considerations make more sense than criteria developed from impulsive or constant frequency disturbance sources.

Time Response Comparison
Large Space Structures Control
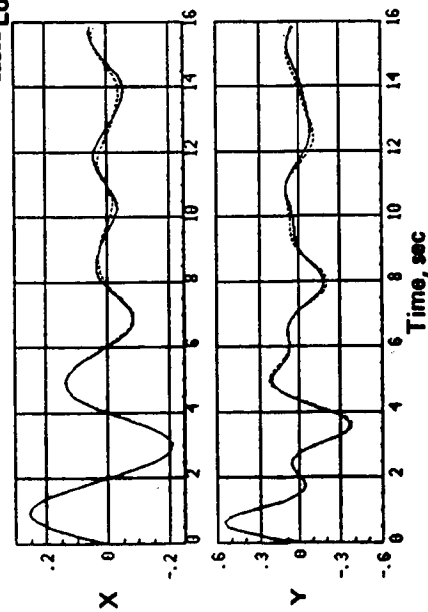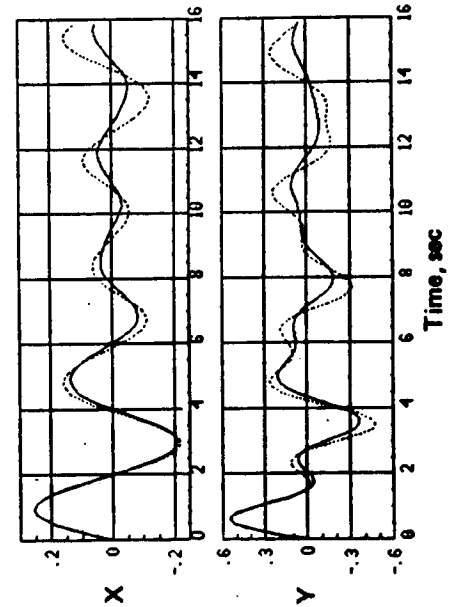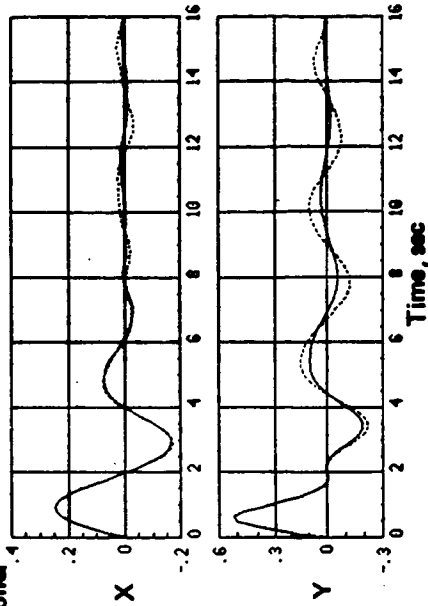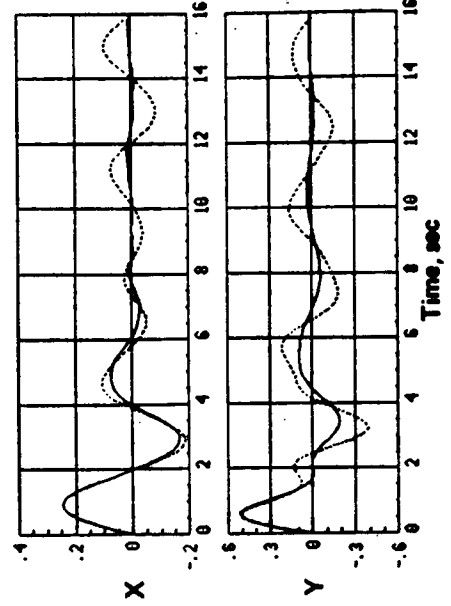
Large Space Structures Control

Singular Value Comparison

The singular value plots on the facing page give a relative performance comparison of 6th order RB controllers for a gain of 10 and 100 respectively. It is noted that the low gain controller is absolutely more robust than the high gain controller. However, the low order controller for the high gain case is relatively more robust to the full order LQG controller than the low gain counterpart.

Singular Value Comparison
Large Space Structures Control
Boeing Aerospace Company

ENGINEERING
TECHNOLOGY

$$\underline{\sigma} = \min_{sv} [\, |\, + (KG)^{-1}\,]$$

535
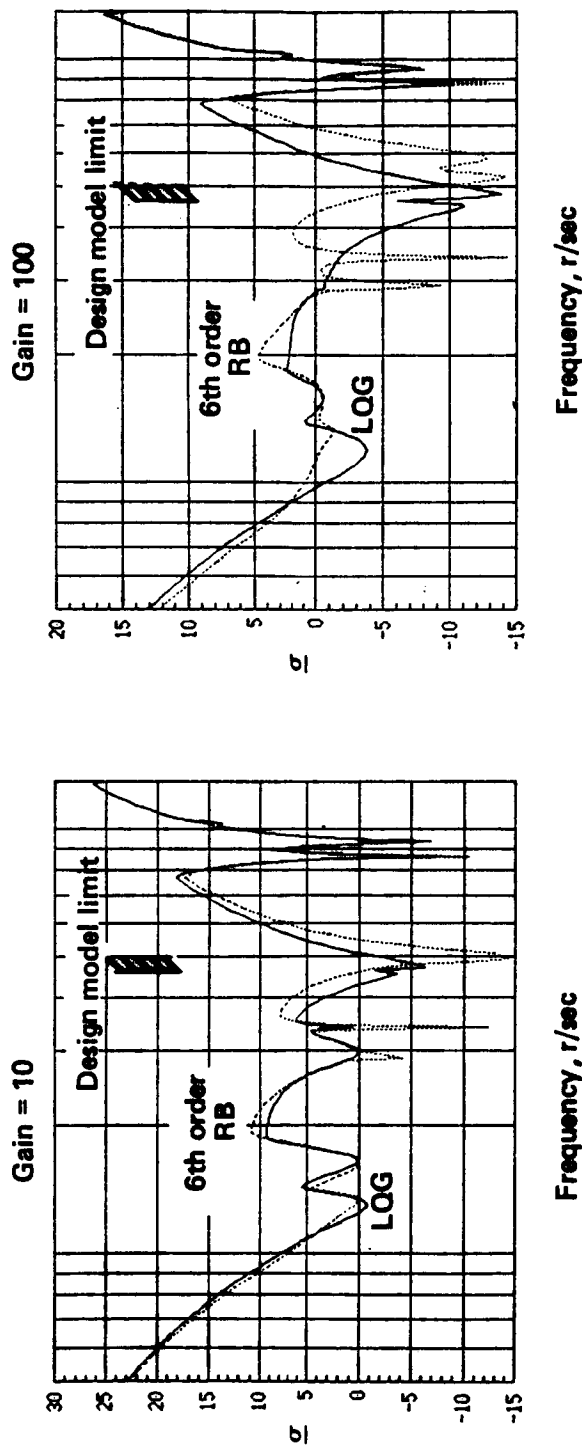
Large Space Structure Control

Conclusions

The conclusion of the study regarding fixed-order controller design along with basic considerations and observations for structural modeling in control applications is given on the facing page.

Control of Flexible Structures

Conclusions

Boeing Aerospace Company

Fixed order controller design

● Model reduction crucial to performance and robustness of closed loop system

● Preferred controller synthesis for highly complex structures is to design high order controller and reduce by projection methods

● q-COVER is the preferred suboptimal projection method for controller reduction

● Frequency shaping in quadratic synthesis of the compensator structure can substantially improve efficiency and performance of LQG designs

● Classified SISO do not accurately represent stability and performance characteristics of structures as multivariable systems

● Singular value decomposition effective for comparative controller robustness assessment but is not a good diagnostic tool

Dynamics of Trusses Having Nonlinear Joints

J. M. Chapman
F. H. Shaw
W. C. Russell

Boeing Aerospace Company
Seattle, Washington

Presented at
Workshop on Structural Dynamics and Control
Interaction of Flexible Structures

Marshall Space Flight Center
Huntsville, Alabama
April 22-24, 1986

DYNAMICS OF TRUSSES HAVING NONLINEAR JOINTS

INTRODUCTION

The current Space Station design includes long beamlike lattices as the primary support structure as shown in Fig. 1. Two basic methods for lattice construction are under evaluation by NASA. The first uses erectable lattice members requiring astronaut EVA for construction while the second uses a pre-assembled but deployable truss requiring little EVA activity. One major disadvantage of deployable trusses is, however, the inherently nonlinear joints used in such structures. Usual analysis and testing techniques therefore become insufficient. The objective of this paper is to present an analysis technique that can perform the nonlinear static and dynamic analyses of a structure having nonlinear joints. Validation of the technique with test results still remains to be demonstrated.
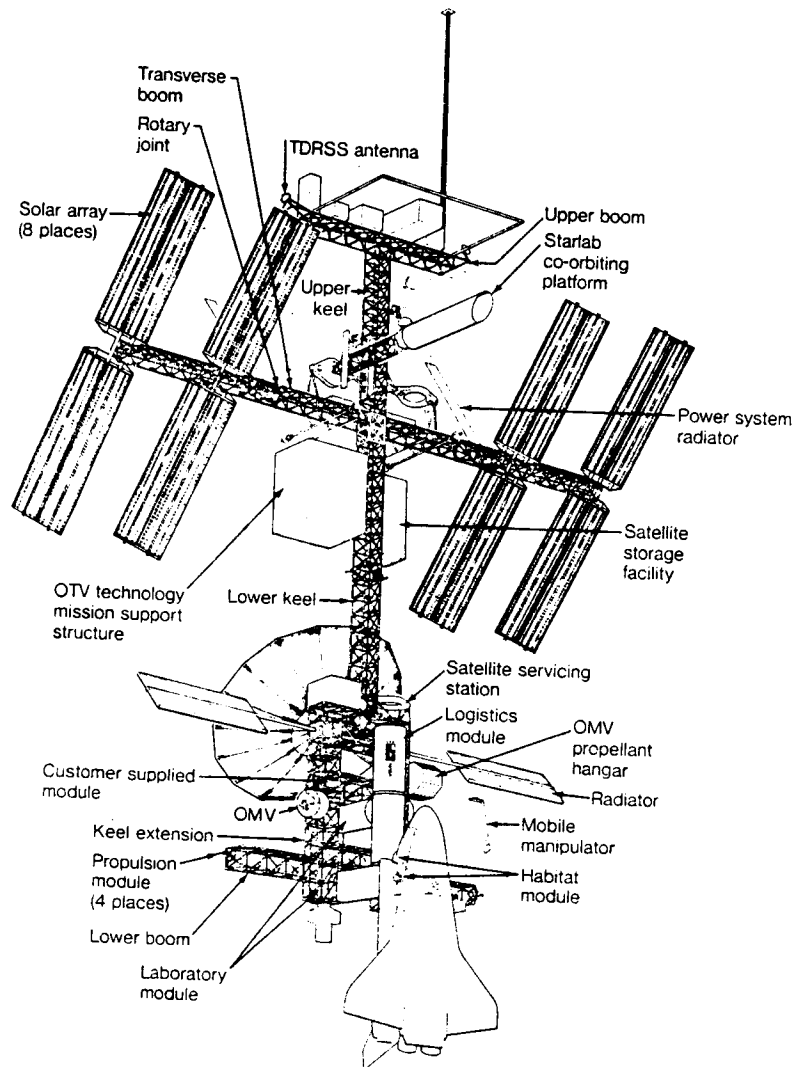
Figure 1

OBJECTIVES

The objectives of the transient analysis techniques are shown in Fig. 2. The technique must account for such nonlinear joint phenomena as free-play and hysteresis. The number of degrees of freedom (dof) describing the dynamic response of the structure must be reduced to a manageable size and the resulting equations of motion must permit a fast numerical algorithm. The analysis method must also permit inclusion of empirical data derived from tests on joints and truss "links". Finally, the analysis method must be be validated by accurately predicting the response of a large multi-jointed test article.

Develop transient analysis techniques that can account for joint free-play and hysteresis

- Reduce the number of governing equations

- Develop a fast numerical integrator

- Validate using test results

Develop testing techniques that can identify and characterize the nonlinear effects of the joints

- Joint tests

- "Link" tests

- Truss tests

Figure 2

Three different analysis procedures were examined rigorously in order to substantiate any particular result derived from one (see Fig. 3).

The "Gap-Element" approach currently exists in general finite element codes such as MSC/NASTRAN and ANSYS but this approach was found to be limited to problems having a small number of nonlinear joints. For large problems the Gap-Element approach became unstable. The general method used in the approach is to update the stiffness matrix each time the properties of a nonlinear element changed. For small problems this approach worked well, but for large problems, a small change in one nonlinear element caused "large" changes in all other elements and a unique stiffness matrix could not be found.

Perturbation techniques using the method of multiple scales were also examined for one and two dof problems yielding corroboration and insight into the behavior of spring-mass systems having free-play. The technique requires, however, an enormous amount of algebraic complexity and may be too limited for an analytic description of trusses having arbitrary joint nonlinearites. Nevertheless, the multiple scale technique remains a valuable tool for future research.

The technique developed in this paper is coined the "residual force" technique. In this method, the linear and nonlinear character of the structure are separately identified and placed, respectively, on the left and right hand sides of the equations of motion. The residual forces appearing on the right hand side (RHS) represent the nonlinear corrections that must be applied to a linear structure in order to replicate the nonlinear response. Having the linear terms on the left hand side (LHS) permits powerful modal analysis techniques as a viable method of size reduction.

Results using the residual force technique have been shown to agree with the results using the gap element and multiple scale solutions for small problems. For large problems, no other known technique exists.

"Gap-element" approach

- Slow—stiffness matrix updated each time step
- Unstable for large problems

Residual force approach

- "Left hand side" of equations of motion linearized
- Nonlinear joint phenomena on "right hand side"

Perturbation techniques

- Method of averaging
- Multiple scale technique

Figure 3

BASIC IDEA OF THE RESIDUAL FORCE

The basic idea of the residual force can best be described by examining the simple one-dof problem shown in Fig. 4. The joint in this spring-mass system is modeled simply as a gap having a total free-play of 2d. The force-displacement curve for this system therefore has a flat spot with zero force while in the gap. This curve can also be reproduced by including a small residual force acting on a linear spring having no gap. The equations of motion then take the form as shown in Fig. 4. Note that the stiffness derived on the "LHS" can be derived by considering the joint to be infinitely stiff.

$$m\ddot{x} + kx = F_{Residual}$$

— Nonlinear terms on "RHS"

LHS constructed with infinitely stiff joints

Figure 4

543
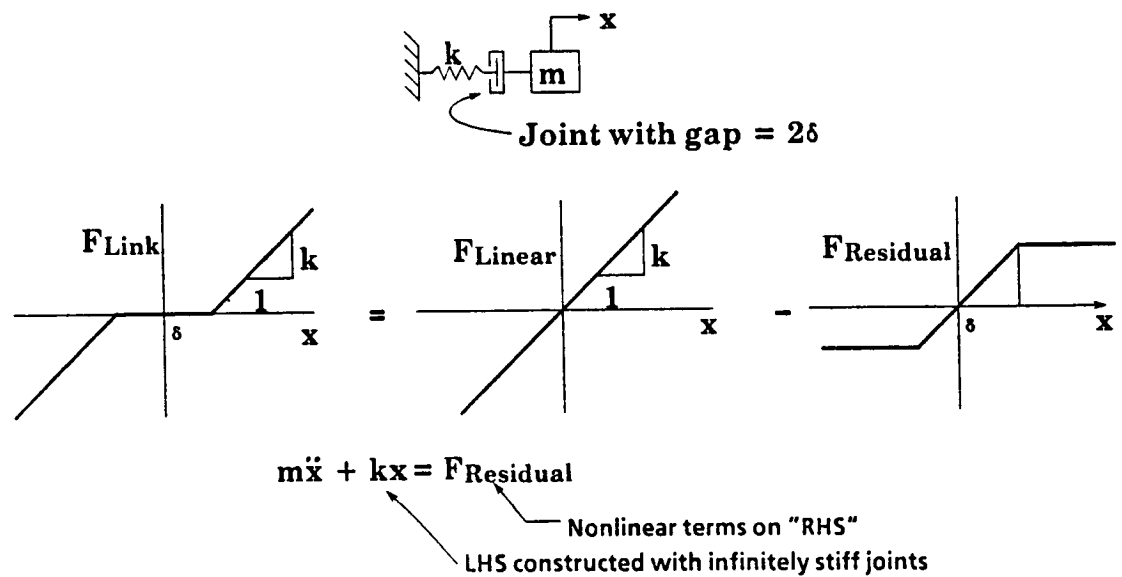
TWO DOF PROBLEM

The equations of motion for a two dof gap problem are shown in Fig. 5. The system consists of two springs, two gaps, and two masses as shown. The linear stiffness matrix of the "LHS" is again constructed by considering the joints to be infinitely stiff, that is, by assuming the gaps to be locked. The nonlinear effects of the gaps are defined by two residual forces appearing on the "RHS" of the equations of motion. Note in Fig. 5 that both the nonlinear forces acting on the system and the relative displacements across each spring-gap element are each defined by the same transfer matrix that depends only upon the geometry and connectivity of the structure.

Results will now be presented for this two dof problem in order to demonstrate certain nonlinear effects that gaps can have on the dynamic response. Afterwards, the equations of motion for a joint dominated structure having arbitrary joint nonlinearities will be presented along with accompanying results for a 10 bay deployable truss.
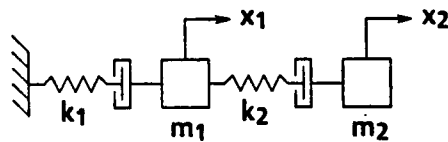
Equations of motion:

$$\begin{bmatrix} m_1 & \\ & m_2 \end{bmatrix} \begin{bmatrix} \ddot{x}_1 \\ \ddot{x}_2 \end{bmatrix} + \begin{bmatrix} k_1+k_2 & -k_2 \\ -k_2 & k_2 \end{bmatrix} \begin{bmatrix} x_1 \\ x_2 \end{bmatrix} = \begin{bmatrix} 1 & -1 \\ 0 & 1 \end{bmatrix} \begin{bmatrix} f_1 \\ f_2 \end{bmatrix}$$
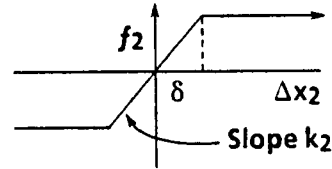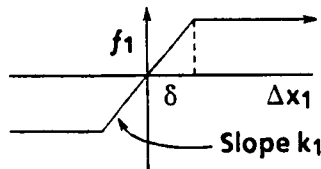
$$\begin{bmatrix} \Delta x_1 \\ \Delta x_2 \end{bmatrix} = \begin{bmatrix} 1 & 0 \\ -1 & 1 \end{bmatrix} \begin{bmatrix} x_1 \\ x_2 \end{bmatrix}$$

Figure 5

544

MODAL RESPONSE OF THE TWO-DOF PROBLEM

The nonlinear modal response of the two dof problem subject to an initial impulse is shown in Fig. 6. The modal response of the linear system having no gaps is also shown. Two effects that gaps have on the modal response are immediately apparent when the linear and nonlinear solutions are compared. First, the maximum modal amplitudes for the nonlinear problem are larger. And second, the modal periods for the gapped system are longer than the periods for the gapless system. Both of these effects are understandable in that the gaps soften the structure and a softer structure would respond with larger amplitude and increased period when excited with the same initial impulse. Other nonlinear effects become apparent, however, when the solution is viewed for longer time periods.
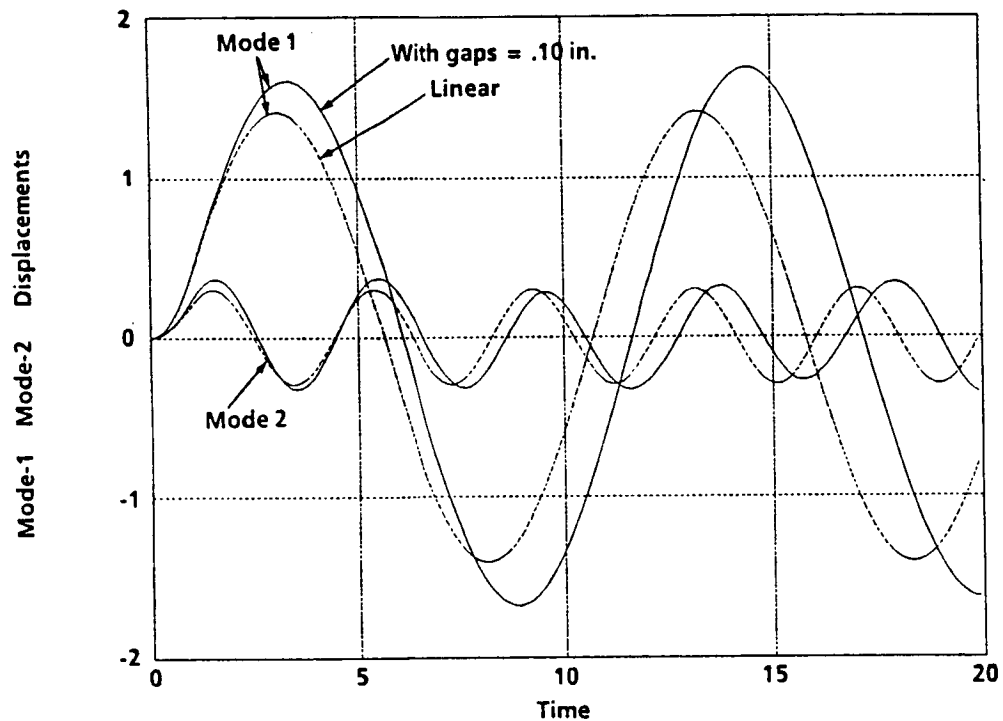
Figure 6

UNDAMPED TWO-DOF PROBLEM

The modal responses of the undamped two-dof gap problem are shown for an extended period of time in Fig. 7. Nonlinear coupling between the modes now becomes apparent in that the free undamped vibration of the two modes exhibit slow sinusoidal variations in their amplitudes. Note that an increase in the maximum amplitude of the second mode is accompanied by a decrease in the amplitude of the first mode. This reciprocal variation in amplitude is understandable since the total energy of the system must remain constant after the initial impulse. The amplitude variations thus indicate a slow sinusoidal energy transfer back and forth between the two modes.

The slow sinusoidal variations in the modal amplitudes may also be shown to exist by using the perturbation theory of multiple-scales on the two-dof gap problem.
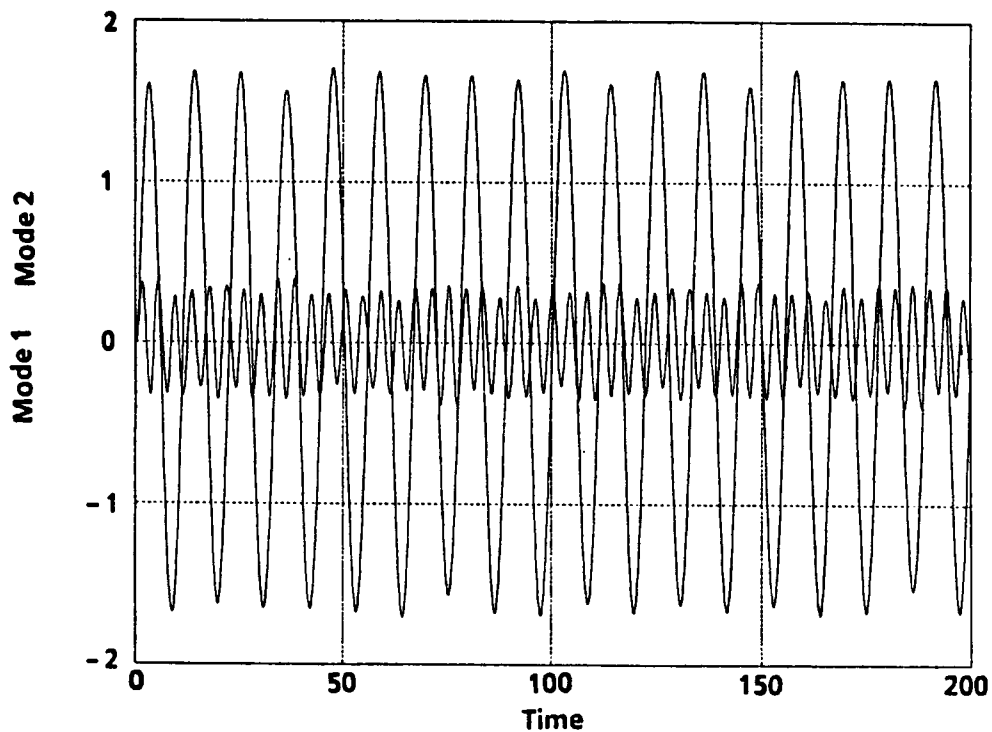
Figure 7

TWO-DOF PROBLEM WITH .5% MODAL DAMPING

The effect of energy transferal between the two modes becomes important when damping is introduced. Fig. 8 shows the response of the two-dof gap problem due to an initial impulse and 0.5 percent modal damping. Slow sinusoidal variations in amplitude are again apparent, but because the second mode has a greater exponential decay, the energy that is transferred from the first mode to the second mode cannot be equally returned. The result is that the second mode seems to reach a quasi-steady state response with the energy dissipation due to modal damping being balanced by the energy transferal from mode one. This also means that the first mode will appear to damp faster than would otherwise be predicted from modal damping alone.

Note also that the amplitude of the second mode is given a substantial boost whenever the two modes are in phase. This suggests that there may be certain conditions determined by the ratio of the two natural modal frequencies and the gap sizes that may cause internal resonance. A complete investigation into the effects that gaps may have on the response of a system must therefore seek to define any conditions that may lead to internal or parametric resonance between the modes.

Figure 8

547
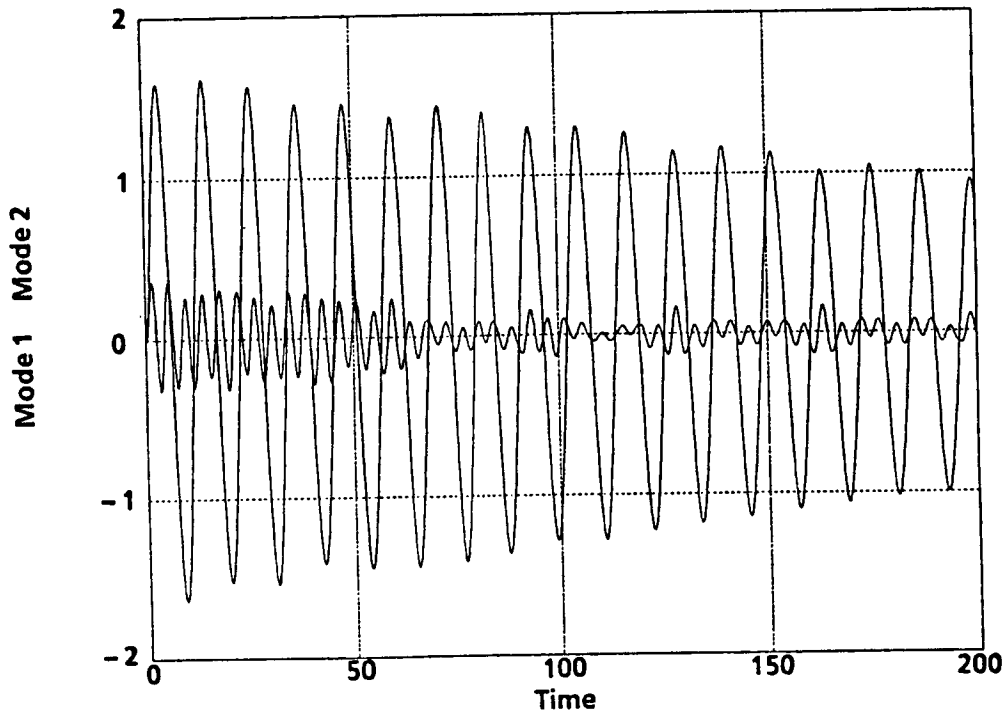
TWO-DOF PROBLEM WITH ENHANCED COUPLING

The coupling between the modes of the two-dof gap problem can be enhanced by a proper choice of the modal frequencies. Forced response of the single dof gap problem shows that resonance can occur when the natural frequency is 1/3, 1/5, 1/7, etc. of the driving frequency. This suggests that choosing the frequency of the second mode to be three times the frequency of the first should define a problem exhibiting large coupling between the two modes. Fig. 9 shows the response of an undamped two-dof gap problem when the ratio of frequencies between the first and second mode is 1/3. This is precisely the condition that one would expect to see resonance of the second mode if such resonance does in fact exist. Fig. 9 shows, however, that while large non-sinusoidal variations do occur in the free vibration of the second mode, time linear growth in the amplitude does not occur. Nevertheless, the slow sinusoidal variations in the amplitude of the second mode are no longer small and indicates a greater coupling between the first and second modes.
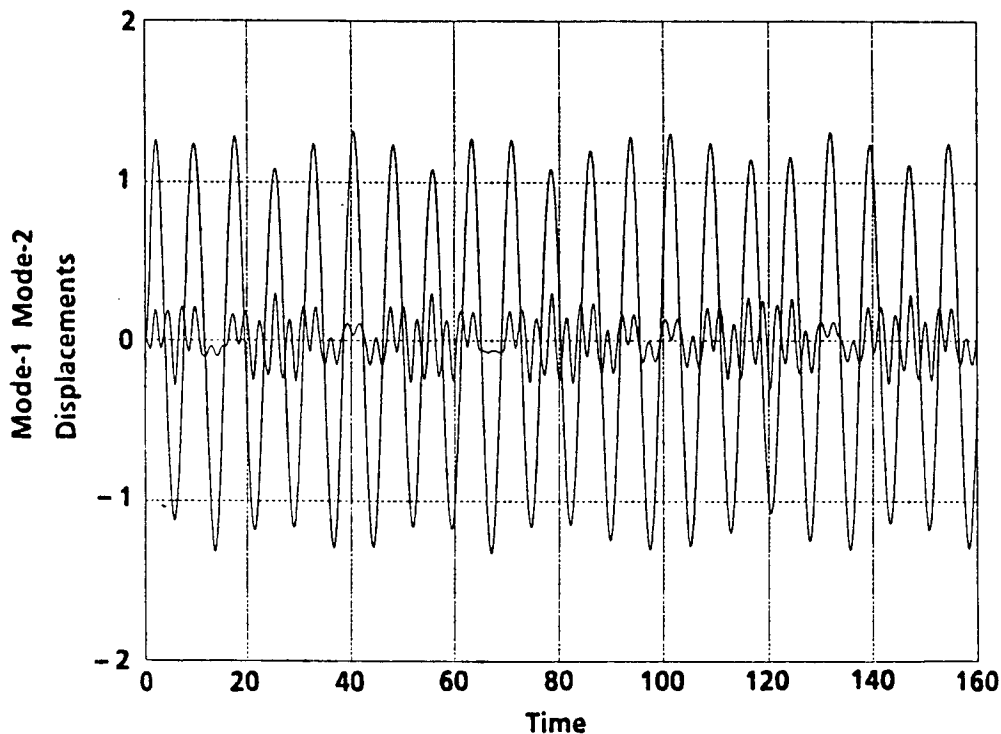
Figure 9

MODELING ASSUMPTIONS

The modeling assumptions used by the residual force technique in the analysis of a typical deployable truss are shown in Fig. 10. As shown, the longerons and lacing members have two or three nonlinear joints that can be characterized using force maps. A force map of a joint is simply a pictorial way of stating that the force in a joint can be defined as a function of both the relative displacement and velocity across the joint. Note that the battens are shown not to have nonlinear joints. This is because stable behavior of trusses (or beamlike lattice structures) generally require that all battens be rigidly attached to the lattice vertices. If the battens are pinned instead of rigidly attached, geometric nonlinearities due to the finite size of the joint must be considered. Moreover, low frequency joint rotation modes will exist unnecessarily complicating the dynamic behavior of the structure. Deployable trusses should therefore avoid pinned battens if at all possible.

Another modeling assumption required in the residual force technique is that the mass of the truss can be lumped at nodes. This approximation is usually valid for low frequency excitation as is generally the case for the Space Station. It remains to be seen if damping effects can be accurately calculated when using the lumped mass approach.

The concept of a truss link is also pictorially shown in Fig. 10. A truss link is defined here as the composite series of joints and members that represent the truss structure between two truss verticies. Truss links are ideally considered as axial load carrying members only and are modeled as a series combination of nonlinear joints and linear springs.

The complete description of the truss link requires, in general, monitoring all the "internal" dof of the link that describe the relative displacements of each joint and spring. In certain special instances however, a composite force map for a massless truss link can be derived. First, if all joint force maps depend only upon displacement then an equivalent force map for the link can be easily derived. Second, if the massless truss link has only two arbitrary but identical joints then a residual force map for the link can be derived. And finally, if the joint stiffness is large, the damping small, and the rates low for each joint, then the force map for the link can again be derived. This last special instance is generally the case for Space Station trusses and suggests that an equivalent force map for the link can be derived directly from testing. If none of the above three special instances apply to the truss being analyzed, then all interior dof of the link must be monitored during the analysis. One easy way to accomplish this is to simply include additional mass freedoms along the truss link.

Special attention has been given to the modeling of the truss links because the success or failure of a transient analysis technique strongly depends upon the ability to accurately monitor the nonlinear stiffness and damping effects of the generally stiff joints. Direct monitoring of the extremely small relative displacements across the joints is impractical. Instead, the residual force method takes advantage of the fact that the joints are in series with a relatively soft spring and a residual force map for the link is derived. In essense, the forces in the joints are monitored instead of the relative displacements.

549

Dynamics of Trusses
Modeling Assumptions

Batten
- ● = Mass node
- □ = Joint having a force map

$$F_J = f(X_J, \dot{X}_J)$$
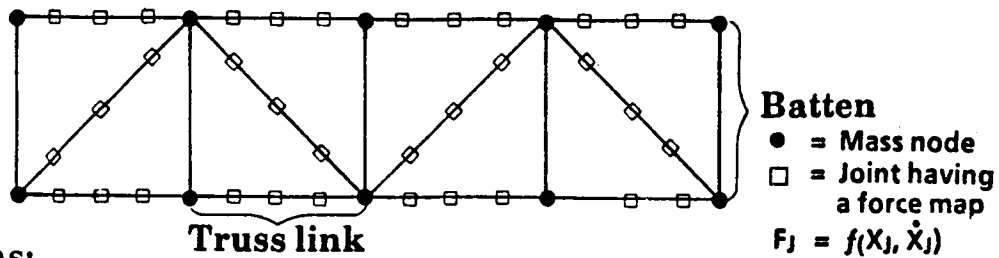
Truss link

Assumptions:
- Battens do not have pinned joints (otherwise joint rotation modes would exist)
- Truss links are axial load carrying members only
- Joints are described by arbitrary force maps
- Inertial effects can be lumped at the mass nodes

Claim:
- The ability or inability to analyze the above truss is determined by the ability or inability to analyze the nonlinear "truss links" with an efficient, stable numerical integrator

Figure 10

RESIDUAL FORCE MAPS

The derivation of a residual force map for a joint in series with a soft spring is given in Fig. 11. The force in the joint can be described by a force map giving the joint force as an arbitrary function of the relative displacement and velocity across the joint. This force must also equal the force in the soft spring, and both the spring force and the joint force are equal to the force in the link.

The first step in generating the residual force map for the link is to transform the displacement axis of the joint force map so that the new force map is a function of the total link displacement and the joint's relative velocity. The equations used in this first step are shown in Fig. 11.

The second step uses the definition of the residual force as the difference between the linear "left hand side" force and the total nonlinear link force. Note that the linear force in Step 2 of Fig. 11 is again obtained by considering the joint to be infinitely stiff. As a result of the above definition for the residual force, it is found that the joint's relative displacement is directly proportional to the residual force. The second step thus transforms two axes of the force map from step 1; the force axis is transformed into a residual force axis, and the velocity axis is transformed to a new axis having the time derivative of the residual force as the independent variable.

The main advantage of the above transformations is that the incrementally small joint displacements and velocities are not monitored directly. Instead, a very small and stretched out residual force map is used offering a numerically more attractive description of the link.

$$F_{Link} = F_{Joint} = F_{Spring}$$

Step 1)

$$\left. \begin{aligned} f_J\left(x_J, \dot{x}_J\right) &= k_s x_s \\ x_L &= x_J + x_S \end{aligned} \right\} \Rightarrow F_{Link} = f_L\left(x_L, \dot{x}_J\right)$$

Step 2)

$$F_R = k_S x_L - F_{Link}$$

$$x_J = x_L - \frac{F_{Link}}{k_S} = \frac{F_R}{k_S} \qquad \Rightarrow F_R = f_R\left(x_L, \dot{F}_R\right)$$

$$\dot{x}_J = \frac{\dot{F}_R}{k_S}$$
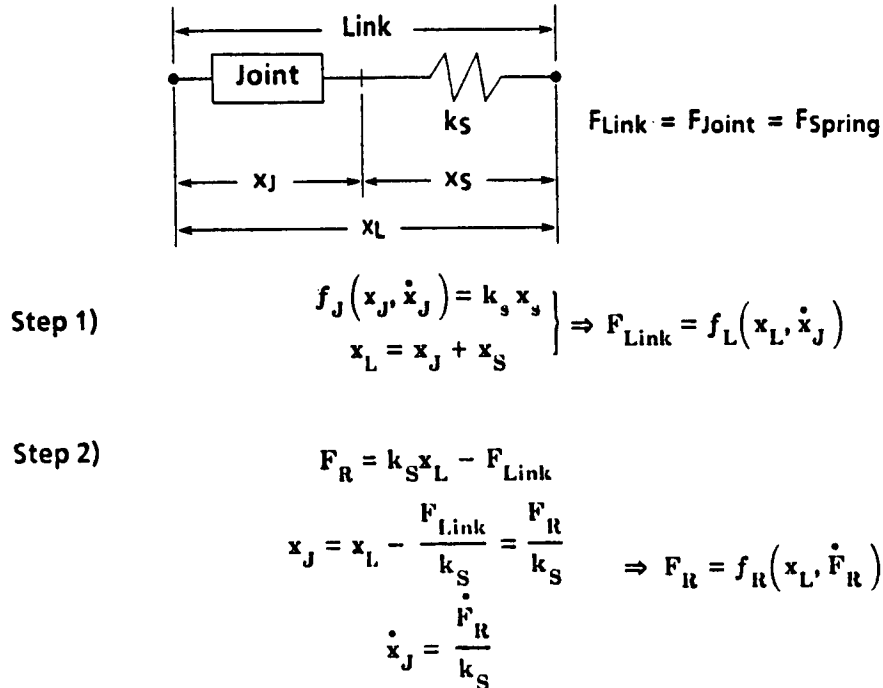
Figure 11

551

RESIDUAL FORCE MAP EXAMPLES

Two examples of residual force maps are given in Fig. 12. The residual force map for a gap in series with a soft spring was derived in Fig. 4 and is shown here again to demonstrate that the residual force for this problem is expressed in terms of the total relative displacement across the link. This result will also be true for any number of joints in series with a soft spring so long as the force maps of the joints are independent of velocity.

The second example is of two identical Voigt joints in series with a soft spring. The truss link is also grounded at one end and attached to a mass at the other to formulate a single dof problem so that all equations of motion may be shown.

Using the procedure of Fig. 11 for calculating the residual force, a linear first order differential equation for the residual force is derived. The equations of motion for the link-mass system are also derived by considering the Voigt joints to be infinitely stiff. All equations are shown in Fig. 12.

There are two interesting observations to be made about the first order differential equation for the residual force. First, the derivative term is normally small suggesting a perturbation solution to the differential equation. And second, the nonhomogeneous term on the right hand side of the differential equation is always small for joints that are much stiffer than the "soft" link spring. Monitoring the residual force therefore appears to be much more numerically attractive than monitoring the incrementally small displacements and velocities across the Voigt joints.

The perturbation solution of the first order differential equation for the residual force also gives an interesting result. As shown in Fig. 12 the perturbation solution for the residual force can be expressed as a function of the link's relative displacement and velocity. This means that the residual force for the link is itself expressable in terms of a force map. This result will always be true whenever the joint stiffness is large, the joint damping is small, and the rates are low.

Gap problem

Link with two linear joints
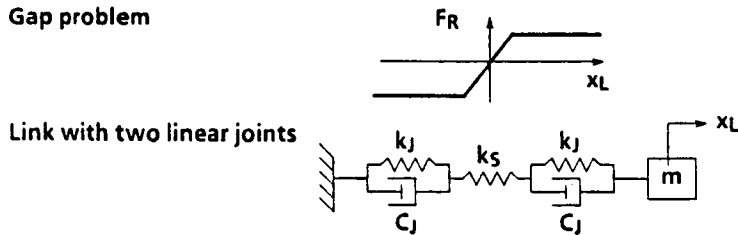
$$m\ddot{x}_L + k_S x_L = F_R$$

$$\frac{C_J}{k_J + 2k_S} \dot{F}_R + F_R = \left(k_S - k_L\right) x_L \qquad \frac{1}{k_L} = \frac{1}{k_S} + \frac{2}{k_J}$$

Also $F_R \simeq \left(k_S - k_L\right) x_L - \dfrac{\left(k_S - k_L\right)}{k_J + 2k_S} C_J \dot{x}_L = f\left(x_L, \dot{x}_L\right)$

when damping is low, joint stiffness is large, and rates are low

Figure 12

EQUATIONS OF MOTION OF A TRUSS HAVING NONLINEAR JOINTS

The equations of motion governing the free and forced dynamic response of a truss having nonlinear joints are shown in Fig. 13. These equations were derived using the residual force technique on a truss satisfying the assumptions listed in Fig. 10. One essential feature of this technique is to replace the arbitrary force maps describing the nonlinear joints with residual force maps describing the truss links. The main advantage of this replacement is that the incrementally small relative displacements and velocities across a joint are not monitored directly thereby avoiding numerical difficulties. Instead, very small and "soft" residual forces are defined giving a numerically attractive form for the equations of motion and thereby permitting numerically stable integration algorithms.

The only mass degrees of freedom shown in Fig. 13 are at the truss verticies but additional mass freedoms along each truss link may be required depending upon the nature of the joint nonlinearities as discussed under the topic of modeling assumptions (Fig. 10). The total number of degrees of freedom defined by the nodal equations of motion shown in Fig. 13 can be on the order of 2000 degrees of freedom for Space Station trusses and methods to reduce this large number are therefore desired.

The modal representation also shown if Fig. 13 is a natural choice for size reduction in that it takes advantage of the linearity of the left hand side of the nodal equations of motion. However, using a truncated set of structural modes generally has the disadvantage of decreasing the represented flexibility of the structure. This disadvantage can be offset by including the residual flexibility due to the neqlected modes in all calculations affecting the dynamic response of the structure. The links' relative displacements and velocities therefore have residual flexibility terms to augment the modal descriptions. Using a truncated set of system modes in the equations of motion then only assumes the inertial loads due to the neglected modes can be ignored. The number of system modes to be retained must therefore be chosen with care.

The residual flexibility matrix operating on the residual forces will in general be very large. Practical inclusion of this matrix is then only possible when the matrix is nearly diagonal. This is expected to be generally the case for trusses but has not yet been demonstrated. However, for problems considered to date, the flexibility terms have not been required. The numerical accuracy of the results were determined simply by including most if not all of the system modes and comparing the results to the truncated solution. Future research will concentrate on the number of retained modes versus residual flexibility issue for various joint nonlinearities.

The two main types of joints investigated so far have been the nonlinear gap joint and the Voigt joint. The Voigt joints considered consist of a stiff spring in parallel with either a lightly damped or heavily damped dashpot. Successful inclusion of these two main types of joints in the transient analysis of a large joint dominated truss should demonstrate the general capability of the residual force approach. Results using these joints are included here for a four bay planar truss and a ten bay 3D deployable truss currently at MARSHALL.

Dynamics of Trusses
Residual Force Technique

Equations of motion

$M\ddot{x} + Kx = CF_R + F_{External}$

x = displacements at mass freedoms only

$x_L = C^Tx$ = deflections across a link

F_R = residual forces in links = $f(x_L, \dot{F}_R)$

Modal representation

$\ddot{Q} + \omega^2Q = \Phi_L{}^T F_R + \Phi^T F_{External}$

$x_L = \Phi_L Q + G_L F_R + G_E F_{External}$

$\dot{x}_L = \Phi_L\dot{Q} + G_L\dot{F}_R + G_E\dot{F}_{External}$

$G_L = C^T G_R C \quad G_E = C^T G_R$

$G_R = (K^{-1} - \Phi \, 1/\omega^2 \, \Phi^T)$ = residual flexibility
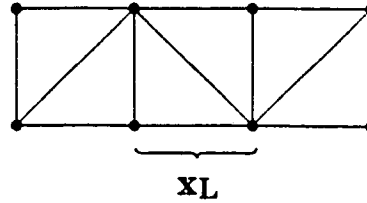
Figure 13

FOUR BAY PLANAR TRUSS

The truss model of a four bay planar truss used to perform several numerical experiments is shown in Fig. 14. Gaps or Voigt joints were considered in all longerons and lacing members but were not included for the battens.

The response after an initial impulse for a truss having gaps of 0.003 inches is shown in Fig. 15 at two different times. The response of the linear truss is also shown for comparison. The nodal equations of motion were integrated so that all modal excitations would be included. Two observations can be made by examining Fig. 15. First, the maximum amplitude of the gapped structure at time 0.270 seconds is larger than the maximum amplitude (nearly) of the linear structure. The larger amplitude appearing for the gapped response results because the gaps introduce greater flexibility to the structure. And second, the nonlinear response has a much greater modal participation than the linear response as seen by observing the structural deformation at time 0.540 seconds.

The tip and modal responses of the gapped truss having 1% modal damping are shown in Fig. 16. The initial large amplitudes in these responses is due to the initial impulse applied to the structure. Free vibration then occurs for times greater than 0.5 seconds. Several interesting observations can be made by examining Fig. 16. First, the tip response is governed primarily by the first mode. Second, as the amplitude decreases due to modal damping, the period increases. Third, very small, slow sinusoidal variations occur in the amplitude of the first mode but these variations are not as pronounced as seen earlier for the two-dof gapped problem. Fourth, the free vibration response of the second mode appears to be strongly coupled to the first and higher modes. Coupling to the first mode can be inferred due to the quasi-steady state response that occurs between four and ten seconds. The energy dissipation that this mode should normally display has been balanced by the net energy transferal from the first mode. Coupling to the higher modes can be inferred by the high frequency content in the free vibration for this mode.

The tip and modal responses of the four bay planar truss having Voigt joints are shown if Fig. 17. The response of this structure to an initial impulse is particularly interesting because all of the damping present is due to the Voigt joints. Modal damping is not present. Several observations concerning this response are also possible, particularly when also compared to the response of Fig. 16. First, the tip response is again dominated by the first mode. Second, the contribution of the second mode is much smaller for the Voigt jointed model than it is for the gapped model. And third, frequency shifts and slow sinusoidal variations do not occur in the decaying response as they do in the gapped problem.

Dynamics of Trusses
2-D Truss With Sloppy Joints

4 @ 53.00"

55.00"

y

E = 9.9 msi
A = .4497 in2

Gap
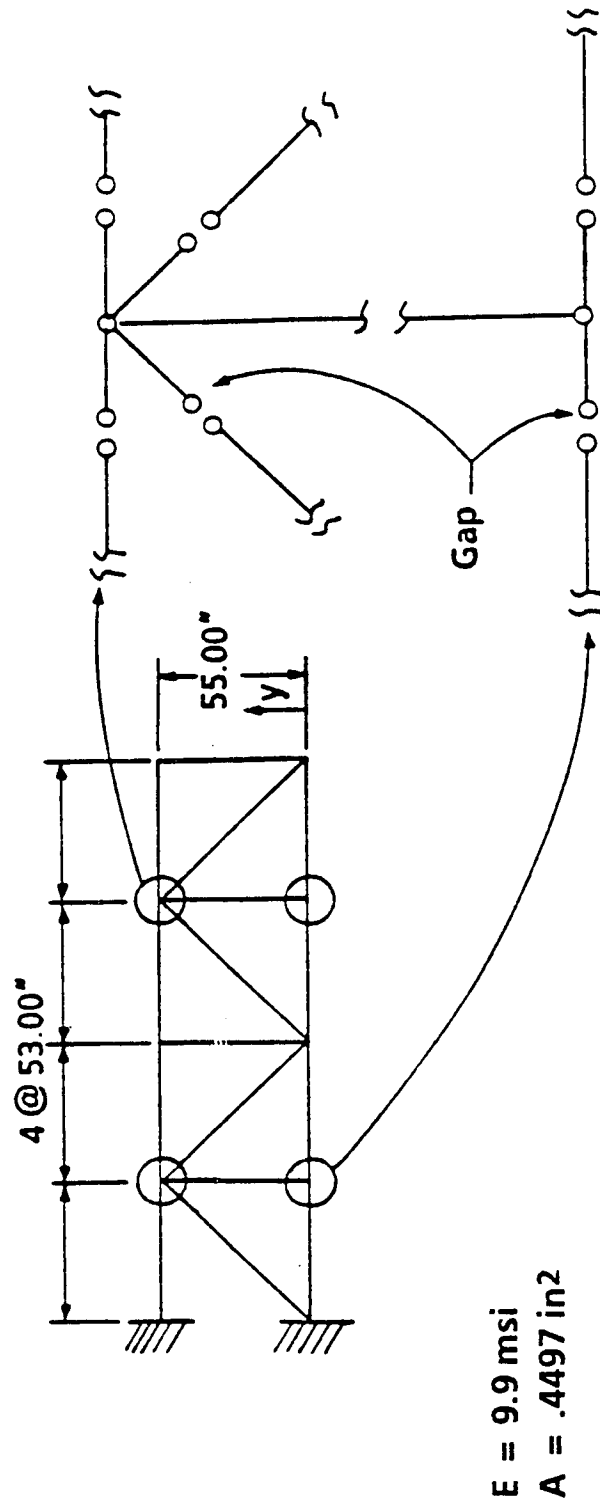
Figure 14

2-D Truss Results
Residual Force Approach

Linear model joint gaps = 0.0"

Nonlinear model joint gaps = 0.003"

.270 seconds

.540 seconds

.270 seconds

.540 seconds
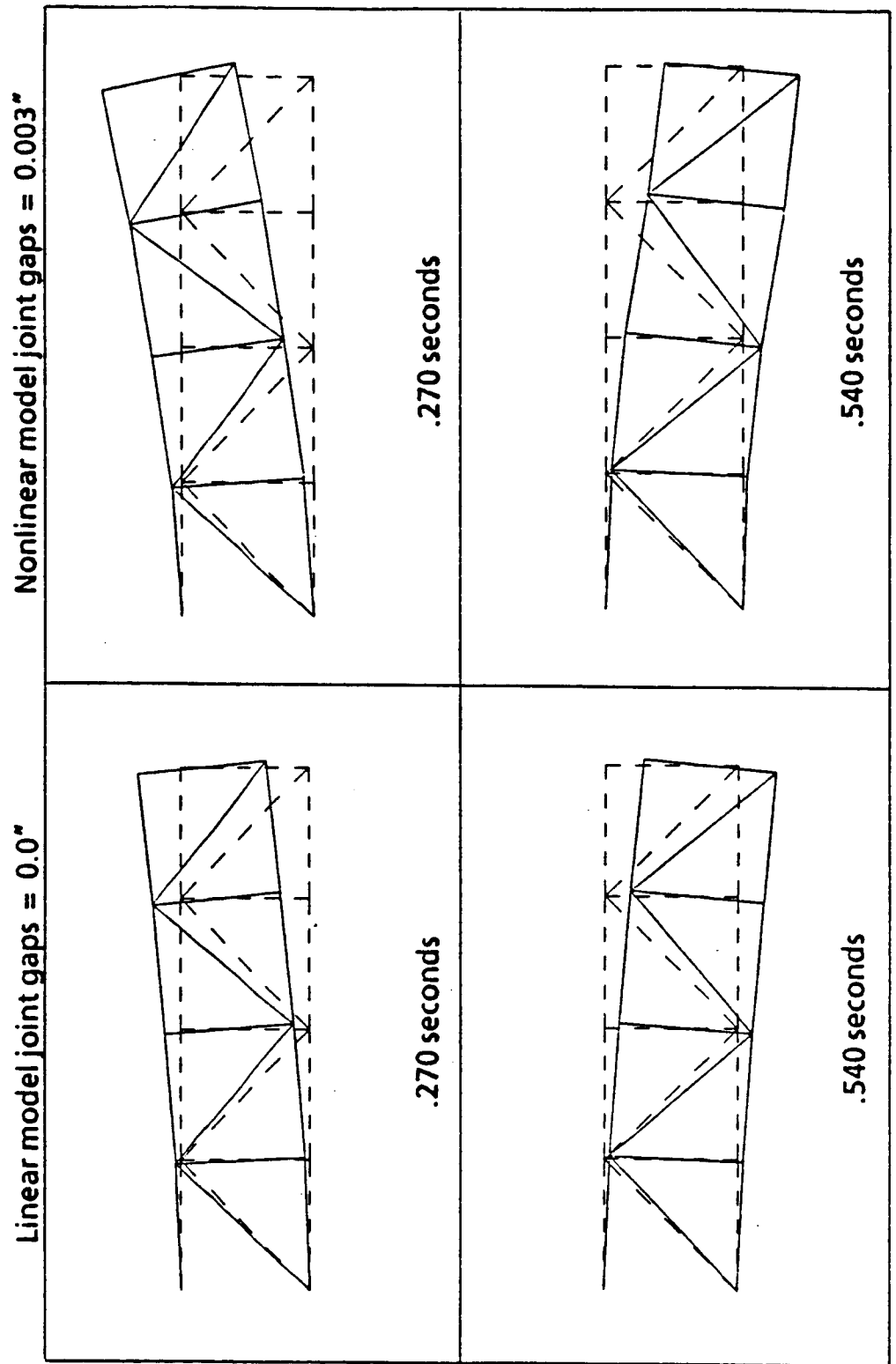
Figure 15

2D Rockwell Truss

Gaps = .003 Inches, 1% Modal Damping

Figure 16

558
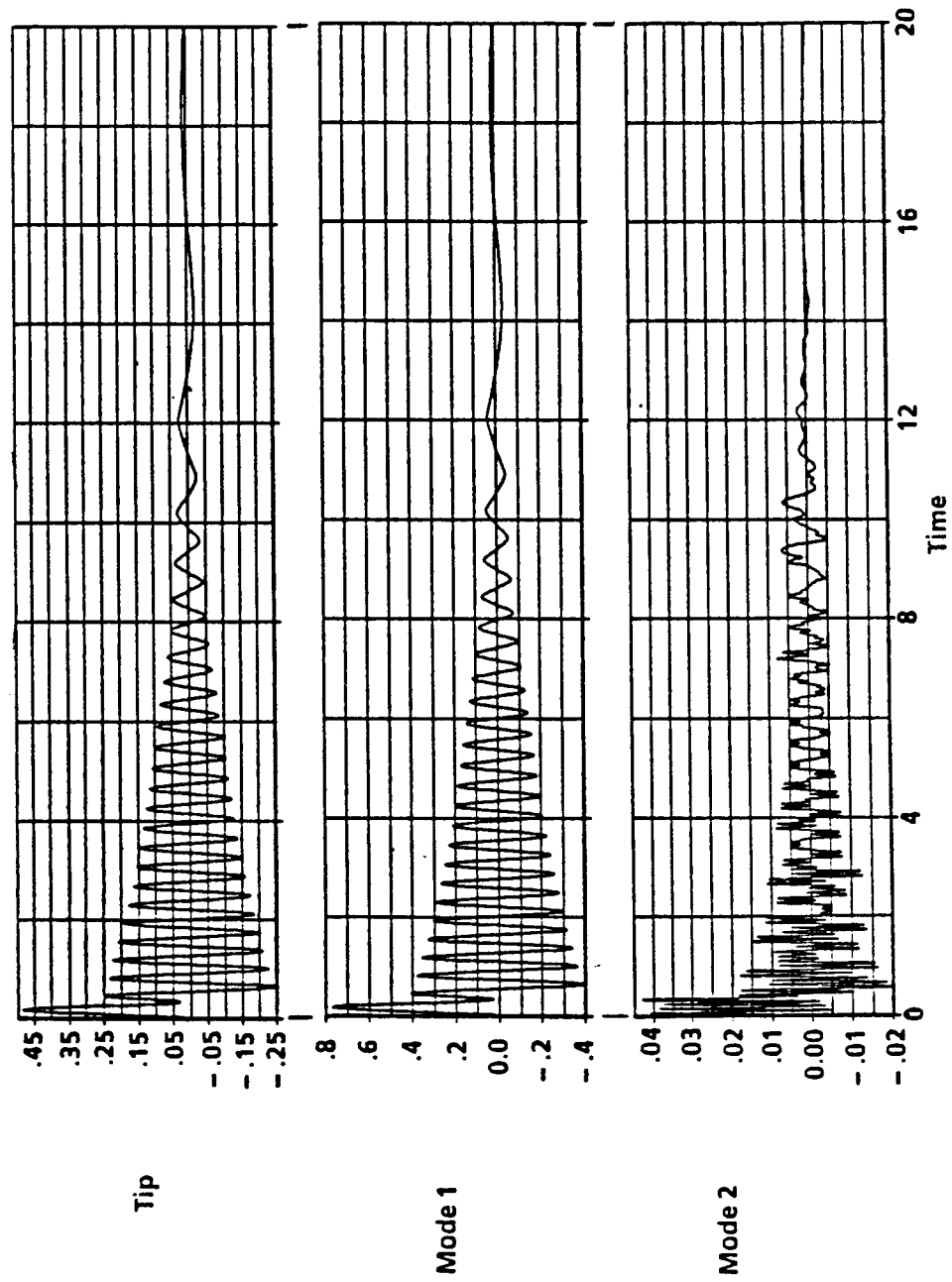
2D Rockwell Truss

Joints = Spring and Dashpot, Damping from Joints Only
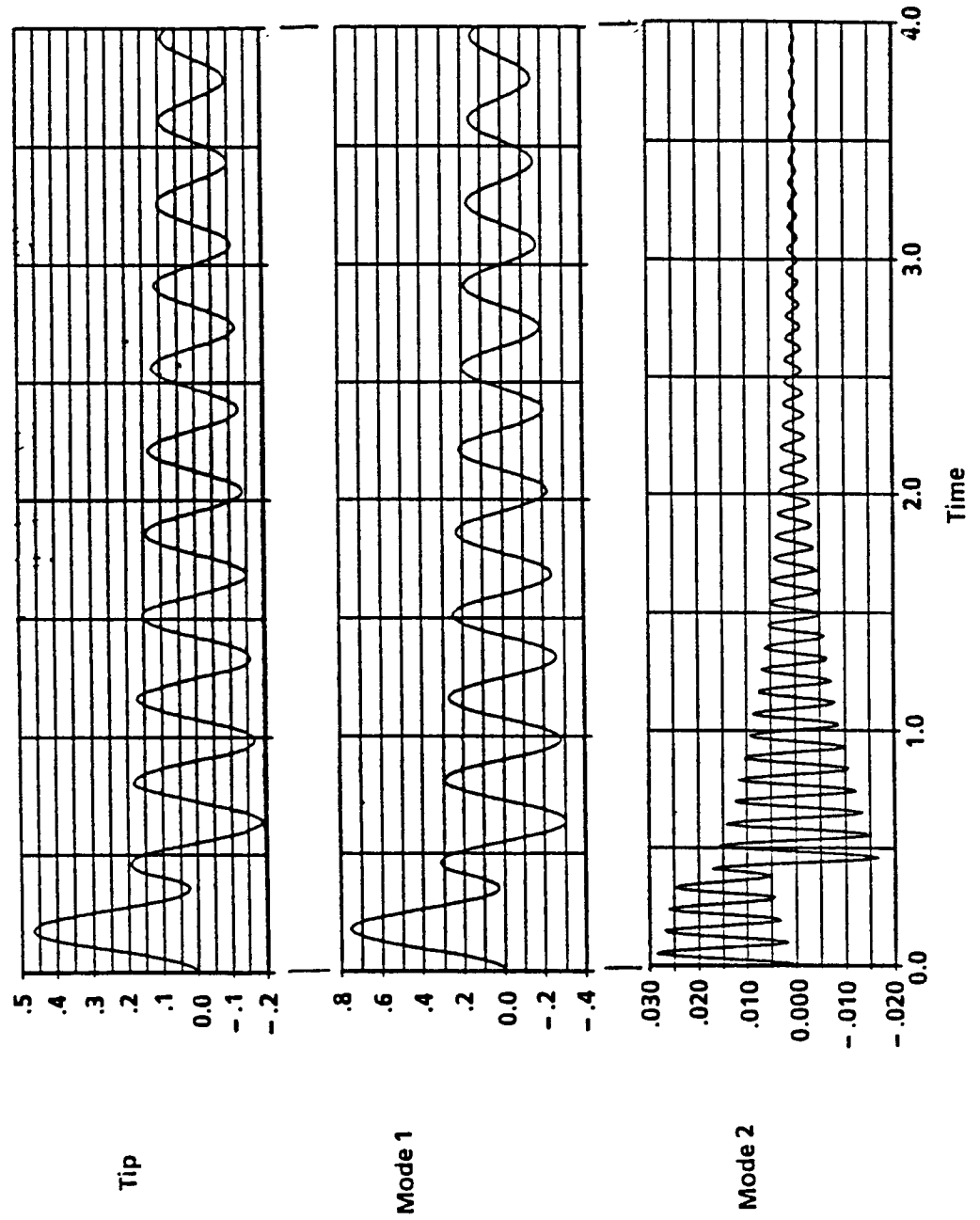
Figure 17

TEN BAY ROCKWELL TRUSS

A nonlinear transient analysis is also performed for a ten bay deployable truss that was designed and constructed by Rockwell and is awaiting testing at MARSHALL. Fig. 18 shows the first and second bending modes for this truss where each bending mode actually represents two orthogonal modes having identical frequencies. Gaps of 0.004 inches were included in all the longerons and lacing links. This gap value is reasonable in that each link has three deployable joints. The longeron links have two pin joints and one hinge joint, and the diagonal links have two pin joints and one telescoping joint.

The tip response of the gapped ten bay cantilevered truss having 1% modal damping subject to an initial impulse is shown in Fig. 19. The response of the linear gapless structure is also shown for comparison. Three observations can be made from Fig. 19. First and second, the amplitude and period of the nonlinear response is greater than those for the linear structure. The most interesting observation, however, is that the damping of the nonlinear structure appears to be greater than 1 percent. Evidently, energy is being transferred from the lower to the higher modes as a result of the nonlinear coupling between the modes. This phenomena was seen earlier for the two-dof problem.

The nonlinear coupling between the modes is clearly shown in Fig. 20. Nearly equal response in modes 1 and 2 as well as in modes 4 and 5 is due to the fact that the initial impulse excited these modes equally. The decaying response of modes 1 and 2 again show the phenomena that the period increases as the amplitude decreases. The response of modes 4 and 5, however, does not appear to be decaying exponentially as expected for modal damping. A strong 2 hertz component in modes 4 and 5 indicates strong coupling with the first bending modes and offers an explanation why decay is not also occurring for the second bending modes. Modes 1 and 2 are evidently driving the response of modes 4 and 5 with sufficient intensity to overcome damping. A net energy drain from modes 1 and 2 to the higher modes will therefore result. This phenomena also explains why the modal damping of modes 1 and 2 seems to be larger than the alloted 1 percent, the difference being madeup by the energy transferal to the higher modes having a greater energy dissipation potential.

Fig. 21 shows the linear and nonlinear responses for mode 4. Note that the maximum response occurs shortly after the initial impulse and that the magnitude of the nonlinear response is much greater than the magnitude of the linear response. Having gaps in the truss therefore permits greater modal participation for the applied tip loading impulse. Note also that if no coupling between the modes were to exist, then mode 4 would decay relatively quickly.

3D Rockwell Truss
10 Bays with 780 lb Tip Mass

1st bending
(Modes 1 and 2)
1.86 Hz

2nd bending
(Modes 4 and 5)
15.2 Hz

Figure 18

561
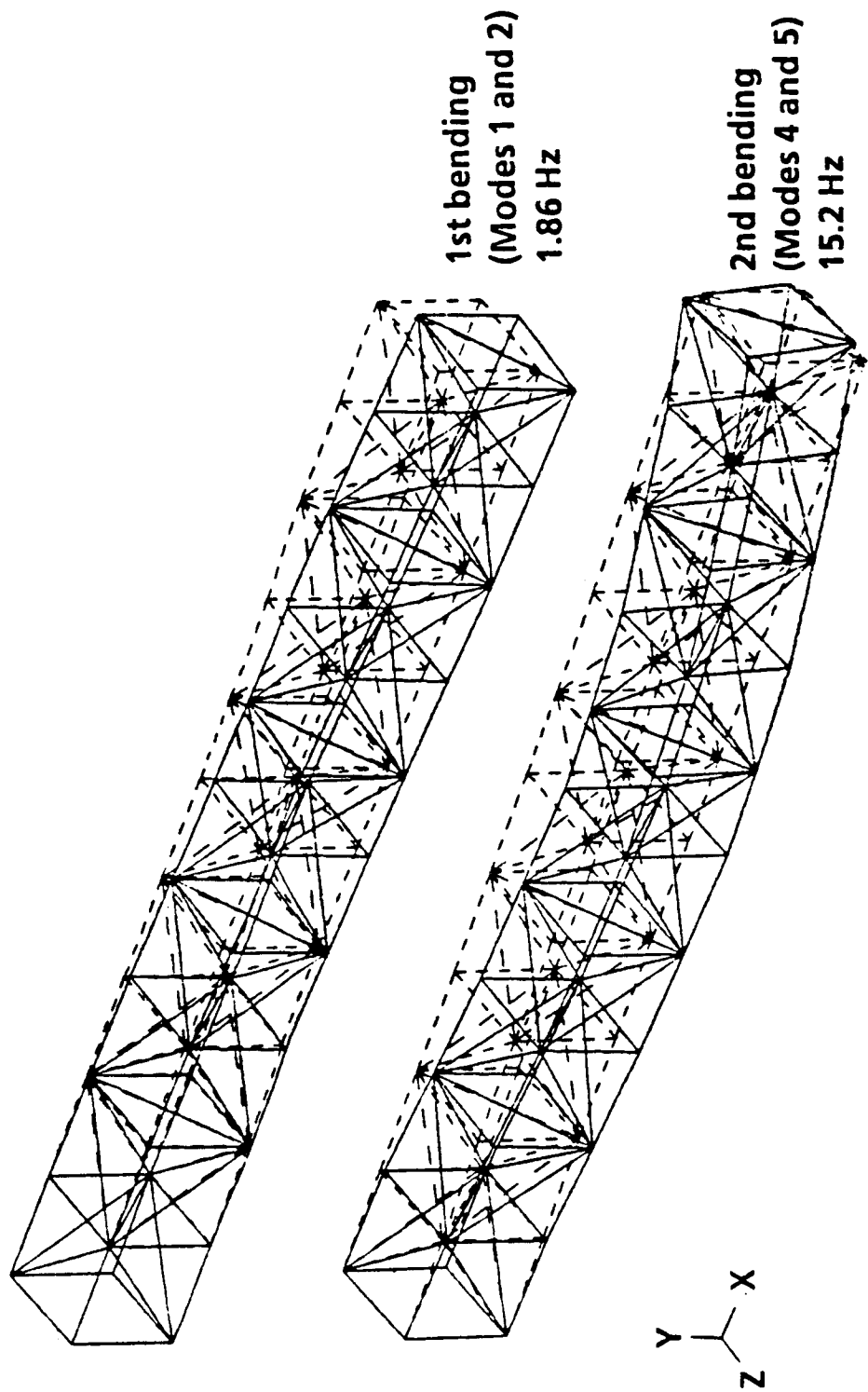
3D Rockwell Truss – Linear Vs Nonlinear

1% Model Damping
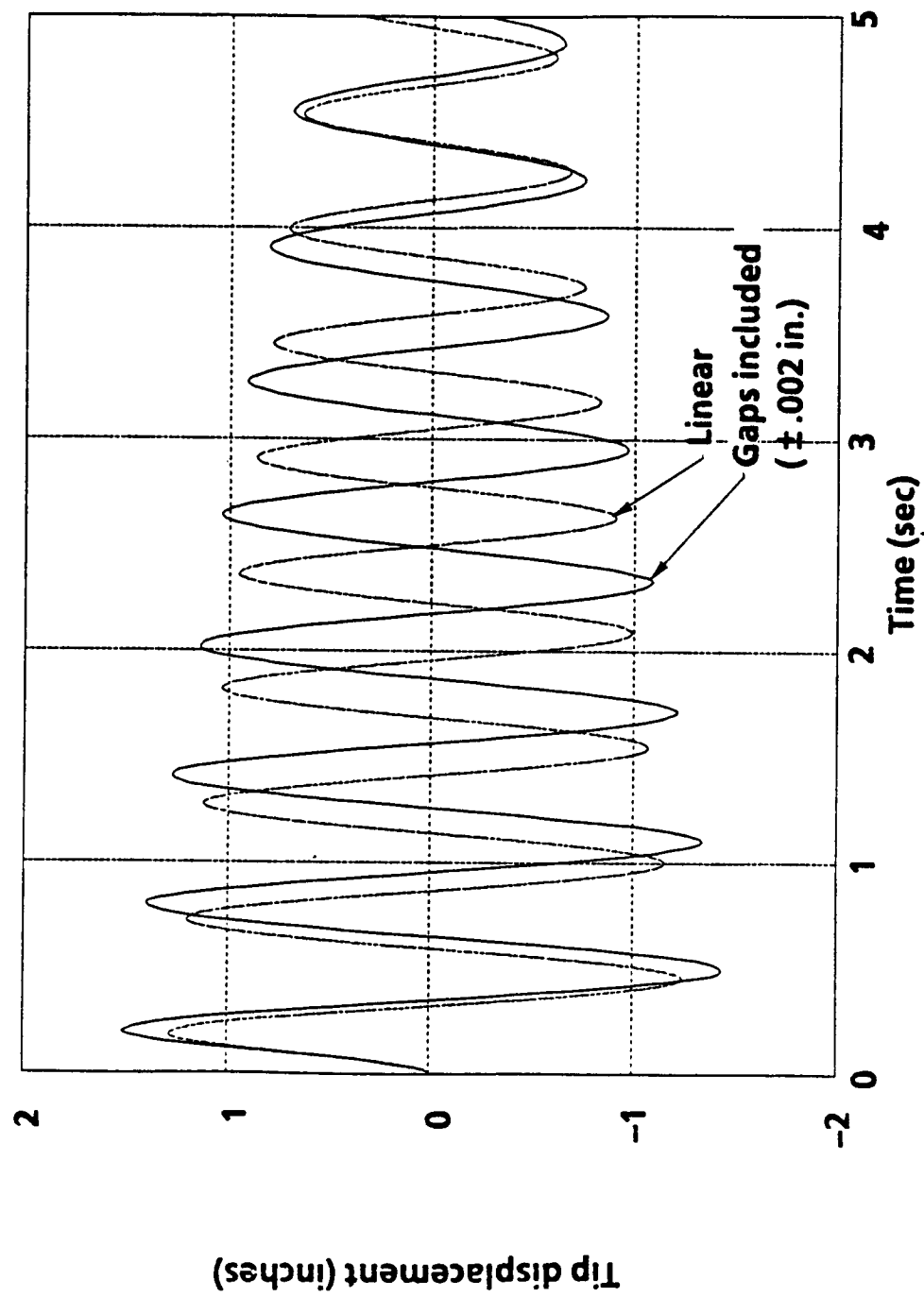
Figure 19

3D Rockwell Truss with 1% Modal Damping
Link Gap = ±.002 in

Figure 20

563

3D Rockwell Truss with 1% Modal Damping

Linear

Mode 4

Nonlinear

Link gap = ± .002 in

Mode 4

Time

Figure 21

564
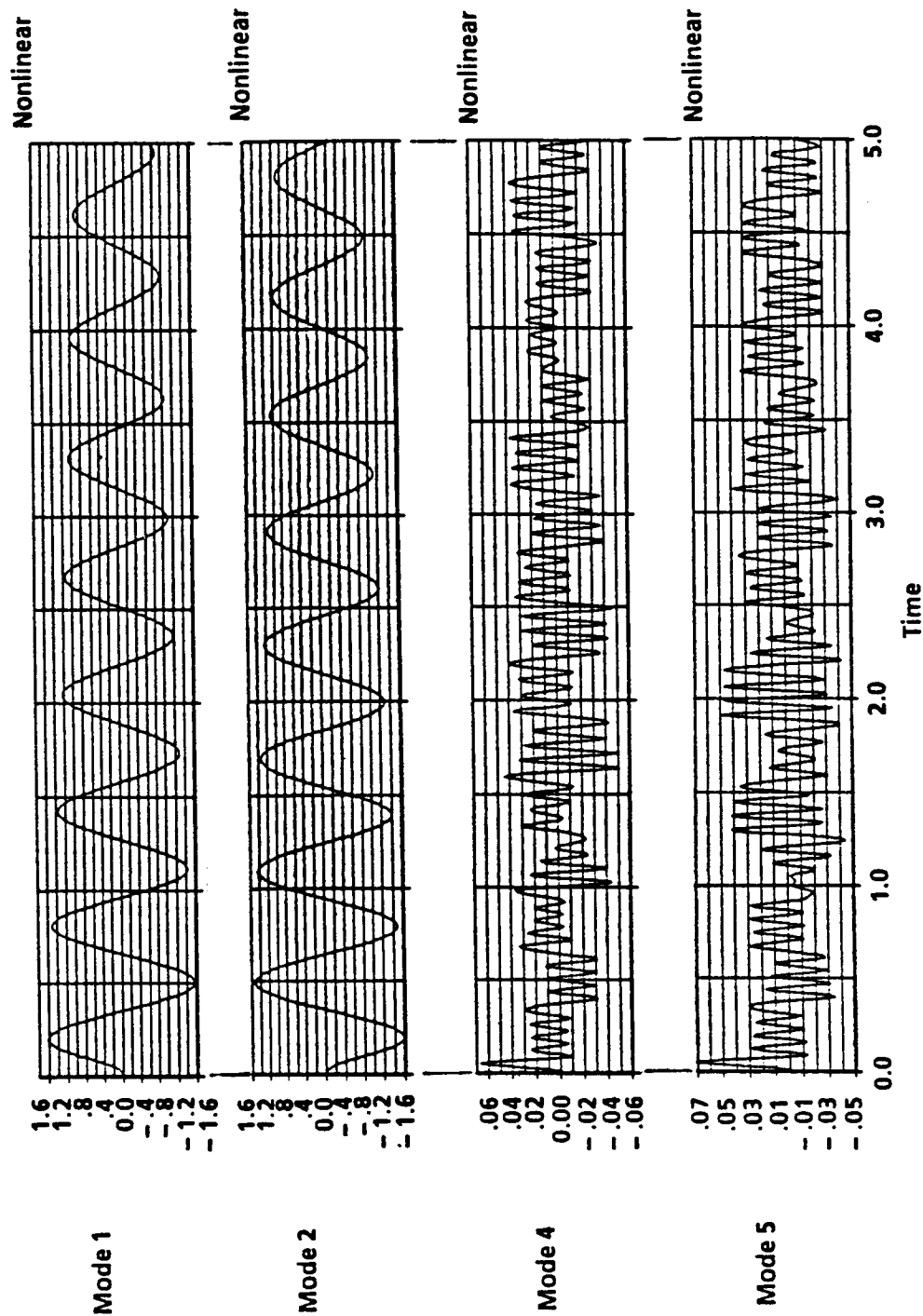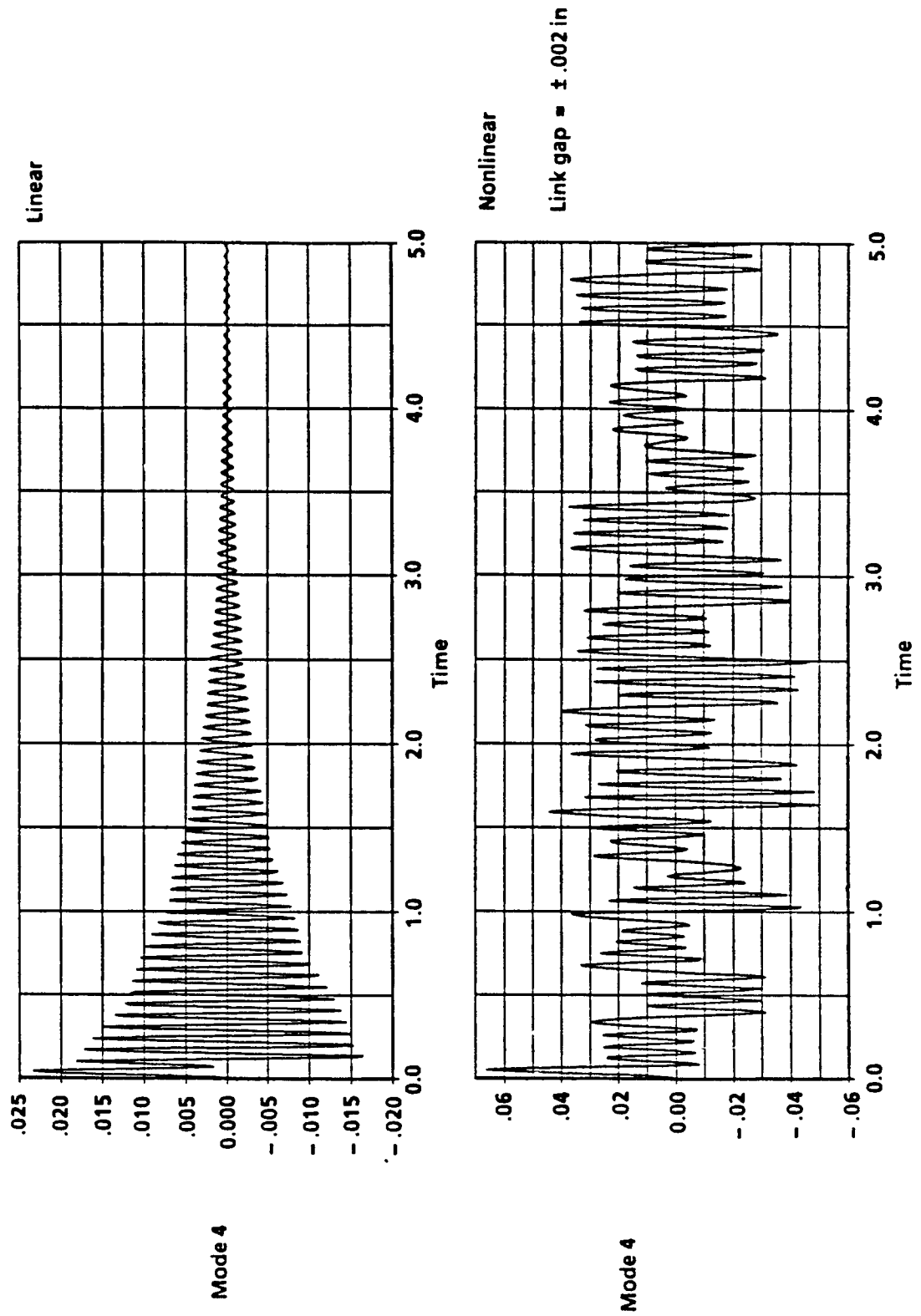
SUMMARY

The transient analysis of trusses having nonlinear joints can be accomplished using the residual force technique. The current technique assumes that the truss links are axial load carrying members only and that the joints have arbitrary force map characterizations. The technique utilizes a "link" concept which has four basic advantages. First, substantial size reduction of the equations of motion is obtained even before modal extraction. Second, numerical difficulties are avoided since the inherently stiff internal degrees of freedom of the links are not monitored. Third, stable integration is achieved by transforming the force maps of the joints to residual force maps of the links. And fourth, direct tests on the links can be performed to validate the analytical assumptions.

The technique was applied a two degree of freedom spring mass system, a four bay planar truss, and an actual ten bay deployable truss at MARSHALL. Joints chosen for analysis were the nonlinear gap joints and the linear Voigt joints. Results from the nonlinear gap analyses generally indicate that coupling between the modes can display some interesting effects during free vibration. One particularly interesting effect was that the damping of the structure appeared to be higher than could be accounted for from modal damping alone. Energy transferral from the lower to the higher modes was found to exist as a result of the modal coupling. The apparently increased damping was due to the fact that the energy transferred to the higher modes is inherently dissipated more quickly. Another interesting phenomenon was that the lower modes could drive the higher modes even during free vibration and that these modes could display a rather large quasi-steady state behavior even when modal damping was present. Gaps were also found to increase the amplitude and period of the free vibration response as expected.

Future work will further examine the effects of modal truncation and residual flexibility that were proposed in the residual force method. Also, other joint nonlinearities will be studied and their effects on the free and forced response of a joint dominated truss determined. Comparison of the analysis predictions with test results also needs to be performed before the residual force technique and truss modeling assumptions can be substantiated.

Equivalent Beam Modeling Using Numerical Reduction Techniques

J. M. Chapman

F. H. Shaw

Boeing Aerospace Company
Seattle, Washington

Presented at

Workshop on Structural Dynamics and Control
Interaction of Flexible Structures

Marshall Space Flight Center
Huntsville, Alabama
April 22-24, 1986

EQUIVALENT BEAM MODELING USING NUMERICAL REDUCTION TECHNIQUES

Introduction

The objective of this paper is to develop numerical procedures that can accomplish model reductions for space trusses. Three techniques will be developed that can be implemented using current capabilities within NASTRAN. The proposed techniques accomplish their model reductions numerically through use of NASTRAN structural analyses and as such are termed numerical in contrast to the analytical techniques developed in References 1-12.

The analytical techniques of Refs. 1-12 can be classified either as substitute continuum, discrete field, periodic difference, or finite difference methodologies. They are generally limited to trusses having either pinned or rigid joints and do not attempt to account for any joint flexibilities. Moreover, only specific trusses are analyzed to derive the "equivalent beam" properties. The primary reason for this limitation is the analytic complexity of treating general truss configurations with arbitrary joint characteristics. These analytic treatments did reveal, however, that equivalent truss models may require more degrees of freedom than allotted to the usual finite element beam.

To eliminate the above restrictions, numerical procedures are developed here that permit reductions of large truss models containing full modeling detail of the truss and its joints. Three techniques are presented that accomplish these model reductions with various levels of structural accuracy. These numerical techniques given in order of increasing accuracy are designated as equivalent beam, truss element reduction, and post-assembly reduction methods.

In the equivalent beam method described herein, the mass and stiffness properties of a simple finite element beam are determined so that the truss structure can be replaced with this equivalent beam element in all static and dynamic structural analyses. This approach is attractive in that once the equivalent beam properties are known, the beam length can be arbitrarily chosen by the analyst to suit the problem at hand. The approach is limited, however, to the usual six degrees of freedom describing the translational and rotational displacements for a beam node.

In the truss element reduction method, the idea of an equivalent structural element is retained but the number of truss bays to be represented must generally be chosen apriori. The advantage of this method is the capability to

retain more than the six degrees of freedom alloted to the equivalent beam. Including warping and shear "degrees of freedom" in the equivalent structural element is an example of this increased capability.

The final approach does not attempt to derive an equivalent structural element for the truss. Instead, a procedure is developed that allows the analyst to identify apriori freedoms that can be reduced out of the model without loss of structural accuracy. This method thus permits a more accurate description of the truss than derived using equivalent structural elements while still allowing significant size reduction of the truss model prior to space station synthesis, modal extraction, or other static and dynamic analyses.

The numerical procedures discussed above all utilize a transformation of coordinates at some step in the reduction procedure. This coordinate transformation defines new "beamlike" degrees of freedom in terms of the original rectangular degrees of freedom describing the translational and rotational displacements of the nodes that are common between truss bays. The transformation of rectangular to beamlike degrees of freedom is described in Figures 1 and 2 for triangular trusses. The transformation for square trusses is similarly described in Figures 1 and 3.

There are two basic advantages arising from these transformations. First, the new beamlike freedoms are largely uncoupled from each other, and second, freedoms which can be reduced out through static condensation are generally more easily recognized.

The utilization of the beamlike transformation for either square or triangular trusses is discussed in Section 1.0 giving the step by step outlines for the three numerical reduction procedures. Results obtained using the three numerical reduction techniques on triangular trusses are given in Section 2.0. Square trusses are similarly discussed in Section 3.0. A preliminary analysis of a ten bay Rockwell truss using the numerical reduction techniques is then given in Section 4.0.

1.0 Step By step Descriptions of the Numerical Reduction Technique

The steps describing the three numerical reduction techniques are given in this section. The reduction procedures do not necessarily have to follow the steps as stated below since some of these steps can be combined and executed more efficiently. The steps as delineated below are given only for discussion purposes.

The first three steps in all three numerical reduction techniques are identical. The first step is to generate a detailed structural model of a single "repeating element" of the truss. The model should include as much definition of the joints as deemed necessary for accurate structural modeling. The second step reduces out all interior degrees of freedom from this single bay element using static condensation and retains freedoms only at the nodes interconnecting truss bays. The third step then connects a predetermined number of these single repeating elements and again reduces out all interior degrees of freedom. The number of bays selected in this step defines the basic mesh size to be used in all numerical reduction methods with the exception of the equivalent beam method. The finite element model resulting from the above three steps will henceforth be referred to as the basic truss cell. Further steps for each numerical procedure are described below.

1.1 Substitute Continuum Beam Method

Additional steps taken for this method are as follows:

i) Construct a truss of one or more basic cells and statically reduce out all interior freedoms resulting from this construction. The number of cells chosen requires a number of computer runs in order to demonstrate convergence of the beam properties derived below.

ii) Transform the degrees of freedom at the end of the truss to the beamlike degrees of freedom and retain only the usual six freedoms describing the translational and rotational displacements of a beam.

iii) Equate the (12 x 12) stiffness matrix resulting from this transformation and reduction to the stiffness matrix for a beam. The following equations are used to generate the E,G,I,J, and K properties of the beam:

$$AE/L = K_{11} \qquad\qquad GA/L = A/J * K_{44}$$

$$EI/L = (K_{55} - L^2 / 4 * K_{22})$$

$$K^{-1} = (GA/L) * \left| \frac{1}{K_{22}} - \frac{L^2}{12\,(EI/L)} \right|$$

$$1 + v = (J/A) * (AE/L) / (2 * K_{44})$$

570

where

A   = arbitrarily chosen to be area of longerons

J/A = radius of gyration squared

K_{ii} = Diagonal terms of the (12 x 12) stiffness matrix

E = elastic modulus

G = shear modulus

v = Poisson's ratio

K = shear stiffness

I = (EI/L) / (AE/L) * A

L = length of segment used to generate the stiffness matrix

The resultant beam properties produce an element stiffness matrix which duplicates the stiffness matrix condensed from the explicit model. This duplication is exact for most truss structure configurations.

The mass of the equivalent beam may be calculated in two different ways. First, internally, using rigid body mass properties for either a consistent or lumped mass approach, and second, explicitly, using the (12 x 12) mass matrix describing the basic truss cell. This second approach has the disadvantage of fixing the beam length in subsequent analyses. If, however, mass per unit length is used as the beam property, then all beam properties are known independent of beam length and, the beam length can be arbitrarily chosen to suit any static or dynamic analysis at hand. This length independence property of the equivalent beam gives it a substantial advantage over the truss element reduction method in parametric studies when the effect of the length of the truss on system response is being examined. Such

parametric studies are envisioned in the early design stages of the space station.

1.2 Truss Element Reduction Method

The additional steps taken in this procedure are as follows:

i) Transform the rectangular degrees of freedom of the interconnecting nodes to the beamlike coordinates.

ii) Eliminate unwanted degrees of freedom either by truncation or by static condensation. Truncation is accomplished in NASTRAN through single point constraint (SPC) and is equivalent to setting the displacement for those selected coordinates to zero. Static condensation is accomplished in NASTRAN by placing those coordinates in the OMIT set and is equivalent to setting the forces on those coordinates to zero.

iii) Form the complete truss structure using either NASTRAN image superelements or NASTRAN general elements (GENEL).

1.3 Post–assembly Reduction Method

The additional steps taken in this procedure are as follows:

i) Connect as many of the basic truss cells as required to define the complete structure and then transform coordinates. These operations may also be reversed so that a basic truss cell element can first be transformed then connected to form the complete truss.

ii) Choose freedoms to be retained for the complete structure. The freedoms retained generally have been selected by previous analytical studies of the truss or by analytical insight to the problem at hand. The reduction is then accomplished using static condensation.

2.0 Reduced Order Model For Triangular Frames and Trusses

The purpose of this section is to apply the three numerical reductions methods to triangular trusses and frames and to compare the results. The analyses are conducted only for cantilevered structures having ten and twenty bays.

Two different triangular frames and one triangular truss are examined (see Fig.4). These are identified as an unbraced Vierendeel frame, a double braced frame, and a double braced truss. A frame is distinguished from a truss by having rigid as opposed to pinned joints. Geometry and material properties are taken from Noor and Nemeth (Ref 1) in order to compare our results with theirs. The double braced frame results are also compared with the double braced truss results in order to bound the effects of joint flexibility on the modes and frequencies of a triangular structure having non-idealized joints.

The "exact" model descriptions of the cantilevered Vierendeel and double braced triangular frames are taken to be represented by finite element models having nodes only at the verticies of the battened triangles. Each node requires six degrees of freedom so that a total of 18 degrees of freedom are required to describe the deflections of one end of a frame bay segment. A total of 180 degrees of freedom are thus required to describe the cantilevered deformation of ten bays.

The primary objective of all three reduction techniques is to significantly reduce the size of the above models. Tables 1 and 2 give the total number of freedoms required by each of the three techniques to calculate the modes and frequencies of the Vierendeel and double-braced structures, respectively. These tables show that the post-assembly reduction technique allows the largest possible reduction of the three techniques considered.

Tables 1 and 2 also show the frequencies of cantilevered structures using various reduction schemes and retained freedoms. These results are also compared with the exact results of Noor and Nemeth.

No final resolution can be given at this time for the differences between our exact results and the exact results of Noor and Nemeth. It appears, however, that the differences may be attributed to the slightly different mass constructions used. MSC/NASTRAN uses a modified consistent mass approach (Ref 13) while Noor and Nemeth use the original consistent mass formulation presented by Archer (Ref 14). Alternatively, differences in modeling detail at

the ends of the truss may account for the discrepancy. Detailed calculations to determine which was the more accurate were not performed.

Evaluations of the results for the various reduction schemes are also given in Tables 1 and 2. In all cases the post-assembly reduction schemes gave excellent results while the equivalent beam and truss element reduction schemes gave satisfactory results only for the double-braced structures. Detailed discussions of the various reduction schemes are given in the following subsections.

2.1 Post-Assembly Reduction

Freedoms that were retained in the post-assembly reductions were chosen simply by examining their modal participation in the frequency range of interest for the unreduced structure. In Table 1, ten, eight, and even four dof were all shown to adequately represent the Vierendeel frame when these dof were retained for every bay. A four dof representation at every other bay length was also shown to adequately represent the Vierendeel structure by showing a maximum of 5.7% error occurring for the fourth torsion mode.

Table 2 shows the results obtained for the double-braced triangular frame. One important conclusion that can be drawn from this table is that excellent results can be obtained for the frame even by considering the joints to be pinned. This conclusion is not suprising since engineers have successfully approximated frames as trusses for years. Excellent results are also expected when the four beamlike coordinates of the truss are retained at multiple bay lengths.

One important inference can be drawn from being able to use pinned instead of rigid joints for the double braced frame. The slight change in frequencies obtained by changing the joint from rigid to pinned is characteristic of a frame having a large area moment of inertia about its centroid. For in this case, the primary strain energy of the frame for low frequency modes can be accounted for by the axial extension or compression of its member elements. As a result of this energy distribution, moment capability of the individual members can be neglected and the joints can be considered pinned. In addition, the most important modeling consideration of a joint for such trusses is to accurately represent its axial stiffness. This in turn implies that free-play in the rotational directions can be ignored and that free-play in the axial direction of each member must be examined carefully to determine its effect on the the truss modes and frequencies.

In conclusion, significant model size reduction for the Vierendeel and double braced frames can be obtained by utilizing the post-assembly reduction technique. The degrees of freedom retained in the reduced models are generally easy to identify by the analyst either by previous analytical studies or by insight. Moreover, the geometrical behavior of the modes are easily recognized when expressed in terms of the beamlike coordinates and do not require mode shape plots in order to visual response.

The mass and stiffness matricies resulting from the post-assembly reduction technique are full, however, and must be repeatedly generated for trusses having different lengths. Such situations would occur in various parametric studies currently envisioned in the early stages of space station design and an "equivalent beam" approach would be preferential for such trade studies.

Model size reduction for double braced triangular frames can also be realized by considering the joints to be pinned. This approximation reduces the size of the problem by one-half when local member modes can be omitted. Further reduction can then be obtained using coordinate transformation followed by static condensation.

2.2 Equivalent Beam and Truss Element Reduction Techniques

The equivalent beam method as defined in this paper is limited to six degrees of freedom. Any extension in the number of retained degrees of freedom for an equivalent structural element necessitates use in MSC/NASTRAN of image super elements. These image super elements can be defined using the numerical truss element reduction technique as presented in this paper or they can be defined using the analytical techniques found in References 1-12. In any event, the 6-dof equivalent beam models are considered in a class of their own due to their ease of use.

The 6-dof equivalent beams are not applicable for all trusses, however, as demonstrated in Table 1 for the Vierendeel frame. In fact any 6-dof equivalent structural element may not be sufficient and additional freedoms may be required. This conclusion is supported for the Vierendeel frame by the unsatisfactory 6-dof element reduction results in Table 1 and by the satisfactory 10-dof analytical results obtained by Noor and Nemeth. It should be noted that the equivalent beam results for the Vierendeel frame are reported in Table 1 even though the beam properties did not converge to a limiting set of values when using successively longer beam segments.

The reason that the 6-dof models are unsatisfactory for the Vierendeel frame is that the frame behaves in a particularly unbeamlike manner.

Qualitatively, this difference may be attributed to the fact that the longerons bend rather than stretch for its fundamental bending modes. The cross sections of the Vierendeel beam therefore do not rotate for these fundamental modes as is normally the case for trusses. Moreover, the torsion modes are unusually coupled with cross-sectional stretching. The 10-dof analytical technique of Noor and Nemeth can account for these effects as demonstrated in Ref 1. Alternatively, the truss element reduction technique using additional retained freedoms can be effectively used as shown in Table 1.

The addition of cross-bracing to the Vierendeel frame increases the shear stiffness of the structure and, as a result, the structure behaves more like a beam. The results of Table 2 indicate that satisfactory results for the double braced frame can be obtained using either the equivalent beam method or the truss element reduction method.

3.0 Reduced Order Models for Square Cross-section Trusses

The purpose of this section is to apply the three numerical reductions methods to square cross-section trusses and to compare the results. The analyses are conducted only for cantilevered structures having ten bays.

The structures analyzed are those defined by Noor in Ref 3. The trusses are square in cross-section and vary in their bracing schemes. Repeating elements have single bracing (two bays per repeating element) and double bracing (one bay per repeating element) . Each configuration is examined with and without cross bracing. The latter configuration is kinematically stable only when rigid boundary conditions are specified. The advantage of such a configuration is that the truss may be folded flat for storage in the Shuttle cargo bay. The disadvantage is that low frequency shear and warping modes are introduced.

Tables 4 through 6 show the frequencies of the cantilevered structures using various reduction schemes and retained freedoms. These results are also compared with the exact results of Noor and Nemeth. Again unexplained differences appear between our exact results and those of Noor and Andersen but these are very small.

Evaluations of the results for the various reduction schemes are also given in Tables 4 through 6. In all cases the post-assembly and element reduction schemes gave excellent results and accounted for the shear and warping modes of the unbraced structures. Table 5 also shows that these shear and warping modes disappear when cross bracing is introduced and that the reduced order

models need only account for the usual six degrees of freedom of an equivalent beam node.

The modeling assumption of using pinned instead of fixed joints was also examined for the single bay, double laced frame with cross bracing. Results are shown in Table 5. Several conclusions may be drawn from the results tabulated there. First, the primary bending and torsion modes are not affected by fixing the joint rotation freedoms. Second, many local member modes which were assumed to be high frequency modes for the pinned structure are in fact low frequency modes. The reason why the local member modes were not calculated for the pinned case is due to the fact that only translational freedoms for nodes only at the ends of each local member were retained. The local member modes would have appeared had nodes been placed midway along each member. And third, while the numerical reduction techniques presented here and Noor's equivalent beam method can all accurately predict the primary modes of a truss, they cannot account for local member modes.

In conclusion, the primary modes of the square trusses studied in this section are almost unaffected by the presence or absence of pins at the joints; warping and shear modes are of course suppressed by fixing the joints. Also, when square trusses have no cross bracing, two extra freedoms must be retained with the usual six beamlike freedoms in order to account for the warping and shear modes exhibited by such a structure.

4.0 Reduced Order Models for The Rockwell Truss

The purpose of this section is to apply the numerical reductions methods to a cantilevered Rockwell truss configuration and to examine various modeling approximations and preload effects on the modes and frequencies. These analyses were performed to get a preliminary understanding of the behavior or the truss.   The Rockwell Truss is a double bay single laced square deployable truss. The batten and intermediate joints are fixed while all other joints are pinned in one direction. Several NASTRAN models of the truss were constructed using either all bar elements, all rod elements except for bars for the battens, or all rod elements. Detailed modeling of the joints were not included in these NASTRAN models of the Rockwell truss. Results of several NASTRAN analyses are summarized below: The cantilevered frequencies resulting from four different modeling schemes are presented in Table 7. The modes are plotted in Figure 5   _   Differences in response between the various element configurations are due primarily to the different mass representations used. The consistent mass formulation produced a model having a higher torsional inertia and accounted for the local batten modes.

C-7

These local modes vanish from the solution when the lumped mass approach was used or when all joints were modeled as pinned. The modeling assumption of using pinned instead of fixed joints had negligible effect on the calculated stiffness of the structure. Table 8 presents the results of the preload study. The truss was subjected to a 100 pound and 200 pound axial preload and the first order nonlinear differential stiffness solution was obtained. Table 8 shows that the change in the frequency is small and varies approximately linearly with the preload. Large geometry effects under preload were not accounted for. Table 9 presents the cantilevered frequencies calculated using various numerical reduction schemes.

Translational degrees of freedom	Rotational degrees of freedom
$X = T * X_B$	$\Theta = R * \Theta_B$
$F_B = T^T * F$	$M_B = R^T * M$
$T^{-1} = D^{-1} * T^T$	$R^{-1} = S^{-1} * R^T$
$D = T^T * T$	$S = R^T * R$

Nomenclature

X,F = Vector of nodal translational displacements and forces, respectively, at the verticies of of the lattice cross-section.

X_B, F_B = Vector of beamlike displacements and loadings, respectively, due to translational displacements and loadings.

Θ,M = Vector of nodal rotational displacements and moments, respectively

Θ_B, M_B = Vector of beamlike rotational displacements and moments, respectively, due to rotatioal degrees of freedom at the nodes.

Figure 1. Beamlike Transformation Relations
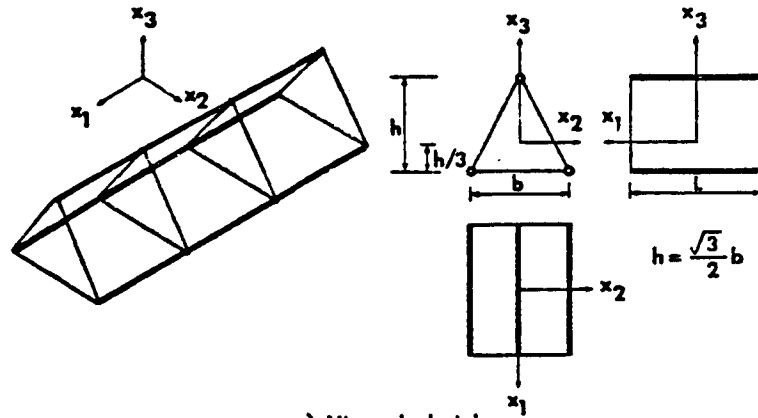
a) Vierendeel girder
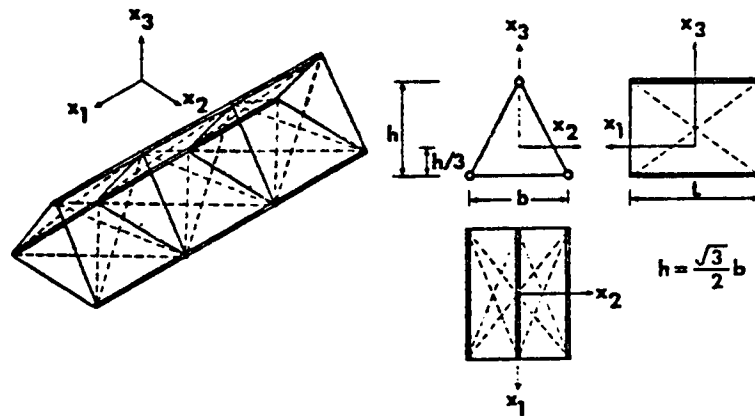
b) Double-laced girder

	C. Sec. Area	Length	Moments of Inertia	Torsional Constant	Material Density	Designation
Longerons	A_ℓ	L	$I_{\ell 2}$, $I_{\ell 3}$	J_ℓ	ρ_ℓ	═══
Battens	A_b	b	I_{b2}, I_{b3}	J_b	ρ_b	───
Diagonals	A_d	d	I_{d2}, I_{d3}	J_d	ρ_d	────

$E = 6.895 \times 10^{10} \text{ N/m}^2$, $A_\ell = 3.0 \times 10^{-5} \text{ m}^2$

$G = 2.652 \times 10^{10} \text{ N/m}^2$, $A_b = A_d = 1.5 \times 10^{-5} \text{ m}^2$

$\rho_\ell = \rho_b = \rho_d = 2768 \text{ Kg}$, $I_{\ell 2} = I_{\ell 3} = I_\ell = 6.0 \times 10^{-9} \text{ m}^4$

$L = 0.75 \text{ m}$, $I_{b2} = I_{b3} = I_{d2} = I_{d3} = 6.5 \times 10^{-10} \text{ m}^4$

$b = 0.75 \text{ m}$, $J_\ell = 1.2 \times 10^{-8} \text{ m}^4$

$J_b = J_d = 1.3 \times 10^{-9} \text{ m}^4$

Figure 2. Beamlike Lattices used in present study.

$$
\begin{bmatrix}
X^{(1)} \\
X^{(2)} \\
X^{(3)} \\
Y^{(1)} \\
Y^{(2)} \\
Y^{(3)} \\
Z^{(1)} \\
Z^{(2)} \\
Z^{(3)}
\end{bmatrix}
=
\begin{bmatrix}
1 & & 2h/3 & 0 & & \\
1 & & -h/3 & b/2 & & \\
1 & & -h/3 & -b/2 & & \\
& 1 & -\frac{2h}{3} & -\frac{2h}{3} & 0 & 0 \\
& 1 & h/3 & h/3 & -s/3 & s/3 \\
& 1 & h/3 & h/3 & s/3 & -s/3 \\
& & 1 & 0 & 0 & 1/3 & 1/3 \\
& & 1 & -b/2 & b/2 & -c/3 & -c/3 \\
& & 1 & b/2 & -b/2 & -c/3 & -c/3
\end{bmatrix}
=
\begin{bmatrix}
X \\
y \\
Z \\
\Theta_x \\
\Theta_y \\
\Theta_z \\
\alpha_x \\
\eta_r \\
\eta_s
\end{bmatrix}
$$
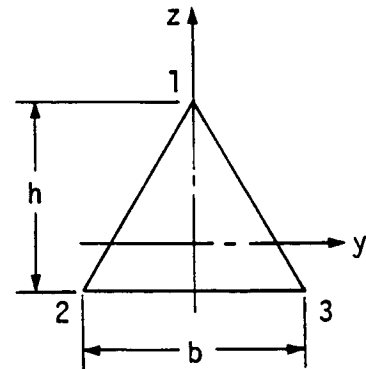
where C = Cos 60 = 1/2 $(X^{(1)}, Y^{(1)}, Z^{(1)})$ = Displacements at Node 1

S = Sin 60 = 1/2 $(0_x^{(1)}, 0_y^{(1)}, 0_z^{(1)})$ = Rotations of Node 1

$h = b_s$

Figure 3 (a). Expanded Transformation For Triangular Trusses $X = X_B$

$$
\begin{bmatrix}
\Theta_x^{(1)} \\
\Theta_x^{(2)} \\
\Theta_x^{(3)} \\
\Theta_y^{(1)} \\
\Theta_y^{(2)} \\
\Theta_y^{(3)} \\
\Theta_z^{(1)} \\
\Theta_z^{(2)} \\
\Theta_z^{(3)}
\end{bmatrix}
\begin{bmatrix}
1 & & 1/2 & 0 & & \\
1 & & -c/2 & 1/2 & & \\
1 & & -c/2 & -1/2 & & \\
& 1 & -1/2 & -1/2 & 0 & 0 \\
& 1 & c/2 & c/2 & -s/3 & s/3 \\
& 1 & c/2 & c/2 & s/3 & -s/3 \\
& & 1 & 0 & 0 & 1/3 & 1/3 \\
& & 1 & -s/2 & s/2 & -c/3 & -c/3 \\
& & 1 & s/2 & -s/2 & -c/3 & -c/3
\end{bmatrix}
\begin{bmatrix}
\phi_x \\
\phi_y \\
\phi_z \\
\phi_1 \\
\phi_2 \\
\phi_3 \\
\phi_4 \\
\phi_5 \\
\phi_6
\end{bmatrix}
$$

Figure   3 (b). Expanded Transformation Relation
$\Theta = R\,\Theta_B$ For Triangular Trusses
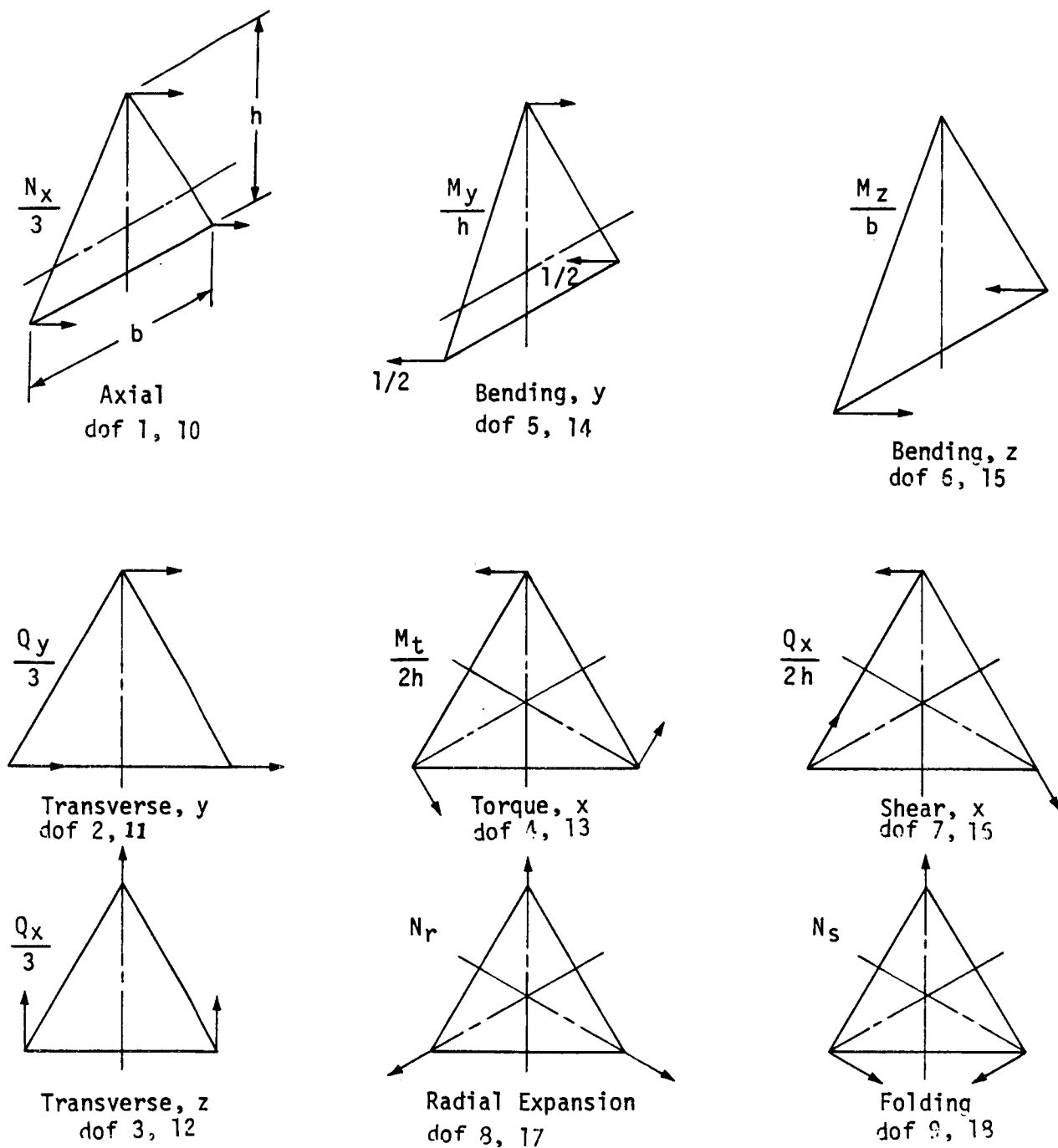
Note: Arrows on Nodes Forces for each Beamlike Loading Condition

Figure 3 (c). Beamlike Loadings For Triangular Trusses

	c1	c2	c3	c4	c5	c6	c7	c8	c9	c10	c11	c12	
N_x	1	1	1	1									$F_x(1)$
Q_y					1	1	1	1					$F_x(2)$
Q_z									1	1	1	1	$F_x(3)$
T_x					h/2	h/2	-h/2	-h/2	b/2	-b/2	-b/2	b/2	$F_x(4)$
M_y	h/2	h/2	-h/2	-h/2									$F_y(1)$
M_z	b/2	-b/2	-b/2	b/2									$F_y(2)$
B_x	1	-1	1	-1									$F_y(3)$
N_y					-1	1	1	-1					$F_y(4)$
N_z									1	1	-1	-1	$F_z(1)$
Q_x					b/2	b/2	-b/2	-b/2	-h/2	h/2	h/2	-h/2	$F_z(2)$
B_y					h/2	-h/2	h/2	-h/2					$F_z(3)$
B_z									b/2	-b/2	b/2	-b/2	$F_z(4)$
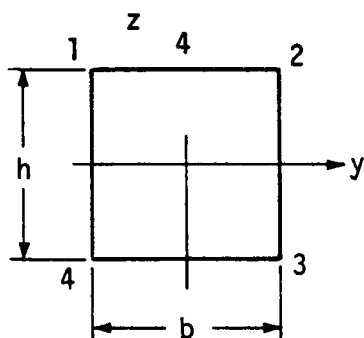
Alternate for N_y and N_z

N_r	0				-h/2	h/2	h/2	-h/2	b/2	b/2	-b/2	-b/2
N_t	0				-b/2	b/2	b/2	-b/2	-h/2	-h/2	h/2	h/2

Figure 4 (a). Expanded Transformation Relation $F_B = T^T F$ For Square Trusses

583
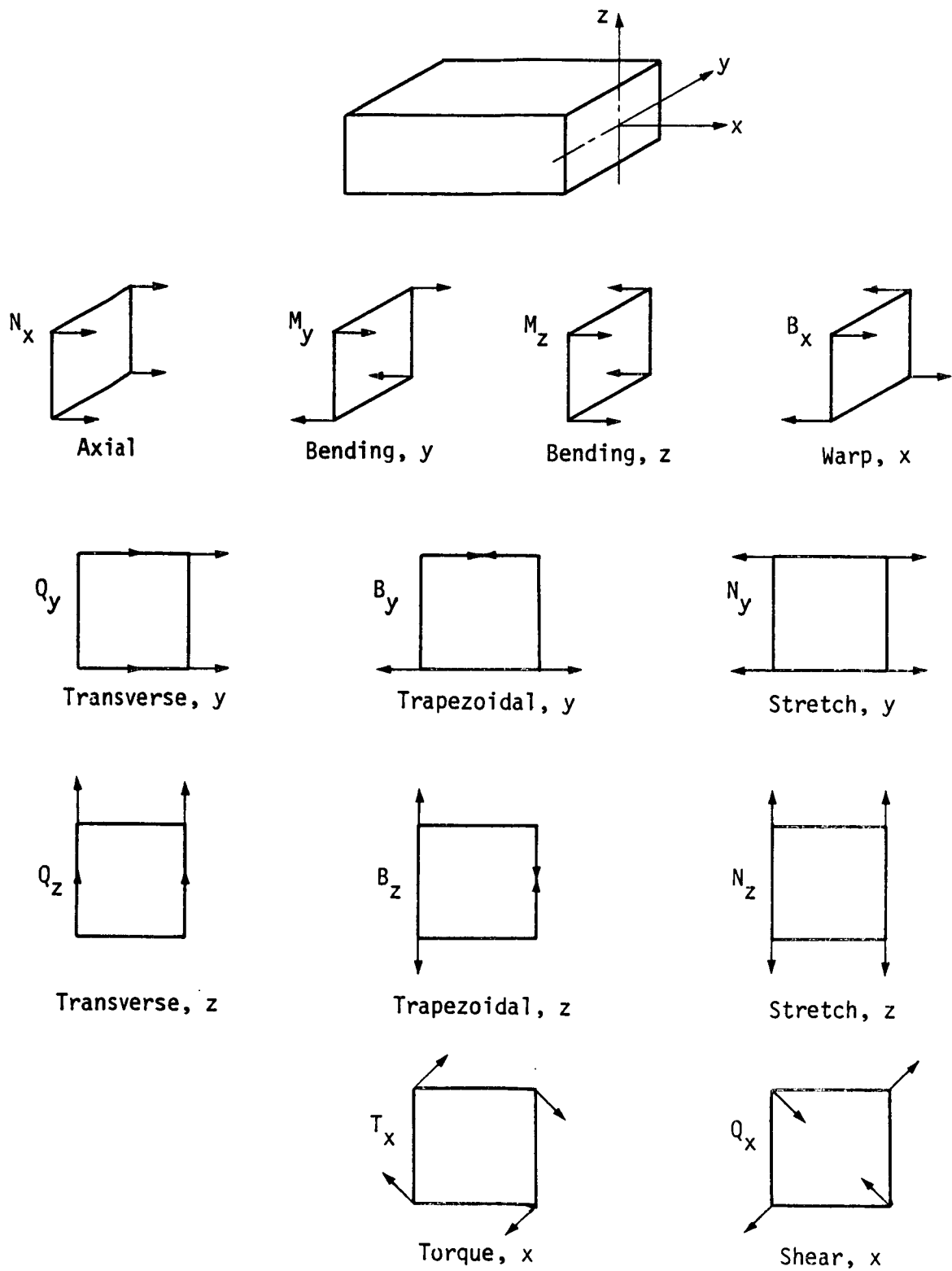
Figure 4 (b). Beamlike Loadings For Square Trusses

10 Bays with 780 lb Tip Mass

1st bending
(Modes 1 and 2)

2nd bending
(Modes 4 and 5)
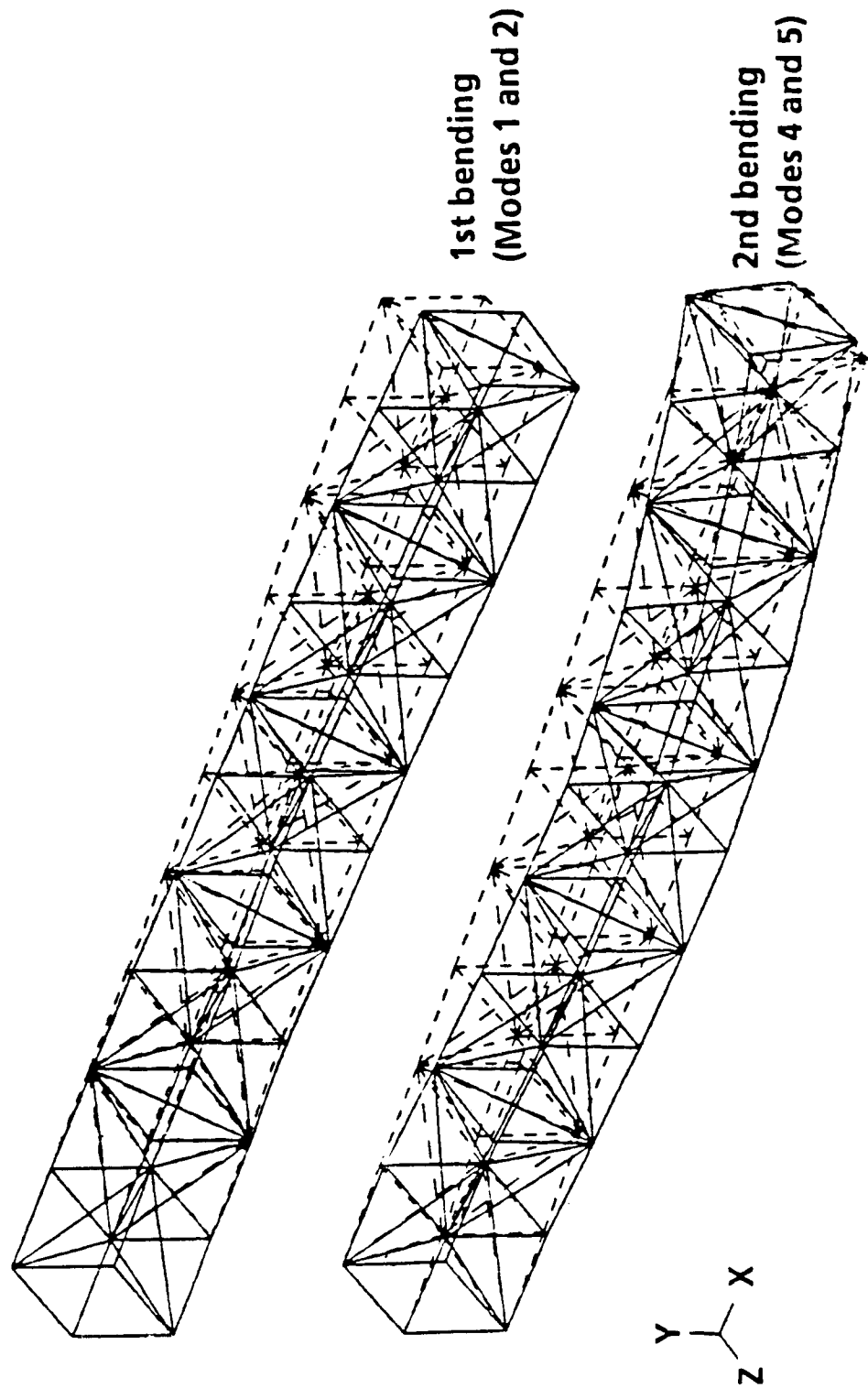
Figure 5.

585

TABLE 1

FREQUENCIES FOR CANTILEVERED 10-BAY VIERENDEEL FRAME

	Finite Element Model		Post-assembly Reduction				Element Reduction			Equivalent Beam	
Mode	Noor	BAC	10-DOF	8-DOF	4-DOF	4-DOF / 2 bays	Guyan 12-DOF	Guyan 6-DOF	SPC 6-DOF	Scalar Mass	(12x12 Mass
1b	2.285	2.244	2.244	2.244	2.244	2.245	2.284	1.975	4.509	2.174	2.245
1t	4.970	4.926	4.926	4.926	4.926	4.931	4.975	3.118	6.769	4.753	4.899
2b	7.554	7.464	7.465	7.465	7.465	7.490	7.550	5.945	13.851	6.471	6.742
2t	14.670	14.602	14.602	14.602	14.604	14.741	14.680	9.391	20.631	14.155	14.719
3b	14.747	14.626	14.631	14.634	14.635	14.841	14.739	10.036	24.700	10.754	11.359
4b	24.449	24.251	24.270	24.276	24.284	25.038	24.438	15.761	----	23.240	21.836
3t	24.253	24.276	24.276	24.276	24.287	25.162	24.264				
4t		34.921	34.921	34.921	34.961	36.932					
5b		36.660	36.719	36.729	36.762	37.854					
DOF used see Fig 4		1-18	1-6 10-12 17	1-4 10-12 17	1-4	1-4	1-6 10-12 14,15,17	1-6	1-6	1-6	1-6
Total DOF	100	180	100	80	40	20	120	60	60	60	60
Evaluation			E	E	E	G	E	U	U	U	U

Note: (b)=bending (t)=torsion (e)=extension ; (E)=Excellent (G)=Good (U)=Unsatisfactory
Each bending listed above represent two bending modes with identical frequecies.

TABLE 2

FREQUENCIES FOR CANTILEVERED 10-BAY DOUBLE BRACED FRAME/TRUSS

	Finite Element Model		Post-assembly Reduction					Element Reduction		Equivalent Beam	
Mode	Noor Exact Frame	BAC Exact Frame	10-DOF Frame	10-DOF Frame	9-DOF Truss	6-DOF Truss	4-DOF Truss	Guyan 6-DOF	SPC 6-DOF	Scalar Mass	(12x12) Mass
1b	8.942	8.796	8.805	8.796	8.877	8.877	8.877	8.802	12.610	8.900	8.792
1t	35.548	35.345	35.345	35.344	35.321	35.321	35.321	35.306	55.372	33.472	34.771
2b	47.930	47.323	48.661	47.327	49.490	49.492	49.492	48.716	54.632	50.276	49.814
3b	96.315(1)	95.990	---	96.039	---	---	---	106.062	110.417	99.594	90.321
1e	104.089	103.083	103.461	103.461	105.271	105.272	105.272				
2t	104.068	103.461	106.512	---	106.946	106.846	106.846				
DOF used See Fig 4	1-18		1-6 10-12 17	2-4 10-15 17	1-9	1-4 7,9	1-4	1-6	1-6	1-6	1-6
Total DOF	180		100	100	90	60	40	60	60	60	60
Evaluation			E	E	E	E	E	E	U	G	G

Note: (b)=bending (t)=torsion (e)=extension (l)=local ; (E)=Excellent (G)=Good (U)=Unsatisfactory
Each bending listed above represent two bending modes with identical frequecies.

587

TABLE 3

FREQUENCIES FOR CANTILEVERED 20-BAY DOUBLE BRACED FRAME/TRUSS

Mode	Finite Element Model BAC Exact Frame	Post-assembly Reduction 4-DOF Frame	9-DOF Truss	4-DOF Truss	Element Reduction 9-DOF Truss	4-DOF Truss	Equivalent Beam 6-DOF Frame	6-DOF Frame
1b	2.256	2.256	2.250	2.251	2.223	2.223	2.258	2.259
2b	13.622	13.691	13.565	13.600	13.397	13.405	13.748	13.751
1t	17.756	17.830	14.421	14.476	14.232	14.232	15.551	15.539
3b	35.711	36.986	35.923	36.564	35.764	35.936	36.873	36.926
2t	52.980	53.617	43.180	44.645	43.799	43.800	46.557	46.235
1e	53.021	54.974	53.410	53.360	52.912	52.913	53.310	53.269
4b	62.732	70.280	65.528	69.101	66.483	67.518	68.305	68.625
DOF used See Fig 4	1-18	1-4 every 2 bays	1-9 every bay	1-4 every 4 bays	1-9 every 4 bays	1-4 every 4 bays	1-6 every bay	1-6 every 2 bays
Total DOF	360	20	180	20	45	20	120	60
Evaluation		E	G	G	G	G	G	G

Note: (b)=bending (t)=torsion (e)=extension (1)=local ; (E)=Excellent (G)=Good
(U)=Unsatisfactory
Each bending listed above represent two bending modes with identical frequecies.

TABLE 4

SINGLE BAY DOUBLE-LACED SQUARE TRUSSES

Pinned Joints and No Batten Cross Bracing
10 Bays Cantilevered

Mode	Finite Element Model			Post-assembly reduction	element reduction
	Noor Beam theory	Noor EXACT	BAC EXACT	8-DOF	8-DOF
1w	0.6060	0.6055	0.6035	0.6035	.6035
1b	0.8335	0.8368	0.8300	0.8286	.8440
2w	3.5742	3.6051	3.5936	3.5936	3.5940
1t	4.1545	4.1542	4.1439	4.1439	4.1439
2b	4.5723	4.6539	4.6192	4.6155	4.6805
3w	9.2143	9.4458	9.4131	9.4131	9.4131
3b	10.9937	11.4168	11.3301	11.3271	11.4420
2t	12.4635	12.4549	12.4144	12.4143	12.4145
1e	12.5104	12.5559	12.4478	12.4276	12.8483
4w	16.3566	17.0596	16.9856	16.9856	16.9857
DOF used	1-8	1-12	1-12	1-8	1-8
Total DOF		120	120	80	80
Evaluation				E	E

Note: (b)=bending (t)=torsion (e)=extension (l)=local   ;
(E)=Excellent (G)=Good (U)=Unsatisfactory
Each bending listed above represent two bending modes with identical
frequecies.

TABLE 5

SINGLE BAY DOUBLE-LACED SQUARE TRUSSES

With Batten Cross Bracing
10 Bays Cantilevered

Mode	Finite Element Model		Post-assembly reduction	element reduction
	Exact Pinned Joints	Exact Fixed Joints	6-DOF Pinned	6-DOF Pinned
1b	0.790	0.784	0.790	0.799
1t	4.062	4.041	4.062	4.062
2b	4.399	4.285	4.399	4.438
3b	10.779	local	10.789	10.849
2t	12.007	"	12.006	12.166
1e	12.166	"	12.166	12.197
4b	18.376	"	18.376	18.457
3t	20.200	"	20.200	20.200
5b	26.643	"	26.664	26.716
DOF used	1-12	1-24	1-6	1-6
Total DOF	120	240	60	60
Evaluation			E	E

Note: (b)=bending (t)=torsion (e)=extension   (l)=local   ;
(E)=Excellent   (G)=Good (U)=Unsatisfactory
Each bending listed above represent two bending modes with
identical frequecies.

TABLE 6

DOUBLE BAY SINGLE-LACED SQUARE TRUSSES

Pinned Joints and No Batten Cross Bracing
10 Bays Cantilevered

Mode	Finite Element Model			Post-assembly reduction		element reduction
	Noor Beam theory	Noor EXACT	BAC EXACT	8-DOF per bay	8-DOF every 2 bays	8-DOF
1w	.6658	.6655	.6603	.6602	.6603	.6603
1b	.8339	.8341	.8229	.8229	.8230	.8229
1t	2.8720	2.8585	2.8585	2.8656	2.8591	2.8586
2w	3.7418	3.7787	3.7514	3.7514	3.7659	3.7527
2b	4.2314	4.2799	4.2314	4.2314	4.2567	4.2341
2t	8.1659	8.5960	8.5542	8.5542	8.7391	8.5697
3w	9.1783	9.3900	9.3251	9.3253	9.5299	9.3446
4b	9.6439	9.8714	9.7668	9.7668	10.0551	9.7990
1e	11.7044	11.6173	11.4990	11.4990	11.5355	11.5005
3t	14.3598	14.3663	14.2857	14.2862	15.0779	14.3579
DOF used	1-8	1-12	1-12	1-8	1-8 every 2 bays	1-8
Total DOF	80	120	120	80	40	80
Evaluation				E	E	E

Note: (b)=bending (t)=torsion (e)=extension (1)=local ;
(E)=Excellent (G)=Good (U)=Unsatisfactory
Each bending listed above represent two bending modes with identi
frequecies.

TABLE 7(a)

EFFECT OF MODEL VARIATIONS ON CANTILEVERED FREQUENCIES OF THE ROCKWELL TRUSS

10 Cantilevered Bays

Mode	Model 1 (hz)	Model 2 (hz)	Model 3 (hz)	Model 4 (hz)
1b(z)	5.361	5.390	5.359	5.360
1b(y)	5.529	5.556	5.527	5.527
1t	22.248	24.248	21.020	21.014
2b(z)	26.734	26.854	26.839	26.843
2b(y)	28.489	28.502	28.597	28.574
local	38.654	----	----	----
local	42.345	----	----	----
2t	53.648	55.396	51.113	55.414

Note: (b)=bending (t)=torsion (e)=extension (l)=local;
(E)=Excellent (G)=Good (U)=Unsatisfactory

TABLE 7(b)

DESCRIPTION OF THE SELECTED NASTRAN MODELS

Description	Model 1	Model 2	Model 3	Model 4
battens	bars	bars	bars	rods
longerons	rods	bars	rods	rods
batten joints	fixed	fixed	fixed	pinned
other joints	pinned	fixed	pinned	pinned
mass dist.	coupled	consistent	lumped	consistent

References

1) Noor, A.K., and Nemeth, M.P., "Analysis of Spatial Beamlike Latticies with Rigid Joints," Computer Methods in Applied Mechanics and Engineering, 1980, pp 35-59.

2) Noor, A.K. ; Anderson, M.S. ; and Greene, W.H. :Continuum Models for Beam and Plate-Like Lattice Structures: AIAA J., vol. 16, no. 12, Dec.1978, pp. 1219-1228.

3) Noor, A.K. ; and Andersen, C.M. : Analysis of Beam-Like Lattice Trusses. Computer Methods in Applied Mechanics and Engineering, vol. 20, no.1, Oct.1979, pp. 53-70

4) Noor, A.K. ; Weisstein, L.S. : Stability of Beamlike Lattice Trusses, Computer Methods in Applied Mechanics and Engineering 25 (1981),pp. 179-193

5) Sun, C.T. ; and Yang, T.Y.: A Continuum Approach Toward Dynamics of Gridworks. Journal of Applied Mechanics, Transactions of ASME, vol. 40, 1973, pp. 186-192

6) Sun, C.T. ; Kim, B.J. and Bogdanoff, J.A. : On the Derivation of Equivalent Simple Models for Beam- and Plate-like Structures in Dynamic Analysis. Proceedings of the AIAA/ASME/ASCE/AHS Structures, Structural Dynamics and Materials Conference, April 1981, pp. 523-532.

7) Dean, D.L. ; and Avent, R.R. : State of the Art of Discrete Field Analysis of Space Structures. Proceedings of the Second International Conference on Space Structures, edited by W.J. Supple, Sept. 1975, pp. 7-11

8) Dean, D.L.: Discrete Field Analysis of Structural Systems. Springer-Verlag, 1976.

9) Anderson, M.S. : Buckling of Periodic Lattice Structures. AIAA J. vol. 19, no. 6, june 1981, pp. 782-788

10) Anderson, M.S. : Vibration of Prestressed Periodic Lattice Structures. AIAA J., vol. 20, no.4, April 1982, pp. 551-555.

11) Anderson, M.S. : Vibration and Buckling of General Periodic Lattice Structures, AIAA paper 84-0979-CP, presented at 25th AIAA/ASME/ASCE/AHS Structures, Structural Dynamics and Materials Conference, May 14-16,1984

12) Renton, J.D. :The Beam-Like Behavior of Space Trusses, AIAA J. vol. 22, no. 2, Feb. 1984, pp. 273-280.

13) NASTRAN theorectical manual, pp 5.5-1 .

14) Archer,J.S.,"Consistent Mass Matrix for Distributed Mass Systems," Journal of Structural Division, Proceeding of the American Society of Civil Engineers, Aug 1963, pp 161.

OTHER REFERENCES PERTINENT TO EQUIVALENT BEAM SOLUTIONS

1) NASA Conference Publication 2258 , Modeling, Analysis, and Optimization Issues for Large Space Structures, Proceedings held in Williamsburg, Virginia, May 13-14, 1982.
2) Berry, D.T. and Yang, T.Y. : Simplified Lattice Beam Finite Elements for Nonlinear Static, Dynamic and Postbuckling Analysis, AIAA J. 1985, pp.316-324.

594

DYNAMIC CHARACTERISTICS OF A VIBRATING BEAM WITH

PERIODIC VARIATION IN BENDING STIFFNESS

JOHN S TOWNSEND

George C. Marshall Space Flight Center
Huntsville, Ala.

DYNAMIC CHARACTERISTICS OF A VIBRATING BEAM WITH

PERIODIC VARIATION IN BENDING STIFFNESS

JOHN S TOWNSEND

ABSTRACT - A detailed dynamic analysis is performed of a vibrating beam with bending stiffness periodic in the spatial coordinate. Using a perturbation expansion technique the free vibration solution is obtained in a closed-form, and the effects of system parameters on beam response are explored. It is found that periodic stiffness acts to modulate the modal displacements from the characteristic shape of a simple sine wave. The results are verified by a finite element solution and through experimental testing.

596

TABLE OF CONTENTS

LIST OF ILLUSTRATIONS

DEFINITION OF SYMBOLS

Symbol		Definiton
A	-	Peak stiffness variation, A = (EImax - EImin) / 2
Anm	-	Factor defined by equation (A-2)
dx	-	Differential element length
$\frac{d}{dx}$, (')	-	Denotes differentiation with respect to position
EIa	-	Geometric average stiffness of beam design, EIa = (EImax + EImin) / 2
EI(x)	-	Bending stiffness function
k	-	Dummy variable referring to mode number
L	-	Span length
Lt	-	Period of the stiffness function
m	-	Dummy variable referring to mode number
$\overline{m}$	-	Mass per unit length
n	-	Vibration mode number
Un(x)	-	Denotes nth mode eigenfunction, bending
x	-	Distance along span measured relative to support
$\tilde{x}$	-	Dimensionless horizontal coordinate, $\tilde{x}$ = x/L
δ_{mn}	-	Kronecker delta function, equation (10)
ϵ	-	Stiffness perturbation parameters, ϵ = A / EIa
λ_n	-	Dimensionless eigenvalue, $\lambda_n^2 = \frac{\overline{m} L^4}{E I_a} \omega_n^2$

599

DEFINITION OF SYMBOLS (cont.)

Symbol		Definiton
λ_{no}	-	Zeroth-order eigenvalue solution
λ_{n1}	-	First-order eigenvalue solution
λ_{n2}	-	Second-order eigenvalue solution
π	-	Pi
ρ	-	Stiffness parameter, $\rho = 1,2,3$ ie., the number of half periods $\rho = 2 L / Lt$
ϕ_n	-	Dimensionless Eigenfunction, $\phi_n = Un / L$
ϕ_{no}	-	Zeroth-order eigenfunction solution
ϕ_{n1}	-	First-order eigenfunction solution
ϕ_{n2}	-	Second-order eigenfunction solution
ω_n	-	Denotes nth mode frequency, bending
∂	-	Partial derivative notation
$\int$	-	Integral sign
$\sum$	-	Summation sign

DYNAMIC CHARACTERISTICS OF A VIBRATING BEAM WITH
PERIODIC VARIATION IN BENDING STIFFNESS

INTRODUCTION

Vibrating beam theory has been considered extensively in the literature for any number of variable property states, ranging from structures with changing cross-sectional geometry to those of a composite nature. Solutions are obtained either in closed-form for a few simple cases, or they are pursued using numerical techniques. In the present study, a perturbation expansion technique applicable to continuous systems is used to develop a closed-form solution to the problem of a vibrating beam with bending stiffness periodic in the spatial coordinate. Results are compared to a finite element solution and verified experimentally using forced vibration of a test span. To the knowledge of the author, this specific beam problem (static or dynamic) has not been addressed in the literature.

Application of periodic stiffness is recognized in the field of vortex-induced motion of transmission power lines [1]. In recent years a conductor, known as twisted-paired, has been developed that uses a variable diameter design to provide a changing conductor profile into the wind. Twisted-paired conductors are constructed by twisting together two identical standard round conductors with 360 degree twists occurring at set intervals along the span. The periodic nature of the twist causes a periodic variation in bending stiffness. Variable profile diameter results in non-uniform shedding of vortices, and hence excitation frequences, along the span. Multiple vortex frequencies act to minimize wind energy transfer and detune vibration response. In conductor systems, influence of bending stiffness effects becomes extremely important in the vicinity of supports.

The purpose of this report is to characterize the dynamic bending behavior of beams with periodic stiffness variation. Also, the models developed will provide insight into the behavior of similar type systems with changing property states.

EQUATIONS OF MOTION AND BASIC ASSUMPTIONS

Consider the problem of the transverse vibrations of a straight beam with periodic variation in bending stiffness along its length. The beam is assumed to be simply supported and long compared to its cross-sectional dimensions, and dynamic shear distortions and rotary inertia are negligible. We will also make the usual simplifying assumptions that Hooke's Law holds and plane sections remain plane. Figure 1 shows a free body sketch of a differential element of the vibrating beam.

We will proceed from the well-known differential equation of motion for the normal mode response of an undamped beam

$$\frac{d^2}{dx^2} \left[EI(x) \; \frac{d^2 U_n(x)}{dx^2} \right] - \bar{m} \, \omega_n^2 \, U_n(x) = 0 \tag{1}$$

where EI(x) is the bending stiffness function, $\bar{m}$ is the mass per unit length, Un(x) is the nth normal mode displacement and ω_n is the nth normal mode frequency. The bending stiffness function is given by

$$EI(x) = EI_a + A \cos \frac{2\pi}{L_T} x \tag{2}$$

where EIa is the geometric average stiffness of the beam design, EIa = [EImax + EImin] / 2 ; and A is the peak stiffness variation, A = [EImax - EImin] / 2. The period of the stiffness function is Lt. Figure 2 plots the function. Notice, at X = 0, the maximum flexural stiffness occurs, and the periodicity of the function is an even multiple of the span length. This particular stiffness function is characteristic of twisted-paired systems [1].

An equation of motion that models an undamped, vibrating beam with periodic bending stiffness is determined by combining equations (1) and (2). The result is a fourth-order differential equation with variable coefficients. A closed-form approximate solution to this boundary value problem is obtained by using a variation of the Rayleigh-Schrodinger expansion [2,3]. The solution in closed-form is extremely useful, since it clearly displays the influence of system parameters on response. Nayfeh [4] presents an application of a similar perturbation formulation for a simple linear second-order eigenvalue problem.
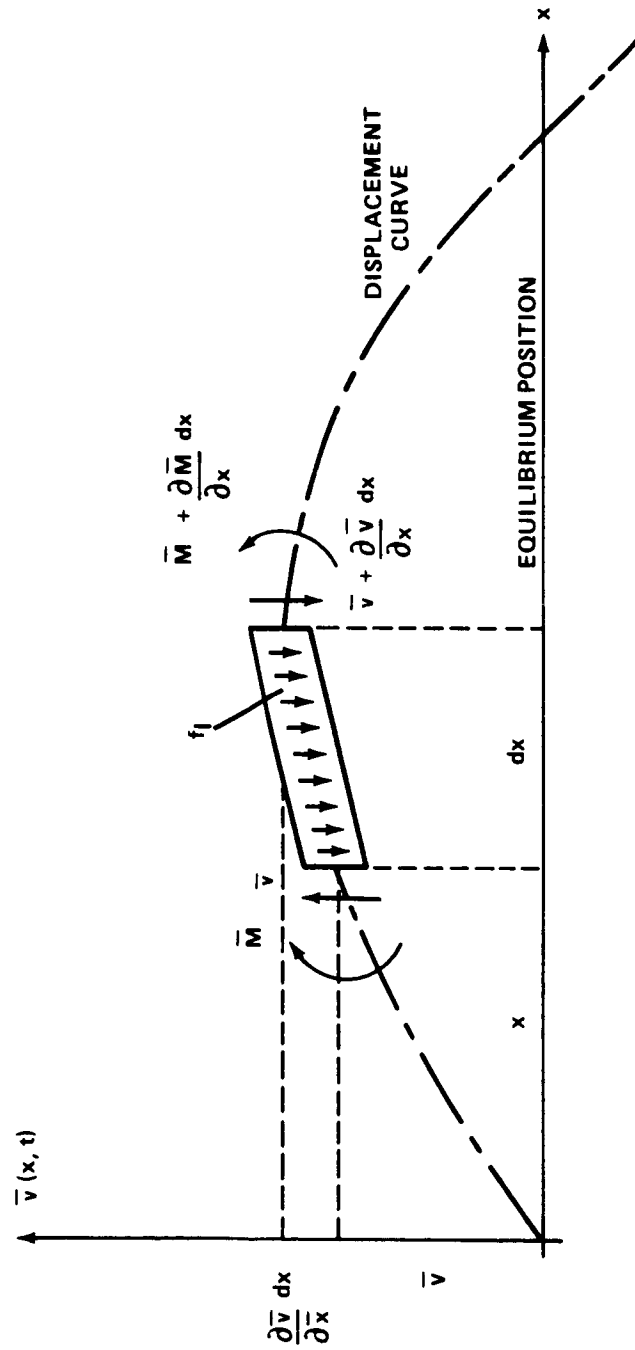
FIGURE 1   DIFFERENTIAL ELEMENT OF A VIBRATING BEAM

$$EI(x) = EI_a + A \cos \frac{2\pi}{L_T} X$$

$$\rho = \frac{2L}{L_T} \quad ; \quad \epsilon = \frac{A}{EI_a}$$
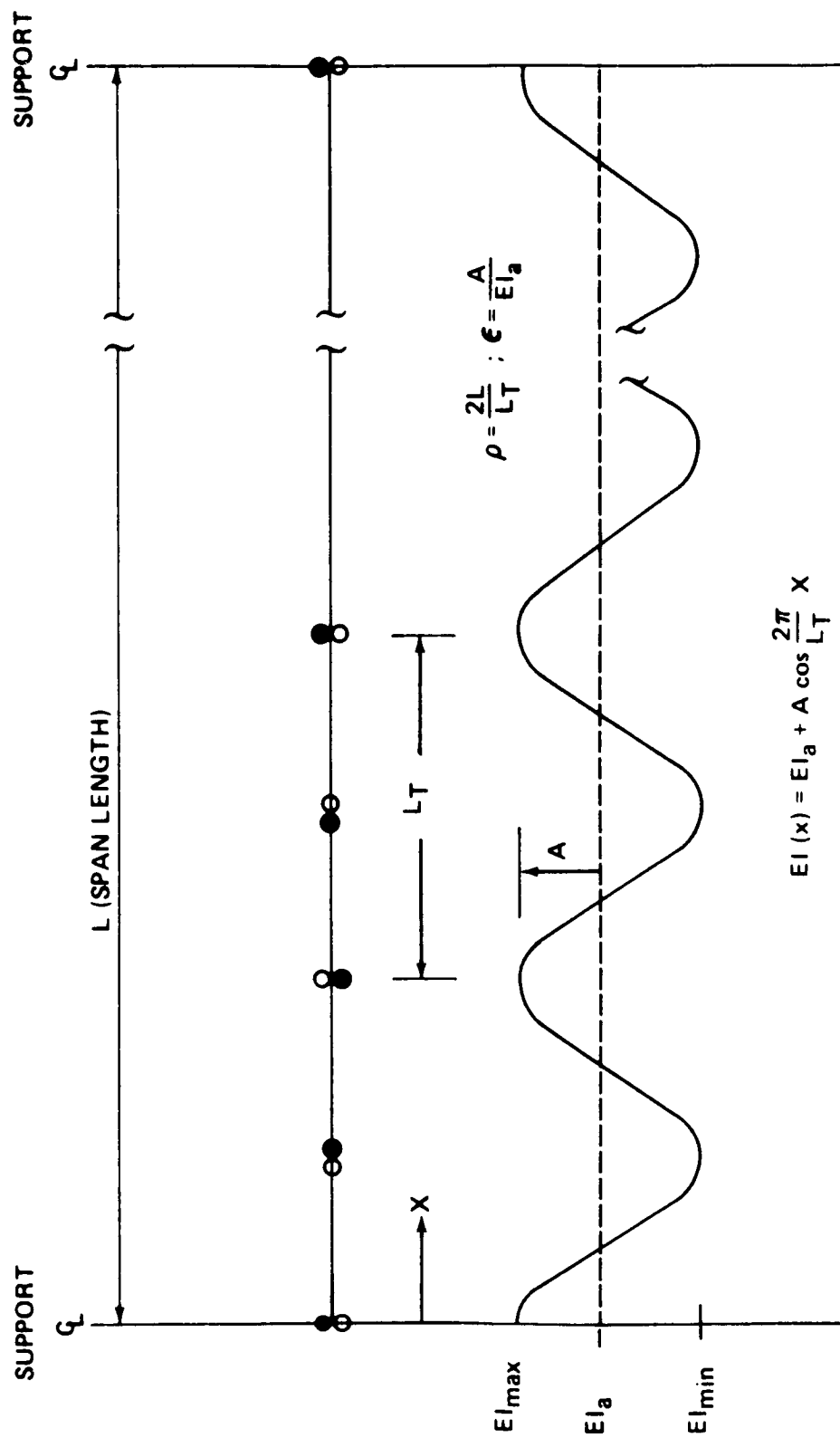
FIGURE 2 PERIODIC BENDING STIFFNESS FUNCTION

A dimensionless form of the governing motion equation is

$$\frac{d^2}{d\tilde{x}^2}\left\{\left[1 + \epsilon \cos\rho\pi\tilde{x}\right]\phi_n''\right\} - \lambda_n^2\phi_n = 0 \qquad (3)$$

(See nomenclature section for a definition of terms.)

and the corresponding boundary conditions for the case of simple supports are

$$\phi_n(0) = \phi_n(1) = 0 \qquad (4)$$

and

$$\phi_n''(0) = \phi_n''(1) = 0 \qquad (5)$$

The quantity [1 + $\epsilon\cos\rho\pi$ x] is the dimensionless bending stiffness. For convenience, the tildes are dropped in the remaining analysis. The coefficient ϵ is a measure of the magnitude of the stiffness variation, ϵ = A / EIa , and the parameter ρ is equal to the number of half periods of the stiffness function in a given span, ρ = 2 L / Lt.

PERTURBATION EXPANSION SOLUTION

The solution (ϕ , λ) of equation (3) is a function of the independent variable x and the parameters ϵ and ρ . If the parameter ϵ is equal to zero, the equation reduces to the case of a vibrating beam with uniform flexural stiffness whose eigenfunctions and eigenvalues are given, respectively, by

$$\phi_n = \sqrt{2} \sin n\pi x \qquad (6)$$

$$\lambda_n^2 = n^4 \pi^4 \qquad (7)$$

The $\sqrt{2}$ coefficient is arbitrary. It is picked so that the eigen-functions are normalized according to the integral function,

$$\int_{0}^{1} \phi_n^2 \, dx = 1 \tag{8}$$

The above eigenfuctions are orthonormal; i.e.,

$$\int_{0}^{1} \phi_n(x) \, \phi_m(x) \, dx = \delta_{mn} \tag{9}$$

where, δ_{mn}, the Kronecker delta function is specified as

$$\delta_{mn} = \begin{cases} 0 & m \neq n \\ 1 & m = n \end{cases} \tag{10}$$

When ϵ does not equal zero, equations (6) and (7) are no longer valid and corrections must be added to them. An approximate solution is obtained by expanding both the eigenfunction and the square of the eigenvalue in the form of a power series in ϵ ; i.e.,

$$\phi_n = \phi_{no} + \epsilon \phi_{n1} + \epsilon^2 \phi_{n2} + \ldots \tag{11}$$

$$\lambda_n^2 = \lambda_{no} + \epsilon \lambda_{n1} + \epsilon^2 \lambda_{n2} + \ldots \tag{12}$$

where ϕ_{no} and λ_{no} are the eigenfunction and the square of the egen-value when ϵ equals zero; equations (6) and (7). An asymptotic expansion is generally valid only if ϵ is small. By definition, the parameter ϵ for beams with periodic stiffness may not be small, but it is always less than one. Corrections of the higher order terms are therfore negligible, and the series converges eventually to the correct solution.

Substituting equations (11) and (12) into equation (3) and equating like powers of ϵ through order ϵ^2, we get the following system of differential equations:

$$O(\epsilon^0): \quad \phi_{no}^{IV} - \lambda_{no}\phi_{no} = 0 \tag{13}$$

$$O(\epsilon^1): \quad \phi_{n1}^{IV} - \lambda_{no}\phi_{n1} = \lambda_{n1}\phi_{no} - \frac{d^2}{dx^2}\left[\phi_{no}'' \cos \rho\pi x\right] \tag{14}$$

$$O(\epsilon^2): \quad \phi_{n2}^{IV} - \lambda_{no}\phi_{n2} = \lambda_{n2}\phi_{no} + \lambda_{n1}\phi_{n1} - \frac{d^2}{dx^2}\left[\phi_{n1}'' \cos \rho\pi x\right] \tag{15}$$

The problem of finding an approximate solution to equation (3) is now simplified to one of obtaining sequential solutions to equations (13), (14), and (15). To illustrate the procedure, the first-order correction is formulated in Appendix A. Equations (A-6) and (A-8) define the correction terms of the eigenvalues and eigenfunctions.

Using equation (A-8) and recalling that $\phi_n = \phi_{no} + \epsilon\phi_{n1}$ where $\rho = 1,2,3, \ldots$, the general eigenfunction solution ϕ_n is expressed in terms of dimensionless parameters for the case when $n \neq \rho/2$ as

$$\phi_n = \sqrt{2} \sin n\pi x$$

$$- \frac{\epsilon n^2}{\sqrt{2}}\left[\frac{(n+\rho)^2}{(n+\rho)^4 - n^4}\right]\sin(n+\rho)\pi x$$

$$- \frac{\epsilon n^2}{\sqrt{2}}\left[\frac{(n-\rho)^2}{(n-\rho)^4 - n^4}\right]\sin(n-\rho)\pi x \tag{16}$$

If $n = \rho/2$, the last term in the series is secular and hence vanishes.

607

Using equations (7), (12), and (A-6), the eigenvalue solution λ_n is given in terms of the first-order correction. The result is expressed in terms of the dimensionless variables as

$$\lambda_n = n^2 \pi^2 \left(1 - \frac{\epsilon}{2} \right)^{\frac{1}{2}} \qquad (17)$$

Equation (17) is valid only for the vibration mode $n = \rho / 2$. For all other vibration states the first-order correction term is zero. The second-order perturbation solution of the eigenvalue is determined using the same techniques previously developed for finding the first-order terms. Details of the formulation are outlined in Reference [1]. The general eigenvalue solution λ_n of the second-order expansion is given as

$$\lambda_n = n^2 \pi^2 \left[1 - \frac{\epsilon}{2} - \frac{\epsilon^2}{4} \left[\frac{(\eta + \rho)^4}{(\eta + \rho)^4 - \eta^4} \right] - \frac{\epsilon^2}{4} \left[\frac{(\eta - \rho)^4}{(\eta - \rho)^4 - \eta^4} \right] \right]^{\frac{1}{2}} \quad (18)$$

The first-order correction term in equation (18) is equal to zero for the vibration modes where $n \neq \rho / 2$. For the case defined by $n = \rho / 2$, the last term in the second-order correction is specified to vanish (ie., this term is secular from ϕ_{n1} solution). Notice that the eigenvalue λ_n simplifies to the case of a beam with uniform stiffness when the perturbation parameter ϵ is equal to zero.

The general behavior of a beam with periodic bending stiffness variation is given by equations (16) and (18). As the vibration state approaches the anomaly occurring at $n = \rho / 2$, the eigenfunction solution deviates from a simple sine wave displacement curve to a mode shape comprising other harmonics. For the case when $n = \rho / 2$, the eigenfunction returns to the sine wave shape. The eigenvalue solution responds in a similar nature. At $n = \rho / 2$ a jump in the eigenvalue occurs, since for this mode the harmonics of the stiffness function are secular. Results of the closed-form perturbation analysis have been checked using finite element results and results of experimentation.

EIGENFUNCTIONS AND EIGENVALUES

Effects of the perturbation terms on the eigenfunction solution are exemplified in Figure 3. The magnitudes of the bracketed terms in equation (16) are plotted as a function of the ρ/n ratio. Two distinct ranges are apparent; $\rho/n < 1$ and near $\rho/n = 2$. In these ranges, the perturbation effects are the strongest. At $\rho/n = 2$, a vibration state is defined where the lengths of the vibration loops match the period of the stiffness function. Based on the stiffness definition given, this mode defines maximum stiffness at the nodes of the vibration loops and minimum siffness at the antinodes. At $\rho/n = 1$, both the maximum and minimum stiffnesses occur at the node positions in alternating sequence along the span.

Figures 4 and 5 give eigenfunction comparisons of vibration modes in the general modal solution range. The vibration displacement amplitudes are normalized and plotted verses the normalized horizontal span coordinate (X/L). Recall, boundary conditions are simple support and beam orientation at the supports is for maximum stiffness. Figure 4 plots eigenfunction solutions near the anomaly $\rho/n = 2$, where $\rho = 64$ and $\epsilon = 0.4$. The effect of periodic stiffness is to modulate the displacements of those vibration modes approaching the anomaly at $n = \rho/2$, or for this case mode 32. Similar displacement curves as patterned for modes 31 and 33 are characteristic of all vibration modes near the anomaly. Close examination of the eigenfunctions reveals that the node (or antinode) locations are adjusting themselves along the span, and the longer vibrating loops result in lower midloop displacement amplitudes. Apparently, the beam attempts to minimize the elastic strain energy stored within the dynamic span by adjusting the lengths of the vibrating loops until the same average bending siffness exists across each individual loop. Equalizing the loop stiffnesses may require the loops to have different legnths depending on the vibration mode, and a longer loop has greater mass. An equal partioning of potential energy and thus kinetic energy between each of the loops results in lower vibration amplitudes for the longer vibrating loops. Loop stiffness calculations verify this reasoning.

At the anomaly, modulation in the mode shape disappears, since for this case the individual loop stiffnesses are equal (ie., the lengths of the vibration loops match the period of the stiffness function). The same basic reasoning holds true for the case where $\rho/n = 1$, see Figure 5. Here also, the mode shape is sinusoidal - no modulation; and average loop stiffnesses are equivalent with maximum and minimum values defining the nodes of each loop. Additional cases identified in Figure 5 are for small and large values of ρ/n. As ρ/n approaches zero, perturbations in the mode shape increase. At the opposite end of the scale, where the ρ/n parameter goes to infinity, the displacement shape is sinusoidal. Figure 6 characterizes the eigenfunction solution as a function of the perturbation parameter, ϵ. As the magnitude of Epsilon (ie., the stiffness variation) increases, the modulation effects become more pronounced.
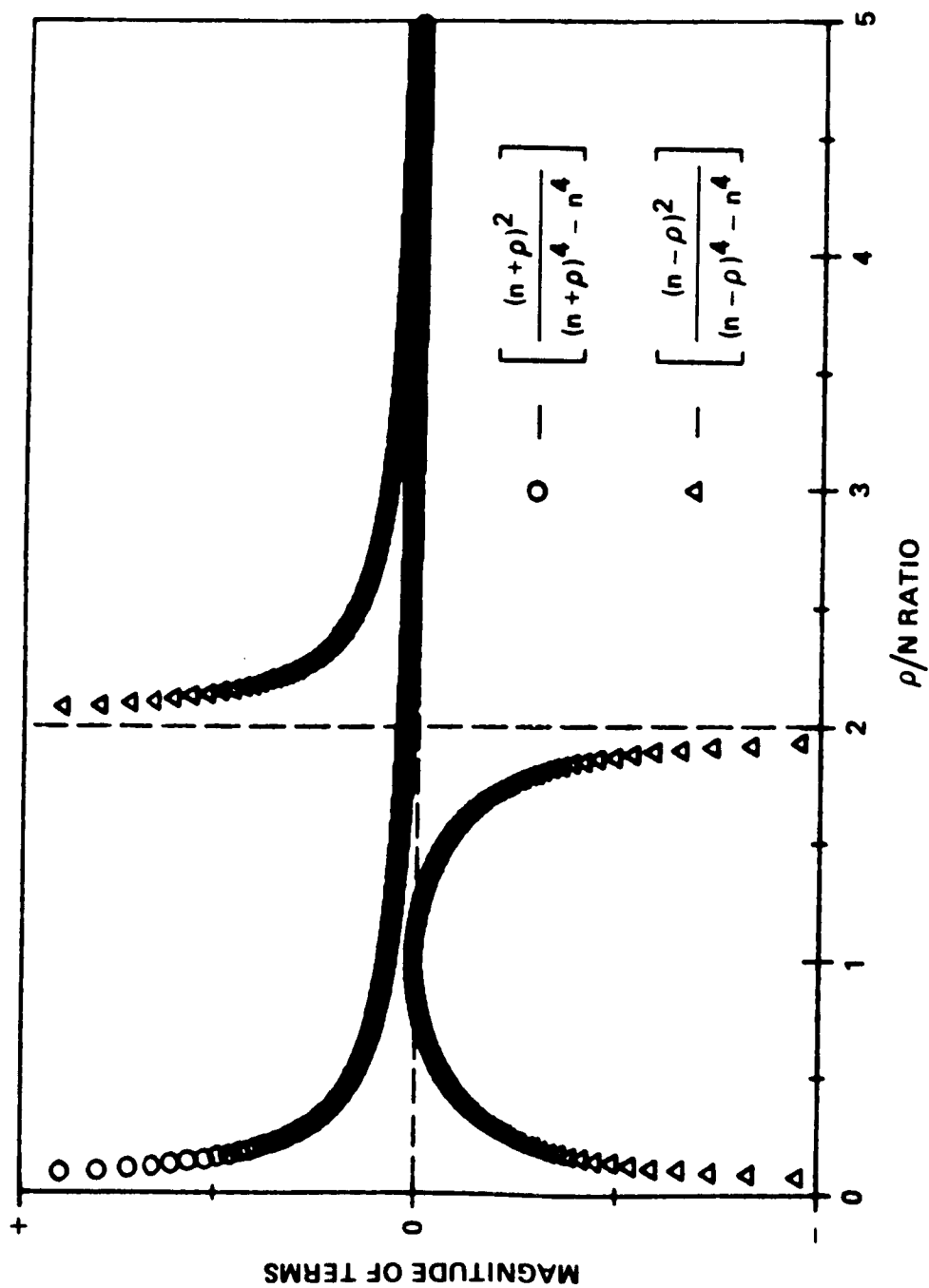
FIGURE 3   EFFECTS OF PERTURBATION TERMS ON EIGENFUNCTION

$$\left[\frac{(n+\rho)^2}{(n+\rho)^4 - n^4}\right]$$

$$\left[\frac{(n-\rho)^2}{(n-\rho)^4 - n^4}\right]$$

ρ/N RATIO

MAGNITUDE OF TERMS

610

EIGENFUNCTION SOLUTION (ρ = 64, ϵ = .4)
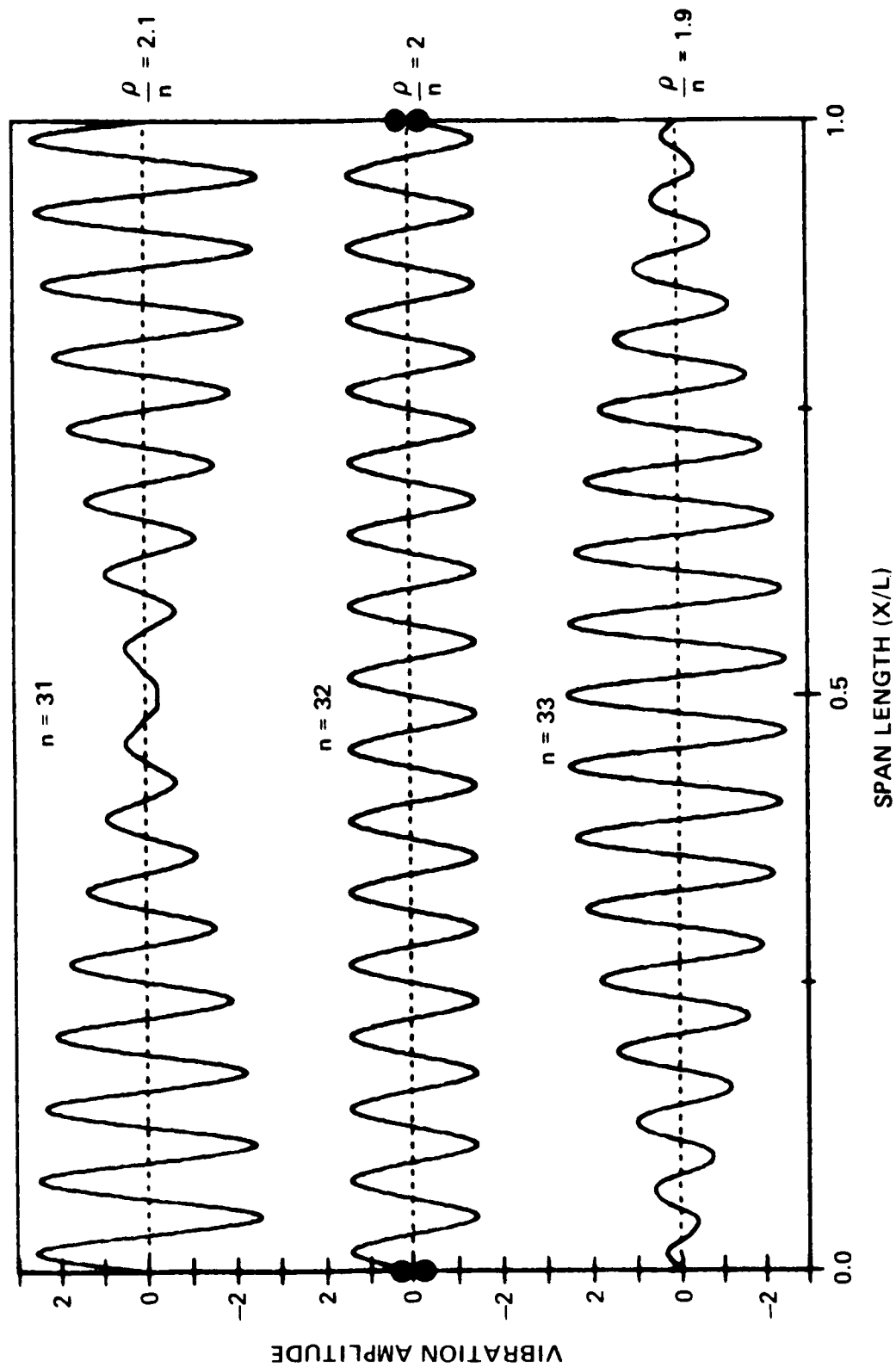
FIGURE 4 EIGENFUNCTION SOLUTIONS NEAR THE ANOMALY, ρ/n = 2
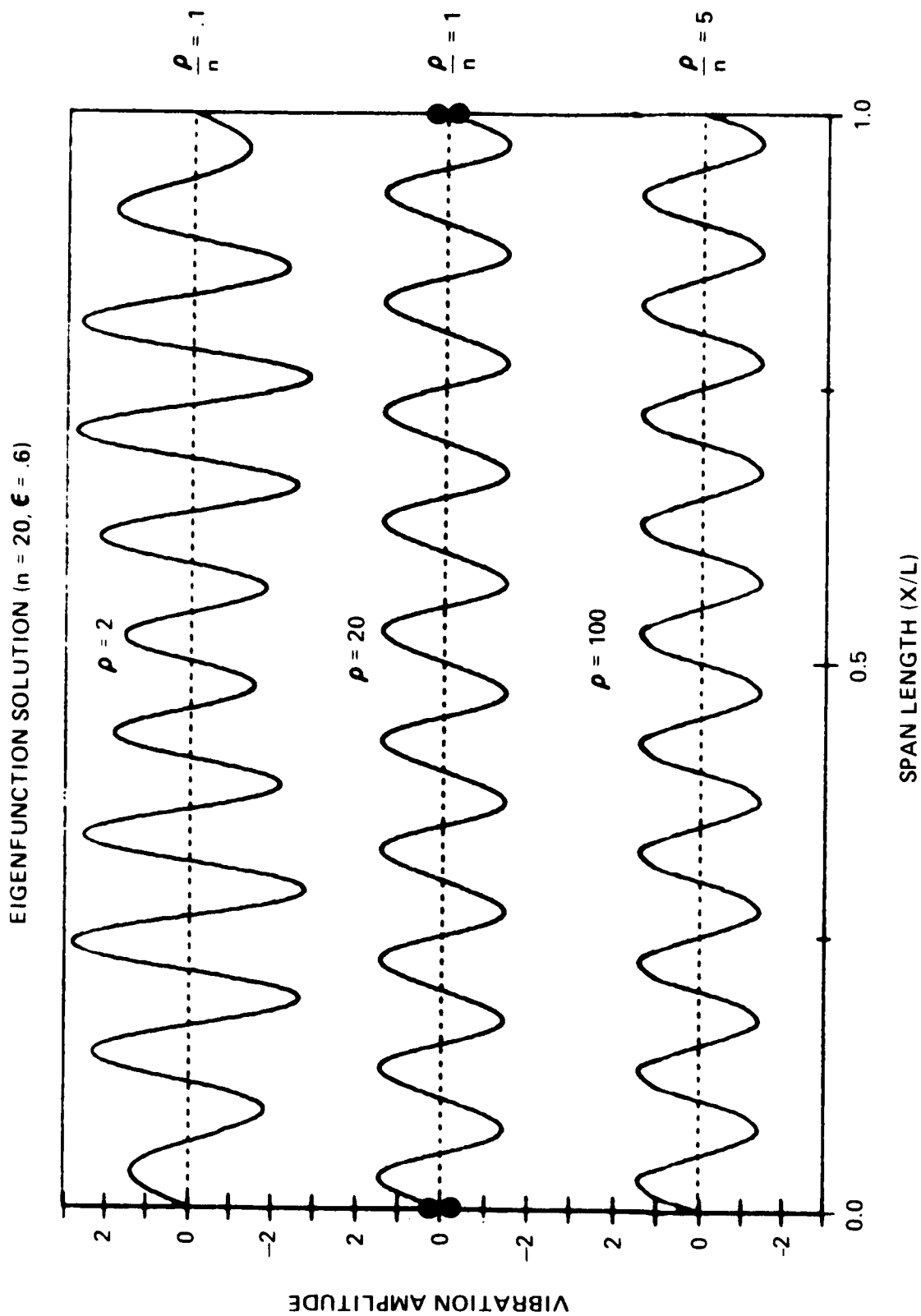
FIGURE 5   EIGENFUNCTION SOLUTIONS IN CHARACTERISTIC RANGES OF VIBRATION

612

EIGENFUNCTION SOLUTION (n = 10, ρ = 21)

VIBRATION AMPLITUDE

SPAN LENGTH (X/L)

ϵ = .2
ϵ = .4
ϵ = .6
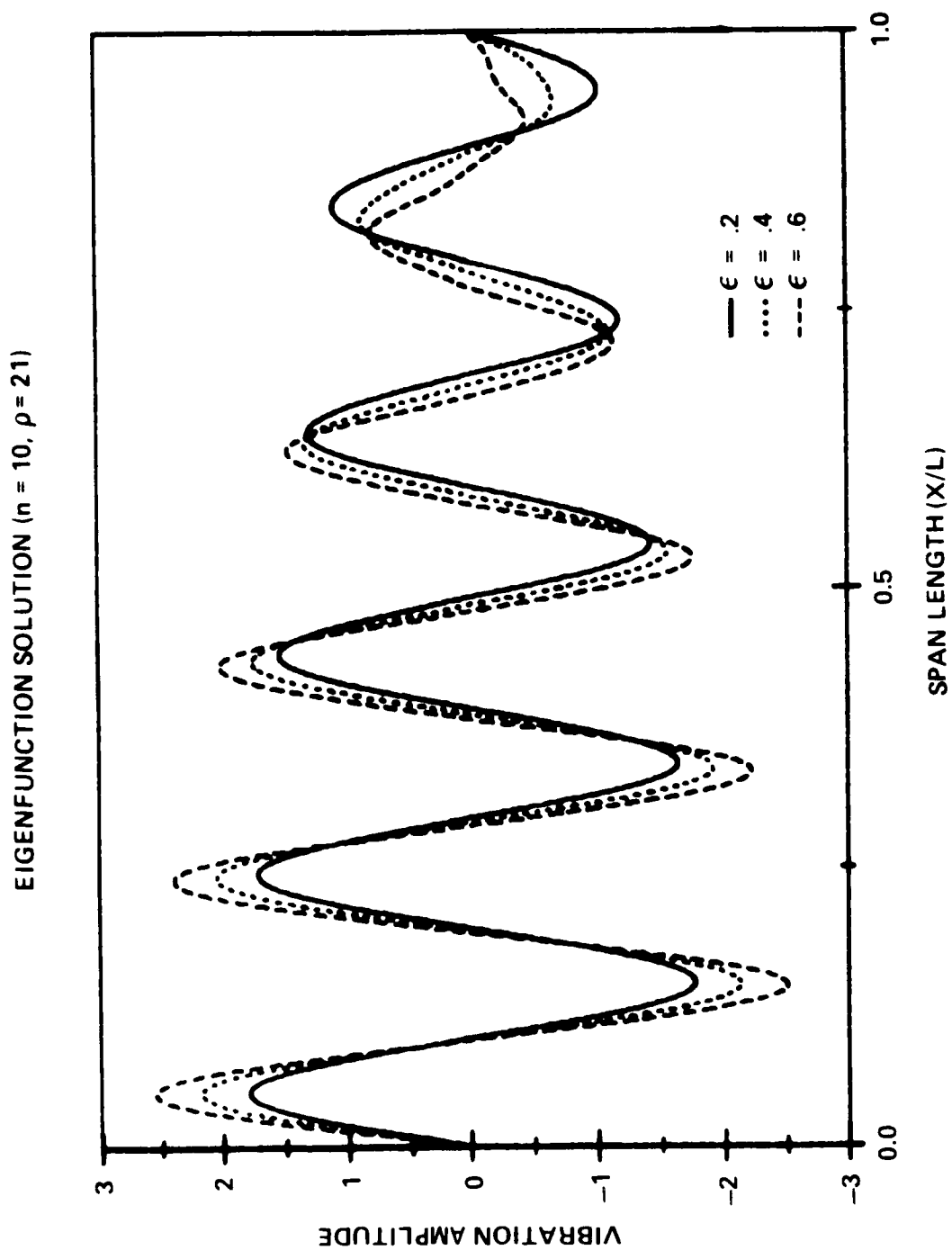
FIGURE 6 EIGENSOLUTION AS A FUNCTION OF EPSILON

EIGENVALVE SOLUTION ($\epsilon = .6$)
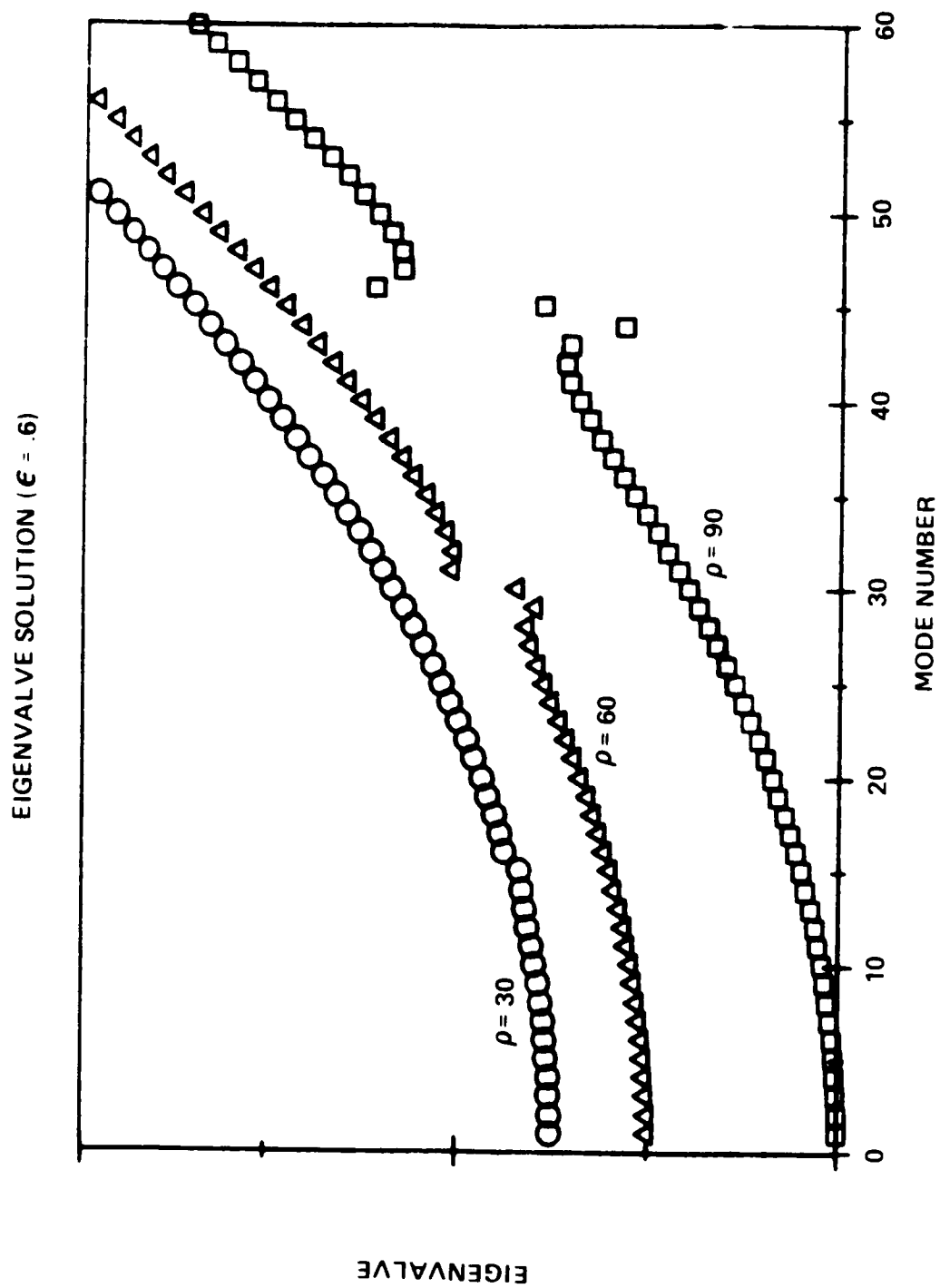
FIGURE 7 EIGENVALVE SOLUTION FOR DIFFERENT CASES OF ρ

Eigenvalue solutions of the 2nd order perturbation expansion for different cases of ρ are plotted in Figure 7 versus the respective vibration mode. At the anomaly, $\rho/n = 2$, a jump in the eigenvalue occurs. The intensity of the jump increases with ρ. Physically, the jump identifies a sharp change in frequency (or stiffness) between characteristic modes of vibration. Mathmatically, the jump is equivalent to removing the secular nature of the stiffness function from the eigenfunction solution.

The closed-form perturbation expansion solution has been verified through comparisons with a finite element solution [1]. Although the findings are not formally documented herein, agreement between the analytical results is excellent. Some discrepancy does occur in the vicinity of the stiffness anomaly. This is apparently due to a sudden change in bending stiffness. Nevertheless, the qualitative picture remains the same. Two characteristic effects of periodic bending stiffness on dynamic response are determined: (1) periodic stiffness forces an anomaly in the system which results in a jump in the natural frequency, and (2) periodic stiffness acts to modulate the modal displacements in distinctive ranges of ρ/n. A qualitative explanation of the modulation and its effects on beam response is given in terms of energy principles.

EXPERIMENTAL VERIFICATION

A series of tests were designed to investigate the dynamic response of beam type systems which have a periodic variation in bending stiffness. A stiff-string structure, known as a twisted-paired conductor, was the test candidate in the program. Table 1 summarizes the experimental test parameters and Figure 8 shows a photograph of the test span. Periodic variation in diameter profile of the twisted-paired conductor is compared to the uniform diameter of a standard conductor design. In stiff-string systems, elastic strain energy is stored in tension and bending. If tension is constant along the span, then tension has minimal effect towards equalizing the variable flexural stiffness of the vibrating loops [1]. In other words, tension effects do not mask the effects of stiffness variation.

Experimental data are compared to the finite element results for free vibration since the fixed boundary conditions are applicable. This type of boundary support keeps the end losses to a minimum. Internal damping of the conductor was also reduced by applying a high tension line force. The procedure of minimizing conductor system damping is necessary; higher harmonics are difficult to excite if mechanical damping is significant. The testing program used forced vibration response to study free vibration. If the span is tuned properly to a single natural frequency, contributions from all other harmonics are minimal. The vibration exciter unit was positioned near the span center to eliminate even harmonics from the general response. The added mass of the moving shaker element and span attachment fixture resulted in a shortening of the drive loop, and thus a lowering

FIGURE 8 PHOTOGRAPH OF TEST SPAN, TWISTED-PAIRED CONDUCTOR
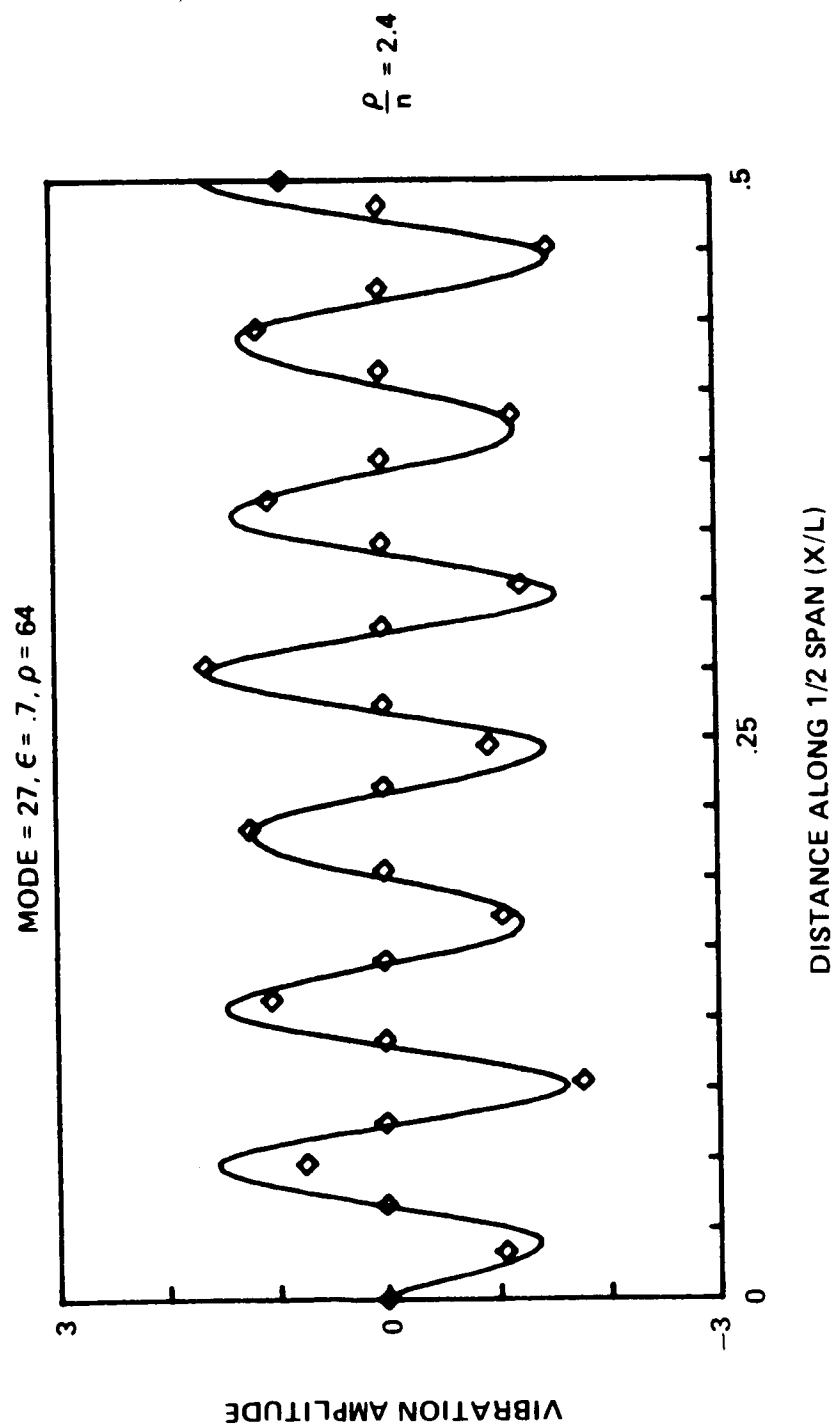
FIGURE 9   COMPARISON OF EIGENSOLUTION WITH
EXPERIMENTAL TEST VALVES, MODE 27

617
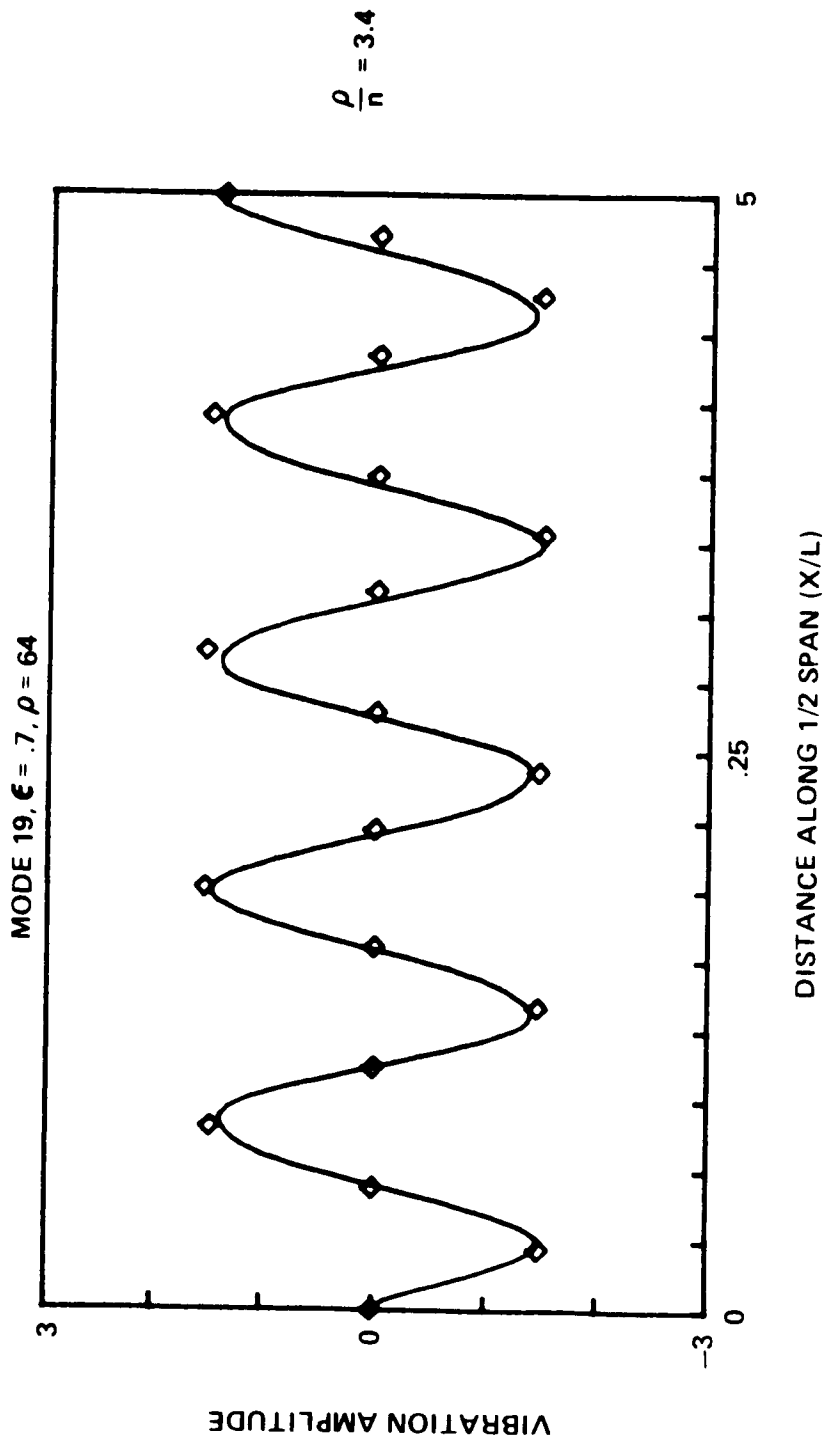
FIGURE 10   COMPARISON OF EIGENSOLUTION WITH
EXPERIMENTAL TEST VALVES, MODE 19

618

of its vibration amplitude. No attempt was made to decouple
shaker mass from the conductor span. A V-scope attached to the
center of each vibrating loop was used to measure the midloop
amplitude displacements. The device is inexpensive and its accuracy
is remarkable at 0.01 inches.

Typical test results are presented in Figures 9 and 10.
Finite element displacement amplitudes are normalized using a
method previously outlined, see equation 8. Experimental
amplitudes are normalized to one of the measured values - chosen
in arbitrary fashion. Span length is used to nondimensionalize
the horizontal coordinate. Since mode shape is symmetric about
the span center, data results are shown only for half the span.
Figure 9 gives the comparison for mode 27, an eigenfunction near
the anomaly in the system occurring at n = 32. Although the com-
parison is not exact, the modulation in the eigenfunction response
is proved physically to exist. The same general results are re-
ported for all other modes near the anomaly. Figure 10 compares
the experimental and analytical data of mode 19, an eigenfunction
well removed from the stiffness anomaly. Agreement between the
analytical and test data is excellent and the mode shape is
sinusoidal. Some discrepancy does occur in the node positions
near the drive location where the measured loop lengths are shorter.
Shacker attachment changes the stiffness and mass of the drive loop.
Shifting of the nodes tends to compensate for these effects.

CONCLUSIONS

The dynamic response of beams with periodic stiffness
contrasts significantly with the vibration behavior of standard
beams. Linear vibration theory was used to develop a stiffness
model and characterize response. Using a perturbation expansion,
a closed-form solution of free vibration was formulated for the
case of simple supports and periodic stiffness variation. The
technique worked exceptionally well when the stiffness parameter
was slowly varying. Applications of variable tension, mass, and
area are natural extensions of the theory. The main conclusions
are summarized below.

1. Periodic bending stiffness forces an anomaly in
    the system which corresponds to the vibration state
    where the loop length matches the period of the
    stiffness function. Physically, the anomaly denotes
    the vibration mode for which loop stiffness changes
    most rapidly. The result is a jump in natural freq-
    uency. The perturbation solution loses some accuracy
    for those vibration modes near the anomaly; however,
    the qualitative characteristics of the response
    remain the same.

2. The stiffness parameter acts to modulate the modal
    displacements in two distinct ranges of vibration:
    $\rho/n < 1$ and near $\rho/n = 2$. Experimental evidence
    is presented which supports these findings.

3. Modulation in modal displacements is explained in terms of energy principles. The beam attempts to minimize the elastic strain energy stored within a dynamic span by adjusting the lengths of the vibrating loops until the same average bending stiffness exists across each individual loop. Equalizing the loop stiffnesses may require the loops to have different lengths depending on the vibration mode, and a longer loop has greater mass. An equal partitioning of potential energy and thus kinetic energy between each of the loops results in lower vibration amplitudes for the longer vibrating loops.

APPENDIX A

FIRST-ORDER CORRECTION TO THE PERTURBATION SOLUTION

The first step in the first-order correction to the perturbation solution is to substitute the zeroth-order solution, equations (6) and (7), into equation (14). After taking the appropriate derivatives and using trigometric identities, the result simplifies to

$$
\phi_{n1}^{IV} - n^4 \pi^4 \phi_{n1} = \sqrt{2} \left\{ \lambda_{n1} \sin n\pi X \right.
$$

$$
\left. - \frac{n^2 \pi^4}{2}(n+\rho)^2 \sin[(n+\rho)\pi X] - \frac{n^2\pi^4}{2}(n-\rho)^2 \sin[(n-\rho)\pi X] \right\} \tag{A-1}
$$

Next, assume that the solution ϕ_{n1} can be expressed as a linear combination of the zeroth-order eigenfunctions ϕ_{n0};

$$
\phi_{n1} = \sqrt{2} \sum_{m=1}^{\infty} A_{nm} \sin m\pi X \tag{A-2}
$$

This solution satifsies the boundary conditions on ϕ_{n1}. Taking derivatives and substituting into equation (A-1) yields

$$
\sum_{m=1}^{\infty} \pi^4 (m^4 - n^4) A_{nm} \sin m\pi X =
$$

$$
\lambda_{n1} \sin n\pi X - \frac{n^2\pi^4}{2}(n+\rho)^2 \sin(n+\rho)\pi X \tag{A-3}
$$

$$
- \frac{n^2 \pi^4}{2}(n-\rho)^2 \sin(n-\rho)\pi X
$$

Multiplying equation (A-3) by $\sin k\pi x$ and interating from 0 to 1 using the orthonormal property, equation (9), we obtain

621

$$\pi^4 \left[K^4 - n^4 \right] A_{nK} = \lambda_{n1}\, \delta_{nK} - n^2 \pi^4 (n+\rho)^2 \int_0^1 \sin(n+\rho)\pi X \sin K\pi X\, dX$$

$$- n^2 \pi^4 (n-\rho)^2 \int_0^1 \sin(n-\rho)\pi X \sin K\pi X\, dX \qquad \text{(A-4)}$$

If k = n, the left-hand side of equation (A-4) vanishes, hence

$$\lambda_{n1} = n^2 \pi^4 (n+\rho)^2 \int_0^1 \sin(n+\rho)\pi X \sin n\pi X\, dX$$

$$+ n^2 \pi^4 (n-\rho)^2 \int_0^1 \sin(n-\rho)\pi X \sin n\pi X\, dX \qquad \text{(A-5)}$$

The above integral expressions evaluate only when n = ⌊ /2, that is when the vibration mode number corresponds to the span length-stiffness function ratio (n = L/Lt). This is the anomaly that makes the periodic stiffness problem so interesting.

Equation (A-5) then calculates the eigenvalues of the first-order expansion as

$$\lambda_{n1} = -\frac{n^4 \pi^4}{2} \qquad \text{WHEN} \quad n = \rho/2 \qquad \text{(A-6)}$$

Note, λ_{n1} = 0 for all other values of n. The above condition removes the secular terms from the solution when k = n. If k ≠ n, then equation (A-4) simplifies to

$$A_{nK} = \frac{-n^2(n+\rho)^2}{K^4 - n^4} \int_0^1 \sin(n+\rho)\pi X \sin K\pi X\, dX$$

$$\frac{-n^2(n-\rho)^2}{K^4 - n^4} \int_0^1 \sin(n-\rho)\pi X \sin K\pi X\, dX \qquad \text{(A-7)}$$

622

Because of the stipulations on the parameter ρ , Ank in equation (A-7) calculates non-zero values only for the two cases: (1) k = n + ρ and (2) k = n - ρ , wher n $\neq$ ρ /2. The general solution of the eigenfunction ϕ_{n1},given by equation (A-2), is finally expressed as

$$\phi_{n1} = \frac{-n^2(n+\rho)^2}{\sqrt{2}\left[(n+\rho)^4 - n^4\right]} \, \sin(n+\rho)\pi\chi$$

(A-8)

$$\frac{-n^2(n-\rho)^2}{\sqrt{2}\left[(n-\rho)^4 - n^4\right]} \, \sin(n-\rho)\pi\chi + \sqrt{2}\, A_{nn}\sin n\pi\chi$$

For the vibration mode corresponding to n = ρ /2, the second term in equation (A-8) vanishes, since for this mode it is secular in nature. Keeping this in mind we can say that the ϕ_{n1} solution is valid for all vibration states where ρ= 1,2,3,. . . The coefficient Ann is determined by the normilizing function

$$\int_0^1 2\,\phi_{no}\,\phi_{n1}\,d\chi = 0$$

(A-9)

For this case, Ann is calculated to equal zero.

LIST OF REFERENCES

1. Townsend, J. S., "Wind Induced Motion of Twisted-Paired Conductors," Ph.D. Dissertation, Washington State University, 1984, pp. 60-121.

2. Hirschfelder, J. O., "Formal Rayleigh-Schrodinger Perturbation Theory for Both Degenerate and Non-Degenerate Energy States," International Journal of Quantum Chemistry, Vol. III, 1969, pp. 731-748.

3. Wilcox, C. H., Perturbation Theory and its Applications in Quantum Mechanics, John Wiley & Sons, Inc., 1966.

4. Nayfeh, A. H., Perturbation Methods, John Wiley & Sons, Inc., 1973, pp. 68-71.

STRUCTURAL DYNAMICS SYSTEM MODEL REDUCTION

JPL

J. C. CHEN

T. L. ROSE

B. K. WADA

Applied Technologies Section

Jet Propulsion Laboratory

California Institute of Technology

Pasadena, California

Workshop on Structural Dynamics and Control

Interaction of Flexible Structures

Marshall Space Flight Center, Alabama

April 22-24, 1986

Loads analysis for structural dynamic systems is usually performed by finite element models. Because of the complexity of the structural system, the model contains large number of degree-of-freedom. The large model is necessary since details of the stress, loads and responses due to mission environments are computed. However, a simplified model is needed for other tasks such as pre-test analysis for modal testing, and control-structural interaction studies. In the present report, a systematic method of model reduction for modal test analysis will be presented. Perhaps it will be of some help in developing a simplified model for the control studies.

The Test-Analysis Model (TAM) serves as the bridge between the loads model and the corresponding modal test whose purpose is to verify the validity of the loads model. It is obvious that the TAM must be compatible with the measurements of the modal test. Since instrumentation limitation, the TAM degrees-of-freedom will be much smaller than that of the loads analysis model.

JPL

LOADS ANALYSIS MODEL REDUCTION

- Test Analysis Model (TAM) Requirement

- Pre-Test Analysis for Primary Modes Determination, Instrumentation Location Selection, Excitation Distribution and etc.

- Compatibility of DOF

- Test - Analysis Correlation

- Analytical Model Updating

629

These are the criteria for TAM.

JPL CRITERIA FOR REDUCED MODEL

- Accuracy in Frequency Prediction for Primary Modes

- Sufficient Resolution of Mode Shape Comparison

- Effective Mass - Completeness

- Accuracy With Respect to External Forcing Function

- Selection of DOF Based on Kinetic Energy

The governing equation begins at the spacecraft/launch vehicle coupled system.

GOVERNING EQUATIONS FOR PAYLOAD/LAUNCH VEHICLE COMPOSITE SYSTEM

$$\begin{bmatrix} m_1 & 0 \\ 0 & m_2 \end{bmatrix} \begin{Bmatrix} \ddot{x}_1 \\ \ddot{x}_2 \end{Bmatrix} + \left(\begin{bmatrix} k_1 & 0 \\ 0 & 0 \end{bmatrix} + \begin{bmatrix} k_{11} & k_{21} \\ k_{12} & k_{22} \end{bmatrix} \right) \begin{Bmatrix} x_1 \\ x_2 \end{Bmatrix} = \begin{Bmatrix} F(t) \\ 0 \end{Bmatrix}$$

$\{x_1\}$ = LAUNCH VEHICLE DEGREES-OF-FREEDOM (DOF)

$\{x_2\}$ = PAYLOAD DOF

$[m_1]$ = MASS MATRIX OF THE LAUNCH VEHICLE

$[m_2]$ = MASS MATRIX OF THE PAYLOAD

$[k_1]$ = STIFFNESS MATRIX OF THE LAUNCH VEHICLE

$[k_{11}], [k_{12}], [k_{21}], [k_{22}]$ = SUB-MATRICES OF THE TOTAL PAYLOAD STIFFNESS MATRIX PARTITIONED INTO LAUNCH VEHICLE/PAYLOAD INTERFACE DOF AND PAYLOAD DOF.

$\{F(t)\}$ = EXTERNAL FORCING FUNCTION

Statically determinate interface between the spacecraft and launch vehicle is assumed.

STATICALLY DETERMINATE SUPPORTED PAYLOAD

$$[k_{11}] = [\phi_R]^T [k_{22}] [\phi_R]$$

$$[k_{21}] = -[\phi_R]^T [k_{22}] = [k_{12}]^T$$

WHERE

$[\phi_R]$ = PAYLOAD RIGID BODY TRANSFORMATION MATRIX DEFINED AS THE PAYLOAD DISPLACEMENT DUE TO UNIT DISPLACEMENT OF THE LAUNCH VEHICLE/ PAYLOAD INTERFACE DOF, $\{x_I\}$.

$\{x_I\}$ = LAUNCH VEHICLE/PAYLOAD INTERFACE DOF CONNECT- ING PAYLOAD TO LAUNCH VEHICLE, A SUBSET OF THE LAUNCH VEHICLE DOF $\{x_I\}$.

The spacecraft responses are decomposed into rigid-body motion and elastic motion. It should be noted that only the elastic motion will cause structural loads.

PAYLOAD MOTION DECOMPOSITION

$$\{x_2\} = [\phi_R]\{x_1\} + \{x_e\}$$

$$\begin{bmatrix} m_1 + m_{rr} & \phi_R^T m_2 \\ m_2 \phi_R & m_2 \end{bmatrix} \begin{Bmatrix} \ddot{x}_1 \\ \ddot{x}_e \end{Bmatrix} + \begin{bmatrix} k_1 & 0 \\ 0 & k_{22} \end{bmatrix} \begin{Bmatrix} x_1 \\ x_e \end{Bmatrix} = \begin{Bmatrix} F(t) \\ 0 \end{Bmatrix}$$

WHERE

$$[m_{rr}] = [\phi_R]^T [m_2][\phi_R]$$

DENOTED AS RIGID-BODY MASS.

637

The accuracy of the response is dependent on the selection of modes. The modes selection should be based on the criteria of providing maximum response, frequency sensitive to the forcing functions and maximum effective mass. The TAM should produce modes which will satisfy all these criteria.

GENERALIZED COORDINATES

$$[m]\{\ddot{x}\} + [k]\{x\} = -[m_2][\phi_R]\{\ddot{x}_I\} \longrightarrow \text{FULL DOF MODEL}$$

MODAL TRUNCATION
SELECT MODES FOR MAX. x

LET $\quad \{x\} = [\phi]\{u(t)\} \longrightarrow$

WHERE $[\phi]$ IS THE NORMAL MODE MATRIX SUCH THAT

$$[\phi]^T[m][\phi] = [\,\ulcorner 1\lrcorner\,], \text{ IDENTITY MATRIX}$$

$$[\phi]^T[k][\phi] = [\,\ulcorner \omega^2\lrcorner\,], \text{ EIGENVALUE}$$

$$\{\ddot{u}\} + [\,\ulcorner 2\rho\omega\lrcorner\,]\{\dot{u}\} + [\,\ulcorner \omega^2\lrcorner\,]\{u\} = \{F(t)\}$$

$\longleftarrow$ **SELECT MODES SENSITIVE TO F(t)**

WHERE

$$\{F(t)\} = -[\phi]^T[m_2][\phi_R]\{\ddot{x}_I\} = \text{GENERALIZED FORCE}$$

$$= -[M_{er}]\{\ddot{x}_I\}$$

RELATED TO EFFECTIVE MASS

This is a typical forcing function in the form of interface acceleration. The shock spectra indicates that that modes with frequency either lower than 2.0 Hz or higher than 40.0 Hz will be of little effect as far as response calculation is concerned.
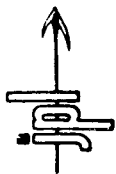
LAUNCH VEHICLE / SPECRAFT
INTERFACE ACCELERATION
LONGITUDINAL (Z) DIRECTION

SHOCK SPECTRA

DATA SET = Q = 50

STIFF1 GLL86 + L/V 7301 0 TUNE -I/F Z

TIME HISTORY

DATA SET = 3

STIFF1 GLL86 + L/V 7301 0 TUNE -I/F Z

641

The model reduction procedure will be demonstrated by the Galileo spacecraft.
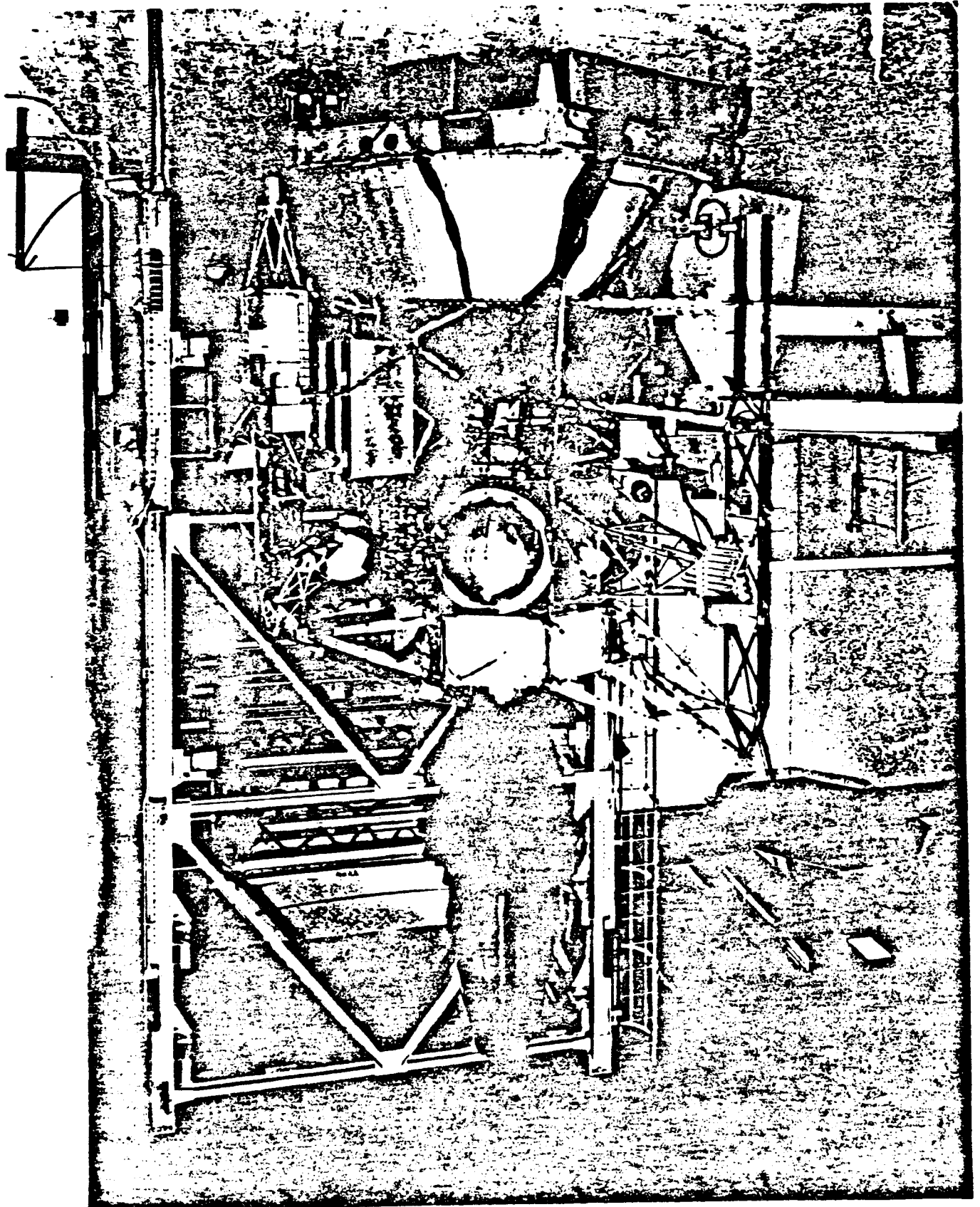
The Galileo spacecraft has a complex structural system. A detailed finite element model is required for the loads analysis.

GALILEO SPACECRAFT CORE STRUCTURES

BUS
(SPUN)

RPM
(SPUN)

SBM SUPPORT
(SPUN)

OUTER CONE
(DESPUN)

LTR
(SPUN)

DESPUN SKIRT
(DESPUN)

PROBE
(DESPUN)

SUPER ZIP
(DESPUN)

ADAPTER
(DESPUN)

SBA
SPUN-DESPUN INTERFACE
400 N. ENGINE

NOTE: 400 N. ENGINE
PLUME SHIELDS
REMOVED FOR CLARITY

645
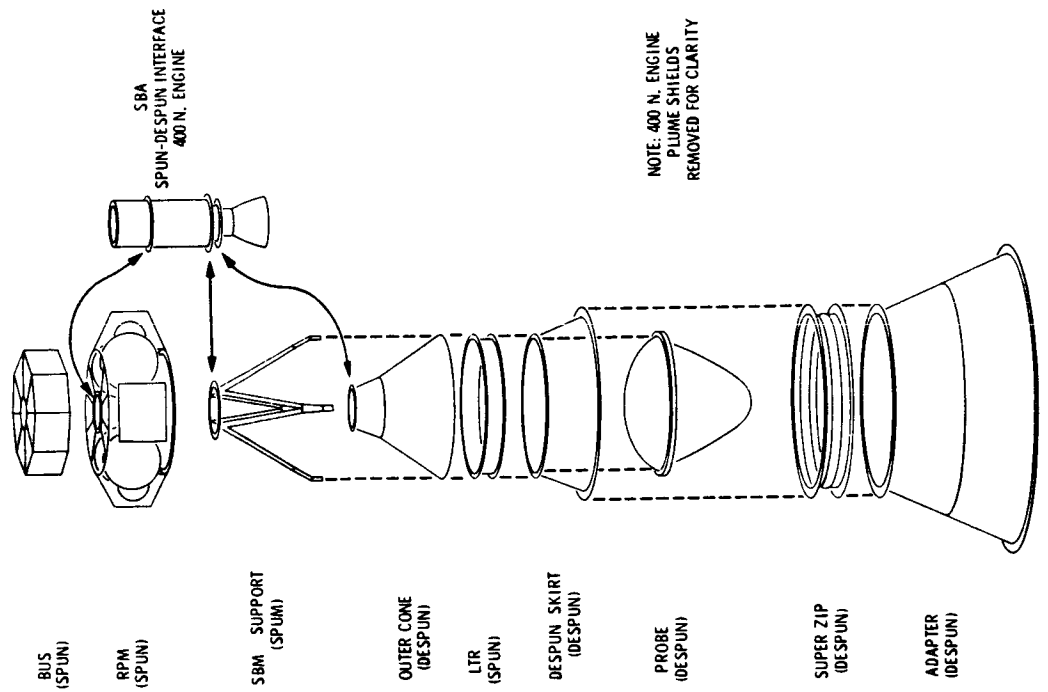
This shows weight distribution of the subsystems.

GALILEO SPACECRAFT MAJOR SUBSYSTEMS

Subsystem	Mass* (kg)	Weight* (lbs)
High Gain Antenna	49.5	109.1
Bus	272.5	600.7
Retro Propulsion Module (RPM)	1216	2681
Despun Box	110.4	243.3
RRH	6.0	13.2
Bay E	14.5	32.0
Science Boom	76.6	168.8
Scan Platform	96.4	212.5
+x RTG	80.2	176.9
-x RTG	77.2	170.2
Probe	341.8	753.4
Spin Bearing	43.1	95.1
Inner Cone		
LTR		
Despun Cone	52.8	116.3
S/C Adapter	50.1	110.6

The final loads model contains 10,000 degrees-of-freedom.

GALILEO NASTRAN MODEL

JPL

649
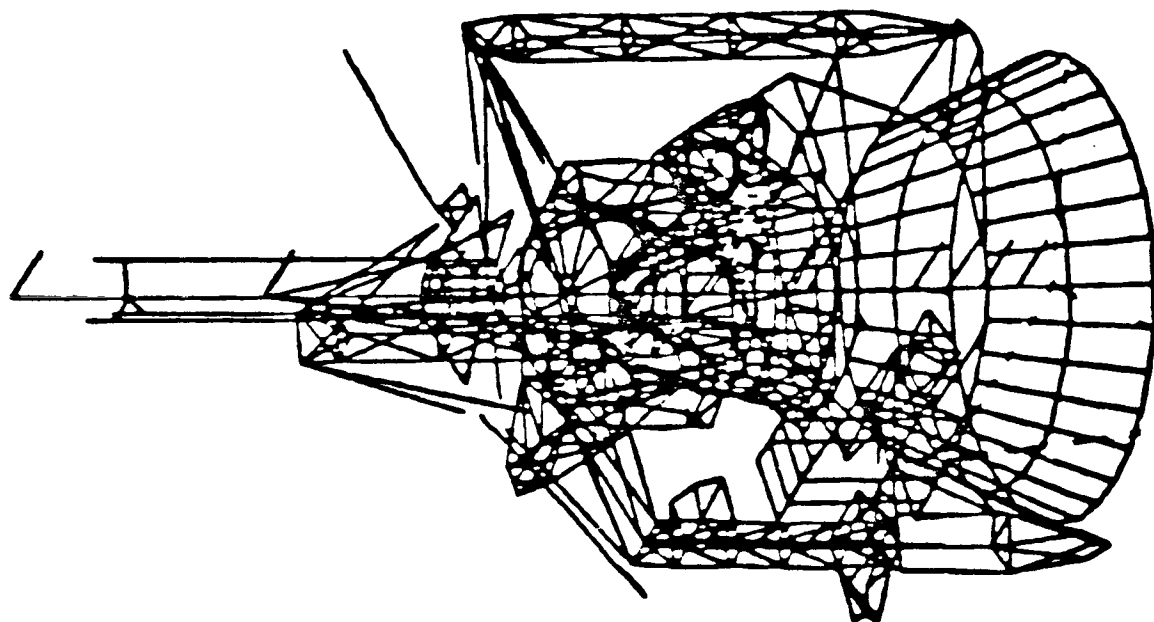
These are the frequencies predicted by the loads model.

FREQUENCY PREDICTION

MODE NO.	FREQ (Hz)	MODE NO.	FREQ (Hz)	MODE NO.	FREQ (Hz)
1	12.78	25	37.49	49	53.42
2	13.04	26	38.48	50	53.90
3	16.59	27	40.22	51	54.58
4	17.45	28	40.54	52	56.02
5	18.42	29	41.34	53	56.45
6	19.36	30	41.60	54	56.76
7	19.77	31	41.93	55	63.35
8	20.86	32	42.09	56	63.89
9	21.94	33	42.16	57	65.07
10	22.69	34	42.25	58	67.94
11	22.88	35	42.33	59	68.35
12	28.01	36	42.78	60	69.04
13	29.11	37	43.38	61	69.94
14	29.51	38	43.48	62	71.02
15	31.17	39	44.08	63	71.63
16	31.44	40	45.23	64	72.56
17	31.44	41	47.25	65	73.38
18	31.90	42	48.43	66	75.04
19	33.44	43	48.89	67	76.07
20	34.57	44	49.74	68	76.55
21	35.21	45	49.98	69	80.19
22	35.99	46	50.23	70	82.88
23	36.07	47	50.89		
24	36.47	48	51.38		

This is the description of the first six modes.

MODES DESCRIPTION

MODE No.	FREQ (Hz)	DESCRIPTION
1	12.78	GLOBAL BENDING IN x-DIRECTION. +x & -x RTG MOTION IN +z & -z DIRECTION RESPECTIVELY, WALKING MODE
2	13.04	GLOBAL BENDING IN y-DIRECTION
3	16.59	LOCAL MODE, MAG. CAN. MOTION IN y-DIRECTION, -x RTG MOTION IN z-DIRECTION
4	17.45	2nd GLOBAL BENDING IN y-DIRECTION
5	18.42	2nd GLOBAL BENDING IN x-DIRECTION
6	19.36	LOCAL MODE, BOTH MAG. CAN. & -x RTG IN z-DIRECTION MOTION, IN PHASE

These are the predicted effective mass in percentage. Those modes with large effective mass are the important modes for the loads analysis and should be predicted by the reduced model. It should be noted that the total effective mass for the first 21 modes constitutes only a portion of the total mass.
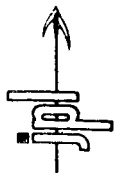
EFFECTIVE MASS

DOF / MODE	x	y	z	θ_x	θ_y	θ_z
1	.3239	.0046	.0001	.0067	.6701	.0007
2	.0028	.3519	.0002	.6678	.0067	0
3	.0569	.0018	.0001	.0005	.0189	.2719
4	.0038	.3392	.0004	.2434	.0024	.0009
5	.1135	.0018	0	.0015	.1118	.0130
6	.0343	.0844	.0016	.0143	.0204	.0008
7	.1520	.0026	.0003	0	.0813	.0171
8	.0031	.0003	.0021	.0005	.0002	.2785
9	0	.0006	.0723	.0024	.0001	.0098
10	.0001	.0005	.0117	.0003	0	0
11	.0001	.0012	.1225	.0013	0	.0021
12	.1453	.0002	.0020	0	.0395	.0141
13	.0006	.0008	0	.0001	.0004	.0037
14	.0007	.0067	0	.0011	.0001	.0009
15	0	0	0	0	0	0
16	0	0	0	0	0	0
17	0	0	0	0	0	0
18	.0001	.0004	.0002	0	.0001	.0009
19	.0059	.0030	.4144	.0002	.0015	0
20	.0009	.0051	.0642	.0001	.0002	.0007
21	.0048	.0010	.0738	.0001	.0011	.0001
SUM	.8488	.8061	.7659	.9403	.9548	.6152

The residual mass is defined as the total mass subtracted by the effective mass. The smaller residual mass is an indication for a better modal truncation.

RESIDUAL MASS

Z-DIRECTION

X-DIRECTION

PERCENTAGE OF RESIDUAL MASS

NUMBER OF MODES
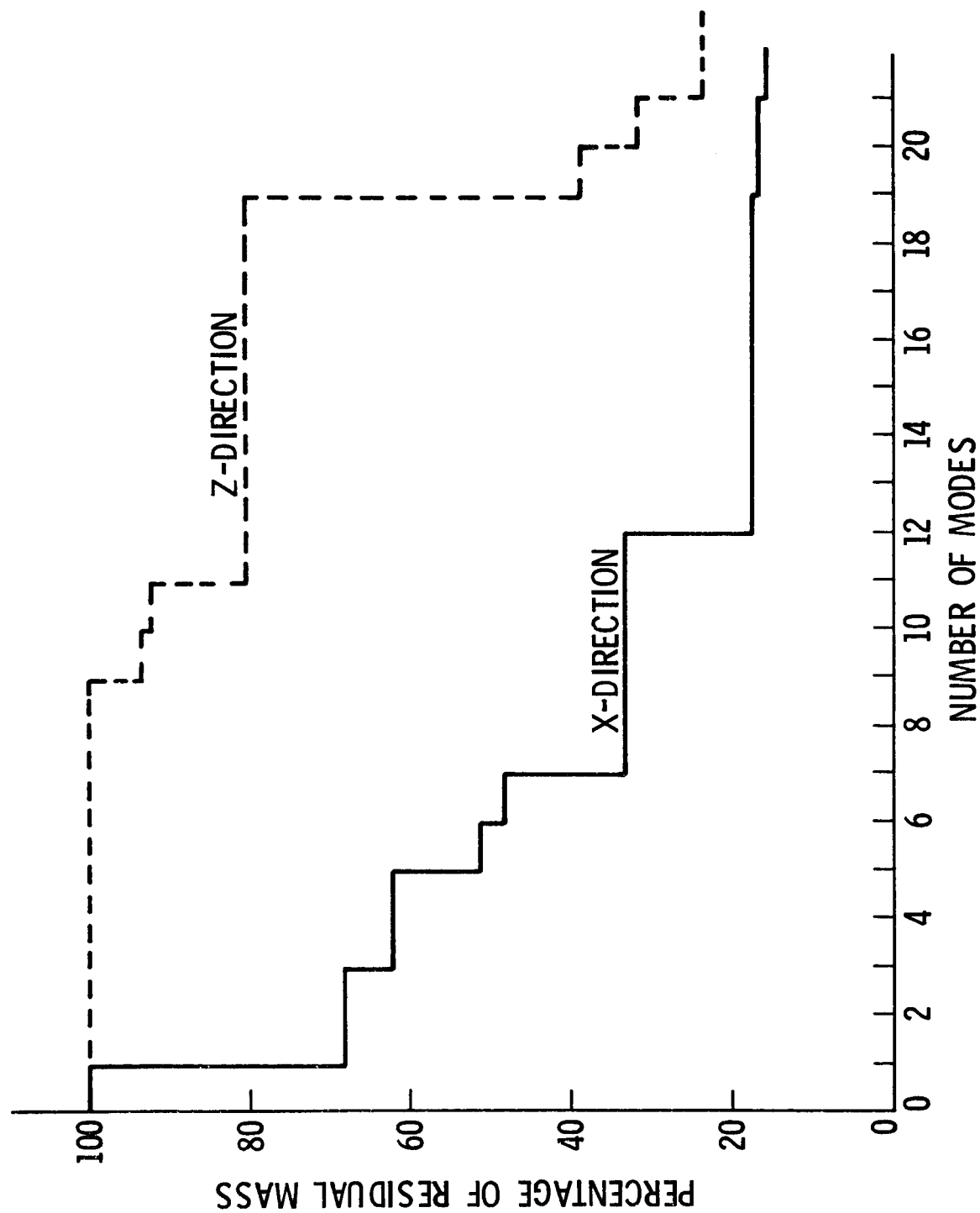
The modal accelerations due to a typical interface acceleration are calculated for the first 21 modes. They are shown here together with the sum of the effective mass. In general, modes with higher effective mass will have higher modal accerlations and they are the important modes. However, there are some modes with smaller effective mass but large modal accelerations such as the 19th mode. These modes may be local modes but they may generate higher loads for the local structures. Therefore, they should be considered as important modes too.

MODAL ACCELERATION

MODE	FREQ (Hz)	EFFECTIVE MASS SUMMATION	MODAL ACCELERATION
1	12.78	1.01	2.00 (g)
2	13.04	1.03	8.52
3	16.59	.35	-1.36
4	17.45	.59	-8.14
5	18.42	.24	1.19
6	19.36	.16	3.15
7	19.77	.25	-1.62
8	20.86	.29	-1.33
9	21.94	.09	4.25
10	22.69	.01	-1.39
11	22.88	.13	4.42
12	28.01	.20	-2.26
13	29.11	.01	.21
14	29.51	.01	.60
15	31.17	0	0
16	31.44	0	-.07
17	31.44	0	-.06
18	31.90	0	-.20
19	33.44	.43	6.35
20	34.57	.07	2.46
21	35.21	.08	2.75

659

As mentioned before, the kinetic energy distribution will be used as the basis for selecting the degree-of-freedom for the reduced model. For this particular mode, the kinetic energy is distributed with 36.20% in x-direction, 40.43% in y-direction and 22.15% in z-direction, a relatively uniform distribution. The degree-of-freedom with higher kinetic energy is indicated. Because of the relatively uniform distribution of kinetic energy, we conside this mode to be a global mode.

KINETIC ENERGY DISTRIBUTION FOR GLOBAL MODE

KINETIC ENERGY FOR MODE 7 JPL DATA

GRID	DOF	X	Y	Z	RX	RY	RZ	
119		0.0039	0.0018					0.0056
379		0.0020	0.0001	0.0008				0.0030
841		0.1195	0.0908	0.0000				0.2103
2130		0.0131	0.0177	0.0038				0.0346
2340		0.0219	0.0404	0.0008				0.0631
2530		0.0129	0.0187	0.0060				0.0377
2740		0.0289	0.0350	0.0011				0.0650
3075		0.0011	0.0012	0.0005				0.0027
3076		0.0007	0.0013	0.0006				0.0026
3160		0.0389	0.0524	0.0159	0.0001	0.0001	0.0000	0.1074
3260		0.0212	0.0288	0.0000	0.0001	0.0000	0.0000	0.0501
3360		0.0303	0.0397	0.0171	0.0001	0.0001	0.0000	0.0873
3460		0.0172	0.0250	0.0000	0.0001	0.0000	0.0000	0.0423
3550		0.0013	0.0016	0.0007				0.0037
3555		0.0008	0.0012	0.0034	0.0000			0.0054
3650		0.0014	0.0017	0.0006				0.0037
3665		0.0009	0.0015	0.0035	0.0000			0.0059
4123		0.0009	0.0007	0.0001				0.0017
4128		0.0013	0.0002	0.0011				0.0025
4235		0.0013	0.0001	0.0003				0.0017
4401		0.0000						0.0000
4418		0.0003	0.0033	0.0007	0.0000	0.0000		0.0043
5001		0.0035	0.0078	0.0040				0.0154
5004		0.0048	0.0000	0.0095				0.0144
5008		0.0045	0.0036	0.0042				0.0123
5009		0.0002	0.0001	0.0007				0.0010
5050				0.0011				0.0011
5052		0.0030		0.0011				0.0041
5072				0.0013				0.0013
5092		0.0019		0.0018				0.0037
5111		0.0019	0.0000	0.0046				0.0065
5112		0.0019	0.0006	0.0038				0.0063
5115		0.0035	0.0001	0.0056				0.0092
5604		0.0003	0.0000					0.0003
5610		0.0001	0.0000					0.0001
6002		0.0002		0.0001				0.0005
6003				0.0001				0.0001
6100		0.0002	0.0007	0.0013	0.0004	0.0000	0.0001	0.0026
6205				0.0004				0.0004
7050		0.0000	0.0001	0.0089	0.0006	0.0001	0.0000	0.0097
7550		0.0000	0.0001	0.1155	0.0002	0.0009	0.0000	0.1165
8050		0.0154	0.0200	0.0000	0.0032	0.0033	0.0000	0.0419
8060		0.0000	0.0000	0.0000	0.0000	0.0000		0.0001
8130		0.0005	0.0077	0.0002	0.0016	0.0010	0.0002	0.0112
9104		0.0000	0.0000					0.0000
9114		0.0000	0.0002					0.0003
9125		0.0002	0.0000					0.0002
9404		0.0000	0.0000					0.0000
9414		0.0000	0.0000					0.0000
9425		0.0000	0.0000					
		0.3620	0.4043	0.2215	0.0064	0.0056	0.0002	1.0000

661

For this mode, almost all the kinetic energy is concentrated at one degree-of-freedom which is a good indication for a local mode.

662

KINETIC ENERGY DISTRIBUTION FOR LOCAL MODE

JPL

KINETIC ENERGY FOR MODE 10 JPL DATA

GRID	DOF	X	Y	Z	RX	RY	RZ	
119		0.0000	0.0000					0.0000
379		0.0000	0.0000	0.0000				0.0000
841		0.0000	0.0000	0.0000				0.0000
2130		0.0000	0.0000	0.0000				0.0000
2340		0.0000	0.0001	0.0000				0.0001
2530		0.0000	0.0002	0.0000				0.0002
2740		0.0000	0.0001	0.0000				0.0001
3075		0.0000	0.0000	0.0000				0.0000
3076		0.0000	0.0000	0.0000				0.0000
3160		0.0000	0.0001	0.0001	0.0000	0.0000	0.0000	0.0001
3260		0.0002	0.0002	0.0000	0.0000	0.0000	0.0000	0.0004
3360		0.0000	0.0001	0.0002	0.0000	0.0000	0.0000	0.0003
3460		0.0001	0.0000	0.0000	0.0000	0.0000	0.0000	0.0001
3550		0.0000	0.0000	0.0000				0.0000
3555		0.0000	0.0001	0.0000	0.0000			0.0001
3650		0.0000	0.0000	0.0000				0.0000
3665		0.0000	0.0001	0.0000	0.0000			0.0001
4123		0.0000	0.0000	0.0000				0.0000
4128		0.0000	0.0000	0.0000				0.0000
4235		0.0000	0.0000	0.0000				0.0000
4401		0.0000						0.0000
4418		0.0000	0.0000	0.0000	0.0000	0.0000		0.0000
5001		0.0000	0.0000	0.0001				0.0001
5004		0.0000	0.0000	0.0005				0.0005
5008		0.0000	0.0000	0.0003				0.0003
5009		0.0000	0.0000	0.0001				0.0001
5050				0.0001				0.0001
5052		0.0000		0.0001				0.0001
5072				0.0001				0.0001
5092		0.0000		0.0001				0.0001
5111		0.0000	0.0000	0.0004				0.0004
5112		0.0000	0.0000	0.0004				0.0004
5115		0.0000	0.0000	0.0004				0.0004
5604		0.0000	0.0000					0.0000
5610		0.0000	0.0000					0.0000
6002		0.0006		0.0018				0.0024
6003				0.0015				0.0015
6100		0.0006	0.0002	0.0046	0.0012	0.0000	0.0004	0.0070
6205				0.9799				0.9799
7050		0.0000	0.0000	0.0000	0.0000	0.0000	0.0000	0.0000
7550		0.0000	0.0000	0.0000	0.0000	0.0000	0.0000	0.0000
8050		0.0000	0.0000	0.0000	0.0008	0.0000	0.0000	0.0008
8060		0.0000	0.0001	0.0000	0.0000	0.0000		0.0001
8130		0.0000	0.0036	0.0000	0.0000	0.0000	0.0000	0.0036
9104		0.0000	0.0000					0.0000
9114		0.0000	0.0000					0.0000
9125		0.0001	0.0000					0.0001
9404		0.0000	0.0000					0.0000
9414		0.0000	0.0000					0.0000
9425		0.0000	0.0000					
		0.0017	0.0050	0.9909	0.0020	0.0000	0.0004	1.0000

663

The degrees-of-freedom with more than 5.0% of kinetic energy in any of the important modes are retained for the reduced model, TAM. A total of 162 degrees-of-freedom are retained out of 10,000 degrees-of-freedom.

TAM PREDICTION

Mode	Frequencies (Hz)	Description
1	13.22	Global bending in X
2	13.44	Global bending in Y
3	16.93	Science boom in X
4	17.90	SXA in Y
5	18.89	SXA in X
6	19.92	-X RTG in Z
7	20.58	+X RGG in Z
8	21.46	Oxidizer 2 in X-Y
9	22.67	±X RTG in Z
10	23.62	Probe in Y
11	28.69	Science in Y
12	29.76	Damper and Science Boom in Y
13	30.26	SXA Local in X-Y
14	31.38	SXA Local in X
15	32.40	SXA Local in Y
16	32.69	Probe in X
17	33.15	Damper in X
18	34.26	Oxidizer in Z
19	36.06	Relay Antenna in Y
20	36.53	Thruster Boom in Y
21	37.35	Thruster Boom in Y

The results of the reduced model, TAM, are compared with those of the loads model. Excellent agreement is obtained. It is concluded that this systematic procedure for model reduction will provide a good representation for a large complex model.

FREQUENCY AND EFFECTIVE MASS COMPARIONS FOR TAM AND LOADS MODEL

	TAM		Loads Model		
Mode	Freq (Hz)	Eff. Mass (kg)	Mode	Freq (Hz)	Eff. Mass (kg)
1	13.22	796.0	1	13.23	786.2
2	13.44	840.0	2	13.50	841.0
3	16.93	142.5	3	16.94	143.4
4	17.90	858.0	4	17.99	852.0
5	18.89	291.0	5	18.98	281.0
6	19.92	293.0	6	19.93	298.0
7	20.58	391.1	7	20.39	395.8
8	21.46	6.0	8	21.47	10.1
9	22.67	120.2	9	22.60	176.2
10	23.62	394.0	10	23.54	391.1
11	28.69	344.6	11	28.84	360.3
13	30.26	15.9	13	30.34	16.6
18	34.26	1091.5	18	34.40	1043.8
23	37.69	55.1	19	35.56	17.1
19	36.06	345.2	20	36.18	176.2
22	37.33	5.9	21	36.76	25.1

WORKSHOP ON STRUCTURAL DYNAMICS AND
CONTROL INTERACTION OF FLEXIBLE STRUCTURES

National Aeronautics and
Space Administration

George C. Marshall Space Flight Center
Marshall Space Flight Center, Alabama 35812

L. P. Davis, J. F. Wilson
Sperry Corporation
Aerospace and Marine Group
Phoenix, Arizona 85036

R. E. Jewell
National Aeronautics and Space Administration
George C. Marshall Space Flight Center
Marshall Space Flight Center, Alabama 35812

April 22-24, 1986

ABSTRACT

The Hubble Space Telescope features the most exacting line of sight jitter requirement thus far imposed on a spacecraft pointing system. Consideration of the fine pointing requirements prompted an attempt to isolate the telescope from the low level vibration disturbances generated by the attitude control system reaction wheels. The primary goal was to provide isolation from axial component of wheel disturbance without compromising the control system bandwidth. At Sperry Corporation, a passive isolation system employing metal springs in parallel with viscous fluid dampers was designed, fabricated, and space qualified. Stiffness and damping characteristics are deterministic, controlled independently, and have been demonstrated to remain constant over at least five orders of input disturbance magnitude. The damping remained purely viscous even at the data collection threshold of $.16 \times 10^{-6}$ in input displacement, a level much lower than the anticipated Hubble Space Telescope disturbance amplitude. Vibration attenuation goals were obtained and ground test of the vehicle has demonstrated the isolators are transparent to the attitude control system.

INTRODUCTION

The Hubble Space Telescope (HST), shown in Figure 1, provides an optical image for five scientific instruments and three Fine Guidance Sensors. The vehicle is approximately 44 feet long and weighs 24,000 pounds. It is designed for STS insertion into a circular orbit of 320 NM for a 15-year mission. On-orbit maintenance and new technology upgrades during the mission are anticipated. To preclude the possibility of contamination of the optical elements no chemical reaction propulsion systems are onboard. Attitude control is provided by the Reaction Wheel Assemblies (RWAs) and the magnetic momentum control system. Reboost following orbital decay will be provided by the orbiter.

POINTING CONTROL SYSTEM

The primary elements of the Pointing Control System (PCS) used for fine pointing are the digital computer, reaction wheels, magnetic momentum system, rate gyro complement, and two of the Fine Guidance Sensors. Pointing torques are applied with the RWAs. The magnetic momentum system is used to desaturate the RWAs and minimize the wheel speed excursions. The four RWAs are positioned with their spin axes inclined at 20 degrees to the telescope optical axis as in Figure 2. Two RWAs provide torque along the pitch and roll axes and two provide torque along the yaw and roll axes. The array is thus redundant in that it can provide control at reduced capacity following the loss of any one RWA. Additional coarse pointing attitude information is available from fixed head star trackers and sun sensors. Finally, a backup control system with backup rate gyros is provided for increased mission reliability.
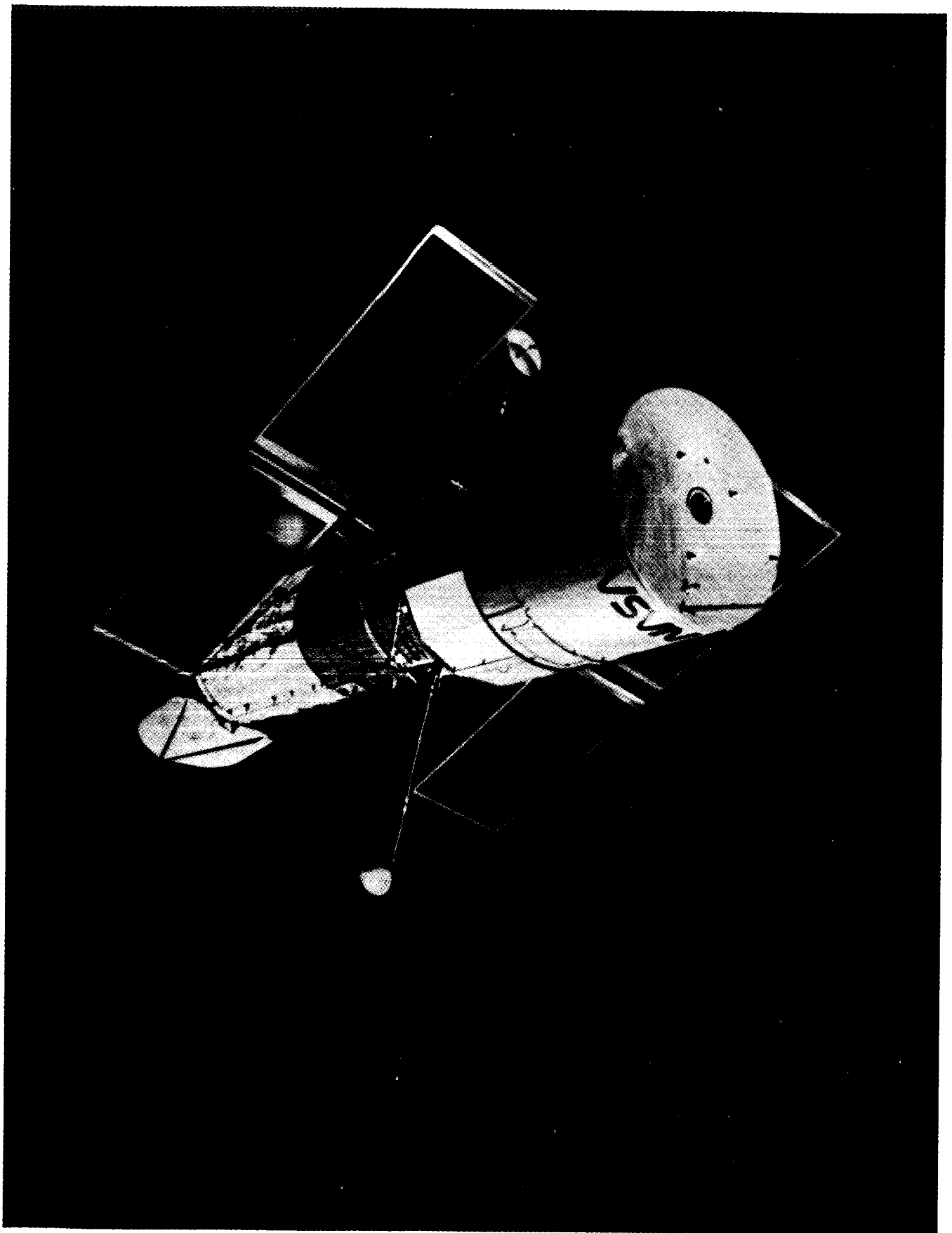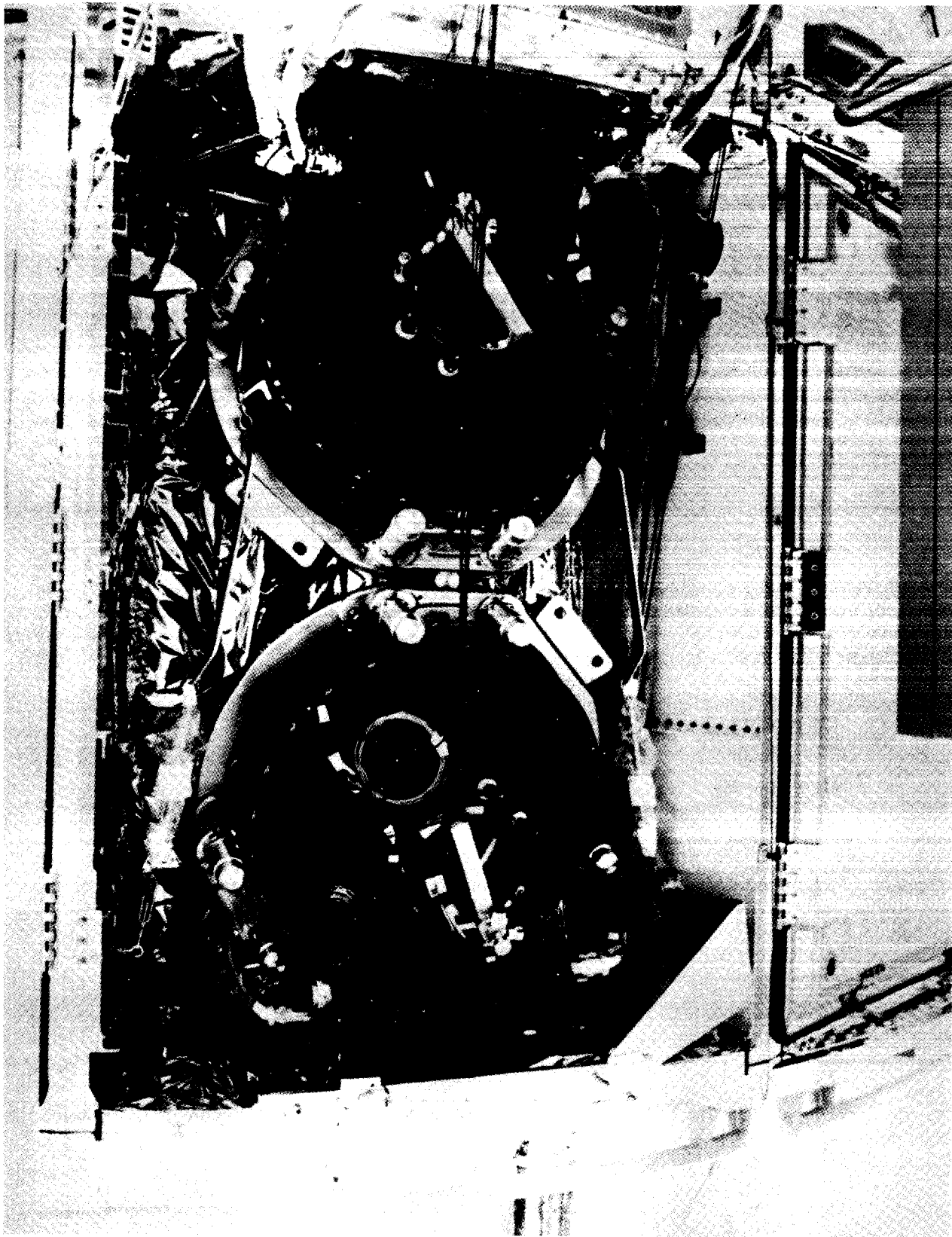
Figure 1

Figure 2

HST pointing accuracy and stability are defined in terms of Line Of Sight (LOS) error of the principal ray at the final imaging element, which includes the errors from all the optical elements in the path. Jitter predictions involve modeling of the disturbance sources, the HST structural transmissivities, and ray tracing between the various optical elements. The HST image stability requirement for periods up to 24 hours is .007 arcsec rms. This requirement is also to be maintained in any period as short as 10 seconds, which limits the averaging of short duration disturbances. The HST pointing repeatability requirement for periods up to 100 hours is .01 arcsec. Pointing performance of a satellite at these levels has not been previously obtained. LOS jitter sources include random sensor noise, coherent sources due to rotating machinery, thermal gradient effects, and residual transients due to recent large amplitude maneuvers. Since the RWAs are the most massive rotating machines onboard and must be operated continuously during science acquisition they received considerable attention in the jitter reduction effort. Jitter models indicated that the LOS was most sensitive to axial RWA disturbances owing to the vehicle configuration.

REACTION WHEEL INDUCED VIBRATION

An RWA produces vibration disturbances when it rotates due to imperfections in the electromagnetics and their drive electronics, unbalance of the rotor, and imperfections in the spin bearings. In the case of the HST RWA, the electromagnetics and electronics were designed to produce negligible disturbances relative to the latter sources. The rotors were balanced to the point that the unbalance was at least as small as and indistinguishable from disturbances due to geometric imperfections in the spin bearings. The bearing geometry disturbances occur at many harmonics of wheel speed, and balancing alters only the once per revolution harmonic, so further improvements in balance are unproductive. The bearing geometry disturbances were minimized through the use of bearings with nearly perfect geometry (equivalent of ABEC 9) and by selectively matching the bearings for lowest net disturbance. This procedure is thought to result in state-of-the-art vibration reduction.

Some of the lower frequency first order disturbances are shown in Figure 3. These are the maximum, average, and minimum force levels for the five flight RWAs and the engineering unit while running at 1500 rpm. Also shown is a table summarizing the sources of these harmonics. In the HST bearing the ball groups rotate .35 times as fast as the rotor so harmonics of 1.0, .35 and their difference occur.

In Figure 4 measured data is shown for the axial force at once per revolution as wheel speed is varied from 0 to 3000 rpm. Also shown is the least square curve fit to the data based on the assumption that force is proportional to the square of wheel speed. A similar correlation with wheel speed squared is found for other harmonics at frequencies below the first resonance of the RWA and test fixture. This correlation suggests that at low frequency the disturbances have the form $f = M\Delta(NW)^2$ where f is the disturbance force, M is the mass of the rotor, Δ is the geometrical runout in the bearing, N is the harmonic number, and W is the wheel speed. Using this assumption, Δ for each harmonic may be determined in the least square sense. This was done for the flight units and is tabulated in Figure 4. Since the predicted geometry errors are within the bearing specification and are not practically measurable this model of the bearing disturbance was accepted.

C - 8

BALL
BEARING
DISTURBANCES

- 0.35 HARMONIC (BALL RETAINER)
- 1.0 HARMONIC (MASS UNBALANCE)
- 2.0 HARMONIC (RACE TO RACE MISALIGNMENT)
- 2.8 HARMONIC (OUTER RACE DEFECTS)
- 5.2 HARMONIC (INNER RACE DEFECTS)
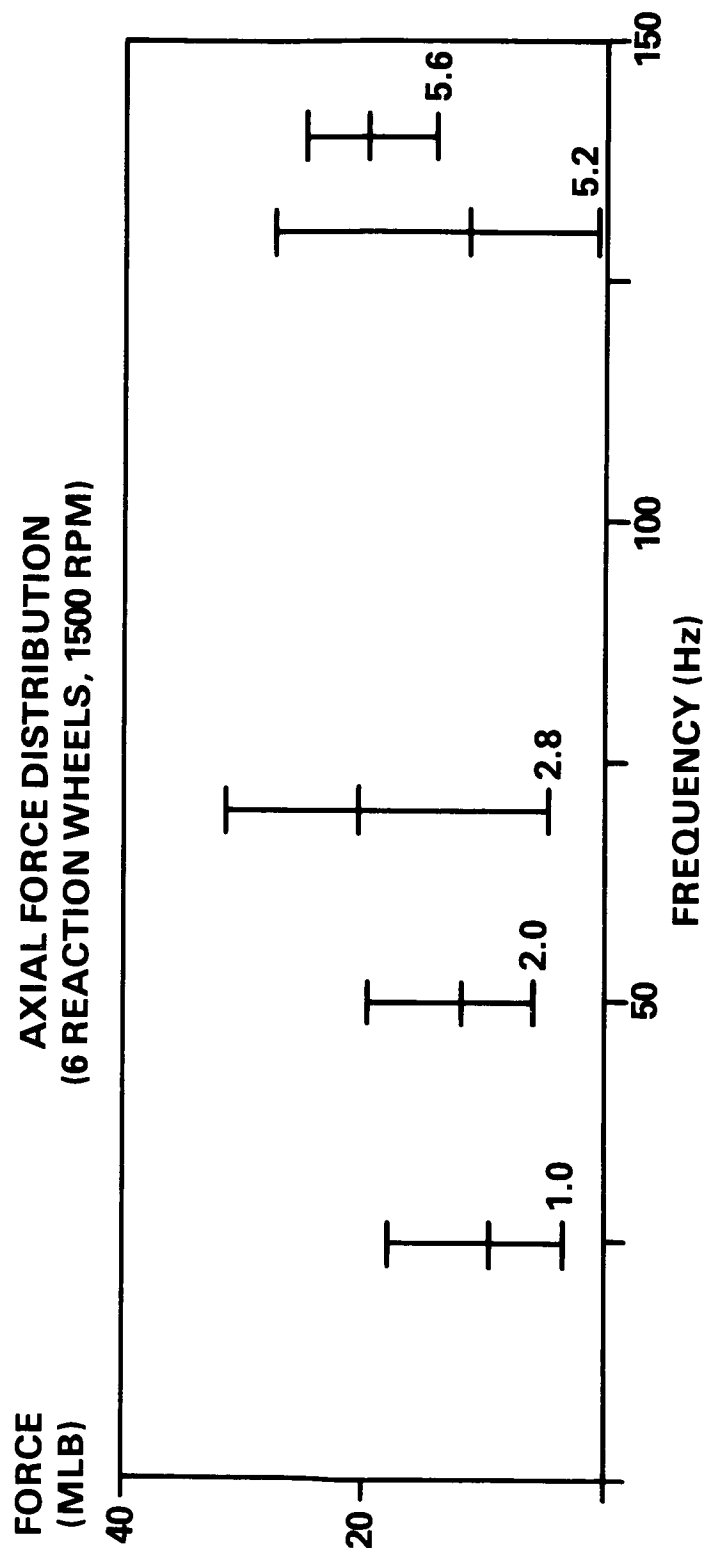- 5.6 HARMONIC (OUTER RACE DEFECTS)

AXIAL FORCE DISTRIBUTION
(6 REACTION WHEELS, 1500 RPM)

Figure 3

1g Hardmount Axial
1.0 Component

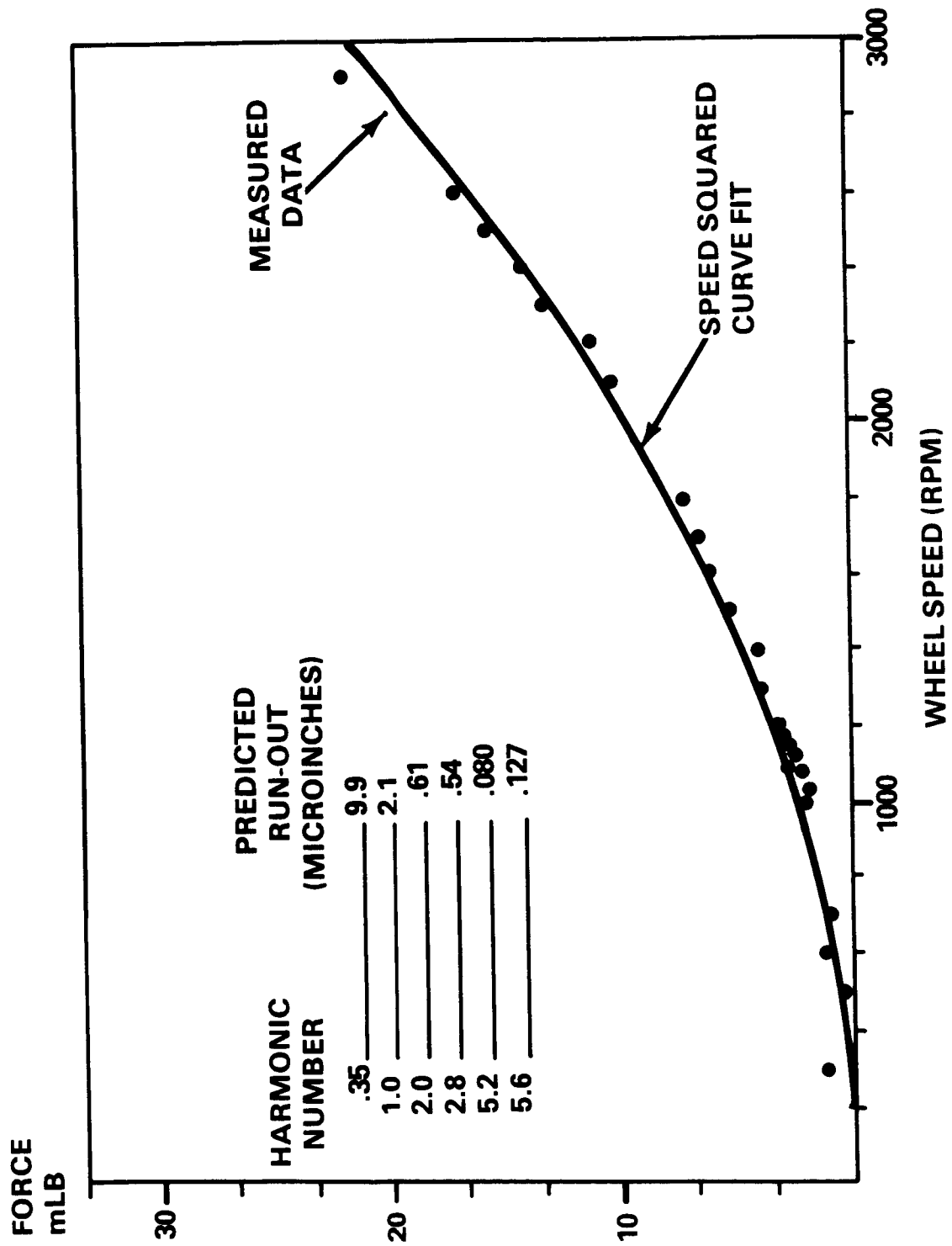| HARMONIC NUMBER	PREDICTED RUN-OUT (MICROINCHES)
.35	9.9
1.0	2.1
2.0	.61
2.8	.54
5.2	.080
5.6	.127

FORCE mLB

MEASURED DATA

SPEED SQUARED CURVE FIT

WHEEL SPEED (RPM)

Figure 4

The nature of the RWA vibration disturbances is that there are many harmonics, sweeping a wide frequency range as wheel speed is run up and down, with amplitudes increasing as the square of speed. LOS jitter models predicted marginal performance due to axial disturbances at the higher wheel speeds above 10 Hz (600 RPM) so passive isolation of the RWAs was a logical approach. Initial evaluations were made with wire rope isolators. The PSD of acceleration response due to force input for this isolator is shown in Figure 5. The input force level was varied from .0045 to .750 pound. The transfer function is nonlinear in stiffness and damping as a function of disturbance amplitude. Both these tendencies are explained to the first order by the loss of sliding friction in the wire rope as the amplitude is reduced. These nonlinearities make accurate modeling of the isolator very difficult. An additional drawback is the lack of strict determinism in the design of the stiffness and damping properties since these characteristics cannot be independently controlled.

These difficulties led to the development of the viscous fluid damped isolator shown in Figure 6. A simplified schematic and a cutaway of the flight design are shown. In the dual chamber schematic damping fluid is contained by two metal bellows supporting the center isolated portion. When the center portion moves axially fluid must flow from one bellows chamber to the other, incurring viscous losses as it flows. The damping value is determined by the viscosity of the fluid and the dimensions of the annular passage between the chambers. The stiffness is determined by the bellows design. These characteristics are deterministic and independent. For radial motion the stiffness is also deterministic although the damping is less so due to the complex flow. The flight design works on the same principal but acquired additional complexity. Coil springs were added in parallel with the bellows which effectively determine the spring rates. A third preloaded bellows chamber was added outboard to accommodate thermal expansion of the fluid. Mechanical stops were built in to limit maximum displacements and a redundant leak-proof seal was added to minimize the chance of fluid escape.

The equivalent lumped mass model and its theoretical transfer function were determined from volume balance equations for the three chambers. Finite element models of the metal parts gave translational and volumetric spring rates. The fluid contributions taken into account were its bulk modulus and viscous loss in the damping chamber. The isolator was assumed to be massless for this model. The equivalent lumped mass model and its theoretical transfer function are shown in Figure 7. It may be seen from the transfer function that high frequency roll-off takes place with a slope of two rather than one as with a simple parallel spring and dashpot. Physically, this is because high frequency motion can be accommodated by volumetric changes in the chambers with no corresponding flow through the damping chamber and hence very low damping. The double peak in the transfer function occurs because with very low damping only k1 is effective whereas with very high damping k1 acts in parallel with the series combination of k2 and k3. The PSD of axial acceleration at various force levels for the viscous isolator are shown in Figure 8. Both stiffness and damping are constant for the range of input considered. Transfer function tests down to the lowest threshold input attainable (.16 μ in.) indicated linear behavior. The damping properties of the isolator and the internal fluid pressure are a function of temperature. The pressure variation is controlled by the design of the thermal compensation bellows. A positive pressure margin is maintained to prevent
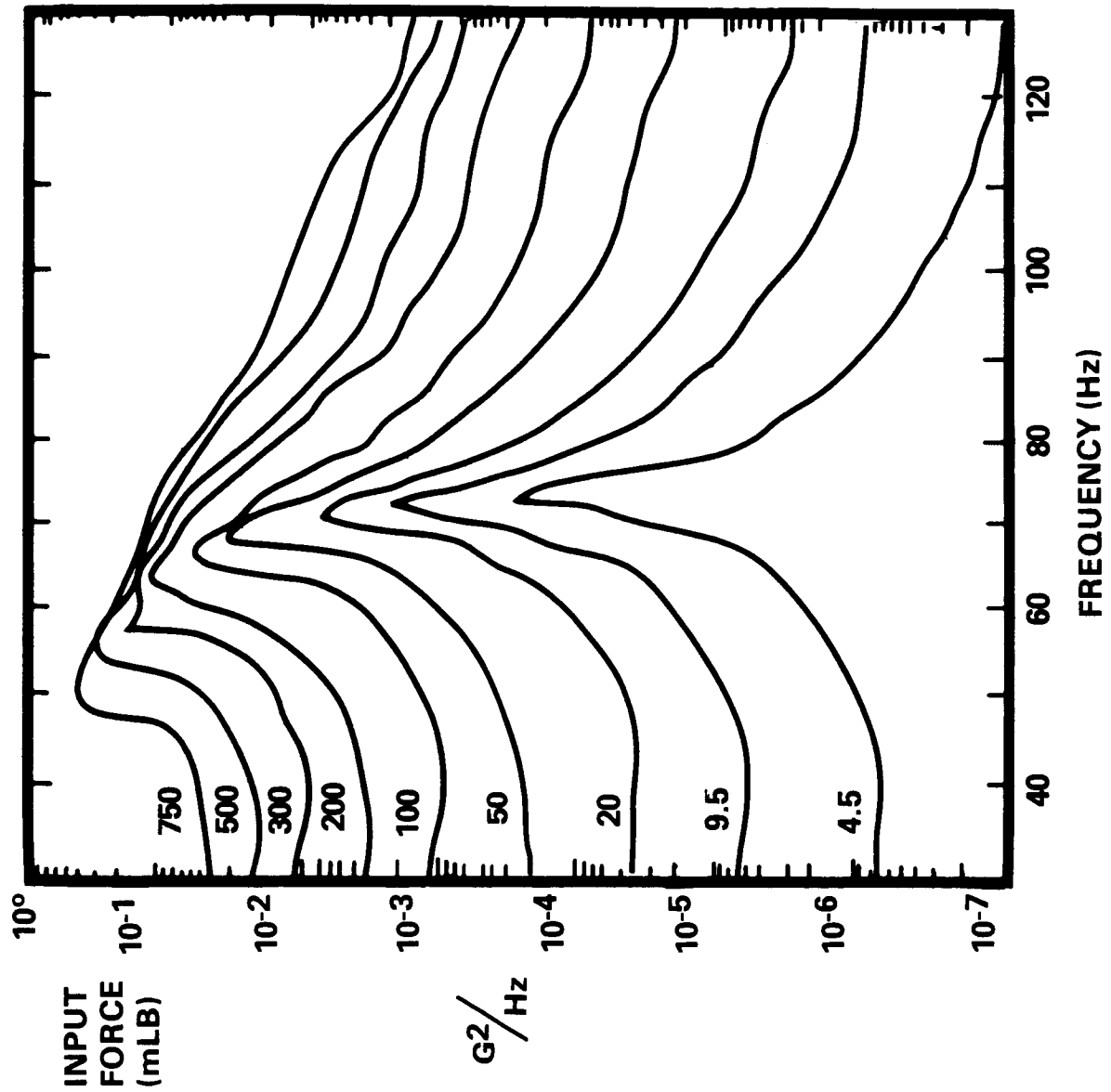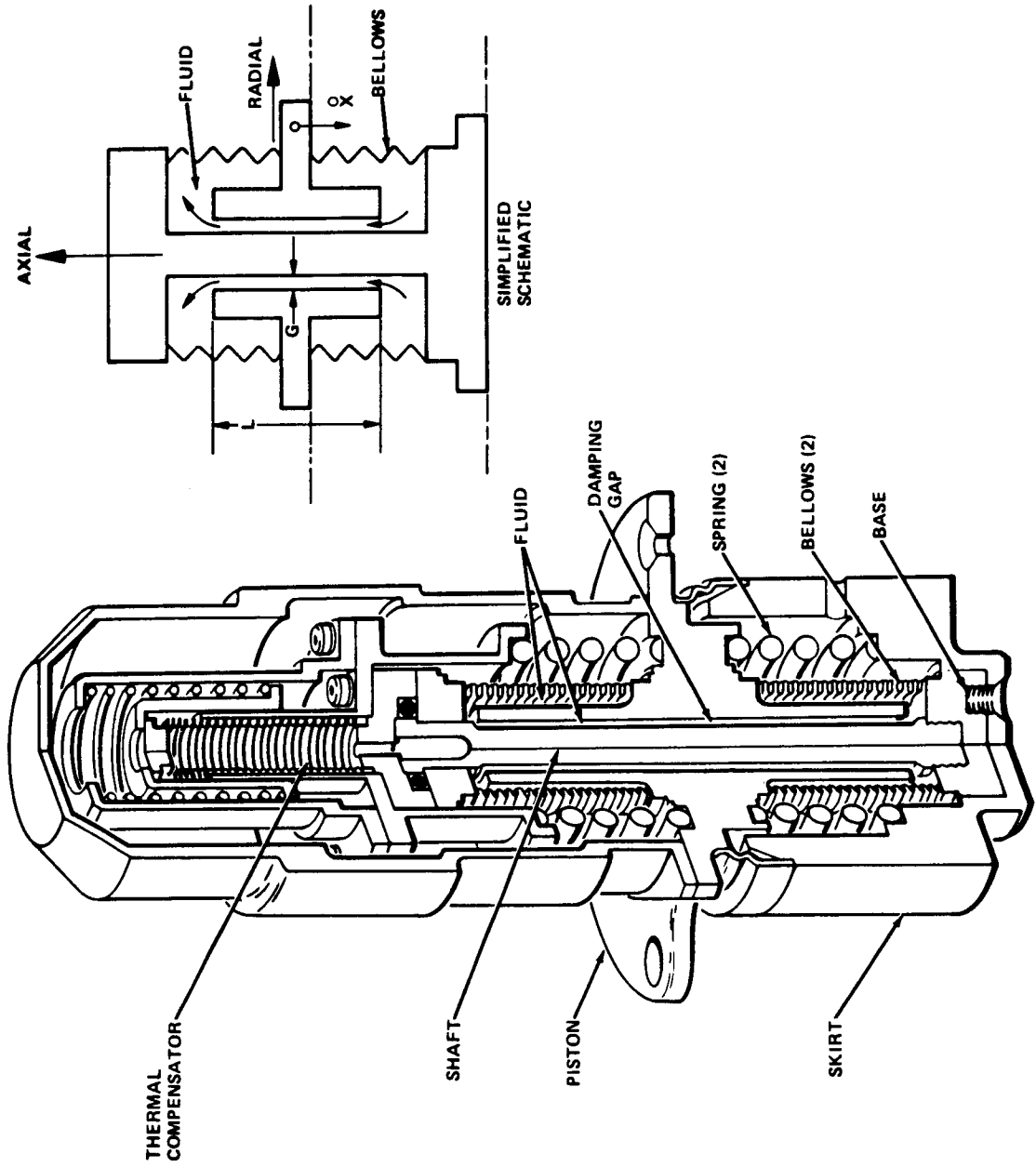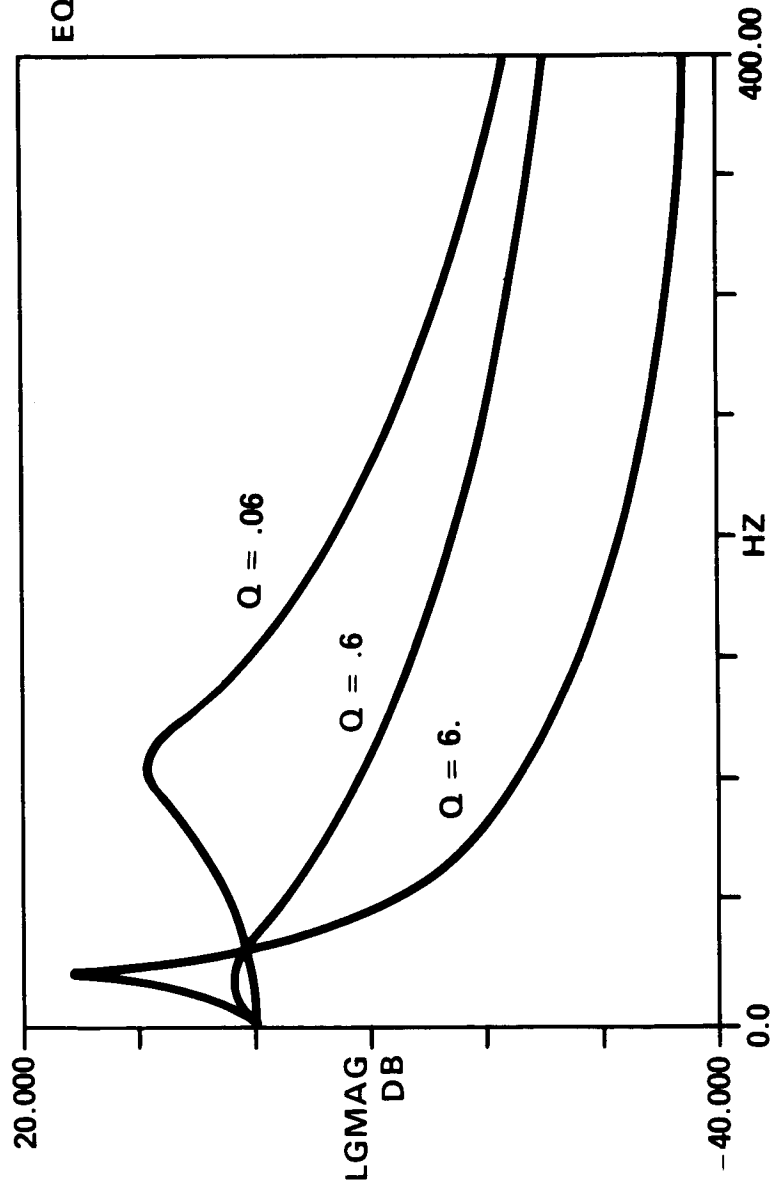
Wire Rope Isolator PSD

FREQUENCY (Hz)

Figure 5

677

Unit Isolator

THERMAL COMPENSATOR

SHAFT

PISTON

SKIRT

FLUID

DAMPING GAP

SPRING (2)

BELLOWS (2)
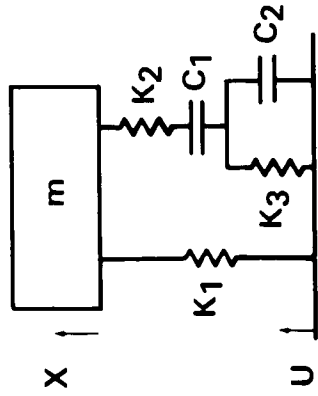
BASE

FLUID

RADIAL

X

BELLOWS

AXIAL

G

L

SIMPLIFIED SCHEMATIC

Figure 6

Theoretical Isolator Transfer Function

$$T = \cfrac{1 + \left(\cfrac{MN + LN + M + N}{MNQ}\right)\left(\cfrac{s}{P}\right) + \left(\cfrac{NMQ^2 + L(N+1)}{NMQ^2}\right)\left(\cfrac{s}{P}\right)^2 + \cfrac{L(N+1)}{NMQ^2}\left(\cfrac{s}{P}\right)^2}{1 + \left(\cfrac{MN + LN + M + N}{MNQ}\right)\left(\cfrac{s}{P}\right)\left(\left(\cfrac{MN + LN + M + N}{MNQ}\right)\left(\cfrac{s}{P}\right) + \cfrac{L(N+1)}{NMQ^2}\left(\cfrac{s}{P}\right)^2\right) + \left(\cfrac{LN + M + N}{NMQ}\right)\left(\cfrac{s}{P}\right)^3 + \cfrac{L}{NMQ^2}\left(\cfrac{s}{P}\right)^4}$$

EQUIVALENT LUMPED MASS MODEL

T = X/U
N = K₂/K₁
M = K₃/K₁
L = C₂/C₁
Q = √(K₁m/c₁)
P = √(K₁m/c₁)

$T = X/U$
$N = K_2/K_1$
$M = K_3/K_1$
$L = C_2/C_1$
$Q = \sqrt{K_1 m / c_1}$
$P = \sqrt{K_1 m / c_1}$

Q = .06
Q = .6
Q = 6.

LGMAG DB
20.000
-40.000
0.0
400.00
HZ

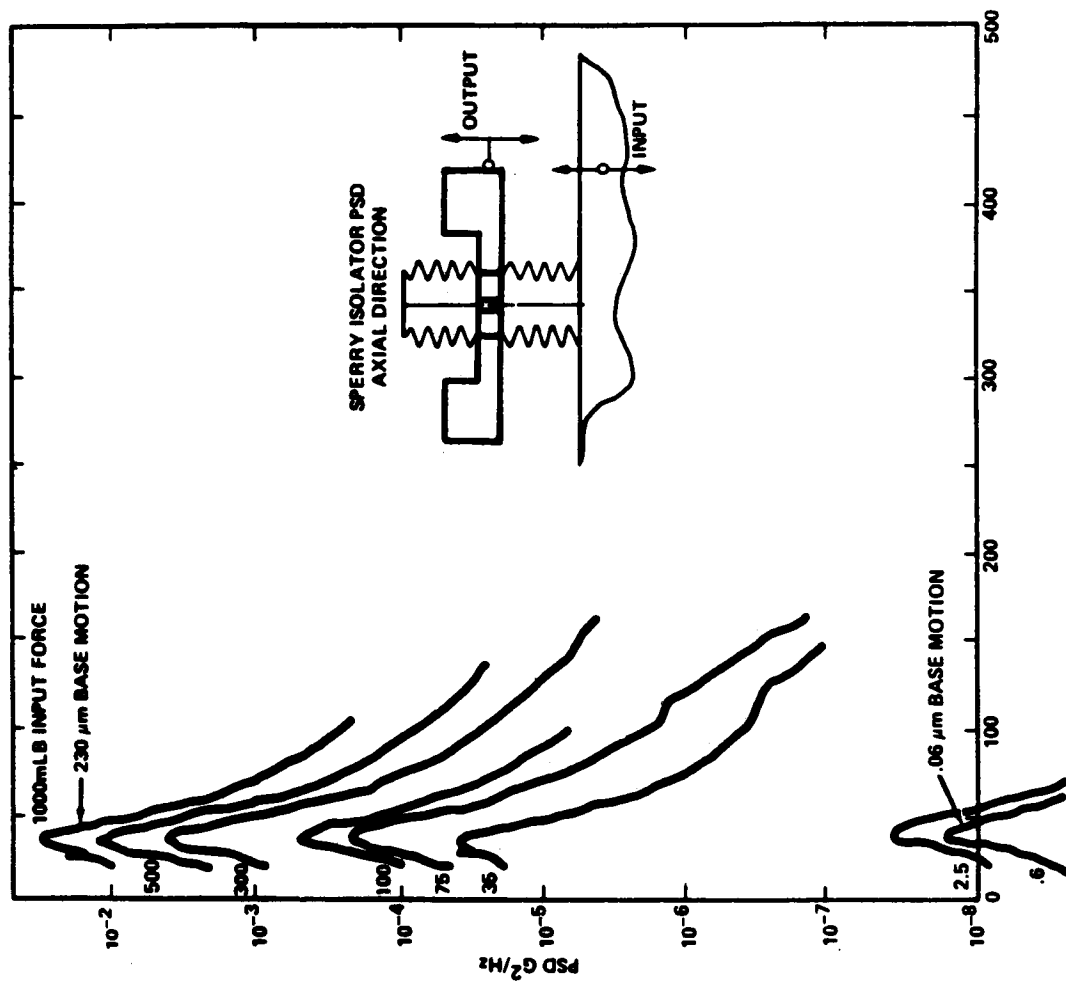Figure 7

Axial Displacement Power Spectral Density

Figure 8

cavitation in the isolator. The variation in damping was deemed acceptable from a dynamic standpoint. An HST RWA mounted on an isolation system is shown in Figure 9. Three sets of two rigidly coupled isolator units are used to support the RWA at three points. For this application, the isolators are aligned for maximum damping in the axial direction. The structural attachments have been designed for on-orbit replacement of the isolation system, RWA, or RWA plus isolation system.

COMPONENT VIBRATION CHARACTERIZATION

The test configuration for characterizing RWAs and isolation systems is shown in Figure 10. The RWA is mounted to a holding fixture through the isolators. The holding fixture is mounted to a large isolation mass through very stiff piezoelectric load cells. The holding fixture is supported by low friction gas bearings to ensure that the preponderance of force transmitted to the isolation block passes through the load cells. Summing networks permit measurements of forces and torques. The holding fixture can be rotated 90 degrees to measure axial or radial disturbances. Radial force measured during a wheel speed rundown without isolation is shown in Figure 11. This plot is a composite of force spectra taken at 16 second intervals during a 1600 second RWA rundown from 3000 rpm to zero wheel speed. The RWA was back-driven with constant torque so the wheel speed varied linearly. In the plot, harmonic disturbances occur at linearly varying frequencies whereas resonances in the RWA and test fixture occur at constant frequency. Peaking occurs where the two coincide. A resonance is evident around 105 Hz. A similar rundown plot for axial force is shown in Figure 12. The peak axial force recorded during the rundown was 3.390 pounds, when the 2X harmonic passed through a resonance at 80 Hz. An axial rundown with the wire rope isolators installed is given in Figure 13. Resonances from 20 to 50 Hz are present. The peak force recorded was .248 pound when the 1X harmonic passed through a resonance near 50 Hz. The ratios of these peaks are not a measure of the isolator attenuation but reflect the ratio of the Q of the RWA at its resonance to the Q of the isolator at its resonance, and also the square of the frequency ratio since force is proportional to speed squared. An axial rundown is plotted in Figure 14 for the Sperry viscous isolator with 200 centistoke damping fluid. An axial resonance lies at 20 Hz and a peak force of .053 pound was measured when the 1X harmonic crossed it. Again the ratio of the peak forces reflects the ratio of the Qs and speeds squared rather than isolator attenuation. When 350 centistoke fluid is used, the peak force is .025 pound. The difference in transmitted energy with and without isolation is dramatic. The LOS jitter predictions show a similar level of improvement with the isolation system.

The HST in dynamic test configuration is shown in Figure 15. It is suspended by three cables from air bags to simulate zero g conditions. The transfer function of vehicle angle response to control system torque was measured with RWAs isolated and nonisolated. The isolators did not alter the transfer characteristic. Figure 16 shows a close-up of the isolators in the test vehicle.
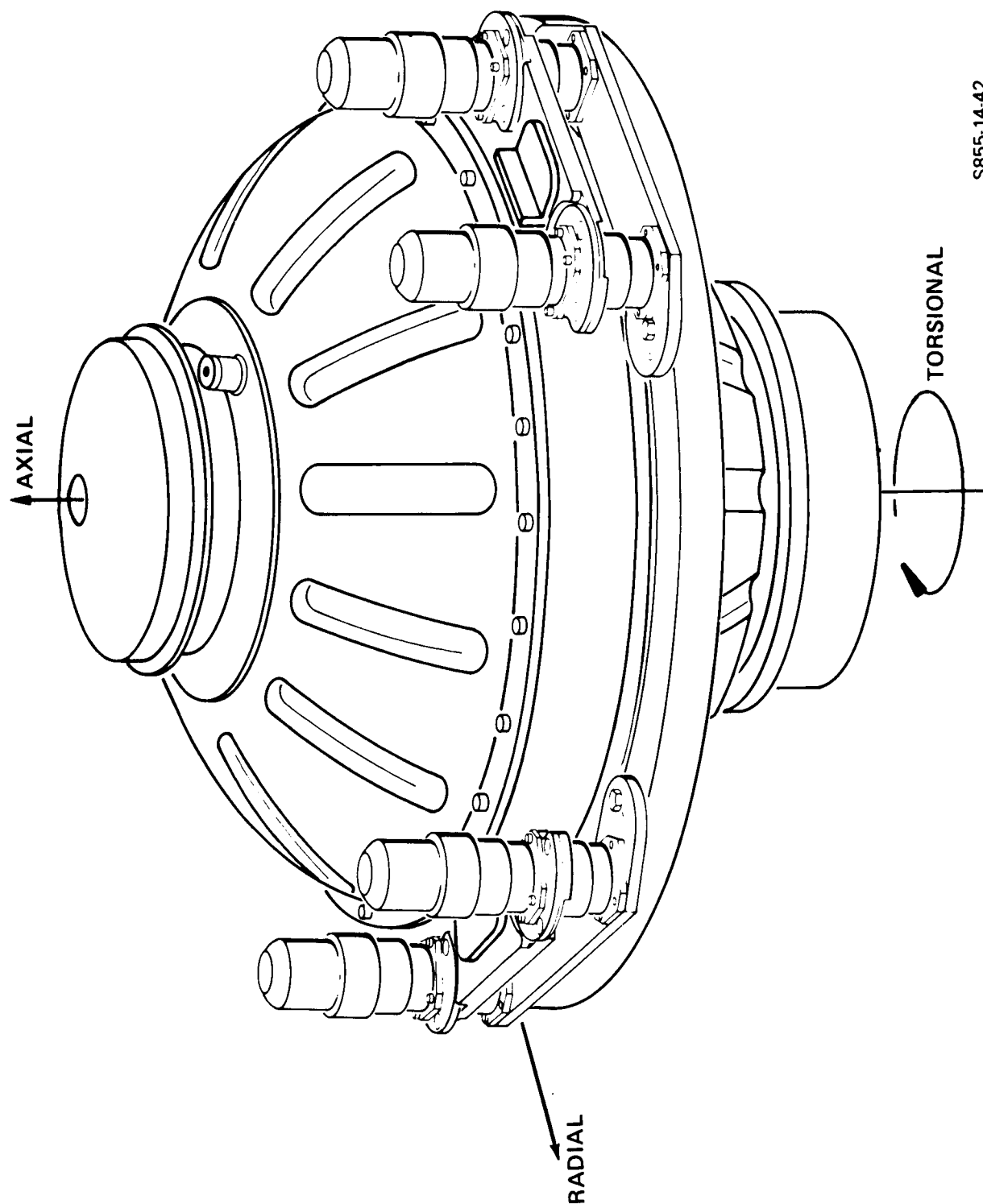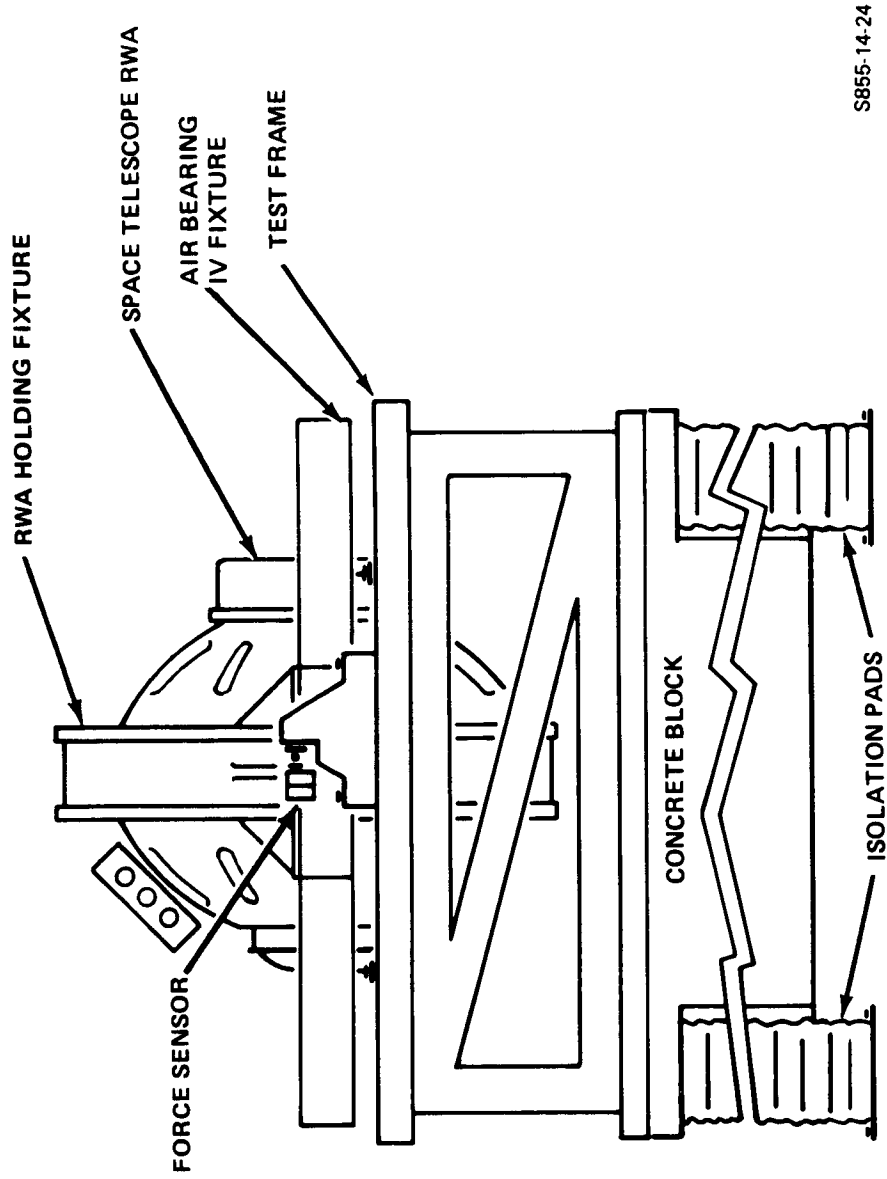
RWA on Isolation System

AXIAL

RADIAL

TORSIONAL

S855-14-42

Figure 9

682

Induced Vibration Measurement System

RWA HOLDING FIXTURE

SPACE TELESCOPE RWA

AIR BEARING
IV FIXTURE

TEST FRAME

FORCE SENSOR

CONCRETE BLOCK

ISOLATION PADS

S855-14-24

Figure 10

683

HARD MOUNTED
REACTION WHEEL RADIAL FORCE
(.782 LB PEAK)
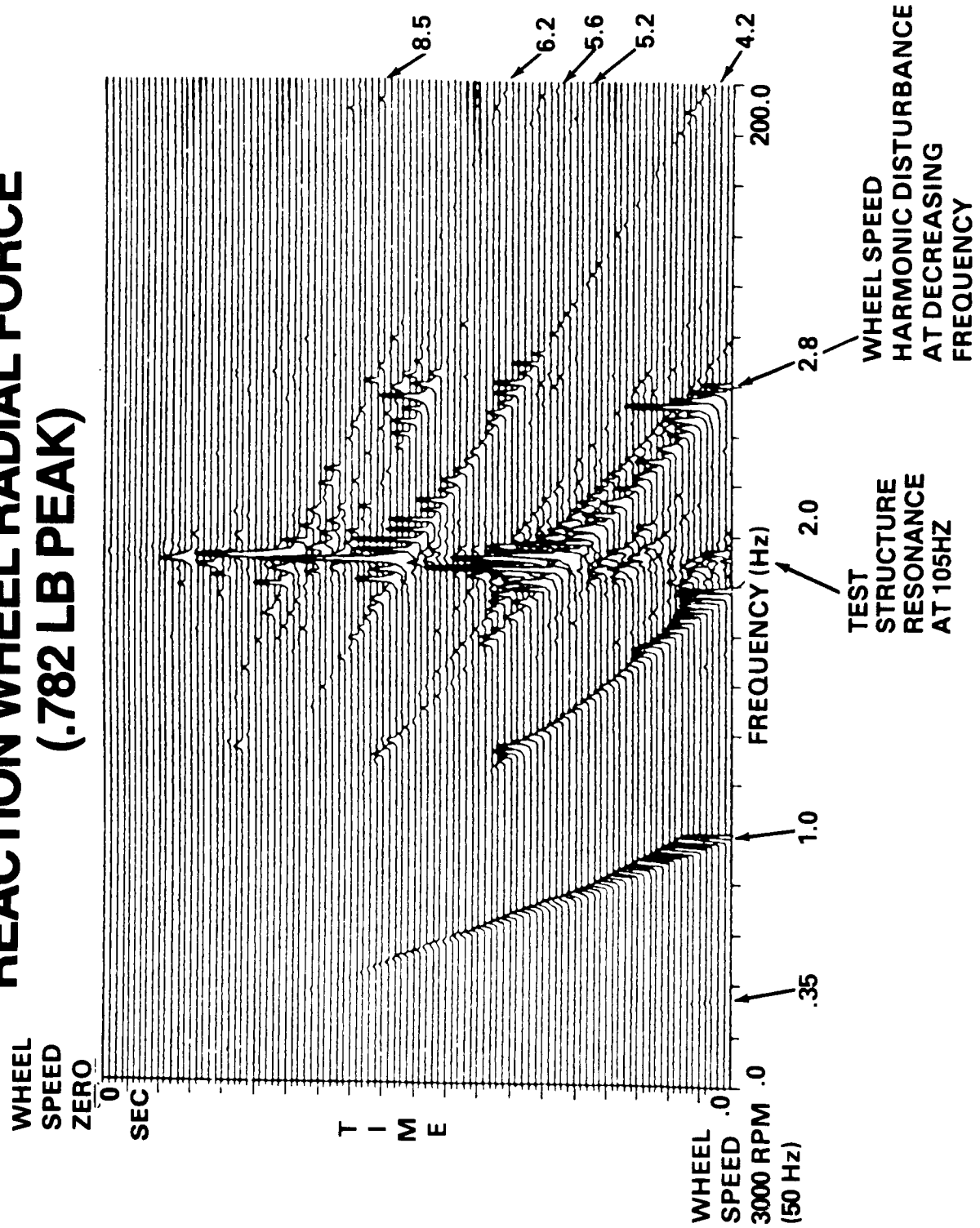
Figure 11

HARD MOUNTED
REACTION WHEEL AXIAL FORCE
(3.39 LB PEAK)
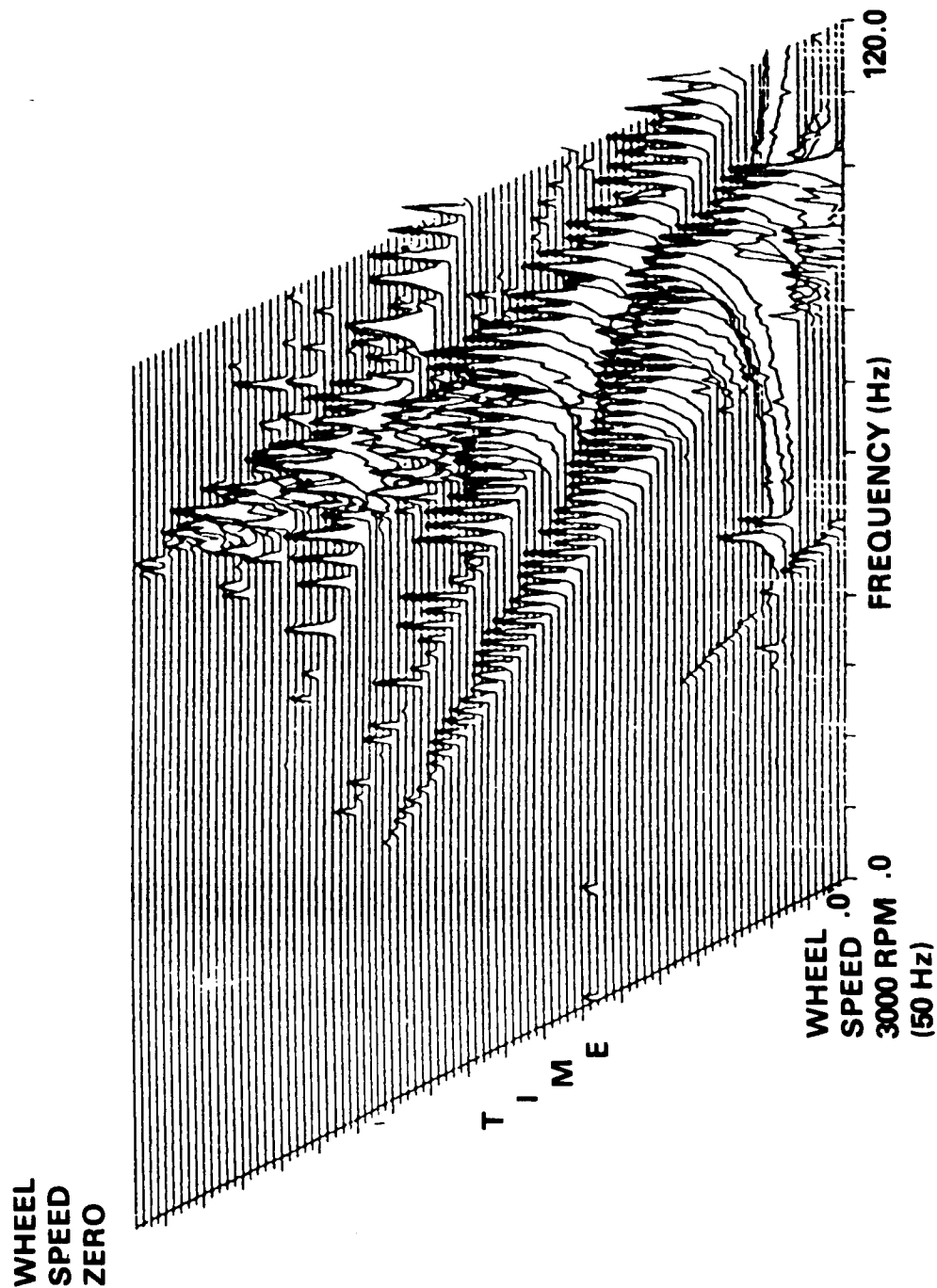
Figure 12

ISOLATED
(WIRE ROPE ISOLATOR)
REACTION WHEEL AXIAL FORCE
(.284 LB PEAK)
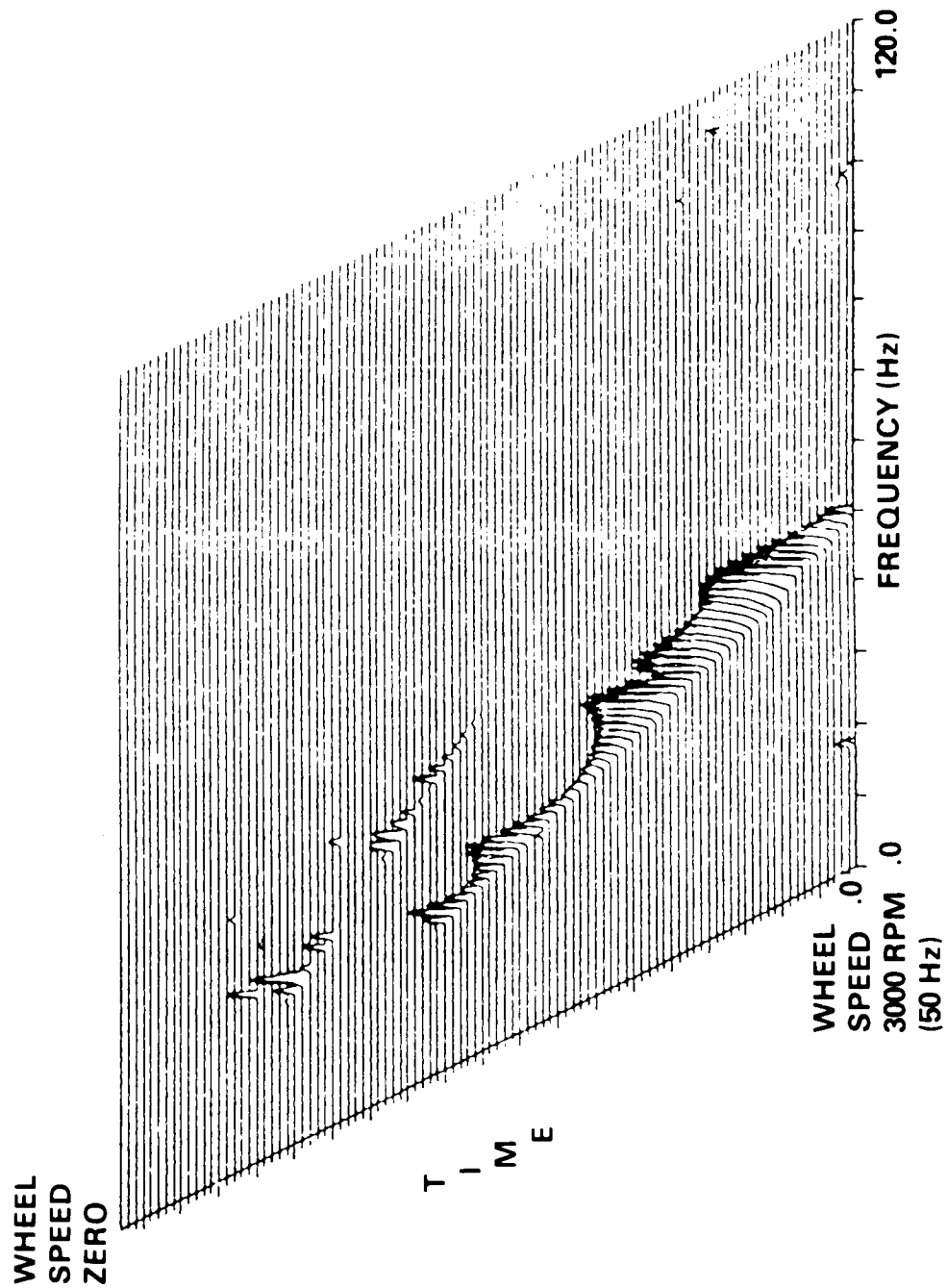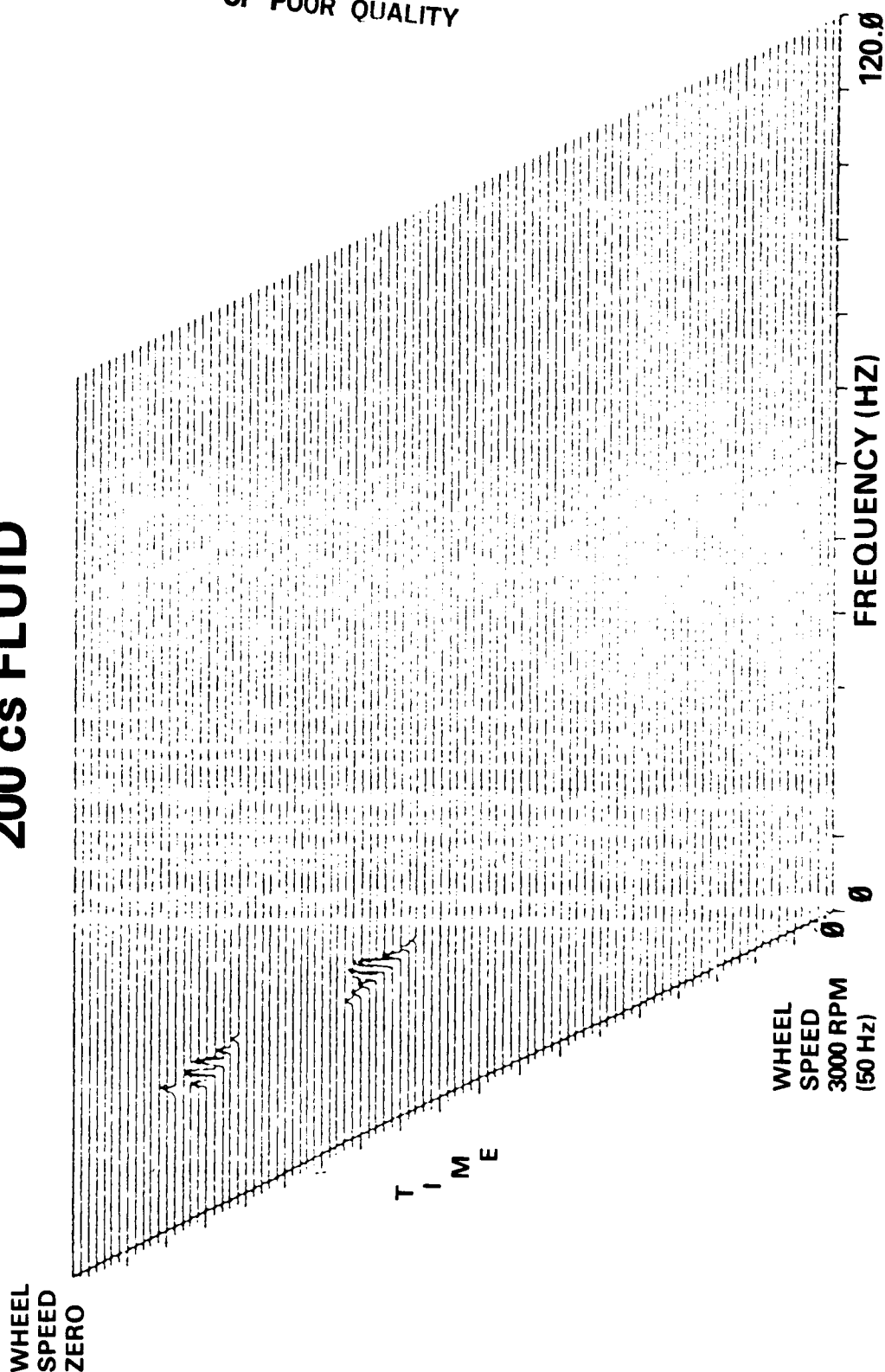

Figure 13

ISOLATED
(SPERRY VISCOUS ISOLATOR)
REACTION SHEEL AXIAL FORCE
(.052 LB PEAK)
200 cs FLUID

Figure 14

687

SUMMARY

The Hubble Space Telescope is a spacecraft with unique sensitivity to vibration disturbances. Its Reaction Wheel Assemblies cause coherent frequency disturbances in the millipound range. There are many harmonics of wheel speed and the disturbances are proportional to the square of wheel speed. A passive isolation system was developed to attenuate the higher frequency disturbances. The isolators utilize a metal spring in parallel with a viscous fluid damper, providing independent, deterministic control of the stiffness and damping characteristics. Second order roll-off of the transfer characteristic is obtained due to the volumetric spring rate of the isolator. Stiffness and damping were found constant over a disturbance amplitude range from $.2 \times 10^{-6}$ to .04 inch of input amplitude. Damping is a function of temperature but for this application no compensation was required. The design has been space qualified and subjected to four times life fatigue testing. Component testing has demonstrated greater than two orders of magnitude reduction in peak axial force transmitted by an RWA. Ground testing has been conducted with the spacecraft suspended by cables from three air bags. Frequency response measurements of vehicle angle due to torque commanded have verified the flexibility of the isolators does not compromise the attitude control loop.
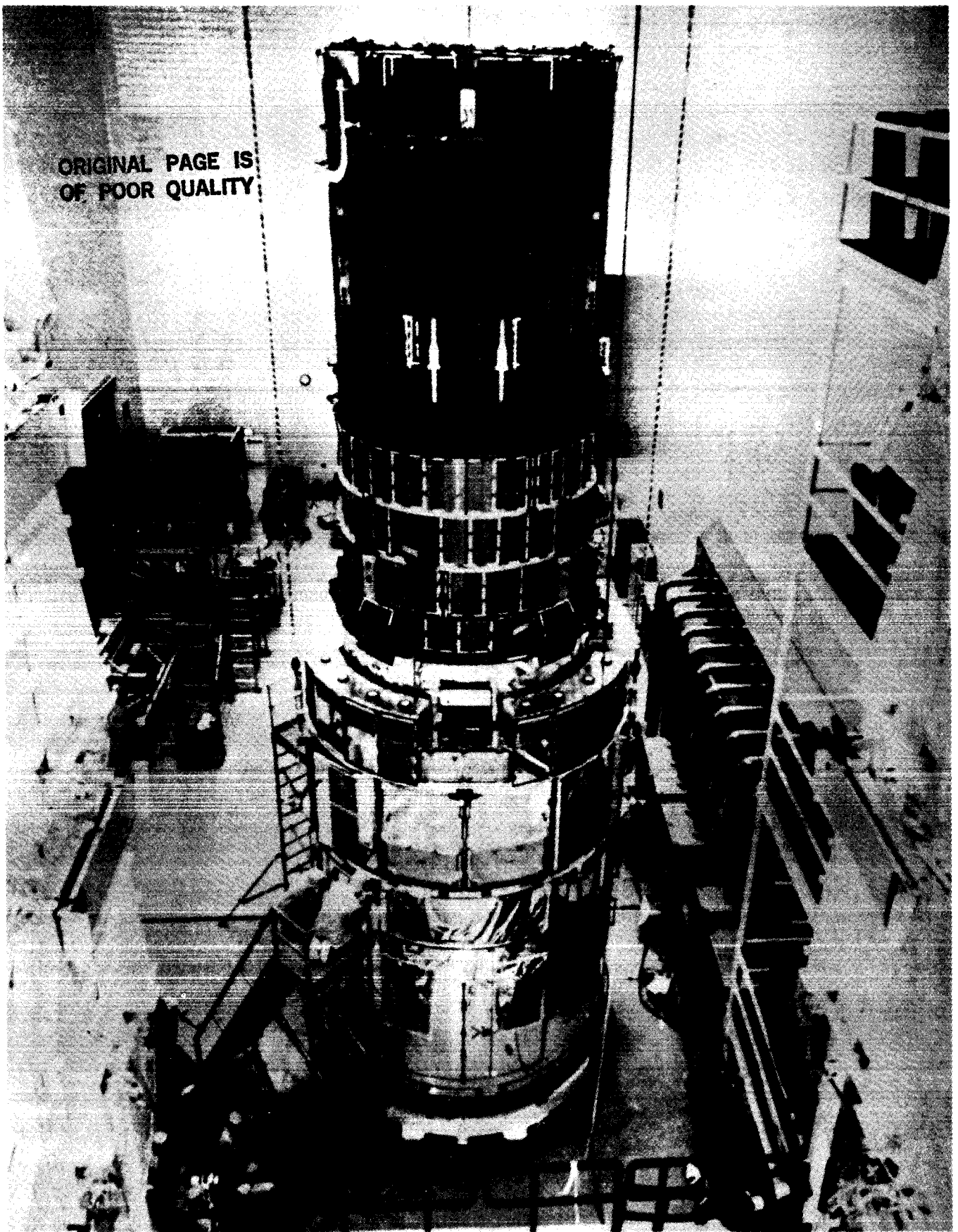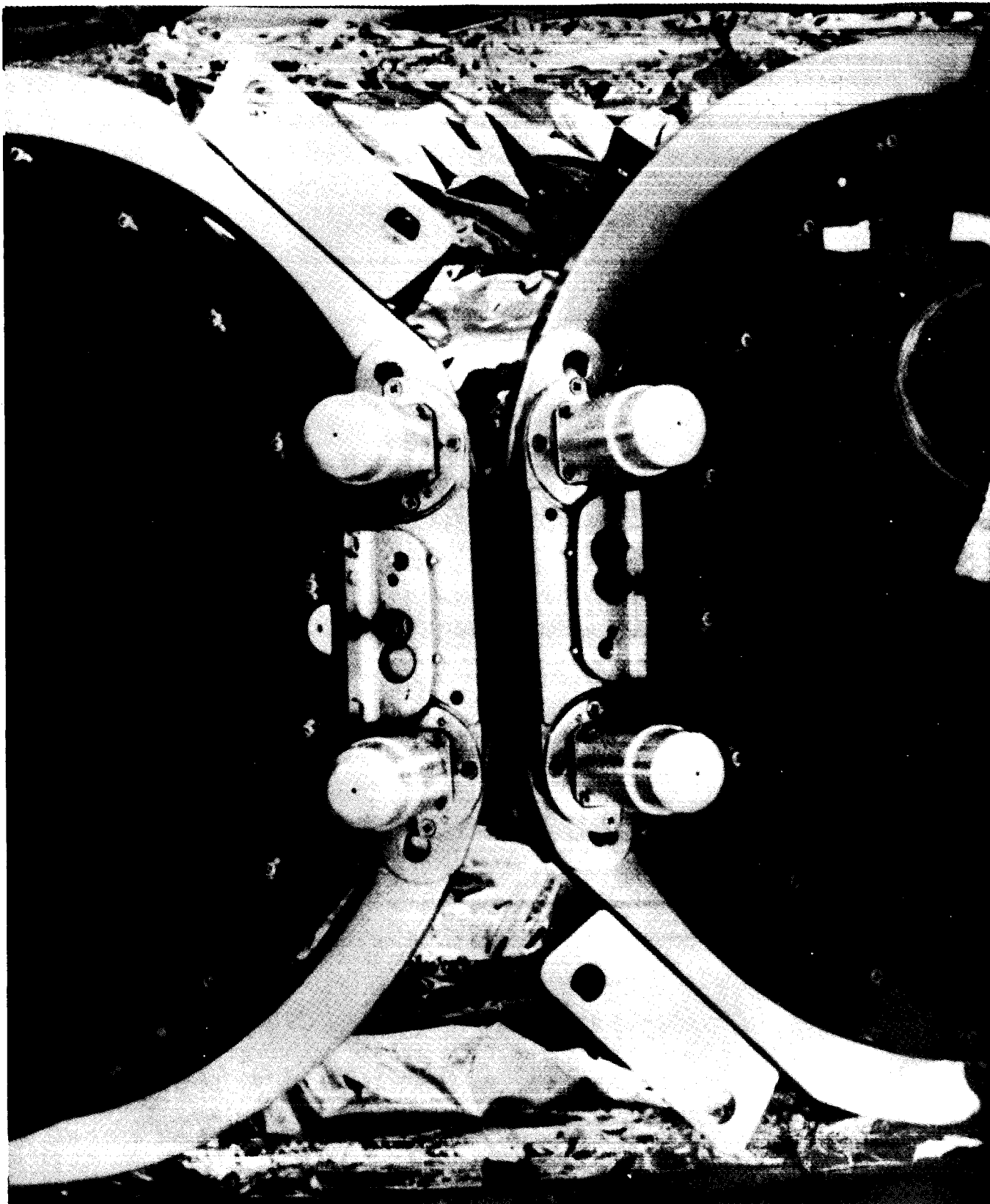
Figure 15

Figure 16

690

April 23, 1986 (Concurrent Sessions on Structures and Control)

Control Session 3A - George B. Doane, III, Chairman

Stiffness Control for Active Damping	J. L. Fanson and J. C. Chen, Jr.
A Quasi-Analytical Method for Non-Iterative Computation of Nonlinear Controls	J. L. Junkins and R. C. Thompson, Texas A&M; J. D. Turner, Cambridge Research
Decentralized Control of Large Space Structures via the GHR	D. K. Lindner, VPI
Control of Flexible Structures and the Research Community	J. S. Pyle and C. R. Keckler, LaRC

Control Session 3B - Robert Skelton, Chairman

Impact of Space Station Appendage Vibrations on the Pointing Performance of Gimballed Payloads	R. Hughes, GE
Maneuvering and Vibration Control of Flexible Spacecraft	L. Meirovitch and R. D. Quinn, VPI
Hubble Space Telescope Disturbances Caused by High Gain Antenna Motions	J. P. Sharkey, MSFC
Preliminary Evaluation of a Reaction Control System for the Space Station	H. H. Woo and J. Finley, RI/SD

This set of viewgraphs presents some of the results of research on control of flexible structures carried out at the California Institute of Technology and the Jet Propulsion Laboratory. This particular work has been underway since the fall of 1983. The research is supported by the JPL Director's Discretionary Fund, the NASA Graduate Student Researchers Program, and the NASA Office of Aeronautics and Space Technology. James Fanson is a graduate student in Applied Mechanics at Caltech, Thomas Caughey is Professor of Applied Mechanics at Caltech, and Jay-Chung Chen is a Member of the Technical Staff at the Jet Propulsion Laboratory.

692

1. REPORT NO. NASA CP-2467, Part 1	2. GOVERNMENT ACCESSION NO.	3. RECIPIENT'S CATALOG NO.
4. TITLE AND SUBTITLE Structural Dynamics and Control Interaction of Flexible Structures		5. REPORT DATE April 1987
		6. PERFORMING ORGANIZATION CODE
7. AUTHOR(S) Edited by Robert S. Ryan and Harold N. Scofield		8. PERFORMING ORGANIZATION REPORT #
9. PERFORMING ORGANIZATION NAME AND ADDRESS George C. Marshall Space Flight Center Marshall Space Flight Center, Alabama 35812		10. WORK UNIT NO. M-554
		11. CONTRACT OR GRANT NO.
		13. TYPE OF REPORT & PERIOD COVERED
12. SPONSORING AGENCY NAME AND ADDRESS National Aeronautics and Space Administration Washington, D.C. 20546		Conference Publication
		14. SPONSORING AGENCY CODE

15. SUPPLEMENTARY NOTES

16. ABSTRACT

A Workshop on Structural Dynamics and Control Interaction of Flexible Structures was held at the Marshall Space Flight Center to promote technical exchange between the structural dynamics and control disciplines, foster joint technology, and provide a forum for discussing and focusing critical issues in the separate and combined areas. This workshop was attended by approximately 150 people from Government, industry, and universities. This document contains all the papers presented. The workshop was closed by a panel meeting. Panel members' viewpoints and their responses to questions are included.

17. KEY WORDS Structural/Control Interaction Structural Dynamics Flexible Structures Systems Identification	18. DISTRIBUTION STATEMENT Unclassified — Unlimited Subject Category: 15	
19. SECURITY CLASSIF. (of this report) Unclassified	20. SECURITY CLASSIF. (of this page) Unclassified	21. NO. OF PAGES 692 / 22. PRICE A99

MSFC - Form 3292 (May 1969)

For sale by National Technical Information Service, Springfield, Virginia 22161